Did a cosmic catastrophe set the stage for life? *p. 116*

Programming a "chemputer" *pp. 122 & 144*

Growing brains in a dish *p. 126*

Science

$15
11 JANUARY 2019
sciencemag.org

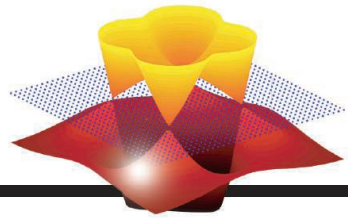
AAAS



DROUGHT RELIEF

How termites benefit a tropical forest during El Niño *p. 174*

CONTENTS



148
Tuning
Weyl points

11 JANUARY 2019 • VOLUME 363 • ISSUE 6423



120 & 166

NEWS

IN BRIEF

106 News at a glance

IN DEPTH

109 SHUTDOWN STARTS TO TAKE A BITE OUT OF SCIENCE
As agency closures enter third week, effects ripple across research community *By D. Malakoff*

110 JAPAN'S EXIT FROM WHALING GROUP MAY BENEFIT WHALES
Commercial whaling will replace a controversial research program, but the market for whale meat is declining *By D. Normile*

111 HOW TO SHINE IN INDONESIAN SCIENCE? GAME THE SYSTEM
Researchers object to a metric that was easy to manipulate *By D. Rochmyaningsih*

112 SHIPS BANNED FROM THROWING UNWANTED FISH OVERBOARD
Controversial European policy worries industry while environmentalists fear rampant cheating *By E. Stokstad*

114 RESEARCHERS OBJECT TO CENSUS PRIVACY MEASURE
New approach to preserving confidentiality could harm data quality, critics say *By J. Mervis*

115 NEW HORIZONS INSPECTS A DISTANT TIME CAPSULE
Kuiper belt "snowman" supports idea that planetary building blocks coalesced from clumps of pebbles *By P. Voosen*

FEATURE

116 SEEING THE DAWN
Evidence lines up to offer a new view of how life on our planet may have emerged *By R. S. Service*

INSIGHTS

PERSPECTIVES

120 ARE CLEVER MALES PREFERRED AS MATES?
Testing this Darwinian hypothesis is a tough nut to crack
By G. F. Striedter and N. T. Burley
▸ REPORT P. 166

122 DEMOCRATIZING SYNTHESIS BY AUTOMATION
Computer code directs interconnected modules that perform primary steps of synthesis *By A. Milo*
▸ RESEARCH ARTICLE P. 144

123 NEURONAL FUNCTION OF ALZHEIMER'S PROTEIN
Cleavage products of an Alzheimer's disease protein are involved in synaptic homeostasis *By M. Korte*
▸ RESEARCH ARTICLE P. 143

124 MANY PATHS TO PRESERVE THE BODY CLOCK
Daily clocks in astrocytes in the brain can drive behavioral rhythmicity
By C. B. Green
▸ REPORT P. 187

126 ASSEMBLING HUMAN BRAIN ORGANOIDS
Three-dimensional assembloids can be used to study human development and disease *By S. P. Paşca*

128 HOW FAST ARE THE OCEANS WARMING?
Observational records of ocean heat content show that ocean warming is accelerating *By L. Cheng* et al.

POLICY FORUM

130 THE MOOC PIVOT
What happened to disruptive transformation of education?
By J. Reich and J. A. Ruipérez-Valiente
▸ PODCAST

BOOKS *ET AL.*

132 CHEAP OIL VS. CLIMATE CHANGE
The Gulf struggles to reform subsidies as temperatures and domestic energy demand rise *By M. R. Aczel*

133 THE FUTURE IS FIBER
Faster, cheaper, and more versatile than traditional telecom hardware, U.S. fiber networks still face policy hurdles *By V. Mayer-Schönberger*

(GRAPHIC) H. JIA *ET AL.*; (PHOTO) ARCO IMAGES GMBH/ALAMY STOCK PHOTO

Downloaded from http://science.sciencemag.org/ on January 14, 2019

Published by AAAS

LETTERS

134 INTEGRATED DATA COULD AUGMENT RESILIENCE
By F. Vahedifard et al.

134 WILDFIRES: OPPORTUNITY FOR RESTORATION?
By A. B. Leverkus et al.

135 PROTECT CATALONIA'S CORALS DESPITE POLITICS
By N. Arafeh-Dalmau et al.

136 TECHNICAL COMMENT ABSTRACTS

RESEARCH

IN BRIEF

137 From *Science* and other journals

REVIEW

140 IMMUNOMETABOLISM
An evolutionary perspective on immunometabolism *A. Wang* et al.
REVIEW SUMMARY; FOR FULL TEXT:
dx.doi.org/10.1126/science.aar3932

RESEARCH ARTICLES

141 MOLECULAR BIOLOGY
Cap-specific terminal N^6-methylation of RNA by an RNA polymerase II–associated methyltransferase *S. Akichika* et al.
RESEARCH ARTICLE SUMMARY; FOR FULL TEXT:
dx.doi.org/10.1126/science.aav0080

142 IMMUNOLOGY
Chronic TLR7 and TLR9 signaling drives anemia via differentiation of specialized hemophagocytes *H. M. Akilesh* et al.
RESEARCH ARTICLE SUMMARY; FOR FULL TEXT:
dx.doi.org/10.1126/science.aao5213

143 NEUROSCIENCE
Secreted amyloid-β precursor protein functions as a $GABA_BR1a$ ligand to modulate synaptic transmission *H. C. Rice* et al.
RESEARCH ARTICLE SUMMARY; FOR FULL TEXT:
dx.doi.org/10.1126/science.aao4827
▸ PERSPECTIVE P. 123

144 CHEMISTRY
Organic synthesis in a modular robotic system driven by a chemical programming language *S. Steiner* et al.
RESEARCH ARTICLE SUMMARY; FOR FULL TEXT:
dx.doi.org/10.1126/science.aav2211
▸ PERSPECTIVE P. 122



REPORTS

145 MEMBRANES
Complete steric exclusion of ions and proton transport through confined monolayer water *K. Gopinadhan* et al.

148 TOPOLOGICAL OPTICS
Observation of chiral zero mode in inhomogeneous three-dimensional Weyl metamaterials *H. Jia* et al.

151 ORGANIC CHEMISTRY
Finite phenine nanotubes with periodic vacancy defects *Z. Sun* et al.

155 SURFACE CHEMISTRY
Site-specific reactivity of molecules with surface defects—the case of H_2 dissociation on Pt *R. van Lent* et al.

158 CHEMICAL PHYSICS
The Sommerfeld ground-wave limit for a molecule adsorbed at a surface *L. Chen* et al.

161 CHEMISTRY
Nematic-to-columnar mesophase transition by in situ supramolecular polymerization *K. Yano* et al.

166 SEXUAL SELECTION
Problem-solving males become more attractive to female budgerigars *J. Chen* et al.
▸ PERSPECTIVE P. 120

168 NEUROSCIENCE
Emergence of preconfigured and plastic time-compressed sequences in early postnatal development *U. Farooq and G. Dragoi*

174 TROPICAL ECOLOGY
Termites mitigate the effects of drought in tropical rainforest *L. A. Ashton* et al.

177 PALEOECOLOGY
A 90,000-year record of Afromontane forest responses to climate change *A.-M. Lézine* et al.

181 ANTIBIOTIC RESISTANCE
Invertible promoters mediate bacterial phase variation, antibiotic resistance, and host adaptation in the gut *X. Jiang* et al.

187 CIRCADIAN RHYTHMS
Cell-autonomous clock of astrocytes drives circadian behavior in mammals *M. Brancaccio* et al.
▸ PERSPECTIVE P. 124

DEPARTMENTS

105 EDITORIAL
A fresh look at nuclear energy *By John Parsons* et al.

198 WORKING LIFE
The scars we bear *By Robert S. Schick*

ON THE COVER



Worker termites (*Longipeditermes longipes*) carry masticated leaves back to their colony in the rainforest of Malaysian Borneo. Processionary termites are important decomposers of leaf litter and can confer ecosystem resilience, as these insects often thrive during periods of environmental stress. Consequently, during drought, an uptick in termite activity and abundance leads to increased soil moisture, soil nutrient heterogeneity, leaf litter decomposition, and seedling survival. See page 174. *Photo: Chien C. Lee*

New Products.....193
Science Careers.....194

SCIENCE (ISSN 0036-8075) is published weekly on Friday, except last week in December, by the American Association for the Advancement of Science, 1200 New York Avenue, NW, Washington, DC 20005. Periodicals mail postage (publication No. 484460) paid at Washington, DC, and additional mailing offices.

Copyright © 2019 by the American Association for the Advancement of Science. The title SCIENCE is a registered trademark of the AAAS.

Domestic individual membership, including subscription (12 months): $165 ($74 allocated to subscription). Domestic institutional subscription (51 issues): $1971; Foreign postage extra: Mexico, Caribbean (surface mail) $55; other countries (air assist delivery): $98. First class, airmail, student, and emeritus rates on request. Canadian rates with GST available upon request, GST #125488122. Publications Mail Agreement Number 1069624. **Printed in the U.S.A.**
Change of address: Allow 4 weeks, giving old and new addresses and 8-digit account number. **Postmaster:** Send change of address to AAAS, P.O. Box 96178, Washington, DC 20090–6178. **Single-copy sales:** $15 each plus shipping and handling; bulk rate on request. **Authorization to reproduce** material for internal or personal use under circumstances not falling within the fair use provisions of the Copyright Act can be obtained through the Copyright Clearance Center (CCC), www.copyright.com. The identification code for *Science* is 0036-8075. *Science* is indexed in the *Reader's Guide to Periodical Literature* and in several specialized indexes.

(PHOTO) ISTOCK.COM/VIORIKA

Downloaded from http://science.sciencemag.org/ on January 14, 2019

Published by AAAS

EDITORIAL

A fresh look at nuclear energy

We are running out of time, as the Intergovernmental Panel on Climate Change (IPCC) warned last October in a special report, *Global Warming of 1.5°C*. National commitments under the 2015 Paris Agreement are only the first step toward decarbonization, but most countries are already lagging behind. It is time to take a fresh look at the role that nuclear energy can play in decarbonizing the world's energy system.

Nuclear is already the largest source of low-carbon energy in the United States and Europe and the second-largest source worldwide (after hydropower). In the September report of the MIT Energy Initiative, *The Future of Nuclear Energy in a Carbon-Constrained World*, we show that extending the life of the existing fleet of nuclear reactors worldwide is the least costly approach to avoiding an increase of carbon emissions in the power sector. Yet, some countries have prioritized closing nuclear plants, and other countries have policies that undermine the financial viability of their plants. Fortunately, there are signs that this situation is changing. In the United States, Illinois, New Jersey, and New York have taken steps to preserve their nuclear plants as part of a larger decarbonization strategy. In Taiwan, voters rejected a plan to end the use of nuclear energy. In France, decisions on nuclear plant closures must account for the impact on decarbonization commitments. In the United Kingdom, the government's decarbonization policy entails replacing old nuclear plants with new ones. Strong actions are needed also in Belgium, Japan, South Korea, Spain, and Switzerland, where the existing nuclear fleet is seriously at risk of being phased out.



Nuclear power generation is increasing in China through the deployment of new power plants such as the one in Haiyang, China.

PHOTO: TANG KE/IMAGINECHINA/AP IMAGES

What about the existing electricity sector in developed countries—can it become fully decarbonized? In the United States, China, and Europe, the most effective and least costly path is a combination of variable renewable energy technologies—those that fluctuate with time of day or season (such as solar or wind energy), and low-carbon dispatchable sources (whose power output to the grid can be controlled on demand). Some options, such as hydropower and geothermal energy, are geographically limited. Other options, such as battery storage, are not affordable at the scale needed to balance variable energy demand through long periods of low wind and sun or through seasonal fluctuations, although that could change in the coming decades. Nuclear energy is one low-carbon dispatchable option that is virtually unlimited and available now. Excluding nuclear power could double or triple the average cost of electricity for deep decarbonization scenarios because of the enormous overcapacity of solar energy, wind energy, and batteries that would be required to meet demand in the absence of a dispatchable low-carbon energy source.

One obstacle is that the cost of new nuclear plants has escalated, especially in the first-of-a-kind units currently being deployed in the United States and Western Europe. This may limit the role of nuclear power in a low-carbon portfolio and raise the cost of deep decarbonization. The good news is that the cost of new nuclear plants can be reduced, not only in the direct cost of the equipment, but also in the associated civil structures and in the processes of engineering, licensing, and assembling the plant. The implication is that a large impact on the cost of new nuclear plants may come from several sources: improvements in project management practices; innovations in the serial construction of standardized designs to minimize reengineering and maximize learning; adoption of modular construction, to shift labor from construction sites to productive factories and shipyards; advanced concrete solutions to reduce the need for reinforcement steel formwork at the site; and seismic isolation to protect the plant against earthquakes, which simplifies the structural design of the plant.

It's time to transform our thinking. Renewable and nuclear energies are not mutually exclusive, but complementary. We should preserve existing nuclear power plants and reimagine how new plants can be delivered.

–John Parsons, Jacopo Buongiorno, Michael Corradini, David Petti

John Parsons
is a senior lecturer at the Sloan School of Management, Massachusetts Institute of Technology (MIT), Cambridge, MA, USA. jparsons@mit.edu

Jacopo Buongiorno
is the TEPCO Professor and associate department head of Nuclear Science and Engineering at MIT, Cambridge, MA, USA. jacopo@mit.edu

Michael Corradini
is a professor emeritus in Nuclear Engineering and Engineering Physics, University of Wisconsin, Madison, WI, USA. corradini@engr.wisc.edu

David Petti
is the director of the Nuclear Fuels and Materials Division at the Idaho National Laboratory, Idaho Falls, ID. USA. david.petti@inl.gov

10.1126/science.aaw5304

Downloaded from http://science.sciencemag.org/ on January 14, 2019

Published by AAAS

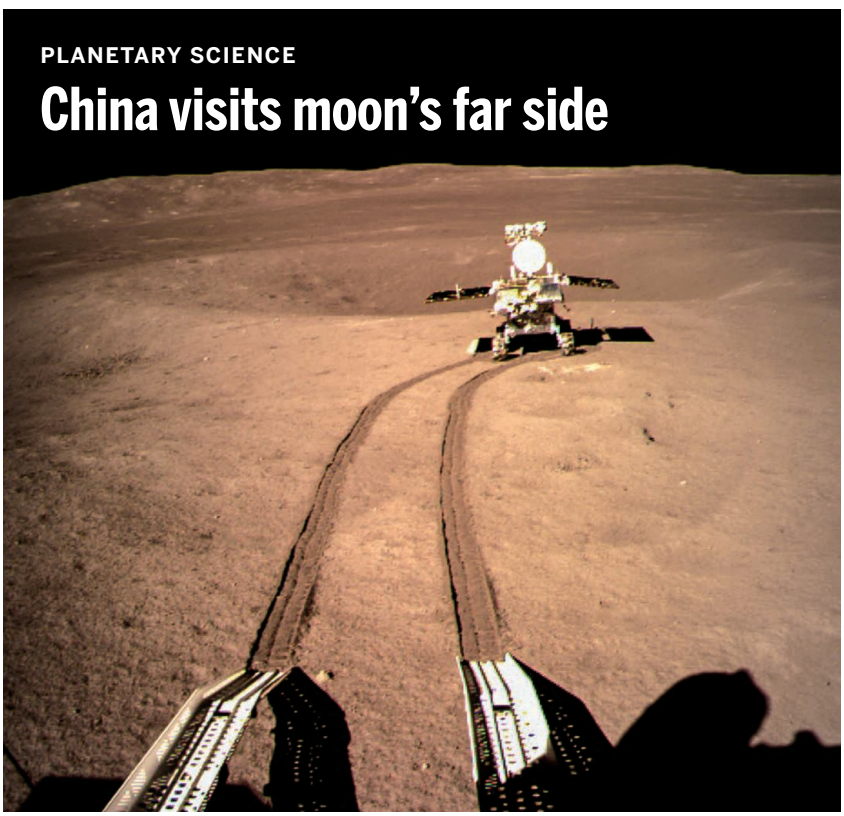
> “We had heard from numerous senators suggesting that this was not a good idea.”
>
> **NASA head Jim Bridenstine,** in *The Washington Post*, on inviting the sanctioned head of the Russian space agency to visit the United States. The invitation was rescinded.

IN BRIEF

Edited by **Jeffrey Brainard**

PLANETARY SCIENCE

China visits moon’s far side



Chang’e-4’s rover, named Yutu 2 (Jade Rabbit 2) for a moon goddess’s companion, rolls into action.

China’s Chang’e-4 lander became the first spacecraft to set down on the far side of the moon on 3 January. Later that day, the China National Space Administration released the first close-up pictures of the surface and confirmed that the mission’s rover safely exited the lander. Because the moon blocks direct radio contact with the lander and rover, Chang’e-4 relies on a communications relay satellite that China placed beyond the moon at a gravitationally locked point. Chang’e-4’s cameras, spectrometers, and ground-penetrating radar may provide new scientific insights into the composition and evolution of the moon. The far side has an older crust and more craters than the near side, where more recent lava flows cover much of the surface. Chang’e-4 is the fourth of China’s lunar missions, all named after a Chinese moon goddess. Chang’e-5 is scheduled for launch later this year and will attempt to gather lunar soil and rock samples and return them to Earth.

Indian researchers fight low pay

SCIENCE FUNDING | India’s early-career researchers last week vowed to intensify their nationwide protests over government stipends, which they say are too low to make ends meet. The payments have remained frozen for the past 4 years while housing costs have risen sharply, and the money often arrives 6 to 12 months late, they say. Scientists who qualify get only 25,000 rupees ($356) per month in the first 2 years and 28,000 rupees monthly in the next 3 years. Those not provided with a hostel room also get a modest rent allowance. For months, thousands of scientists have held protests at India’s research institutes and universities and outside the federal science ministry in New Delhi, but they complain these have not yielded results. Now, they plan to hold sit-ins and hunger strikes. They are demanding that stipends rise by at least 80% now, increase annually, and be paid on time.

Ocean plastic cleanup stumbles

MARINE ECOLOGY | A high-profile trash collector designed to remove plastic from the Pacific Ocean is limping back to port after a mechanical failure. The 600-meter-long device was built by the Ocean Cleanup, a nonprofit based in Rotterdam, the Netherlands. Boyan Slat founded the group as an 18-year-old inventor, raised $31.5 million, and hired 80 engineers and scientists. They designed a U-shaped pontoon that, pushed by wind and waves, would collect plastic with a skirt. Ships could occasionally haul the trash away. Boyan has said that a fleet of 60 such pontoon collectors could remove half of the Great Pacific Garbage Patch—a large accumulation of waste between Hawaii and California—in 5 years. But skeptics questioned the plan’s feasibility and cost. In November 2018, the team discovered the prototype tested in the garbage patch was not retaining trash, perhaps because it was not moving fast enough. Then, in late December 2018, an 18-meter-long section broke off, apparently because of material fatigue. Engineers will try to repair and improve the device after it reaches Honolulu on 13 January.

PHOTO: CHINA NATIONAL SPACE ADMINISTRATION

Downloaded from http://science.sciencemag.org/ on January 10, 2019

Published by AAAS



Galápagos Island officials worried that loud noises threatened endemic species, such as the land iguana.

CONSERVATION

A ban on kabooms in the Galápagos

The governing council of the Galápagos Islands has banned noisemaking fireworks to protect the sensitive and unusual species living there. In its 28 December 2018 decision, just in time for New Year's Eve, the council said pyrotechnic bangs had harmed local animals, inducing rapid heart rates, cardiac diseases, and stress that threatened their survival. Fireworks that produce light but not sound are permitted. A public outreach campaign was carried out in 2017 to discourage the use of pyrotechnics in the islands. Many Galápagos species live nowhere else, including 20 of 22 species of reptiles, such as the giant tortoise and marine iguana. Conservationists continue to pursue other protections for native flora and fauna, including controlling invasive species and limiting human inhabitants.

Ancient flaying temple discovered

ARCHAEOLOGY | The first temple dedicated to Xipe Tótec, or the "Flayed Lord," a deity widely worshiped in Mesoamerica who was honored through ritual sacrifices of human captives, has been found, scientists announced last week. One thousand years ago in what is now the Mexican state of Puebla, priests flayed captives' bodies and donned their skins in rituals related to agricultural renewal and fertility; the god himself was depicted as a skeleton wearing a human skin. Archaeologists from Mexico's National Institute of Anthropology and History in Mexico City said they found the temple at a Puebla site called Ndachjian-Tehuacán. A sculpture at the temple depicts Xipe Tótec's torso with an extra hand dangling off of one arm, a stark illustration of him wearing the skin of a sacrificial victim.

Senate confirms science heads

SCIENCE AGENCIES | The U.S. Senate last week confirmed meteorologist Kelvin Droegemeier to lead the White House Office of Science and Technology Policy and political scientist Steven Dillingham to head the Census Bureau, although at press time, those agencies remained closed because of the partial government shutdown. Lawyer Daniel Simmons is more fortunate, having won approval to manage the renewable energy research programs at the Department of Energy (DOE), which remains open for business. The 115th Congress adjourned on 2 January without approving several other nominees to lead science agencies, so President Donald Trump must resubmit their names or offer new ones. Those left in limbo include neuroscientist Christopher Fall to run DOE's science programs and investment banker Lane Genatowski to lead its Advanced Research Projects Agency-Energy, as well as former AccuWeather CEO Barry Myers as administrator of the National Oceanic and Atmospheric Administration.

Taiwanese academic exonerated

CRIMINAL JUSTICE | A former head of Taiwan's Academia Sinica was cleared of corruption charges by a district court on 28 December 2018. Wong Chi-Huey, a biochemist, was head of Taiwan's premier collection of research institutes when in 2017 he was accused of accepting shares in a pharmaceutical startup in exchange for allowing the company to develop his discoveries into a breast cancer drug. In a statement, Wong wrote that the charges—the first in Taiwan related to technology

PHOTO: GUDKOV ANDREY/SHUTTERSTOCK

Downloaded from http://science.sciencemag.org/ on January 10, 2019

Published by AAAS

transfer—resulted from "misconceptions about the technologies in question" and practices in technology transfer. Wong resigned because of the controversy and is now a professor at Scripps Research in San Diego, California.

Law boosts quantum science

COMPUTING | The U.S. Congress last month approved a law, signed by President Donald Trump, that authorizes increased spending and federal coordination for quantum information science that could reshape computing, sensors, and communications. The National Quantum Initiative Act recommends $1.275 billion from 2019 to 2023 to support such research at three federal agencies—the Department of Energy, the National Institute of Standards and Technology, and the National Science Foundation. (Appropriators in Congress decide how much each agency actually gets—often less than authorized spending.) That would be an increase from the current estimated spending on this topic of about $200 million per year. The law's proponents say more money will help the United States keep up with China and Europe in a quantum research arms race.

Departing head knocks vax policy

PUBLIC HEALTH | The leader of Italy's main health research agency resigned in December 2018, accusing government officials of "unscientific or frankly antiscientific positions on many issues." Walter Ricciardi told the *Corriere della Sera* newspaper that he decided to step down from the National Institute of Health because of the anti-vaccine stances of the coalition government that came to power last June. Ricciardi is an expert on vaccination who supported a law that made 10 childhood vaccinations mandatory and that the new government has partly repealed. He also called out Italy's Deputy Prime Minister Matteo Salvini as falsely claiming that migrants carry diseases, which Ricciardi said caused "discomfort in health agencies, forcing them into a kind of self-censorship not to contradict politicians."

Voyager illuminates dark matter

COSMOLOGY | NASA's Voyager 1 spacecraft has dented the idea that mysterious dark matter consists of countless tiny primordial black holes lingering from the big bang. Launched in 1977, Voyager 1 escaped the protective bubble of the sun's magnetic field in 2012. It can now detect low-energy positrons and electrons spewing into space from the edge of black holes in a process proposed by the late Stephen Hawking. However, Voyager 1 has recorded few of these particles. The observed flux reveals that black holes the size of atomic nuclei, each weighing as much as 10 billion tons, make up less than 1% of our galaxy's dark matter, argue Mathieu Boudaud and Marco Cirelli of Sorbonne University in Paris in a paper in press at *Physical Review Letters*.



Anak Krakatau on 23 December 2018 as it erupted.

PHOTO: NURUL HIDAYAT/BISNIS INDONESIA VIA AP

GEOPHYSICS

Volcano's tsunami threat continues

The Anak Krakatau volcano continued to explosively erupt this week in Indonesia, raising fears of a repeat of the surprising landslide-induced tsunami late last month that killed more than 400 people and injured more than 7000. On 23 December 2018, following a year of eruptions, the volcano collapsed. Its peak dropped by a kilometer and more than half of the island built by the volcano slid into the ocean, sending tsunami waves more than 3 meters high crashing into the coasts of the Indonesian islands of Java and Sumatra. In 2012, volcanologists predicted that Anak Krakatau posed such a risk and warned that landslide tsunamis are a neglected hazard; they said proper monitoring could help alert nearby residents. Thousands remain in evacuation camps, having lost their homes to the sea.

EYE ON ENERGY

1.9%

Estimated increase in emissions of carbon dioxide from U.S. power generation in 2018, making it harder for the United States to meet its obligations under the Paris agreement (*Rhodium Group*).

14.3

Gigawatts (GW) of U.S. coal-fired power plant capacity estimated to have been retired in 2018, out of 246 GW in total capacity. An additional 22.9 GW is expected to be retired from 2019 to 2024 (*S&P Global Market Intelligence*).

40%

Portion of Germany's public electricity supply that came from renewable sources in 2018, exceeding for the first time the share from coal-fired plants (*Fraunhofer Institute for Solar Energy Systems*).

SCIENCEMAG.ORG/NEWS
Read more news from *Science* online.

Downloaded from http://science.sciencemag.org/ on January 10, 2019

Published by AAAS



Congress has refused to give President Donald Trump the funding he wants for a border wall, triggering a partial government shutdown.

U.S. FUNDING

Shutdown starts to take a bite out of science

As agency closures enter third week, effects ripple across research community

By **David Malakoff**

Rattlesnakes, bears, hurricanes, and freezing weather haven't stopped ecologist Jeff Atkins from taking weekly hikes into Virginia's Shenandoah National Park for the past 8 years to collect water samples from remote streams. But Atkins is now facing an insurmountable obstacle: the partial shutdown of the U.S. government, in its third week as *Science* went to press.

Park managers have barred Atkins from entering since 22 December 2018, when Congress and President Donald Trump failed to agree on a deal to fund about one-quarter of the federal government, including the National Park Service. That has shut down the sampling, part of a 40-year-old effort to monitor how the streams are recovering from the acid rain that poisoned them in past decades.

"It's very frustrating to have this needless disruption" in what is one of the park system's longest continuous data sets, says Atkins, a postdoctoral researcher at Virginia Commonwealth University in Richmond. "This is the biggest [sampling] gap we've had. … Now, there is always going to be this hole."

Atkins is one of tens of thousands of U.S. scientists feeling the pain caused by the shutdown, which resulted after Congress refused to give Trump the $5.7 billion he wants for a wall along the U.S.-Mexico border. The impasse has all but halted work at more than a half-dozen agencies that fund or conduct research, including NASA, the National Science Foundation (NSF), the U.S. Department of Agriculture (USDA), the National Oceanic and Atmospheric Administration (NOAA), and parts of the Smithsonian Institution.

Many of the scientists at those shuttered agencies have been furloughed without pay, barred from working at home, and prohibited from checking their government email. A travel ban has hurt attendance at several major conferences and caused organizers to cancel other events.



The shutdown is complicating studies of endangered bumble bees at Michigan State University.

The shutdown is also creating chaos for university researchers, private contractors, and others who collaborate with idled federal scientists, or depend on affected agencies for funding, facilities, and data. Besides doing lasting damage to some research projects, the standstill is threatening livelihoods. "In a moment's notice, I went from believing I had secure income to not knowing when I would be paid," says Marshall McMunn, an ecologist at the University of California (UC), Davis, on an NSF postdoctoral fellowship. He can't even find out whether it's OK to take a part-time job to help pay his bills.

Amy Freitag, a social scientist who does contract work for NOAA at the Cooperative Oxford Laboratory in Maryland, says the shutdown has "made it very hard to make progress on any research that involves my [NOAA] colleagues … or do any kind of planning." Freitag has been able to continue to work—from home and coffee shops—because her private employer is paid in advance. To stay on the job, however, she'll need new assignments. But key NOAA managers have been furloughed.

Atmospheric scientist Rachel Storer, who works at NASA's Jet Propulsion Laboratory (JPL) in Pasadena, California, but is employed by Colorado State University in Fort Collins, says, "My paycheck isn't in immediate danger." But Storer has suspended work on building digital simulations of cloud formation because she can't get access to NASA

PHOTOS: (TOP TO BOTTOM) MARK WILSON/GETTY IMAGES; RUFUS ISAACS/MICHIGAN STATE UNIVERSITY

Downloaded from http://science.sciencemag.org/ on January 10, 2019

Published by AAAS

supercomputers. (JPL is open because it is operated by the California Institute of Technology, a contractor.) "I have other work to fill my time … but it's a setback," she says.

The shutdown has also stung entomologist Rufus Isaacs of Michigan State University in East Lansing. Some endangered bumble bees he has collected are now "sitting in a fridge in my lab" and can't be shipped to USDA laboratories until they reopen. He notes that a few months' delay in agricultural research "can mean a whole year of progress is lost, because if we don't have the answers from the recent experiments, we don't know how to prepare for the coming growing season."

Marine biologist Mykle Hoban, a doctoral student at the Hawaii Institute of Marine Biology in Kaneohe, was to begin a 10-week project on fish taxonomy this week at the Smithsonian's National Museum of Natural History in Washington, D.C. The museum is closed, and he can't reach the researcher he's supposed to work with, but Hoban still plans to make the trip "and hope for the best."

Even researchers funded by agencies not affected by the shutdown are feeling the pinch. Rita Hamad, a health policy researcher at UC San Francisco, is supported by the National Institutes of Health, which is open. But she relies on data handled by staffers at the U.S. Census Bureau, which is closed. The result? "I can't publish timely evidence on policies that I study," she says.

Other scientists have been forced to cancel long-planned trips and meetings. USDA's Forest Service pulled the plug on what would have been the 30th annual Interagency Forum on Invasive Species, scheduled for this week in Annapolis. "It's just a very sad day for science," says retired federal entomologist Michael McManus, who organized the forum and was expecting 200 attendees.

The travel ban forced hundreds of federal scientists to drop trips to major meetings held by the American Meteorological Society and the American Astronomical Society—in Phoenix and Seattle, Washington, respectively—where they had planned to present work. U.S. scientists will also be absent from a technical meeting of the Intergovernmental Panel on Climate Change scheduled for this week in Vancouver, Canada.

On Twitter, astrophysicist Jane Rigby of NASA's Goddard Space Flight Center in Greenbelt, Maryland, mused about the implications of being furloughed. "Can't work. Can't travel for work. … Can't use work laptop," she wrote. "Can I think about the universe? Unclear." ■

With reporting by Daniel Clery, Kelly Servick, and Paul Voosen.

CONSERVATION

Japan's exit from whaling group may benefit whales

Commercial whaling will replace a controversial research program, but the market for whale meat is declining

By **Dennis Normile**, *in Tokyo*

Japan's 26 December 2018 announcement that it will withdraw from the International Whaling Commission (IWC) and resume commercial whaling in its own waters triggered fierce criticism around the world. U.K. environment secretary Michael Gove was "extremely disappointed." Greenpeace called the decision "out of step with the international community" and its timing in the middle of the holiday season "sneaky."

But some conservationists say the hand wringers are missing the point. What matters most is that Japan has decided "to stop large-scale whaling" on the high seas under the mantle of scientific research, says Justin Cooke, a marine population assessment specialist at the Center for Ecosystem Management Studies in Emmendingen, Germany. Given the declining appetite for whale meat, Japan is unlikely to start to catch many more whales in its own waters than it already does, he adds: "There won't be much change on the ground."

Patrick Ramage, a whaling specialist at the International Fund for Animal Welfare in Yarmouth, Massachusetts, agrees. "It's good news for whales," he says—and also for IWC, which can finally end its "food fights over whaling" and focus on other issues in whale conservation.

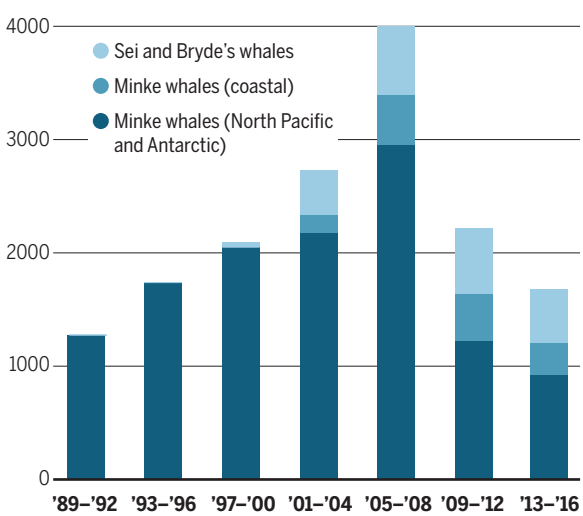
Japan has never hidden its hope of resuming commercial whaling, banned under an IWC moratorium since 1986. In the meantime, it has used a clause in the IWC treaty that allows members to capture whales for scientific purposes—and sell the meat. The Institute of Cetacean Research (ICR) here has primarily harvested minke whales, with minor catches of sei whales, Bryde's whales, and a few other species (see graphic, below). Japanese scientists claimed whale autopsies were essential to determine the animals' diet and age, among other things, but critics dismissed the research as a fig leaf for commercial whaling and said it produced few meaningful data.

In March 2014, the International Court of Justice sided with the critics in a suit brought by Australia, ordering Japan to halt its Antarctic whaling research. (The case did not address Japan's North Pacific research programs.) Japan canceled its Antarctic research cruises for a year, then resumed them under new programs it deemed compliant with the court's ruling.

But at IWC's biannual meeting in September 2018 in Brazil, Japan also proposed a fresh plan to resume commercial whaling, which it said can be done in a sustainable way. IWC concedes that the current population of several hundred thousand minke whales in the Antarctic is "clearly not endangered." But the fight is no longer just about sustainability; whaling opponents say the bloody hunt for the majestic mammals is simply inhumane. IWC rejected the Japanese

Whaling takes a dive

In its scientific programs, Japan has harvested thousands of minke whales and smaller numbers of other species. Numbers have fallen, in part because demand for whale meat has dropped, and may fall further when whaling is limited to a commercial hunt in coastal waters.



CREDITS: (GRAPHIC) J. BRAINARD/*SCIENCE*; (DATA) INTERNATIONAL WHALING COMMISSION

Downloaded from http://science.sciencemag.org/ on January 10, 2019

Published by AAAS

proposal, and the meeting adopted a resolution emphasizing that IWC's purpose is to ensure the recovery of cetacean populations to preindustrial levels and reaffirming the moratorium on commercial whaling. That one-two punch triggered Japan's December announcement.

Although Japan will now abandon its scientific whaling programs, what will happen to ICR, which has a $68 million annual budget, is unclear. "It's likely to have some role as a research institute contributing to cetacean science, though its magnitude may not be so significant," says Masayuki Komatsu, a former delegate to IWC now at the Tokyo Foundation for Policy Research.

Meanwhile, Japan's whaling efforts will shift to its own coastal waters and the 320-kilometer exclusive economic zone around them. Whether whales there will now be at risk is a subject of debate. The Northern Hemisphere minke population as a whole "is not threatened," says Cooke, but waters near the Koreas and Japan are home to an "unusual and possibly unique" population, called the J-stock, that breeds in the summer instead of the winter, he says.

Japanese fishers already catch about 100 minke whales each year in these waters, Komatsu says. (Rather than the traditional harpoons, they use nets, which is allowed under the IWC moratorium.) But increasing the harvest with harpoon whaling could put pressure on the J-stock. Japan's December announcement said catch limits will be set "to avoid negative impact on cetacean resources" but provided no details.

Market forces may settle the issue. Joji Morishita, a fisheries expert at the Tokyo University of Marine Science and Technology who finished a 2-year stint as IWC chair in September 2018, believes whaling remains a "viable" business. Others are doubtful. Shifting consumer tastes and a growing environmental awareness have already led to a steep decline in Japanese whale meat consumption, from 203,000 tons in 1965 to just 4000 tons in 2015. Three major fishing companies appear to have no interest in commercial whaling. Cooke suspects Japan will go the way of Norway, where "a niche operation is feeding a niche market but with decreasing interest in the market and decreasing interest in going whaling."

Although Japan intends to continue to participate in IWC as an observer, it will no longer contribute to the group's budget. (In 2017, it provided about 6% of IWC's $2.7 million total income.) The upside is that, with Japan gone, IWC can spend more time on other threats to whales, including ship strikes, bycatches, habitat loss, and what Ramage calls the "existential question" for whales' future: the effects of climate change. ■

PHOTO: NATIONAL GEOGRAPHIC IMAGE COLLECTION/ALAMY STOCK PHOTO



An Indonesian scientist at work on Borneo. The country's new index seeks to capture academics' performance.

RESEARCH METRICS

How to shine in Indonesian science? Game the system

Researchers object to a metric that was easy to manipulate

By **Dyna Rochmyaningsih**, *in Jakarta*

Last July, when Indonesia's Ministry of Research, Technology and Higher Education (RISTEK) here honored eight researchers, along with institutions and journals, for their exceptional contributions to science, observers noticed something odd. Many of the laureates were relatively unknown academics from second-tier universities; underdogs had apparently become leaders.

It didn't take curious scientists long to figure out why. The honors went to top scorers in Indonesia's Science and Technology Index (SINTA), a system introduced in early 2017 to measure research performance. Critics showed that several winners had inflated their SINTA score by publishing large numbers of papers in low-quality journals, citing their own work excessively, or forming networks of scientists who cited each other.

It's unclear whether formal rules were broken, but SINTA's architects concede they were outwitted. And the revelations have led to a fierce discussion about SINTA, a unique nationwide attempt to capture the output of every academic in a single formula. Some say it should not be used to produce rankings, or should even be abandoned. But the government is undeterred: After a meeting on 3–4 January, it announced the rollout later this year of an improved version. SINTA "gives recognition to Indonesian scientists, triggers competition among them, and motivates them to be better," says Sadjuga, RISTEK's director of intellectual property management. (Like many Indonesians, he goes by only one name.)

Indonesia has introduced several other policies in the past 6 years to boost research output from its more than 250,000 academics, who work at more than 4000 universities. University professors may lose almost half of their salary if they don't publish in international journals, for instance. As a result, the number of papers published by authors in Indonesia has soared from just under 7000 in 2014 to more than 28,000 last year, according to Scopus, a database operated by Dutch publisher Elsevier (see graphic, p. 112). Indonesia seems set to overtake Malaysia as the region's biggest research producer by 2020.

SINTA—also the name of a Sanskrit goddess—turned the pressure up a notch. It combines data from Scopus and Google Scholar with information submitted by Indonesian academics to track published papers, citations, and researchers' h-index, a controversial metric reflecting both output quantity and citations. These numbers are used to calculate a personal score that is taken into account when academics apply for research grants; a high score may also help with promotions and salary negotiations.

Many other countries use publication and citation data to evaluate research; some pay hefty cash bonuses for papers in top-tier journals. But, "There is nothing like [SINTA] that I know of," says Diana Hicks, a research

Downloaded from http://science.sciencemag.org/ on January 10, 2019

Published by AAAS

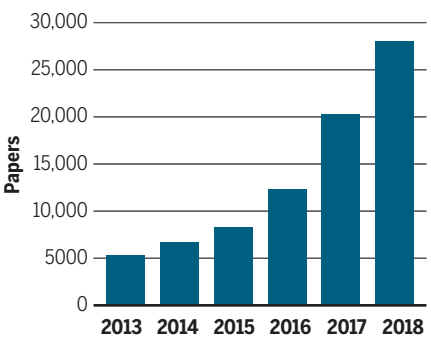
metrics expert at the Georgia Institute of Technology in Atlanta. The extra push was welcome, says Danang Birowosuto, an Indonesian physicist at CINTRA, an international research group in Singapore: "Our international competence in science is still very low."

But many Indonesian academics worried that SINTA might harm their reputations. Thousands joined groups on social media to help each other navigate the new numbers-driven landscape. "Although the original aim was sincere," discussions soon turned to gaming the system, says plant biologist Andik Wijayanto of the State University of Malang.

In October 2018, Anis Fuad, a health informatician at Gadjah Mada University in Yogyakarta, presented RISTEK with a detailed analysis of the problems. Indonesia's most-cited 2018 paper so far wasn't a major breakthrough, Fuad noted, but a study titled "Analysis of Student Satisfaction Toward Quality of Service Facility," presented at a workshop co-organized by the Indonesian Publications Collaboration Community (KO2PI) and published in conference proceedings, a type of publication that gets minimal peer review. The study had been cited 42 times, often in papers on unrelated topics—including mosque architecture and cold storage of fish—that were also published in conference series or in low-quality open-access journals no longer indexed in Scopus.

Surging ahead

New incentives have driven a sharp rise in Scopus-indexed papers from Indonesia.



One of the paper's 10 authors was statistician Ansari Saleh Ahmar of the State University of Makassar, who won SINTA awards in two categories last July; he co-authored more than 100 papers in 2017 and 2018 and has been cited almost 600 times. Ahmar is also president of KO2PI, which has run workshops in an extraordinary range of scientific fields. On a poster produced in early 2017, KO2PI promised participants a paper in a Scopus-indexed proceeding in return for a 1.5 million rupiah ($106) fee. Ahmar says he was "surprised" by his own citation rate, but says statistical papers are often cited in seemingly unrelated fields. He says he is no longer active in KO2PI and, given the controversy, would now like to return his award.

After asking Ahmar and other academics suspected of gaming the system for an explanation, RISTEK has deleted their SINTA accounts, Sadjuga says, but it has not withdrawn the awards because "the public shaming is punishment enough." Sadjuga says problematic data in Scopus and scientists' unethical behavior contributed to the problem but does not blame SINTA itself. (An Elsevier spokesperson says Scopus has stopped indexing three journals that many Indonesian scientists have published in and is investigating "concerns" about the conference series used by KO2PI, which is published by the U.K. Institute of Physics.)

Gaming aside, Indonesia's research evaluation should not rely on a commercial database, says Dasapta Erwin Irawan, a hydrogeologist at Bandung Institute of Technology. He also says the system's preference for Scopus-indexed international journals is misguided, because research in Indonesian journals may be just as good and sometimes more relevant. RISTEK doesn't entirely ignore local journals: It has created an online portal, named Garuda, to more than 7000 journals in the Indonesian language, as well as a journal accreditation system. But researchers win far fewer SINTA points when papers in local journals are cited and none at all for publishing in them.

That lack of appreciation for locally relevant research violates the "Leiden Manifesto for research Metrics," an influential paper Hicks and three co-authors published in 2015. Hicks says SINTA falls short on several other principles in the manifesto, which stipulates that metrics should "support a qualitative, expert assessment" and "account for variation by field in publication and citation practices." SINTA currently does neither.

A new version of SINTA, set to be launched this year, will integrate data from several additional sources, including the Web of Science and the Indonesian National Library. It will also give researchers credit for other types of output, such as books, artwork, and patents. A new tool will flag self-citation and the ministry will disseminate scientific integrity guidelines to Indonesian universities.

But Mikrajuddin Abdullah, a physicist at Bandung Institute of Technology, says RISTEK should still review last year's awards and retract them if they were based on misconduct: "It will teach us that scientific achievement does not come suddenly, but is the result of a long period of perseverance." ■

Dyna Rochmyaningsih is a journalist based in Deli Serdang, Indonesia.

FISHERIES SCIENCE

Ships banned from throwing unwanted fish overboard

Controversial European policy worries industry while environmentalists fear rampant cheating

By **Erik Stokstad**

Long before fillets reach your dinner plate, lots of seafood is thrown away. Overboard, actually. As fishing crews sort through their catches, they toss unwanted fish back into the sea—as much as 20% of the global catch. The vast majority die. On 1 January, the wasteful practice became illegal in waters of the European Union. Scientists believe the policy will lead to more efficient fisheries and eventually boost stocks, while incentivizing more selective fishing gear and strategies. But in the short term it could mean hardship for the industry and perhaps even compromise fisheries data, if hidden cheating becomes widespread. "This is one of the most dramatic changes in EU fisheries policy," says Peder Andersen, an economist at the University of Copenhagen.

Regulators began to phase in the discard ban, formally known as the Landing Obligation, in 2015. To ease the pain, they started with vessels that didn't discard much because they catch schools of herring and other single species. Now comes the bigger challenge: fisheries where many species live together, such as those in the North Sea. When vessels drag nets near or along the bottom, they end up with a jumble of species and sizes. Until now, vessels only kept the valuable portion of their catch. The discarding of young fish, which haven't yet reproduced much, has hit struggling populations especially hard.

Under the ban, fishing vessels must bring back all regulated species, a significant headache. More time will be spent sorting fish, as even the unwanted ones must be tallied and brought to port. Holds will fill up faster, meaning more trips to sea and higher fuel costs. And unwanted fish will be sold for a fraction of the price of the normal catch, if it can be sold at all.

Downloaded from http://science.sciencemag.org/ on January 10, 2019

CREDITS: (GRAPHIC) M. ENSERINK/*SCIENCE*; (DATA) RISTEK

Published by AAAS



A new European policy bans the discarding of regulated fish, such as this cod.

PHOTO: JAMES BOARDMAN/ALAMY STOCK PHOTO

A second problem for industry is that the ban creates the prospect of "choke species" that threaten to shut down fishing. In a fishery with a mix of species, a vessel might catch the same proportion of species each time it trawls, despite varying quotas for the allowed catch of each. Before the discard ban, this wasn't a problem: Fishers could keep catching haddock and whiting, for example, even after reaching their cod quota. Following the law, they simply threw away any new cod caught.

Now, vessels in some places will have to stop fishing once they reach their quota for choke species like cod. Haddock or whiting quotas will go unused—a lost economic opportunity. "Choke species are a huge problem," says Daniel Voces de Onaindi, managing director of Europêche, a lobbying group in Brussels. "We're talking about destroying boats, and unemployment." The discard ban does exempt species, such as Norway lobster, that typically survive after they are returned to the water. And last month, EU fisheries ministers boosted quotas for five species, despite scientific advice to protect these stocks.

Still, case studies from DiscardLess, an EU-funded research project that wraps up this month, suggest the fishing industry could suffer losses on the order of 10% for several years if the ban is enforced.

Over the longer term, the discard ban will boost fish stocks and benefit the overall ecosystem, according to modeling led by Marie Savina-Rolland of the French Research Institute for the Exploitation of the Sea, an oceanographic research center in Lorient. That could eventually translate to higher quotas and profits, says Andersen, who co-led economic research for the DiscardLess project.

The ban could also stimulate more research on new fishing gear and tactics to avoid unwanted catches. Researchers have already shown benefits from separator trawls, which have a horizontal panel at the opening. Haddock and whiting tend to swim upward when the trawl approaches. The panel diverts them into an upper net, whereas cod and monkfish are collected by a lower net. Unwanted species can escape through an opening in the net. Equipping fishing gear with light-emitting diodes can also help reduce bycatch, DiscardLess researchers have found, by discouraging some unwanted species from entering trawl nets. But these techniques also lose some of the commercial catch, so industry has not adopted them widely. "It's rare to get a situation where you can avoid unwanted sizes or species and not pay a penalty with the fish you do want," says David Reid, a fisheries ecologist at the Marine Institute in Oranmore, Ireland.

> ***"It could bring about a very big, negative change. I get very worried about European fisheries management."***
> **Lisa Borges**, FishFix

More quota trading could also help industry cope. If a vessel or fleet has run out of quota to catch cod in its mixed trawls, for example, it could offer its quota of whiting to a fleet with the opposite problem. Last month, EU fisheries ministers increased pressure on nations to start trading quotas. "It's basically banging their heads together and saying you must swap quotas for this to work," says Andrew Clayton, who directs the Pew Charitable Trusts's campaign to end overfishing in northwest Europe and is based in London.

Few expect all fishing vessels to obey the discard ban. "Put yourself in the boots of a fishermen who can see he will run out of quota for a species. If he does, he would have to tie up for the rest of the year. He might have to sell the boat, or sell the house," says Barrie Deas, CEO of the National Federation of Fishermen's Organisations in York, U.K. "What's he going to do?"

Scofflaws could jeopardize not just fish stocks, but also data about how they are faring. Researchers, who suggest catch levels to regulators, get their discard data largely from independent observers on just a few boats—less than 1% of the EU fleet. Observed boats are now likely to discard much fewer fish than other vessels, leaving an official undercount of the discard rate and a falsely rosy picture of how heavily stocks are fished, says Lisa Borges, a fisheries biologist who runs a consultancy called FishFix in Lisbon. "It could bring about a very big, negative change," Borges says. "I get very worried about European fisheries management."

Environmentalists want to toughen up enforcement by installing cameras on ships, the practice in New Zealand and a few other places with discard bans. But Voces de Onaindi says this is impractical on some vessels and raises privacy concerns. Countries where discard bans have succeeded, including Norway and Iceland, have gradually introduced incentives and controls to develop the economic use of unwanted fish and create a culture of regulatory compliance. Those steps, Andersen says, lessen conflict but can take decades to achieve. ■

Downloaded from http://science.sciencemag.org/ on January 10, 2019

Published by AAAS

SOCIAL SCIENCE

Researchers object to census privacy measure

New approach to preserving confidentiality could harm data quality, critics say

By **Jeffrey Mervis**

The U.S. Census Bureau says it is making a "sea change" in how it safeguards the confidentiality of the vast amount of data released from the decennial census. That decision is making waves among social scientists.

In September 2018, the bureau announced it would apply a mathematical concept called differential privacy to 2020 census data. Officials say the move addresses a serious weakness in current methods of ensuring the data cannot be linked to individuals. And supporters of the decision say that privacy concern is even more urgent in light of plans to add a citizenship question to the 2020 census.

Critics, however, think the agency is trying to fix a system that isn't broken. "Differential privacy goes above and beyond what is necessary to keep data safe under census law and precedent," says Steven Ruggles, a population historian at the University of Minnesota in Minneapolis. Critics fear the change will degrade the quality of information used by thousands of researchers, businesses, and government agencies, and also make the data less accessible.

The Census Bureau's job is to collect, analyze, and disseminate information about the U.S. population. There's a lot to manage: The 2010 census, for example, generated 7.8 billion statistics about 308 million people. But the agency must tread carefully. Federal law prohibits it from publishing information that would reveal the identity of any "establishment or individual."

To prevent reidentification, census officials have long employed a bag of statistical tricks that provides protection without significantly undermining data quality. For example, in some cases they will delete outliers—such as the income of a multimillionaire—or swap similar but not identical information about people living in different locales.

But census officials have concluded that such methods, known as adding "noise" to the data, are no longer sufficient. They cite recent work by mathematicians showing it's possible to reidentify people in an anonymized database, given a sufficiently large amount of other information, such as credit reports, voter rolls, and property records.

To better understand the risks, the Census Bureau ran its own computer-intensive experiment targeting records from the 2010 census. First, the researchers reconstructed records for unnamed individuals—say, a 55-year-old Hispanic woman—by mining aggregated census tables. Then, they tried to match reconstructed individuals to more detailed census block records (which lacked names); they found "putative matches" about half the time on a limited set of characteristics. Finally, they compared the putative matches to commercially available credit databases in hopes of attaching a name to a record. Even when they succeeded, however, the team didn't know whether it had actually found the right person.



The bureau has yet to release detailed results, but the simulated attack showed reidentification "can be done," says John Abowd, the bureau's chief scientist and associate director in Suitland, Maryland. "It exposes a vulnerability that we're not designing our systems to address."

A labor economist on leave from Cornell University, Abowd has led the bureau's push to adopt differential privacy, which he says represents a needed "sea change for the way that official statistics are produced and published." It isn't a substitute for swapping and other ways to perturb the data, he notes. Rather, it will allow the bureau to measure the likelihood that enough information will "leak" from its data set to open the door to reconstruction. The bureau can then insert just enough noise to prevent that, with especially sensitive data receiving more protection.

Ruggles and others have argued in print that traditional methods of preserving confidentiality have worked and that the bureau should rethink its strategy. At a meeting last month of one of the agency's advisory committees, members questioned whether the reconstruction experiment really indicated an urgent need to adopt differential privacy. They weren't impressed with the 50% "hit" rate. And they noted that the ability to reconstruct records is not the same as reidentifying individuals.

There is also disagreement about the law. Ruggles believes the bureau is required to mask only the identity of individuals, not their characteristics (such as sex and age). Abowd disagrees. "Steve has gotten it wrong," he says. "What is prohibited is releasing the data in an identifiable way."

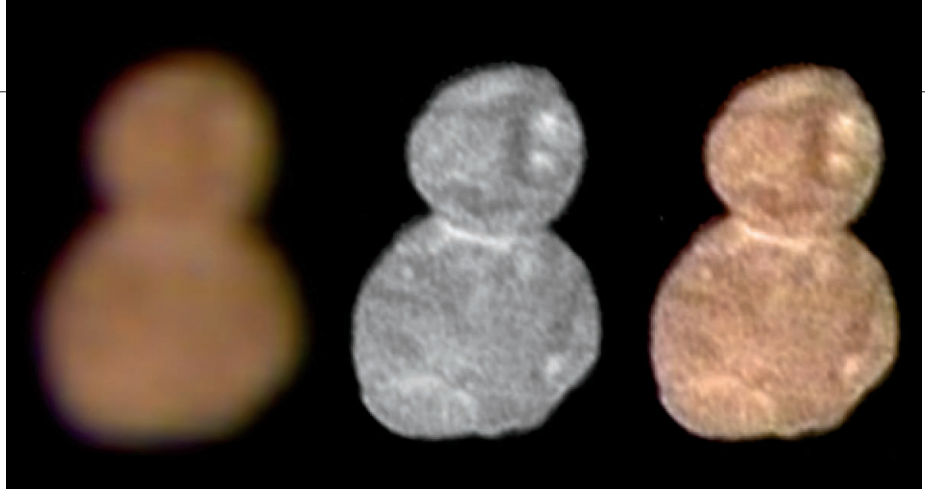
Critics of the change also say officials haven't thought enough about its negative impact on users, including a ripple effect on the many public and private organizations that conduct surveys based on census data. "If the Census Bureau wants to provide the same level of protection against reidentification that current methods do, you're going to have to do a lot more damage to the data than is done now," Ruggles says.

Even advocates of applying differential privacy concede there might be fallout. "Surveys could take longer, cost more, and may be less accurate," says John Thompson, a former Census Bureau director who recently retired as head of the Council of Professional Associations on Federal Statistics in Arlington, Virginia. But he thinks the bureau "doesn't have a choice. … The problem is real, and it is something you have to deal with."

Even if differential privacy is inevitable, Ruggles thinks census officials could do a lot more to smooth the transition. "There are better and worse ways to implement it," he says. "I would like them to consider the trade-offs, and not take such an absolutist stand on the risks." ■

IMAGE: WILLIAM DUKE/PHOTO BY DAXIAO PRODUCTIONS/SHUTTERSTOCK

Published by AAAS



A pinkish snowman took shape when blurry color and sharper black and white images were merged.

PLANETARY SCIENCE

New Horizons inspects a distant time capsule

Kuiper belt "snowman" supports idea that planetary building blocks coalesced from clumps of pebbles

By **Paul Voosen**, *in Laurel, Maryland*

Anders Johansen, an astrophysicist at Lund University in Sweden, was at home with his 7-year-old daughter on New Year's Day, watching the first close-up images of a small icy body at the fringes of the solar system. "My jaw just dropped," he says. Sent back by NASA's New Horizons spacecraft, the photos showed two nearly perfect spheres of ice and rock nestled together—a 33-kilometer-long interplanetary snowman. It was a shape Johansen had seen before. He had created it himself, in computer simulations of how the solar system formed.

Although the payoffs from New Horizons's flyby of 2014 MU_{69} have only just begun, the mission has already given humanity its first good look at a pristine relic of the solar system's earliest days, says Jeff Moore, a planetary scientist at NASA's Ames Research Center in Mountain View, California, and the mission's geology lead. Objects like MU_{69} "are the only remaining basic building blocks" of planets. And seeing a relic planetesimal up close bolsters a new picture of planet formation.

New Horizons zipped past its primary target, Pluto, in 2015. The dwarf planet belongs to the Kuiper belt, a diffuse array of hundreds of thousands of small icy bodies beyond Neptune, many of them little changed since the early days of the solar system. But Pluto itself has had a turbulent history. Tiny MU_{69}, the spacecraft's second target, looked like a better time capsule.

At 12:33 a.m. EST on New Year's morning, New Horizons skimmed past at a distance of just 3500 kilometers. Delayed by the finite speed of light, word that the probe had survived took 10 hours to reach mission controllers here at the Johns Hopkins University Applied Physics Laboratory (APL). "In lock with telemetry," Alice Bowman, the mission operation manager, called out in APL's control room. The instruments reported "green"—healthy. And, most important: The hard drives were full of new science data. "We've just accomplished the most distant flyby," Bowman said. A half-hour later, the New Horizons team poured into an APL auditorium to a standing ovation. New approach to preserving confidentiality could harm data quality, critics say.

Over the next 2 days, the team laid out initial findings from a low-resolution image taken early in the flyby, from 28,000 kilometers away. The researchers had puzzled over MU_{69}'s oblong shape, which telescopes had glimpsed when it was silhouetted against stars. Was it two icy objects orbiting each other, or a single "peanut"? Both, the team now concludes. MU_{69}'s dark red lobes formed as two bodies gently smooshed together billions of years ago. Gravitational attraction keeps them married despite their gentle, 15-hour rotation.

That shape bolsters a new view of how planetesimals first took shape. Scientists believe static electricity caused grains in the dusty disk around the newborn sun to stick together into centimeter-size pebbles. The problem was forming boulders bigger than a meter: In those cases, the collisions would quickly grow violent enough to break up the fragile objects, stalling growth.

In 2005, as New Horizons neared launch, astrophysicists Andrew Youdin, now at the University of Arizona in Tucson, and Jeremy Goodman of Princeton University discovered a way around the problem. The churn of the primordial disk could have caused pebbles to flock together in ever-larger clouds, like cyclists drafting in a peloton. Johansen came to a similar conclusion. In 2007, Johansen, Youdin, and others showed that these pebble clumps could grow large enough to gravitationally collapse into spherical planetesimals kilometers across.

At that point, planetesimals in the rich inner disk could grow into full-fledged planets by vacuuming up remaining gas and dust. But in the sparse Kuiper belt, the planetesimals would have been the end of the process—as attested to by MU_{69}'s relatively smooth, crater-free surface. The theory also explains why it appears to have started out as a binary, like about a third of the other Kuiper belt objects seen so far. Like figure skaters pulling in their arms, a pebble cloud rotates faster as it collapses. Turbulence develops, and it fractures into two or three spheres. "Clearly, understanding binarity holds a key to understanding the early stages of solar system history," Youdin says.

MU_{69}'s shape supports suggestions that comet 67P/Churyumov-Gerasimenko, a rubber duck–shaped visitor from the Kuiper belt that the European Space Agency's Rosetta spacecraft explored, is also a binary planetesimal, degraded by interactions with the sun. "This really puts the nail in the coffin now," says Alan Stern, the mission's principal investigator and a planetary scientist at the Southwest Research Institute in Boulder, Colorado. "We know this is how many objects like this form."

Much remains to be learned about MU_{69}. The early images were too coarse to reveal small impact craters, which could expose a glimpse of its interior. Detailed surface composition is not yet known. And so far the images have not shown small moons, which could be used to gauge MU_{69}'s mass and help explain its gentle assembly. The best imagery won't arrive until next month, and the spacecraft will take 20 months to beam all its data back. Along the way, it will stay busy, using its telescope to survey two dozen other bodies similar to MU_{69}.

This week, the sun came between Earth and New Horizons, interrupting its data stream for a few days. The team dispersed from APL. And the spacecraft left MU_{69} behind, traveling deeper into the ink of the Kuiper belt. ■

IMAGES: NASA/JOHNS HOPKINS UNIVERSITY APPLIED PHYSICS LABORATORY/SOUTHWEST RESEARCH INSTITUTE

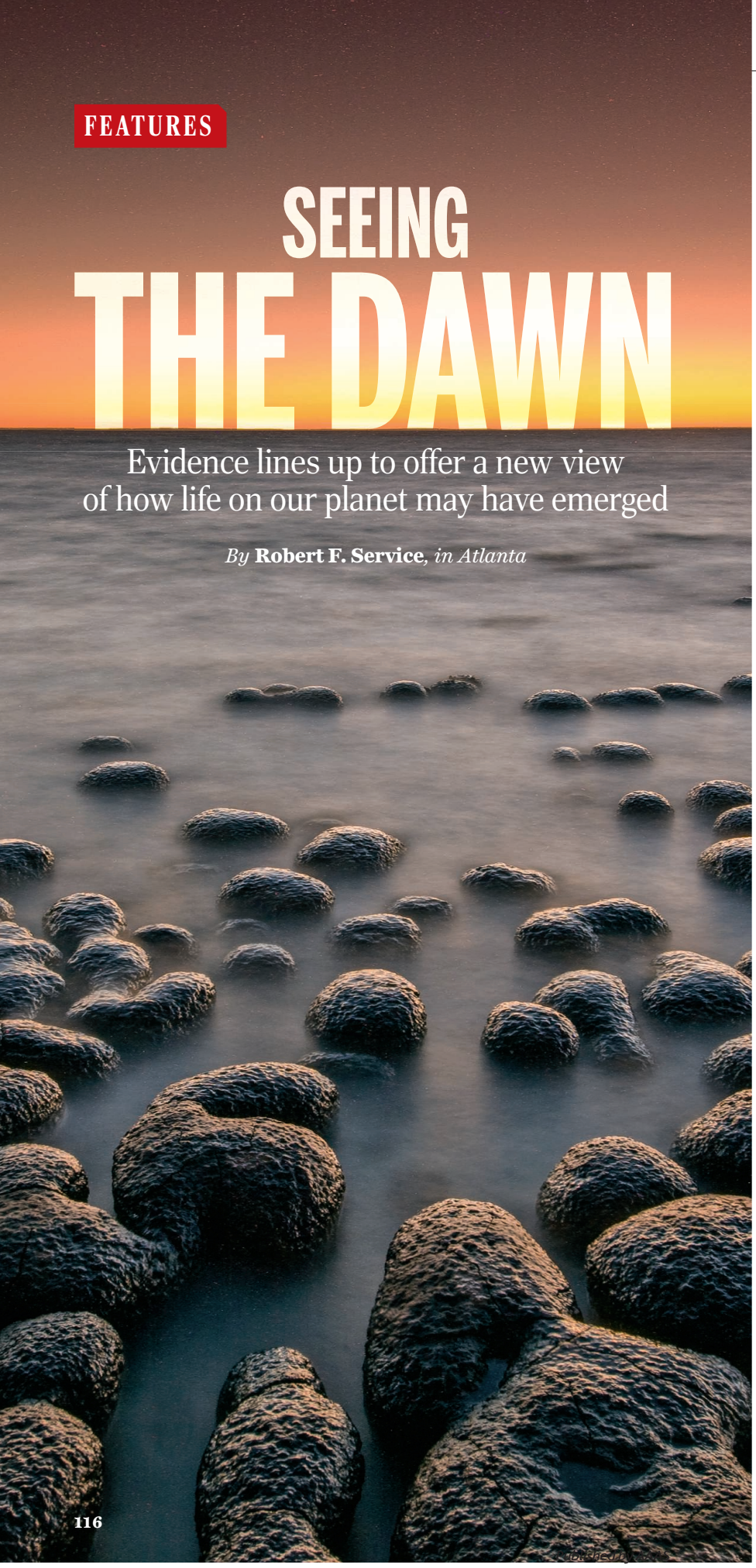
Downloaded from http://science.sciencemag.org/ on January 10, 2019

Published by AAAS

SEEING THE DAWN

Evidence lines up to offer a new view of how life on our planet may have emerged

By **Robert F. Service**, *in Atlanta*



Microbial mats called stromatolites emerged early in life's history—and still persist at Shark Bay in Australia.

PHOTO: FRANS LANTING/NATIONAL GEOGRAPHIC IMAGE COLLECTION

A cataclysm may have jump-started life on Earth. A new scenario suggests that some 4.47 billion years ago—a mere 60 million years after Earth took shape and 40 million years after the moon formed—a moon-size object sideswiped Earth and exploded into an orbiting cloud of molten iron and other debris.

The metallic hailstorm that ensued likely lasted years, if not centuries, ripping oxygen atoms from water molecules and leaving hydrogen behind. The oxygens were then free to link with iron, creating vast rust-colored deposits of iron oxide across our planet's surface. The hydrogen formed a dense atmosphere that likely lasted 200 million years as it ever so slowly dissipated into space.

After things cooled down, simple organic molecules began to form under the blanket of hydrogen. Those molecules, some scientists think, eventually linked up to form RNA, a molecular player long credited as essential for life's dawn. In short, the stage for life's emergence was set almost as soon as our planet was born.

That scenario captivated participants at an October 2018 conference here, where geologists, planetary scientists, chemists, and biologists compared notes on the latest thinking on how life got its start. No rocks or other direct evidence remain from the supposed cataclysm. Its starring role is inferred because it would solve a bevy of mysteries, says Steven Benner, an origin of life researcher at the Foundation for Applied Molecular Evolution in Alachua, Florida, who organized the Origins of Life Workshop.

The metal-laden rain accounts for the distribution of metals across our planet's surface today. The hydrogen atmosphere would have favored the emergence of the simple organic molecules that later formed more complex molecules such as RNA. And the planetary crash pushes back the likely birthdate for RNA, and possibly life's emergence, by hundreds of millions of years, which better aligns with recent geological evidence suggesting an early emergence of life.

The impact scenario joins new findings from laboratory experiments suggesting how the chemicals spawned on early Earth might have taken key steps along the road to life—steps that had long baffled researchers. Many in the field see a consistent narrative describing how and when life was born starting to take shape. "Fifteen years ago, we only had a few hazy ideas" about how life may have come about, says Andrej Lupták, a chemist at the University of California (UC), Irvine, who attended the meet-

Downloaded from http://science.sciencemag.org/ on January 10, 2019

ing. "Now, we're seeing more and more pieces come together."

The case isn't settled, Lupták and others say. Researchers still disagree, for example, over which chemical path most likely gave rise to RNA and how that RNA combined with proteins and fats to form the earliest cells. Nevertheless, Benner says, "The field is in a new place. There is no question."

LIFE AS WE KNOW IT likely emerged from an "RNA world," many researchers agree. In modern cells, DNA, RNA, and proteins play vital roles. DNA stores heritable information, RNA ferries it inside cells, and proteins serve as chemical workhorses. The production of each of those biomolecules requires the other two. Yet, the idea that all three complex molecules arose simultaneously seems implausible.

Since the 1960s, a leading school of thought has held that RNA arose first, with DNA and proteins evolving later. That's because RNA can both serve as a genetic code and catalyze chemical reactions. In modern cells, RNA strands still work alongside proteins at the heart of many crucial cellular machines.

In recent years, chemists have sketched out reactions that could have produced essential building blocks for RNA and other compounds. In 2011, for example, Benner and his colleagues showed how boron-containing minerals could have catalyzed reactions of chemicals such as formaldehyde and glycolaldehyde, which were probably present on early Earth, to produce the sugar ribose, an essential component of RNA. Other researchers have laid out how ribose may have reacted with other compounds to give rise to individual RNA letters, or nucleosides.

But critics such as Robert Shapiro, a biochemist at New York University in New York City who died in 2011, often pointed out that when researchers produced one pre-RNA chemical component or another, they did so under controlled conditions, adding purified reagents in just the right sequence. How all those steps could have occurred in the chaotic environment of early Earth is unclear at best. "The analogy that comes to mind is that of a golfer, who having played a golf ball through an 18-hole course, then assumed that the ball could also play itself around the course in his absence," Shapiro wrote in 2007 in *Scientific American*. He favored a "metabolism first" view of life's origin, in which energetic small molecules trapped inside lipidlike membranes or other compartments established chemical cycles resembling metabolism, which transformed into more complex networks. Other researchers, meanwhile, have argued that simple proteins were a more likely driver of early life because their amino acid building blocks are far simpler than the nucleotides in RNA.

Arguments have sometimes been heated. At a 2008 meeting on the origin of life in Ventura, California, Shapiro and John Sutherland, a chemist at the University of Cambridge in the United Kingdom, wound up shouting at each other. "Bob was very critical about published routes to prebiotic molecules," Sutherland says. If the chemistry wasn't ironclad, "he felt it failed."

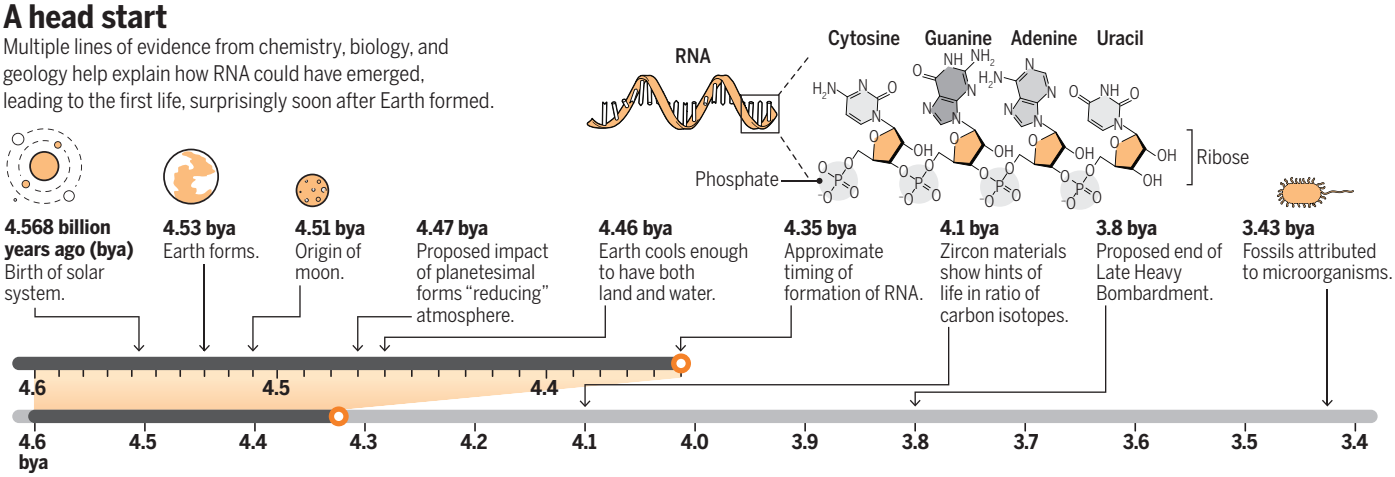
Today, Benner says, "The amount of yelling has gone down." A steady stream of new data has bolstered scenarios for how RNA could have arisen. For example, although Benner and his colleagues had previously shown how ribose may have formed, they could not explain how some of its ingredients—namely, the highly reactive small molecules formaldehyde, glycolaldehyde, and glyceraldehyde—could have survived. Geochemists have long thought that reactions sparked by lightning and ultraviolet (UV) light could have produced such compounds. However, Benner says, "There's no way to build up a reservoir" of those compounds. They can react with one another, devolving into a tarlike glop.

Benner now has a possible solution, which builds on recent work suggesting early Earth had a wet-dry cycle. On the basis of evidence from tiny, almost indestructable mineral crystals called zircons, researchers think a modest amount of dry land was occasionally doused with rain. In a not-yet-published study, he and colleagues in the United States and Japan have found that sulfur dioxide, which would have belched from volcanoes on early Earth, reacts with formaldehyde to produce a compound called hydroxymethanesulfonate (HMS). During dry times, HMS would have accumulated on land "by the metric ton," Benner says. The reverse reaction would have happened more slowly, regenerating formaldehyde. Then, when rains came, it could have washed in a steady trickle into puddles and lakes, where it could react to form other small organic molecules essential for building RNA. Similar processes, Benner says, could have provided a steady supply of glycolaldehyde and glyceraldehyde as well.

The sugar ribose is only one piece of RNA. The molecule also strings together four ring-shaped bases, which comprise the letters of the genetic code: cytosine (C), uracil (U), adenine (A), and guanine (G). Making them requires a supply of electron-rich nitrogen compounds, and identifying a plausible source for those has long challenged origin of life researchers. But other recent advances in prebiotic chemistry, which assume a supply of those compounds, have identified a set of reactions that could have produced all four of RNA's genetic letters at the same time and place. In 2009, for example, Sutherland and his colleagues reported a plausible prebiotic reaction for making C

A head start

Multiple lines of evidence from chemistry, biology, and geology help explain how RNA could have emerged, leading to the first life, surprisingly soon after Earth formed.



GRAPHIC: N. DESAI/*SCIENCE*

Downloaded from http://science.sciencemag.org/ on January 10, 2019

Published by AAAS

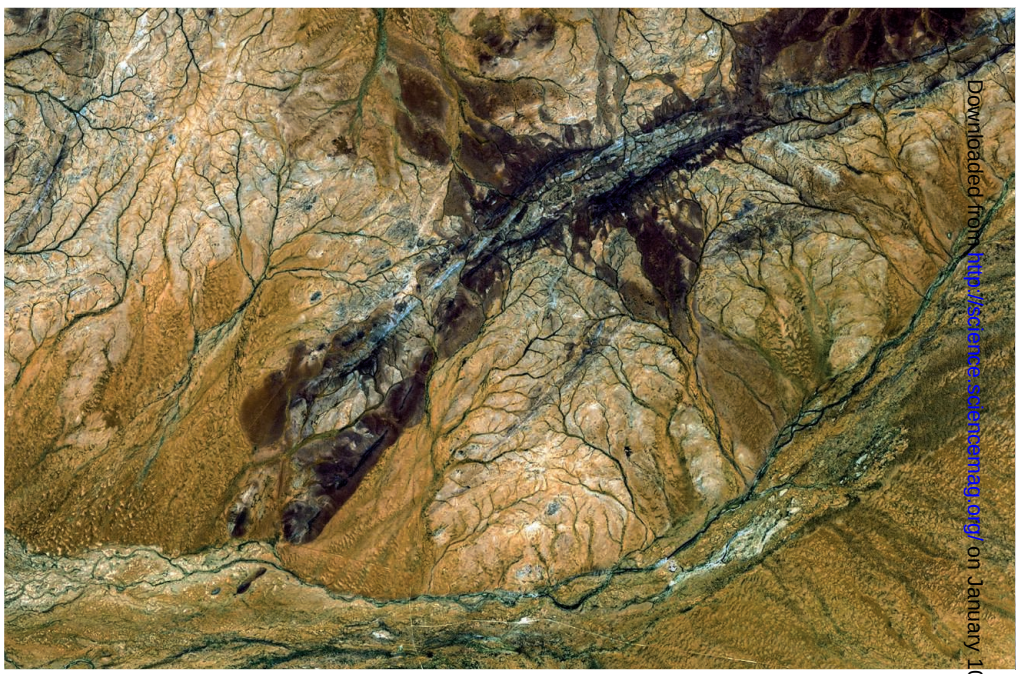
and U, chemically related letters known as pyrimidines. Then, in 2016, a team led by chemist Thomas Carell from Ludwig Maximilian University in Munich, Germany, reported coming up with a plausible way to make A and G, known as purines. The trouble was that Sutherland's and Carell's routes to pyrimidines and purines required different reaction conditions, making it difficult to imagine how they could have taken place side by side.

At the workshop, Carell reported a possible solution. He and his colleagues found that simple compounds likely present on early Earth could react in several steps to produce pyrimidines. Nickel and other common metals trigger the last step in the sequence by swiping electrons from intermediate compounds, causing them to react with one another. It turns out that gaining electrons enables the metals to then carry out a final step in synthesizing purines. What's more, those steps can produce all four nucleosides in one pot, thereby offering the first plausible explanation for how all four RNA letters could have arisen together.

Benner calls Carell's solution very clever. But not everyone is on board. Sutherland notes that those reactions are inefficient; any nucleosides they produced might fall apart faster than they could accumulate. To address that concern, others argue that more stable RNA-like compounds, rather than RNA itself, might have emerged first and helped form the first chemical system that could reproduce itself. Later, those RNA mimics might have given way to more efficient modern biomolecules such as RNA.

Whichever route RNA's letters took, other researchers have recently worked out how minerals likely present on early Earth could have added phosphate groups to RNA nucleosides, an essential step toward linking them into long strings of RNA that could then have acted as catalysts and a rudimentary genetic code. And many experiments have confirmed that once RNA chains begin to grow, they can swap RNA letters and even whole sections with other strands, building complexity, variation, and new chemical functions. At the meeting, for example, Niles Lehman, a chemist at Portland State University in Oregon, described experiments in which pairs of 16-letter-long RNA chains, known as 16-mers, rearranged to form 28-mers and 4-mers. "This is how we can go from short things that can be made prebiotically to more complex molecules," Lehman said. Later, he quipped, "If you give me 8-mers, I'll give you life."

That process may help explain how more complex RNA molecules arose, including those that can propel the synthesis of simple proteins. At the meeting in Atlanta, chemist Ada Yonath presented one such prototypical proteinmaking RNA. Yonath, of the Weizmann Institute of Science in Rehovot, Israel, shared the 2009 Nobel Prize in Chemistry for working out the atomic structure of the ribosome, the complex molecular machine inside today's cells that translates the genetic code into proteins. Yonath's original structure was of a bacterium's ribosome. Since then, she and her colleagues, along with other groups, have mapped the ribosomes of many other species. Modern ribosomes are behemoths, made up of dozens of protein and RNA components. But at their core, all ribosomes have a sinuous string of RNA with a narrow slit through which budding proteins emerge. The structure is virtually identical across species, unchanged after billions of years of evolution.



Her group has now synthesized that ribosomal core, which she refers to as the protoribosome. At the meeting, she reported that her team's protoribosome can stitch together pairs of amino acids, the building blocks of proteins. "I think we're seeing back to how life began billions of years ago," Yonath says.

All that is still a long way from demonstrating the emergence of life in a test tube. Nevertheless, Clemens Richert, a chemist at the Institute of Organic Chemistry at the University of Stuttgart in Germany, says the recent progress has been heartening. "We're finding reactions that work," he says. "But there are still gaps to get from the elements to functional biomolecules."

ONE MAJOR GAP is identifying a source for the energetic nitrogen-containing molecules needed to make the RNA bases. Lightning and UV light acting on compounds in the atmosphere may have made enough of them, says Jack Szostak, an origin of life expert at Harvard University. At the meeting, Stephen Mojzsis, a geologist at the University of Colorado in Boulder, argued that the moon-size impact is a more plausible spark.

Mojzsis didn't set out to grapple with the origin of life. Rather, he and his colleagues were looking for ways to make sense of a decades-old geological conundrum: the surprising abundance of platinum and related metals in Earth's crust. In the standard picture of Earth's formation, they simply shouldn't be there. The violent assembly of the planet from smaller bodies 4.53 billion years ago would have left it as a boiling sea of magma for millions of years. Dense elements, such as iron, gold, platinum, and palladium, should have sunk to the planet's core, whereas silicon and other light elements floated nearer the surface. Yet as the wares in any jewelry store testify, those metals remain plentiful near the planet's surface. "Precious metals in the crust are thousands of times more abundant than they should be," Mojzsis says.

The long-standing explanation has been that after Earth cooled enough to form a crust, additional metals arrived in a hail of meteors. On the basis of ages of moon rocks brought back by Apollo astronauts, geologists suspected this assault was particularly intense from 3.8 billion to 4.1 billion years ago, a period they refer to as the Late Heavy Bombardment (LHB).

But that scenario has problems, Benner says. For starters, fossil evidence of com-

PHOTO: NASA/MCT/MCT VIA GETTY IMAGES

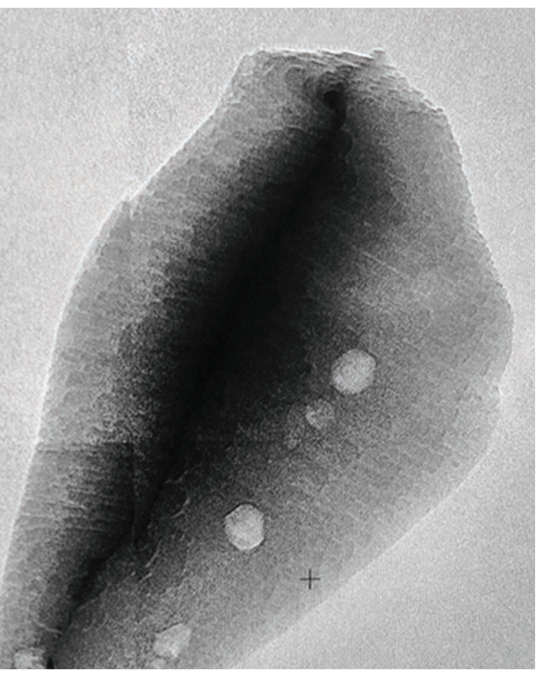
Downloaded from http://science.sciencemag.org/ on January 10, 2019

Published by AAAS

plex microbial mats called stromatolites shows up in rocks just a few hundred million years younger than the hypothetical bombardment. That's a narrow window in which to move from zero organic molecules to full-blown cellular life.

Zircons—those tiny, durable crystals—also pose a challenge, says Elizabeth Bell, a geologist at UC Los Angeles. Zircons are hardy enough to have remained intact even as the rocks that originally housed them melted while cycling into and out of the planet's interior.

In 2015, Bell and her colleagues reported in the *Proceedings of the National Academy of Sciences* that zircons



This 4.1-billion-year-old zircon mineral (x-ray image, right) contains carbon isotopes suggestive of life. Even older zircons have come from Australia's Jack Hills (aerial view, left).

dated to 4.1 billion years ago contain flecks of graphitic carbon with a life-like combination of carbon isotopes—biased toward carbon's lighter isotope over its heavier one. Bell concedes that an as-yet-unknown nonbiological process might account for that isotope mix, but she says it suggests life was already widespread 4.1 billion years ago, before the end of the LHB. Other recent zircon data, including samples from as long ago as 4.32 billion years, hint that very early Earth had both liquid water and dry land, suggesting it was more hospitable to life than originally thought. "We're pushing back further and further the time when life could have been formed on Earth," Bell says.

MOJZSIS ARGUES that a moon-size cataclysm 4.47 billion years ago could explain both Earth's veneer of precious metals and an early start for life. In December 2017, he and two colleagues published a set of extensive computer simulations in *Earth and Planetary Science Letters* showing how the current distribution of metals could have originated in the rain of debris from such an impact. Simone Marchi, a planetary scientist at the Southwest Research Institute in Boulder, and colleagues reached much the same conclusion in a paper the same month in *Nature Geoscience*. Marchi's team, however, simulated not one moon-size impactor, but several smaller bodies, each about 1000 kilometers across.

Whether one impact or a few, those collisions would have melted Earth's silicate crust, an event that appears to be recorded in data on isotopes of uranium and lead, according to Mojzsis. The collisions also would have profoundly affected Earth's early atmosphere. Before the impact, the cooling magma and rocks on the surface would have spurted out gases, such as carbon dioxide, nitrogen, and sulfur dioxide. None of those gases is reactive enough to produce the organic compounds needed to make RNA. But Benner notes the blanket of hydrogen generated by the impact's metallic hail would have formed exactly the kind of chemically reducing atmosphere needed to produce the early organics. Robert Hazen, a geologist at the Carnegie Institution's Geophysical Laboratory in Washington, D.C., agrees that hydrogen could help. With that reducing atmosphere, the wide array of minerals on the planet's surface could have acted as catalysts to propel the chemical reactions needed to make simple organics, Hazen says.

Just before the impact, Mojzsis says, "there was no persistent niche for the origin of life." But after the impact and a brief period of cooling, he adds, "at 4.4 billion years ago, there are settled niches for the propagation of life."

"I'm delighted," Benner says. "Steve [Mojzsis] is giving us everything we need" to seed the world with prebiotic chemicals. And by eliminating the need for the LHB, the impact scenario implies organic molecules, and possibly RNA and life, could have originated several hundred million years earlier than thought. That would allow plenty of time for complex cellular life to evolve by the time it shows up in the fossil record at 3.43 billion years ago.

NOT EVERYBODY accepts that tidy picture. Even if geologists' new view of early Earth is correct, the RNA world hypothesis remains flawed, says Loren Williams, a physical chemist at the Georgia Institute of Technology here and an RNA world critic who attended the workshop. "I like talking to Steve Benner," Williams says. "But I don't agree with him."

One major problem with the RNA world, he says, is that it requires a disappearing act. An RNA molecule capable of faithfully copying other RNAs must have arisen early, yet it has vanished. "There's no evidence for such a thing in modern biology," Williams says, whereas other vestiges of ancient RNA machines abound. The ribosome's RNA core, for example, is virtually unchanged in every life form on the planet. "When biology makes something, it gets taken and used over and over," Williams notes. Instead of an RNA molecule that can copy its brethren, he says, it's more likely that early RNAs and protein fragments called peptides coevolved, helping each other multiply more efficiently.

Advocates of the RNA world hypothesis concede they can't explain how early RNA might have copied itself. "An important ingredient is still missing," Carell says. Researchers around the globe have designed RNA-based RNA copiers in the lab. But those are long, complex molecules, made from 90 or more RNA bases. And the copiers tend to copy some RNA letters better than others.

Still, enough steps of an RNA-first scenario have come into focus to convince advocates that others will follow. "We are running a thought experiment," says Matthew Powner, a chemist at University College London. "All we can do is decide what we think is the simplest trajectory."

That thought experiment was on full display in the workshop's final session. Ramon Brasser of the Tokyo Institute of Technology, one of Mojzsis's collaborators, stood at the front of a small conference room and drew a timeline of Earth's earliest days. A red slash at 4.53 billion years ago on the left side of Brasser's flip chart marked Earth's initial accretion. Another slash at 4.51 billion years ago indicated the moon's formation. A line at 4.47 billion years ago marked the hypothetical impact of the planetesimal that gave rise to an atmosphere favorable to organic molecules.

Benner asked Brasser how long Earth's surface would have taken to cool below 100°C after the impact, allowing liquid water to host the first organic chemical reactions. Probably 50 million years, Brasser said. Excited, Benner rushed up to the timeline and pointed to a spot at 4.35 billion years ago, adding a cushion of extra time. "That's it, then!" Benner exclaimed. "Now we know exactly when RNA emerged. It's there—give or take a few million years." ■

PHOTO: CRYSTAL SHI

Downloaded from http://science.sciencemag.org/ on January 10, 2019

Published by AAAS



Downloaded from http://science.sciencemag.org/ on January 13, 2019

PERSPECTIVES

EVOLUTIONARY BIOLOGY

Are clever males preferred as mates?

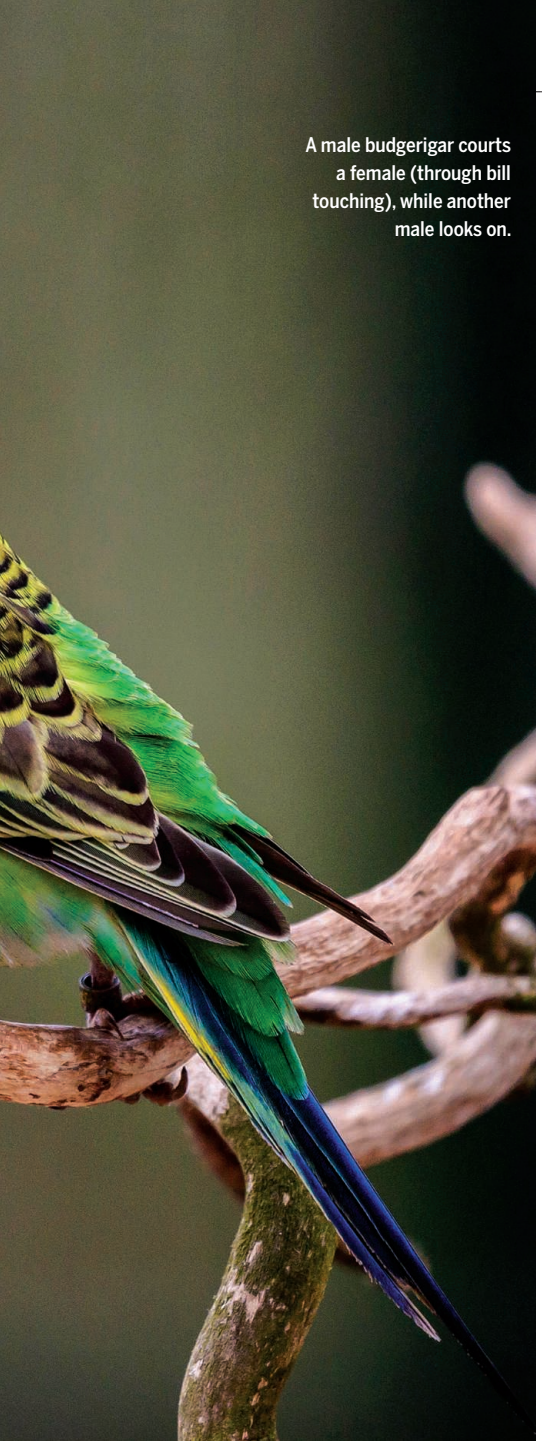
Testing this Darwinian hypothesis is a tough nut to crack

By **Georg F. Striedter**[1] *and* **Nancy T. Burley**[2]

Being smart is a good thing, or so smart people like to think. Indeed, the possibility that superior cognition confers an evolutionary advantage, specifically a reproductive fitness benefit, is intuitively appealing. Of the three general fitness components—survivorship/longevity, fecundity, and mating success—the best-documented association involves survivorship. Across species, comparatively large-brained mammals and birds, which are thought to have superior cognitive capacities, show greater longevity than their smaller-brained relatives (*1*, *2*). In addition, within-species comparisons of problem-solving ability, especially in foraging contexts, have shown positive correlations with fecundity (*3*, *4*). Yet, what is arguably the most famous hypothesized fitness benefit of superior cognition has seldom been studied in nonhumans: the sexual selection hypothesis that clever in-

PHOTO: ARCO IMAGES GMBH/ALAMY STOCK PHOTO

Published by AAAS



A male budgerigar courts a female (through bill touching), while another male looks on.

dividuals are preferred as mating partners (*5*, *6*). Recent research on several species of birds does suggest that females are attracted to males that are adept at problem-solving (*7*, *8*). In most instances, however, researchers have inferred female preference for cognitive superiority from the expression of traits (e.g., plumage or song) that correlate with cognitive performance. Unfortunately, such correlative studies cannot establish that superior cognitive ability per se is the basis of an observed mate preference. On page 166 of this issue, Chen *et al.* (*9*) report tackling this problem by directly testing female preference for male problem-solving ability, using a small Australian parrot, the budgerigar.

Chen *et al.*'s approach was to observe female budgerigars choose between two males in an apparatus where they could only interact with one male at a time—a design that previously revealed preferences of female budgerigars for male plumage and vocal traits (*10*, *11*). Chen *et al.* did not attempt to gauge natural variation in male problem-solving ability. Instead, they tested each female with a unique set of two males to establish her relative preference for them. Then, away from the female's observing eyes, they trained the male she did not prefer to open translucent containers filled with seed. The preferred males and females, meanwhile, were exposed to already-opened containers, so they could not attempt to solve the foraging task. Next, each female was allowed to observe the trained male solve the tasks repeatedly. In alternate trials, she watched the untrained male being unable to open the containers. During this period, seed containers were present in her cage, but they were taped shut. Finally, after the observation period, each female was retested with her original set of males. Remarkably, the females shifted their preference toward the previously nonpreferred, "problem-solving" males. Control trials revealed that the shift in female preference did not result from simply observing the trained males eating seed. Nor did females exhibit a preference for other females trained on the foraging task, indicating that the main finding was specific to an intersexual context. Thus, Chen *et al.* offer convincing evidence that female budgerigars modified their mate preference in favor of trained males after observing them perform complex foraging tasks.

"...female budgerigars preferred trained males for their apparent problem-solving prowess."

Although the main result is straightforward, its interpretation is less clear-cut. Given the growing evidence of complex cognition in an array of species (*7*, *12*), it is tempting to infer that female budgerigars preferred trained males for their apparent problem-solving prowess. However, the fact that females lacked the opportunity to perform the foraging task themselves suggests that they may have had little basis for understanding the exercise as a problem in need of a clever solution. Instead, they might have attributed male success in opening the containers to superior physical strength. Alternatively, the extensive training paradigm may have elicited subtle behavioral differences between trained and untrained males, such that (for example) the untrained males showed less foraging effort during the observation period or less exploratory behavior during the posttraining choice trials. Unfortunately, it is difficult to rule out such alternative explanations in most studies of comparative cognition (*12*).

Despite these concerns, the approach employed by Chen *et al.* has considerable promise for advancing empirical research on mate choice for cognitive traits. Numerous species display the capacity to choose mates using more than one trait, and the full set of relevant traits is not known for any species. As a result, mate choice experiments that focus on one particular set of traits almost always contain additional variation in other traits, some of which may be correlated with the traits of interest. Although the experimenters may be oblivious to those potentially confounding traits, the choosing individuals may be attending to them. Chen *et al.*'s approach mitigates this problem by giving the choosers additional information about their potential partners after the initial choice is made and then asking whether this additional information alters their preference. Confounding variables may still exist in such designs, especially when the additional information involves complex behavior (*13*), but they are minimized. Therefore, we anticipate that this methodology will become an important tool for mate choice research in future studies. ■

[1]Department of Neurobiology and Behavior, University of California, Irvine, CA, USA. [2]Department of Ecology and Evolutionary Biology, University of California, Irvine, CA, USA. Email: georg.striedter@gmail.com

REFERENCES

1. C. González-Lagos, D. Sol, S. M. Reader, *J. Evol. Biol.* **23**, 1064 (2010).
2. P. Minias, P. Podlaszczuk, *Ecol. Evol.* **7**, 3558 (2017).
3. E. F. Cole, J. Morand-Ferron, A. E. Hinks, J. L. Quinn, *Curr. Biol.* **22**, 1808 (2012).
4. D. P. Wetzel, *Ethology* **123**, 475 (2017).
5. C. Darwin, *The Descent of Man, and Selection in Relation to Sex* (Murray, London, 1871).
6. G. F. Miller, P. M. Todd, *Trends Cogn. Sci.* **2**, 190 (1998).
7. N. J. Boogert, T. W. Fawcett, L. Lefebvre, *Behav. Ecol.* **22**, 447 (2011).
8. F. Mateos-Gonzalez, J. Quesada, J. C. Senar, *Biol. Lett.* **7**, 668 (2011).
9. J. Chen, Y. Zou, Y.-H. Sun, C. ten Cate, *Science* **363**, 166 (2019).
10. S. M. Pearn, A. T. D. Bennett, I. C. Cuthill, *Proc. Biol. Sci.* **268**, 2273 (2001).
11. M. L. Moravec, G. F. Striedter, N. T. Burley, *Ethology* **116**, 961 (2010).
12. S. J. Shettleworth, *Cognition, Evolution, and Behavior* (Oxford Univ. Press, Oxford, ed. 2, 2010).
13. A. G. Hile, N. T. Burley, C. B. Coopersmith, V. S. Foster, G. F. Striedter, *Ethology* **111**, 901 (2005).

10.1126/science.aaw1811

Published by AAAS

Downloaded from http://science.sciencemag.org/ on January 13, 2019

CHEMISTRY

Democratizing synthesis by automation

Computer code directs interconnected modules that perform primary steps of synthesis

By **Anat Milo**

There is something particularly satisfying in watching an automaton as it impeccably performs its task, be it an Archimedean screw pump or a machine for making cookie cutters. In this vein, the videos accompanying the article on page 144 by Steiner *et al.* (*1*), depicting their self-driven synthetic chemistry setup—in effect, an automated chemical assembly line—are mesmerizing. The authors constructed a broad-purpose chemical synthesis system comprising interconnected modules coupled with a standardized computer code and architecture. Put in simpler terms, they built a fully equipped fume hood that functions without the need of a human operator. Validating their approach, the synthesizer autonomously prepared three pharmaceutical compounds—diphenhydramine hydrochloride, rufinamide, and sildenafil—according to tailored computer codes provided by the authors.

This work follows several recent efforts to build flexible automated machines that can execute full synthetic routes for a broad range of synthetic procedures (*2*–*5*). Machines perform the tasks of synthetic chemistry in ways that are repeatable, consistent, and fast, and in principle could outperform humans in reaction procedures that require accuracy, reproducibility, and reliability. Furthermore, automation fulfills the promise of technology disburdening people from drudgery and danger, and could free chemists to work on more creative aspects of chemistry. From an industrial perspective, it may lead to faster and more reliable processing.

Automation does not simply imply taking processes and using a robot to perform them as a human would. The process of automating a task inevitably changes the task, occasionally to its very core. In chemistry, synthetic methodologies often must be modified before they can be executed successfully by machines. For example, before the introduction of automated methods for peptide synthesis, robust peptide-coupling methodologies had to be accessible, and together these outcomes resulted in enormous advances in biological chemistry (*6*). As another example, to enable high-throughput screening at the nanoliter scale using a robotics system, a carbon-nitrogen coupling reaction had to be optimized to work in an unusual solvent, dimethyl sulfoxide (DMSO), that provided much greater solubility at room temperature (*7*). On-demand synthesis and purification of radiolabeled fluorinated compounds for positron emission tomography, which is dictated by the short half-life of ^{18}F, has been transformed by considering automation constraints at the earliest stages of reaction development (*8*–*11*). Flow chemistry relies on accurate control of reaction component ratios and mixing rates as well as mass and heat transfer, all of which are streamlined by automation. It is hardly surprising that an automated synthesis system capable of purifying several pharmaceuticals has already been enabled by an integrated continuous-flow strategy (*12*, *13*). More recently, by combining this strategy with in-line analytical capabilities, a reconfigurable continuous-flow system was designed for automated optimization of reaction conditions (*14*). These examples demonstrate how automation has already altered synthesis.

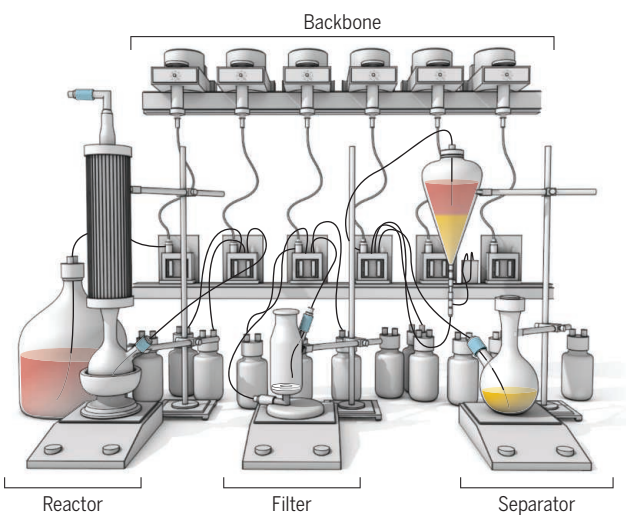
Synthetic chemists often take for granted the senses and skills required to perform simple lab operations. Steiner *et al.* mimicked many of these to construct their robotic system—for example, using an external magnet to capture the stirring bar after a reaction. In other cases, they had to adjust the way synthesis is performed. They struggled to find an automated means for detecting phase separations that would allow them to replicate a decision-based procedure that trained chemists would accomplish visually. Their solution consisted of a conductivity sensor to differentiate between the two phases, which is not only highly resourceful but could potentially outperform visual detection. Such scenarios, in which the machine applies strategies that distinguish it from a human counterpart, may be stepping stones toward superior performance on a particular task. In general, the advantage of using a machine is bolstered by endowing it with abilities that humans do not possess, such as the use of regions of the spectrum undetectable by the human eye or the use of electrical signals as sensors.

The rigorously designed synthetic platform presented by Steiner *et al.* is complemented by the approach they developed for controlling the modules. They first deconstructed and generalized the different steps common to most synthetic procedures and then broke these steps down into machine operations, designing drivers for each module to run these operations (see the figure). The physical connections between the modules are saved as graphs, allowing the system to be truly modular and easily reconfigured to include additional modules.

To bring the software and hardware together, Steiner *et al.* coded a compiler that

The synthesis engine under the fume hood

The main flow controller of the autonomous synthesis robot designed by Steiner *et al.* is illustrated. The modules shown include a reactor, a filter, and a separator, connected by a "backbone" of six-way valves and syringe pumps that move the reaction mixture between modules.



GRAPHIC: C. BICKEL/*SCIENCE*

Department of Chemistry, Ben-Gurion University of the Negev, Beer Sheva 84105, Israel. Email: anatmilo@bgu.ac.il

Downloaded from http://science.sciencemag.org/ on January 10, 2019

Published by AAAS

produces low-level commands for controlling the modules when given a graph of the physical setup and an input of high-level instructions. These instructions are coded with an extensible descriptive programming language (XDL) to allow users with no programming knowledge to easily encode machine- and human-readable synthetic protocols. This code is then transcribed into a machine-readable chemical assembly (ChASM) script that serves to break down the higher-level abstractions (e.g., reflux) into operations performed by the modules (e.g., stirring and heating). If widely accepted, this protocol could standardize the way procedures are reported and minimize ambiguity. Here again, automation may be responsible for a change in the very task it sought to automate. Ultimately, this type of approach could democratize the automation of synthetic protocols by allowing chemists to straightforwardly adapt and build upon the developed hardware and software.

In the short term, automation can lead to standardization and growth, but what are the long-term consequences of the changes that make a system amenable to automation? Would automation limit inventiveness in molecular sciences once many tasks are shaped into automatable categories? Would the application of automation in exploratory studies enable or hinder the identification of unexpected new phenomena? How would we fill the gap created by automation in the profession of making molecules? Would it ratchet us up to greater unforeseen progress, or would it facilitate indolence? These questions and many more need to be addressed in the coming years as the automation revolution unfolds. In this respect, the availability of technologies and computer codes heralds the automation of chemical synthesis and allows us to be involved in a process that will eventually redefine what it means to be a chemist. ■

REFERENCES

1. S. Steiner *et al.*, *Science* **363**, eaav2211 (2019).
2. J. Li *et al.*, *Science* **347**, 1221 (2015).
3. K. Sanderson, *Nat. Rev. Drug Discov.* **14**, 299 (2015).
4. M. Peplow, *Nature* **512**, 20 (2014).
5. K. J. Kilpin, R. J. Whitby, *Chem. Cent. J.* **9**, 43 (2015).
6. A. R. Mitchell, *Biopolymers* **90**, 175 (2008).
7. A. Buitrago Santanilla *et al.*, *Science* **347**, 49 (2015).
8. C. M. Waldmann, A. Lebedev, N. Allison, S. Sadeghi, *Appl. Radiat. Isot.* **127**, 245 (2017).
9. M. S. McCammant *et al.*, *Org. Lett.* **19**, 3939 (2017).
10. M. G. Campbell, T. Ritter, *Org. Process Res. Dev.* **18**, 474 (2014).
11. M. Tredwell *et al.*, *Angew. Chem. Int. Ed.* **53**, 7751 (2014).
12. A. Adamo *et al.*, *Science* **352**, 61 (2016).
13. P. L. Heider *et al.*, *Org. Process Res. Dev.* **18**, 402 (2014).
14. A.-C. Bédard *et al.*, *Science* **361**, 1220 (2018).

10.1126/science.aav8816

GRAPHIC: A. KITTERMAN/*SCIENCE*

NEUROSCIENCE

Neuronal function of Alzheimer's protein

Cleavage products of an Alzheimer's disease protein are involved in synaptic homeostasis

By **Martin Korte**

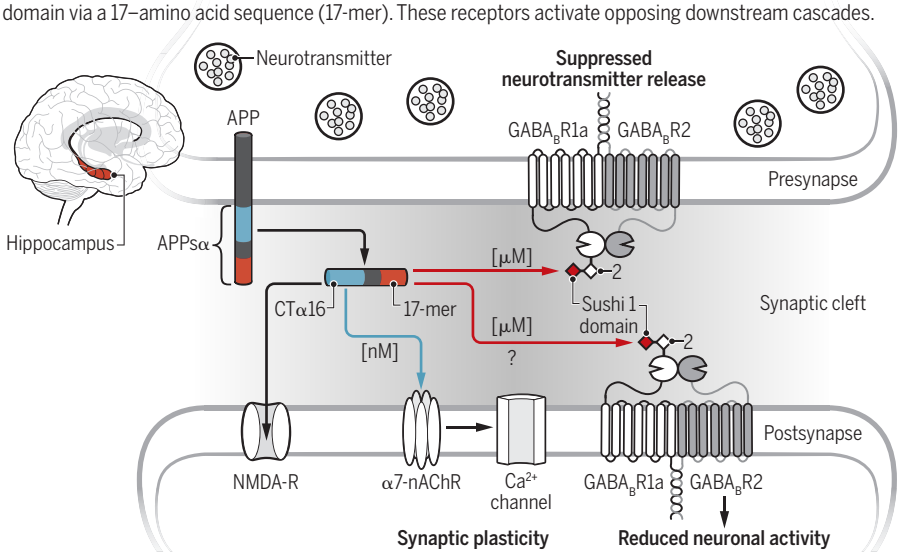
For a long time, the huge importance of the cleavage product of the amyloid precursor protein (APP), amyloid-β (Aβ), in the etiology of Alzheimer's disease (AD) (*1*) has occluded the view of the physiological function of APP. But over the years, it has become clear that APP and its proteolytic products have important physiological functions (*2*) during brain development or in the adult brain in processes of activity-dependent synaptic plasticity (*3*) and possibly even protection against neurodegeneration (*4*, *5*). On page 143 of this issue, Rice *et al.* (*6*) discovered that a sushi-containing neurotransmitter receptor in the brain, $GABA_BR1a$ (γ-aminobutyric acid type B receptor subunit 1a), has a new interaction partner, APP. This provides important insights about the physiological function of APP and might open new avenues to treat AD—not only through targeting Aβ but also by strengthening alternate routes of cleaving APP and utilizing nonamylogenic pathways.

Unraveling APP functions and its binding partners has not been trivial, because APP undergoes complex processing, and this results in numerous fragments, which have different and sometimes opposing functional properties. Furthermore, APP functions are partially shared by APP-like protein 1 (APLP1) and APLP2, which confounds some experimental approaches. But what became clear is that one of the main APP proteolytic pathways leads to the secretion of large soluble ectodomains, called APPsα, APPsβ, and APPη (*2*). The main physiologically active agent seems to be APPsα, which is possibly neurotrophic and neuroprotective and may promote the strengthening of synapses, termed long-term potentiation (LTP), in the hippocampus (*3*), which is a cellular mechanism for learning and memory. Accumulating evidence suggests that AD symptoms are caused by both an overload of toxic substances, including Aβ, as well as deficits of protective molecules, such as low concentrations of APPsα.

Zoological Institute, Division of Cellular Neurobiology, Technische Universität Braunschweig, 38106 Braunschweig, Germany, and AG Neuroinflammation and Neurodegeneration (NIND), Helmholtz Centre for Infection Research (HZI), 38124 Braunschweig, Germany. Email: m.korte@tu-bs.de

Cleavage products of APP regulate synaptic function

At nM concentration, APPsα is an allosteric activator of α7-nAChR, mediated by C-terminal 16 amino acids (CTα16). At μM concentrations, Rice *et al.* identified the $GABA_BR1a$ as a target of APPsα, binding the sushi 1 domain via a 17–amino acid sequence (17-mer). These receptors activate opposing downstream cascades.



Published by AAAS

Downloaded from http://science.sciencemag.org/ on January 10, 2019

Rice *et al.* investigated APP in the adult hippocampus, where it regulates synaptic plasticity and memory (*3*). But what is the receptor through which APPsα mediates these functions? The authors confirmed that APP is expressed at presynaptic terminals of excitatory and inhibitory hippocampal neurons. They found that APPsα and APPsβ are strong binding partners of $GABA_BR1a$. This metabotropic receptor for the inhibitory neurotransmitter GABA regulates presynaptic neurotransmitter release and postsynaptic membrane excitability (*7*). This suggests that the APP-$GABA_BR1a$ interaction acts as an activity-dependent negative-feedback mechanism to preserve homeostatic control of neural circuits in the aged brain. Indeed, it is currently an open question why Aβ plaques in the brains of patients with AD form and how they become toxic. Alternatively, as suggested by results from Rice *et al.* and others (*4*, *8*, *9*), perhaps the deposition of toxic plaques is caused by the loss of homeostasis in neuronal networks, such as hyperexcitability and hypersynchronization, which might precede AD clinical symptoms (*10*).

Rice *et al.* found that the extension domain (ExD) of APP was the minimal domain required to bind to $GABA_BR1a$-expressing cells. From the ExD domain, the authors synthesized a 17–amino acid peptide (APP 17-mer) that was long enough to bind with high affinity to the $GABA_BR1a$ sushi 1 domain. Many proteins contain multiple, repeating sushi domains, which are a conserved protein domain with a protein loop within another loop (*11*). These domains are thought to act as protein binding regions. Consistent with their results in cell cultures and brain slices, the application of APP 17-mer reduced neuronal activity in mice. Taken together, these findings show that proteolytic cleavage products of APP inhibit neuronal activity and that the $GABA_BR1a$ binding domain of APP is sufficient for such inhibition. This opens the possibility that the APP 17-mer peptide—or a similarly acting compound—might be used to treat early symptoms of AD, as shown by others in an animal model of AD treated with APPsα (*4*).

Rice *et al.* now add a new player—$GABA_BR1a$—to the physiology of APP in the regulation of neuronal communication. It was shown previously that APPsα might alter *N*-methyl-D-aspartate (NMDA) receptor function (*8*, *12*), an important glutamate receptor involved in activity-dependent synaptic plasticity that initiates learning-induced neuronal changes in synaptic strength. Furthermore, APPsα was shown to be an allosteric activator of the excitatory α-7 nicotinic receptor (α7-nAChR), through binding to its 16–amino acid carboxyl terminus (*9*). Owing to different receptor associations, opposing downstream cascades might be initiated by APP ectodomain cleavage products. The APP 17-mer subdomain might regulate presynaptic release of neurotransmitter at the presynaptic cleft by $GABA_BR1a$ activation to promote homeostasis, whereas the 16–amino acid carboxyl terminus might induce Ca^{2+}-mediated postsynaptic effects via α7-nAChR activation to support synaptic plasticity (see the figure). It needs to be determined how, in a complex hippocampal or cortical neuronal network, these pleiotropic actions of APPsα subdomains are executed in order to maintain homeostasis and promote learning and memory. There is also a discrepancy with the existing literature about the action of APPsβ and APPsα or even smaller peptides, which were reported to have no effect on baseline synaptic transmission (*8*, *13*), whereas Rice *et al.* observed less synaptic activity when these APP cleavage products were applied. Perhaps concentration differences of the peptides used might explain the discrepancy. Another interesting topic for future research is how much of the effects are really presynaptically mediated, because $GABA_BR1a$ is also expressed postsynaptically and causes hyperpolarization of the postsynaptic neuron (*7*).

Rice *et al.* determined an interesting new binding partner, $GABA_BR1a$, to specific parts of APP that induces beneficial changes in synapse function. This could lead to new ways of preserving or even restoring synaptic function in patients with AD. The long-term application of APPsα can indeed ameliorate and possibly reduce the cellular and cognitive effects of Aβ deposits in mice (*4*), and such a long-term study is needed with APP 17-mer. The next steps should include the use of induced pluripotent stem cell–derived neurons from humans to validate animal findings. Moreover, because several studies have shown that APPsα levels are decreased in the cerebrospinal fluid of patients with AD (*14*) and correlate with poor memory performance (*15*), the findings presented by Rice *et al.* are of considerable interest to understand AD etiology. ■

REFERENCES

1. D. J. Selkoe, J. Hardy, *EMBO Mol. Med.* **8**, 595 (2016).
2. U. C. Müller *et al.*, *Nat. Rev. Neurosci.* **18**, 281 (2017).
3. S. Ludewig, M. Korte, *Front. Mol. Neurosci.* **9**, 161 (2017).
4. R. Fol *et al.*, *Acta Neuropathol.* **131**, 247 (2016).
5. V. T. Y. Tan *et al.*, *Mol. Brain* **11**, 7 (2018).
6. H. C. Rice *et al.*, *Science* **363**, eaao4827 (2019).
7. M. Gassmann, B. Bettler, *Nat. Rev. Neurosci.* **13**, 380 (2012).
8. C. J. Taylor *et al.*, *Neurobiol. Dis.* **31**, 250 (2008).
9. K. N. Richter *et al.*, *EMBO J.* **37**, 139 (2018).
10. S. Frere, I. Slutsky, *Neuron* **97**, 32 (2018).
11. A. Meindl *et al.*, *Hum. Mol. Genet.* **4**, 2339 (1995).
12. L. Moreno *et al.*, *J. Alzheimers Dis.* **48**, 927 (2015).
13. M. Hick *et al.*, *Acta Neuropathol.* **129**, 21 (2015).
14. L. Lannfelt *et al.*, *Nat. Med.* **1**, 829 (1995).
15. O. Almkvist *et al.*, *Arch. Neurol.* **54**, 641 (1997).

10.1126/science.aaw0636

NEUROSCIENCE

Many paths to preserve the body clock

Daily clocks in astrocytes in the brain can drive behavioral rhythmicity

By **Carla B. Green**

Robust daily oscillations in behavior, physiology, and biochemistry are driven by endogenous timekeeping machinery called the circadian clocks. Circadian clocks in mammals were originally considered properties of the nervous system, and the anatomical locus of this clock was determined to be the suprachiasmatic nucleus (SCN) in the hypothalamus. The neurons that make up this structure are highly interconnected (coupled) and exhibit robust and coordinated rhythms of activity, and loss of rhythmicity results in loss of behavioral rhythms such as daily activity. On page 187 of this issue, Brancaccio *et al.* (*1*) reveal that SCNs that have been rendered "clockless" through genetic perturbation in mice can be restored to rhythmicity by rescuing the clocks in only the astrocytes, a type of glial cell. The idea that rhythmic astrocytes are sufficient to generate a functional circadian clock that can control behavioral rhythms is surprising and suggests that the SCN can produce rhythms by means of more than one mechanism.

The SCN, a paired nucleus of ~20,000 neurons, was identified through experiments that included the introduction of lesions that rendered the animals' behavior arrhythmic, track tracing of neural circuits from the retina (which provides the light input that regulates the circadian clock), and the rescue of arrhythmic animals by transplanting fetal SCNs from donor animals with different period lengths and showing that these restored rhythms had periods of the donor animals (*2*). Although these experiments demonstrated conclusively that the SCN was necessary for circadian rhythms of behavior, subsequent discoveries of the genes and proteins that make up this timekeeping mechanism revealed

Department of Neuroscience, UT Southwestern Medical Center, 5323 Harry Hines Boulevard, Dallas, TX 75390-9111, USA. Email: carla.green@utsouthwestern.edu

Downloaded from http://science.sciencemag.org/ on January 10, 2019

Published by AAAS

that the circadian clockwork was present in nearly every cell of the body and could drive cell-autonomous rhythms independently of the SCN. Despite this, the SCN is considered the master clock that receives synchronizing light information from the environment and coordinates the rhythms of the many cellular clocks throughout the body through humoral and neuronal signals (*3*). Furthermore, the SCN has been shown to have special properties, resulting from its highly coupled neuronal network, which makes it robust and resistant to damping and to some genetic perturbations (*4*).

The core circadian clockwork consists of a transcription-translation negative feedback loop in which the heterodimeric transcription factor composed of CLOCK and BMAL1 drives expression of the repressors, including *Period* genes (*Per1*, *Per2*, and Per*3*) and the *Cryptochrome* genes (*Cry1* and *Cry2*). Cells or animals with deficits in the various components of this system have compromised clocks with altered period lengths or are arrhythmic (*5*). Within the SCN, *Per* and *Cry* genes are expressed rhythmically, with a spatiotemporal wave of expression that starts from the dorsomedial edge and proceeds ventrally across the nucleus in a highly coordinated manner each day. This coupling is important for the high-amplitude robust rhythms generated by this structure, which synchronizes clocks throughout the body (*6*).

Dissecting the roles of the neuronal cell types within the SCN has been a major focus of research. The generation of chimeric mice with different proportions and distributions of wild-type and *Clock* mutant cells within the SCN demonstrated that not all SCN neurons need to have an intrinsic clock in order for the ensemble to operate correctly (*7*). Other studies have used cell-type overexpression of mutant CLOCK proteins or cell-type–specific ablation of circadian clock genes to examine the roles of different cell types in driving rhythmicity (*8*, *9*). Brancaccio *et al.* used an opposite approach on the basis of a previous discovery that the circadian clock in mice with arrhythmic SCN in which *Cry1* and *Cry2* are ablated can be rescued by rhythmically expressing either *Cry1* or *Cry2* (*10*, *11*). They used this to test the roles of astrocytes and neurons within the SCN for their ability to generate a competent SCN clock in arrhythmic mice. As expected, they found that introduction of *Cry1* into either cell type in slice cultures was sufficient to rescue rhythms in the cells in which *Cry1* was expressed. However, the free-running periods of the restored rhythms were different for the different cell types, with the astrocyte clock running faster than the neuron clock, demonstrating that both astrocytes and neurons are timekeepers, or pacemakers, within the SCN, but with different intrinsic properties.

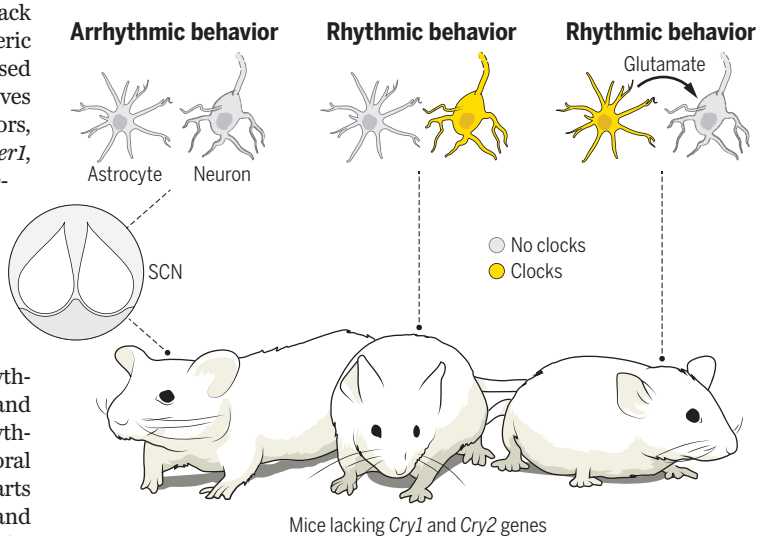
Even more surprising, rescue of the astrocyte clock caused robust rhythms in gene expression in the clockless neurons. In addition, the spatiotemporal wave across the SCN was restored, suggesting that network properties within the SCN pacemaker were rescued. Furthermore, rescue of the astrocyte clock in otherwise arrhythmic mice rescued the behavioral activity rhythms, such as periodic wheel-running, demonstrating that functional circadian clocks in the astrocytes are sufficient to generate a rhythmic animal (see the figure). Moreover, the free-running periods matched that of the endogenous astrocyte clock.

Brancaccio *et al.* determined that astrocytes with restored rhythms periodically released glutamate [a major glial neurotransmitter in the SCN (*12*)] and that this glutamate was required to restore the rhythms to the SCN neurons by somehow activating the existing SCN circuit. What is not clear from these studies is whether the neuronal rhythms depend on some component(s) of the circadian clock that remain in the absence of the two *Cry* genes or whether the periodic glutamate directly drives the rhythms. It has been shown that SCNs of mice in which *Cry1* and *Cry2* are ablated have some residual rhythmicity that quickly dissipates (*13*), suggesting that some pacemaker function is still present. Additionally, loss of the *Bmal1* gene in subsets of SCN neurons result in long periods and unstable rhythms, likely through loss of interneuronal coupling (*8*, *9*), suggesting that at least some components of the circadian clock are needed in neurons to enable normal behavior. Additional experiments using neurons that lack other components of the circadian clock will be necessary to answer these questions.

Although sufficient, astrocytes are not necessary for rhythmic behavior because neuron-only reintroduction of circadian clock genes also rescues circadian rhythms in mice, and astrocyte-specific perturbation of the circadian clock does not ablate rhythms, although it does alter the period length (*14*), suggesting that the normal clock requires interactions between these two cell types. The study of Brancaccio *et al.* supports the idea that the SCN has redundant and robust mechanisms for maintaining circadian rhythms, complementing earlier findings (*4*) that this master timekeeper is distinctly resilient to perturbation. Clearly, the importance of maintaining rhythmicity has resulted in the evolutionary selection of many solutions for maintaining circadian rhythms. ■

Astrocyte clocks can drive rhythms in mice

In arrhythmic mice, the circadian clock is genetically perturbed in all cells. Rhythmic behavior can be rescued by restoring the clock in astrocytes in the SCN, which periodically release glutamate. Restoring clocks in SCN neurons can also restore the circadian rhythms in these mice.



REFERENCES

1. M. Brancaccio *et al.*, *Science* **363**, 187 (2019).
2. D. R. Weaver, *J. Biol. Rhythms* **13**, 100 (1998).
3. M. H. Hastings *et al.*, *Nat. Rev. Neurosci.* **4**, 649 (2003).
4. A. C. Liu *et al.*, *Cell* **129**, 605 (2007).
5. C. Rosensweig, C. B. Green, *Eur. J. Neurosci.* 10.1111/ejn.14254 (2018).
6. E. D. Herzog, T. Hermanstyne, N. J. Smyllie, M. H. Hastings, *Cold Spring Harb. Perspect. Biol.* **9**, a027706 (2017).
7. S. S. Low-Zeddies, J. S. Takahashi, *Cell* **105**, 25 (2001).
8. M. Mieda *et al.*, *Neuron* **85**, 1103 (2015).
9. I. T. Lee *et al.*, *Neuron* **85**, 1086 (2015).
10. M. D. Edwards *et al.*, *Proc. Natl. Acad. Sci. U.S.A.* **113**, 2732 (2016).
11. M. Ukai-Tadenuma *et al.*, *Cell* **144**, 268 (2011).
12. M. Brancaccio *et al.*, *Neuron* **93**, 1420 (2017).
13. D. Ono, S. Honma, K. Honma, *Nat. Commun.* **4**, 1666 (2013).
14. C. F. Tso *et al.*, *Curr. Biol.* **27**, 1055 (2017).

10.1126/science.aav9706

GRAPHIC: V. ALTOUNIAN/*SCIENCE*

Downloaded from http://science.sciencemag.org/ on January 10, 2019

Published by AAAS

NEUROSCIENCE

Assembling human brain organoids

Three-dimensional assembloids can be used to study human development and disease

By **Sergiu P. Pașca**

Brain development is a remarkable self-organization process in which cells proliferate, differentiate, migrate, and wire to form functional neural circuits. In humans, this process takes place over a long fetal phase and continues into the postnatal period, but it is largely inaccessible for direct, functional investigation at a cellular level. Therefore, the features that make the human central nervous system unique and the sequence of molecular and cellular events underlying brain disorders remain largely uncharted. Human pluripotent stem (hPS) cells, including those obtained by reprogramming somatic cells, have the ability to self-organize and differentiate when grown in three-dimensional (3D) aggregates rather than in direct contact with a flat plastic surface (*1*). Such 3D neural cultures, also known as organoids and organ spheroids, recapitulate many aspects of human brain development in vitro (*1*) and have the potential to accelerate progress in human neurobiology. Here, I discuss the emerging approaches to produce brain assembloids—the next generation of brain organoids that combine multiple cell lineages in 3D. These cultures can be used to model interactions between various brain regions in vitro, and ultimately may be applied to understand the assembly of neural circuits and to capture complex cell-cell interactions in the brain.

Brain organoids have been generated from hPS cells to resemble the dorsal forebrain, which generates the cerebral cortex (see the figure). These cerebral cortical organoids contain glutamatergic neurons of various layers that are synaptically connected, and their generation is followed by the production and maturation of starlike glial cells, called astrocytes (*2*). During development in utero, the formation of specific brain regions is shaped by interactions with other brain regions through long-distance projections as well as by wiring locally into microcircuits with neurons that have migrated from other regions in the central nervous system. To capture these cell-cell interactions in vitro, ventral forebrain organoids that contain γ-aminobutyric acid (GABA)–ergic cortical interneurons can be combined with a dorsal forebrain organoid (*3*). GABAergic cortical neurons migrate, modify their morphology, and make synapses with cortical glutamatergic neurons, generating a functional neural network in a 3D cellular structure called a multiregion assembloid (*3*–*5*). This process of cortical interneuron migration takes place in late stages of human development, up to 2 years after birth, and assembloids of the ventral and dorsal forebrain offer a unique opportunity to study primate-specific features of GABAergic interneuron development as well as investigate how their migration may go awry, using cultures from patients with epilepsy or autism spectrum disorders (*3*). Moreover, this approach can be used to combine other region-specific organoids, such as the striatum and midbrain, to study glutamatergic and dopaminergic inputs to the basal ganglia and the spinal cord to model cortico-spinal projections, or combinations with the thalamus to model cortico-thalamic interactions and how this cross-talk shapes cortical circuits. However, more work is needed to reliably assess connectivity in vitro and to learn to what extent this platform can capture more subtle inter-brain regional changes associated with complex psychiatric disease.

Besides input from other brain regions, neural development and function is shaped by interactions with other cell types, which are often specified outside the nervous system, such as yolk sac–derived microglia, which are resident immune cells in the central nervous system, or mesoderm-derived blood vessels. It is increasingly recognized that neuroimmune and neurovascular interactions are important in brain development. These interactions can be modeled in vitro by adding primary or hPS cell–derived microglia and pericytes and brain endothelial cells (that compose blood vessels) to brain region–specific organoids at various stages of differentiation to form multilineage assembloids. For example, hPS cell–derived microglia-like cells have been integrated in cortical organoids that display aggregates of the β-amyloid (Aβ) protein, which is the main component in amyloid plaques, and have subsequently been used to model features of Alzheimer's disease (AD) (*6*). More specifically, microglia-like cells carrying the AD high-risk allele, apolipoprotein E4 variant (*APOE4*), embedded into 3D brain organoids showed longer processes and took up less Aβ than cells expressing the low-risk *APOE3* allele. Alternatively, primary microglia isolated from patient postmortem cerebral cortex could be integrated into brain organoids to investigate their function in neurodevelopmental or neurodegenerative disease. Glial cells, such as microglia and astrocytes, actively sculpt neural circuits and regulate synaptic plasticity by engulfing synapses, and assembloids containing human glial cells as well as neurons could be used to study the role of immune-related pathways in synapse elimination, such as understanding how variants in the complement *C4* gene regulate synapse function in humans and how they contribute to schizophrenia risk (*7*). Ultimately, multilineage assembloids could be used to elucidate fundamental questions in neuroglial cross-talk, such as: How do glial cells regulate synapse number and function in humans during development and in disease? How did human glial cells evolve to control synapse formation and elimination compared with other mammals, and how does this contribute to the unique features of the expanded human cerebral cortex that controls higher-order cognition and complex behaviors? Neural-glial interactions and chronic exposure in the context of late-onset neurodegenerative disorders will be more challenging to study because most assembloid cultures resemble early stages of development, and strategies for accelerating maturation in vitro are required.

Mutations in genes expressed in myeloid cells, such as monocytes and microglia, have been associated with neuropsychiatric diseases, but how dysfunction in immune cells influences brain function is unknown (*8*). Recently, a triculture 3D assembloid system that includes neurons, astrocytes, and microglia has been used to study neural-glial interactions and mimic neuroinflammation-like processes (*9*). Building on these efforts, multilineage brain assembloids could model cell-cell interactions using autologous immune cells, which carry the immunological history of the individual, such as exposure to various antigens. For example, how neurons in the hypothalamus producing the arousal-associated neuropeptide hypocretin are specifically lost in the severe sleep disorder narcolepsy is still unclear. Epidemiological studies and strong genetic association with human leukocyte antigen (*HLA*) and T cell recep-

Department of Psychiatry and Behavioral Sciences and Human Brain Organogenesis Program, Stanford University, Stanford, CA, USA. Email: spasca@stanford.edu

Downloaded from http://science.sciencemag.org/ on January 15, 2019

Published by AAAS

tor (*TCR*) genes suggest immune involvement (*10*). Hypothalamic organoids that contain neurons that produce hypocretin and other neural and glial populations could be assembled with immune cells harvested from the same narcolepsy patients to elucidate the sequence of cellular events leading to cell loss. Similarly, immune cells from patients with multiple sclerosis could be included in an autologous assembloid system that also includes myelin-producing oligodendrocytes to understand the pathological process of demyelination.

Other examples of multilineage assembloids are gut organoids that were combined with neural crest cells, which migrate into the organoid and differentiate to form a neural plexus that gives rise to rhythmic waves of activity (*11*), or cancer cells that can be assembled with brain organoids to investigate tumorigenesis in the nervous system. For instance, genetic manipulation of oncogenes and tumor suppressor genes was recently used to initiate and directly image tumorigenesis in a brain organoid system (*12*). Moreover, patient-derived tumor organoids were fused to brain organoids to study the cell biology of tumor invasion. This approach could be used to ask questions about metastasis and why some tumors are more aggressive than others.

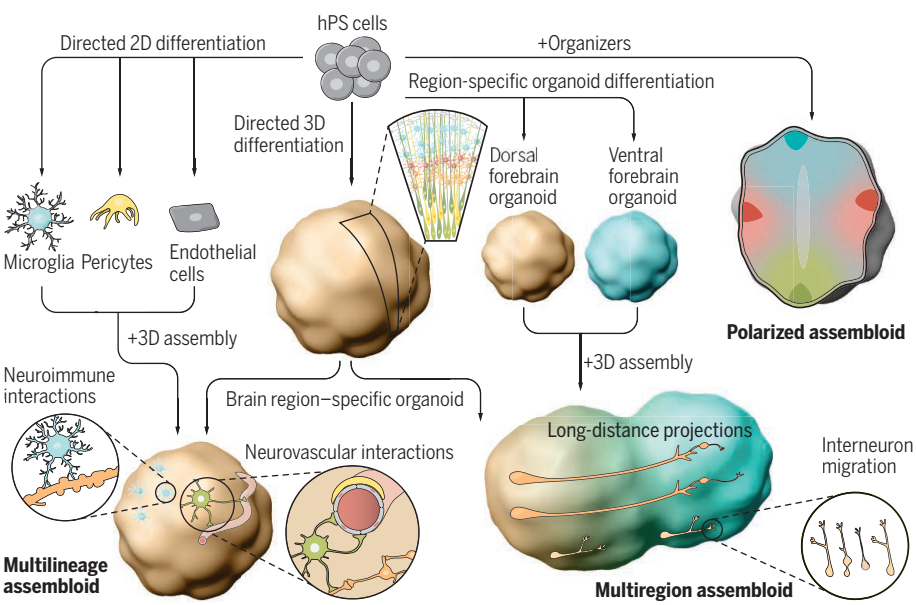
Moving forward, a key challenge in building and assembling human brain organoids in vitro is the ability to control polarity and obtain predictable 3D cellular architectures that recapitulate anatomical and functional aspects of the human brain. To form anteroposterior (head-to-tail) and dorsoventral (back-to-belly) axes in vivo, the neuroepithelium progressively subdivides into distinct regions under the influence of specialized groups of cells called organizers. These organizers instruct the cell fate and morphogenesis of neighboring cell populations by emitting molecular signals, and once this polarity has been established, the interactions necessary to form the central nervous system become possible. Future brain assembloids could include gel beads or tubes carrying morphogens or populations of organizer-like cells derived from hPS cells or isolated from animals to generate polarized assembloids. For example, cells resembling the floor plate region of the developing neural tube and expressing the morphogen sonic hedgehog (SHH) could be included to induce ventral cell identities, whereas roof plate–like cells that secrete the morphogens bone morphogenetic proteins (BMPs) and WNTs, could be used to specify dorsal fates.

Such strategies could allow the development of a polarized 3D spinal cord in vitro, for example, which would enable the exploration of regional diversity of neural and glial cells and how their specification is shaped by neural activity. This organoid could also be assembled with cortical organoids to study ascending and descending neural pathways in motor processing and with muscle tissue to develop human models of neuromuscular function and cortical control. Similarly, other morphogen-secreting regions in the developing central nervous system, such as prechordal plate–like cells and cortical hem-like cells, could be used to specify and spatially organize within the same organoid subdomains of the forebrain. Lastly, the recent differentiation in vitro from hPS cells of groups of cells that can organize axes in the early embryo (*13*) will enable the dissection of the mechanisms behind the formation of embryo body plan and neural axis in the human nervous system. However, as 3D cell cultures develop polarity, the use of in situ molecular biology will be essential for identifying cell fates and cell states with high resolution over time and for avoiding biases due to cell dissociation and other processing steps during assembloid manipulation.

Although a comprehensive understanding of the programs driving the development of all cells and regions in the central nervous system is lacking, identifying the minimal signals necessary for specification and self-organization will be essential in developing other region-specific organoids as well as polarized multiregion brain structures in vitro. However, even if this is achieved for a number of domains or regions of the nervous system, the sensory input that shapes the developing brain is missing, and this aspect may be critical to capture subtle functional imbalances underlying psychiatric disorders. Transplantation of intact brain organoids into mammalian brain tissue (*14*) could have applications for regenerative medicine and constitutes one way by which integration into larger neural networks that receive sensory input could be achieved in the future. Understanding the mechanisms of psychiatric disorders will require more accurate models of the human brain, but as approaches for deriving brain tissue in the lab are further refined to recapitulate in vivo function, more discussions about the ethical implications will be needed (*15*). ■

Generating assembloids

Brain region–specific organoids are generated from human pluripotent stem (hPS) cells and can be assembled with other cell types (multilineage assembloids), with other organoids (multiregion assembloids), or with morphogens or organizer-like cells (polarized assembloids). Brain organoids and assembloids can be used to model complex cell-cell interactions and neural circuit formation in the human nervous system.



GRAPHIC: N. DESAI/*SCIENCE*

REFERENCES

1. S. P. Paşca, *Nature* **553**, 437 (2018).
2. A. M. Paşca *et al.*, *Nat. Methods* **12**, 671 (2015).
3. F. Birey *et al.*, *Nature* **545**, 54 (2017).
4. J. A. Bagley *et al.*, *Nat. Methods* **14**, 743 (2017).
5. Y. Xiang *et al.*, *Cell Stem Cell* **21**, 383 (2017).
6. Y. T. Lin *et al.*, *Neuron* **98**, 1294 (2018).
7. A. Sekar *et al.*, *Nature* **530**, 177 (2016).
8. J. Herz *et al.*, *Immunity* **46**, 943 (2017).
9. J. Park *et al.*, *Nat. Neurosci.* **21**, 941 (2018).
10. B. R. Kornum *et al.*, *Curr. Opin. Neurobiol.* **21**, 897 (2011).
11. M. J. Workman *et al.*, *Nat. Med.* **23**, 49 (2017).
12. J. Ogawa *et al.*, *Cell Reports* **23**, 1220 (2018).
13. I. Martyn *et al.*, *Nature* **558**, 132 (2018).
14. A. A. Mansour *et al.*, *Nat. Biotechnol.* **36**, 432 (2018).
15. N. A. Farahany *et al.*, *Nature* **556**, 429 (2018).

10.1126/science.aau5729

Downloaded from http://science.sciencemag.org/ on January 15, 2019

Published by AAAS

CLIMATE CHANGE

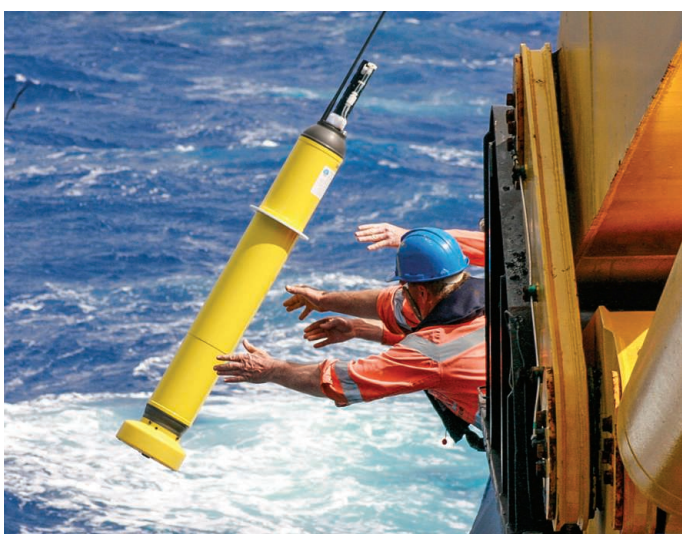
How fast are the oceans warming?

Observational records of ocean heat content show that ocean warming is accelerating

By Lijing Cheng[1], John Abraham[2], Zeke Hausfather[3], Kevin E. Trenberth[4]

Climate change from human activities mainly results from the energy imbalance in Earth's climate system caused by rising concentrations of heat-trapping gases. About 93% of the energy imbalance accumulates in the ocean as increased ocean heat content (OHC). The ocean record of this imbalance is much less affected by internal variability and is thus better suited for detecting and attributing human influences (*1*) than more commonly used surface temperature records. Recent observation-based estimates show rapid warming of Earth's oceans over the past few decades (see the figure) (*1*, *2*). This warming has contributed to increases in rainfall intensity, rising sea levels, the destruction of coral reefs, declining ocean oxygen levels, and declines in ice sheets; glaciers; and ice caps in the polar regions (*3*, *4*). Recent estimates of observed warming resemble those seen in models, indicating that models reliably project changes in OHC.

The Intergovernmental Panel on Climate Change's Fifth Assessment Report (AR5), published in 2013 (*4*), featured five different time series of historical global OHC for the upper 700 m of the ocean. These time series are based on different choices for data processing (see the supplementary materials). Interpretation of the results is complicated by the fact that there are large differences among the series. Furthermore, the OHC changes that they showed were smaller than those projected by most climate models in the Coupled Model Intercomparison Project 5 (CMIP5) (*5*) over the period from 1971 to 2010 (see the figure).



Scientists deploy an Argo float. For over a decade, more than 3000 floats have provided near-global data coverage for the upper 2000 m of the ocean.

Since then, the research community has made substantial progress in improving long-term OHC records and has identified several sources of uncertainty in prior measurements and analyses (*2*, *6*–*8*). In AR5, all OHC time series were corrected for biases in expendable bathythermograph (XBT) data that had not been accounted for in the previous report (AR4). But these correction methods relied on very different assumptions of the error sources and led to substantial differences among correction schemes. Since AR5, the main factors influencing the errors have been identified (*2*), helping to better account for systematic errors in XBT data and their analysis.

Several studies have attempted to improve the methods used to account for spatial and temporal gaps in ocean temperature measurements. Many traditional gap-filling strategies introduced a conservative bias toward low-magnitude changes (*9*). To reduce this bias, Domingues *et al.* (*10*) used satellite altimeter observations to complement the sparseness of in situ ocean observations and update their global OHC time series since 1970 for the upper 700 m. Cheng *et al.* (*2*) proposed a new gap-filling method that used multimodel simulations to provide an improved prior estimate and error covariance. This method allowed propagation of information from data-rich regions to the data gaps (data are available for the upper 2000 m since 1940). Ishii *et al.* (*6*) completed a major revision of their estimate in 2017 to account for the previous underestimation and also extended the analysis down to 2000 m and back to 1955. Resplandy *et al.* (*11*) used ocean warming outgassing of O_2 and CO_2, which can be isolated from the direct effects of anthropogenic emissions and CO_2 sinks, to independently estimate changes in OHC over time after 1991.

These recent observation-based OHC estimates show highly consistent changes since the late 1950s (see the figure). The warming is larger over the 1971–2010 period than reported in AR5. The OHC trend for the upper 2000 m in AR5 ranged from 0.20 to 0.32 W m^{-2} during this period (*4*). The three more contemporary estimates that cover the same time period suggest a warming rate of 0.36 ± 0.05 (*6*), 0.37 ± 0.04 (*10*), and 0.39 ± 0.09 (*2*) W m^{-2}. [Note that the analysis in Domingues *et al.* (*10*) is combined with that in Levitus *et al.* (*12*) for 700 to 2000 m to produce a 0 to 2000 m time series.] All four recent studies (*2*, *6*, *10*, *11*) show that the rate of ocean warming for the upper 2000 m has accelerated in the decades after 1991 from 0.55 to 0.68 W m^{-2} (calculations provided in the supplementary materials).

Multiple lines of evidence from four independent groups thus now suggest a stronger observed OHC warming. Although climate model results (see the supplementary materials) have been criticized during debates about a "hiatus" or "slowdown" of global mean surface temperature, it is increasingly clear that the pause in surface warming was at least in part due to the redistribution of heat within the climate system from Earth surface into the ocean interiors (*13*). The recent OHC warming estimates (*2*, *6*, *10*, *11*) are quite similar to the average of CMIP5 models, both for the late 1950s until present and during the 1971–2010 period highlighted in AR5 (see the figure). The ensemble average of the models has a linear ocean warming trend of 0.39 ± 0.07 W m^{-2} for the upper 2000 m

[1]International Center for Climate and Environment Sciences, Institute of Atmospheric Physics, Chinese Academy of Sciences, Beijing 100029, China. [2]School of Engineering, University of St. Thomas, 2115 Summit Avenue, St. Paul, MN, USA. [3]Energy and Resources Group, University of California, Berkeley, 310 Barrows Hall, Berkeley, CA 94720, USA. [4]National Center for Atmospheric Research, Post Office Box 3000, Boulder, CO 80307, USA. Email: chenglij@mail.iap.ac.cn

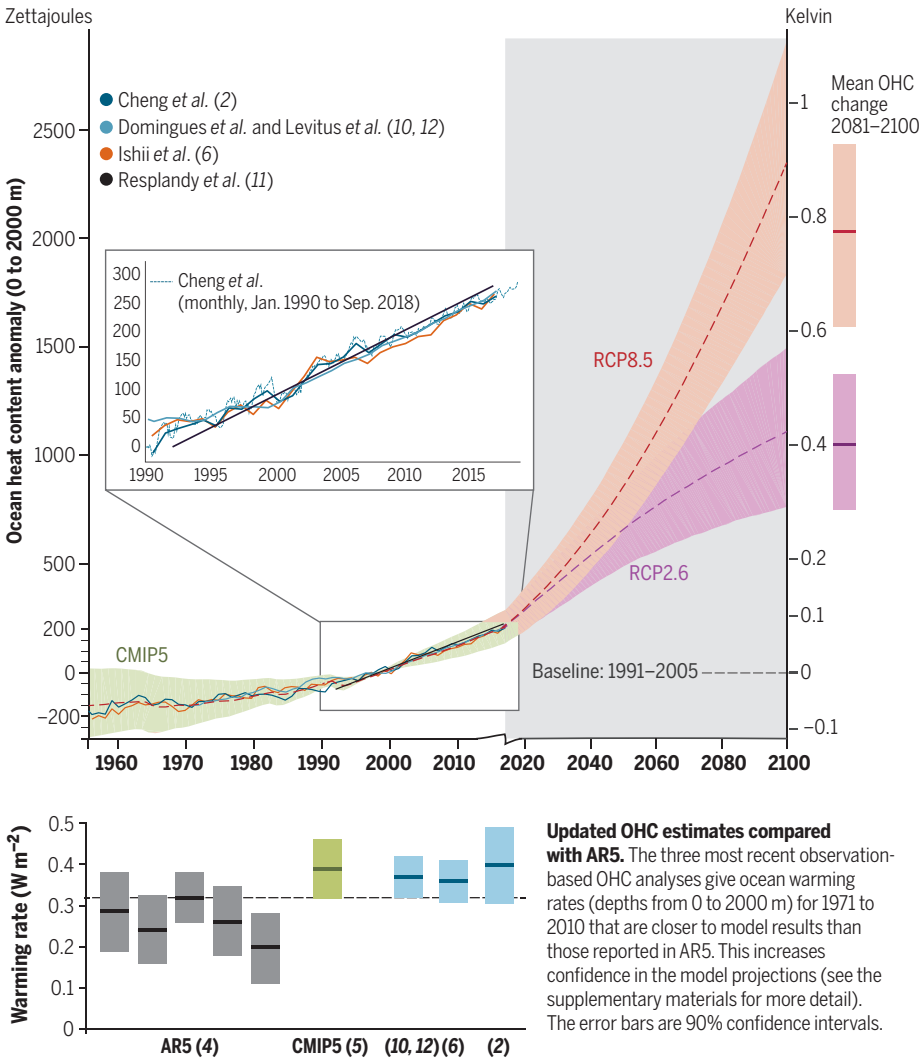
Downloaded from http://science.sciencemag.org/ on January 15, 2019

PHOTO: ALICIA NAVIDAD/CSIRO

Published by AAAS

Past and future ocean heat content changes

Annual observational OHC changes are consistent with each other and consistent with the ensemble means of the CMIP5 models for historical simulations pre-2005 and projections from 2005–2017, giving confidence in future projections to 2100 (RCP2.6 and RCP8.5) (see the supplementary materials). The mean projected OHC changes and their 90% confidence intervals between 2081 and 2100 are shown in bars at the right. The inset depicts the detailed OHC changes after January 1990, using the monthly OHC changes updated to September 2018 [Cheng *et al*. (*2*)], along with the other annual observed values superposed.



Updated OHC estimates compared with AR5. The three most recent observation-based OHC analyses give ocean warming rates (depths from 0 to 2000 m) for 1971 to 2010 that are closer to model results than those reported in AR5. This increases confidence in the model projections (see the supplementary materials for more detail). The error bars are 90% confidence intervals.

from 1971–2010 compared with recent observations ranging from 0.36 to 0.39 W m^{-2} (see the figure).

The relatively short period after the deployment of the Argo network (see the photo) in the early 2000s has resulted in superior observational coverage and reduced uncertainties compared to earlier times. Over this period (2005–2017) for the top 2000 m, the linear warming rate for the ensemble mean of the CMIP5 models is 0.68 ± 0.02 W m^{-2}, whereas observations give rates of 0.54 ± 0.02 (*2*), 0.64 ± 0.02 (*10*), and 0.68 ± 0.60 (*11*) W m^{-2}. These new estimates suggest that models as a whole are reliably projecting OHC changes.

However, some uncertainties remain, particularly for deep and coastal ocean regions and in the period before the deployment of the Argo network. It is important to establish a deep ocean observation system to monitor changes below 2000 m (*14*). It is also essential to improve the historical record, for example, by recovering undigitized OHC observations.

Simulations of future climate use a set of scenarios or plausible radiative forcing pathways based on assumptions about demographic and socioeconomic development and technological changes (*5*). Two scenarios shown in the figure project a substantial warming in the 21st century. For the Representative Concentration Pathways (RCP) 2.6 scenario, the models project an ocean warming (0 to 2000 m) of 1037 zettajoules (ZJ) (~0.40 K) at the end of the 21st century (mean of 2081–2100 relative to 1991–2005); this pathway is close to the Paris Agreement goal of limiting global warming to well below 2°C. For the RCP8.5 scenario, a business-as-usual scenario with high greenhouse gas emissions, the models project a warming of 2020 ZJ (~0.78 K). This level of warming would have major impacts on ocean ecosystems and sea level rise through thermal expansion; 0.78 K warming at 2100 is roughly equal to a sea level rise of 30 cm. This is in addition to increased sea level rise caused by land ice melt.

The fairly steady rise in OHC shows that the planet is clearly warming. The prospects for much higher OHC, sea level, and sea-surface temperatures should be of concerngiven the abundant evidence of effects on storms, hurricanes, and the hydrological cycle, including extreme precipitation events (*3*, *15*). There is a clear need to continue to improve the ocean observation and analysis system to provide better estimates of OHC, because it will enable more refined regional projections of the future. In addition, the need to slow or stop the rates of climate change and prepare for the expected impacts is increasingly evident. ■

REFERENCES AND NOTES

1. L. Cheng *et al.*, *Eos (Wash. D.C.)* **98**, 14 (2018).
2. L. Cheng *et al.*, *Sci. Adv.* **3**, e1601545 (2017).
3. K. E. Trenberth, A. Dai, R. M. Rasmussen, D. B. Parsons, *Bull. Am. Meteorol. Soc.* **84**, 1205 (2003).
4. M. Rhein *et al.*, in *Climate Change 2013: The Physical Science Basis. Contribution of Working Group I to the Fifth Assessment Report of the Intergovernmental Panel on Climate Change*, T. F. Stocker *et al.*, Eds. (Cambridge Univ. Press, 2013), pp. 215–315.
5. K. E. Taylor, R. J. Stouffer, G. A. Meehl, *Bull. Am. Meteorol. Soc.* **93**, 485 (2012).
6. M. Ishii *et al.*, *Sci. Online Lett. Atmos.* **13**, 163 (2017).
7. T. Boyer *et al.*, *J. Clim.* **29**, 4817 (2016).
8. J. P. Abraham *et al.*, *Rev. Geophys.* **51**, 450 (2013).
9. P. Durack, P. J. Gleckler, F. Landerer, K. E. Taylor, *Nat. Clim. Chang.* **4**, 999 (2014).
10. C. M. Domingues *et al.*, *Nature* **453**, 1090 (2008).
11. L. Resplandy *et al.*, *Nature* **563**, 105 (2018).
12. S. Levitus *et al.*, *Geophys. Res. Lett.* **39**, L10603 (2012).
13. M. A. Balmaseda, K. E. Trenberth, E. Källén, *Geophys. Res. Lett.* **40**, 1754 (2013).
14. G. C. Johnson, J. M. Lyman, S. G. Purkey, *J. Atmos. Ocean. Technol.* **32**, 2187 (2015).
15. K. E. Trenberth, L. Cheng, P. Jacobs, Y. Zhang, J. T. Fasullo, *Earth's Future* **6**, 730 (2018).

ACKNOWLEDGMENTS

This study is supported by the National Key R&D Program of China (2017YFA0603202). The National Center for Atmospheric Research (NCAR) is sponsored by the National Science Foundation. We thank the climate modeling groups (listed in table S1) for producing and making available their model output, and we acknowledge J. Fasullo for calculating OHC in CMIP5 models and making the data available to the authors. Institute of Atmospheric Physics data and the CMIP5 time series are available at http://159.226.119.60/cheng/.

SUPPLEMENTARY MATERIALS

www.sciencemag.org/content/363/6423/128/suppl/DC1

10.1126/science.aav7619

GRAPHIC: N. CARY/SCIENCE

Downloaded from http://science.sciencemag.org/ on January 15, 2019

Published by AAAS

POLICY FORUM

SCIENCE EDUCATION

The MOOC pivot

What happened to disruptive transformation of education?

By **Justin Reich** *and* **José A. Ruipérez-Valiente**

When massive open online courses (MOOCs) first captured global attention in 2012, advocates imagined a disruptive transformation in postsecondary education. Video lectures from the world's best professors could be broadcast to the farthest reaches of the networked world, and students could demonstrate proficiency using innovative computer-graded assessments, even in places with limited access to traditional education. But after promising a reordering of higher education, we see the field instead coalescing around a different, much older business model: helping universities outsource their online master's degrees for professionals (*1*). To better understand the reasons for this shift, we highlight three patterns emerging from data on MOOCs provided by Harvard University and Massachusetts Institute of Technology (MIT) via the edX platform: The vast majority of MOOC learners never return after their first year, the growth in MOOC participation has been concentrated almost entirely in the world's most affluent countries, and the bane of MOOCs—low completion rates (*2*)—has not improved over 6 years.

MOOC providers explored several potential revenue models in their first years, but selling certificates of completion was the most prominent. In early public talks (*3*, *4*), Coursera cofounder Daphne Koller described their business model as a blue ccean strategy (*5*): Rather than focus on existing consumers of higher education, they would sustain a new global service by converting nonconsumers of higher education—especially in places with limited access—into online learners at the world's best universities. MOOC providers would make learning materials freely and widely available and would earn revenue from a portion of learners who purchased the opportunity to earn verified certificates and credentials.

Data on enrollment, intention, and completion show the challenges with this model.

Massachusetts Institute of Technology, Cambridge, MA, USA. Email: jreich@mit.edu

We analyzed data from all MOOCs taught on edX by its founding partners MIT and Harvard University, from the start of the initiative in October 2012 to May 2018 (organized into annual cohorts starting in June). The dataset includes 565 course iterations from 261 different courses, with a combined 12.67 million course registrations from 5.63 million learners. Data from other edX partners or MOOC providers might reveal different dynamics, but we have a detailed view of two of the largest course providers.

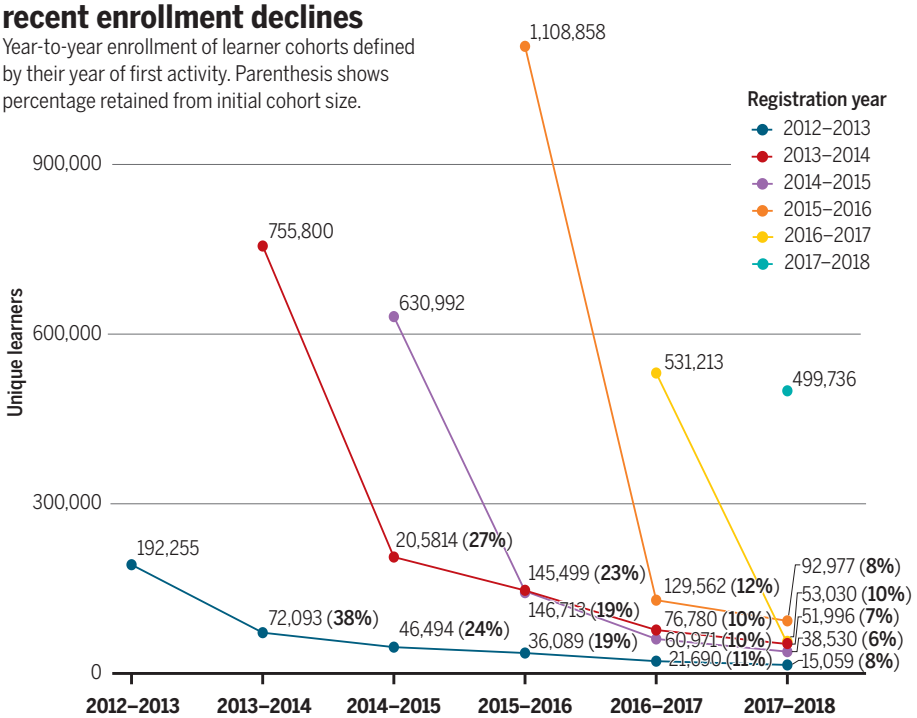
MOOC researchers realized early on that most MOOC registrants leave soon after enrollment. Of those who register for a course, 52% never enter the courseware (table S4), and attrition typically remains high in the first 2 weeks of a course (*2*). We see similar patterns when looking at engagement over multiple years. New individual learners increased from 2012 to 2016 but have declined since (see the first figure). The largest initial cohort was in 2015 to 2016, but only 12% of those 1.1 million individual learners took an additional HarvardX or MITx course in the following year. Second-year retention rates have declined with every cohort, from 38% in the first cohort to 7% in the 2016–2017 cohort. A growing global demand for ongoing learning from MOOCs that might have maintained a blue ocean strategy never materialized.

It was clear from the first few years of MOOC research that MOOCs disproportionately drew their learners from affluent countries and neighborhoods, and markers of socioeconomic status were correlated with greater persistence and certification (*6*, *7*). In 2012 to 2013, 80% of learners came from countries rated with high or very high United Nations Human Development Index ratings (*8*). That proportion grew slightly through 2015 to 2016, so that the majority of new registrations and certifications came from the world's most affluent countries (see the second figure). Rather than creating new pathways at the margins of global higher education, MOOCs are primarily a complementary asset for learners within existing systems.

Last, MOOCs' low completion rate has barely budged (fig. S1), despite 6 years of investment in course development and learning research (*9*). A strategy that depends on bringing new learners into higher education cannot succeed if educational institutions cannot support learners in converting their time and financial investment into completing a course to earn a credential with labor market value.

Consistently low retention and recent enrollment declines

Year-to-year enrollment of learner cohorts defined by their year of first activity. Parenthesis shows percentage retained from initial cohort size.



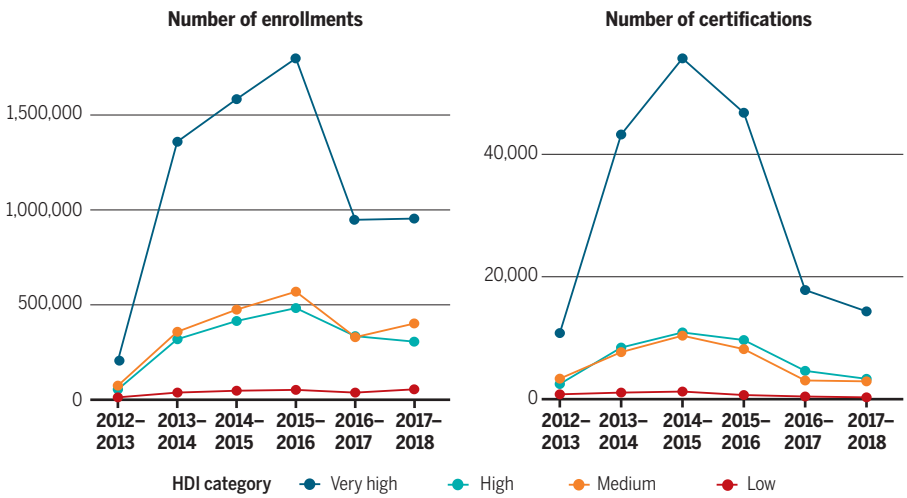
GRAPHIC: N. CARY/*SCIENCE*

Downloaded from http://science.sciencemag.org/ on January 15, 2019

Published by AAAS

Disproportionate participation from affluent countries

Number of enrollments and certifications per year divided into quartiles based on the UN Human Development Index (HDI) rating of each registrant's home country.



In light of these trends, financial sustainability for MOOC platforms may depend on reaching smaller numbers of people with greater financial means that are already embedded in higher-education systems rather than bringing in new nonconsumers from the margins.

In October 2018, edX became the last of the major MOOC providers to announce partnerships with universities to offer fully online professional master's degrees (*10*), 5 years after Udacity made the first such partnership with Georgia Tech. EdX's move into fully online master programs was followed by their December 2018 decision—mirroring earlier decisions by Coursera and Udacity—to begin building paywalls around their previously freely available content (*11*).

In these initiatives, MOOC providers will compete with well-established, for-profit companies in helping universities to outsource their online degrees. For two decades, a class of companies called "online program managers" or "school-as-a-service" companies—Pearson Embanet, 2U, and Wiley Education Services—have supported colleges in creating online degrees (*1*). Universities choose how much of the total student experience to outsource to these providers, who offer services that include marketing and recruitment, admissions, online course management, curriculum design, and course instruction and assessment. School-as-a-service providers typically earn revenue by taking a fraction of the tuition of each student enrolled.

MOOC providers are reorienting to compete directly with these companies in one market segment: professional master's degrees, credentialed by near-top universities, in fields with well-established return on investment, such as data science, computer programming, business, and related fields. The primary competitive advantage of MOOCs relative to established school-as-a-service providers involves cutting labor costs through automation. Many "traditional" online programs include small class sizes, synchronous sessions with instructors, and human-graded assignments. Many degrees offered by universities with the technology and support of Coursera and edX will be one-half or one-quarter as expensive as typical U.S. professional online credentials, with the bulk of savings coming from a combination of larger class sizes, fewer or no synchronous sessions, reduced contact with instructors, and more autograded assignments (*12*).

Because MOOC platforms support programs that look more like "traditional" online higher education, the literature on online learning can provide guidance. By most indications, students typically do worse in online courses than in on-campus courses, and the challenges of online learning are particularly acute for the most vulnerable populations of first-generation college students, students from low-income families, and underrepresented minorities (*13*). If low-cost, MOOC-based degrees end up recruiting the kinds of students who have historically been poorly served by online degree programs, student support programs will be vital. Some recent research has explored online and text-message–based interventions for supporting these students, but most research suggests that human connections through advisers, tutors, and peer groups provide the most important student supports (*14*). These human supports will push against lower tuition costs. MOOC-based degree providers may find that highly effective online learning for diverse populations costs about the same to provide as highly effective residential learning (*12*).

MOOCs will not transform higher education and probably will not disappear entirely. Rather, they will provide new supports for specific niches within already existing education systems, primarily supporting already educated learners. The 6-year saga of MOOCs provides a cautionary tale for education policy-makers facing whatever will be the next promoted innovation in education technology, be it artificial intelligence or virtual reality or some unexpected new entrant. New education technologies are rarely disruptive but instead are domesticated by existing cultures and systems. Dramatic expansion of educational opportunities to underserved populations will require political movements that change the focus, funding, and purpose of higher education; they will not be achieved through new technologies alone. ■

GRAPHIC: N. CARY/*SCIENCE*

REFERENCES AND NOTES

1. P. Hill, *Educause Review* **47**, PP (2012).
2. J. Reich, MOOC completion and retention in the context of student intent. *Educause Rev.* (2014); https://er.educause.edu/articles/2014/12/mooc-completion-and-retention-in-the-context-of-student-intent.
3. W. C. Kim, R. Mauborgne, *Calif. Manage. Rev.* **47**, 105 (2005).
4. D. Koller, "The Online Revolution: Learning Without Limits," in Proceedings of the 20th International Conference for Online Learning (2013); review retrieved from https://sloanc2013.wordpress.com/2013/11/21/moocs-the-blue-ocean-strategy.
5. M. Trucano, MOOCs in Africa. *EduTech* (2013); http://blogs.worldbank.org/edutech/moocs-in-africa.
6. J. D. Hansen, J. Reich, *Science* **350**, 1245 (2015).
7. R. F. Kizilcec, A. J. Saltarelli, J. Reich, G. L. Cohen, *Science* **355**, 251 (2017).
8. United Nations (UN), *Human Development Indices and Indicators: 2018 Statistical Update* (UN, 2018); http://hdr.undp.org/sites/default/files/hdr2018_technical_notes.pdf.
9. J. Reich, *NAE Bridge* **46**, 29 (2016).
10. A. Agarwal, Fully online, top-ranked master's degrees now available on edX. *edX blog* (2018); https://blog.edx.org/fully-online-top-ranked-masters-degrees-now-available-edx.
11. A. Agarwal, Updates to our platform: Achieving long-term sustainability. *edX blog* (2018); https://blog.edx.org/updates-platform-achieving-long-term-sustainability.
12. P. Hill, Coursera CEO interview: Betting on OPM market and shift to low-cost masters degrees. *E-literate* (2018); https://mfeldstein.com/coursera-ceo-interview-betting-on-opm-market-and-shift-to-low-cost-masters-degrees.
13. D. Xu, S. S. Jaggars, *J. Higher Educ.* **85**, 633 (2014).
14. D. Xu, S. Solanki, P. McPartlan, B. Sato, *Educ. Res.* **47**, 435 (2018).
15. G. Lopez, D. T. Seaton, A. Ang, D. Tingley, I. Chuang, Proceedings of the Fourth ACM Conference on Learning @ Scale, 10.1145/3051457.3053980 (2017).

ACKNOWLEDGMENTS

Funding: No specific funding sources supported this commentary. **Author contributions:** J.R. conceptualized the paper, wrote the original draft, and revised the paper. J.A.R.-V. conceptualized the paper, conducted data analysis, and revised the paper. **Competing interests:** Authors declare no competing interests. **Data and materials availability:** Data are described in the supplementary materials.

SUPPLEMENTARY MATERIALS

www.sciencemag.org/content/363/6423/130/suppl/DC1

10.1126/science.aav7958

Downloaded from http://science.sciencemag.org/ on January 15, 2019

Published by AAAS



ENERGY POLICY

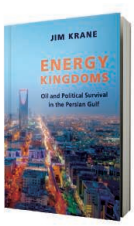
Cheap oil vs. climate change

The Gulf struggles to reform subsidies as temperatures and domestic energy demand rise

By **Miriam R. Aczel**

Since the discovery of oil in the 1930s, the six Gulf monarchies—Saudi Arabia, Qatar, Kuwait, Oman, Bahrain, and the United Arab Emirates—have become known for their seemingly endless supply of cheap energy and a growing domestic appetite for it. However, in the face of a changing climate, the very policies that led to their development and prosperity are today posing a threat as the region faces record-breaking temperatures. Jim Krane's compelling *Energy Kingdoms* takes readers inside this critical energy conundrum.

Krane evaluates the forces behind the Gulf region's "feverish demand for its chief export commodity" and argues that the monarchies' economic and political systems have created contradictory phenomena: Subsidization of energy, a key political institution, undermines oil and gas exporting, their main economic institution. "[L]ong term, these two crucial components of governance cannot remain in conflict. Either the political structures will bend or the economy will yield."



Energy Kingdoms
Jim Krane
Columbia University Press, 2019. 220 pp.

Before the discovery of oil, the geographic isolation of the Arabian Peninsula enabled the Gulf sheikdoms to develop "a robust tribal culture and distributional autocratic rule" that would make them ideal hosts for commercial oil development because the autocracies allowed for direct negotiation with rulers. Moreover, oil in these regions was relatively close to the surface, and mineral rights were held by the state.

By 1973, the Organization of Petroleum Exporting Countries (OPEC) controlled 51% of global oil output. That year, the Gulf OPEC members tested their market power by raising oil prices and exercised their collective power by initiating a targeted oil embargo. Krane explains how this reversed existing trade terms, leading to frantic attempts by importing countries to reduce Middle East "dependence" and gain "energy security," buzzwords that endure today.

Overseas profits meant that Gulf states did not need to raise income through taxation. The kingdoms began to subsidize internal energy services, including electricity, water, and fuel, thus widening the difference between these commodities' local costs and their overseas selling prices. As their populations grew more prosperous, the subsidies were no longer needed, but the states continued to provide them. "Subsidies, ruling families learned, are sticky: easy to hand out, much tougher to retract," observes Krane.

Krane reviews four policy options available to the monarchies, who today face an ever-growing increase in domestic demand for energy. These options include (i) to invest upstream or increase oil production; (ii) to diversify energy supply through the development of alternate energy sources; (iii) to diversify economies beyond hydrocarbons; or (iv) to reduce demand, allowing maintenance of export levels. Currently, the monarchies partially exercise all four options, but without retracting subsidies, reducing demand has proven particularly difficult.

In 2010, Iran and Dubai launched ambitious energy price reforms to manage the impacts of domestic subsidies. The lessons Krane draws from these cases are that governments must allow public discussion of proposals ("citizens are more likely to get behind painful policy if it's explained and makes sense") and that policy-makers are likely overly cautious; if rulers "level with their people," citizens may be more willing to accept adversity, as long as it is distributed fairly.

But Krane concludes that there is a more important energy problem facing the Gulf than responding to increased demand. Climate change, he writes, "represents a potential catastrophe for all of humanity, but the Gulf monarchies play starring roles as both major perpetrators and early victims." Because fossil fuels are responsible for the majority of greenhouse gas emissions leading to climate change, reducing emissions is crucial.

The sustainability of both the Gulf's economy and its climate cannot be guaranteed unless the energy subsidies are reformed, according to Krane. Flexibility in policy will be crucial as the autocracies prepare for another chaotic change period: the "post-oil age." Ultimately, Krane posits that the Gulf monarchies will need to diversify their economies in order to remain viable—a change to the states' status quo.

In the end, *Energy Kingdoms* provides a fascinating look at the double-edged sword that is the Gulf monarchies' greatest resource. The states face an extraordinary challenge as "[t]he magical fluid that dragged them from poverty and isolation just a few short generations ago now threatens to render their already intense climate intolerable." How they choose to proceed will affect the region and the world at large for generations to come. ■

10.1126/science.aav7012

Energy subsidies helped cities like Dubai flourish, but fossil fuels may also be their downfall.

PHOTO: ISTOCK.COM/RASTISLAVSEDLAK

The reviewer is at the Centre for Environmental Policy, Imperial College London, London SW7 2AZ, UK. Email: miriam.aczel14@imperial.ac.uk

Downloaded from http://science.sciencemag.org/ on January 10, 2019

Published by AAAS

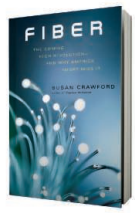
TELECOMMUNICATIONS

The future is fiber

Faster, cheaper, and more versatile than traditional telecom hardware, U.S. fiber networks still face policy hurdles

By **Viktor Mayer-Schönberger**

Fiber
The Coming Tech Revolution—And Why America Might Miss It
Susan Crawford
Yale University Press, 2018. 260 pp.



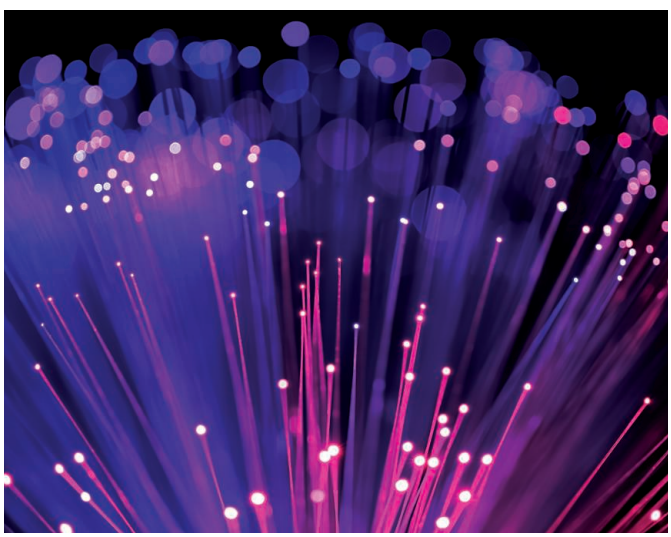
In her latest book, *Fiber*, legal scholar Susan Crawford writes about the role of fiber optic cables as the enormously capable conduits of digital data flows. According to Crawford, fiber is the technological enabler that affords true high-speed internet connectivity. But even though the technology is well understood, incumbent telecommunications providers in the United States have so far failed to bring fiber to most homes.

This has locked the American people into slow and outdated internet connections that are grossly overpriced, especially outside major urban areas, stifling innovation and economic growth and perpetuating social, economic, and geographic inequalities. And whereas in other nations, from Singapore to Sweden, regulators have worked to make fiber available and affordable for many, in the United States, federal and state policies have acted as impediments to widespread fiber availability.

It's a shocking reality of our times that in the United States, the cradle of the internet revolution, few have unhindered access to the fruits of that revolution. Crawford's narrative is a damning indictment, grounded in facts, and a critically important story. But *Fiber* also offers a way out of connectivity misery, and as the book title suggests, bringing fiber into homes is the crucial element.

Even for those familiar with the subject, *Fiber* offers a number of valuable insights. Crawford reveals, for example, that we cannot innovate a work-around to compensate for the lack of fiber. She explains why in the context of so-called "5G" mobile connectivity, the wireless transmission technology that is the next step after the currently used Long-Term Evolution standard. But the point she makes is generalizable: The more data we want to convey, the fatter the "pipes" we need to deliver it all. In the wireless context, this translates into more wireless spectrum, higher frequencies, and dramatically more transmission stations (which all need to be connected to a fast-speed data network). Compared with over-the-air transmission, fiber is far more powerful and versatile.

A second and related point in favor of fiber's superiority is its inherent upgradeability: Even decades-old fiber strands can be transformed into the fastest data highways by swapping the equipment at the end points that translates data into laser pulses. Much like with the original internet, the "intelligence" of fiber is on either end, not in the physical infrastructure that's buried deep in the ground or strung high on telephone poles. That makes fiber networks surprisingly future-proof, a crucial advantage over alternative transmission technologies.



Despite its benefits, telecom companies have been resistant to invest in fiber.

Perhaps Crawford's most important point, however, has less to do with the technological viability of fiber and more to do with a different sort of challenge. The real obstacle to widespread fiber adoption in the United States, she argues, is regulatory policy. Incumbent telecommunications companies install outdated copper or coaxial cables into the homes of most of their customers and have thus far shown little interest in investing in high-speed fiber. To insulate themselves from the forces of competition, they have successfully lobbied federal and state legislatures to maintain innumerous hurdles for would-be fiber competitors.

After a few years of investing in fiber networks, even Google, with its deep financial pockets, has scaled back its ambition. This has left thousands of small and medium-sized communities without real high-speed access to the internet. In response, some municipalities and local cooperatives have taken over where Google and other alternative providers left off.

Crawford is at her best when describing the astonishingly innovative organizational setups of community-based fiber initiatives and how they came about, when detailing the machinations of telecom incumbents and their lobbyists to cripple these initiatives, and when explaining how local champions of fiber have sometimes been able to neutralize attempts to derail them.

Quite often, the Goliaths still win. But Crawford also portrays the Davids that succeeded. In doing so, she makes clear that there is no one-sized solution that fits all contexts. Rather, local victory requires a combination of guts and persistence combined with an inclusive plan that addresses the real needs of the community in question.

The final ingredient required for successful fiber implementation, Crawford suggests, is leadership. This is where I have a small gripe with the book. In Singapore, one of Crawford's key examples of comprehensive fiber connectivity, it was a tireless American named Andrew Haire, working in a key role in the Singapore telecommunications regulatory agency, who championed and ensured a regulatory structure that kept connectivity high, rates low, and incumbents in check. Unfortunately, Haire isn't mentioned in *Fiber*, even though his is an example that offers telling evidence that when national and state politicians fail to step up to the plate, others can lead. ■

10.1126/science.aav7139

The reviewer is at the Oxford Internet Institute, University of Oxford, Oxford OX1 3JS, UK. Email: viktor.ms@oii.ox.ac.uk

PHOTO: ISTOCK.COM/VIORIKA

Downloaded from http://science.sciencemag.org/ on January 10, 2019

Published by AAAS

LETTERS

Edited by **Jennifer Sills**

Integrated data could augment resilience

The massive November 2018 Camp Fire set the record for the deadliest and most destructive wildfire in California's history (*1*). By the time the blaze was contained, it had scorched 153,336 acres, destroyed 18,804 structures, displaced approximately 52,000 people, and killed 85 people (*1*, *2*). Insured losses are estimated to be between $7.5 and $10 billion (*3*). The damages and losses will likely increase, as there is a risk of potential cascading hazards, such as toxic ash, poor air quality, and mudslides and debris flow (*4*). California has experienced an increase in wildfire activity over the past few years (*5*), and the trend is projected to continue (*6*). Going forward, scientists must help decision-makers and first responders prevent extreme hazards like the Camp Fire from turning into massive human disasters.

Lack of an integrated framework for circulating information among decision-makers and passing it to residents exacerbated the devastating impact of the wildfire. Reports unanimously point to shortcomings in disseminating critical information to residents before and during the wildfire (*7*). The data crisis further increased in areas where cellular and telecommunication infrastructure was damaged, limiting internet access (*8*).

Investment in an integrated data system for identifying, harnessing, synthesizing, and communicating pertinent data will enable decision-makers and communities to better anticipate, prepare for, respond to, and recover from extreme events such as the Camp Fire. We must identify relevant stakeholders, examine the required data, collect public and relevant private data efficiently, and develop platforms for processing datasets such as weather data, cell phone GPS data as proxy for people, social media feeds, and traffic cameras and sensors. We then need strategies to convert datasets into usable information by using artificial intelligence technologies for decision-support systems. To communicate the resulting information effectively, we need a reliable data infrastructure for real-time analysis that could alert residents by email, phone messages, text warning, television, radio, and "reverse 911" (*9*).

California's wildfires are just one example of emerging compound natural hazards. By augmenting existing resiliency platforms, we can mitigate the destruction caused by future natural disasters. These augmented platforms will require regionalized resiliency indices that can be tested, verified, and updated after each extreme event. Successfully integrating and communicating data cannot be achieved without close collaboration with data stakeholders, community-level stakeholders, and state-level institutions.

Farshid Vahedifard[1]*, Alireza Ermagun[1], Kimia Mortezaei[1,2], Amir AghaKouchak[3]
[1]Department of Civil and Environmental Engineering, Mississippi State University, Mississippi State, MS 39762, USA. [2]Center for Advanced Vehicular Systems (CAVS), Mississippi State University, Mississippi State, MS 39762, USA. [3]Department of Civil and Environmental Engineering, University of California, Irvine, CA 92697, USA.
*Corresponding author.
Email: farshid@cee.msstate.edu

REFERENCES

1. "Top 20 most destructive California wildfires," CalFire (2018); www.fire.ca.gov/communications/downloads/fact_sheets/Top20_Destruction.pdf.
2. "Camp Fire incident update, Date: 11/25/2018, Time: 7:00 a.m," CalFire (2018); http://cdfdata.fire.ca.gov/pub/cdf/images/incidentfile2277_4326.pdf.
3. "Latest Estimates of Insured Losses from California Wildfires at $9B to $13B," *Insurance Journal* (2018); www.insurancejournal.com/news/west/2018/11/19/509677.htm.
4. A. AghaKouchak *et al.*, *Nature* **561**, 458 (2018).
5. National Interagency Fire Center, "2018 national year-to-date report on fires and acres burned" (2018); https://gacc.nifc.gov/sacc/predictive/intelligence/NationalYTDbyStateandAgency.pdf.
6. J. D. Radke *et al.*, "Assessing extreme weather-related vulnerability and identifying resilience options for California's interdependent transportation fuel sector" (Center for Catastrophic Risk Management, University of California, Berkeley, 2018); www.climateassessment.ca.gov/techreports/docs/20180827-Energy_CCCA4-CEC-2018-012.pdf.
7. E. Levenson, "Many Camp Fire victims didn't get emergency alerts. Those who did got them too late," CNN (2018); www.cnn.com/2018/11/15/us/california-fire-emergency-alert/index.html.
8. "California Camp Fire threatens fiber optics," GeoTel Communications (2018); www.geo-tel.com/2018/california-camp-fire-threatens-fiber-optics/.
9. J. Rainey, "Paradise Fire survivors say warnings were too little, too late," NBC (2018); www.nbcnews.com/news/us-news/paradise-fire-survivors-say-warnings-were-too-little-too-late-n935846.

10.1126/science.aaw2236



PHOTO: JUSTIN SULLIVAN/GETTY IMAGES

Wildfires: Opportunity for restoration?

Wildfires are increasingly making global headlines due to their destructive effects. In many parts of the world, climate change (*1*), accelerating land-use alterations (*2*), and other factors are making large wildfires more frequent and their ecological effects more severe (*3*). Most organisms in the world's fire-prone ecosystems have evolutionary adaptations to cope with natural fire cycles (*2*). However, ongoing changes in fire regimes, coupled with drier climate and other associated natural and anthropogenic disturbances (*4*–*6*), can surpass the capacity of organisms to cope with disturbance (*7*) and ultimately trigger ecosystem collapse (*5*). As a result, wildfires are one of the major drivers of change in forest cover worldwide (*8*). Yet, under some circumstances, wildfires can also provide an opportunity for ecosystem restoration.

About 2 billion hectares of the world's terrestrial ecosystems are considered degraded and in need of ecological restoration (*9*), and most ecosystems are under the threat of changing climatic conditions. Wildfires can provide a window of opportunity in which scientists and forest managers can

Downloaded from http://science.sciencemag.org/ on January 10, 2019

Published by AAAS



Better data integration and dissemination could mitigate the effects of hazards such as the November 2018 Camp Fire.

take action to restore degraded ecosystems, eradicate undesirable species and pests, and favor vegetation that is better adapted to future climatic conditions. For example, dense, monospecific pine plantations from the 20th century, which are often unproductive because of climate and soil limitations, abound across the Mediterranean Region (*10*). They were originally planted to retain soil and regain plant cover, but they now generate many ecological challenges, such as increasing the risk of high-intensity fire and hindering the development of native vegetation (*10*). Wildfires may thus release the native vegetation from the fierce competition of the dense pine canopy [e.g., (*11*)] and provide management opportunities to favor more diverse and resilient—and less flammable—communities, including species adapted to future fires and to drier conditions. Such management can involve letting preexistent natural communities, previously oppressed by competitive planted canopies, regenerate on their own through passive restoration, or providing some help through population reinforcement. In other cases, postfire restoration could be a time to conduct assisted migration to reduce forest vulnerability to future fire and drought conditions (*6*).

Wildfires generally trigger management actions and attract funding to implement them. Forest managers and scientists should leverage these opportunities to address long-term goals that could not be easily achieved in the absence of wildfires because of public opposition, lack of access through dense vegetation, lack of funding, or too much bureaucracy. Moreover, forest policy should include contingencies for wildfires so that, in case one occurs, appropriate management actions are predefined to address not only the imminently necessary treatments identified during the emergency situation but also mid- and long-term goals.

We do not minimize the problems and risks associated with wildfires, nor do we wish to stimulate the spread of uncontrolled fires with potentially tragic consequences. However, once a wildfire has occurred and the immediate danger has passed, we urge scientists and forest managers to seize the opportunity to rethink forest management and foster more resilient landscapes.

Alexandro B. Leverkus[1]*, Pablo García Murillo[2], Vicente Jurado Doña[3], Juli G. Pausas[4]

[1]Field Station Fabrikschleichach, Department of Animal Ecology and Tropical Biology (Zoology III), Julius-Maximilians-University Würzburg, 96181 Rauhenebrach, Germany. [2]Departamento de Biología Vegetal y Ecología, Universidad de Sevilla, E-41012 Sevilla, Spain. [3]Departamento de Geografía Física y Análisis Geográfico Regional, Universidad de Sevilla, E-41004 Sevilla, Spain. [4]Centro de Investigaciones sobre Desertificación (CIDE-CSIC), 46113 Montcada, Valencia, Spain.
*Corresponding author.
Email: alexandro.leverkus@uah.es

REFERENCES

1. R. Seidl *et al.*, *Nat. Clim. Change* **7**, 395 (2017).
2. J. G. Pausas, J. E. Keeley, *Bioscience* **59**, 593 (2009).
3. C. I. Millar, N. L. Stephenson, *Science* **349**, 823 (2015).
4. A. B. Leverkus, D. B. Lindenmayer, S. Thorn, L. Gustafsson, *Glob. Ecol. Biogeogr.* **27**, 1140 (2018).
5. D. B. Lindenmayer, C. Sato, *Proc. Natl. Acad. Sci. U.S.A.* **115**, 5181 (2018).
6. C. D. Allen, D. D. Breshears, N. G. McDowell, *Ecosphere* **6**, 1 (2015).
7. J. F. Johnstone *et al.*, *Front. Ecol. Environ.* **14**, 369 (2016).
8. P. G. Curtis, C. M. Slay, N. L. Harris, A. Tyukavina, M. C. Hansen, *Science* **361**, 1108 (2018).
9. R. Cernansky, *Nature* **560**, 542 (2018).
10. J. G. Pausas, S. Fernández-Muñoz, *Clim. Change* **110**, 215 (2012).
11. A. B. Leverkus, J. M. Rey Benayas, J. Castro, *Ecology* **97**, 2628 (2016).

10.1126/science.aaw2134

Protect Catalonia's corals despite politics

The Mediterranean red coral (*Corallium rubrum*), sold as a precious organic gemstone and homoeopathic product, is classified as endangered by the IUCN (*1*–*3*). In January 2017, a regional report concluded that 90% of red coral populations in Catalonia had failed to reach the minimum harvest size and were on the verge of collapse (*3*). In response, the Catalan Parliament declared the first moratorium of red coral in the Mediterranean basin (*4*). In October 2017, the General Fisheries Commission for the Mediterranean (GFCM) made a recommendation consistent with Catalonia's decision: The GFCM declared that if a Mediterranean country finds that

Published by AAAS

Downloaded from http://science.sciencemag.org/ on January 10, 2019

25% of the total red coral catch, in a given zone, is undersized (less than 7 mm basal diameter), then that country should close the area to red coral fishing as a precautionary measure to protect red coral stocks (*5*). As the GFCM recommendation confirmed, Catalonia's action was consistent with scientific evidence and the protection afforded by European regulations (*6*). However, politics has undermined Catalonia's efforts.

On 27 October 2017, Catalonia declared its independence (*7*). Three days later, the Spanish government applied Article 155 to gain control over all Catalan institutions (*8*). In November 2017, the Spanish Ministry of Agriculture disregarded Catalan's coral moratorium and granted 12 red coral fishing licenses in Catalonia's exterior waters, under Spanish jurisdiction (*9*). In May 2018, Catalonia regained control of its institutions. A month later, the government of Spain was disbanded after a vote of no confidence due to corruption, and the parties formed a new government (*10*). Despite hopes of a new era of diplomacy between Spain and Catalonia, on 14 November 2018, the new Spanish Ministry of Agriculture upheld the red coral fishing licenses (*11*). A few days later, more than 80 research institutions, nongovernmental organizations, and activists sent a letter (for the third time) asking the ministry to revoke the decision (*12*), but no action has been taken.

The European Commission has the authority to protect endangered marine species through several conservation mechanisms supported by international policies and management strategies (*6*). Member states are responsible for complying with GFCM regulations. Given that Spain is not honoring Catalonia's moratorium, the commission should use its powers to protect red coral not only from overexploitation but also from political conflicts that endanger its persistence.

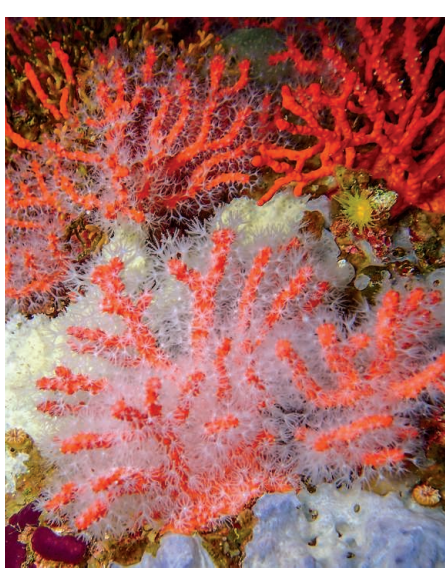
Nur Arafeh-Dalmau[1]*, Cristina Linares[2], Bernat Hereu[2], Hernan Caceres-Escobar[1,3], Duan Biggs[1,4,5], Hugh Possingham[1,6]

[1]ARC Centre of Excellence for Environmental Decisions, Centre for Biodiversity and Conservation Science, School of Biological Sciences, University of Queensland, Brisbane, QLD 4072, Australia. [2]Departament de Biologia Evolutiva, Ecologia i Ciències Ambientals, Institut de Recerca de la Biodiversitat (IRBIO), University of Barcelona, 08028 Barcelona, Spain. [3]National Environmental Science Programme Threatened Species Recovery Hub, The University of Queensland, Brisbane, QLD 4072, Australia. [4]Environmental Futures Research Institute, Griffith University, Nathan, QLD 4111, Australia. [5]Department of Conservation Ecology and Entomology, Stellenbosch University, Matieland 7602, South Africa. [6]Office of the Chief Scientist, The Nature Conservancy, Arlington, VA 22203–1606, USA.
*Corresponding author.
Email: n.arafehdalmau@uq.net.au

REFERENCES

1. M. M. Otero *et al*., "Overview of the conservation status of Mediterranean anthozoans" (IUCN, Malaga, Spain, 2017); pp. 36–41.
2. A. W. Bruckner, *Mar. Ecol. Prog. Ser.* **397**, 319 (2009).
3. J. Garrabou *et al*., "Informe sobre l'estat de les poblacions de coral vermell (*Corallium rubrum*) a les aigües de Catalunya," (Generalitat de Catalunya, 2017); www.cibsub.cat/rcs_actu/2017_Informe_estat_poblacions_corall_costa_catalana.pdf [in Catalan].
4. Order ARP/59/2017 of 18 April 2017, *Diari Oficial de la Generalitat de Catalunya*, No. 7351 (2017); https://portaldogc.gencat.cat/utilsEADOP/PDF/7351/1604661.pdf [in Catalan].
5. Recommendation GFCM/41/2017/5 on the establishment of a regional adaptive management plan for the exploitation of red coral in the Mediterranean Sea (2017); www.fao.org/gfcm/decisions/en/.
6. C. Regulation, No. 1967/2006 of 21 December 2006, *Official Journal of the European Union L, 409* (2016); http://publications.europa.eu/resource/cellar/f7b0a754-4a19-4cf9-8040-aeae2faace38.0005.01/DOC_1.
7. Proposta de resolució que regula la proclamació de la República Catalana, of 27 October 2017, No. 72032 (2017); www.ara.cat/2017/10/27/255_00004_11_RG72032_GP_JxSI_GP_CUP_20171027-1.pdf [in Catalan].
8. Order PRA/1034/2017 of 27 October 2017, *Boletín Oficial del Estado,* No 260 (2017); www.boe.es/boe/dias/2017/10/27/pdfs/BOE-A-2017-12328.pdf [in Spanish].
9. Order APM/1101/2017 of 16 November 2017, *Boletín Oficial del Estado*, No. 278 (2017); http://noticias.juridicas.com/base_datos/Admin/608222-om-apm-1101-2017-de-2-nov-convoca-el-procedimiento-de-autorizacion-para-la.html [in Spanish].
10. S. Jones, "Mariano Rajoy ousted as Spain's prime minister," *The Guardian* (2018); www.theguardian.com/world/2018/jun/01/mariano-rajoy-ousted-as-spain-prime-minister.
11. Order APA/1186/2018 of 14 November 2018, *Boletín Oficial del Estado*, No. 277 (2018); www.boe.es/boe/dias/2018/11/16/pdfs/BOE-A-2018-15612.pdf [in Spanish].
12. F. Segura Castro (Ecologistes en Acció de Cataluunya), "Letter to: Teresa Ribera Rodríguez (Minister of Ecological Transition) and Luis Planas Puchades (Minister of Agriculture, Fisheries and Food)" (2018); www.ecologistasenaccion.org/wp-content/uploads/2018/11/20181126-Carta-Coral-Rojo-relación-entidades.pdf [in Spanish].

10.1126/science.aav8710



The Spanish government has disregarded Catalonia's efforts to protect red coral (*Corallium rubrum*).

PHOTO: CRISTINA LINARES

TECHNICAL COMMENT ABSTRACTS

Comment on "Tropical forests are a net carbon source based on aboveground measurements of gain and loss"

Matthew C. Hansen, Peter Potapov, Alexandra Tyukavina

Baccini *et al.* (Reports, 13 October 2017, p. 230) report MODIS-derived pantropical forest carbon change, with spatial patterns of carbon loss that do not correspond to higher-resolution Landsat-derived tree cover loss. The assumption that map results are unbiased and free of commission and omission errors is not supported. The application of passive moderate-resolution optical data to monitor forest carbon change overstates our current capabilities.

Full text: dx.doi.org/10.1126/science.aar3629

Response to Comment on "Tropical forests are a net carbon source based on aboveground measurements of gain and loss"

A. Baccini, W. Walker, L. Carvalho, M. Farina, R. A. Houghton

The Hansen *et al.* critique centers on the lack of spatial agreement between two very different datasets. Nonetheless, properly constructed comparisons designed to reconcile the two datasets yield up to 90% agreement (e.g., in South America).

Full text: dx.doi.org/10.1126/science.aat1205

Comment on "Impacts of species richness on productivity in a large-scale subtropical forest experiment"

Hua Yang, Zhongling Guo, Xiuli Chu, Rongzhou Man, Jiaxin Chen, Chunjiang Liu, Jing Tao, Yong Jiang

Huang *et al.* (Reports, 5 October 2018, p. 80) report significant increases in forest productivity from monocultures to multispecies mixtures in subtropical China. However, their estimated productivity decrease due to a 10% tree species loss seems high. We propose that including species richness distribution of the study forests would provide more meaningful estimates of forest-scale responses.

Full text: dx.doi.org/10.1126/science.aav9117

Response to Comment on "Impacts of species richness on productivity in a large-scale subtropical forest experiment"

Helge Bruelheide, Yuxin Chen, Yuanyuan Huang, Keping Ma, Pascal A. Niklaus, Bernhard Schmid

Yang *et al.* have raised criticism that the results reported by us would not be relevant for natural forests. We argue that productivity is positively related to species richness also in subtropical natural forests, and that both the species pools and the range of tree species richness used in our experiment are representative of many natural forests of this biome.

Full text: dx.doi.org/10.1126/science.aav9863

Downloaded from http://science.sciencemag.org/ on January 10, 2019

Published by AAAS

TECHNICAL COMMENT

CARBON CYCLE

Comment on "Tropical forests are a net carbon source based on aboveground measurements of gain and loss"

Matthew C. Hansen*, Peter Potapov, Alexandra Tyukavina

Baccini *et al*. (Reports, 13 October 2017, p. 230) report MODIS-derived pantropical forest carbon change, with spatial patterns of carbon loss that do not correspond to higher-resolution Landsat-derived tree cover loss. The assumption that map results are unbiased and free of commission and omission errors is not supported. The application of passive moderate-resolution optical data to monitor forest carbon change overstates our current capabilities.

Baccini *et al.* (*1*) report net tropical forest aboveground carbon stock change from Moderate Resolution Imaging Spectroradiometer (MODIS) data and purport to capture all forest carbon dynamics resulting from both natural and anthropogenic processes. We believe their method and results overstate current monitoring capabilities and may confuse the global community of practitioners working to establish robust and defensible forest carbon monitoring systems.

Our methods for mapping tree cover (*2*, *3*) are very similar to those of Baccini *et al.* for mapping aboveground carbon; we use the same passive optical data (they use a simpler set of annual composite images that do not capture phenological variation) and the same data-mining tool (regression trees in a random forest implementation). The approaches differ principally in the dependent variable. Our research characterizing global tree cover uses MODIS and Landsat passive optical sensing systems. Land cover, including tree cover, is directly sensed in passive optical Earth observations because the multitemporal, multispectral reflectance variations directly relate to biophysical surface properties and vegetation types. Forest carbon is a more challenging variable to characterize, requiring knowledge about the volume and carbon density of vegetation—parameters that are not directly related to surface reflectance. Although the empirical model built by Baccini *et al.* suggests a relationship between passive optical imagery and forest carbon, it is likely the very same signal we use in mapping tree cover. Tree cover is largely discriminated using a spectral signature that is a combination of high reflectance in the near-infrared, associated with dense vegetation cover, and low reflectance in other bands due to light extinction from canopy shadowing and absorption from healthy vegetation cover. There is no physical basis for passive optical reflectance data being sensitive to changes in forest carbon parameters such as diameter at breast height or stem wood density.

Land change maps derived from satellite data consist of accurately mapped change along with inevitable omission and commission errors, whether the mapped variables are categorical or continuous. For data derived from MODIS, accurate mapping of land change is limited by its coarse spatial resolution (~500 m), as substantial areas of subpixel land change are not reliably quantified. For example, Hansen *et al.* (*4*) showed that area estimation of stand-replacement tree cover loss from Landsat samples at 30-m spatial resolution was twice that of a MODIS-derived tree cover loss map product. If MODIS data are forced to reproduce all of the area detected by Landsat, change maps quickly turn into noise, or more correctly, unconstrained omission and commission errors. The use of independent probability-based reference data to assess error rates and bias is standard practice and has been recommended by the IPCC (*5*–*8*).

Baccini *et al.* attempt to track changes in forest carbon stocks directly with propagated model uncertainties presented in place of accuracy assessments. Admittedly, an accuracy assessment of forest carbon change is difficult and would need to consist of a probability-based sample of time 1 and time 2 carbon stock measurements at the scale of observation. Regardless, in a modeling approach like that of Baccini *et al.*, map biases and associated omission and commission errors are undetermined. This is critical, as the mapping challenge is greater for Baccini *et al.*, given a dependent variable (aboveground carbon change) that has a much more tenuous relation to the MODIS-derived independent spectral reflectance variables. Baccini *et al.* state that their map is free from bias because they use a "single predictive model" applied to carbon stock gain and loss estimation. However, the distribution of map commission and omission errors is a function not only of model choice, but also of spatio-temporal variations of forest change, sensitivity

Department of Geographical Sciences, University of Maryland, College Park, MD 20740, USA.
*Corresponding author. Email: mhansen@umd.edu

Table 1. Disaggregation of Baccini *et al.* aboveground loss by percent tree cover, tree cover loss, forest intactness, and colocated tree cover loss and gain.

Baccini *et al.* (*1*) aboveground loss		Tropical America	Tropical Africa	Tropical Asia
By percent tree cover category of Hansen *et al.* (*2*)	≥60% tree cover	86.1%	40.9%	74.1%
	30–59% tree cover	7.9%	24.4%	15.0%
	10–29% tree cover	3.4%	30.4%	6.8%
	0–9% tree cover	2.6%	4.2%	4.1%
Within Hansen *et al.* (*2*) mapped tree cover loss	≥60% tree cover	27.1%	13.4%	47.9%
	30–59% tree cover	3.0%	8.9%	6.6%
	10–29% tree cover	0.9%	6.1%	2.0%
	0–9% tree cover	0.2%	0.0%	0.4%
Outside of Hansen *et al.* (*2*) mapped tree cover loss		68.7%	71.5%	43.2%
Within an intersection of intact (*9*) and hinterland (*10*) forest maps		25.3%	7.9%	2.5%
Within hinterland forests (*10*)		28.9%	10.5%	3.7%
For colocated tree cover loss and tree cover gain from Hansen *et al.* (*2*)		0.65%	0.00%	5.45%

Downloaded from http://science.sciencemag.org/ on January 15, 2019

to different land cover dynamics, data quality, and optical reflectance relationships with aboveground carbon.

We compared our tree cover loss data with Baccini *et al.*'s carbon loss estimates for the period 2003–2014 to assess map correspondence (Table 1 and Figs. 1 to 3). We found that 69%, 72%, and 43% of estimated carbon losses for Latin America, Africa, and Southeast Asia, respectively, are not colocated with Landsat-scale forest disturbances, defined as any MODIS grid cell with ≥10% Landsat-derived tree cover loss. The carbon losses reported by Baccini *et al.* must therefore be due to factors other than observable land cover and land use forest disturbances. Unfortunately, there is no evidence in their paper or in the literature to explain such large-scale biomass change dynamics for regions without tree cover loss. Other anomalous results include more than 25% of carbon loss in South America being located within intact forest landscapes with no observable human or natural disturbance (*9*, *10*) and more than 30% of tropical Africa's aboveground carbon loss found in parklands of 10 to 30% tree cover (*2*). On the basis of our experience with MODIS (*3*, *4*, *11*), much of the carbon loss presented by Baccini *et al.* is likely commission error.

Moreover, Baccini *et al.* state that carbon change per MODIS cell is a net estimate, resulting in conservative aggregate gain and loss values. To assess this supposition, we examined MODIS grid cells with >10% loss and >10% gain from Landsat (*2*). Areas of both loss and gain accounted for 6%, 7%, and 21% of Landsat-defined mapped tree cover loss for tropical America, Africa, and Asia, respectively. We found no appreciable carbon loss in the data of Baccini *et al.* for these areas (bottom row of Table 1), supporting the idea that net change is low or absent in areas of colocated tree cover loss and gain. However, we posit that for other

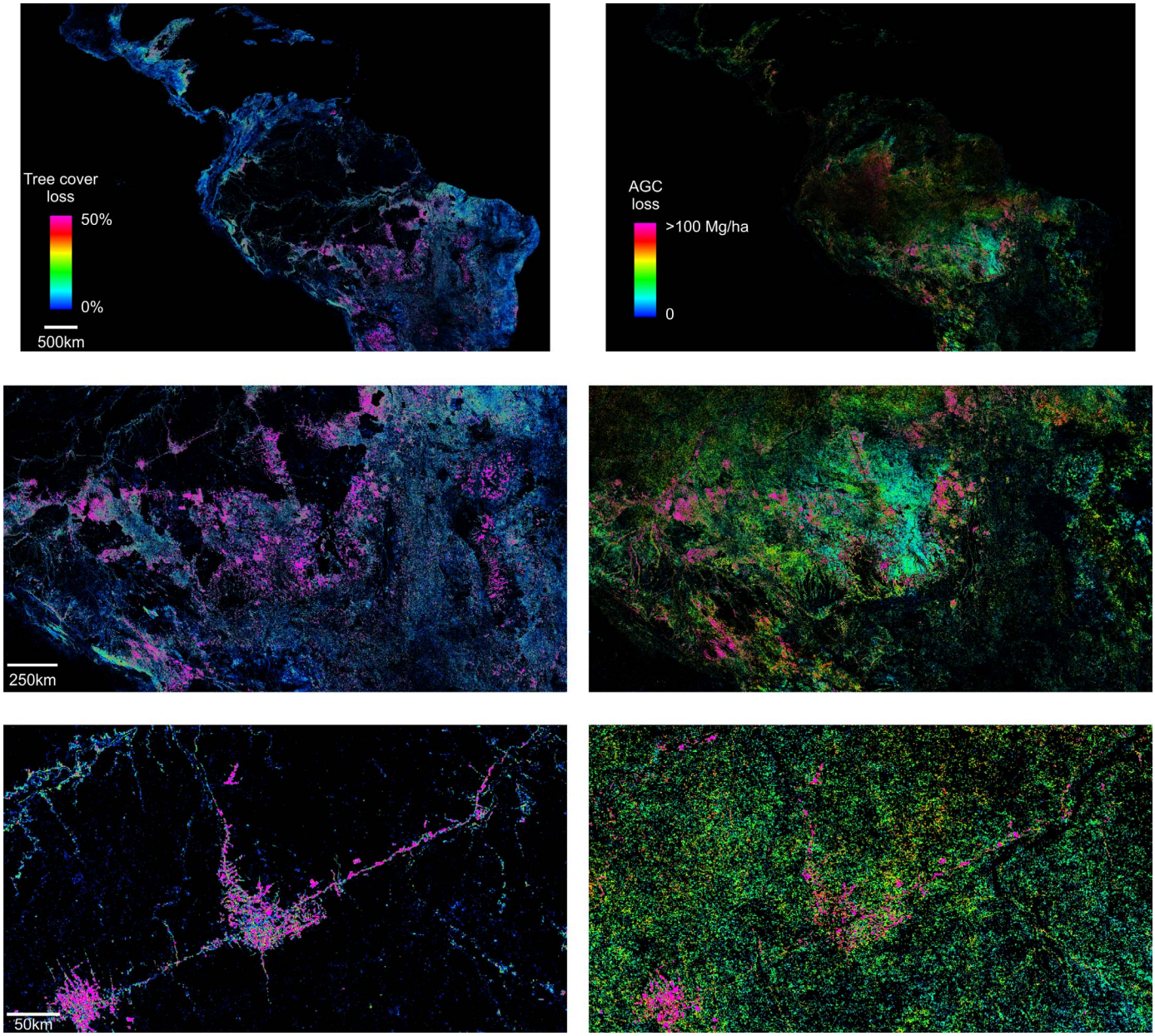


Fig. 1. Tropical America. Except for some large industrial-scale clearings, mapped carbon losses within the Amazon Basin are largely uncorrelated with Landsat-derived tree cover loss. Left: Tropical America tree cover loss from Hansen *et al*. (*2*). Right: Aboveground carbon (AGC) loss from Baccini *et al*. (*1*). Top row: Extent of study area of Baccini *et al*. for tropical America. Middle row: 2800 km × 1500 km subset centered on Mato Grosso state, Brazil. Bottom row: 530 km × 290 km subset of Amazonas state, Brazil.

Downloaded from http://science.sciencemag.org/ on January 15, 2019

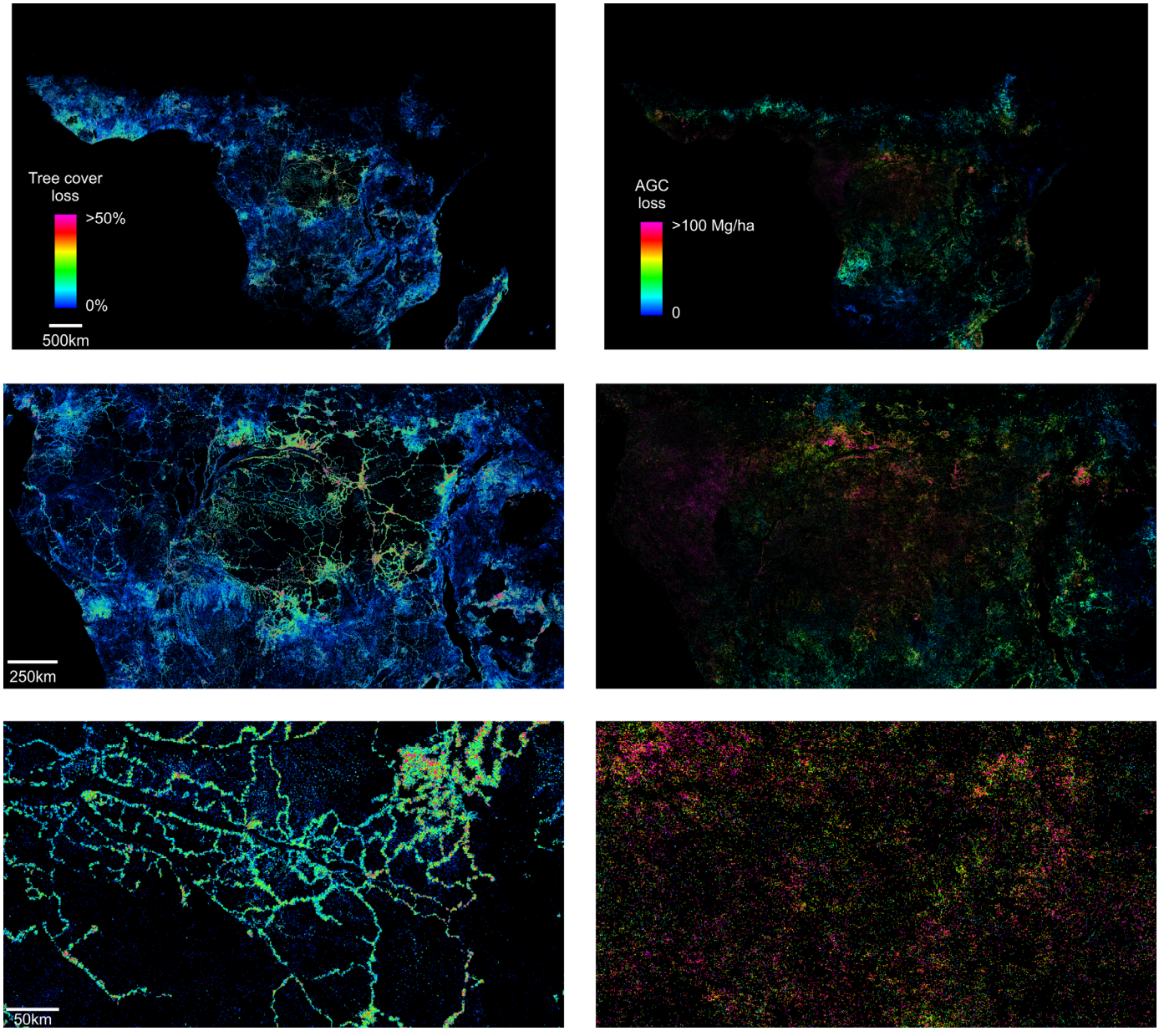


Fig. 2. Tropical Africa. The pattern of smallholder forest clearing along rural roads in the Congo Basin (*12*), which includes carbon loss due to the expansion of agriculture into primary forest, is wholly absent. Left: Tropical Africa tree cover loss from Hansen *et al*. (*2*). Right: Aboveground carbon (AGC) loss from Baccini *et al*. (*1*). Top row: Extent of study area of Baccini *et al*. for tropical Africa. Middle row: 2800 km × 1500 km subset centered on the Congo Basin. Bottom row: 530 km × 290 km subset of Tshuapa province, Democratic Republic of Congo.

tree cover loss–dominated areas, carbon loss should be present. For tropical America, Africa, and Asia, Baccini *et al.* estimate no carbon loss for 68%, 76% and 72% of Landsat-derived tree cover loss–dominant cells; we identify these as errors of omission (Figs. 1 to 3) (*12*, *13*).

Despite the likely presence of substantial spatial error and claims of capturing carbon losses from disturbances beyond deforestation, the carbon loss estimates of Baccini *et al.* are lower than those of Tyukavina *et al.* (*14*), which relied on robust and statistically accurate area estimation methods. Given the lower overall carbon loss estimate of Baccini *et al.*—an estimate not accounted for by colocated gain and loss, and consisting of considerable commission error—it follows that their estimates of carbon losses over landscapes experiencing land cover and land use change are underestimated. On the other hand, if we accept that the carbon losses as depicted are accurate, their results overturn our current understanding of where the global climate change science and policy communities should be focused in mitigating emissions from deforestation and forest degradation (i.e., not focused on tropical forest clearing). According to Baccini *et al.*, deforestation is a minority source of emissions and is not colocated with forests experiencing degradation (i.e., sites spread diffusely throughout tropical forests, including forests heretofore thought to be intact) (Table 1 and Figs. 1 to 3).

We know the limitations of MODIS data in mapping forest cover, including signal saturation within high canopy cover and the impacts of spatial resolution, atmospheric contamination, and sensor degradation (*15*). Even if these effects could be accounted for, map characterizations inevitably contain error and bias. Baccini *et al.* provide per-pixel estimates of carbon stock changes from 1 to >1000 tonnes per hectare—a capability not previously demonstrated experimentally,

Downloaded from http://science.sciencemag.org/ on January 15, 2019

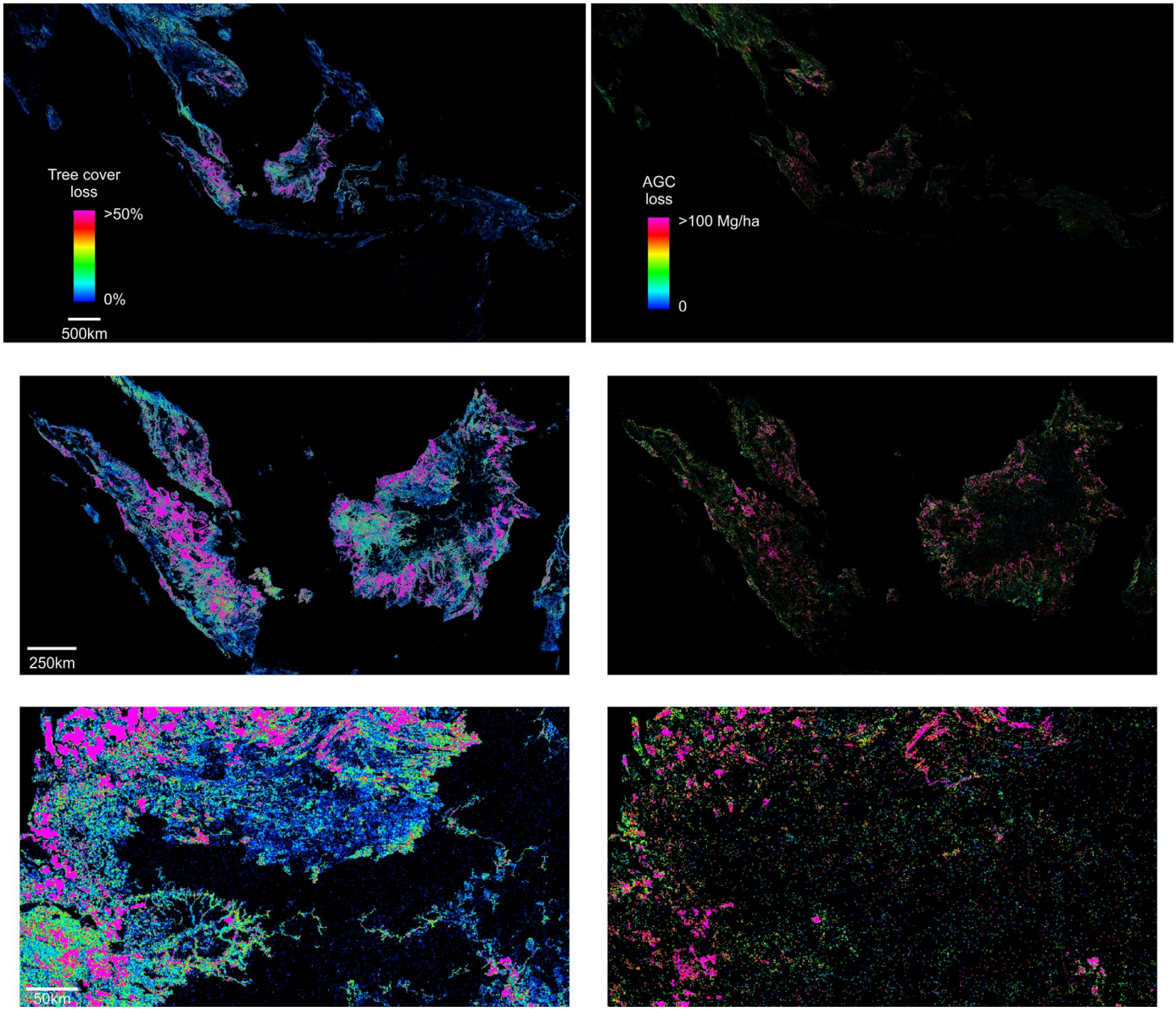


Fig. 3. Tropical Asia. The documented difference in logging within the primary forests of the Malaysia/Indonesia border (*13*) is wholly absent in the carbon loss map. Left: Tropical Asia tree cover loss from Hansen *et al*. (*2*) Right: Aboveground carbon (AGC) loss from Baccini *et al*. (*1*). Top row: Extent of study area of Baccini *et al*. for tropical Asia (east and west edges truncated). Middle row: 2800 km × 1500 km subset centered the islands of Sumatra and Borneo. Bottom row: 530 km × 290 km subset of central Borneo along the Malaysia/Indonesia border.

much less at scale. We believe that the results of their study should be considered with an appropriate level of scientific skepticism, and that other approaches should be used until carbon stock change mapping can be more definitively demonstrated. We advocate the use of carbon stock strata—that is, areas of known mean carbon and associated uncertainty derived using probability-based forest inventory or other data. When such carbon stock data are combined with accurate estimates of forest/tree cover area change, forest carbon change can be quantified without bias and with known uncertainty (*14*).

REFERENCES

1. A. Baccini *et al*., *Science* **358**, 230–234 (2017).
2. M. C. Hansen *et al*., *Science* **342**, 850–853 (2013).
3. M. C. Hansen *et al*., *Earth Interact.* **7**, 10 (2003).
4. M. C. Hansen, P. Potapov, S. Turubanova, in *Global Forest Monitoring from Earth Observation*, F. Achard, M. Hansen, Eds. (Taylor and Francis, 2012), pp. 93–110.
5. P. Olofsson *et al*., *Remote Sens. Environ.* **148**, 42–57 (2014).
6. S. V. Stehman, *Int. J. Remote Sens.* **35**, 4923–4939 (2014).
7. Intergovernmental Panel on Climate Change, *Good Practice Guidance for Land Use, Land-Use Change and Forestry* (IPCC National Greenhouse Gas Inventories Programme, Hayama, Japan, 2003).
8. United Nations Food and Agriculture Organization, *Integration of Remote-Sensing and Ground-Based Observations for Estimation of Emissions and Removals of Greenhouse Gases in Forests: Methods and Guidance from the Global Forest Observations Initiative* (ed. 2.0, 2016).
9. P. Potapov *et al*., *Sci. Adv.* **3**, e1600821 (2017).
10. A. Tyukavina, M. C. Hansen, P. V. Potapov, A. M. Krylov, S. J. Goetz, *Glob. Ecol. Biogeogr.* **25**, 151–163 (2016).
11. M. C. Hansen, S. V. Stehman, P. V. Potapov, *Proc. Natl. Acad. Sci. U.S.A.* **107**, 8650–8655 (2010).
12. G. Molinario *et al*., *Environ. Res. Lett.* **12**, 104001 (2017).
13. M. Broich, M. Hansen, P. Potapov, M. Wimberly, *Int. J. Remote Sens.* **34**, 5748–5760 (2013).
14. A. Tyukavina *et al*., *Environ. Res. Lett.* **10**, 074002 (2015).
15. Y. Zhang, C. Song, L. E. Band, G. Sun, J. Li, *Remote Sens. Environ.* **191**, 145–155 (2017).

30 October 2017; accepted 8 November 2018
10.1126/science.aar3629

Downloaded from http://science.sciencemag.org/ on January 15, 2019

TECHNICAL RESPONSE

CARBON CYCLE

Response to Comment on "Tropical forests are a net carbon source based on aboveground measurements of gain and loss"

A. Baccini[1]*, W. Walker[1], L. Carvalho[2], M. Farina[1], R. A. Houghton[1]

The Hansen *et al*. critique centers on the lack of spatial agreement between two very different datasets. Nonetheless, properly constructed comparisons designed to reconcile the two datasets yield up to 90% agreement (e.g., in South America).

The Comment by Hansen *et al*. (*1*) provides the opportunity to distinguish our research, which quantifies dynamics in carbon density, from studies focused on the binary classification of changes in forest area (*2*). We use a multisensor (ICESat/MODIS), multistage approach combined with field measurements to map net change (i.e., losses and gains) in carbon density for the period 2003–2014 for each 463 m × 463 m (21.4 ha) pixel in our dataset. Within each pixel, dynamic processes occurring at both the tree and stand level are necessarily considered in aggregate, meaning that losses and gains are happening always and concurrently wherever woody biomass is present. A loss is registered when losses are greater than gains, and vice versa. In this way, we estimate the aboveground contribution to what the atmosphere "sees" at the scale of individual pixel-level units of measurement.

Hansen *et al*. (*2*) provided pixel-level (30 m) estimates of forest cover loss and gain from 2000 to 2012. Forest cover loss is defined as "stand-replacement disturbance"—that is, any instance where forest cover decreases from >50% to 0% (e.g., deforestation). Trees must be taller than 5 m and forest degradation is not estimated. Gain is the inverse of loss and is defined as any instance of a forest cover increase from 0% to 50%. Whereas loss is reported annually, gain is reported as a 12-year total. The data of (*2*) are, strictly speaking, binary insofar as a given pixel in a given year is either forest (>50% cover) or nonforest (<50% cover). Moreover, the data are effectively gross binary estimates, meaning that once a loss is recorded in a pixel, a second loss event cannot be recorded even if (i) a second loss event in fact occurs following (ii) a gain being recorded for the same pixel in the gain layer. In short, the forest cover gross loss and gain layers have no influence on the present or future states of one another.

With these inherent differences in mind, the data products can be compared in regions such as central Africa, where slash-and-burn agriculture is a dominant land-use practice. In the Democratic Republic of Congo (DRC), Barbosa *et al*. (*3*) report that 92.2% of forest cover loss is linked to small-scale shifting agriculture. In these systems, the data of (*2*) record successive loss pixels annually as forest (i.e., >50% cover) is converted to small-scale agriculture (i.e., 0% cover). Despite the cyclical on-the-ground pattern of forest loss and gain observed in any one location, (*2*) captures only gross losses, recording a loss only once per pixel during the period of study. Similarly, the gain layer captures only gross gains, recording a gain only once per pixel but without reporting the timing of the gain.

The dataset of (*4*) produces a fundamentally different result in a shifting agriculture system (Fig. 1). Assuming a case where an entire 21.4-ha pixel is dominated by a slash-and-burn mosaic where the ratio of forest to nonforest is approximately 50/50 at any one time, the Baccini *et al*. product would record no change in carbon density in that pixel over the 12-year period of study because, from a net carbon accounting perspective (Fig. 1), the amount of biomass measured aboveground remains constant even though its spatial distribution "shifts." In other words, the atmosphere registers neither a loss nor a gain in carbon. If the ratio of forest to nonforest is instead 45/55, a small net loss would be recorded. Conversely, if the ratio of forest to nonforest is 55/45, a small net gain would be recorded. That is, a net gain in carbon density would be recorded in the same location where (*2*) record a gross loss in forest area. On the basis of this example alone, it is not at all surprising—indeed, it is expected—

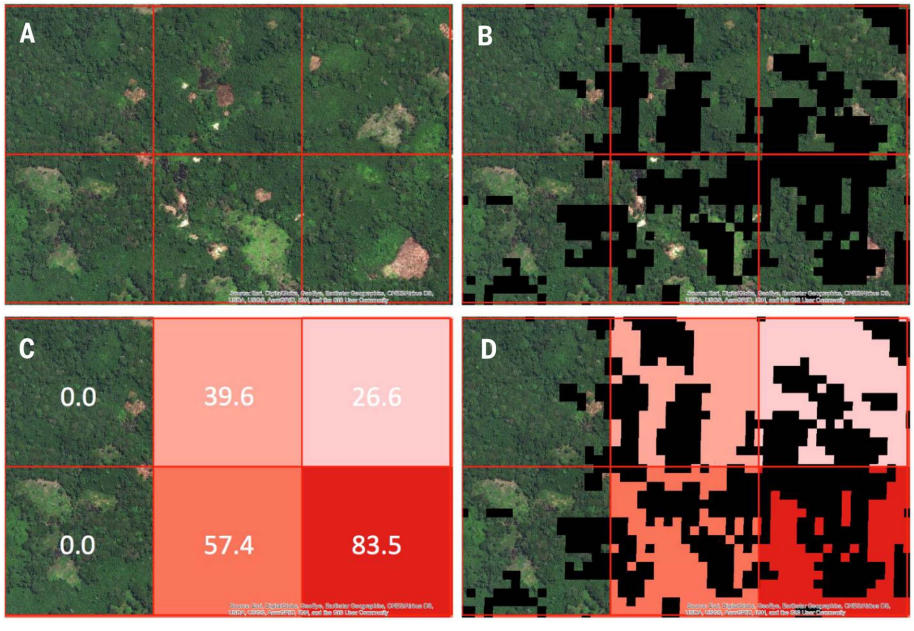


Fig. 1. Comparison of spatial patterns in Hansen *et al*. and Baccini *et al*. datasets. (**A**) Digital Globe image (2013) of shifting cultivation in South Kivu province, Democratic Republic of Congo, with Baccini *et al*. 21.4-ha pixel boundaries shown in red. (**B**) Hansen *et al*. 30-m forest area loss pixels (2003–2014) shown in black. (**C**) Baccini *et al*. carbon density change (2003–2014) pixels with loss values in Mg ha^{-1} shown in white. (**D**) Combination of (B) and (C). Hansen *et al*. losses (black) inside Baccini *et al*. pixels (red) can and do agree in terms of overall trend (four eastern pixels); however, depending on the underlying pattern of land use, below some threshold of loss, carbon density change tends toward zero (net neutral; two western pixels) because gains are observed to be equivalent to losses over time. Hence, Hansen *et al*. records gross forest area loss, whereas Baccini *et al*. records no net carbon density change.

[1]Woods Hole Research Center, Falmouth, MA 04523, USA.
[2]Department of Mathematics and Statistics, Boston University, Boston, MA, USA.
*Corresponding author. Email: abaccini@whrc.org

Downloaded from http://science.sciencemag.org/ on January 15, 2019

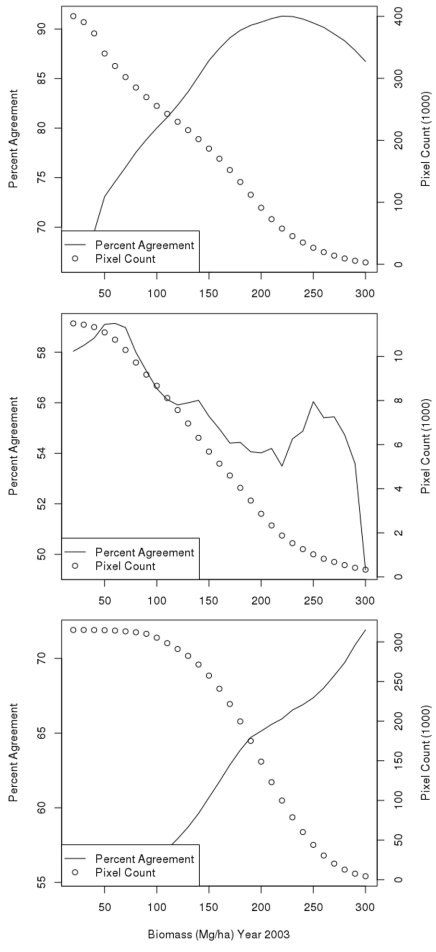


Fig. 2. Agreement between Hansen *et al.* and Baccini *et al.* data products. Tropical America, Africa, and Asia (top to bottom), expressed as a percentage for Baccini *et al.* loss pixels having ≥90% of forest area loss as determined by Hansen *et al.*

that (*2*) find a lack of spatial agreement between the two datasets.

A comprehensive diagnosis of the lack of agreement between the two datasets is additionally dependent on their inherent error and uncertainty. At the pixel level, Baccini *et al.* (*4*) record a net change only if the change is statistically significant at the 95% level ($P \leq 0.05$). For each significant change pixel, the standard error can then be used to compute the 95% confidence interval (CI; uncertainty envelope) for each change value [figure S6 of (*4*)]. We maintain that our estimates are unbiased, meaning not skewed by magnitude (large versus small) or type (loss versus gain) of change; however, we do not claim that they are without error.

Conversely, (*2*) report no measures of error or uncertainty at the pixel level but rather cite accuracy assessments derived from probability-based samples [table S5 of (*2*)], which are relevant only at the biome scale. Although they are useful for applying corrections to biome-level summary statistics on forest area change, they allow for no inferences to be made about pixel-level uncertainty or about the geographic distribution of errors across the landscape. Subsequent to the publication of (*2*), an error assessment was reported by Tyukavina *et al.* (*5*), which indicates area-based errors in the forest cover loss map of 21% for the Pan-Amazon, 92% for humid tropical Africa, and 6% for South/Southeast Asia. The pantropical total was estimated to be 24%. Hansen *et al.* do not refer to nor account for these errors in their Comment, further undermining their comparison.

Above, we summarize the two main reasons why the datasets in question should differ: (i) inherent differences in what is being measured and (ii) inherent error and uncertainty characteristics. As a result, the comparisons made by Hansen *et al.* lack merit; however, an example of a proper comparison based on independent carbon density data can be found in figure S10 of (*4*). That said, Fig. 2 presents what we think is a fair method of comparing the datasets, all things (above) considered. Given the characteristics of (*4*), agreement with (*2*) is expected to increase with increasing "loss purity" at the pixel level, defined here as 21.4-ha pixels in (*4*) where (i) the majority of the area (≥90% or ≥19.3 ha) is subject to forest conversion during the study period and (ii) biomass density at the beginning of the study period (2003) is relatively high. Focusing the analysis on "pure loss" pixels minimizes the net signal effect [i.e., concurrent losses/gains within a pixel of (*4*)], which necessarily differs from the gross signal that the data in (*2*) are designed to detect. The results indicate that as loss purity increases, the agreement with the forest area loss data of (*2*) also increases, reaching more than 90% agreement in tropical America where the prevalence of large-scale deforestation is a dominant contributing factor. In tropical Africa, the agreement is much lower (averaging ~54%), given the dominance of mixed pixels across the mosaic of shifting agriculture.

In conclusion, we would like to address the claim in (*1*) that our data "overstate current monitoring capabilities and may serve to confuse … practitioners working to establish robust … carbon monitoring systems." This statement fails to acknowledge the substantial shortcomings of current monitoring capabilities, which discount degradation and disturbance as noncontributors to emissions. The statement also fails to acknowledge that the status quo often relies upon carbon density data very similar to those being criticized here (*6*). The intent of our research is to reduce the uncertainty in current emissions estimates. This has meant, among other things, rendering data on forest area change unnecessary to the calculation. Although some may find this departure from standard practice confusing and even concerning, practitioners and policy makers should have every confidence that this new approach can be leveraged to provide estimates of forest carbon dynamics—including contributions from forest cover loss, losses from forest degradation and disturbance, and gains from forest growth—that are overall more comprehensive, more consistent, and less uncertain than before.

REFERENCES

1. M. C. Hansen, P. Potapov, A. Tyukavina, *Science* **363**, eaar3629 (2019).
2. M. C. Hansen *et al.*, *Science* **342**, 850–853 (2013).
3. C. Barbosa *et al.*, "New map helps distinguish between cyclical farming and deforestation in the Congo Basin" (2018); https://blog.globalforestwatch.org/data/new-map-helps-distinguish-between-cyclical-farming-and-deforestation-in-the-congo-basin.
4. A. Baccini *et al.*, *Science* **358**, 230–234 (2017).
5. A. Tyukavina *et al.*, *Environ. Res. Lett.* **10**, 074002 (2015).
6. D. Zarin *et al.*, *Glob. Change Biol.* **22**, 1336–1347 (2016).

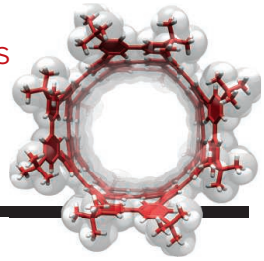
9 March 2018; accepted 8 November 2018
10.1126/science.aat1205

Downloaded from http://science.sciencemag.org/ on January 15, 2019

RESEARCH

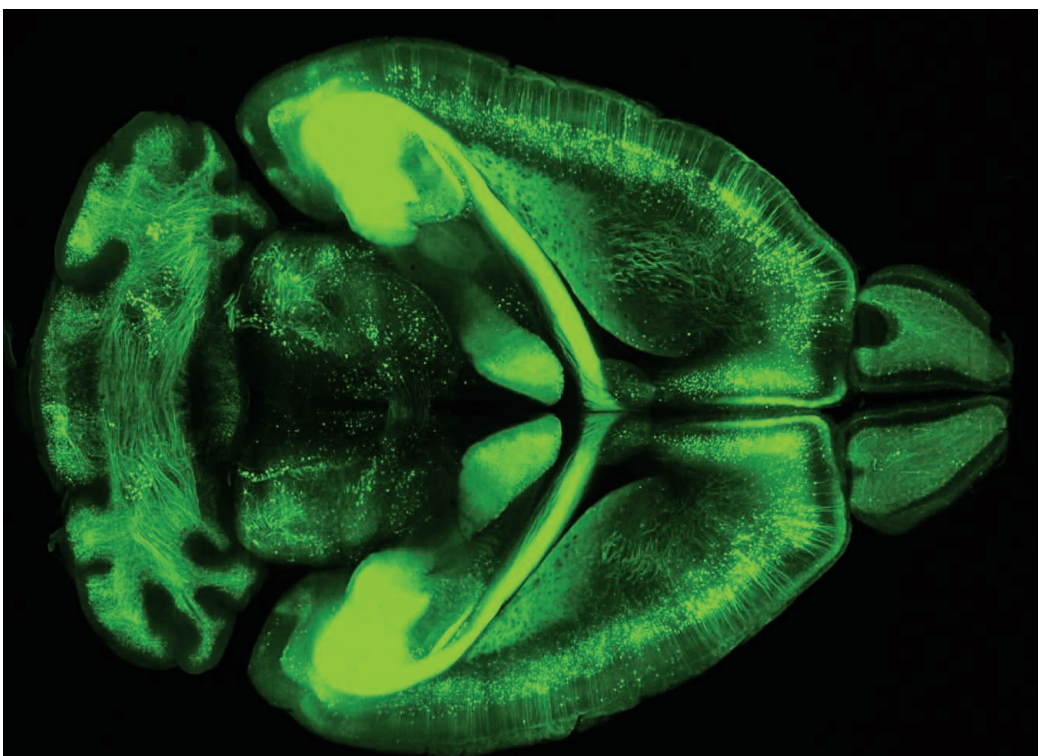
A step toward nanotubes with holes in the walls

Sun et al., *p. 151*



IN *SCIENCE* JOURNALS

Edited by **Stella Hurtley**



RESEARCH METHODS

Advancing 3D imaging of organs

Viewing intact tissue structures is crucial to biological research. The current methods for obtaining three-dimensional (3D) images of tissues and even whole organs, characterized by the clearing of the tissue with an organic solvent, are still limited by the level of clarity, transparency, and efficiency at which they can produce samples. Qi *et al.* developed an advanced optical clearing method, FDISCO, that overcomes some of these limitations. The authors used this method to gather high-resolution images of neuronal and vascular structures in the brain, kidney, and muscles. —PJB

Sci. Adv. 10.1126/sciadv.aau8355 (2018).

Light-sheet fluorescent image of whole mouse brain cleared by FDISCO.

IMAGE: QI *ET AL.*

MEMBRANES

Only the water may pass

Removing objects by size to keep only the smallest ones is simple in theory, but it requires a sieve, membrane, or filter with holes small enough to allow only the smallest objects to pass. Gopinadhan *et al*. engineered two-dimensional water channels by removing an atomic plane of atoms from a sandwich made from bulk crystal with a graphene spacer. Water flowed through the channels without resistance, but the channels excluded all ions except for protons because the ion hydration shells could not squeeze through the channels. —MSL

Science, this issue p. 145

TOPOLOGICAL OPTICS

A photonic Weyl system by design

Theoretically proposed exotic physics is now being explored and realized in condensed matter and photonic systems. Weyl physics arises when the valence band and conduction bands meet at discrete points in the band structure. Jia *et al*. designed and fabricated a photonic metamaterial in which the position of the Weyl points in momentum space could be tuned using a huge artificial magnetic field. Because these points are stable, the ability to design and control such a Weyl system with a robust chiral optical mode could be exploited in future optical information processing applications. —ISO

Science, this issue p. 148

SURFACE CHEMISTRY

Broken on impact

Two competing models have been proposed for the adsorption of molecular hydrogen on platinum surfaces. Both invoke dissociation at surface defects but differ on whether hydrogen molecules diffuse along the surface before encountering a defect or adsorb only if they initially impact a defect site. Van Lent *et al*. studied the sticking of hydrogen molecules from a molecular beam scanned across a curved platinum single-crystal surface that varied in the density and type of defects exposed. Modeling of the results was consistent only with the second model invoking direct impact. —PDS

Science, this issue p. 155

Published by AAAS

CHEMISTRY

Mating disks and rods into an ordered phase

Disk-shaped molecules tend to stack in columns, whereas rod-shaped ones tend to align parallel to each other. When the two types of molecules are mixed, they tend to phase separate. Yano *et al*. found the right recipe that allowed enough affinity between the disks and rods so that they formed a blended twisted columnar phase. The phase could be stabilized by polymerizing the disks. The orientation of the twisted columns could be altered using electric fields, whereas optical stimuli could lead to a second ordering transition. —MSL

Science, this issue p. 161

TROPICAL ECOLOGY

Forest termites mitigate the effects of drought

In many tropical regions, where drought is predicted to become more frequent in the coming years, termites are key components of ecosystem function. Ashton *et al*. experimentally manipulated termite communities to quantify their role during the 2015–2016 "super El Niño" drought in a Malaysian tropical rainforest. Termite relative abundance more than doubled in control plots during drought, maintaining three major ecosystem processes: decomposition, nutrient heterogeneity, and moisture retention. Seedling mortality increased where termites were suppressed. —AMS

Science, this issue p. 174

SEXUAL SELECTION

Who's a clever boy then?

There is considerable value in choosing a smart mate. The suggestion that mate choice has thus shaped the evolution of cognition has been around since Darwin's time, but testing this hypothesis is difficult. Chen *et al*. found that female budgerigars shifted their preference to previously nonpreferred males after these males demonstrated the ability to solve a problem that stumped the originally preferred males (see the Perspective by Striedter). This preference shift was specific to problem-solving and to choosing males. —SNV

Science, this issue p. 166; see also p. 120

CIRCADIAN RHYTHMS

Astrocytes can drive the master clock in the brain

The neurons of the suprachiasmatic nucleus (SCN) of the hypothalamus function as a central circadian clock, coordinating mammalian physiology with the 24-hour light-dark cycle. Brancaccio *et al*. found that these neurons have help from neighboring astrocytes (see the Perspective by Green). In mice lacking the *Cry* gene, which encodes a critical clock component, restoration of *Cry* expression and molecular clock function in the astrocytes, but not the neighboring neurons, restored rhythmic transcriptional oscillations in the SCN and reestablished circadian behaviors in the mice. —LBR

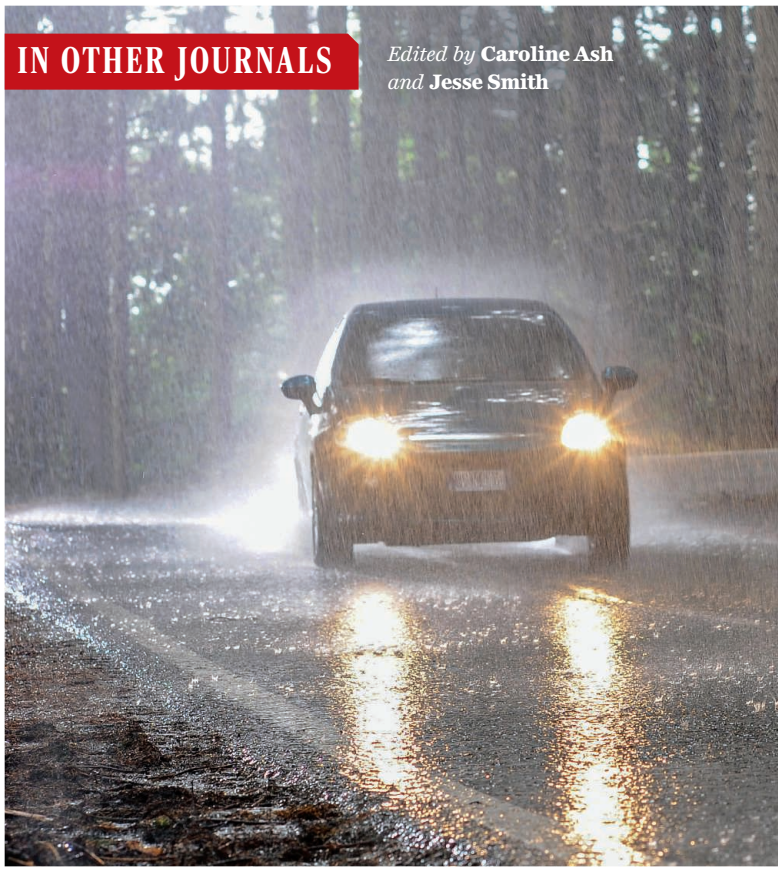
Science, this issue p. 187; see also p. 124

OPIOID OVERDOSE

A step toward preventing overdose

Opioid addiction and overdose remain serious health concerns in the United States. Naloxone can reverse opioid overdose but must be administered in a timely manner. Toward this goal, Nandakumar *et al.* configured a smartphone to detect changes in respiration that precede opioid overdose. Using sonar, the smartphone detected respiratory depression and apnea (temporary lack of breathing) after self-injected drug use in a supervised injection facility. Respiratory changes while under general anesthesia, which simulates opioid-induced overdose, were also detected in a clinical setting. —CC

Sci. Transl. Med. **11**, eaau8914 (2019).



IN OTHER JOURNALS

Edited by **Caroline Ash** *and* **Jesse Smith**

NEUROSCIENCE

Chronic short sleep and neurodegeneration

The locus ceruleus is a brain region that is critical for optimal cognitive performance and brain health. Its neurons degenerate during mild cognitive impairment and the early stages of Alzheimer's disease (AD). Zhu *et al.* investigated the role of chronic sleep deprivation on the protein tau, which is found abundantly in the brain and is associated with AD. In mice, a shortage of sleep in early life advanced the temporal progression of toxic tau accumulation, worsened neurobehavioral impairment, and increased the abundance of soluble tau oligomers within the locus ceruleus and other regions. Lack of sleep promoted neurodegeneration in the locus ceruleus and other tau-affected areas, and the effects persisted for months. Chronic sleep disruption may thus contribute to the progression of AD and related diseases. —PRS

J. Neurosci. **38**, 10255 (2018).

INFLUENZA

More tricks up its sleeve

Influenza viruses are famous for generating variants that evade immune surveillance—and our vaccines. Vahey and Fletcher describe another way these viruses elude control. The authors made a strain of influenza A virus that expressed fluorescently labeled components and used them to infect cells. Live-cell imaging was then used to monitor the composition and morphology of virus particles as they were released from infected cells. Influenza A was found to produce very variable virus particles, unlike many other human viruses whose morphology and composition are consistent. This variability appears to be stochastic and allows progeny viruses to escape the effects of neuraminidase drugs, which would normally prevent successful infections. —SMH

Cell 10.1016/j.cell.2018.10.056 (2019).

PHOTOS: (TOP) PIRTUSS/SHUTTERSTOCK; (FACING PAGE) FOTOTRIPS/SHUTTERSTOCK

Published by AAAS



RAIN

The meteorological future is here

Climatologists have predicted that anthropogenic climate change will cause more and more intense rainfall (along with other meteorological extremes), and it seems like that is occurring, but have precipitation patterns really changed enough to be objectively noticeable? Lehmann *et al.* present data showing that this impression does accurately reflect reality. They show that heavy rainfall events now occur more frequently than they did only 40 years ago in most of the world, except in Central Africa, where record-dry months have become more common. These trends are consistent with the changes in mean monthly precipitation expected to accompany climate change and should become more extreme in the future. —HJS

Geophys. Res. Lett. 10.1029/2018GL079439 (2018).

Extreme rainfall events are becoming more common with climate changes in many regions around the world.

IMMUNOLOGY

Fungi affect gut-lung cross-talk

Fungal dysbiosis in the gut may occur after antibiotic treatment. This happens because specific microorganisms that support natural resistance are eliminated. In certain cases, fungal dysbiosis can promote allergic airway disease (AAD). Li *et al.* administered fluconazole to mice and found that it exacerbated AAD responses to house dust mite. An environment free of fungi abrogated this effect, whereas feeding mice dysbiosis-associated fungi enhanced AAD, even in mice with otherwise normal microflora. The researchers then examined the role of CX3CR1^{+} mononuclear phagocytes (MNPs), which recognize and take up fungi in the gut. Syk-mediated activation of CX3CR1^{+} MNPs was required, potentially through the priming of fungal-specific helper T cells. —STS

Cell Host Microbe **24**, 847 (2018).

ANIMAL MECHANICS

Water-speed–record geckos

House geckos are most commonly observed in acrobatic hunting chases across ceilings of buildings. They are not normally thought of as aquatic. But Nirody *et al.* have discovered that geckos are adept at hydroplaning across the surface of ponds in Singapore. This lizard's quadrupedal slapping gait creates air cavities under its feet that serve to keep its head above water while leaving its tail underwater. If soap is added to water, the geckos struggle, because they also exploit surface tension. Plus, they can undulate their bodies and tails in the style of alligators. Thus, a complete range of acrobatic and anatomical talent is put to good effect in the gecko's unimpeded scampering across water, all of which might inform future robot design. —CA

Curr. Biol. **28**, 4046 (2018).



House geckos' agility, gait, and anatomy allow them to run on water just as fast as they do on ceilings.

ULTRAFAST METROLOGY

Getting your timing right

The generation of femtosecond and attosecond pulses of light and electrons in the laboratory provides the ability to probe the dynamics of some of the fastest processes that occur in nature. For larger facilities, however, achieving such performance levels requires synchronization across many components, operational wavelengths, and sometimes across infrastructure separated by kilometers. Xin *et al.* review the various approaches and characterization technologies being developed to synchronize the operation of large-scale systems, outlining the obstacles and possible directions to take on the way to meeting those precision timing challenges. Matching the timing capability in large user facilities with devices such as free-electron lasers and extreme light sources would allow these facilities to reach their potential for imaging ultrafast processes in biological and condensed matter systems. —ISO

Optica **5**, 1564 (2018).

FUNCTIONAL MATERIALS

A functional materials map

Chemical bonding is important for understanding and designing new functional materials. In two papers, Wuttig *et al.* and Raty *et al.* propose a bonding type they term "metavalent." Metavalent materials lie between covalently and metallically bound ones but are distinctly different from both. Several of the compounds that plot in the metavalent field have unique and important physical properties that make for good thermoelectric, phase-change, and other functional materials. The new bonding category potentially provides a guide for the development of interesting new materials. —BG

Adv. Mater. 10.1002/adma.201803777, 10.1002/adma.201806280 (2018).

Published by AAAS

ALSO IN *SCIENCE* JOURNALS

Edited by **Stella Hurtley**

IMMUNOMETABOLISM

Metabolism as a driver of immune response

All living organisms need energy and metabolic building blocks to sustain biological processes. Wang *et al*. review immunometabolism, applying the principles of life history theory. They highlight recent advances showing the reciprocal interactions between systemic metabolism and immunity, as well as how inflammation can alter the functional state of metabolic organs and their central control by the hypothalamus. Such coordinated cross-talk between whole-body and immune cell metabolism is involved in a variety of health and disease states. —PNK

Science, this issue p. 140

MOLECULAR BIOLOGY

A cap-specific m^6A writer

N^{6},2′-*O*-dimethyladenosine (m^6Am) is present at the transcription start nucleotide of capped mRNAs in vertebrates. Akichika *et al*. quantified the abundance of this modification in the transcriptome and identified the writer protein, cap-specific adenosine methyltransferase (CAPAM), needed for this modification. CAPAM contains a unique structure that recognizes cap-specific *N*^{6}-methyladenosine (m^6A) as the substrate. The protein interacts with RNA polymerase II, suggesting that the modification occurs cotranscriptionally. The m^6Am promotes the translation of capped mRNAs in a eIF4E-independent fashion. —SYM

Science, this issue p. 141

IMMUNOLOGY

Unmasking an agent of inflammatory anemia

Infectious and autoimmune diseases are associated with anemia and thrombocytopenia. A severe form of inflammatory cytopenia called macrophage activation syndrome (MAS) may occur during rheumatological disorders and viral infections. Akilesh *et al*. show that monocyte recognition of self- or pathogen-derived nucleic acids via Toll-like receptors 7 and 9 (TLR7 and TLR9) drives MAS-like disease in mice. TLR7 or TLR9 signaling in monocytes causes these cells to differentiate into inflammatory hematophagocytes (iHPCs), which are similar to but distinct from red pulp macrophages. Preventing iHPC differentiation by depleting monocytes relieves MAS-like symptoms. When mice were subjected to a model of malarial anemia, MyD88- and endosomal TLR-dependent iHPC differentiation also occurred. Thus, iHPCs may play a role in both MAS-driven and malarial anemia, as well as thrombocytopenia. —STS

Science, this issue p. 142

NEUROSCIENCE

A physiological function for sAPP?

Although the pathological role of the amyloid-β precursor protein (APP) in Alzheimer's disease is well studied, the physiological role of this protein has remained elusive. Rice *et al*. found that the secreted ectodomain of APP (sAPP) binds to $GABA_BR1a$, the metabotropic receptor for the inhibitory neurotransmitter γ-aminobutyric acid (GABA) (see the Perspective by Korte). Binding suppressed synaptic vesicle release and modulated synaptic transmission and plasticity in mice. A short, 17–amino acid peptide in APP bound to $GABA_BR1a$'s sushi 1 domain, conferring structure to this unstructured domain. Therapeutics targeting this interaction could potentially benefit a range of neurological disorders in which GABA signaling is implicated. —SMH

Science, this issue p. 143; see also p. 123

CHEMISTRY

Clear directions for a robotic platform

The chemistry literature contains more than a century's worth of instructions for making molecules, all written by and for humans. Steiner *et al*. developed an autonomous compiler and robotic laboratory platform to synthesize organic compounds on the basis of standardized methods descriptions (see the Perspective by Milo). The platform comprises conventional equipment such as round-bottom flasks, separatory funnels, and a rotary evaporator to maximize its compatibility with extant literature. The authors showcase the system with short syntheses of three common pharmaceuticals that proceeded comparably to manual synthesis. —JSY

Science, this issue p. 144; see also p. 122

ORGANIC CHEMISTRY

Toward nanotubes with periodic gaps

Carbon nanotubes consist of a continuous array of benzene rings fused along their edges. It is not straightforward to excise regular fragments in a top-down fashion to produce periodic gaps. Sun *et al*. showcase the beginnings of a bottom-up strategy toward this end. They used borylations and catalytic cross-coupling chemistry to prepare a discrete cylindrical carbon compound composed of 40 benzene rings bonded to one another at the 1, 3, and 5 positions to leave regular void spaces in the walls. Catenation of multiple similar segments could ultimately lead to an extended nanotube with periodic wall defects. —JSY

Science, this issue p. 151

CHEMICAL PHYSICS

Climbing vibrational levels

Vibrational excitation of molecules adsorbed on a surface is usually limited because the vibrational energy is rapidly transferred into phonons, the vibrational modes of the substrate. Chen *et al*. found that this is not the case for CO molecules adsorbed on a surface of NaCl. The CO molecules efficiently transferred vibrational energy within groups of molecules from one high excitation state to another until they reached the dissociation limit. This process was possible because of the close proximity of the molecules and the limited transfer of energy to just one phonon mode in the salt surface. —PDS

Science, this issue p. 158

NEUROSCIENCE

Memory capabilities develop with age

During memory formation, time-compressed neuronal sequences underlie consolidation as well as encoding of novel information. Such memory traces are largely contributed by a selection of preconfigured neuronal patterns. However, when and how these preconfigured patterns first emerge in the hippocampus is unknown. Farooq and Dragoi identified an age-dependent development of network preconfiguration into trajectory-like sequences. This preconfiguration was expressed spontaneously during sleep and emerged from the assembly of persistent, location-depicting ensembles, largely controlled by intrinsic developmental programs. Thus, the compressed binding of adjacent locations into spatial trajectories during navigation and their experience-dependent replay emerge in coordination from spontaneous preconfigured sequences. —PRS

Science, this issue p. 168

Published by AAAS

PALEOECOLOGY

Ancient changes in the African tropics

Long-term records of past vegetation change are key to understanding how climate change affects ecosystems, but data are scarce—especially in highly biodiverse regions in the tropics. Lezine *et al*. present a detailed 90,000-year pollen core from an upland crater-lake site in the west African tropical montane forest, which is important from conservation and biogeographic standpoints. The upper treeline moved in response to climate change during the Pleistocene glacial and interglacial periods, whereas the lower limit of the Afromontane forest was stable. The constituent species of the forest also changed. This record resolves debates concerning the biogeographic history of Afromontane vegetation. —AMS

Science, this issue p. 177

ANTIBIOTIC RESISTANCE

Switching ON resistance

Clonal bacterial colonies will often grow dissimilar patches, similar to a tortoiseshell pattern. These differing phenotypes arise by reversible mechanisms called phase variation. Jiang *et al*. developed an algorithm to survey bacterial genomes for invertible promoters that cause phase variation. Inverted repeats signal the presence of these promoters, which can flip between ON and OFF states catalyzed by phage integrase analogs called invertases. Invertible promoters linked to antibiotic resistance genes were widespread among vertebrate gut–associated organisms, including Bacteroidetes, Spirochaetes, and Verrucomicrobia. These bacteria are thus equipped and prepared for sudden environmental stress, including antibiotic exposure. —CA

Science, this issue p. 181

CLIMATE CHANGE

Getting warmer, faster

Rising greenhouse gas concentrations are warming Earth's atmosphere and oceans. However, it has been difficult to reconcile model results and observational time series. In a Perspective, Cheng *et al.* highlight recent studies that have improved the methods used to account for systematic errors and for gaps in the observational record; one study reports an independent measure of ocean heat content changes. The results from these studies are close to those seen in models, suggesting that the models reliably capture the overall change in ocean heat content. Accelerating ocean warming since 1991 underscores the urgency of both mitigating and adapting to climate change. —JFU

Science, this issue p. 128

NEUROSCIENCE

Combining organoids to assemble brain regions

Organoids are three-dimensional cultures of cells, which form complex morphological structures. Recently, numerous advances in organoid culture of cells from human brain regions have helped us understand how the cells behave in a more native, three-dimensional environment. In a Perspective, Paşca discusses how brain organoids derived from cells in different regions of the human brain can be combined, and how multiple cell types can be combined in one organoid, to produce complex brain assembloids. These could be used to understand how brain regions interconnect and develop, as well as how neurodegeneration and neuropsychiatric disorders might arise. —GKA

Science, this issue p. 126

T CELLS

T cells need nuclear F-actin

T cell activation is regulated by numerous mechanisms upon T cell antigen receptor (TCR) engagement, including induction of specific cytokines by transcription factors such as NF-κB and NFAT. Tsopoulidis *et al*. found that TCR engagement caused rapid nuclear actin polymerization to create a dynamic actin filament network critical for $CD4^+$ T cell effector functions. Nuclear actin filament polymerization involved the nuclear Arp2/3 complex induced by nuclear Ca^{2+} and regulated by N-Wasp and NIK. Specific inhibition of nuclear actin filament formation impaired T cell effector responses, including cytokine expression and $CD4^+$ T cell help for antibody production. —CNF

Sci. Immunol. **4**, eaav1987 (2019).

INFLAMMATION

Manganese mobilizes microglial exosomes

Chronic occupational exposure to manganese is associated with the development of Parkinson's disease. Sarkar *et al.* found that exposure of primed microglia or mice to manganese increased the levels and activation of the NLRP3 inflammasome, an inflammation-promoting protein complex. Manganese treatment of microglia caused mitochondrial dysfunction and the release of exosomes containing the inflammasome adaptor protein ASC. Serum exosomes from welders contained more ASC and were more inflammatory than those from normal donors. —ERW

Sci. Signal. **12**, eaat9900 (2019).

Published by AAAS

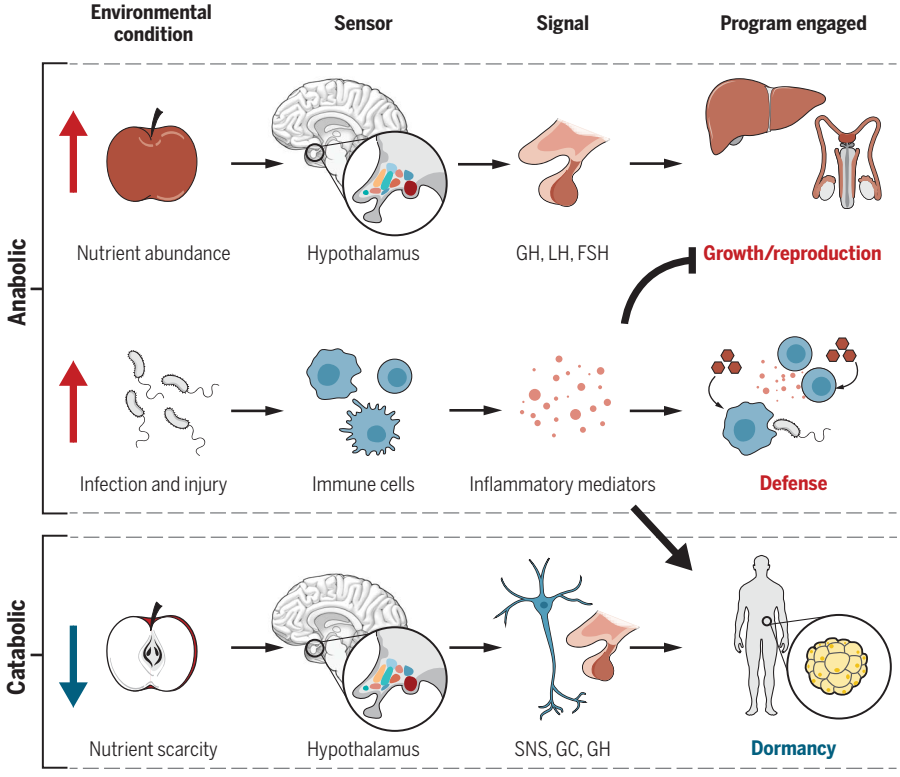
REVIEW SUMMARY

IMMUNOMETABOLISM

An evolutionary perspective on immunometabolism

Andrew Wang*, Harding H. Luan*, Ruslan Medzhitov†

BACKGROUND: Metabolism can be broadly divided into anabolic, energy-consuming, biosynthetic processes and energy-generating catabolic processes. Different biological functions rely on primarily catabolic or primarily anabolic metabolism. The field of immunometabolism has advanced our understanding of how allocation of metabolic resources (energy and metabolites) supports host defenses. On cellular, tissue, and organismal levels, emerging evidence demonstrates a complex interplay between metabolism and inflammation that must be precisely regulated to support biological functions. It is now well established that inflammatory signals tend to activate anabolic processes necessary to support immune responses. Additionally, macrophages, dendritic cells, and T cells can undergo metabolic reprogramming to support different types of cellular functions and activities; thus, naïve and memory T cells rely on catabolic metabolism, whereas effector T cells and macrophages stimulated through Toll-like receptors engage in glycolysis and anabolic metabolism. In addition, at least some anti-inflammatory signals promote metabolic programs that are not supportive of the inflammatory response. The dysregulation of these processes underlies many modern human diseases such as sepsis, diabetes, and obesity.



A life history perspective of metabolic programs. In favorable environmental conditions, growth and reproduction programs are engaged, which rely on anabolic metabolism. Under unfavorable environmental conditions, maintenance programs are engaged. There are two types of maintenance programs: dormancy and defense. Dormancy is induced by nutrient scarcity and relies on energy-preserving catabolic metabolism, whereas defense is induced by infections (and other hostile factors) and requires the support of anabolic metabolism. GH, growth hormone; LH, luteinizing hormone; FSH, follicle-stimulating hormone; SNS, sympathetic nervous system; GC, glucocorticoid.

ADVANCES: We apply evolutionary and ecological principles of life history to discuss the recent advances in immunometabolism within a unifying framework. From this perspective, we highlight the parallels between cellular and systemic control of metabolism. According to life history theory, biological programs can be broadly divided into growth, reproduction, and maintenance. The choice among these programs is dictated by the quality of the environment. Thus, favorable environments promote growth and reproduction, whereas hostile environments promote maintenance and survival programs. These life history programs operate at both organismal and cellular levels. At the organismal level, different hypothalamic-pituitary axes control the engagement of metabolic programs that support organismal growth, reproduction, and maintenance. At the cellular level, activated and quiescent states also broadly correspond to cellular growth and reproduction (proliferation) versus maintenance (quiescence), respectively.

ON OUR WEBSITE

Read the full article at http://dx.doi.org/10.1126/science.aar3932

We propose that maintenance programs can be further subdivided into defense and dormancy. This is because the environment can be hostile for two different reasons: It can lack what an organism needs (nutrients and other resources), or it may have what an organism does not want (pathogens, predators, toxins, etc.). Dormancy and defense deal with these two types of hostile environments, respectively. Dormancy (or quiescence) is an energy-preserving state that permits survival in the face of nutrient scarcity. Defenses, on the other hand, are energy-consuming processes that protect from hostile factors, such as pathogens. We then apply these concepts to immunometabolism and highlight important implications for the logic behind the coordination of cellular function with corresponding metabolic programs.

OUTLOOK: Dysregulation of metabolism and inflammation is a common feature of most of the prevalent modern human diseases. Understanding the complex cellular, tissue, and organismal biology that drive disease pathogenesis is an urgent need. The conceptual framework presented here highlights the logic of metabolic control and the parallels between systemic and cellular metabolism; moreover, it illuminates important areas of exploration in the fields of neuroendocrinology, metabolism, and inflammation biology. ■

The list of author affiliations is available in the full article online.
*These authors contributed equally to this work.
†Corresponding author. Email: ruslan.medzhitov@yale.edu
Cite this article as A. Wang *et al.*, *Science* **363**, eaar3932 (2019). DOI: 10.1126/science.aar3932

Downloaded from http://science.sciencemag.org/ on January 14, 2019

REVIEW

IMMUNOMETABOLISM

An evolutionary perspective on immunometabolism

Andrew Wang[1]*, Harding H. Luan[2]*, Ruslan Medzhitov[2,3]†

Metabolism is at the core of all biological functions. Anabolic metabolism uses building blocks that are either derived from nutrients or synthesized de novo to produce the biological infrastructure, whereas catabolic metabolism generates energy to fuel all biological processes. Distinct metabolic programs are required to support different biological functions. Thus, recent studies have revealed how signals regulating cell quiescence, proliferation, and differentiation also induce the appropriate metabolic programs. In particular, a wealth of new studies in the field of immunometabolism has unveiled many examples of the connection among metabolism, cell fate decisions, and organismal physiology. We discuss these findings under a unifying framework derived from the evolutionary and ecological principles of life history theory.

Metabolism is the core process underlying all biological phenomena. All biological processes require energy sources and metabolic building blocks. Metabolism generally falls into (i) anabolic, energy-consuming, biosynthetic pathways or (ii) catabolic, energy-producing pathways. Historically, our knowledge of these core biochemical pathways was primarily gleaned from research of post-mitotic cells. Recent studies of the immune system have demonstrated a dynamic and finely tuned connection between metabolic programs and the specialized cellular functions they support during the course of the immune response. A number of specific regulatory pathways demonstrating the crucial role of metabolism in immunity have been elegantly characterized and have resulted in the emergence of the new field of immunometabolism. Several excellent recent reviews summarize these advances (*1*–*6*) and demonstrate that on the cellular, tissue, and organismal level, there is a critical role for metabolism in controlling immunity and that inflammation, in turn, has a profound impact on metabolism. This reciprocal relationship is fundamental to the immune response and is at the center of a myriad of modern human diseases including obesity, diabetes, sepsis, and autoimmune/autoinflammatory diseases.

At the heart of immunometabolism is the regulated allocation of metabolic resources (energy and building blocks) required to support host defense and survival. Here, we discuss a unifying framework for these complex interactions based on general concepts of life history theory that explains evolutionary patterns of resource allocation in diverse environments.

Life history theory as an organizing principle in biology

Living creatures use different strategies to optimize reproductive success in the face of constraints imposed by the environment. These strategies are specific combinations of so-called "life history traits" such as size at birth, temporal pattern of growth, age and size at reproductive maturity, fertility, and lifespan, which vary vastly among species. For example, krill grow to only a couple of centimeters and lay thousands of eggs per brood, while the blue whales that dine on them can grow to nearly 100 feet and only give birth once every several years. Life history theory aims to explain this tremendous diversity of lifestyles through analysis and modeling of various resource distribution strategies in the context of species-specific sets of environmental challenges (*7*).

Since its conception in the 1950s, life history theory has clearly demonstrated that in order to maximize reproductive success, organisms must effectively optimize distribution of finite resources into growth, reproduction, and environment-specific survival strategies (maintenance) (*7*). Traditionally, life history theory has identified growth, reproduction, and maintenance as the three fundamental biological programs into which resources can be invested depending on the quality of the environment. Favorable environmental conditions, including abundance of nutrients, promote investment in the anabolic and energy-consuming processes of growth and reproduction, whereas unfavorable conditions, including nutrient scarcity, require reallocation of available resources into stress-specific catabolic and energy-saving maintenance mechanisms (*7*).

Two types of maintenance programs: Defense and dormancy

There are two ways in which the environment can be unfavorable: absence of sufficient resources (typically nutrients), or presence of factors with negative impact on fitness (e.g., predators, pathogens, and toxins). Accordingly, maintenance programs induced by these adverse environments are of two types: dormancy and defense, respectively (Fig. 1). Scarcity of resources induces states of dormancy, where non-essential functions, including growth and reproduction, are temporarily suppressed. Dormancy programs promote energy conservation, rely on catabolic metabolism, and are generally associated with high resistance to environmental stressors. At the extremes, these programs can take the form of suspended animation, such as hibernation and dauer. Hibernating mammals, which build up tremendous stores of fat reserves prior to hibernation, drastically decrease their metabolic rate and rely on catabolic programs associated with the metabolism of fatty acids (*8*). Hibernating mammals have elevated resistance to multiple stressors, including oxidative damage (*9*), traumatic injury (*10*), and hypothermia (*11*). Dormancy programs in lower organisms, such as dauer in *Caenorhabditis elegans* (*12*) and extreme abiotic states in tardigrades (*13*), also show pronounced resilience to environmental stressors. Concordantly, transcriptional analyses of these organisms demonstrate a shift toward catabolic programs and fatty acid metabolism (*14*, *15*).

Like dormancy, defense programs occur at the expense of growth and reproduction, but unlike dormancy, they are energy-consuming and rely on anabolic metabolism to fuel protective responses against pathogens and other hostile environmental factors (Fig. 1B). For example, immune response to pathogens relies on anabolic programs associated with glucose and glutamine utilization, necessary to support leukocyte proliferation and biosynthesis of proteins and other biomolecules involved in defenses (*1*–*3*). Thus, dormancy and defense, although both are part of maintenance, rely on different metabolic programs. Note also that a response to some adverse environments can belong to either dormancy or defense, depending on the animal group. For example, the maintenance program induced by cold temperature could be classified as dormancy in poikilothermic animals, yet be considered as defense in homeothermic animals.

Although life history theory was originally developed as an organizing framework for evolutionary ecology, similar principles can also be applied at the level of organisms and cells. In this context, growth, reproduction, and maintenance can be referred to as life history programs. This view can provide a unifying framework for control and coordination of cellular and organismal metabolism.

The hypothalamus as a central coordinator of organismal life history programs

On the organismal level, the growth, reproduction, and maintenance programs identified in life

[1]Department of Medicine (Rheumatology), Yale University School of Medicine, New Haven, CT 06520, USA. [2]Department of Immunobiology, Yale University School of Medicine, New Haven, CT 06520, USA. [3]Howard Hughes Medical Institute, Yale University School of Medicine, New Haven, CT 06520, USA.
*These authors contributed equally to this work.
†Corresponding author. Email: ruslan.medzhitov@yale.edu

Downloaded from http://science.sciencemag.org/ on January 14, 2019

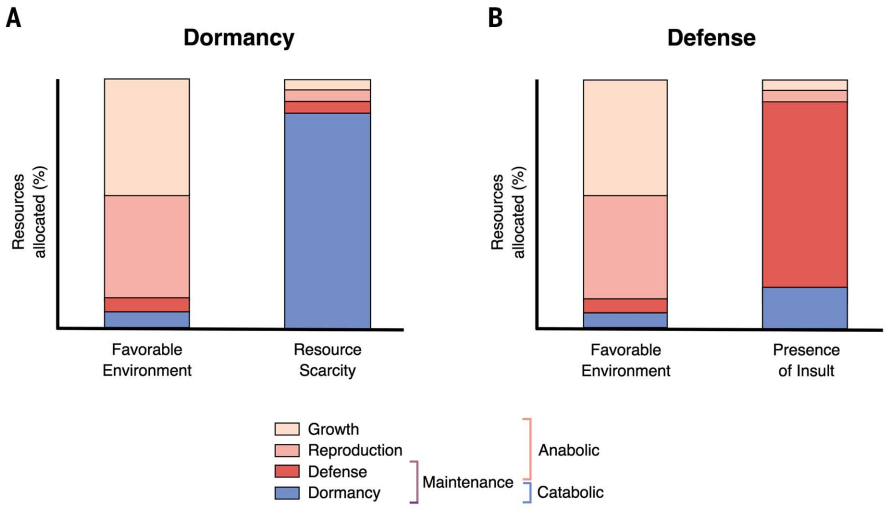


Fig. 1. Dormancy and defense are distinct programs of maintenance. Favorable environments promote investment in growth and reproduction. Unfavorable environments are of two types—resource scarcity and presence of insult (pathogen, toxin, etc.)—and both lead to divestment in growth and reproduction. (**A**) Resource scarcity induces dormancy states, which are characterized by divestment in non-essential functions, energy conservation, and reliance on catabolic metabolism. These programs are generally tissue-protective and cytoprotective. (**B**) Presence of insult induces defense states, which are characterized by energy consumption and anabolic metabolism. Components of the system that are not required for defense engage dormancy both for protection and to divert resources to the defense arm, which requires high energy consumption.

history theory bear distinct resemblance to the three neuroendocrine pathways known as the hypothalamic-pituitary (HP) axes (Fig. 2). Control of somatic growth is largely governed by the growth hormone–insulin-like growth factor (GH-IGF) axis (*16*). Growth hormone (GH) is secreted from somatotroph cells in the anterior pituitary gland. The secretion of GH from the anterior pituitary is promoted by growth hormone–releasing hormone (GHRH) produced by neurons in the periventricular nucleus of the hypothalamus. GH acts through the growth hormone receptor on hepatocytes and other cell types to promote secretion of insulin-like growth factor 1 (IGF-1), which acts on multiple tissues to promote anabolic growth programs. Reproduction is regulated by the hypothalamic-pituitary-gonadal (HPG) axis (*17*). This system begins with hypothalamic neurons in the arcuate nucleus and preoptic area, which secrete gonadotropin-releasing hormone (GnRH). GnRH acts on gonadotrophs in the anterior pituitary gland to induce secretion of luteinizing hormone (LH) and follicle-stimulating hormone (FSH), which promote a variety of sex-specific reproductive functions, in large part by inducing gonadal secretion of the sex hormones, testosterone and estrogen. Finally, the hypothalamic-pituitary-adrenal (HPA) axis controls glucocorticoid production, which, in addition to sympathetic tone, is a common feature of the response to a variety of environmental stressors (infection, cold, predation, etc.) (*18*). Neurons in the paraventricular nucleus of the hypothalamus secrete corticotropin-releasing hormone (CRH). CRH induces corticotrophs in the anterior pituitary gland to release adrenocorticotropic hormone (ACTH) into the blood stream. ACTH then acts on the cells in the cortex of the adrenal gland to promote glucocorticoid secretion. Thus, these three hypothalamic-pituitary axes act as central coordinators of organismal life history programs.

Life history programs on an organismal level are coupled to specific metabolic programs. The GH-IGF axis ultimately results in secretion of IGF-1, which has been shown to promote anabolic metabolism, growth, and storage of excess energy (*19*). Similarly, sex hormones have well-known anabolic effects, which can facilitate energy storage in various ways, such as increased muscle and adipose mass (*20*). In contrast, the effect of glucocorticoids on tissues is primarily catabolic (*21*, *22*). Thus, the physiological effects of the three hypothalamic-pituitary axes correspond to the three life history programs (growth, reproduction, and maintenance), with growth and reproduction being anabolic and maintenance being catabolic.

Because all three of these axes are initiated at the level of the hypothalamus, the hypothalamus can be thought of as the sensor of environmental quality that then directs engagement of appropriate organismal life history programs. Evidence for hypothalamic sensing of environmental quality is abundant. The medial basolateral hypothalamus is particularly well positioned for direct sensory function because it is not protected by the blood-brain barrier, allowing it to access and evaluate the contents of the blood (*23*). Neurons in this anatomic area, including neuropeptide Y/agouti-related protein (NPY/AgRP) and pro-opiomelanocortin (POMC) neurons, can sense nutritional status, either directly (*24*, *25*) or through the effects of insulin and leptin (*26*). The hypothalamus has also been shown to sense other environmental conditions, including hot (*27*) and cold (*28*) temperature, thirst (*29*, *30*), and infection (*31*, *32*).

There is strong evidence that hypothalamic sensing of a hostile environment can lead to direct suppression of the GH-IGF and HPG axes at the hypothalamic level. Following the example of NPY/AgRP and POMC neurons above, α-melanocyte stimulating hormone secreted by POMC neurons (in response to nutrient abundance) has been shown to activate a large fraction of GnRH neurons, whereas NPY, which can be secreted by NPY/AgRP neurons (in response to nutrient scarcity), has been shown to suppress GnRH neurons (*33*). NPY/AgRP neurons have also been shown to inhibit Kiss1-expressing neurons (*34*), which are critical drivers of reproductive maturation and function. AgRP neuron activation may also lead to suppression of the GH–IGF-1 axis (*35*). Finally, CRH can directly suppress GnRH secretion as well as GHRH-induced GH secretion (*36*). Taken together, these examples illustrate how the hypothalamus controls the choice of life history programs as a function of the quality of the environment and orchestrates the suppression of growth and reproductive functions while engaging maintenance programs in unfavorable environments.

Cellular life history programs

At the cellular level, life history programs of cell growth, reproduction (proliferation), and maintenance are reflected in the organization of cell signaling pathways. Engagement of the cellular equivalents of life history programs is dictated by sensing of local cellular environment (nutrient and oxygen availability and various stress factors) and global organismal state (which in turn reflects the organismal environment).

Cells receive information about the organismal environment via various endocrine signals, including signals for growth (GH, IGF-1, and other growth factors), reproduction (estrogen and androgen), and maintenance (glucocorticoids), as well as endocrine hormones which communicate systemic status, such as those permissive for growth and reproduction (i.e., insulin and leptin) or maintenance [i.e., glucagon, ghrelin, fibroblast growth factor (FGF) 21, and inflammatory cytokines]. Interestingly, GH has a dual role in controlling organismal life history programs: In addition to being involved in the GH–IGF-1 axis that controls growth and anabolic metabolism, GH is induced by ghrelin during fasting and promotes lipolysis and gluconeogenesis to enable adaptation to starvation (*37*, *38*). Which of the two opposing pathways is induced by GH is likely dictated by the metabolic status of the organism, such that GH promotes IGF-1–mediated anabolic growth programs in fed states, whereas GH promotes catabolic maintenance programs in fasted states. The details of how

Downloaded from http://science.sciencemag.org/ on January 14, 2019

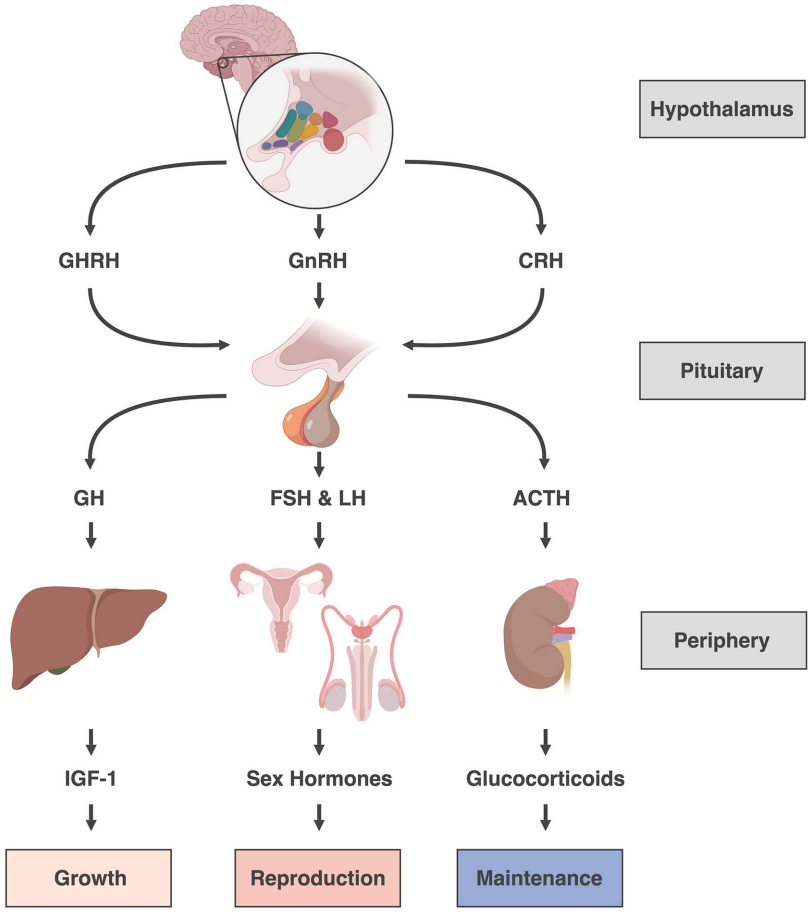


Fig. 2. The hypothalamus as a central coordinator of organismal life history programs. The growth, reproduction, and maintenance arms of life history theory correspond on the organismal level to the growth hormone–insulin-like growth factor (GH-IGF), hypothalamic-pituitary-gonadal (HPG), and hypothalamic-pituitary-adrenal (HPA) axes, respectively. These axes all initiate at the level of the hypothalamus and can be engaged or disengaged, depending on inputs reporting on the quality of the environment. The GH-IGF axis regulates hepatic secretion of IGF-1, which is known to be essential to growth. The HPG axis controls the gonadal secretion of sex hormones, which are necessary for reproductive maturation and function. The HPA axis governs adrenal secretion of glucocorticoids, which are a common component of responses to environmental stress.

these effects of GH are regulated remain to be established.

The local cellular environment is sensed by various nutrient sensors, including adenosine 5′-monophosphate–activated protein kinase (AMPK), which senses adenosine triphosphate; carbohydrate response element–binding protein (ChREBP), which senses glucose; general control nonderepressible 2 (GCN2) and mechanistic target of rapamycin (mTOR), which sense amino acids; sterol regulatory element–binding protein 2 (SREBP-2), which senses sterols; and peroxisome proliferator–activated receptor α (PPARα) and PPARγ, which sense fatty acids (*39*, *40*). Oxygen level is sensed by hypoxia-inducible factor 1 and 2 (HIF-1/2)–prolyl hydroxylase (PHD) sensors (*41*). In addition to nutrient and oxygen availability, cells sense the local presence of various negative microenvironmental factors, including pathogens [Toll-like receptors (TLRs), retinoic acid inducible gene I (RIG-I), melanoma differentiation-associated protein 5 (MDA-5)], oxidative stress [nuclear factor erythroid 2 related factor 2 (NRF-2)], DNA damage (p53), deviations in pH (G-coupled protein receptors GPR132, GPR4, GPR68, and GPR65), heavy metals [metal regulatory transcription factor I (MTF-1)], and protein damage [X-box binding protein I (XBP-1) and heat shock factor I (HSF-1)] (*42*). Activation of these pathways is generally known as the cellular stress response.

Cells engage in their own version of life history programs in reaction to the local environmental and organismal state: When the environment is sensed as favorable, cells grow, proliferate, and engage specific signaling pathways and transcriptional programs that execute these cellular functions. When the environment is sensed as unfavorable, cells engage defense or dormancy programs orchestrated by the corresponding signaling and transcriptional programs (Table 1). The functions of p53 provide a particularly well-studied example illustrating the regulation of cellular life history programs: In response to sensing an adverse cellular state (DNA damage and other stressors), p53 suppresses growth factor signaling and anabolic metabolism required to support cell proliferation, while promoting catabolic metabolism, autophagy, and dormancy (*43*).

Cellular detection of nutrient scarcity leads to activation of catabolic processes characterized by engagement of AMPK, FOXO1/FOXO3a, fatty acid oxidation, and autophagy pathways (*44*). Additionally, these programs repress the anabolic processes of cellular growth and proliferation programs through suppression of the phosphatidylinositol 3-kinase (PI3K)–protein kinase B (AKT) and mTOR pathways (*45*–*47*). A fundamental aspect of a cell's life history program choice is between quiescence (and self-renewal in stem/progenitor cells) and proliferation and differentiation. Stem/progenitor cell quiescence and self-renewal are promoted by resource scarcity and are controlled by the same pathways that control dormancy—AMPK, FoxO, STAT3 (signal transducer and activator of transcription 3), and SMADs—whereas proliferation and differentiation are promoted by PI3K-AKT, mTOR, and other regulators of anabolic metabolism (*4*). Interestingly, asymmetric cell division of stem cells results in unequal partitioning of these signaling components between self-renewing and differentiating daughter cells (*48*–*51*), reflecting the fundamental role these pathways play in cell fate decisions along life history programs. Quiescence/dormancy and self-renewal rely on catabolic metabolism, including oxidative phosphorylation (OxPhos), whereas cell activation, proliferation, and differentiation require glucose and glutamine, aerobic glycolysis, and anabolic metabolism. This is clearly seen in the well-studied examples of T cell metabolism, where naïve and memory T cells (self-renewing/quiescent states) rely on OxPhos, whereas activated/effector T cells rely on aerobic glycolysis and require activation of PI3K-AKT and mTOR pathways (*1*).

Thus, when viewing metabolic reprogramming from a cellular life history perspective, it is clear that the same signaling pathways and transcriptional programs that enable specific cellular functions such as proliferation also engage specific metabolic programs to support these functions. Growth, proliferation, and other resource-utilizing processes are supported by anabolic metabolism, whereas maintenance relies on either catabolic (dormancy) or anabolic (defense) metabolic programs, as we discuss next (Fig. 3A).

Dealing with infection: Immune resistance (defense) and tolerance (dormancy)

For an organism to survive infection, it must reduce the microbial burden (through immune resistance mechanisms) and tolerate the damage caused by infection (through various tissue-protective and survival mechanisms unrelated to pathogen control) (*52*, *53*). Immune resistance requires the proliferation of immune cells and

Downloaded from http://science.sciencemag.org/ on January 14, 2019

Table 1. Cellular life history programs and their associated signaling and transcriptional programs. ER, estrogen receptor; AR, androgen receptor; RIP140, receptor interacting protein 140; $G\alpha_i$ and $G\alpha_s$, Gs and Gi α subunits; ATF4, activating transcription factor 4; GSK3b, glycogen synthase kinase 3β; GR, glucocorticoid receptor; PGC-1α, peroxoisome proliferator-activated receptor γ coactivator 1-α; ERRα, estrogen-related receptor α; cAMP, cyclic adenosine monophosphate; CREB, cAMP response element–binding protein.

	Growth/proliferation	Maintenance/dormancy
Cellular-level signaling	PI3K-AKT	AMPK
	mTOR	GCN2-ATF4, AMPK
	c-Myc, ChREBP	FoxO
	STAT5	STAT3, SMAD2, SMAD3
	Ras-Raf-Erk	GSK3b
	ER, AR	GR, PPARα
	RIP140	PGC-1α, ERRα
	$G\alpha_i$	$G\alpha_s$-cAMP-CREB
Organismal-level signaling	Insulin	Glucagon
	Leptin	Ghrelin
	IGF1, sex hormones	Glucocorticoids
	Growth hormone*	Growth hormone*

*Growth hormone is induced in both favorable and unfavorable environments. How it instructs growth as part of the GH-IGF axis while also acting downstream of ghrelin to promote adaptation to nutrient scarcity is unknown.

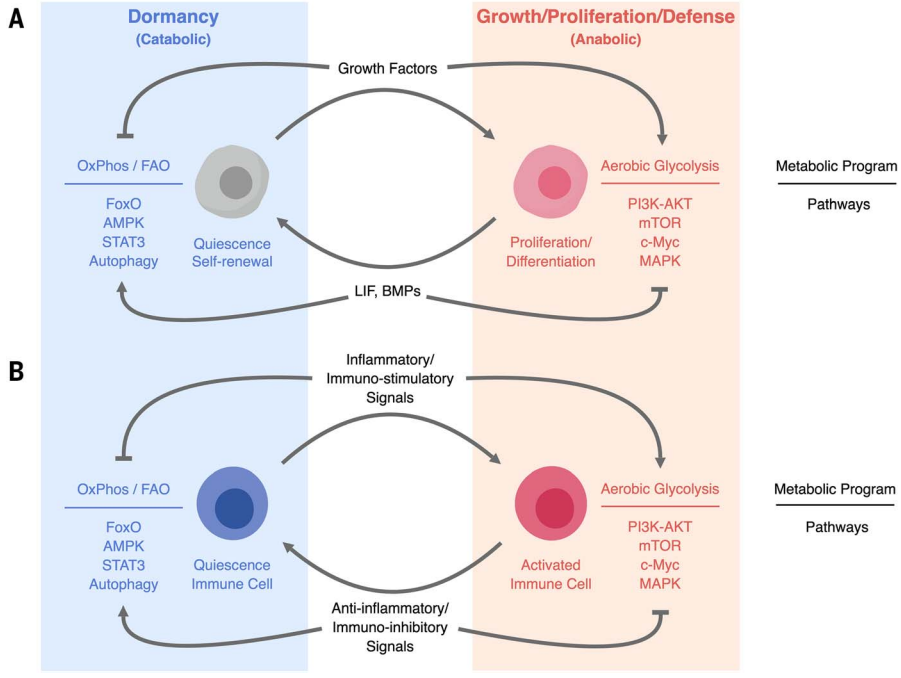


Fig. 3. Cellular life history programs and their corresponding metabolic programs. (**A**) Cells generally use aerobic glycolysis and anabolic pathways after receiving growth and differentiation signals in order to grow, proliferate, and actively suppress catabolic pathways. Signals that inhibit differentiation and proliferation and promote quiescence generally suppress anabolic pathways and use catabolic pathways associated with fatty acid oxidation (FAO) and oxidative phosphorylation (OxPhos). (**B**) Inflammatory and immunostimulatory signals (e.g., TCR, CD28, Toll-like receptors) are mitogenic signals for immune cells and use the same pathways as growth and differentiation factors. These signals direct the activation of macrophages, dendritic cells, and T cells. Anti-inflammatory signals such as IL-10, TGF-β (macrophages), and PD1 (T cells) inhibit metabolic pathways associated with activation and drive catabolic pathways and FAO. Similarly, signals such as IL-4 (macrophages) (*107*) and IL-7 (T cells) promote corresponding quiescent cellular states (alternatively activated macrophages and memory T cells, respectively), which also use FAO and catabolic pathways. MAPK, mitogen-activated protein kinase; LIF, leukemia inhibitory factor; BMPs, bone morphogenetic proteins.

generation of lipid and protein mediators that direct the immune response. These rely on the same energy-consuming anabolic pathways as growth and proliferation induced by growth factors. Thus, the immune response corresponds to the defense component of maintenance programs (Fig. 3B). On the other hand, at least some tolerance mechanisms, which confer stress resistance and tissue protection from inflammatory and pathogen-induced damage, may largely rely on catabolic metabolism and correspond to the dormancy component of maintenance programs. Indeed, as noted earlier, dormancy programs rely on catabolic metabolism and confer stress resistance. We further propose that these dormancy programs are likely induced by specialized signals (including adenosine, ketone bodies, FGF21, and glucocorticoids) that coordinate organ-specific switches to tissue-protective, dormant metabolic states.

Immune resistance (defense)

It is now well established that for immune cells to execute their specialized functions during an infection, they must engage anabolic metabolism. Under homeostatic conditions (in the absence of infection), macrophages maintain homeostatic proliferation in the presence of mitogens (growth and proliferation) in a c-Myc–dependent fashion, but upon activation with lipopolysaccharide (LPS) they actively suppress c-Myc expression and switch to a mTOR-HIF1α–dependent metabolic program (*54*). This example illustrates that although both growth/proliferation and defense rely on anabolic programs, they have distinct features and are controlled by different signaling and transcriptional programs (in this example, c-Myc versus HIF1α). In addition to activating anabolic metabolism, TLR signals induced by LPS in macrophages actively suppresses catabolic programs. LPS stimulation leads to inhibition of AMPK (a key activator of catabolic metabolism) (*55*) and up-regulation of inducible nitric oxide synthase (iNOS) and NO production, which nitrosylates proteins in the mitochondrial electron transport chain, leading to suppression of OxPhos (*56*, *57*). In contrast, the inflammatory functions of macrophages are dependent on aerobic glycolysis and anabolic programs. Upon stimulation by LPS, macrophages activate mTOR (*58*) while increasing phosphofructokinase 2 (μ-PFK2) and thus enhancing aerobic glycolysis (*59*). In a coordinated fashion, LPS activates mTOR-HIF1α pathways, leading to increased transcription of glucose transporter 1 (GLUT1) (*60*) to fuel aerobic glycolysis. The production of interleukin (IL)–1β also requires the activation of mTOR-HIF1α (*61*, *62*) as well as fatty acid synthase (*63*) and the suppression of AMPK and autophagy (*64*, *65*). AMPK suppression in macrophages has also been shown to be critical for maximal induction of tumor necrosis factor (TNF), IL-6, and eicosanoids (*66*). In all cases, limiting glucose or interfering with the subsequent anabolic pathways ablates macrophage inflammatory responses (*59*–*62*).

Dendritic cells (DCs) also switch to aerobic glycolysis upon activation and actively suppress

Downloaded from http://science.sciencemag.org/ on January 14, 2019

OxPhos through the actions of NO and mTOR-HIF1α (67). mTOR-HIF1α has been shown to be required for up-regulation of the costimulatory molecules CD80 and CD86 (68) as well as the production of cytokines (69). Thus, dendritic cell functions are also coupled with supportive anabolic metabolic programs.

Aerobic glycolysis in activated T cells generates the supply of substrates used for growth and proliferation and regulates the efficient production of effector cytokines critical for the immune response (3, 70). Unlike macrophages and DCs, T cell activation initiated by T cell receptor (TCR)/CD28 also augments OxPhos to support rapid increase in energy demand (71, 72). It was recently shown that subsequent to TCR engagement, the mitochondrial proteome is remodeled to promote one-carbon metabolism (73). Ablation of serine hydroxymethyltransferase 2 (SHMT2), the first enzyme in this pathway, impairs CD4 T cell survival and proliferation (74). Consistent with this finding is the observation that unequal elimination of mitochondria in daughter cells after TCR activation leads to different functional outcomes (48, 75). Maintenance of mitochondria has been linked to anabolic metabolism and enhanced glycolysis via PI3K and mTOR pathways and suppression of AMPK and autophagy, whereas mitochondrial clearance has been linked to a catabolic program activated by FOXO1 (75). This process was shown to be critical for control of differentiation (defense, PI3K, mTOR) versus self-renewal (dormancy, FOXO1) (75). Consistent with these findings, one general feature of long-lived memory T cells is their dependence on OxPhos metabolism and fatty acid utilization as well as active suppression of glycolysis and glucose utilization (70, 76).

Given that immune cell activation requires anabolic metabolism, one way that anti-inflammatory signals can operate is by suppressing nutrient acquisition and anabolic programs in immune cells. Indeed, IL-10 negatively regulates macrophage inflammatory response by suppressing GLUT1 cell surface expression, glycolytic flux, and mTOR activity while simultaneously promoting OxPhos and mitophagy, which negatively regulate macrophage activation (64). Transforming growth factor–β (TGF-β) was also recently shown to negatively regulate macrophages by interfering with mitochondrial dynamics (77). In T cells, engagement of the inhibitory receptor PD1 (programmed cell death protein 1) leads to inhibition of glycolysis and promotion of fatty acid oxidation (78, 79). Taken together, these examples suggest that one major mode of action of anti-inflammatory and immune-suppressive signals might be through the suppression of anabolic metabolic programs required for activation of immune and inflammatory responses (Fig. 3B).

Disease tolerance (dormancy)

Surviving an infection requires both pathogen clearance (resistance to infection) and tissue protection from pathogens and inflammatory damage (tolerance to infection). Although immune resistance relies on anabolic metabolism, we propose that some (but not all) aspects of tolerance may primarily be based on catabolic dormancy programs. Indeed, the inflammatory response activates many components of dormancy programs typically induced by nutrient scarcity (Fig. 4A).

A prominent component of acute inflammation illustrating this point is sickness behaviors, which include anorexia, loss of libido, social withdrawal, fatigue, and somnolence (80). Sickness behaviors are thought to have a protective role during an infection, although there is limited understanding of the mechanistic basis for this notion. However, sickness behaviors can be seen from the perspective of life history programs as organismal states associated with dormancy and organ protection. All sickness behaviors appear to be induced through the effects of inflammatory mediators, especially prostaglandins, on the corresponding areas of the hypothalamus (81, 82). Thus, sickness behaviors can be thought of as behavioral manifestations of divestment in growth and reproduction (anorexia and loss of libido) and entry into dormancy (hypersomnia, fatigue, malaise, social withdrawal). Consistent with this, under inflammatory challenges, the HPA axis (for maintenance/catabolic programs) is engaged while the HPG and IGF-1 pathways (growth and reproduction/anabolic programs) are suppressed (83, 84). Inflammatory mediators such as TNF, IL-6, IL-1β, type I interferon, and prostaglandins have all independently been shown to directly induce anorexia (82, 85, 86). In addition to the catabolic state induced by activation of the HPA axis, TNF directly liberates free fatty

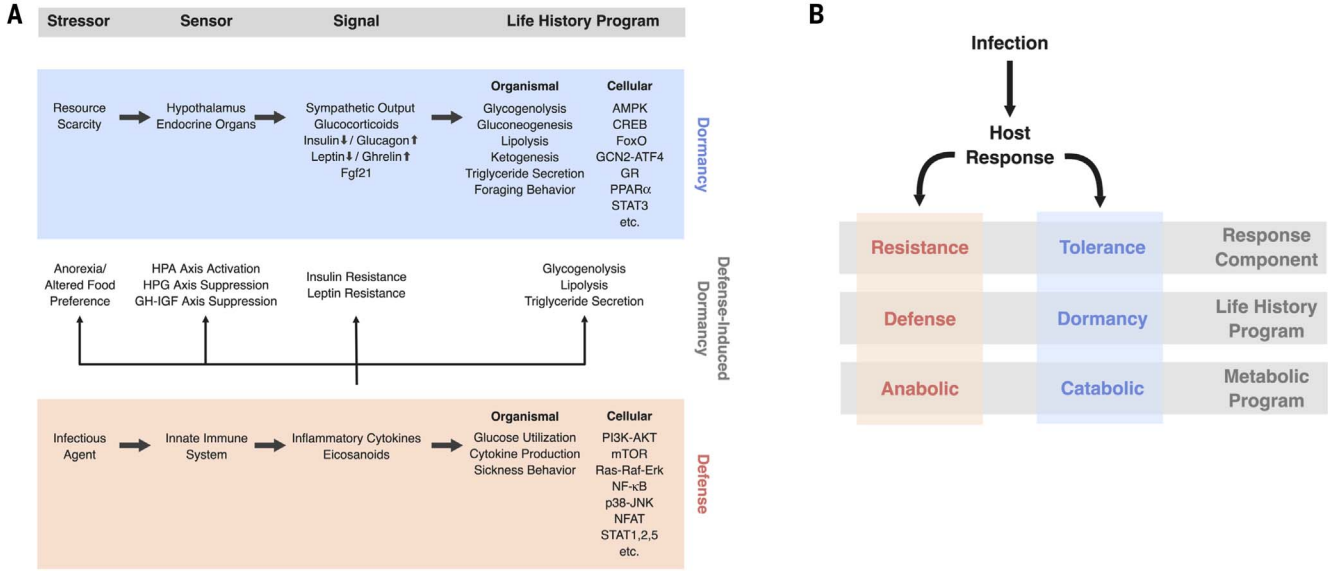


Fig. 4. Inflammation engages both defense and dormancy programs. Dormancy programs are induced by resource scarcity. Resource scarcity is sensed by the hypothalamus and endocrine organs, which then send signals that activate catabolic cellular and organismal programs associated with quiescence and stress resistance. Defense programs are induced by environmental insults such as infectious agents. These are sensed by the immune system, which then uses inflammatory mediators to activate anabolic cellular and organismal programs associated with proliferation and biogenesis. (**A**) During the inflammatory response to infection, inflammatory mediators engage dormancy-associated programs. While the immune system is engaged in defense programs, other parts of the organism are engaged in dormancy programs, which confer stress resilience and tissue protection. (**B**) The host response to infection is divided into immune resistance and immune tolerance. Immune resistance is a defense life history program used by the immune system, whereas immune tolerance is a dormancy life history program activated by the immune system; they use corresponding anabolic and catabolic metabolic programs, respectively.

Downloaded from http://science.sciencemag.org/ on January 14, 2019

acids through lipolysis (87) while simultaneously reducing glucose utilization in skeletal muscle and adipose tissue, both by decreasing insulin secretion by pancreatic β cells and by inducing insulin resistance in these organs (88, 89). Leptin resistance has also been demonstrated in a variety of inflammatory contexts (90). Furthermore, inflammation and inflammation-induced anorexia induce a modified version of a fasted metabolic state, which is characterized by lipolysis and the liberation of free fatty acids from adipose tissue as well as PPARα-regulated synthesis and secretion of ketone bodies and FGF21 by the liver (91). Moreover, both fasting and infection-induced IL-6 induce hepatic triglyceride secretion (92). Plasma angiopoietin-like 4 (Angptl4) levels also rise during inflammation, which inhibits lipoprotein lipase activity in adipose tissue, such that the increased triglycerides in circulation are readily available for utilization rather than taken up for storage (93). The ability to produce glucocorticoids, liberate alternative fuels through lipolysis, stimulate triglyceride secretion, perform ketogenesis, and induce FGF21 have all been shown to be necessary for surviving inflammatory conditions (91, 94, 95). Conversely, agonism of PPARα and FGF21 pathways has been shown to improve survival (96, 97).

It is becoming increasingly clear that a shift to dormancy-associated metabolic programs in vital organs during an immune response confers tissue protection. For example, alternative fuels such as ketone bodies have been shown to have direct cytoprotective effects, primarily by reducing oxidative damage (98, 99) but also by directly signaling to negatively regulate inflammation, as in the cases of the β-hydroxybutyrate receptor Gpr109a (100, 101) and the effect of ketone bodies on the NLRP3 (nucleotide-binding oligomerization domain-like receptor family pyrin domain containing 3) inflammasome (102). On the cellular level, upon oxidative stress, hematopoietic stem cells shift metabolic programs to OxPhos and fatty acid metabolism in a cytochrome c oxidase 2–dependent fashion, which improves their survival (103). Indeed, engagement of catabolic/maintenance programs has been observed to confer stress resistance in a variety of settings, such as in the beneficial tissue-protective effects seen in calorie restriction (104), ischemic preconditioning (105), and therapeutic hypothermia (106).

In summary, the inflammatory response to infection (a maintenance program) suppresses growth and reproduction and is a composite of resistance (defense component of maintenance), which relies on anabolic programs and promotes pathogen clearance, and tolerance (dormancy component of maintenance), which relies on catabolic programs and promotes tissue protection (Fig. 4B). Finally, it should be noted that although dormancy is perhaps the most universal mechanism of tolerance, there are many other processes that can promote survival, depending on what is the limiting factor in a given context. For example, tissue repair is an anabolic process (and thus fits better with the definition of defense), but it can clearly contribute to tolerance. Dormancy, on the other hand, can make tissues less susceptible to damage in the first place.

Perspectives

When the life history theory–derived framework is applied in the context of the immune response, it becomes clear why metabolic reprogramming on both the cellular and organismal level is a critical aspect of the host response to infection. On the cellular level, activated immune cells largely require glucose to mount a robust response. This is consistent with the anabolic processes that immune cell activation entails, including rapid proliferation and synthesis of cytokines, antimicrobial proteins, and lipid mediators. Simultaneously, tissues not directly involved in the immune response engage catabolic metabolism and switch fuel usage from glucose to fatty acids and ketones, which support tissue-protective pathways, as dormancy programs are generally highly resistant to stress.

Life history programs encapsulate the fundamental processes of life. Species, organisms, and cells must all grow and reproduce, proliferate, or survive dynamic environments with a limited pool of resources. Proper allocation of these resources (metabolic programming) is necessary to achieve these basic processes of life. Metabolic and inflammatory disorders, such as diabetes, obesity, sepsis, and autoimmune and autoinflammatory diseases, are increasing at alarming rates, with little progress made toward mitigating mortality and morbidity despite substantial technological advancements. The evolutionary perspective on immunity and metabolism may provide a useful framework within which to understand the biology underlying these diseases.

REFERENCES AND NOTES

1. M. D. Buck, R. T. Sowell, S. M. Kaech, E. L. Pearce, Metabolic Instruction of Immunity. *Cell* **169**, 570–586 (2017). doi: 10.1016/j.cell.2017.04.004; pmid: 28475890
2. L. A. O'Neill, E. J. Pearce, Immunometabolism governs dendritic cell and macrophage function. *J. Exp. Med.* **213**, 15–23 (2016). doi: 10.1084/jem.20151570; pmid: 26694970
3. E. L. Pearce, M. C. Poffenberger, C. H. Chang, R. G. Jones, Fueling immunity: Insights into metabolism and lymphocyte function. *Science* **342**, 1242454 (2013). doi: 10.1126/science.1242454; pmid: 24115444
4. S. A. Nish, W. W. Lin, S. L. Reiner, Lymphocyte Fate and Metabolism: A Clonal Balancing Act. *Trends Cell Biol.* **27**, 946–954 (2017). doi: 10.1016/j.tcb.2017.07.005; pmid: 28818395
5. G. S. Hotamisligil, Foundations of Immunometabolism and Implications for Metabolic Health and Disease. *Immunity* **47**, 406–420 (2017). doi: 10.1016/j.immuni.2017.08.009; pmid: 28930657
6. Y. S. Lee, J. Wollam, J. M. Olefsky, An Integrated View of Immunometabolism. *Cell* **172**, 22–40 (2018). doi: 10.1016/j.cell.2017.12.025; pmid: 29328913
7. S. Stearns, *The Evolution of Life Histories* (Oxford Univ. Press, 1992).
8. G. L. Florant, Lipid Metabolism in Hibernators. *Integr. Comp. Biol.* **38**, 331–340 (1998).
9. J. P. Otis, A. C. Pike, J. R. Torrealba, H. V. Carey, Hibernation reduces cellular damage caused by warm hepatic ischemia-reperfusion in ground squirrels. *J. Comp. Physiol. B* **187**, 639–648 (2017). doi: 10.1007/s00360-017-1056-y; pmid: 28144740
10. P. A. Iaizzo, T. G. Laske, H. J. Harlow, C. B. McClay, D. L. Garshelis, Wound healing during hibernation by black bears (Ursus americanus) in the wild: Elicitation of reduced scar formation. *Integr. Zool.* **7**, 48–60 (2012). doi: 10.1111/j.1749-4877.2011.00280.x; pmid: 22405448
11. V. Matos-Cruz *et al.*, Molecular Prerequisites for Diminished Cold Sensitivity in Ground Squirrels and Hamsters. *Cell Rep.* **21**, 3329–3337 (2017). doi: 10.1016/j.celrep.2017.11.083; pmid: 29262313
12. N. Fielenbach, A. Antebi, C. elegans dauer formation and the molecular basis of plasticity. *Genes Dev.* **22**, 2149–2165 (2008). doi: 10.1101/gad.1701508; pmid: 18708575
13. T. Hashimoto *et al.*, Extremotolerant tardigrade genome and improved radiotolerance of human cultured cells by tardigrade-unique protein. *Nat. Commun.* **7**, 12808 (2016). doi: 10.1038/ncomms12808; pmid: 27649274
14. B. Mali *et al.*, Transcriptome survey of the anhydrobiotic tardigrade Milnesium tardigradum in comparison with Hypsibius dujardini and Richtersius coronifer. *BMC Genomics* **11**, 168 (2010). doi: 10.1186/1471-2164-11-168; pmid: 20226016
15. A. M. Burnell, K. Houthoofd, K. O'Hanlon, J. R. Vanfleteren, Alternate metabolism during the dauer stage of the nematode Caenorhabditis elegans. *Exp. Gerontol.* **40**, 850–856 (2005). doi: 10.1016/j.exger.2005.09.006; pmid: 16221538
16. M. B. Ranke, J. M. Wit, Growth hormone - past, present and future. *Nat. Rev. Endocrinol.* **14**, 285–300 (2018). doi: 10.1038/nrendo.2018.22; pmid: 29546874
17. A. Acevedo-Rodriguez *et al.*, Emerging insights into hypothalamic-pituitary-gonadal axis regulation and interaction with stress signalling. *J. Neuroendocrinol.* **30**, e12590 (2018). doi: 10.1111/jne.12590; pmid: 29524268
18. S. M. Smith, W. W. Vale, The role of the hypothalamic-pituitary-adrenal axis in neuroendocrine responses to stress. *Dialogues Clin. Neurosci.* **8**, 383–395 (2006). pmid: 17290797
19. W. Boron, E. Boulpaep, *Medical Physiology* (Elsevier, ed. 3, 1992).
20. S. Melmed, K. Polonsky, P. R. Larsen, H. Kronenberg, *Williams Textbook of Endocrinology* (Elsevier, ed. 13, 2015).
21. P. O. Hasselgren, Glucocorticoids and muscle catabolism. *Curr. Opin. Clin. Nutr. Metab. Care* **2**, 201–205 (1999). doi: 10.1097/00075197-199905000-00002; pmid: 10456248
22. C. Xu *et al.*, Direct effect of glucocorticoids on lipolysis in adipocytes. *Mol. Endocrinol.* **23**, 1161–1170 (2009). doi: 10.1210/me.2008-0464; pmid: 19443609
23. L. E. Olofsson, E. K. Unger, C. C. Cheung, A. W. Xu, Modulation of AgRP-neuronal function by SOCS3 as an initiating event in diet-induced hypothalamic leptin resistance. *Proc. Natl. Acad. Sci. U.S.A.* **110**, E697–E706 (2013). doi: 10.1073/pnas.1218284110; pmid: 23386726
24. T. K. Lam, R. Gutierrez-Juarez, A. Pocai, L. Rossetti, Regulation of blood glucose by hypothalamic pyruvate metabolism. *Science* **309**, 943–947 (2005). doi: 10.1126/science.1112085; pmid: 16081739
25. T. K. Lam, G. J. Schwartz, L. Rossetti, Hypothalamic sensing of fatty acids. *Nat. Neurosci.* **8**, 579–584 (2005). doi: 10.1038/nn1456; pmid: 15856066
26. M. O. Dietrich, T. L. Horvath, Hypothalamic control of energy balance: Insights into the role of synaptic plasticity. *Trends Neurosci.* **36**, 65–73 (2013). doi: 10.1016/j.tins.2012.12.005; pmid: 23318157
27. C. L. Tan *et al.*, Warm-Sensitive Neurons that Control Body Temperature. *Cell* **167**, 47–59.e15 (2016). doi: 10.1016/j.cell.2016.08.028; pmid: 27616062
28. Z. D. Zhao *et al.*, A hypothalamic circuit that controls body temperature. *Proc. Natl. Acad. Sci. U.S.A.* **114**, 2042–2047 (2017). doi: 10.1073/pnas.1616255114; pmid: 28053227
29. C. A. Zimmerman *et al.*, Thirst neurons anticipate the homeostatic consequences of eating and drinking. *Nature* **537**, 680–684 (2016). doi: 10.1038/nature18950; pmid: 27487211
30. W. E. Allen *et al.*, Thirst-associated preoptic neurons encode an aversive motivational drive. *Science* **357**, 1149–1155 (2017). doi: 10.1126/science.aan6747; pmid: 28912243
31. G. Matarese *et al.*, Hunger-promoting hypothalamic neurons modulate effector and regulatory T-cell responses. *Proc. Natl. Acad. Sci. U.S.A.* **110**, 6193–6198 (2013). doi: 10.1073/pnas.1210644110; pmid: 23530205
32. M. S. Kim *et al.*, Rapid linkage of innate immunological signals to adaptive immunity by the brain-fat axis. *Nat. Immunol.* **16**, 525–533 (2015). doi: 10.1038/ni.3133; pmid: 25848866
33. J. Roa, A. E. Herbison, Direct regulation of GnRH neuron excitability by arcuate nucleus POMC and NPY neuron neuropeptides in female mice. *Endocrinology* **153**, 5587–5599 (2012). doi: 10.1210/en.2012-1470; pmid: 22948210

Downloaded from http://science.sciencemag.org/ on January 14, 2019

34. S. L. Padilla *et al*., AgRP to Kiss1 neuron signaling links nutritional state and fertility. *Proc. Natl. Acad. Sci. U.S.A.* **114**, 2413–2418 (2017). doi: 10.1073/pnas.1621065114; pmid: 28196880
35. H. Sasanuma, M. Nakata, K. Parmila, J. Nakae, T. Yada, PDK1-FoxO1 pathway in AgRP neurons of arcuate nucleus promotes bone formation via GHRH-GH-IGF1 axis. *Mol. Metab.* **6**, 428–439 (2017). doi: 10.1016/j.molmet.2017.02.003; pmid: 28462077
36. K. Kageyama, Regulation of gonadotropins by corticotropin-releasing factor and urocortin. *Front. Endocrinol.* **4**, 12 (2013). doi: 10.3389/fendo.2013.00012; pmid: 23431022
37. R. L. Li *et al*., Profound hypoglycemia in starved, ghrelin-deficient mice is caused by decreased gluconeogenesis and reversed by lactate or fatty acids. *J. Biol. Chem.* **287**, 17942–17950 (2012). doi: 10.1074/jbc.M112.358051; pmid: 22474325
38. A. A. Sakharova *et al*., Role of growth hormone in regulating lipolysis, proteolysis, and hepatic glucose production during fasting. *J. Clin. Endocrinol. Metab.* **93**, 2755–2759 (2008). doi: 10.1210/jc.2008-0079; pmid: 18413425
39. A. Efeyan, W. C. Comb, D. M. Sabatini, Nutrient-sensing mechanisms and pathways. *Nature* **517**, 302–310 (2015). doi: 10.1038/nature14190; pmid: 25592535
40. R. A. Saxton, D. M. Sabatini, mTOR Signaling in Growth, Metabolism, and Disease. *Cell* **168**, 960–976 (2017). doi: 10.1016/j.cell.2017.02.004; pmid: 28283069
41. A. J. Majmundar, W. J. Wong, M. C. Simon, Hypoxia-inducible factors and the response to hypoxic stress. *Mol. Cell* **40**, 294–309 (2010). doi: 10.1016/j.molcel.2010.09.022; pmid: 20965423
42. D. Kültz, Molecular and evolutionary basis of the cellular stress response. *Annu. Rev. Physiol.* **67**, 225–257 (2005). doi: 10.1146/annurev.physiol.67.040403.103635; pmid: 15709958
43. T. J. Humpton, K. H. Vousden, Regulation of Cellular Metabolism and Hypoxia by p53. *Cold Spring Harb. Perspect. Med.* **6**, a026146 (2016). doi: 10.1101/cshperspect.a026146; pmid: 27371670
44. R. Singh, A. M. Cuervo, Autophagy in the cellular energetic balance. *Cell Metab.* **13**, 495–504 (2011). doi: 10.1016/j.cmet.2011.04.004; pmid: 21531332
45. N. Moreno-Marín *et al*., Aryl Hydrocarbon Receptor Promotes Liver Polyploidization and Inhibits PI3K, ERK, and Wnt/β-Catenin Signaling. *iScience* **4**, 44–63 (2018). doi: 10.1016/j.isci.2018.05.006
46. R. L. Vidal, C. Hetz, Unspliced XBP1 controls autophagy through FoxO1. *Cell Res.* **23**, 463–464 (2013). doi: 10.1038/cr.2013.9; pmid: 23337584
47. Z. Feng, A. J. Levine, The regulation of energy metabolism and the IGF-1/mTOR pathways by the p53 protein. *Trends Cell Biol.* **20**, 427–434 (2010). doi: 10.1016/j.tcb.2010.03.004; pmid: 20399660
48. Y. H. Chen *et al*., Asymmetric PI3K Activity in Lymphocytes Organized by a PI3K-Mediated Polarity Pathway. *Cell Rep.* **22**, 860–868 (2018). doi: 10.1016/j.celrep.2017.12.087; pmid: 29420173
49. K. C. Verbist *et al*., Metabolic maintenance of cell asymmetry following division in activated T lymphocytes. *Nature* **532**, 389–393 (2016). doi: 10.1038/nature17442; pmid: 27064903
50. K. N. Pollizzi *et al*., Asymmetric inheritance of mTORC1 kinase activity during division dictates CD8(+) T cell differentiation. *Nat. Immunol.* **17**, 704–711 (2016). doi: 10.1038/ni.3438; pmid: 27064374
51. W. H. Lin *et al*., Asymmetric PI3K Signaling Driving Developmental and Regenerative Cell Fate Bifurcation. *Cell Rep.* **13**, 2203–2218 (2015). doi: 10.1016/j.celrep.2015.10.072; pmid: 26628372
52. J. S. Ayres, D. S. Schneider, Tolerance of infections. *Annu. Rev. Immunol.* **30**, 271–294 (2012). doi: 10.1146/annurev-immunol-020711-075030; pmid: 22224770
53. M. P. Soares, R. Gozzelino, S. Weis, Tissue damage control in disease tolerance. *Trends Immunol.* **35**, 483–494 (2014). doi: 10.1016/j.it.2014.08.001; pmid: 25182198
54. L. Liu *et al*., Proinflammatory signal suppresses proliferation and shifts macrophage metabolism from Myc-dependent to HIF1α-dependent. *Proc. Natl. Acad. Sci. U.S.A.* **113**, 1564–1569 (2016). doi: 10.1073/pnas.1518000113; pmid: 26811453
55. D. Sag, D. Carling, R. D. Stout, J. Suttles, Adenosine 5′-monophosphate-activated protein kinase promotes macrophage polarization to an anti-inflammatory functional phenotype. *J. Immunol.* **181**, 8633–8641 (2008). doi: 10.4049/jimmunol.181.12.8633; pmid: 19050283
56. R. B. Lorsbach, W. J. Murphy, C. J. Lowenstein, S. H. Snyder, S. W. Russell, Expression of the nitric oxide synthase gene in mouse macrophages activated for tumor cell killing. Molecular basis for the synergy between interferon-γ and lipopolysaccharide. *J. Biol. Chem.* **268**, 1908–1913 (1993). pmid: 7678412
57. E. Clementi, G. C. Brown, M. Feelisch, S. Moncada, Persistent inhibition of cell respiration by nitric oxide: Crucial role of S-nitrosylation of mitochondrial complex I and protective action of glutathione. *Proc. Natl. Acad. Sci. U.S.A.* **95**, 7631–7636 (1998). doi: 10.1073/pnas.95.13.7631; pmid: 9636201
58. A. J. Covarrubias, H. I. Aksoylar, T. Horng, Control of macrophage metabolism and activation by mTOR and Akt signaling. *Semin. Immunol.* **27**, 286–296 (2015). doi: 10.1016/j.smim.2015.08.001; pmid: 26360589
59. J. C. Rodríguez-Prados *et al*., Substrate fate in activated macrophages: A comparison between innate, classic, and alternative activation. *J. Immunol.* **185**, 605–614 (2010). doi: 10.4049/jimmunol.0901698; pmid: 20498354
60. A. J. Freemerman *et al*., Metabolic reprogramming of macrophages: Glucose transporter 1 (GLUT1)-mediated glucose metabolism drives a proinflammatory phenotype. *J. Biol. Chem.* **289**, 7884–7896 (2014). doi: 10.1074/jbc.M113.522037; pmid: 24492615
61. G. M. Tannahill *et al*., Succinate is an inflammatory signal that induces IL-1β through HIF-1α. *Nature* **496**, 238–242 (2013). doi: 10.1038/nature11986; pmid: 23535595
62. J. S. Moon *et al*., mTORC1-Induced HK1-Dependent Glycolysis Regulates NLRP3 Inflammasome Activation. *Cell Rep.* **12**, 102–115 (2015). doi: 10.1016/j.celrep.2015.05.046; pmid: 26119735
63. J. S. Moon *et al*., UCP2-induced fatty acid synthase promotes NLRP3 inflammasome activation during sepsis. *J. Clin. Invest.* **125**, 665–680 (2015). doi: 10.1172/JCI78253; pmid: 25574840
64. W. K. E. Ip, N. Hoshi, D. S. Shouval, S. Snapper, R. Medzhitov, Anti-inflammatory effect of IL-10 mediated by metabolic reprogramming of macrophages. *Science* **356**, 513–519 (2017). doi: 10.1126/science.aal3535; pmid: 28473584
65. M. Takahama, S. Akira, T. Saitoh, Autophagy limits activation of the inflammasomes. *Immunol. Rev.* **281**, 62–73 (2018). doi: 10.1111/imr.12613; pmid: 29248000
66. K. C. Carroll, B. Viollet, J. Suttles, AMPKα1 deficiency amplifies proinflammatory myeloid APC activity and CD40 signaling. *J. Leukoc. Biol.* **94**, 1113–1121 (2013). doi: 10.1189/jlb.0313157; pmid: 23883517
67. B. Everts *et al*., Commitment to glycolysis sustains survival of NO-producing inflammatory dendritic cells. *Blood* **120**, 1422–1431 (2012). doi: 10.1182/blood-2012-03-419747; pmid: 22786879
68. J. Jantsch *et al*., Hypoxia and hypoxia-inducible factor-1α modulate lipopolysaccharide-induced dendritic cell activation and function. *J. Immunol.* **180**, 4697–4705 (2008). doi: 10.4049/jimmunol.180.7.4697; pmid: 18354193
69. W. Cao *et al*., Toll-like receptor-mediated induction of type I interferon in plasmacytoid dendritic cells requires the rapamycin-sensitive PI(3)K-mTOR-p70S6K pathway. *Nat. Immunol.* **9**, 1157–1164 (2008). doi: 10.1038/ni.1645; pmid: 18758466
70. M. D. Buck, D. O'Sullivan, E. L. Pearce, T cell metabolism drives immunity. *J. Exp. Med.* **212**, 1345–1360 (2015). doi: 10.1084/jem.20151159; pmid: 26261266
71. C. H. Chang *et al*., Posttranscriptional control of T cell effector function by aerobic glycolysis. *Cell* **153**, 1239–1251 (2013). doi: 10.1016/j.cell.2013.05.016; pmid: 23746840
72. L. A. Sena *et al*., Mitochondria are required for antigen-specific T cell activation through reactive oxygen species signaling. *Immunity* **38**, 225–236 (2013). doi: 10.1016/j.immuni.2012.10.020; pmid: 23415911
73. M. D. Buck *et al*., Mitochondrial Dynamics Controls T Cell Fate through Metabolic Programming. *Cell* **166**, 63–76 (2016). doi: 10.1016/j.cell.2016.05.035; pmid: 27293185
74. N. Ron-Harel *et al*., Mitochondrial Biogenesis and Proteome Remodeling Promote One-Carbon Metabolism for T Cell Activation. *Cell Metab.* **24**, 104–117 (2016). doi: 10.1016/j.cmet.2016.06.007; pmid: 27411012
75. W. C. Adams *et al*., Anabolism-Associated Mitochondrial Stasis Driving Lymphocyte Differentiation over Self-Renewal. *Cell Rep.* **17**, 3142–3152 (2016). doi: 10.1016/j.celrep.2016.11.065; pmid: 28009285
76. G. Cui *et al*., IL-7-Induced Glycerol Transport and TAG Synthesis Promotes Memory CD8$^+$ T Cell Longevity. *Cell* **161**, 750–761 (2015). doi: 10.1016/j.cell.2015.03.021; pmid: 25957683
77. J. R. Grunwell *et al*., TGF-β1 Suppresses the Type I IFN Response and Induces Mitochondrial Dysfunction in Alveolar Macrophages. *J. Immunol.* **200**, 2115–2128 (2018). doi: 10.4049/jimmunol.1701325; pmid: 29427413
78. N. Patsoukis *et al*., PD-1 alters T-cell metabolic reprogramming by inhibiting glycolysis and promoting lipolysis and fatty acid oxidation. *Nat. Commun.* **6**, 6692 (2015). doi: 10.1038/ncomms7692; pmid: 25809635
79. B. Bengsch *et al*., Bioenergetic Insufficiencies Due to Metabolic Alterations Regulated by the Inhibitory Receptor PD-1 Are an Early Driver of CD8$^+$ T Cell Exhaustion. *Immunity* **45**, 358–373 (2016). doi: 10.1016/j.immuni.2016.07.008; pmid: 27496729
80. R. Dantzer, K. W. Kelley, Twenty years of research on cytokine-induced sickness behavior. *Brain Behav. Immun.* **21**, 153–160 (2007). doi: 10.1016/j.bbi.2006.09.006; pmid: 17088043
81. S. Jin *et al*., Hypothalamic TLR2 triggers sickness behavior via a microglia-neuronal axis. *Sci. Rep.* **6**, 29424 (2016). doi: 10.1038/srep29424; pmid: 27405276
82. C. B. Saper, A. A. Romanovsky, T. E. Scammell, Neural circuitry engaged by prostaglandins during the sickness syndrome. *Nat. Neurosci.* **15**, 1088–1095 (2012). doi: 10.1038/nn.3159; pmid: 22837039
83. A. P. Herman, D. Tomaszewska-Zaremba, Effect of endotoxin on the expression of GnRH and GnRHR genes in the hypothalamus and anterior pituitary gland of anestrous ewes. *Anim. Reprod. Sci.* **120**, 105–111 (2010). doi: 10.1016/j.anireprosci.2010.03.011; pmid: 20427135
84. W. Umławska, A. Prusek-Dudkiewicz, Growth retardation and delayed puberty in children and adolescents with juvenile idiopathic arthritis. *Arch. Med. Sci.* **6**, 19–23 (2010). doi: 10.5114/aoms.2010.13501; pmid: 22371715
85. L. R. Leon, A. A. White, M. J. Kluger, Role of IL-6 and TNF in thermoregulation and survival during sepsis in mice. *Am. J. Physiol.* **275**, R269–R277 (1998). pmid: 9688988
86. T. Blank *et al*., Brain Endothelial- and Epithelial-Specific Interferon Receptor Chain 1 Drives Virus-Induced Sickness Behavior and Cognitive Impairment. *Immunity* **44**, 901–912 (2016). doi: 10.1016/j.immuni.2016.04.005; pmid: 27096319
87. J. Laurencikiene *et al*., NF-κB is important for TNF-α-induced lipolysis in human adipocytes. *J. Lipid Res.* **48**, 1069–1077 (2007). doi: 10.1194/jlr.M600471-JLR200 pmid: 17272828
88. G. S. Hotamisligil, N. S. Shargill, B. M. Spiegelman, Adipose expression of tumor necrosis factor-α: Direct role in obesity-linked insulin resistance. *Science* **259**, 87–91 (1993). doi: 10.1126/science.7678183; pmid: 7678183
89. C. Park *et al*., Inhibitory effects of streptozotocin, tumor necrosis factor-α, and interleukin-1β on glucokinase activity in pancreatic islets and gene expression of GLUT2 and glucokinase. *Arch. Biochem. Biophys.* **362**, 217–224 (1999). doi: 10.1006/abbi.1998.1004; pmid: 9989930
90. C. B. de La Serre, G. de Lartigue, H. E. Raybould, Chronic exposure to low dose bacterial lipopolysaccharide inhibits leptin signaling in vagal afferent neurons. *Physiol. Behav.* **139**, 188–194 (2015). doi: 10.1016/j.physbeh.2014.10.032; pmid: 25446227
91. K. R. Feingold *et al*., FGF21 is increased by inflammatory stimuli and protects leptin-deficient ob/ob mice from the toxicity of sepsis. *Endocrinology* **153**, 2689–2700 (2012). doi: 10.1210/en.2011-1496; pmid: 22474187
92. K. Nonogaki *et al*., Interleukin-6 stimulates hepatic triglyceride secretion in rats. *Endocrinology* **136**, 2143–2149 (1995). doi: 10.1210/endo.136.5.7720663; pmid: 7720663
93. N. Tjeerdema *et al*., Inflammation increases plasma angiopoietin-like protein 4 in patients with the metabolic syndrome and type 2 diabetes. *BMJ Open Diabetes Res. Care* **2**, e000034 (2014). doi: 10.1136/bmjdrc-2014-000034; pmid: 25512873
94. A. Wang *et al*., Opposing Effects of Fasting Metabolism on Tissue Tolerance in Bacterial and Viral Inflammation. *Cell* **166**, 1512–1525.e12 (2016). doi: 10.1016/j.cell.2016.07.026; pmid: 27610573
95. L. Lichtenstein *et al*., Angptl4 protects against severe proinflammatory effects of saturated fat by inhibiting fatty acid uptake into mesenteric lymph node macrophages. *Cell Metab.* **12**, 580–592 (2010). doi: 10.1016/j.cmet.2010.11.002; pmid: 21109191

Downloaded from http://science.sciencemag.org/ on January 14, 2019

96. A. Budd *et al*., Increased survival after gemfibrozil treatment of severe mouse influenza. *Antimicrob. Agents Chemother.* **51**, 2965–2968 (2007). doi: 10.1128/AAC.00219-07; pmid: 17562808
97. C. R. Cámara-Lemarroy *et al*., Gemfibrozil attenuates the inflammatory response and protects rats from abdominal sepsis. *Exp. Ther. Med.* **9**, 1018–1022 (2015). doi: 10.3892/etm.2015.2190; pmid: 25667670
98. D. Y. Kim *et al*., Ketone bodies are protective against oxidative stress in neocortical neurons. *J. Neurochem.* **101**, 1316–1326 (2007). doi: 10.1111/j.1471-4159.2007.04483.x; pmid: 17403035
99. T. Shimazu *et al*., Suppression of oxidative stress by β-hydroxybutyrate, an endogenous histone deacetylase inhibitor. *Science* **339**, 211–214 (2013). doi: 10.1126/science.1227166; pmid: 23223453
100. M. Rahman *et al*., The β-hydroxybutyrate receptor HCA2 activates a neuroprotective subset of macrophages. *Nat. Commun.* **5**, 3944 (2014). doi: 10.1038/ncomms4944; pmid: 24845831
101. N. Singh *et al*., Activation of Gpr109a, receptor for niacin and the commensal metabolite butyrate, suppresses colonic inflammation and carcinogenesis. *Immunity* **40**, 128–139 (2014). doi: 10.1016/j.immuni.2013.12.007; pmid: 24412617
102. Y. H. Youm *et al*., The ketone metabolite β-hydroxybutyrate blocks NLRP3 inflammasome-mediated inflammatory disease. *Nat. Med.* **21**, 263–269 (2015). doi: 10.1038/nm.3804; pmid: 25686106
103. W. Du, S. Amarachintha, A. F. Wilson, Q. Pang, SCO2 Mediates Oxidative Stress-Induced Glycolysis to Oxidative Phosphorylation Switch in Hematopoietic Stem Cells. *Stem Cells* **34**, 960–971 (2016). doi: 10.1002/stem.2260; pmid: 26676373
104. L. M. Redman *et al*., Metabolic Slowing and Reduced Oxidative Damage with Sustained Caloric Restriction Support the Rate of Living and Oxidative Damage Theories of Aging. *Cell Metab.* **27**, 805–815.e4 (2018). doi: 10.1016/j.cmet.2018.02.019; pmid: 29576535
105. D. M. Yellon, D. J. Hausenloy, Realizing the clinical potential of ischemic preconditioning and postconditioning. *Nat. Clin. Pract. Cardiovasc. Med.* **2**, 568–575 (2005). doi: 10.1038/ncpcardio0346; pmid: 16258568
106. A. L. Schenone *et al*., Therapeutic hypothermia after cardiac arrest: A systematic review/meta-analysis exploring the impact of expanded criteria and targeted temperature. *Resuscitation* **108**, 102–110 (2016). doi: 10.1016/j.resuscitation.2016.07.238; pmid: 27521472
107. D. Vats *et al*., Oxidative metabolism and PGC-1β attenuate macrophage-mediated inflammation. *Cell Metab.* **4**, 13–24 (2006). doi: 10.1016/j.cmet.2006.05.011; pmid: 16814729

ACKNOWLEDGMENTS

We thank members of the R.M. lab for helpful discussion. **Funding:** Supported by the HHMI, Else Kröner Fresenius Foundation, and the Blavatnik Family Foundation (R.M.); NIH grant K08 AI128745 (A.W.); and NIH grant T32 AI007019 and the Gruber Science Fellowship (H.H.L.). **Author contributions:** A.W., H.H.L., and R.M. wrote the manuscript and generated the accompanying figures. **Competing interests:** The authors declare no competing interests.

10.1126/science.aar3932

Downloaded from http://science.sciencemag.org/ on January 14, 2019

RESEARCH ARTICLE SUMMARY

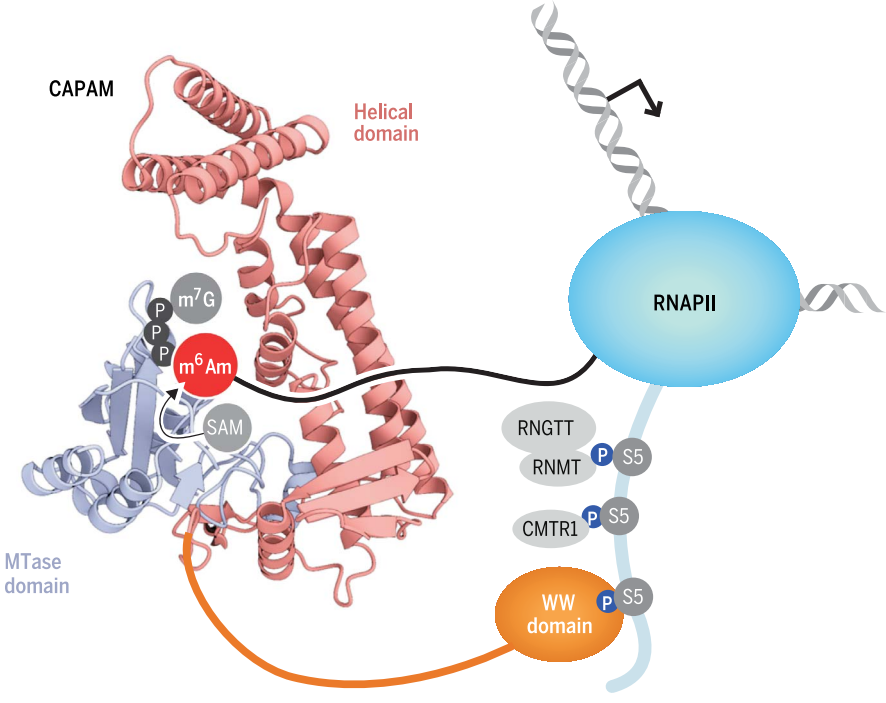
MOLECULAR BIOLOGY

Cap-specific terminal N^6-methylation of RNA by an RNA polymerase II–associated methyltransferase

Shinichiro Akichika*, Seiichi Hirano*, Yuichi Shichino, Takeo Suzuki, Hiroshi Nishimasu, Ryuichiro Ishitani, Ai Sugita, Yutaka Hirose, Shintaro Iwasaki, Osamu Nureki†, Tsutomu Suzuki†

INTRODUCTION: N^6-methyladenosine (m^6A), an abundant modification in eukaryotic mRNAs and long-noncoding RNAs, has been recognized as a major epitranscriptome mark that plays critical roles in RNA metabolism and function. In addition to the internal m^6A, N^6, 2′-*O*-dimethyladenosine (m^6Am) is present at the transcription start site of capped mRNAs in vertebrates. Previous studies reported that an eraser protein, FTO, demethylates N^6-methyl group of m^6Am and destabilizes a subset of mRNAs, suggesting a possible function of m^6Am in stabilizing A-starting capped mRNAs. However, the biogenesis and functional role of m^6Am remain elusive.

RATIONALE: To reveal the functional and physiological roles of m^6Am, it is necessary to identify a writer protein for N^6-methylation of m^6Am. We first established a highly sensitive method to analyze 5′-terminal chemical structures of the capped mRNAs using mass spectrometry (RNA-MS), and then measured m^6Am methylation status accurately. We employed RNA-MS to identify the writer gene by a reverse genetic approach. We chose several candidates of uncharacterized methyltransferases (MTases) that are conserved in vertebrates, but not in yeast, which does not have m^6Am. Each of the candidates was knocked out in human cells. If the target gene is disrupted, RNA-MS can detect the absence of m^6Am in mRNAs prepared from the knockout cells.



Sequential and cotranscriptional m^6Am formation mediated by CAPAM. CAPAM is recruited to the early elongation stage of RNAPII through specific interaction between the WW domain and Ser^5-phosphorylated CTD. The m^7G cap MTase (RNMT) complexed with the capping enzyme (RNGTT) and 2′-*O*-MTase (CMTR1) are also recruited to this complex, indicating a hierarchical formation of m^7Gpppm^6Am—pppA, GpppA, m^7GpppA, m^7GpppAm, and m^7Gpppm^6Am.

RESULTS: RNA-MS analysis revealed that m^6Am modification in human mRNAs is more abundant (92%) than previously estimated. We identified human PCIF1 as cap-specific adenosine-N^6-MTase (CAPAM) responsible for N^6-methylation of m^6Am. Indeed, m^6Am disappeared completely and converted to Am modification in mRNAs prepared from the *CAPAM* knockout (KO) cells. The *CAPAM* KO cells were viable, but sensitive to oxidative stress, implying the physiological importance of m^6Am. We showed that CAPAM catalyzes N^6-methylation of m^6Am in the capped mRNAs in an *S*-adenosylmethionine (SAM)–dependent manner. A series of biochemical studies revealed that CAPAM specifically recognizes the 7-methylguanosine (m^7G) cap structure and preferentially N^6-methylates $m^7GpppAm$ rather than m^7GpppA, indicating the importance of the 2′-*O*-methyl group of the target site for efficient m^6Am formation. CAPAM has a N-terminal WW domain that specifically interacts with the Ser^5-phosphorylated C-terminal domain (CTD) of RNA polymerase II (RNAPII), suggesting that the CAPAM is recruited to the early elongation complex of RNAPII and introduces m^6Am in a nascent mRNA chain cotranscriptionally. We also solved the crystal structure of CAPAM complexed with the cap analog and SAM analog. The core region of CAPAM is composed of MTase and helical domains. The m^7G cap is bound to a pocket formed by these two domains. The SAM analog is recognized by an active site with the characteristic NPPF motif in the MTase domain. This structure reveals the molecular basis of cap-specific m^6A formation. RNA-sequencing analysis of the *CAPAM* KO cells revealed that loss of m^6Am does not affect transcriptome alteration. This result does not support the proposed function of m^6Am in stabilizing A-starting capped mRNAs. Instead, ribosome profiling of the *CAPAM* KO cells showed that N^6-methylation of m^6Am promotes the translation of capped mRNAs.

ON OUR WEBSITE

Read the full article at http://dx.doi.org/10.1126/science.aav0080

CONCLUSION: We identified PCIF1/CAPAM as a cap-specific m^6A writer for vertebrate mRNAs. Structural analysis revealed the molecular basis of cap-specific m^6A formation by CAPAM. The ribosome profiling experiment revealed that CAPAM-mediated m^6Am formation promotes translation of A-starting mRNAs, rather than stabilization of mRNAs. ■

The list of author affiliations is available in the full article online.
*These authors contributed equally to this work.
†Corresponding author. Email: ts@chembio.t.u-tokyo.ac.jp (Ts.S.); nureki@bs.s.u-tokyo (O.N.)
Cite this article as S. Akichika *et al.*, *Science* **363**, eaav0080 (2019). DOI: 10.1126/science.aav0080

Downloaded from http://science.sciencemag.org/ on January 15, 2019

RESEARCH ARTICLE

MOLECULAR BIOLOGY

Cap-specific terminal N^6-methylation of RNA by an RNA polymerase II–associated methyltransferase

Shinichiro Akichika[1]*, Seiichi Hirano[2]*, Yuichi Shichino[3], Takeo Suzuki[1], Hiroshi Nishimasu[2], Ryuichiro Ishitani[2], Ai Sugita[4], Yutaka Hirose[4], Shintaro Iwasaki[3,5], Osamu Nureki[2]†, Tsutomu Suzuki[1]†

N^6-methyladenosine (m^6A), a major modification of messenger RNAs (mRNAs), plays critical roles in RNA metabolism and function. In addition to the internal m^6A, N^6, 2′-*O*-dimethyladenosine (m^6Am) is present at the transcription start nucleotide of capped mRNAs in vertebrates. However, its biogenesis and functional role remain elusive. Using a reverse genetics approach, we identified PCIF1, a factor that interacts with the serine-5–phosphorylated carboxyl-terminal domain of RNA polymerase II, as a cap-specific adenosine methyltransferase (CAPAM) responsible for N^6-methylation of m^6Am. The crystal structure of CAPAM in complex with substrates revealed the molecular basis of cap-specific m^6A formation. A transcriptome-wide analysis revealed that N^6-methylation of m^6Am promotes the translation of capped mRNAs. Thus, a cap-specific m^6A writer promotes translation of mRNAs starting from m^6Am.

RNA molecules are enzymatically modified after transcription. Indeed, more than 160 chemical modifications have been found in various RNAs across all domains of life (*1*, *2*). Recent studies using deep sequencing methods detected several species of modifications in eukaryotic mRNAs and noncoding RNAs in a transcriptome-wide manner (*3*–*5*). These findings raise the concept of "epitranscriptome" and highlight the importance of RNA modifications as regulatory elements in gene expression.

N^6-methyladenosine (m^6A) is an abundant modification in mRNAs and plays a key regulatory role in various biological events, including meiosis (*6*, *7*), cell differentiation (*8*–*10*), neuronal function (*11*, *12*), cancer proliferation (*13*, *14*), circadian rhythm (*15*), sex determination (*16*), and chromosomal silencing (*17*). The biogenesis and dynamics of m^6A have been studied extensively; the modification is introduced by the writer complex METTL3-METTL14-WTAP (*18*) and METTL16 (*19*), and it is demethylated by eraser proteins (ALKBH5 and FTO) (*18*). Internal m^6As are decoded differently by several reader proteins, including YTH family proteins, hnRNP C, and eIF3 (*20*), thereby leading to diverse fates of mRNAs.

The 7-methylguanosine (m^7G) cap is a characteristic 5′-terminal structure of eukaryotic mRNAs (Fig. 1A) (*21*). In the nucleus, this modification not only stabilizes mRNAs, but also promotes their transcription, splicing, polyadenylation, and nuclear export (*22*). In the cytoplasm, the m^7G cap is required for translation of the majority of mRNAs. The m^7G cap is introduced at the 5′ terminus of nascent mRNAs via 5′ to 5′ linkage at the initial stage of transcription, following the recruitment of the capping enzyme complex (RNGTT and RNMT) to the Ser^5-phosphorylated C-terminal domain (CTD) of RNA polymerase II (RNAPII) in the early elongation complex (*23*). After the m^7G cap formation, the 2′ hydroxyl group of the transcription start nucleotide is cotranscriptionally methylated by CMTR1 (*24*, *25*) and that of the second nucleotide is methylated by CMTR2 (*26*) (Fig. 1A). The interferon-induced factor, IFIT1, recognizes hypomethylated viral RNAs and prevents their translation; the 2′-*O*-methylation at the first nucleotide of mRNAs antagonizes IFIT1, allowing them to escape the innate immune system (*27*, *28*). In vertebrate mRNAs, if the transcription start nucleoside is adenosine, its N^6 position is methylated to form N^6, 2′-*O*-dimethyladenosine (m^6Am) (Fig. 1A) (*29*, *30*). Recent studies reported FTO-mediated demethylation of m^6Am and its association with RNA metabolism (*31*, *32*). The biogenesis and physiological importance of this cap-specific m^6A modification have not been fully understood.

Here we identified PCIF1 as a cap-specific adenosine N^6-methyltransferase (CAPAM) responsible for N^6-methylation of m^6Am. CAPAM interacts with the Ser^5-phosphorylated CTD of RNAPII, resulting in the formation of m^6Am at the early stage of the transcription cycle. The crystal structures of CAPAM complexed with substrates revealed the cap-specific m^6A formation mediated by a helical domain of CAPAM. A ribosome profiling experiment showed that m^6Am promotes cap-dependent translation. Our results highlight CAPAM as an m^6A writer for mRNAs.

Mass spectrometric analysis of m^6Am in capped mRNAs

To accurately measure m^6Am frequency, we first conducted a direct analysis of capped mRNAs using RNA mass spectrometry (Fig. 1B). Polyadenylated [poly(A)$^+$] RNAs from human embryonic kidney 293T (HEK293T) cells were partially fragmented with Zn^{2+} and immunoprecipitated with an antibody against m^7G to isolate the 5′-capped fragments. The fragments were digested with ribonuclease (RNase) T_1 and analyzed by capillary liquid chromatography (LC)–nano-electrospray ionization (ESI)–mass spectrometry (RNA-MS) (*33*). We explored the m^7G-capped dimers (m^7GpppN_1Gp) to pentamers ($m^7GpppN_1N_2N_3N_4Gp$) containing 0 to 3 methyl groups and detected 52 species of 5′-capped fragments (Fig. 1CD and table S1). Each fragment was further probed and sequenced by collision-induced dissociation (CID) (Fig. 1, E and F). Using this approach, we detected 15 species of 5′-capped fragments bearing m^6Am at the first position (table S1). Notably, m^7Gpppm^6AmGp was detected as a major species, and $m^7GpppAmGp$ was detected as a minor species in the mass chromatograms (Fig. 1D). Neither $m^7GpppAGp$ nor m^7Gpppm^6AGp was detected, suggesting that CMTR1-mediated 2′-*O*-methylation was efficiently introduced prior to m^6A formation at the first position. The result showed that 5′-capped mRNAs contain 92% m^6Am and 8% Am (Fig. 1D). Consistently, $m^7GpppGmGp$, but not $m^7GpppGp$, was efficiently detected (Fig. 1D). This finding suggested that m^6Am modification is more dominant than previously estimated; 67% in HeLa S3 (*30*) and 48 to 75% in HEK293T cells (*31*).

To estimate the m^7G immunoprecipitation (IP) experiment, we analyzed the flow-through fraction and detected no m^7G-capped RNA fragments, suggesting that a large majority of the capped mRNAs were immunoprecipitated (fig. S1). Although this antibody has a specificity to N^2, N^2, 7-trimethylguanosine (TMG)–capped RNAs, we could not detect any 5′ termini of U-snRNAs (small nuclear RNAs) in the elution fraction (fig. S1), indicating that they were removed during the poly(A)$^+$ preparation.

Identification of cap-specific adenosine N^6-methyltransferase (CAPAM)

To identify the factor responsible for N^6-methylation of m^6Am at the first position of capped mRNAs, we used a reverse genetics

[1]Department of Chemistry and Biotechnology, Graduate School of Engineering, The University of Tokyo, 7-3-1 Hongo, Bunkyo-ku, Tokyo 113-8656, Japan. [2]Department of Biological Sciences, Graduate School of Science, The University of Tokyo, 7-3-1 Hongo, Bunkyo-ku, Tokyo 113-0033, Japan. [3]RNA System Biochemistry Laboratory, Cluster for Pioneering Research, RIKEN, 2-1 Hirosawa, Wako, Saitama 351-0198, Japan. [4]Laboratory of Gene Regulation, Graduate School of Medicine and Pharmaceutical Sciences, University of Toyama, 2630 Sugitani, Toyama 930-0194, Japan. [5]Department of Computational Biology and Medical Sciences, Graduate School of Frontier Sciences, The University of Tokyo 277-8562, Japan.
*These authors contributed equally to this work.
†Corresponding author. Email: ts@chembio.t.u-tokyo.ac.jp (Ts.S.); nureki@bs.s.u-tokyo.ac.jp (O.N.)

Downloaded from http://science.sciencemag.org/ on January 15, 2019

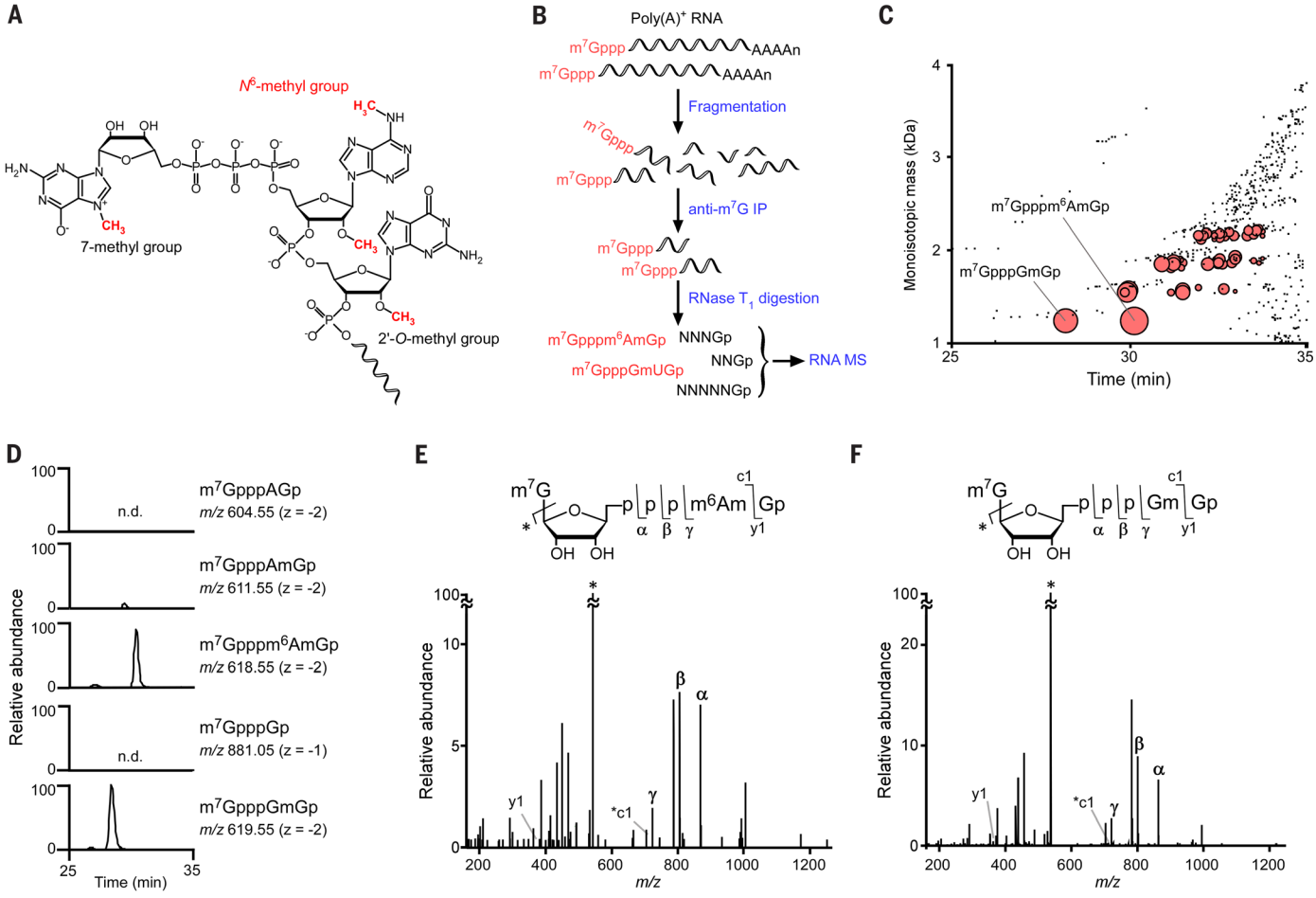


Fig. 1. Comprehensive analysis of mRNA 5′-terminal modification. (**A**) Chemical structure of the 5′-terminus of a typical human mRNA. (**B**) Overview of the mass spectrometric analysis of 5′-capped fragments of human mRNAs. (**C**) Bubble chart showing mass spectrometric profiling of 5′-capped fragments (red circles) of mRNAs. Black circles indicate the noncapped fragments. The bubble sizes are in proportion to the square root of their intensity (red) or the $\log_{10}$ (black). (**D**) Extracted-ion chromatograms (XICs) for 5′-capped RNase T_1-digested fragments of mRNAs. The sequence, mass/charge ratio (*m/z*), and charge state are shown on the right. n.d., not detected. (**E** and **F**) CID spectra of m^7Gpppm^6AmGp and $m^7GpppGmGp$. The product ions were assigned as indicated. Asterisks represent 7-methylguanine dissociation.

approach coupled with RNA-MS (*33*). First, we chose 15 previously uncharacterized methyltransferase (MTase) genes that are not conserved in budding yeast, because m^6Am is not present in fungi. Among them, we focused on PCIF1, which was originally identified as a factor that interacts with the phosphorylated CTD of RNAPII (*34*, *35*) and has an uncharacterized domain similar to that of DNA m^6A MTases M.EcoKI and M.TaqI (*36*). This led us to speculate that PCIF1 is a factor responsible for m^6Am formation on the nascent transcript by association with RNAPII. Therefore, we knocked out this gene in HEK293T cells using the CRISPR-Cas9 system (Fig. 2A) and obtained two knockout (KO) cell lines (KO#1 and KO#2) in which both alleles had frameshift mutations. Western blotting confirmed the absence of endogenous PCIF1 in these KO cell lines (Fig. 2B). The 5′-capped fragments of mRNAs were isolated from *PCIF1* KO#1 and subjected to RNA-MS (Fig. 2C). Notably, m^7Gpppm^6AmGp disappeared completely; instead, $m^7GpppAmGp$ was accumulated in *PCIF1* KO#1. When the KO cells were rescued by plasmid-encoded PCIF1, m^6Am was efficiently restored, demonstrating that PCIF1 is responsible for the conversion of Am to m^6Am at the first position of capped mRNAs (Fig. 2C). Because PCIF1 has an uncharacterized m^6A MTase domain with the conserved NPPF motif (fig. S5C) (*36*), we constructed a mutant of *PCIF1* with Asn^{553}→Ala (N553A) substitution in the NPPF motif. The N553A mutant did not efficiently restore m^6Am in the *PCIF* KO cells (Fig. 2C), indicating the importance of Asn^{553} for m^6Am formation in cells. To examine whether PCIF1 is also involved in the internal m^6A formation, we analyzed the nucleoside composition of poly(A)$^+$ RNAs using LC-MS and found no substantial decrease in internal m^6A in *PCIF1* KO#1 relative to wild-type (WT) cells (fig. S2). Hence, we renamed PCIF1 as cap-specific adenosine-N^6-methyltransferase, or CAPAM.

We next measured in vitro methylation activity of purified CAPAM protein toward a 5′-capped mRNA substrate and clearly observed m^6A formation in the presence of both CAPAM and *S*-adenosylmethionine (SAM) (Fig. 2D). A small amount of m^6A was detected even in the absence of SAM, indicating that some endogenous SAM was bound to the recombinant CAPAM. CID analysis of the methylated fragment confirmed that m^6A indeed occurred at the first position of the capped fragment (fig. S3). Little activity of N^6-methylation was observed in both G-capped mRNA (GpppA) and noncapped mRNA (pppA) (Fig. 3A), suggesting that CAPAM specifically recognizes the m^7G cap structure. We then compared m^6A-forming efficiency of the capped mRNA substrate with or without 2′-*O*-methylation at the first position and found that N^6-methylation of $m^7GpppAm$ is faster than that of m^7GpppA (Fig. 3A and fig. S4A). The K_m (Michaelis constant) values of $m^7GpppAm$ and m^7GpppA were determined to be 3.5 and 28 μM, respectively (Fig. 3B), demonstrating that CAPAM preferentially recognizes the capped mRNAs with Am modification. Consistently, the efficient N^6-methylation of

Downloaded from http://science.sciencemag.org/ on January 15, 2019

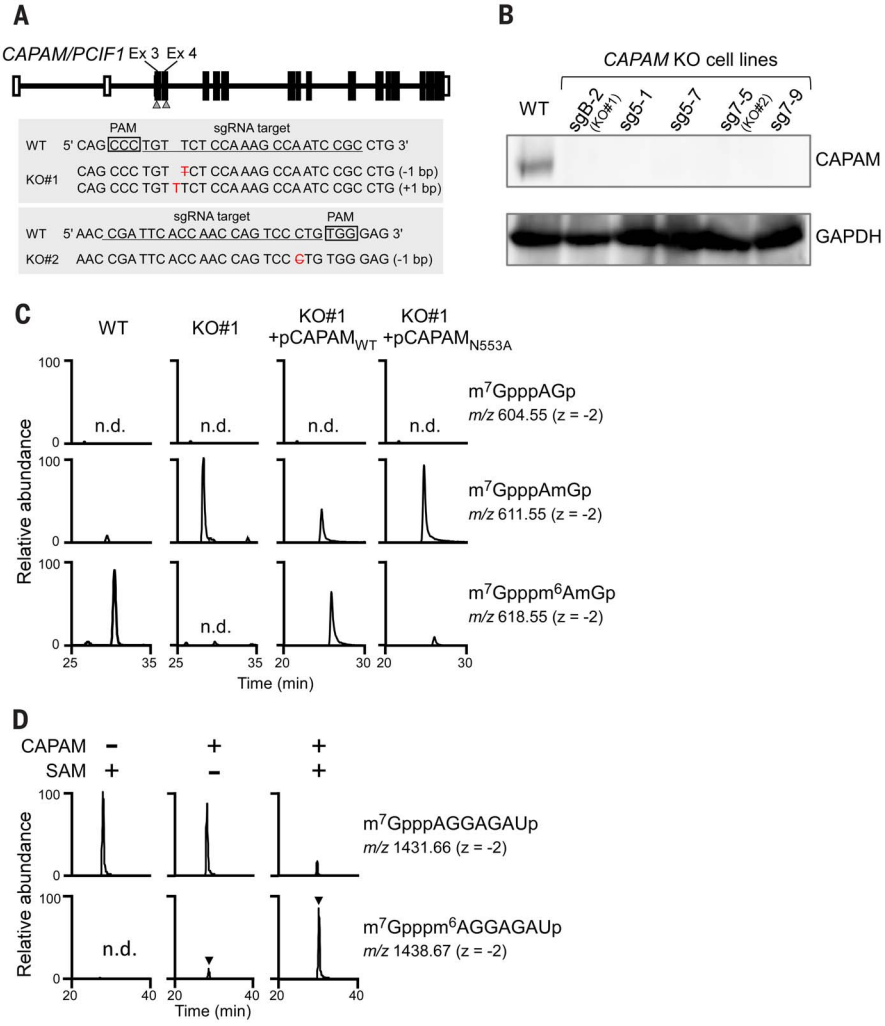


Fig. 2. Identification of CAPAM. (**A**) Schematic illustration of the human *CAPAM* locus and the indels (insertions and deletions) (red) introduced by the CRISPR-Cas9 system targeted by two sgRNAs in the *CAPAM* KO strains. The protospacer and protospacer adjacent motif (PAM) on the sense strand are underlined and boxed, respectively. The arrowheads in exons 3 and 4 indicate the target sites of sgB-2 (KO#1) and sg7-5 (KO#2), respectively. (**B**) Western blot analysis showing the absence of CAPAM in KO cells. (**C**) XICs for the 5′-capped RNase T_1-digested fragments (with A at the first position) of mRNAs obtained from WT (left), KO#1 (left-middle), KO#1 rescued by plasmid-encoded human WT CAPAM (right-middle), and the N553A mutant (right). The fragment information is the same as that shown in Fig. 1D. n.d., not detected. (**D**) In vitro methylation assay of human CAPAM in the presence (+) or absence (-) of SAM. XICs of the 5′-capped RNase A–digested fragments without (upper panels) or with (bottom panels) m^6A. n.d., not detected.

m^7GpppAm was reported in a previous study using HeLa cell lysate (*30*). Our results indicated the hierarchical formation of m^7Gpppm^6Am. To examine the substrate specificity, we compared m^6A methylation activities of CAPAM toward 10 RNA substrates with different sequences at positions 2 and 3 (fig. S4B). CAPAM showed some preference for the 5′-terminal sequence of mRNAs, but did not have a strong sequence specificity. In addition, we measured the activities of CAPAM toward a series of capped RNA substrates with different lengths. CAPAM did not efficiently introduce m^6A on the 3- to 5-nucleotide (mer) substrates, whereas CAPAM methylated the 6-mer substrate as efficiently as the 110-mer substrate (Fig. 3C). Thus, 6-mer is the minimum substrate for the CAPAM-mediated m^6A formation.

CAPAM has a WW domain at its N-terminal region (fig. S5A) (*34*). This domain is homologous to the Pin1 WW domain, which binds to the phosphorylated Ser-Pro motif (*37*). Therefore, we examined the specificity of the CAPAM WW domain for RNAPII CTD peptides with phosphorylation at Ser^2 or Ser^5 (Fig. 3D). The CAPAM WW domain interacted specifically with the Ser^5-phosphorylated CTD, whereas the Pin 1 WW domain interacted with both peptides (Fig. 3D). We next examined a specific interaction between CAPAM and RNAPII with the Ser^5–phosphorylated CTD in HeLa cells. CAPAM and RNAPII with the Ser^5-phosphorylated CTD were coimmunoprecipitated (Fig. 3E), indicating that CAPAM is recruited to the early elongation complex of RNAPII.

Molecular basis of CAPAM-mediated N^6-methylation

To elucidate the mechanism of N^6-methylation by CAPAM, we determined the crystal structure of the CAPAM complex containing m^7G-capped RNA and a cofactor analog, *S*-adenosylhomocysteine (SAH). For crystallization, we constructed human and zebrafish CAPAMs (hCAPAM and zCAPAM, respectively) with truncation of the N-terminal WW domain and the C-terminal part (Fig. 4A and fig. S5A), because the WW domain did not affect the in vitro MTase activity of CAPAM (fig. S5B). We determined the crystal structures of hCAPAM (Apo and SAH-bound forms) and zCAPAM (Apo, SAH-bound, m^7GpppA/SAH-bound, and m^7GpppAmG/SAH-bound forms) at 1.8 to 2.9 Å resolutions (fig. S6 and table S2). Because these six overall structures are similar [root mean square deviation (RMSD) of <1.5 Å for aligned Cα atoms], we hereafter describe the structure of m^7GpppA/SAH-bound zCAPAM unless otherwise stated.

The core region of CAPAM contains the helical and MTase domains (Fig. 4, A and B). The helical domain consists of three-helix bundles (α1-α6-α8 and α4-α5-α6), a four-helix bundle (α1-α2-α3-α6), and β sheets (β1-β2 and β3-β4-β5) (Fig. 4B and fig. S7). A Dali search (*38*) detected no structural similarities between the helical domain and any known protein structure. The MTase domain adopts a canonical Rossmann fold containing a conserved catalytic motif (residues 558 to 561) (Fig. 4B and fig. S7). SAH is bound to a catalytic pocket of CAPAM in a manner similar to that of class I MTases, such as DNA m^6A MTase M.TaqI (Fig. 4C and figs. S8A and S9A). The m^7G cap is bound to the "m^7G site" located between the helical and MTase domains (Fig. 4, B and D, and fig. S8B). The ribose and guanine moieties of m^7G are recognized by Arg^{239}/Arg^{269}/Glu^{563} and Glu^{563}/Trp^{593}/Pro^{596}/Pro^{597}, respectively (Fig. 4D). A mutational assay confirmed the importance of Arg^{239}/Arg^{269}/Glu^{563} for m^7G cap recognition (Fig. 4F). The m^7G cap, but not the target adenosine adjacent to the m^7G cap, was visible in the electron density map (fig. S8B), suggesting that the target nucleotide is disordered in the crystal structure. Based on the reported structure of M.TaqI MTase bound to a DNA substrate (*39*), we modeled a 2′-*O*-methyladenosine (Am) at the active site of CAPAM (fig. S9, B and C). Although M.TaqI is bound to a double-stranded DNA, the active site of M.TaqI recognizes the adenine base flipped out from the double helix (fig. S9, A and C). In addition, the MTase domain of CAPAM is highly homologous to that of M.TaqI, and the characteristic (DNSH)PP(YFW) motif is conserved in all m^6A MTases (*36*). Thus, we modeled the target Am in the active site of CAPAM, based on the M.TaqI complex structure. The model suggested that the adenine moiety of Am forms

Downloaded from http://science.sciencemag.org/ on January 15, 2019

hydrogen-bonding interactions with Asn^{558}/Pro^{559}/Phe^{561} and π-stacking interactions with Phe^{561}/Phe^{619}, and the ribose moiety of Am forms van der Waals interactions with His^{621}. A mutation study supported the importance of these residues for m^6A formation (Fig. 4, E and F, and fig. S9B). Notably, the helical domain forms a positively charged groove (fig. S10, A and B) and is highly conserved in animals (fig. S10C), suggesting that the RNA strand following the 5′ cap binds to this positive groove. We mutated six basic residues in the helical domain of CAPAM and found that five of them reduced m^6A-forming activities significantly (fig. S10D). The result suggests that the basic helical domain serves as the RNA-binding surface. Overall, our structural and mutagenesis data provide mechanistic insights into m^7G-capped RNA recognition and m^6A formation by CAPAM.

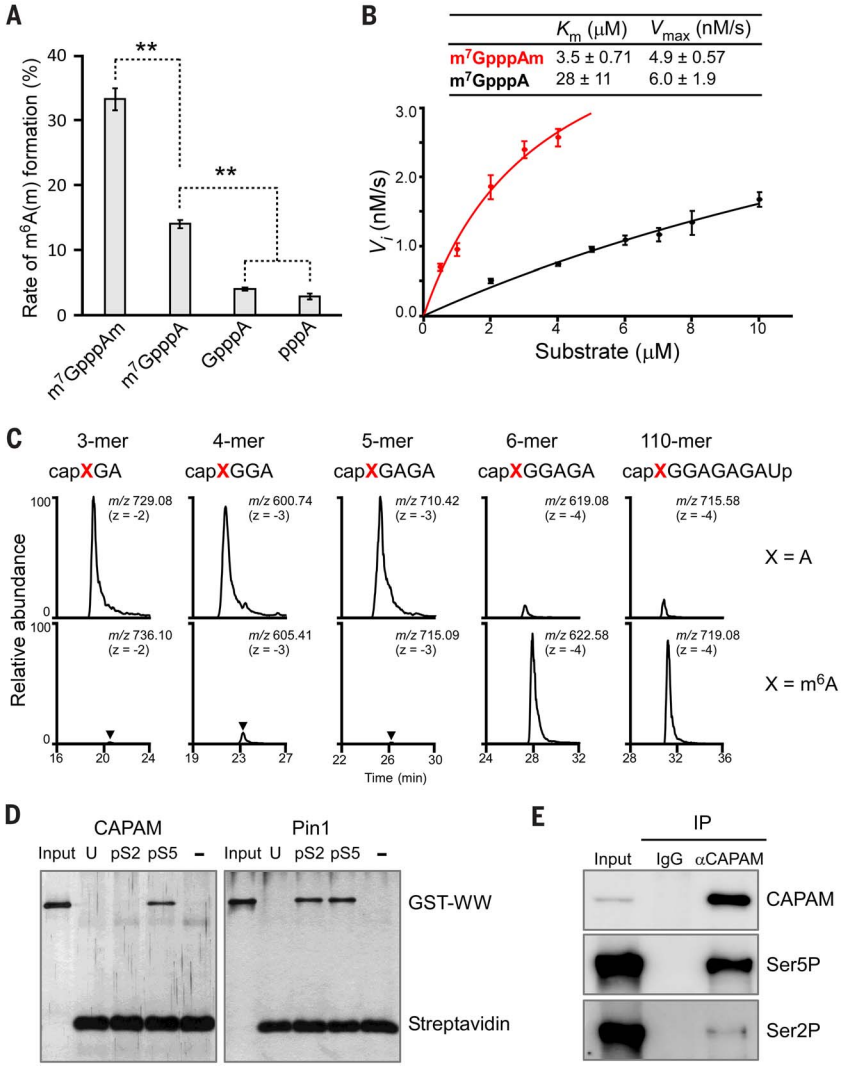


Fig. 3. Biochemical characterization of CAPAM. (**A**) In vitro methylation efficiency of mRNA substrates (110 mer) bearing different 5′-terminal structures (m^7GpppAm-, m^7GpppA-, GpppA-, and pppA-) by human CAPAM. The rate of m^6A(m) formation (percentage) was measured as the mean ± SD (n = 4 independent experiments) of the molar ratio of the incorporated methyl group calculated from the ^{14}C radioactivity to the substrate RNA at each time point. $^{**}P < 1.0 \times 10^{-6}$ by Student's t test. (**B**) Kinetic analysis of in vitro methylation of 5′-capped mRNA substrates (110 mer) with Am (red line) or A (black line) at the first nucleotide by human CAPAM. The initial velocity (V_i) was calculated as the mean ± SD (n = 3 independent experiments). The K_m and V_{max} values were calculated using Prism 7. (**C**) In vitro methylation of 5′-capped mRNA substrates with different lengths, as indicated. XICs for the RNA fragments with A (upper panels) or m^6A (bottom panels). (**D**) The human CAPAM WW domain binds specifically to Ser^5-phosphorylated CTD. Glutathione S-transferase–tagged WW domains derived from CAPAM (left) and Pin1 (right) were pulled down with four different CTD peptides (heptad repeats) immobilized to streptavidin beads. U: unphosphorylated peptide; pS2: Ser^2-phosphorylated; pS5: Ser^5-phosphorylated; (-): without peptide. (**E**) Immunoprecipitation of CAPAM from whole-cell extracts from HeLa cells using CAPAM-specific antibody and normal rabbit immunoglobulin G (control), followed by immunoblotting with antibodies against the indicated proteins.

Physiological role of *CAPAM*

To investigate the biological role of *CAPAM*, we explored the phenotypic features of *CAPAM* KO cell lines. Although *CAPAM* KO cells grew well and showed a growth rate similar to that of WT cells under normal culture conditions, they showed defective growth under oxidative stress conditions (Fig. 5A). This finding indicates that *CAPAM* is involved in the cellular response to oxidative stress.

Next, we performed RNA sequencing (RNA-seq) to compare the transcriptomes of *CAPAM* KO and WT HEK293T cells. A comparison of the steady-state levels of all detected transcripts between *CAPAM* KO and WT cells revealed 25 up-regulated mRNAs and 36 down-regulated mRNAs [false discovery rate (FDR) <0.01] upon KO of *CAPAM* (fig. S11). A previous study reported that demethylation of m^6Am by overexpression of the eraser protein FTO results in significant destabilization of a subset of mRNAs starting with m^6Am (*31*). To confirm this result, we classified mRNAs into five groups according to their first nucleotides (m^6Am, Am, Gm, Cm, and Um) based on the published miCLIP and CAGE data (*31*, *40*), and calculated fold-changes in their steady-state levels upon KO of *CAPAM* (Fig. 5B and fig. S12A). In contrast to the previously reported effect of FTO overexpression (*31*), we observed a slight increase in the level of mRNAs with m^6Am upon KO of *CAPAM*. This result does not support the proposed function of m^6Am to stabilize A-starting capped mRNAs. Consistently, a recent report showed that FTO mainly affects the expression levels of mRNA containing internal m^6A rather than mRNA starting with m^6Am (*32*).

Translational regulation by m^6Am

Given that the 5′-cap structure plays a critical role in translation initiation, we examined whether the m^6Am modification is involved in protein synthesis. To this end, we performed ribosome profiling and RNA-seq to compare translation efficiency (TE) profiles of *CAPAM* KO and WT HEK293T cells. To reveal the effect of m^6Am modification on translation, we classified mRNAs as described above (m^6Am, Am, Gm, Cm, and Um). We observed a significant decrease in translation of mRNAs with m^6Am upon KO of *CAPAM* (Fig. 5C and fig. S12B). Indeed, we found a strong correlation between the TE change of m^6Am-starting transcripts in the two *CAPAM* KO strains versus WT strains with high correlation coefficient (R = 0.81) (fig. S12E), suggesting that N^6-methylation of m^6Am up-regulates the translation. A comparison of the translation efficiency of all detected transcripts between *CAPAM* KO and WT cells revealed 3 up-regulated mRNAs and 75 down-regulated mRNAs (FDR <0.05) upon KO of *CAPAM* (Fig. 5D and fig. S12, C and D). The down-regulated

Downloaded from http://science.sciencemag.org/ on January 15, 2019

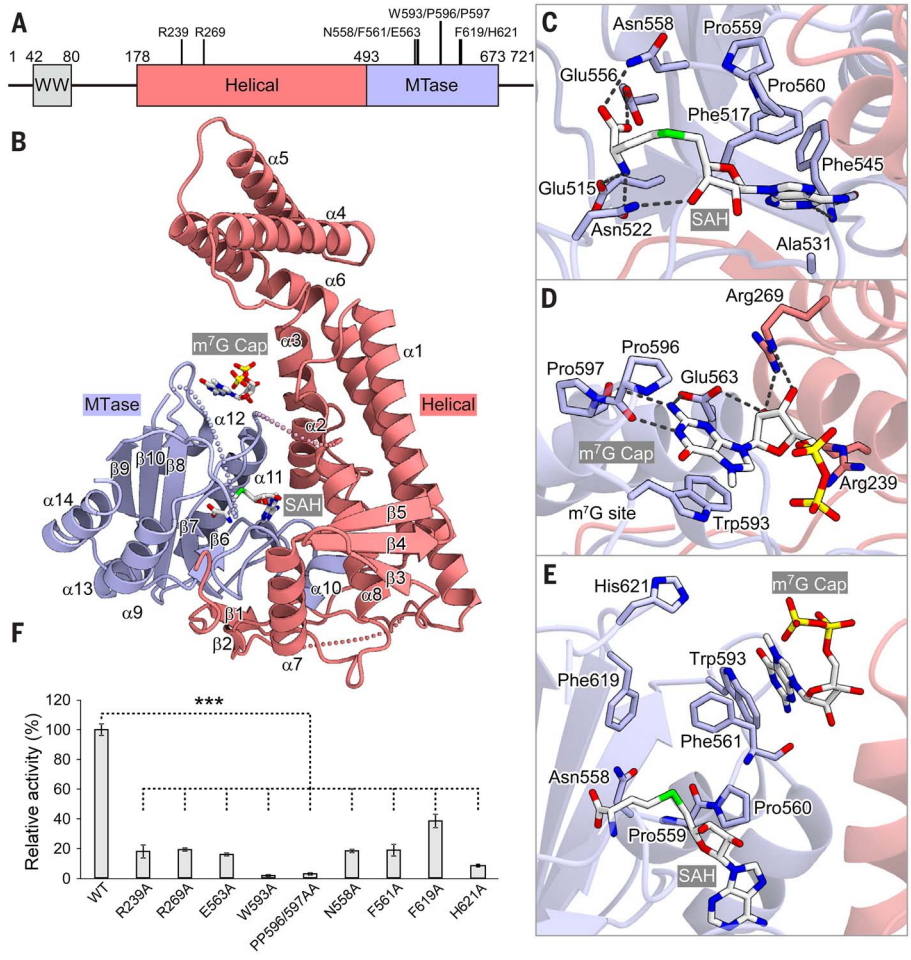


Fig. 4. Crystal structure of CAPAM. (**A**) Domain organization of zCAPAM. (**B**) Overall structure of zCAPAM in complex with m^7GpppA and SAH. (**C** and **D**) Recognition of SAH and the m^7G cap. Hydrogen bonds are shown as dashed lines. (**E**) Putative binding site of the target Am nucleotide. (**F**) In vitro MTase activities of zCAPAM mutants. The substrate used for this assay was 5′-capped mRNA (110 mer). The relative rate of m^6Am formation was calculated as the mean ± SD (n = 4 independent experiments). $^{**}P < 1.0 \times 10^{-6}$ by Student's t test.

genes in the *CAPAM* KO cells, but not up-regulated genes, showed significant enrichment of m^6Am-starting transcripts (Fig. 5E and table S3). A Gene Ontology enrichment analysis revealed that the down-regulated genes are associated with mRNA transport and metabolic processes, and with translation (fig. S13, A and B). We carried out a metagene analysis of ribosomal protected fragments (RPFs) around start codons for m^6Am-starting transcripts and other transcripts (fig. S14), but found no significant difference between WT and *CAPAM* KO cells, indicating that m^6Am modification does not influence ribosome distribution in each mRNA. We also analyzed translation efficiencies of upstream open reading frames (uORFs) and found no obvious effect of m^6Am on the uORF expression upon KO of *CAPAM* (fig. S15).

The eukaryotic translation initiation factor eIF4E directly recognizes the cap structure of mRNAs and is essential for cap-dependent translation initiation (*41*). In addition, the binding affinity of eIF4E for the cap structure is modulated by the first nucleotide of capped mRNAs (*42*). Hence, we examined the binding affinity of eIF4E for capped mRNAs with m^7Gpppm^6Am or m^7GpppAm using an electrophoretic mobility shift assay (EMSA). We observed no significant effect on the binding affinity of eIF4E for mRNAs with or without N^6-methylation of m^7Gpppm^6Am (fig. S16), suggesting that other factors and mechanisms independent of eIF4E are involved in the m^6Am-mediated translational regulation.

Discussion

Using direct RNA-MS analysis of capped mRNAs from HEK293T cells, we found that 92% of A-starting mRNAs have the m^6Am modification, and the remainder have the Am modification, suggesting that the m^6Am frequencies observed in previous studies were underestimated. Because we did not detect m^7GpppAGp and m^7Gpppm^6AGp in this study, it is likely that Am formation by CMTR1 precedes m^6A formation by CAPAM. This finding is consistent with the observation that CAPAM preferentially N^6-methylates Am rather than unmodified A (Fig. 3, A and B) (*30*). In our model structure, the target Am can be recognized in a pocket formed by N^{558}, F^{561}, F^{619}, and H^{621} (Fig. 4E and fig. S9B). Hydrophobic interaction conferred by 2′-*O*-methyl group of Am might be involved in the strong binding to this pocket. Otherwise, C3′ *endo* ribose puckering of Am conferred by 2′-*O*-methylation might be a preferable conformation recognized by CAPAM. These speculations show how the Am is specifically recognized by the enzyme. We also showed that the CAPAM WW domain binds specifically to the Ser^5-phosphorylated CTD, indicating that CAPAM is recruited to the early elongation complex of RNAPII and that N^6-methylation of m^6Am takes place cotranscriptionally. Our results suggested a hierarchical formation of m^7Gpppm^6Am—pppA, GpppA, m^7GpppA, m^7GpppAm, and m^7Gpppm^6Am in the nascent transcript at the early stage of transcription elongation by RNAPII.

Structural comparison with other m^6A writers, METTL3-METTL14 (*43*) and METTL16 (*44*), revealed their diverse mechanisms of RNA substrate recognition and m^6A modification. Whereas these m^6A writers share the common MTase domain with a Rossmann fold, they have additional domains or subunits that define the RNA substrate specificity (fig. S17). In CAPAM, the helical domain forms a positively charged groove that can bind 5′-capped single-stranded RNA. The METTL3-METTL14 complex has a positively charged surface near the active site, which may bind single-stranded RNA containing the consensus motif. In METTL16, the N-terminal domain forms a wide groove that accommodates its structured RNA substrates. These distinct structural features of the m^6A writers likely contribute to their functional divergence in the RNA recognition and m^6A modification.

Our finding that *CAPAM* KO cells grew well under normal conditions suggests that N^6-methylation of m^6Am is not required for cell viability. Nonetheless, *CAPAM* KO cells showed strong sensitivity to H_2O_2 treatment, indicating that m^6Am plays a regulatory role in gene expression in response to oxidative stress. Among m^6Am-starting transcripts, translation efficiency of the *SOD1* mRNA, which encodes superoxide dismutase, was significantly decreased upon KO of *CAPAM* (table S3). This finding might partly explain why *CAPAM* KO strains are sensitive to oxidative stress. An RNA interference–based genetic screen identified *CAPAM/PCIF1* as a putative tumor suppressor in a bladder cancer model (*45*), indicating that it might be involved in cell proliferation under certain conditions. Further studies seem necessary to unveil the physiological role of this gene. Here, we found that N^6-methylation of m^6Am has an ability to up-regulate cap-dependent translation; however, N^6-methylation of m^6Am did not modulate binding of eIF4E to the cap structure. Other cap-binding proteins might be involved in this process.

Downloaded from http://science.sciencemag.org/ on January 15, 2019

Methods summary

5′-capped RNA fragments of poly(A)$^+$ RNAs from HEK293T cells were enriched by antibodies against m^7G cap and subjected to capillary liquid chromatography coupled with nano-electron spray ionization mass spectrometry (*33*) to directly detect m^7G-capped oligomers with m^6Am at the transcription start site. *CAPAM* was knocked out in HEK293T cells by the CRISPR-Cas9 system using two single guide RNAs (sgRNAs) with different target sites. For in vitro reconstitution of m^6A, His-SUMO–tagged CAPAM was recombinantly expressed in *E. coli*, and substrate RNAs were transcribed using T7 RNA polymerase in the presence of cap analogs. Polyclonal antibody against CAPAM was affinity purified from rabbit serum. CAPAM was crystallized with or without SAH and a cap analog, and x-ray diffraction data were collected on beamlines at SPring-8 and Swiss Light Source. The cDNA libraries for RNA-seq analysis were prepared according to the Illumina Truseq protocol, and ribosome profiling was performed as described (*46*).

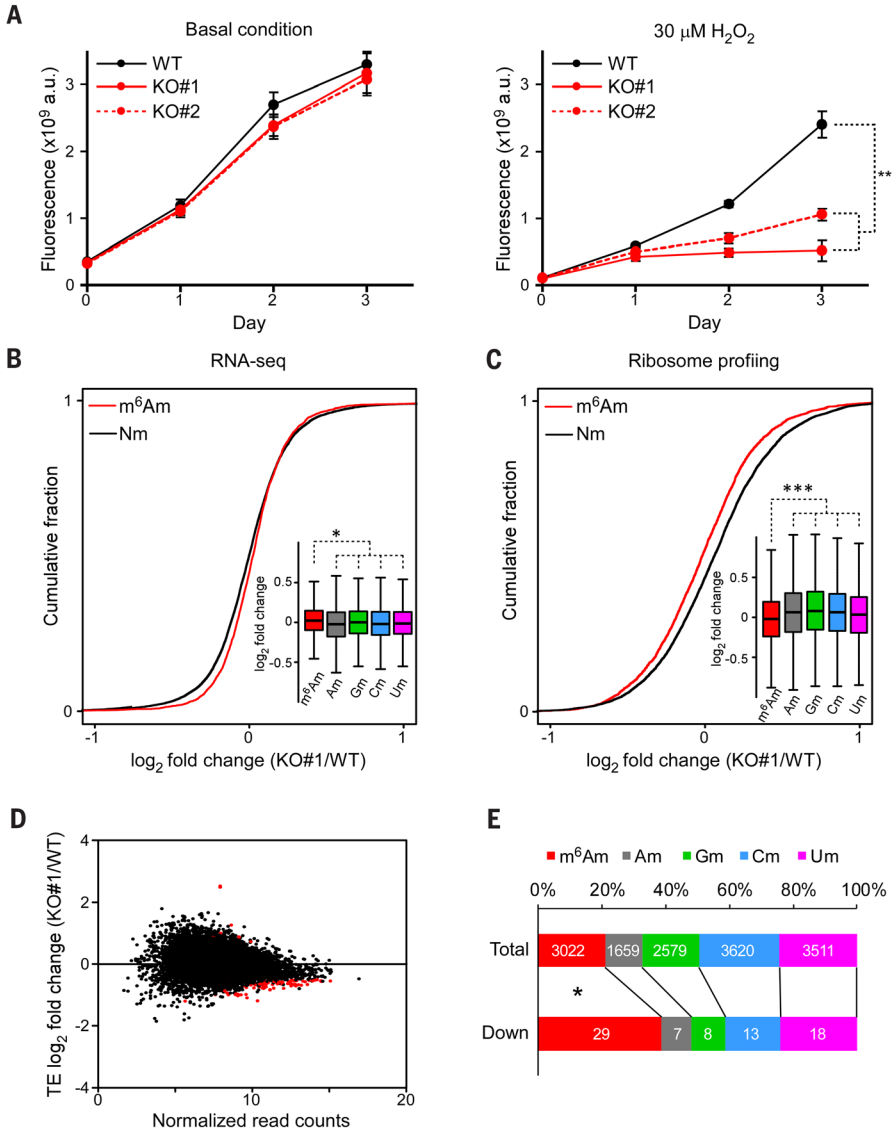


Fig. 5. Physiological importance and translation regulation by m^6Am. (**A**) Growth curves of WT, KO#1, and KO#2 cell lines cultured in normal medium (left) or medium containing 30 μM H_2O_2 (right). Fluorescence was calculated as the mean ± SD (n = 5 independent biological replicates). $^{**}P < 1.0 \times 10^{-7}$ by Student's t test. (**B**) Cumulative plot of the fold-changes in mRNA expression in KO#1 versus WT cells. The mRNAs were classified into five groups based on the first nucleotides (m^6Am, Am, Gm, Cm, and Um), and fold-changes in the steady-state levels of the groups were determined. Each box in the inset panel shows the first quartile, median, and third quartile, and the whiskers represent the 1.5 × interquartile ranges. $^{*}P < 1.0 \times 10^{-4}$ versus m^6Am and Am/Gm/Cm/Um by Wilcoxon's rank sum test. (**C**) Cumulative plot of the fold-change in TE in KO#1 versus WT cells. TE was calculated as the ratio of the normalized read counts obtained from RNA-seq and ribosome profiling. The mRNAs were classified as described for (B). $^{***}P < 1.0 \times 10^{-11}$ versus m^6Am and Am/Gm/Cm/Um by Wilcoxon's rank sum test. (**D**) Differential TEs between WT and KO#1. The $\log_2$ fold-change of each TE was plotted against the normalized read counts from RNA-seq (plots with $P < 0.05$ in red). (**E**) Stacked bar chart of the number of total and down-regulated mRNAs. The number in each box represents the number of classified mRNAs with different first nucleotides. $^{*}P < 1.0 \times 10^{-3}$ versus total m^6Am start mRNAs and down-regulated m^6Am start mRNAs by a binomial test.

REFERENCES AND NOTES

1. P. Boccaletto *et al.*, MODOMICS: A database of RNA modification pathways. 2017 update. *Nucleic Acids Res.* **46** (D1), D303–D307 (2018). doi: 10.1093/nar/gkx1030; pmid: 29106616
2. M. Frye, B. T. Harada, M. Behm, C. He, RNA modifications modulate gene expression during development. *Science* **361**, 1346–1349 (2018). doi: 10.1126/science.aau1646; pmid: 30262497
3. E. M. Harcourt, A. M. Kietrys, E. T. Kool, Chemical and structural effects of base modifications in messenger RNA. *Nature* **541**, 339–346 (2017). doi: 10.1038/nature21351; pmid: 28102265
4. I. A. Roundtree, M. E. Evans, T. Pan, C. He, Dynamic RNA modifications in gene expression regulation. *Cell* **169**, 1187–1200 (2017). doi: 10.1016/j.cell.2017.05.045; pmid: 28622506
5. M. Frye, S. R. Jaffrey, T. Pan, G. Rechavi, T. Suzuki, RNA modifications: What have we learned and where are we headed? *Nat. Rev. Genet.* **17**, 365–372 (2016). doi: 10.1038/nrg.2016.47; pmid: 27140282
6. S. Schwartz *et al.*, High-resolution mapping reveals a conserved, widespread, dynamic mRNA methylation program in yeast meiosis. *Cell* **155**, 1409–1421 (2013). doi: 10.1016/j.cell.2013.10.047; pmid: 24269006
7. M. J. Clancy, M. E. Shambaugh, C. S. Timpte, J. A. Bokar, Induction of sporulation in *Saccharomyces cerevisiae* leads to the formation of N^6-methyladenosine in mRNA: A potential mechanism for the activity of the IME4 gene. *Nucleic Acids Res.* **30**, 4509–4518 (2002). doi: 10.1093/nar/gkf573; pmid: 12384598
8. P. J. Batista *et al.*, m(6)A RNA modification controls cell fate transition in mammalian embryonic stem cells. *Cell Stem Cell* **15**, 707–719 (2014). doi: 10.1016/j.stem.2014.09.019; pmid: 25456834
9. Y. Wang *et al.*, N^6-methyladenosine modification destabilizes developmental regulators in embryonic stem cells. *Nat. Cell Biol.* **16**, 191–198 (2014). doi: 10.1038/ncb2902; pmid: 24394384
10. S. Geula *et al.*, Stem cells. m^6A mRNA methylation facilitates resolution of naïve pluripotency toward differentiation. *Science* **347**, 1002–1006 (2015). doi: 10.1126/science.1261417; pmid: 25569111
11. Y. L. Weng *et al.*, Epitranscriptomic m^6A Regulation of Axon Regeneration in the Adult Mammalian Nervous System. *Neuron* **97**, 313–325.e6 (2018). doi: 10.1016/j.neuron.2017.12.036; pmid: 29346752
12. D. Merkurjev *et al.*, Synaptic N^6-methyladenosine (m^6A) epitranscriptome reveals functional partitioning of localized transcripts. *Nat. Neurosci.* **21**, 1004–1014 (2018). doi: 10.1038/s41593-018-0173-6; pmid: 29950670
13. D. Dai, H. Wang, L. Zhu, H. Jin, X. Wang, N^6-methyladenosine links RNA metabolism to cancer progression. *Cell Death Dis.* **9**, 124 (2018). doi: 10.1038/s41419-017-0129-x; pmid: 29374143
14. S. Lin, J. Choe, P. Du, R. Triboulet, R. I. Gregory, The m(6)A Methyltransferase METTL3 Promotes Translation in Human Cancer Cells. *Mol. Cell* **62**, 335–345 (2016). doi: 10.1016/j.molcel.2016.03.021; pmid: 27117702
15. J. M. Fustin *et al.*, RNA-methylation-dependent RNA processing controls the speed of the circadian clock. *Cell* **155**, 793–806 (2013). doi: 10.1016/j.cell.2013.10.026; pmid: 24209618
16. T. Lence *et al.*, m^6A modulates neuronal functions and sex determination in Drosophila. *Nature* **540**, 242–247 (2016). doi: 10.1038/nature20568; pmid: 27919077

Downloaded from http://science.sciencemag.org/ on January 15, 2019

17. D. P. Patil *et al*., m(6)A RNA methylation promotes XIST-mediated transcriptional repression. *Nature* **537**, 369–373 (2016). doi: 10.1038/nature19342; pmid: 27602518
18. B. S. Zhao, I. A. Roundtree, C. He, Post-transcriptional gene regulation by mRNA modifications. *Nat. Rev. Mol. Cell Biol.* **18**, 31–42 (2017). doi: 10.1038/nrm.2016.132; pmid: 27808276
19. K. E. Pendleton *et al*., The U6 snRNA m^6A Methyltransferase METTL16 Regulates SAM Synthetase Intron Retention. *Cell* **169**, 824–835.e14 (2017). doi: 10.1016/j.cell.2017.05.003; pmid: 28525753
20. D. P. Patil, B. F. Pickering, S. R. Jaffrey, Reading m^6A in the Transcriptome: M^6A-Binding Proteins. *Trends Cell Biol.* **28**, 113–127 (2018). doi: 10.1016/j.tcb.2017.10.001; pmid: 29103884
21. I. Topisirovic, Y. V. Svitkin, N. Sonenberg, A. J. Shatkin, Cap and cap-binding proteins in the control of gene expression. *Wiley Interdiscip. Rev. RNA* **2**, 277–298 (2011). doi: 10.1002/wrna.52; pmid: 21957010
22. V. H. Cowling, Regulation of mRNA cap methylation. *Biochem. J.* **425**, 295–302 (2010). doi: 10.1042/BJ20091352; pmid: 20025612
23. S. Moteki, D. Price, Functional coupling of capping and transcription of mRNA. *Mol. Cell* **10**, 599–609 (2002). doi: 10.1016/S1097-2765(02)00660-3; pmid: 12408827
24. F. Bélanger, J. Stepinski, E. Darzynkiewicz, J. Pelletier, Characterization of hMTr1, a human Cap1 2′-O-ribose methyltransferase. *J. Biol. Chem.* **285**, 33037–33044 (2010). doi: 10.1074/jbc.M110.155283; pmid: 20713356
25. T. Haline-Vaz, T. C. Lima Silva, N. I. Zanchin, The human interferon-regulated ISG95 protein interacts with RNA polymerase II and shows methyltransferase activity. *Biochem. Biophys. Res. Commun.* **372**, 719–724 (2008). doi: 10.1016/j.bbrc.2008.05.137; pmid: 18533109
26. M. Werner *et al*., 2′-*O*-ribose methylation of cap2 in human: Function and evolution in a horizontally mobile family. *Nucleic Acids Res.* **39**, 4756–4768 (2011). doi: 10.1093/nar/gkr038; pmid: 21310715
27. J. L. Hyde, M. S. Diamond, Innate immune restriction and antagonism of viral RNA lacking 2′-*O* methylation. *Virology* **479-480**, 66–74 (2015). doi: 10.1016/j.virol.2015.01.019; pmid: 25682435
28. Y. M. Abbas *et al*., Structure of human IFIT1 with capped RNA reveals adaptable mRNA binding and mechanisms for sensing N1 and N2 ribose 2′-*O* methylations. *Proc. Natl. Acad. Sci. U.S.A.* **114**, E2106–E2115 (2017). doi: 10.1073/pnas.1612444114; pmid: 28251928
29. A. K. Banerjee, 5′-terminal cap structure in eucaryotic messenger ribonucleic acids. *Microbiol. Rev.* **44**, 175–205 (1980). pmid: 6247631
30. J. M. Keith, M. J. Ensinger, B. Mose, HeLa cell RNA (2′-*O*-methyladenosine-N^6-)-methyltransferase specific for the capped 5′-end of messenger RNA. *J. Biol. Chem.* **253**, 5033–5039 (1978). pmid: 670176
31. J. Mauer *et al*., Reversible methylation of m^6A_m in the 5′ cap controls mRNA stability. *Nature* **541**, 371–375 (2017). doi: 10.1038/nature21022; pmid: 28002401
32. J. Wei *et al*., Differential m^6A, m^6A_m, and m^1A Demethylation Mediated by FTO in the Cell Nucleus and Cytoplasm. *Mol. Cell* **71**, 973–985.e5 (2018). doi: 10.1016/j.molcel.2018.08.011; pmid: 30197295
33. T. Suzuki, Y. Ikeuchi, A. Noma, T. Suzuki, Y. Sakaguchi, Mass spectrometric identification and characterization of RNA-modifying enzymes. *Methods Enzymol.* **425**, 211–229 (2007). doi: 10.1016/S0076-6879(07)25009-8; pmid: 17673085
34. H. Fan *et al*., PCIF1, a novel human WW domain-containing protein, interacts with the phosphorylated RNA polymerase II. *Biochem. Biophys. Res. Commun.* **301**, 378–385 (2003). doi: 10.1016/S0006-291X(02)03015-2; pmid: 12565871
35. Y. Hirose *et al*., Human phosphorylated CTD-interacting protein, PCIF1, negatively modulates gene expression by RNA polymerase II. *Biochem. Biophys. Res. Commun.* **369**, 449–455 (2008). doi: 10.1016/j.bbrc.2008.02.042; pmid: 18294453
36. L. M. Iyer, D. Zhang, L. Aravind, Adenine methylation in eukaryotes: Apprehending the complex evolutionary history and functional potential of an epigenetic modification. *BioEssays* **38**, 27–40 (2016). doi: 10.1002/bies.201500104; pmid: 26660621
37. P. J. Lu, X. Z. Zhou, M. Shen, K. P. Lu, Function of WW domains as phosphoserine- or phosphothreonine-binding modules. *Science* **283**, 1325–1328 (1999). doi: 10.1126/science.283.5406.1325; pmid: 10037602
38. L. Holm, P. Rosenström, Dali server: Conservation mapping in 3D. *Nucleic Acids Res.* **38**, W545–W549 (2010). doi: 10.1093/nar/gkq366; pmid: 20457744
39. K. Goedecke, M. Pignot, R. S. Goody, A. J. Scheidig, E. Weinhold, Structure of the N^6-adenine DNA methyltransferase M.TaqI in complex with DNA and a cofactor analog. *Nat. Struct. Biol.* **8**, 121–125 (2001). doi: 10.1038/84104; pmid: 11175899
40. B. Linder *et al*., Single-nucleotide-resolution mapping of m^6A and m^6Am throughout the transcriptome. *Nat. Methods* **12**, 767–772 (2015). doi: 10.1038/nmeth.3453; pmid: 26121403
41. N. Sonenberg, A. G. Hinnebusch, Regulation of translation initiation in eukaryotes: Mechanisms and biological targets. *Cell* **136**, 731–745 (2009). doi: 10.1016/j.cell.2009.01.042; pmid: 19239892
42. A. Tamarkin-Ben-Harush, J. J. Vasseur, F. Debart, I. Ulitsky, R. Dikstein, Cap-proximal nucleotides via differential eIF4E binding and alternative promoter usage mediate translational response to energy stress. *eLife* **6**, e21907 (2017). doi: 10.7554/eLife.21907; pmid: 28177284
43. X. Wang *et al*., Structural basis of N(6)-adenosine methylation by the METTL3-METTL14 complex. *Nature* **534**, 575–578 (2016). doi: 10.1038/nature18298; pmid: 27281194
44. K. A. Doxtader *et al*., Structural Basis for Regulation of METTL16, an *S*-Adenosylmethionine Homeostasis Factor. *Mol. Cell* **71**, 1001–1011.e4 (2018). doi: 10.1016/j.molcel.2018.07.025; pmid: 30197297
45. J. Hensel *et al*., Patient Mutation Directed shRNA Screen Uncovers Novel Bladder Tumor Growth Suppressors. *Mol. Cancer Res.* **13**, 1306–1315 (2015). doi: 10.1158/1541-7786.MCR-15-0130; pmid: 26078295
46. N. J. McGlincy, N. T. Ingolia, Transcriptome-wide measurement of translation by ribosome profiling. *Methods* **126**, 112–129 (2017). doi: 10.1016/j.ymeth.2017.05.028; pmid: 28579404

ACKNOWLEDGMENTS

We are grateful to the lab members, especially to Y. Sakaguchi and S. Ito, for technical assistance. We thank C. K. Ho and S. Shuman for providing materials. **Funding:** This work was supported by Grants-in-Aid for Scientific Research on Priority Areas from the Ministry of Education, Culture, Sports, Science, and Technology of Japan (MEXT); Japan Society for the Promotion of Science (JSPS) (26113003, 26220205, and 18H05272 to Ts.S., 21115003 and 18K19141 to Ta.S., 17K07282 to Y.H., JP17H05679 and JP17H04998 to S.I.), and the Basic Science and Platform Technology Program for Innovative Biological Medicine from the Japan Agency for Medical Research and Development (AMED) to O.N. This work used the Vincent J. Coates Genomics Sequencing Laboratory at the University of California Berkeley, supported by NIH S10 OD018174 Instrumentation Grant, and Bioinformatics Analysis Environment Service on RIKEN Cloud at RIKEN Advanced Center for Computing and Communications. **Author contributions:** S.A. performed all biochemical and genetic works assisted by Ta.S. S.H. performed structural studies assisted by H.N. and R.I. Y.S. performed ribosome profiling and data analysis supported by S.I. Y.H. and A.S. performed the IP experiment. S.A., S.H., H.N. and Ts.S. wrote this paper. All authors discussed the results and revised this paper. Ts.S. and O.N. designed and supervised all the work. **Competing interests:** The authors declare that they have no competing interests. **Data and materials availability:** Ribosome profiling and RNA-seq data are deposited in NCBI (accession numbers: GSE122071). The coordinates of CAPAM structures are deposited in the Protein Data Bank (accession numbers 6IRV, 6IRW, 6IRX, 6IRY, 6IRZ, 6ISO).

SUPPLEMENTARY MATERIALS

www.sciencemag.org/content/363/6423/eaav0080/suppl/DC1
Materials and Methods
Figs. S1 to S17
Tables S1 to S4
References (47–66)

5 August 2018; accepted 14 November 2018
Published online 22 November 2018
10.1126/science.aav0080

Downloaded from http://science.sciencemag.org/ on January 15, 2019

RESEARCH ARTICLE SUMMARY

IMMUNOLOGY

Chronic TLR7 and TLR9 signaling drives anemia via differentiation of specialized hemophagocytes

Holly M. Akilesh, Matthew B. Buechler, Jeffrey M. Duggan, William O. Hahn, Bharati Matta, Xizhang Sun, Griffin Gessay, Elizabeth Whalen, Michael Mason, Scott R. Presnell, Keith B. Elkon, Adam Lacy-Hulbert, Betsy J. Barnes, Marion Pepper, Jessica A. Hamerman*

INTRODUCTION: Inflammatory disorders and infections are associated with cytopenias, including anemia and thrombocytopenia. Common to these conditions is activation of the innate immune system, which includes the monocyte/macrophage lineage, through receptors that recognize pathogen-derived molecules. Toll-like receptors (TLRs) are one family of pathogen sensors that recognize bacterial and viral ligands, including pathogen-derived nucleic acids through TLR7 and TLR9. TLRs not only recognize pathogens, leading to clearance of infection, they are also implicated in inflammatory and autoimmune disease. How signaling through TLRs in monocytes and/or macrophages may participate in inflammation- and infection-associated cytopenias is not completely understood.

RATIONALE: The phagocytosis of red blood cells (RBCs), platelets, and leukocytes can be a major contributor to acute cytopenias. Thus, we reasoned that specialized phagocytes may develop in inflammatory conditions in response to the signaling of pattern-recognition receptors, such as TLRs. In vitro, TLR signaling can directly induce macrophage development. However, whether TLR-induced differentiation specifies a particular macrophage fate that is distinct from homeostatic macrophage differentiation is not clear. To address this question, we undertook in vitro and in vivo studies to investigate TLR-induced macrophage differentiation and the role of this process in inflammatory cytopenias.

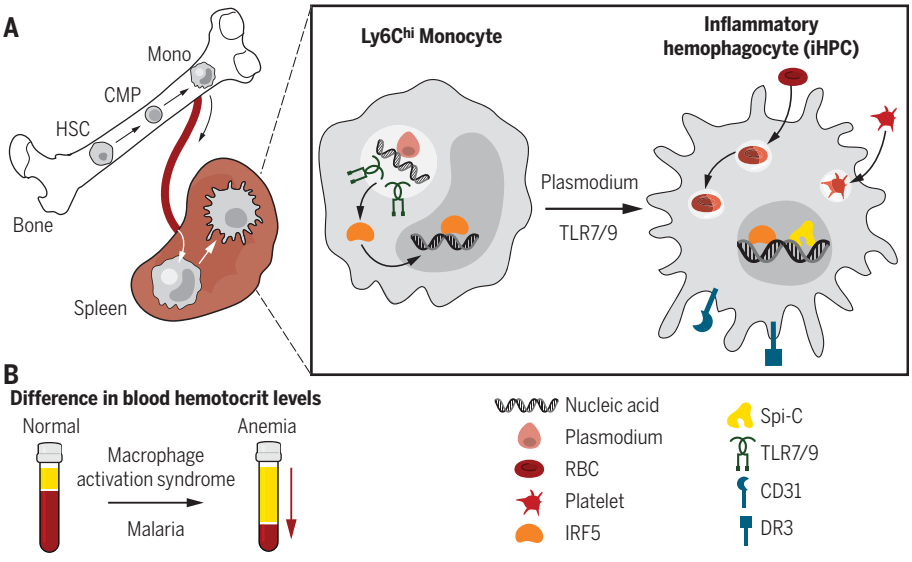
RESULTS: Transcriptional profiling of macrophages differentiated through TLR7 signaling in vitro showed that these cells have a gene signature similar to red pulp macrophages (RPMs), the steady-state hemophagocytes of the spleen. Using a mouse model of TLR7-driven inflammation (the TLR7.1 mouse), we found a population of hemophagocytes that were distinct from RPMs by cell-surface phenotype and that were not found in uninflamed wild-type mice. Therefore, we have termed these cells "inflammatory hemophagocytes," or iHPCs. iHPCs shared expression of the transcription factor Spi-C with RPMs but showed higher phagocytic uptake of RBCs. Thus, iHPCs, although similar to RPMs, are a distinct population of hemophagocytes.

ON OUR WEBSITE

Read the full article at http://dx.doi.org/10.1126/science.aao5213

iHPCs required cell-intrinsic TLR7 signaling for their development and differentiated from inflammatory Ly6C^{hi} monocytes by way of IRF5. Signaling in these monocytes through TLR7 or TLR9—but not through TLR4, TLR3, interleukin-1β, or interferon-γ—induced the iHPC phenotype, and chronic depletion of monocytes caused a severe reduction in iHPC numbers. TLR7.1 mice showed progressive severe anemia and thrombocytopenia with age, and blocking iHPC differentiation through monocyte depletion rescued these inflammatory cytopenias. We next asked whether infection-driven anemia and thrombocytopenia also involved iHPCs. Infection of mice with RBC stage *Plasmodium yoelii* 17XNL, a model of malarial anemia, showed MyD88 and endosomal TLR-dependent iHPC differentiation. Thus, iHPCs differentiate in situations of both sterile and infectious cytopenias.

CONCLUSION: We identified a previously unknown TLR7/9-driven monocyte differentiation pathway associated with inflammatory cytopenias. We propose that macrophage activation syndrome (MAS), a life-threatening complication of rheumatological diseases or viral infection associated with acute cytopenias, may be caused by iHPCs and that these cells also drive severe malarial anemia. Our studies suggest unexplored avenues to treat MAS, severe malarial anemia, and "anemia of inflammation." ■



iHPCs differentiate in response to TLR7 and TLR9 signals and participate in inflammation-induced anemia. (**A**) Before release into the circulation, Ly6C^{hi} monocytes develop in the bone marrow from hematopoietic stem cells (HSCs) and common myeloid progenitors (CMPs). During inflammation, including TLR7 overexpression and *Plasmodium* infection, Ly6C^{hi} monocytes differentiate into hemophagocytes in response to signaling from the endosomal nucleic acid–sensing receptors TLR7 and TLR9 by means of the IRF5 transcription factor. These splenic iHPCs phagocytose RBCs and express the transcription factor Spi-C and cell-surface proteins CD31 and DR3. (**B**) iHPCs drive inflammatory anemia and thrombocytopenia, such as that seen in MAS and severe malarial anemia.

The list of author affiliations is available in the full article online.
*Corresponding author. Email: jhamerman@benaroyaresearch.org
Cite this article as H. M. Akilesh *et al.*, *Science* **363**, eaao5213 (2019). DOI: 10.1126/science.aao5213

Downloaded from http://science.sciencemag.org/ on January 12, 2019

RESEARCH ARTICLE

IMMUNOLOGY

Chronic TLR7 and TLR9 signaling drives anemia via differentiation of specialized hemophagocytes

Holly M. Akilesh[1,2], Matthew B. Buechler[1,3], Jeffrey M. Duggan[1,3], William O. Hahn[3,4], Bharati Matta[5], Xizhang Sun[2], Griffin Gessay[1], Elizabeth Whalen[6], Michael Mason[6], Scott R. Presnell[6], Keith B. Elkon[1,2], Adam Lacy-Hulbert[1,3], Betsy J. Barnes[5], Marion Pepper[3], Jessica A. Hamerman[1,3]*

Cytopenias are an important clinical problem associated with inflammatory disease and infection. We show that specialized phagocytes that internalize red blood cells develop in Toll-like receptor 7 (TLR7)–driven inflammation. TLR7 signaling caused the development of inflammatory hemophagocytes (iHPCs), which resemble splenic red pulp macrophages but are a distinct population derived from Ly6C^{hi} monocytes. iHPCs were responsible for anemia and thrombocytopenia in TLR7-overexpressing mice, which have a macrophage activation syndrome (MAS)–like disease. Interferon regulatory factor 5 (IRF5), associated with MAS, participated in TLR7-driven iHPC differentiation. We also found iHPCs during experimental malarial anemia, in which they required endosomal TLR and MyD88 signaling for differentiation. Our findings uncover a mechanism by which TLR7 and TLR9 specify monocyte fate and identify a specialized population of phagocytes responsible for anemia and thrombocytopenia associated with inflammation and infection.

Inflammatory disorders and infections are associated with cytopenias, including anemia and thrombocytopenia. However, the mechanisms underlying these phenomena are poorly understood. A particularly acute and life-threatening form of inflammatory cytopenia is seen in macrophage activation syndrome (MAS), in which activated macrophages containing red blood cells (RBCs) and leukocytes are found in the bone marrow, spleen, and liver (*1*, *2*). MAS is a severe complication of some rheumatological diseases, most commonly in systemic juvenile idiopathic arthritis (sJIA) and pediatric lupus, or MAS can develop after viral infections, such as with Epstein–Barr virus (*1*, *3*, *4*). Severe cytopenias, principally anemia and thrombocytopenia, also occur during acute malaria infection, particularly in young children, in whom it can cause mortality (*5*–*7*). Thus, an understanding of the mechanisms underlying cytopenias that accompany inflammatory disease and infection is important in order to identify points of therapeutic intervention for these conditions.

[1]Immunology Program, Benaroya Research Institute, Seattle, WA, USA. [2]Division of Rheumatology, Department of Medicine, University of Washington, Seattle, WA, USA. [3]Department of Immunology, University of Washington, Seattle, WA, USA. [4]Division of Allergy and Infectious Disease, Department of Medicine, University of Washington, Seattle, WA, USA. [5]Center for Autoimmune, Musculoskeletal and Hematopoietic Disease, The Feinstein Institute for Medical Research, Manhasset, NY, USA. [6]Systems Immunology Program, Benaroya Research Institute, Seattle, WA, USA.
***Corresponding author. Email: jhamerman@benaroyaresearch.org**

The phagocytosis of RBCs, platelets, and leukocytes can be a major contributor to acute cytopenias. Thus, we reasoned that specialized phagocytes may develop in inflammatory conditions in response to the signaling of pattern-recognition receptors, such as Toll-like receptors (TLRs). TLRs are well known to trigger cytokine production from mature myeloid cells, such as macrophages. However, little is known about the role of TLRs in specifying myeloid cell development. TLRs are highly expressed on hematopoietic stem and progenitor cells (HSPCs), beginning with hematopoietic stem cells (HSCs) through to more committed myeloid progenitor cells, such as common myeloid progenitors (CMPs). The treatment of HSPCs with TLR agonists in vitro can induce macrophage differentiation in the absence of the homeostatic macrophage differentiation factor M-CSF (macrophage colony-stimulating factor) (*8*–*10*). However, it is unclear whether this occurs in vivo. Viral or bacterial infection or injection of mice with TLR agonists leads to characteristic changes in HSPCs, which correlate with the increased production of neutrophils and monocytes in a process termed "emergency myelopoiesis" or "demand-adapted hematopoiesis" (*11*). However, many of these effects depend on the TLR-induced production of inflammatory cytokines—including interleukin-3 (IL-3), IL-6, interferon-γ (IFNγ), and type I IFN—from mature myeloid cells or nonhematopoietic cells that promote myelopoiesis (*10*, *12*). Thus, in contrast to its potent effects in vitro, the cell-intrinsic role of TLR signaling in directing monocyte/macrophage differentiation in vivo remains an open question.

TLR7 promotes hemophagocyte development in vitro and in vivo

We hypothesized that TLR signaling may drive a specialized macrophage phenotype. To test this hypothesis, we used an in vitro culture system in which bone marrow CMPs were cultured with the TLR7 agonist R848. This approach efficiently induced the differentiation of CD11b^{+}F4/80^{+} macrophages after 4 days (Fig. 1A) (*9*). We compared the transcriptional profiles of macrophages differentiated from CMPs with R848 with those differentiated with the homeostatic macrophage-differentiating growth factor M-CSF and found 813 up-regulated and 1020 down-regulated transcripts [greater than or equal to twofold, false discovery rate (FDR) ≤ 0.05] in macrophages from R848 compared with M-CSF cultures (Fig. 1B). The gene encoding the transcription factor Spi-C (*Spic*), which governs splenic red pulp macrophage (RPM) development (*13*) was significantly up-regulated, suggesting that TLR7 signaling in CMPs may preferentially promote differentiation of RPM-like cells (Fig. 1B). These R848-differentiated macrophages most strongly resembled RPMs in comparison with microglia, peritoneal macrophages, and alveolar macrophages (Fig. 1C). Furthermore, they were enriched for a core set of genes that distinguish RPMs from these other tissue macrophage populations (Fig. 1D) (*14*). The hallmark function of RPMs is the phagocytosis of RBCs ("hemophagocytosis") (*15*). R848-differentiated macrophages efficiently phagocytosed RBCs (Fig. 1E). Thus, TLR7 signaling in CMPs dictates the development of hemophagocytic RPM-like macrophages in vitro.

To examine whether TLR7 signaling increased hemophagocyte development in vivo, we used TLR7.1 mice (*16*), which overexpress TLR7 approximately 10-fold under its own regulatory elements, including in HSPCs and mature myeloid cells (*12*). Among CD45^{+} leukocytes that had internalized RBCs (as determined with intracellular anti-Ter-119 staining), we identified a small number of hemophagocytic leukocytes in the spleens of wild-type (WT) mice, which exhibited cell-surface staining CD11b$^{int/lo}$F4/80^{hi} consistent with RPMs (Fig. 2, A to C). Significantly higher numbers of hemophagocytes were found in the spleen and bone marrow of TLR7.1 mice (Fig. 2, A and B, and fig. S1). These cells had increased levels of intracellular anti-Ter-119 staining, suggesting that hemophagocytes in TLR7.1 mice were more phagocytic than in WT mice. Furthermore, although a small population of hemophagocytes in TLR7.1 mice resembled RPMs through F4/80 and CD11b staining, the majority were CD11b$^{int/hi}$F4/80^{lo} (Fig. 2C). These hemophagocytes lacked the high vascular cell adhesion molecule (VCAM) and CD64 expression associated with RPMs and expressed higher levels of CD31 and CD55. They also expressed similar levels of SIRPα (signal regulatory protein α) and TREML4 (triggering receptor expressed on myeloid cells like 4) compared with RPMs (Fig. 2D). Thus, most hemophagocytes in

Downloaded from http://science.sciencemag.org/ on January 12, 2019

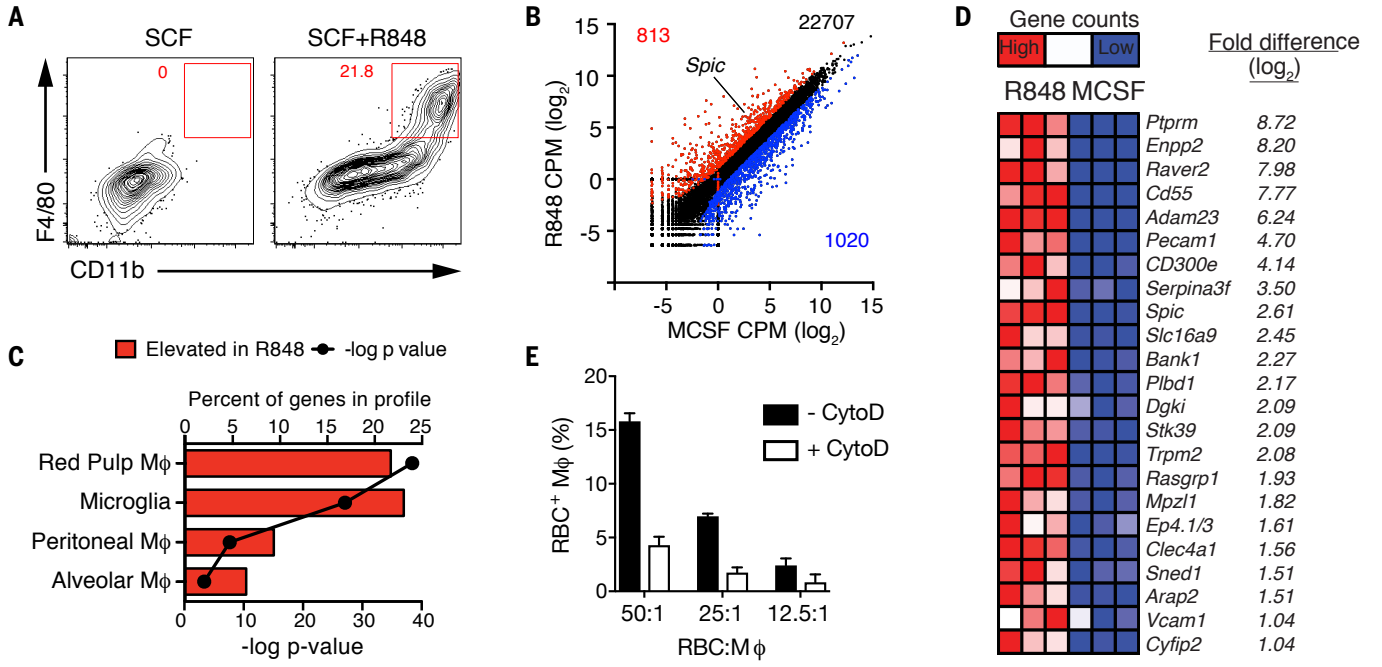


Fig. 1. TLR7 promotes RPM-like hemophagocyte development in vitro. (**A**) Representative flow cytometric staining of CMPs cultured with SCF or SCF+R848. (**B** to **D**) RNA-seq analysis of CD11b^{+}F4/80^{+} macrophages sorted from CMPs differentiated in R848 or M-CSF. (B) Of the 22,707 total protein coding genes, 813 were up-regulated and 1020 were down-regulated in R848-differentiated macrophages with to M-CSF–differentiated macrophages (greater than or equal to twofold, FDR ≥ 0.05). Three independent biological replicates were sequenced for each condition. (C) Red bars indicate the percent of genes in a tissue macrophage core transcriptional signature (*14*) that were significantly increased in R848-differentiated compared with M-CSF–differentiated macrophages. Black line indicates −log *P* value calculated by using exact hypergeometric probability with a normal approximation. (D) Heat map of increased genes (greater than or equal to twofold, FDR ≥ 0.05) in R848-differentiated compared with M-CSF–differentiated macrophages in RPM core signature. (**E**) R848-differentiated macrophages were treated with or without cytochalasin D (CytoD) then allowed to phagocytose CFSE-labeled RBC for 15 min at indicated ratios. Percent of CD11b^{+}F4/80^{+} macrophages that had phagocytosed RBC is shown. Data are representative of four experiments, $n = 3$ technical replicates per condition/experiment. (E) Mean values + SD are shown.

TLR7.1 mice appeared to represent a population of hemophagocytes distinct from RPMs. Hemophagocytes with the identical phenotype were found in the spleen after daily injection with the TLR7 agonist R848 (fig. S2). Because these CD11b$^{int/hi}$F4/80^{lo} hemophagocytes did not exist in untreated or non-inflamed WT mice, we have termed them "inflammatory hemophagocytes," or iHPCs.

Gating iHPCs and RPMs by using only cell-surface markers (fig. S3) showed that TLR7.1 iHPCs were approximately two- to threefold more phagocytic than RPMs from either WT or TLR7.1 mice as measured with intracellular anti-Ter-119 staining (Fig. 2E). Sorting of iHPCs and RPMs followed by hematoxylin and eosin (H&E) staining confirmed that the anti-Ter-119 staining corresponded to internalized RBCs and showed that more iHPCs contained multiple RBCs, confirming that these cells were more phagocytic than RPMs (Fig. 2, F and G). Thus, iHPCs, although similar to RPMs, are a distinct population of hemophagocytes.

iHPCs differentiate in response to cell-intrinsic TLR7 signals and do not require Spi-C

We next investigated the developmental pathway of iHPCs. To determine whether iHPCs require cell-intrinsic TLR7 signaling to develop or whether the inflammation present in TLR7.1 mice is sufficient for this process, we used mixed bone marrow chimeras. Whereas splenic B cells and monocytes reconstituted at the 1:1 ratio of the input bone marrow, iHPCs were almost solely derived from TLR7.1 bone marrow with an ~100:1 ratio of TLR7.1:WT iHPCs (Fig. 3A and fig. S4, A to C). Thus, iHPCs specifically develop in response to cell-intrinsic chronic TLR7 signaling.

We used the R848 injection model to determine whether TLR7 signaling is required for iHPC development. After R848 injection in mixed WT:*Tlr7*$^{-/-}$ bone marrow chimeras, monocytes were found at the 1:1 WT:*Tlr7*$^{-/-}$ ratio of the input bone marrow. However, iHPCs were heavily skewed toward WT cells at a ratio of ~100:1 (Fig. 3B and fig. S5, A and B). Thus, cell-intrinsic TLR7 signaling promotes and is required for iHPC development in vivo. Therefore TLR7 signaling plays a critical role in the induction of a specific macrophage phenotype induced during TLR7-driven inflammation.

The transcription factor Spi-C is required for RPM development (*13*) and is also highly expressed in macrophages generated by TLR7 signaling in vitro (Fig. 1, B and D). Splenic iHPCs sorted directly ex vivo from TLR7.1 mice also expressed high levels of *Spic* mRNA comparable with RPMs, and in contrast to splenic Ly6C^{hi} monocytes (fig. S6A). Because of the functional similarities between RPMs and iHPCs and our observation that both express high levels of Spi-C, we hypothesized this transcription factor would be required for iHPC differentiation. Therefore, we generated TLR7.1/*Spic*$^{-/-}$ mice. As expected, both *Spic*$^{-/-}$ and TLR7.1/*Spic*$^{-/-}$ mice had few splenic RPMs, and *Spic*$^{-/-}$ mice showed a significant reduction in total hemophagocytes in comparison with WT mice (fig. S6, B to D) because most of these cells are *Spic*-dependent RPMs. Surprisingly, TLR7.1/*Spic*$^{-/-}$ mice had similar numbers of splenic hemophagocytes as TLR7.1/*Spic*$^{+/+}$ and TLR7.1/*Spic*$^{+/-}$ mice (fig. S6C). When the total hemophagocyte population was separated into RPMs and iHPCs (fig. S6, D and E), there was no difference in iHPC frequency or number in TLR7.1 mice regardless of *Spic* expression. Similarly, in our in vitro differentiation system, there was no difference in R848-induced macrophage differentiation from *Spic*$^{+/-}$ and *Spic*$^{-/-}$ CMPs (fig. S6F). Thus, Spi-C is not required for iHPC development in vivo or in vitro, demonstrating that iHPCs develop through a program distinct from RPMs.

iHPCs differentiate from Ly6C^{hi} monocytes

In the steady state, many tissue macrophages, including RPMs, are derived from embryonic

Downloaded from http://science.sciencemag.org/ on January 12, 2019

yolk sac– or fetal liver–derived progenitors that locally self-renew. However, monocytes can replenish some but not all of these populations both in the steady state or during inflammation or other perturbations (*17*–*19*). For example, RPMs can be replaced by "classical" or "inflammatory" Ly6C^{hi} monocyte–derived cells after RPM death because of heme-mediated toxicity (*20*). Thus, we asked whether TLR7-induced iHPCs are derived from Ly6C^{hi} inflammatory monocytes. iHPCs did not express the defining inflammatory monocyte markers CCR2 or Ly6C and had low expression of the tissue macrophage marker CD64 similar to Ly6C^{hi} monocytes (Fig. 4A). Ly6C^{hi} monocytes also expressed low levels of the iHPC marker

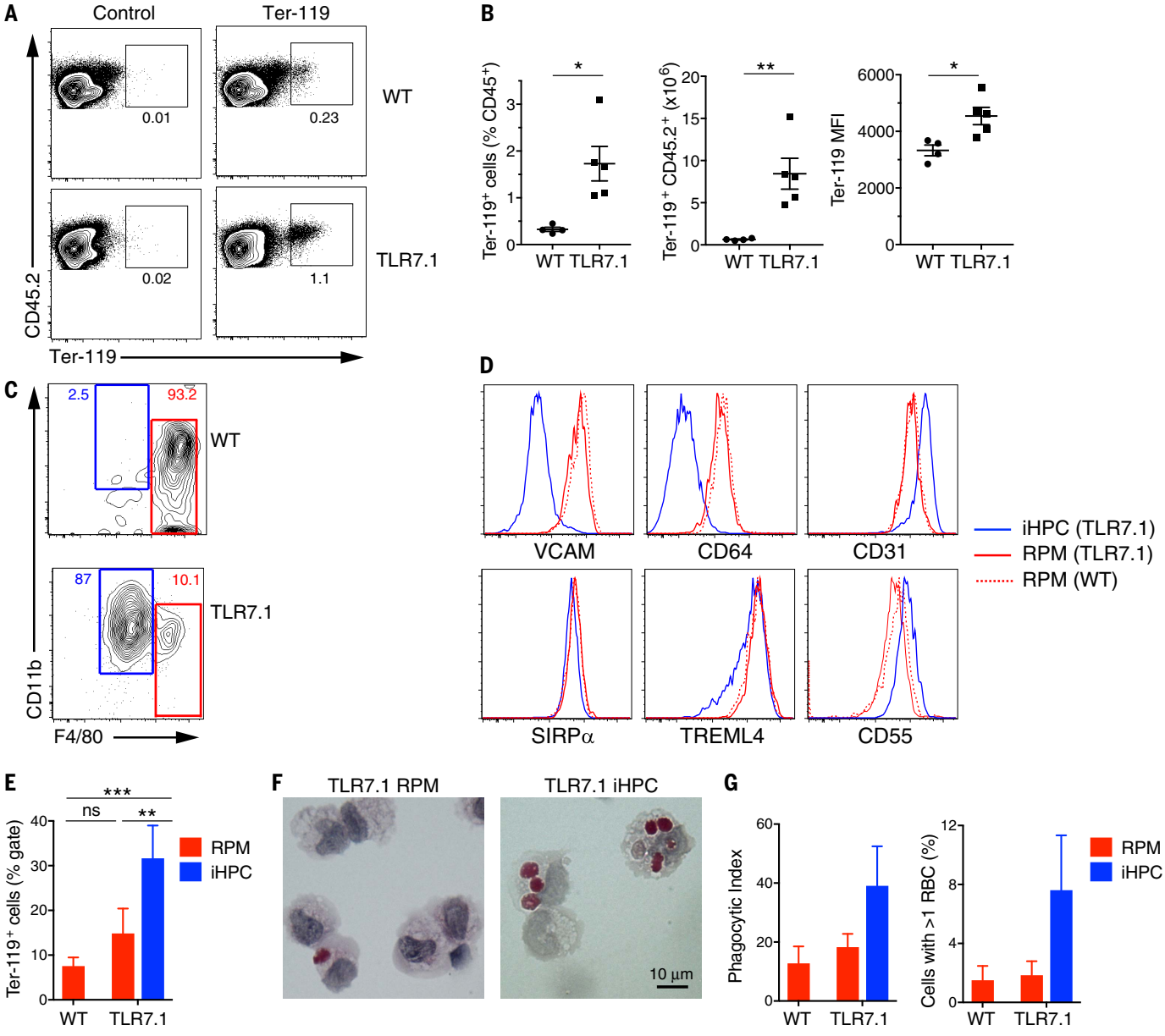


Fig. 2. TLR7 signaling drives formation of hemophagocytes distinct from RPMs in vivo. (**A** to **D**) Splenocytes from WT and TLR7.1 mice were surface-stained for CD11b, CD45.2, F4/80, Ly6G, and Siglec-F and then intracellularly stained with monoclonal antibody to Ter-119 to detect leukocytes that had phagocytosed RBCs. (A) Representative flow cytometry pre-gated as live singlets, CD45.2$^+$ cells. Before intracellular staining with fluorescently labeled antibody to Ter-119, some samples were blocked with unconjugated Ter-119 (control). Other samples were not blocked before staining (Ter-119). (B) Frequency and number of CD45.2$^+$Ly6G$^-$Siglec-F$^-$Ter-119$^+$ cells and mean fluorescence intensity (MFI) of Ter-119 staining in CD45.2$^+$Ter-119$^+$ cells were then quantified. Data are representative of four experiments. (C) CD11b and F4/80 expression on CD45.2$^+$Ly6G$^-$Siglec-F$^-$Ter-119$^+$ splenocytes. iHPCs are in blue, and RPMs are in red. Data are representative of four experiments. (D) RPMs were gated as CD45.2$^+$Ly6G$^-$Siglec-F$^-$Ter-119$^+$ cells that were CD11b$^{int/lo}$F4/80^{hi}, and iHPCs were gated as CD45.2$^+$Ter-119$^+$ cells that were CD11b$^{int/hi}$F4/80^{lo}. Histograms of indicated surface staining are shown. Data are representative of four experiments. (**E**) Percentage of RPMs or iHPCs that were Ter-119$^+$ from WT and TLR7.1 mice quantified by means of flow cytometry. Data are representative of four experiments, $n = 5$ mice per group. (**F** and **G**) RPMs and iHPCs were fluorescence-activated cell–sorted and stained with H&E. Intracellular RBCs were quantitated by means of microscopy. (G) Phagocytic index (number of intracellular RBCs per 100 cells) (left) and percentage of cells with at least one RBC (right) were calculated. Data are representative of two experiments, $n = 3$ to 4 mice per group. In (B), mean ± SEM; in (F) and (G), mean + SEM; and in (B), each symbol represents an individual mouse. *$P < 0.05$, **$P < 0.01$, ***$P < 0.001$, ****$P < 0.0001$, two-tailed, unpaired Student's t test (B). One-way analysis of variance (ANOVA) with Tukey's post test (E).

Downloaded from http://science.sciencemag.org/ on January 12, 2019

CD31. Culture of Ly6C^{hi} monocytes with TLR7 ligands induced phenotypic changes associated with iHPCs, including the induction of *Spic* and *Pecam1* (encoding CD31) and the reduced expression of *Ccr2* and *Ly6c1* (Fig. 4B). Thus, although Ly6C^{hi} monocytes had a distinct cell-surface phenotype from iHPCs, TLR7 signaling in Ly6C^{hi} monocytes caused transcriptional changes associated with the iHPC phenotype, suggesting that iHPCs differentiate from Ly6C^{hi} monocytes in response to TLR7 signals.

To directly assess whether iHPCs derive from Ly6C^{hi} monocytes, we crossed TLR7.1 mice to *Ccr2*-DTR mice, in which injection of diphtheria toxin (DT) results in the depletion of Ly6C^{hi} monocytes within 24 hours and which can be maintained over time with subsequent DT injections (*21*–*23*). Ly6C^{hi} monocyte depletion over 2.5 weeks (fig. S7, A and B) caused a significant reduction in total splenic hemophagocytes and iHPCs in TLR7.1/*Ccr2*-DTR mice, in comparison with TLR7.1 mice not expressing the *Ccr2*-DTR transgene (Fig. 4, C and D). Consistent with the fact that iHPCs do not express CCR2 (Fig. 4A), a single DT injection into TLR7.1/*Ccr2*-DTR mice depleted Ly6C^{hi} monocytes but not iHPCs after 24 hours (fig. S7, B and C). Thus, iHPCs were not directly depleted by DT injections. Two and a half weeks of DT treatment also significantly reduced RPM numbers in TLR7.1/*Ccr2*-DTR mice (fig. S7E), suggesting that during chronic TLR7-driven inflammation, not only are iHPCs derived from Ly6C^{hi} monocytes but RPMs are also replaced by monocyte-derived cells.

The transcriptional changes in Ly6C^{hi} monocytes associated with the iHPC phenotype were not specific to TLR7 signaling. Signaling via TLR9 through CpG DNA also induced *Spic* and *Pecam1* and reduced *Ccr2* and *Ly6c1* in Ly6C^{hi} monocytes (Fig. 4E). Signaling via TLR4 only caused some of the iHPC transcriptional changes; lipopolysaccharide (LPS) induced *Spic* and reduced *Ccr2* but did not induce *Pecam1* or reduce *Ly6c1* expression (Fig. 4E). We also assessed IL-1β, which, similar to TLRs, signals by means of MyD88. IL-1β signaling was similar to LPS in that it induced *Spic* but not *Pecam1* (fig. S8A). We also tested signaling with polyinosinic:polycytidylic acid [poly(I:C)] through TLR3, which uses TRIF exclusively and is expressed at low levels on Ly6C^{hi} monocytes (*14*). TLR3 signaling did not significantly induce *Spic* and *Pecam1* or reduce *Ly6c1* expression. However TLR3 signaling did significantly reduce *Ccr2* expression to a lesser extent than other TLR agonists tested (fig. S8B). Last, IFNγ, a classic monocyte activator, did not induce any of the transcriptional changes associated with iHPC differentiation in Ly6C^{hi} monocytes (fig. S8A). Thus, TLR7 and TLR9 signaling alone drive the iHPC phenotype in Ly6C^{hi} monocytes.

To further assess how iHPCs are related to Ly6C^{hi} monocytes and RPMs, we performed RNA-sequencing (RNA-seq) analysis of these populations from naïve WT and TLR7.1 mice. Principal component analysis of these data revealed that TLR7.1 iHPCs cluster separately from both Ly6C^{hi} monocytes and RPMs, whether they were derived from WT or TLR7.1 mice (Fig. 4F), reinforcing their particular iHPC identity. Unsupervised hierarchical clustering of iHPCs, Ly6C^{hi} monocytes, and RPMs from TLR7.1 mice by using significantly differentially expressed genes [fold-change (FC) > 1.5, FDR < 0.05] between these three populations also highlighted these differences and demonstrated a closer relationship between iHPCs and Ly6C^{hi} monocytes than between iHPCs and RPMs. We also used this dataset to identify distinct surface markers of iHPCs to better distinguish them from Ly6C^{hi} monocytes and RPMs by means of flow cytometry (fig. S9A). Of those tested, DR3, encoded by *Tnfrsf25*, was best at identifying iHPCs because it is expressed in neither Ly6C^{hi} monocytes nor RPMs. DR3 used in conjunction with CD31 reliably identified TLR7.1 splenic iHPCs that were uniformly expressing Spi-C and enriched for hemophagocytes (fig. S9, B to D). Thus, transcriptional profiling supports our contention that iHPCs are a distinct population of Ly6C^{hi} monocyte-derived cells.

Monocyte-derived iHPCs drive TLR7 and TLR9-induced MAS-like disease

The presence of iHPCs in TLR7.1 mice was associated with anemia characterized by reduced RBC count that typically developed by 3 months of age (Fig. 5A) (*16*). The percent and number of splenic iHPCs was inversely correlated with the RBC count in a cohort of TLR7.1 mice (Fig. 5B). The lack of RPMs, but not iHPCs, in TLR7.1/*Spic*$^{-/-}$ mice allowed us to assess the contribution of RPMs versus iHPCs in anemia. Similar to published results, we found no difference in RBC count between *Spic*$^{+/+}$, *Spic*$^{+/-}$, and *Spic*$^{-/-}$ mice, suggesting that in the steady state, Spi-C–dependent RPMs are not major contributors to RBC homeostasis (*13*). TLR7.1/*Spic*$^{-/-}$ mice developed anemia similarly to TLR7.1/*Spic*$^{+/+}$ and TLR7.1/*Spic*$^{+/-}$ mice (Fig. 5C), showing that RPMs do not contribute to TLR7-driven anemia and suggesting that iHPCs are sufficient to cause this outcome.

The lack of iHPCs in DT-injected TLR7.1/*Ccr2*-DTR mice allowed us to ask whether iHPCs drive anemia in the TLR7.1 model by beginning depletions once anemia was detected (fig. S7A). TLR7.1 mice not expressing the *Ccr2*-DTR transgene became progressively more anemic during the course of DT treatment, whereas anemia was completely reversed in the DT-treated TLR7.1/*Ccr2*-DTR mice (Fig. 5D). Taken together with the sustained anemia in TLR7.1/*Spic*$^{-/-}$ mice that lack RPMs, we conclude that hemophagocytosis by iHPCs is required for TLR7-driven anemia. We also investigated a model of anemia caused by chronic TLR9 signaling induced with repetitive CpG DNA injection in *Ccr2*-DTR mice (*21*). Similar effects of monocyte and iHPC depletion were observed in this TLR9-dependent model (Fig. 5E), indicating that hemophagocytosis by iHPCs may be a common mechanism of anemia associated with TLR7- and/or TLR9-dependent inflammation.

The anemia in TLR7.1 mice is reminiscent of the spectrum of diseases defined as MAS, in which activated macrophages cause severe cytopenias by phagocytosing RBCs as well as leukocytes and platelets (*1*, *2*). We confirmed that TLR7.1 mice have very low platelet counts (*16*), even when the RBC count is still close to the range of wild-type mice (Fig. 5F). Similar to RBC counts, platelet counts were completely restored after 2.5 weeks of Ly6C^{hi} monocyte depletion in TLR7.1/Ccr2-DTR mice (Fig. 5F). Thus, iHPCs contribute to both anemia and thrombocytopenia and likely to other aspects of the MAS-like disease in TLR7.1 mice.

This led us to ask which receptors might allow iHPCs to phagocytose RBC and, potentially, platelets and other cells. Analysis of receptors, bridging molecules, and transcription factors that have been implicated in phagocytosis of self cells in our RNA-seq dataset showed that there is a subset of these molecules expressed more highly in iHPCs than monocytes and RPMs, including genes encoding the αv integrin chain, CD300f,

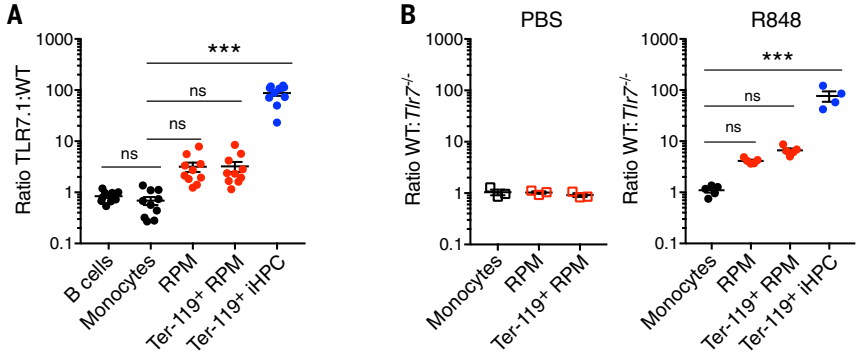


Fig. 3. iHPCs differentiate in response to cell-intrinsic TLR7 signals. (**A**) The ratio of TLR7.1 to WT BM-derived cells in mixed bone marrow chimeras of indicated populations after reconstitution. Data are representative of two experiments with n = 8 to 10 mice per experiment. (**B**) The ratio of WT to *Tlr7*$^{-/-}$ BM-derived cells in mixed bone marrow chimeras injected with the TLR7 agonist R848 (right) or PBS (left) for 13 days. Data are representative of two experiments, with n = 3 to 5 mice per group per experiment. In (A) and (B), mean ± SEM; in (A) and (B), each symbol represents an individual mouse. *P < 0.05, **P < 0.01, ***P < 0.001, ****P < 0.0001, one-way ANOVA with Dunnett's post test [(A) and (B)].

Downloaded from http://science.sciencemag.org/ on January 12, 2019

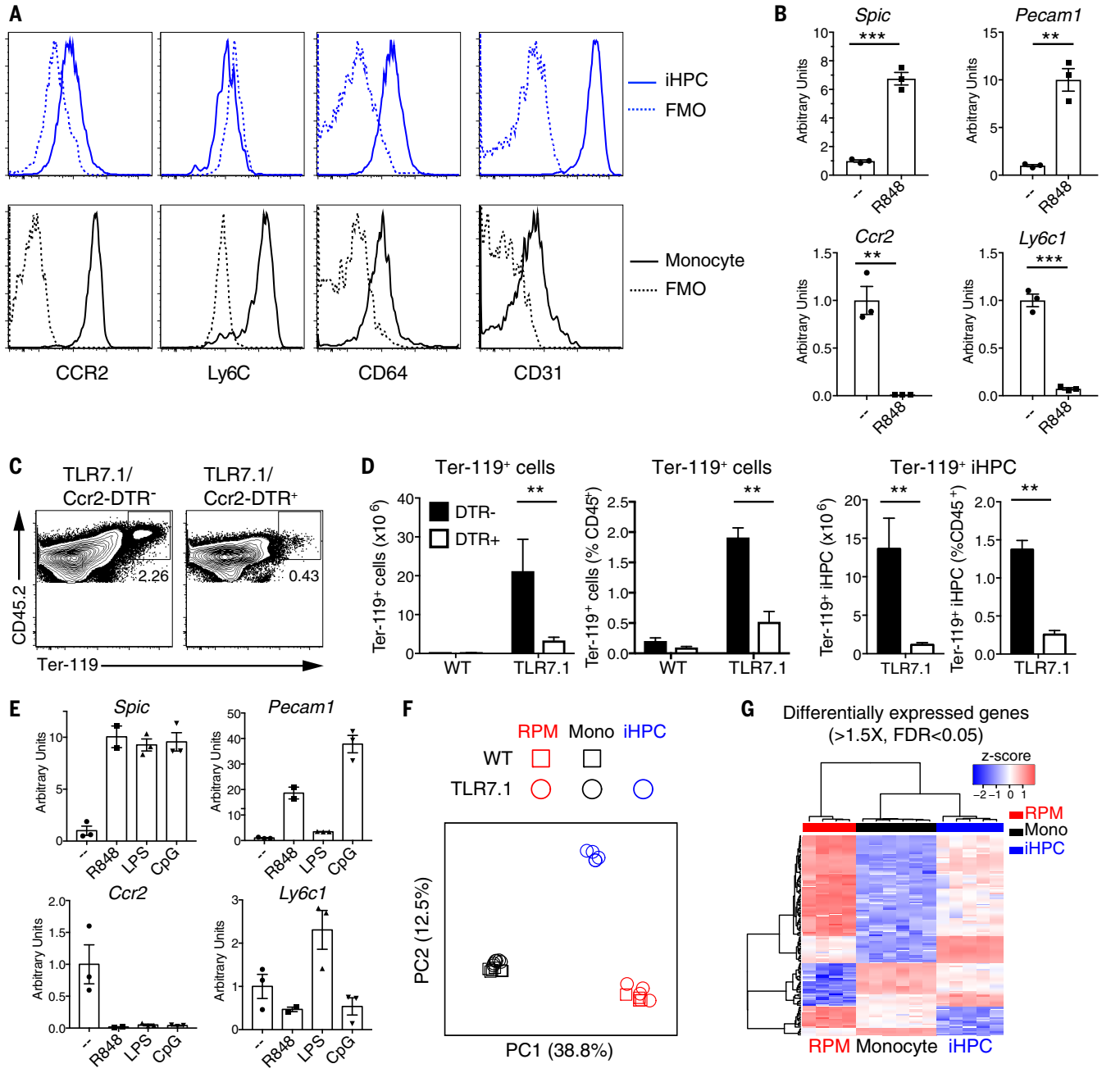


Fig. 4. iHPCs are derived from Ly6C^{hi} monocytes. (**A**) Splenic monocytes (live singlets, CD11b$^+$F4/80$^-$Ly6G$^-$Ly6C^{hi} or CCR2$^+$ cells) (black) and iHPCs (live singlets, F4/80^{lo}Ly6G$^-$Ter-119$^+$VCAM1^{lo} or CD31^{hi} cells) (blue) were assessed for the expression of the cell-surface proteins indicated (solid lines) compared with fluorescence minus one (FMO) control stains (dashed lines). Data are representative of three experiments. (**B**) Bone marrow Ly6C^{hi} monocytes were sorted from WT B6 mice and cultured for 21 hours with media alone (–) or with R848. *Spic*, *Pecam1*, *Ccr2*, and *Ly6c1* transcripts were quantified by means of quantitative polymerase chain reaction (PCR). Data are representative from five experiments, with $n = 3$ mice per experiment. (**C** and **D**) Ccr2-DTR$^-$, Ccr2-DTR$^+$, TLR7.1/Ccr2-DTR$^-$, and TLR7.1/Ccr2-DTR$^+$ mice ($n = 5$ to 7 mice per group) were injected with DT every other day for 17 days. (C) Representative flow cytometry of Ter-119$^+$ hemophagocytes pre-gated on live singlets, CD45.2$^+$Ly6G$^-$Siglec-F$^-$ cells from the spleens of TLR7.1/Ccr2-DTR$^-$ and TLR7.1/Ccr2-DTR$^+$ mice determined by means of flow cytometry. (D) Frequency and number of the indicated cell populations were quantitated from the spleens of Ccr2-DTR$^-$, Ccr2-DTR$^+$, TLR7.1/Ccr2-DTR$^-$, and TLR7.1/Ccr2-DTR$^+$ mice by means of flow cytometry. Data are combined from three experiments. (**E**) Bone marrow Ly6C^{hi} monocytes were sorted from WT B6 mice and cultured for 21 hours with media alone (–), R848, LPS, or CpG. *Spic*, *Pecam1*, *Ccr2*, and *Ly6c1* transcripts were quantified by means of quantitative PCR. Data are representative from two experiments. (**F** and **G**) RNA-seq analysis of RPMs and Ly6C^{hi} monocytes sorted from spleens of WT B6 mice and TLR7.1 mice and iHPCs from spleens of TLR7.1 mice. $n = 5$ mice (TLR7.1 iHPC), $n = 4$ mice (WT and TLR7.1 RPM), and $n = 6$ mice (WT and TLR7.1 Mono). (F) Principal components analysis of indicated populations. (G) Heat map of differentially expressed genes between the three populations (RPMs, Ly6C^{hi} monocytes, and iHPCs) sorted from TLR7.1 mice. Mean values + SEM (D), ±SEM [(B) and (E)]. $^*P < 0.05$, $^{**}P < 0.01$, $^{***}P < 0.001$, $^{****}P < 0.0001$, two-tailed, unpaired Student's *t* test (B) and Mann-Whitney *U* test (D).

Downloaded from http://science.sciencemag.org/ on January 12, 2019

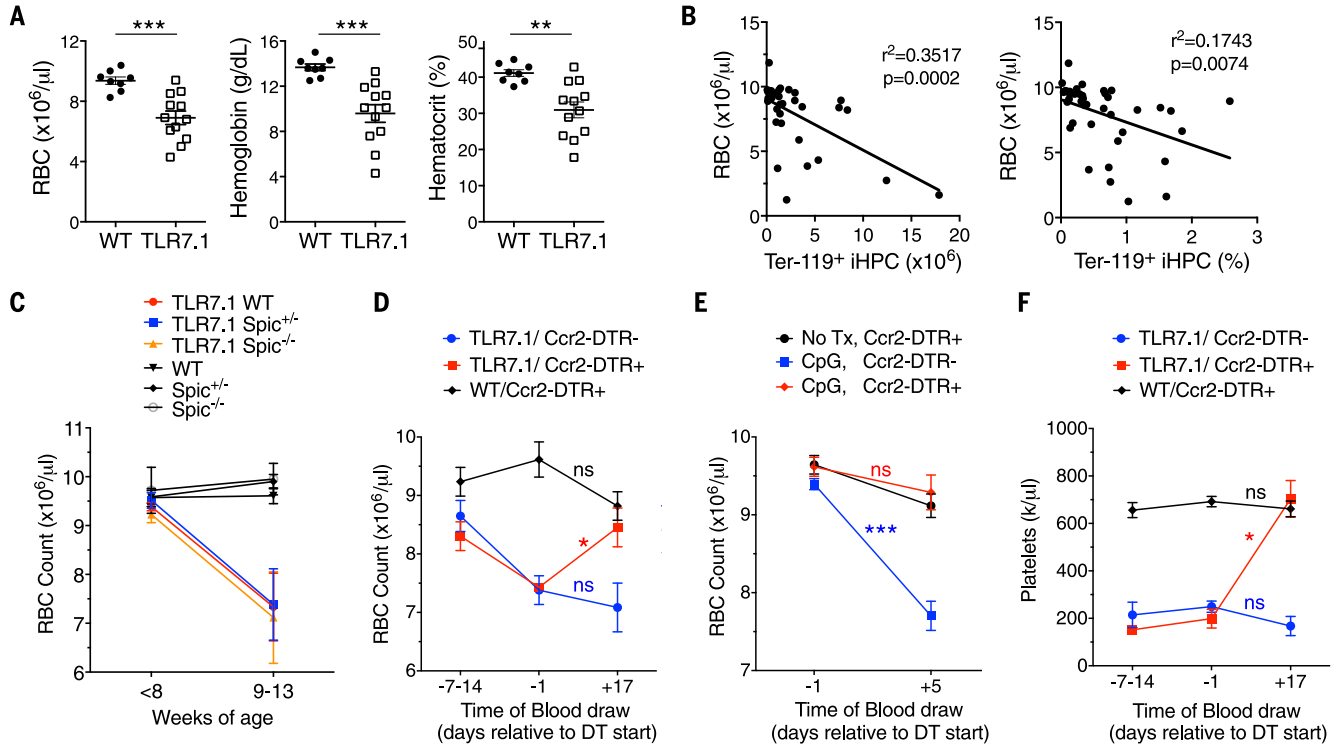


Fig. 5. Monocyte-derived iHPCs drive anemia. (**A**) RBC count, hemoglobin levels, and hematocrit from 3-month-old WT and TLR7.1 mice. Each symbol represents an individual mouse, n = 8 to 12 mice per group. (**B**) Correlation between RBC count and number (left) and frequency (right) of splenic Ter-119$^+$ iHPCs in TLR7.1 mice. (**C**) RBC count of TLR7.1 WT, TLR7.1 Spic$^{+/-}$, TLR7.1 Spic$^{-/-}$, and control mice that were bled before 8 weeks and between 9 and 13 weeks of age. n = 7 to 14 mice per group. (**D**) TLR7.1/Ccr2-DTR$^-$ and TLR7.1/Ccr2-DTR$^+$ mice were treated with DT every other day for 17 days beginning when RBC count was below 8. RBC count was measured at indicated times. n = 5 to 7 mice per group. (**E**) Ccr2-DTR$^-$ and Ccr2-DTR$^+$ mice were treated with DT every day for 6 days and CpG daily starting 1 day after beginning DT treatment. RBC count was measured before and at the end of treatment. Data are representative of two experiments, n = 3 (No Tx) and n = 7 (CpG) mice per group. (**F**) Platelet counts in TLR7.1/Ccr2-DTR$^-$ and TLR7.1/Ccr2-DTR$^+$ mice treated as in (D). Mean values ± SEM [(A) and (C) to (F)] are shown. In (A) and (B), each symbol represents an individual mouse.*P < 0.05, **P < 0.01, ***P < 0.001, ****P < 0.0001; ns, not significant; Mann-Whitney (A), Wilcoxon paired t test of days −1 and +17 for TLR7.1 experiment and −1 and +5 for CpG injection [(D) to (F)].

and the β2 integrin chain (*22*) (fig. S10). Additionally, genes for hemophagocytosis may be shared with RPMs, indicating possible roles for C1q, Mer (encoded by *Mertk*), and LXRα (encoded by *Nr1h3*), which are all more highly expressed in iHPCs and RPMs than monocytes.

IRF5 participates in iHPC differentiation

We propose that cytopenias in MAS can be caused by direct chronic endosomal TLR signaling in monocytes or myeloid progenitor cells. Whether because of infection, genetic perturbations in TLR signaling, and/or the increased availability of nucleic acid endosomal TLR ligands, this may directly lead to the differentiation of pathogenic iHPCs. Some forms of MAS are associated with variants in the gene encoding the IRF5, a transcription factor activated downstream of TLR signaling in monocytes and macrophages (*23*, *24*). The MAS-associated SNPs in *IRF5* are proposed to increase TLR signals (*25*–*27*). Accordingly, we investigated whether IRF5 is involved in TLR7-induced iHPC differentiation. Induction of *Spic* and *Pecam1* was significantly reduced in IRF5-deficient Ly6C^{hi} monocytes compared with WT monocytes, whereas down-regulation of *Ccr2* and *Ly6c1* did not depend on IRF5 (Fig. 6A). The in vivo induction of iHPCs after R848 injection was significantly reduced in *Irf5*$^{-/-}$ mice compared with WT mice (Fig. 6, B and C). Thus, IRF5 is required for optimal iHPC differentiation, and increased IRF5 signaling is genetically associated with MAS.

iHPCs differentiate in response to endosomal TLR signaling in a preclinical model of severe malarial anemia

In addition to MAS, severe cytopenias accompany malaria caused by infection with *Plasmodium falciparum* and *Plasmodium vivax*, particularly the anemia and thrombocytopenia seen in severe malarial anemia (*5*–*7*). Reasoning that iHPCs may also develop during malaria, we infected mice with *Plasmodium yoelii* 17XNL–infected RBCs, a preclinical, nonlethal model of blood stage malaria that causes severe anemia and thrombocytopenia (Fig. 7A). RBC-stage *P. yoelii* infection induced hemophagocytosis (Fig. 7, B and C) (*7*). iHPCs were seen as early as day 5 after infection, and iHPC number peaked at the time of most severe anemia and correlated inversely with RBC count (Fig. 7, D and E). We also found iHPC differentiation during mouse cytomegalovirus (MCMV) infection of young Balb/c mice in a model of virally induced MAS (fig. S11) (*28*). Thus, iHPCs also differentiate during infection.

We next investigated whether TLR signals are required for *Plasmodium*-induced iHPC differentiation. *P. yoelii*–infected *Myd88*$^{-/-}$ mice, which lack most TLR signaling as well as IL-1R and IL-18R signaling, showed significantly reduced iHPC differentiation and anemia compared with that of WT mice (Fig. 7, F and G). *Myd88*$^{-/-}$ mice showed reduced parasitemia compared with that of WT mice, which may reflect the increased RBC count in *Myd88*$^{-/-}$ mice or a role for iHPCs in the clearance or sequestration of infected RBC in tissues. Mixed bone marrow chimeras showed a cell-intrinsic requirement for the TLR signaling adapters MyD88 and TRIF and for the endosomal TLR chaperone UNC93B1 in iHPC differentiation during RBC stage *P. yoelii* 17XNL infection (Fig. 7, H and I). Thus, cell-intrinsic endosomal TLR signaling, likely via TLR7 and/or TLR9, also drives iHPC differentiation during experimental malarial anemia.

Discussion

TLR signaling has previously been shown to cause macrophage differentiation in vitro. However, in vivo evidence for a cell-intrinsic role of

Downloaded from http://science.sciencemag.org/ on January 12, 2019

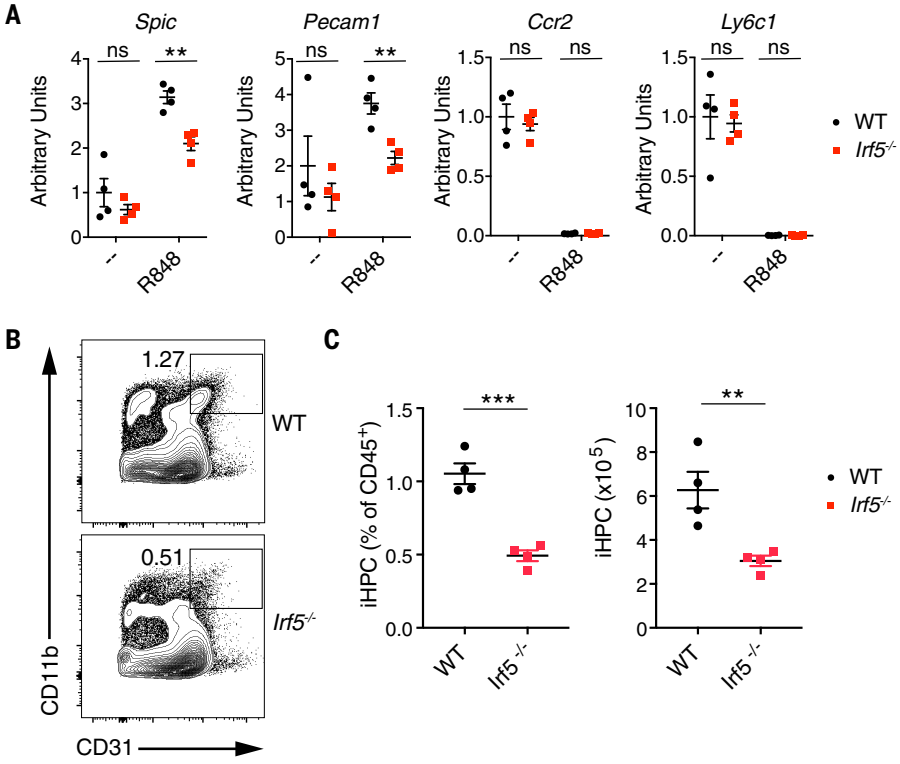


Fig. 6. iHPC differentiation depends on IRF5. (**A**) Bone marrow Ly6C^{hi} monocytes were sorted from WT and *Irf5*$^{-/-}$ mice and cultured for 21 hours with media alone (−) or with R848. *Spic*, *Pecam1*, *Ccr2*, and *Ly6c1* transcripts were quantified by means of quantitative PCR. Data are representative from two experiments with n = 2 to 4 mice per group per experiment. (**B** and **C**) WT and *Irf5*$^{-/-}$ mice were injected with R848 intraperitoneally daily for 2 days. Splenocytes were analyzed by means of flow cytometry. (B) Representative flow plots of WT and *Irf5*$^{-/-}$ CD11b^{+}CD31^{+} iHPCs (gated on live singlets, CD45.2^{+}F4/80^{-}Ly6G^{-}Siglec-F^{-} cells). (C) Frequency (left) and number (right) of iHPCs in WT and *Irf5*$^{-/-}$ spleens. Data are representative from two experiments with n = 4 mice per group per experiment. Mean values±SEM [(A) and (C)] are shown. In (A) and (C)], each symbol represents an individual mouse. *P < 0.05, **P < 0.01, ***P < 0.001, ****P < 0.0001, two-tailed, unpaired Student's t test [(A) and (C)].

TLRs in this process and in defining macrophage fate has been lacking. Our work reveals a distinct developmental pathway by which myeloid progenitors and Ly6C^{hi} monocytes respond directly to chronic TLR7 and TLR9 signaling in vitro and in vivo by inducing hemophagocytes similar to, yet distinct from, RPMs. We identified iHPCs not only in a transgenic model of TLR7 overexpression resulting in a MAS-like disease but also during RBC-stage *P. yoelii* 17XNL infection and during infection with MCMV. Thus, iHPCs differentiate in a broad array of situations that have systemic TLR7 and/or TLR9 activation in common (*29*–*37*). Not only do these models share innate sensors, they also share anemia and thrombocytopenia during the course of infection or disease.

The iHPC program is specific to TLR7 and TLR9 signaling. In vivo, both chronic TLR7 and TLR9 signaling drive anemia, and we have precisely assessed the contribution of TLR7 to iHPC differentiation in the TLR7.1 model. During *P. yoelii* 17XNL infection, both MyD88 and UNC93B1-dependent endosomal TLRs promote iHPC differentiation, and MyD88 participates in the anemia seen in this infection. In vitro, TLR4, TLR7, and TLR9 agonists and IL-1β can all induce the iHPC- and RPM-expressed transcription factor *Spic* in bone marrow Ly6C^{hi} monocytes, suggesting that MyD88 signaling is sufficient for Spi-C expression. This is a distinct pathway leading to Spi-C induction; previously, myeloid Spi-C expression was only linked developmentally to RPMs and a subset of bone marrow macrophages or to heme-induced signals in monocytes (*13*, *20*, *38*). Although Spi-C is critical for RPM differentiation and can repress inflammation in intestinal Cx$_3$CR1^{+} macrophages (*38*), we found no role for Spi-C in iHPC differentiation or in TLR7-mediated MAS-like disease, although it remains possible that Spi-C subtly affects iHPC function in a manner not yet determined.

Distinct from Spi-C expression, only TLR7 and TLR9 signaling induced Ly6C^{hi} monocyte *Pecam1* transcripts that encode CD31, which is a robust marker for iHPCs in all in vivo settings we examined. Whether TLR3—an endosomal TLR that signals via TRIF—can induce the iHPC program was not tested in vivo. However, Ly6C^{hi} monocytes did not induce *Spic* or *Pecam1* after treatment with poly(I:C) in vitro, suggesting that TLR3/TRIF may be unable to signal for iHPC differentiation. Alternatively, the low expression of TLR3 on Ly6C^{hi} monocytes may be insufficient. This leaves us to ask why only TLR7 and TLR9 signaling can cause iHPC differentiation. One possibility is that IRF5, which we show contributes to iHPC differentiation, couples more strongly to these endosomal TLRs than to cell-surface TLRs. Although IRF5 is activated downstream of TLR4, perhaps the balance of nuclear factor κB (NF-κB) and IRF5 activation differs downstream of surface-expressed TLR4 and endosome-expressed TLR7 and TLR9, leading to differential gene transcription. Alternatively, Ly6C^{hi} monocytes may not use IRF5 for TLR4 signaling, unlike bone marrow–derived macrophages and other cell types, in which most of the work on IRF5 in LPS responses has been performed (*23*, *39*). Polymorphisms in *IRF5* are linked to increased susceptibility to systemic lupus erythematosus (SLE), a disease associated with innate responses to nucleic acids and in which IRF5 is constitutively activated in human CD14^{+} classical monocytes (*40*–*44*), the corresponding population to mouse Ly6C^{hi} monocytes. Further studies are required to determine the mechanisms by which IRF5 mediates transcriptional responses for iHPC differentiation. Particularly intriguing is the potential interplay between IRF5, Spi-C, and NF-κB p65 (*38*). Additionally, specific signaling components downstream of TLR7 and TLR9 in Ly6C^{hi} monocytes may be involved in iHPC differentiation.

iHPCs are required to cause anemia and thrombocytopenia in TLR7.1 mice, which have a mild lupus-like disease, which we propose here is a model of MAS, a complication of SLE and more frequently sJIA. Although sJIA has an autoinflammatory component and can be successfully treated with IL-1–pathway blockers, sJIA patients can develop MAS on these therapies, in which MAS can be associated with infection (*45*). MAS, also called secondary hemophagocytic lymphohistiocytosis (HLH), can also be caused by viral infection. *IRF5* polymorphisms have also been associated with increased risk of these hemophagocytic diseases (*25*, *26*), similar to SLE. Primary or familial HLH—caused by defects in cell-mediated cytotoxicity, including mutations in *PRF1* encoding perforin—may be caused by lack of viral clearance by natural killer cells and CD8^{+} T cells, resulting in chronic viral infection (*46*). Thus, a common thread among MAS or HLH may be chronic or excessive TLR7 and/or TLR9 activation, leading to iHPC differentiation.

iHPCs correlate with anemia in a malaria model, suggesting a similarity in mechanisms between MAS and severe malarial anemia. When numbers of *Plasmodium*-induced iHPCs are very low because of MyD88-deficiency, not only was anemia reduced but also parasitemia, suggesting that iHPCs may be exploited by *Plasmodium* to

Downloaded from http://science.sciencemag.org/ on January 12, 2019

promote infection. Additionally, "anemia of inflammation," in which individuals with infections develop mild to moderate anemia, may be a mild form of MAS caused by sustained TLR7 or TLR9 signaling during infection (*47*). This TLR-driven anemia may have protective roles against secondary bacterial infections after viral infection by reducing the amount of iron available from RBC hemolysis. Our studies not only define a distinct monocyte/macrophage induced through TLR7 and TLR9 signaling but also suggest unexplored avenues by which to treat MAS, severe malarial anemia, and "anemia of inflammation" by interfering with iHPC generation and function or by their selective depletion.

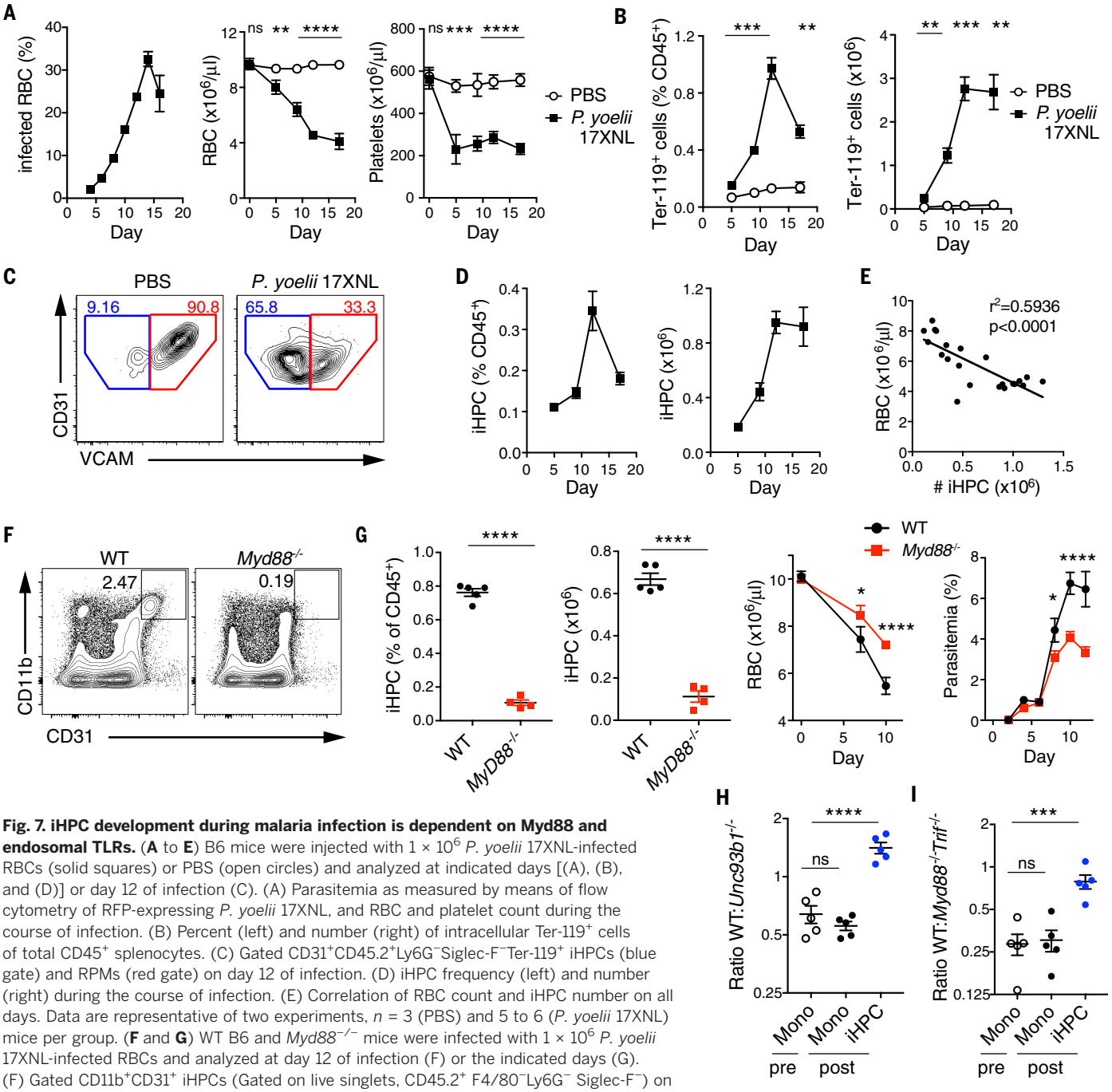


Fig. 7. iHPC development during malaria infection is dependent on Myd88 and endosomal TLRs. (**A** to **E**) B6 mice were injected with 1 × 10^6 *P. yoelii* 17XNL-infected RBCs (solid squares) or PBS (open circles) and analyzed at indicated days [(A), (B), and (D)] or day 12 of infection (C). (A) Parasitemia as measured by means of flow cytometry of RFP-expressing *P. yoelii* 17XNL, and RBC and platelet count during the course of infection. (B) Percent (left) and number (right) of intracellular Ter-119$^+$ cells of total CD45$^+$ splenocytes. (C) Gated CD31$^+$CD45.2$^+$Ly6G$^-$Siglec-F$^-$Ter-119$^+$ iHPCs (blue gate) and RPMs (red gate) on day 12 of infection. (D) iHPC frequency (left) and number (right) during the course of infection. (E) Correlation of RBC count and iHPC number on all days. Data are representative of two experiments, n = 3 (PBS) and 5 to 6 (*P. yoelii* 17XNL) mice per group. (**F** and **G**) WT B6 and *Myd88*$^{-/-}$ mice were infected with 1 × 10^6 *P. yoelii* 17XNL-infected RBCs and analyzed at day 12 of infection (F) or the indicated days (G). (F) Gated CD11b$^+$CD31$^+$ iHPCs (Gated on live singlets, CD45.2$^+$ F4/80$^-$Ly6G$^-$ Siglec-F$^-$) on day 12 of infection. (G) iHPC frequency and number per spleen at day 12 of infection (left); RBC count and parasitemia at the indicated days (right). Data are representative of two experiments, n = 5 (WT) and n = 4 to 5 (*Myd88*$^{-/-}$) mice per group. (**H** and **I**) The ratio of WT to *Unc93b1*$^{-/-}$ (H) or WT to *Myd88*$^{-/-}$*Trif*$^{-/-}$ (I) BM-derived cells in mixed bone marrow chimeras of indicated populations before (pre) and on day 8 after (post) infection with 1 × 10^6 *P. yoelii* 17XNL-infected RBCs. Ly6C^{hi} monocytes preinfection are from blood (open circles). Ly6C^{hi} monocytes postinfection (black circles) and iHPCs postinfection (blue circles) are from spleen. Data are representative of two experiments. Mean values ± SEM [(A), (B), (D), (G), (H), and (I)] are shown. In (E), (G) left, (H), and (I), Each symbol represents an individual mouse. *P < 0.05, **P < 0.01, ***P < 0.001, ****P < 0.0001, two-tailed, unpaired Student's t test [(A), (B), and (G)], linear regression (E), one-way ANOVA with Tukey's post test [(H) and (I)].

Downloaded from http://science.sciencemag.org/ on January 12, 2019

Materials and methods

Mice, BM chimeras, and in vivo treatments

TLR7.1 mice were obtained from S. Bolland (NIH) (*16*), *Spic*$^{-/-}$ (*Spic*^{tm1Kmm}) *Myd88*$^{-/-}$(*Myd88*$^{tm1.1Defr}$/J), and *Spic*$^{iGFP/+}$ (*Spic*$^{tm2.1Kmm}$) mice from Jackson Labs (*13*, *20*, *48*), *Ccr2*-DTR mice from T. Hohl (MSKCC) (*49*), and BALB/c, C57BL/6, and B6.SJL mice from Jackson Labs. *Irf5*$^{-/-}$ mice were used on both C57BL/6 and BALB/c backgrounds (*23*). Bones from *Tlr7*$^{-/-}$, *MyD88/Trif*$^{-/-}$, and *Unc93b1*$^{-/-}$ mice were obtained from G. Barton (UC Berkeley). All experiments were performed under approved protocols from the Benaroya Research Institute or Feinstein Institute Institutional Animal Care and Use Committee.

Mixed bone marrow chimeras were generated by lethally irradiating (1,000 rad) recipient C57BL/6×B6.SJL F1 mice and reconstituting with a 1:1 ratio of 5×10^6 B6.SJL (CD45.1$^+$) and 5 × 10^6 of either C57BL/6, *Tlr7*$^{-/-}$, TLR7.1, or *MyD88/Trif*$^{-/-}$ (CD45.2$^+$) bone marrow cells. For *Unc93b1*$^{-/-}$: WT mixed bone marrow chimeras and controls, B6.SJL (CD45.1$^+$) recipient mice were lethally irradiated (1,000 rad) and reconstituted with a 1:1 ratio of 5×10^6 C57BL/6×B6.SJL F1(CD45.1$^+$CD45.2$^+$) and 5 × 10^6 *Unc93b1*$^{-/-}$ or C57BL/6 (CD45.2) bone marrow cells. For experiments with TLR7.1/*Ccr2*-DTR mice, mice were injected intraperitoneally with 10 ng DT/g of body weight (List Biological Laboratories) in phosphate-buffered saline every other day for 17 days. In experiments with *Tlr7*$^{-/-}$ and B6.SJL mixed bone marrow chimeras, mice were injected intraperitoneally daily with 100 μg of R848 (Enzo Life Sciences) for 13 days. In experiments with *Irf5*$^{-/-}$, mice were injected daily for 2 days with 100 μg of R848 (Invivogen). In CpG injection experiments with *Ccr2*-DTR mice, mice were injected intraperitoneally with 40 μg daily of CpG-B (ODN1826) for 5 days (Integrated DNA Technologies). To assess anemia and thrombocytopenia, mice were bled retro-orbitally with heparinized capillary tubes. Blood was run on a Hemavet Hematology Analyzer (Drew Scientific).

In malaria infection experiments, *P. yoelii* 17XNL expressing RFP, provided by S. Kappe and A. Vaughn (*50*), was passaged through a donor mouse by infection i.p. with 2 × 10^6 frozen infected RBCs. From day 2 of infection, the donor mouse was monitored for parasitemia by tail vein prick and flow cytometric analysis of blood. When parasitemia reached ~1%, the donor mouse was sacrificed and blood harvested. Recipient mice were each injected i.p. with 1 × 10^6 infected RBCs.

MCMV (Smith strain) salivary gland viral stocks were provided by J. Sun (MSKCC) (*51*). Five-week-old BALB/c mice were infected with 8 × 10^3 plaque-forming units (PFU) MCMV i.p. and monitored daily for weight loss. On day 5, mice were sacrificed. Splenocytes were then stained for iHPCs and analyzed by flow cytometry.

Cell isolation, flow cytometry, and cell sorting

CMPs were isolated as described (*9*). RPMs and iHPCs were isolated from spleen by digestion in a cocktail of Liberase TL (Sigma) at 0.17 mg/ml and DNase1 (Sigma) at 40 μg/ml in complete RPMI (Hyclone). Bone marrow cells were isolated by centrifugation. Splenocytes and bone marrow cells were blocked with polyclonal rat IgG (65 μg/ml, Sigma) and purified anti-mouse Ter-119 (Ter-119, 71.4 μg/ml, Biolegend) prior to cell surface staining with fluorescently labeled antibodies as indicated in Supplementary Materials and Methods. Cells were then washed and incubated in Fixable Viability Dye eF780 (eBioscience) or Live/Dead Fixable Blue Dead Cell Stain (Invitrogen). Cells were washed and prepared for intracellular staining with Fixation and Permeabilization buffer (BD Biosciences), washed in Perm/Wash buffer (BD Biosciences) and then stained with fluorescently labeled anti-Ter-119 to detect cells that had phagocytosed RBCs. To accurately assess phagocytosis, some samples were blocked intracellularly with purified anti-mouse Ter-119 (25 μg/ml) prior to intracellular staining with fluorescently labeled anti-Ter-119. To assess spleen and bone marrow cells without Ter-119 stain, cells were blocked with polyclonal rat IgG and polyclonal mouse IgG (65 μg/ml, Sigma), stained with appropriate antibodies, and then fixed with 2% paraformaldehyde. Data were acquired on an LSRII or FACSCanto (BD Biosciences) and analyzed using FlowJo (Tree Star).

For isolation of iHPCs, RPMs, and monocytes for quantitative real-time PCR and microscopic analysis, splenocytes isolated as above were stained with APC-conjugated rat anti-mouse SIRPα (P84, 1 μg/ml), incubated with anti-APC beads (Miltenyi), and positively selected on LS columns (Miltenyi). Following isolation, cells were then stained as indicated in Supplemental Materials and Methods and sorted on a FACSAria (BD Biosciences). For experiments requiring only monocytes, bone marrow was depleted using biotinylated antibodies to hamster anti-mouse CD3ε (eBio500A2, eBioscience), rat anti-mouse CD19 (6D5, Biolegend), rat anti-mouse Ly6G (1A8, Biolegend), and mouse anti-mouse NK1.1 (PK136, eBioscience) (all at 5 μg/ml), anti-biotin beads (Miltenyi), and LS columns (Miltenyi). Negatively selected bone marrow was then stained with rat anti-mouse Ly6C (HK1.4), rat anti-mouse Siglec-F (E50-2440), rat anti-mouse Ly6G (1A8), rat anti-mouse/human CD11b (M1/70), rat anti-mouse MHCII (M5/114.15.2), and hamster anti-mouse CD11c (N418). Cells were then sorted on a FACSAria (BD Biosciences) as in fig. S3.

In vitro cell culture

Sorted bone marrow CMPs were plated as previously described (*9*). CMPs (2500–20,000) were plated per well in 96-well plates in complete serum-free StemPro-34 media (Life Technologies) with 20 ng/ml of stem cell factor (Peprotech) for all experiments. Unless otherwise noted, 1 μg/ml of R848 (Invivogen) and 20 ng/ml of M-CSF (Peprotech) were used. For flow cytometric quantification of CD11b$^+$ F4/80$^+$ cells, adherent cells were isolated using cell dissociation buffer (Life Technologies) and stained with antibodies to CD11b and F4/80. Cell yield was quantified using polystyrene microspheres (Polysciences) and flow cytometry as the number of CD11b$^+$F4/80$^+$ events per well divided by the number of polystyrene bead events per well multiplied by the total number of polystyrene beads per well.

For gene expression analysis, sorted monocytes were plated in either RPMI alone, 100 ng/ml of LPS (List Biologicals), 3 μM CpG-C ODN2395 (Integrated DNA Technologies), 10 μg/ml of R848 (Invivogen), 40 ng/ml of MCSF (Peprotech), 100 ng/ml of IFNγ (Peprotech), 100 ng/ml of IL-1β (Miltenyi), or 25–50 μg/ml of Poly(I:C) (Invivogen).

Hemophagocytosis assay

CMPs were sorted as above and then placed in culture at 10,000 cells/well in either 10 μg/ml of R848 or 40 ng/ml of M-CSF. On day 4, cells were harvested from wells with cell dissociation buffer (Gibco), washed in Dulbecco's Modified Eagle Medium (Gibco) supplemented with 10% fetal bovine serum (Sigma-Aldrich), plated at 50,000 cells per well in non-tissue culture treated flat bottom 96-well plates, and rested overnight. On day 5, heparinized blood was harvested from a C57BL/6 mouse, and 40 μl of whole blood (or approximately 4 × 10^8 RBCs) were then washed in PBS and resuspended at 2 × 10^7/ml in 20 ml of PBS containing 5 μM carboxyfluorescein diacetate succinimidyl ester (CFSE) (Sigma-Aldrich) and incubated at 37°C for 10 min while shaking to obtain CFSE-labeled RBCs. Following incubation, the reaction was stopped with DMEM with 10% FBS for 10 min on ice, and then washed three times. R848-differentiated macrophages were pretreated with 2 μM cytochalasin D (Calbiochem) or DMSO (Fisher) vehicle for 30 min and 10 μg/ml of purified anti-SIRPα antibody (P84) for 15 min, prior to the addition of CFSE-labeled RBCs. Following a 15-min incubation with RBCs, assay wells were washed with cold PBS and extracellular RBCs were lysed with cold ACK lysis buffer (Lonza) for 5 min on ice. Cells were then washed with cold DMEM with 10% FBS, followed by cold PBS. Macrophages were then harvested from assay plates with cell dissociation buffer (Gibco, ThermoFisher) at 37°C on a shaker for 10 min. Cells were blocked for Fc receptor binding with polyclonal rat IgG and polyclonal mouse IgG (65 μg/ml, Sigma) and stained for CD11b and F4/80 for 20 min. Samples were then washed, fixed with 2% paraformaldehyde, and analyzed on a FACSCanto (BD Biosciences) and using FlowJo software (Tree Star).

Microscopy

RPMs and iHPCs were sorted from spleens of TLR7.1 and WT mice, cytospun onto slides (Cytospin 4, Thermo Scientific), and stained by hematoxylin and eosin. At least two fields per sample were quantified for phagocytic index using a Leica DM2500 microscope with SPOT Software 5.1 and SPOT Insight Wide-field 4 Mp Monochrome FireWire Digital Camera. A total of 43–409 cells per sample were counted. The phagocytic index was calculated by using the following formula: PI = (% phagocytic cells containing ≥ 1 RBC) × (mean number of RBC/phagocytic cell containing RBCs).

Downloaded from http://science.sciencemag.org/ on January 12, 2019

Quantitative RT-PCR

RNA was generated using RNeasy Plus Mini Kit and RNeasy MinElute Cleanup kit (Qiagen). cDNA was synthesized using Primescript (Takara) and Invitrogen reagents with random hexamers and OligoDT primers. qPCR was performed using SYBR green reagents (Takara) on a 7500 Fast Real-Time PCR System (Applied Biosystems). Arbitrary units were calculated using the ΔΔCT method normalized to HPRT. The values were then normalized again by setting either media alone (–) or monocyte values to 1.

RNA-seq and bioinformatic analysis

CMP+R848 versus CMP+M-CSF RNA-Seq

Samples were generated by sorting CMPs and plating 10,000 cells per well of a 96-well plate in complete serum-free StemPro 34 (Gibco) media with 20 ng/ml Stem Cell Factor (Peprotech) for 4 days with 1 μg/ml of R848 (Invivogen) or 20 ng/ml of M-CSF (Peprotech). At day 4, cells were washed with Dulbecco's Modified Eagle Medium (Gibco) supplemented with 10% fetal bovine serum (Sigma-Aldrich), rested for 24 hours, and isolated using cell dissociation buffer. Samples were sorted as propidium iodide$^-$ CD11b$^+$F4/80$^+$ cells directly into RLT plus lysis buffer (Qiagen). RNA was generated using RNeasy kit and MinElute cleanup kit (Qiagen). RNA from three independent sorts for each M-CSF and R848-diferentiated macrophages were used for RNA sequencing.

RNA-Seq libraries were constructed from 100 ng of RNA using the TruSeq RNA Sample Preparation V2 kit (Illumina). Libraries were clustered on a flowcell using the TruSeq SR Cluster Kit, v3 using a cBot (Illumina), followed by single read sequencing on a HiSeq2500 (Illumina) for 100 cycles. FASTQ files were downloaded from https://basespace.illumina.com.

Libraries were processed via Galaxy on a local computer cluster. Libraries were aligned via TopHat (v1.4.1) to Ensembl's *Mus musculus* GRCm38.78 gtf (http://may2012.archive.ensembl.org/Mus_musculus/Info/Index). The –single-paired flag was set to "single," whereas all other TopHat parameters were set to defaults. HTSeq-count (*52*) was used to generate gene counts with mode as "Intersection (nonempty)" and Minimum alignment quality set to 0; all others were set to default parameters.

Analysis of the 37,991 Ensembl ID count data was performed using the edgeR package (*53*) in the R software environment (R Core Team (2017). R: A language and environment for statistical computing. R Foundation for Statistical Computing, Vienna, Austria. www.R-project.org). For each gene, a negative binomial general linear model (*54*) appropriate for count data was used for the two-group comparisons of R848 versus M-CSF. The Ensembl IDs were filtered to those that had a TMM normalized count of at least one in at least one library, which resulted in 13,690 Ensembl IDs used in the general linear model. The two-group comparison had an 18% biological coefficient of variation and 1833 protein coding Ensembl IDs had a false discovery rate less than 0.05 and fold change greater than 2 (in either direction) (Shilin Zhao, Yan Guo, Quanhu Sheng and Yu Shyr (2015). heatmap3: An Improved Heatmap Package. R package version 1.1.1. https://CRAN.R-project.org/package=heatmap3).

Tissue macrophage gene signatures were identified in Gautier *et al.* 2012 (*14*). Analysis of tissue macrophage signature overlap was conducted by comparing the number of genes significantly upregulated (>2-fold) in R848-derived macrophages versus M-CSF–derived macrophages to the number of significantly enriched genes in each tissue macrophage signature (*14*) using an online tool (http://nemates.org/MA/progs/overlap_stats.html).

iHPC, RPM, and Ly6C^{hi} monocyte RNA-seq

Five hundred cells were sorted into lysis buffer from the SMART-Seq v4 Ultra Low Input RNA Kit for Sequencing (Takara). Reverse transcription was performed followed by PCR amplification to generate full-length amplified cDNA. Sequencing libraries were constructed using the NexteraXT DNA sample preparation kit (Illumina) to generate Illumina-compatible barcoded libraries. Libraries were pooled and quantified using a Qubit Fluorometer (Life Technologies). Dual-index, single-read sequencing of pooled libraries was carried out on a HiSeq2500 sequencer (Illumina) with 58-base reads, using HiSeq v4 Cluster and SBS kits (Illumina) with a target depth of 5×10^6 reads per sample. Basecalls were processed to FASTQs on BaseSpace (Illumina), and a base call quality trimming step was applied to remove low-confidence base calls from the ends of reads.

Libraries were processed via Galaxy as above. Analysis of the 37,991 Ensembl ID count data was performed using voom from the limma package updated for RNA-sequencing experiments (*55*) in the R software environment. The Ensembl IDs were filtered to those that encoded for protein coding genes, and had a TMM normalized count of at least one count per million in at least 10% of the libraries, which resulted in 12,856 Ensembl IDs used in the general linear model. Samples were removed from analysis if the number of aligned reads was less than 500,000. Two-group comparisons were filtered for a false discovery rate of 0.05 after multiple testing correction, and a fold change of 1.5 or greater. Heatmaps were constructed using the heatmap3 package (*54*).

RNA-seq data are available in GEO SuperSeries GSE117718 containing CMP dataset (GSE70520) and iHPC dataset (GSE117711).

REFERENCES AND NOTES

1. C. Bracaglia, G. Prencipe, F. De Benedetti, Macrophage activation syndrome: Different mechanisms leading to a one clinical syndrome. *Pediatr. Rheumatol. Online J.* **15**, 5 (2017). doi: 10.1186/s12969-016-0130-4; pmid: 28095869
2. S. W. Canna, E. M. Behrens, Not all hemophagocytes are created equally: Appreciating the heterogeneity of the hemophagocytic syndromes. *Curr. Opin. Rheumatol.* **24**, 113–118 (2012). doi: 10.1097/BOR.0b013e32834dd37e; pmid: 22089101
3. A. Ravelli, A. A. Grom, E. M. Behrens, R. Q. Cron, Macrophage activation syndrome as part of systemic juvenile idiopathic arthritis: Diagnosis, genetics, pathophysiology and treatment. *Genes Immun.* **13**, 289–298 (2012). doi: 10.1038/gene.2012.3; pmid: 22418018
4. T. D. Bennett *et al.*, Macrophage activation syndrome in children with systemic lupus erythematosus and children with juvenile idiopathic arthritis. *Arthritis Rheum.* **64**, 4135–4142 (2012). doi: 10.1002/art.34661; pmid: 22886474
5. T. Taylor *et al.*, Standardized data collection for multi-center clinical studies of severe malaria in African children: Establishing the SMAC network. *Trans. R. Soc. Trop. Med. Hyg.* **100**, 615–622 (2006). doi: 10.1016/j.trstmh.2005.09.021; pmid: 16551469
6. D. J. Perkins *et al.*, Severe malarial anemia: Innate immunity and pathogenesis. *Int. J. Biol. Sci.* **7**, 1427–1442 (2011). doi: 10.7150/ijbs.7.1427; pmid: 22110393
7. A. A. Lamikanra *et al.*, Malarial anemia: Of mice and men. *Blood* **110**, 18–28 (2007). doi: 10.1182/blood-2006-09-018069; pmid: 17341664
8. Y. Nagai *et al.*, Toll-like receptors on hematopoietic progenitor cells stimulate innate immune system replenishment. *Immunity* **24**, 801–812 (2006). doi: 10.1016/j.immuni.2006.04.008; pmid: 16782035
9. M. B. Buechler, H. M. Akilesh, J. A. Hamerman, Cutting Edge: Direct sensing of TLR7 ligands and type I IFN by the common myeloid progenitor promotes mTOR/PI3K-dependent emergency myelopoiesis. *J. Immunol.* **197**, 2577–2582 (2016). doi: 10.4049/jimmunol.1600813; pmid: 27566824
10. S. Boettcher, M. G. Manz, Sensing and translation of pathogen signals into demand-adapted myelopoiesis. *Curr. Opin. Hematol.* **23**, 5–10 (2016). doi: 10.1097/MOH.0000000000000201; pmid: 26554891
11. H. Takizawa, S. Boettcher, M. G. Manz, Demand-adapted regulation of early hematopoiesis in infection and inflammation. *Blood* **119**, 2991–3002 (2012). doi: 10.1182/blood-2011-12-380113; pmid: 22246037
12. M. B. Buechler, T. H. Teal, K. B. Elkon, J. A. Hamerman, Cutting edge: Type I IFN drives emergency myelopoiesis and peripheral myeloid expansion during chronic TLR7 signaling. *J. Immunol.* **190**, 886–891 (2013). doi: 10.4049/jimmunol.1202739; pmid: 23303674
13. M. Kohyama *et al.*, Role for Spi-C in the development of red pulp macrophages and splenic iron homeostasis. *Nature* **457**, 318–321 (2009). doi: 10.1038/nature07472; pmid: 19037245
14. E. L. Gautier *et al.*, Gene-expression profiles and transcriptional regulatory pathways that underlie the identity and diversity of mouse tissue macrophages. *Nat. Immunol.* **13**, 1118–1128 (2012). doi: 10.1038/ni.2419; pmid: 23023392
15. T. Ganz, Macrophages and systemic iron homeostasis. *J. Innate Immun.* **4**, 446–453 (2012). doi: 10.1159/000336423; pmid: 22441209
16. J. A. Deane *et al.*, Control of toll-like receptor 7 expression is essential to restrict autoimmunity and dendritic cell proliferation. *Immunity* **27**, 801–810 (2007). doi: 10.1016/j.immuni.2007.09.009; pmid: 17997333
17. M. Guilliams, C. L. Scott, Does niche competition determine the origin of tissue-resident macrophages? *Nat. Rev. Immunol.* **17**, 451–460 (2017). doi: 10.1038/nri.2017.42; pmid: 28461703
18. I. Amit, D. R. Winter, S. Jung, The role of the local environment and epigenetics in shaping macrophage identity and their effect on tissue homeostasis. *Nat. Immunol.* **17**, 18–25 (2016). doi: 10.1038/ni.3325; pmid: 26681458
19. E. G. Perdiguero, F. Geissmann, The development and maintenance of resident macrophages. *Nat. Immunol.* **17**, 2–8 (2016). doi: 10.1038/ni.3341; pmid: 26681456
20. M. Haldar *et al.*, Heme-mediated SPI-C induction promotes monocyte differentiation into iron-recycling macrophages. *Cell* **156**, 1223–1234 (2014). doi: 10.1016/j.cell.2014.01.069; pmid: 24630724
21. E. M. Behrens *et al.*, Repeated TLR9 stimulation results in macrophage activation syndrome-like disease in mice. *J. Clin. Invest.* **121**, 2264–2277 (2011). doi: 10.1172/JCI43157; pmid: 21576823
22. S. Nagata, Apoptosis and clearance of apoptotic cells. *Annu. Rev. Immunol.* **36**, 489–517 (2018). doi: 10.1146/annurev-immunol-042617-053010; pmid: 29400998
23. A. Takaoka *et al.*, Integral role of IRF-5 in the gene induction programme activated by Toll-like receptors. *Nature* **434**, 243–249 (2005). doi: 10.1038/nature03308; pmid: 15665823
24. A. Schoenemeyer *et al.*, The interferon regulatory factor, IRF5, is a central mediator of toll-like receptor 7 signaling. *J. Biol. Chem.* **280**, 17005–17012 (2005). doi: 10.1074/jbc.M412584200; pmid: 15695821
25. M. Yanagimachi *et al.*, Association of IRF5 polymorphisms with susceptibility to macrophage activation syndrome in patients

Downloaded from http://science.sciencemag.org/ on January 12, 2019

with juvenile idiopathic arthritis. *J. Rheumatol.* **38**, 769–774 (2011). doi: 10.3899/jrheum.100655; pmid: 21239750
26. M. Yanagimachi *et al.*, Association of IRF5 polymorphisms with susceptibility to hemophagocytic lymphohistiocytosis in children. *J. Clin. Immunol.* **31**, 946–951 (2011). doi: 10.1007/s10875-011-9583-x; pmid: 21898142
27. M. Hedl, J. Yan, C. Abraham, IRF5 and IRF5 disease-risk variants increase glycolysis and human M1 macrophage polarization by regulating proximal signaling and Akt2 activation. *Cell Reports* **16**, 2442–2455 (2016). doi: 10.1016/j.celrep.2016.07.060; pmid: 27545875
28. E. Brisse *et al.*, Mouse cytomegalovirus infection in BALB/c mice resembles virus-associated secondary hemophagocytic lymphohistiocytosis and shows a pathogenesis distinct from primary hemophagocytic lymphohistiocytosis. *J. Immunol.* **196**, 3124–3134 (2016). doi: 10.4049/jimmunol.1501035; pmid: 26903481
29. R. T. Gazzinelli, P. Kalantari, K. A. Fitzgerald, D. T. Golenbock, Innate sensing of malaria parasites. *Nat. Rev. Immunol.* **14**, 744–757 (2014). doi: 10.1038/nri3742; pmid: 25324127
30. A. Baccarella, M. F. Fontana, E. C. Chen, C. C. Kim, Toll-like receptor 7 mediates early innate immune responses to malaria. *Infect. Immun.* **81**, 4431–4442 (2013). doi: 10.1128/IAI.00923-13; pmid: 24042114
31. A. Baccarella, B. W. Huang, M. F. Fontana, C. C. Kim, Loss of Toll-like receptor 7 alters cytokine production and protects against experimental cerebral malaria. *Malar. J.* **13**, 354 (2014). doi: 10.1186/1475-2875-13-354; pmid: 25192715
32. P. Parroche *et al.*, Malaria hemozoin is immunologically inert but radically enhances innate responses by presenting malaria DNA to Toll-like receptor 9. *Proc. Natl. Acad. Sci. U.S.A.* **104**, 1919–1924 (2007). doi: 10.1073/pnas.0608745104; pmid: 17261807
33. X. Wu, N. M. Gowda, S. Kumar, D. C. Gowda, Protein-DNA complex is the exclusive malaria parasite component that activates dendritic cells and triggers innate immune responses. *J. Immunol.* **184**, 4338–4348 (2010). doi: 10.4049/jimmunol.0903824; pmid: 20231693
34. S. Pichyangkul *et al.*, Malaria blood stage parasites activate human plasmacytoid dendritic cells and murine dendritic cells through a Toll-like receptor 9-dependent pathway. *J. Immunol.* **172**, 4926–4933 (2004). doi: 10.4049/jimmunol.172.8.4926; pmid: 15067072
35. X. Yu *et al.*, Cross-regulation of two type I interferon signaling pathways in plasmacytoid dendritic cells controls anti-malaria immunity and host mortality. *Immunity* **45**, 1093–1107 (2016). doi: 10.1016/j.immuni.2016.10.001; pmid: 27793594
36. T. Delale *et al.*, MyD88-dependent and -independent murine cytomegalovirus sensing for IFN-α release and initiation of immune responses in vivo. *J. Immunol.* **175**, 6723–6732 (2005). doi: 10.4049/jimmunol.175.10.6723; pmid: 16272328
37. N. Zucchini *et al.*, Cutting edge: Overlapping functions of TLR7 and TLR9 for innate defense against a herpesvirus infection. *J. Immunol.* **180**, 5799–5803 (2008). doi: 10.4049/jimmunol.180.9.5799; pmid: 18424698
38. H. Kayama *et al.*, Heme ameliorates dextran sodium sulfate-induced colitis through providing intestinal macrophages with noninflammatory profiles. *Proc. Natl. Acad. Sci. U.S.A.* **115**, 8418–8423 (2018). doi: 10.1073/pnas.1808426115; pmid: 30061415
39. D. G. Saliba *et al.*, IRF5:RelA interaction targets inflammatory genes in macrophages. *Cell Reports* **8**, 1308–1317 (2014). doi: 10.1016/j.celrep.2014.07.034; pmid: 25159141
40. R. R. Graham *et al.*, Three functional variants of IFN regulatory factor 5 (IRF5) define risk and protective haplotypes for human lupus. *Proc. Natl. Acad. Sci. U.S.A.* **104**, 6758–6763 (2007). doi: 10.1073/pnas.0701266104; pmid: 17412832
41. D. S. Cunninghame Graham *et al.*, Polymorphism at the TNF superfamily gene TNFSF4 confers susceptibility to systemic lupus erythematosus. *Nat. Genet.* **40**, 83–89 (2008). doi: 10.1038/ng.2007.47; pmid: 18059267
42. J. B. Harley *et al.*, Genome-wide association scan in women with systemic lupus erythematosus identifies susceptibility variants in ITGAM, PXK, KIAA1542 and other loci. *Nat. Genet.* **40**, 204–210 (2008). doi: 10.1038/ng.81; pmid: 18204446
43. G. Hom *et al.*, Association of systemic lupus erythematosus with C8orf13-BLK and ITGAM-ITGAX. *N. Engl. J. Med.* **358**, 900–909 (2008). doi: 10.1056/NEJMoa0707865; pmid: 18204098
44. R. C. Stone *et al.*, Interferon regulatory factor 5 activation in monocytes of systemic lupus erythematosus patients is triggered by circulating autoantigens independent of type I interferons. *Arthritis Rheum.* **64**, 788–798 (2012). pmid: 21968701
45. A. A. Grom *et al.*, Rate and clinical presentation of macrophage activation syndrome in patients with systemic juvenile idiopathic arthritis treated with canakinumab. *Arthritis Rheumatol.* **68**, 218–228 (2016). doi: 10.1002/art.39407; pmid: 26314396
46. H. Al-Samkari, N. Berliner, Hemophagocytic lymphohistiocytosis. *Annu. Rev. Pathol.* **13**, 27–49 (2018). doi: 10.1146/annurev-pathol-020117-043625; pmid: 28934563
47. E. E. Zoller *et al.*, Hemophagocytosis causes a consumptive anemia of inflammation. *J. Exp. Med.* **208**, 1203–1214 (2011). doi: 10.1084/jem.20102538; pmid: 21624938
48. B. Hou *et al.*, Selective utilization of Toll-like receptor and MyD88 signaling in B cells for enhancement of the antiviral germinal center response. *Immunity* **34**, 375–384 (2011). doi: 10.1016/j.immuni.2011.01.011; pmid: 21353603
49. T. M. Hohl *et al.*, Inflammatory monocytes facilitate adaptive CD4 T cell responses during respiratory fungal infection. *Cell Host Microbe* **6**, 470–481 (2009). doi: 10.1016/j.chom.2009.10.007; pmid: 19917501
50. J. L. Miller, A. Harupa, S. H. I. Kappe, S. A. Mikolajczak, Plasmodium yoelii macrophage migration inhibitory factor is necessary for efficient liver-stage development. *Infect. Immun.* **80**, 1399–1407 (2012). doi: 10.1128/IAI.05861-11; pmid: 22252874
51. N. M. Adams *et al.*, Transcription factor IRF8 orchestrates the adaptive natural killer cell response. *Immunity* **48**, 1172–1182.e6 (2018). doi: 10.1016/j.immuni.2018.04.018; pmid: 29858012
52. S. Anders, P. T. Pyl, W. Huber, HTSeq—A Python framework to work with high-throughput sequencing data. *Bioinformatics* **31**, 166–169 (2015). doi: 10.1093/bioinformatics/btu638; pmid: 25260700
53. M. D. Robinson, D. J. McCarthy, G. K. Smyth, edgeR: A Bioconductor package for differential expression analysis of digital gene expression data. *Bioinformatics* **26**, 139–140 (2010). doi: 10.1093/bioinformatics/btp616; pmid: 19910308
54. D. J. McCarthy, Y. Chen, G. K. Smyth, Differential expression analysis of multifactor RNA-Seq experiments with respect to biological variation. *Nucleic Acids Res.* **40**, 4288–4297 (2012). doi: 10.1093/nar/gks042; pmid: 22287627
55. M. E. Ritchie *et al.*, limma powers differential expression analyses for RNA-sequencing and microarray studies. *Nucleic Acids Res.* **43**, e47 (2015). doi: 10.1093/nar/gkv007; pmid: 25605792

ACKNOWLEDGMENTS

The authors thank R. Doty and the Hamerman laboratory members for helpful discussions, D. Campbell and S. Ziegler for review of the manuscript, T. Hohl for *Ccr2*-DTR mice, J. Sun for MCMV, G. Barton for bones from *MyD88/Trif*$^{-/-}$ and *Unc93b1*$^{-/-}$ mice, A. Vaughn and S. Kappe for RFP-expressing *P. yoelii* 17XNL, S. Bolland for TLR7.1 mice, and J. Abkowitz for Hemavet use. We also thank the Benaroya Research Institute Flow Cytometry Core Lab and Genomics Core for technical support and the Vivarium staff for support. We also acknowledge technical support from BioRender with the print page summary figure. **Funding:** This work was supported by NIH T32 AR007108 and an AAI Fellowship (H.M.A.); NSF Graduate Research Fellowship DGE-0718124 (M.B.B.); NIH T32 AI007044-39 (W.O.H.); NIH T32 AI106677 (J.M.D.); NIH R21 CA195256; DOD BCRP W81XWH-08-1-0570; Lupus Research Alliance (B.J.B.); NIH R01 DK09369 (A.L-H.); NIH R01 AI118803 (M.P.); NIH R01 AI081948, NIH R01 AI113325, and NIH R21 AI138067 (J.A.H.); and NIH R21 ES024437 (K.B.E.). **Author contributions:** H.M.A, M.B.B and J.A.H. conceived and designed the study. H.M.A, M.B.B, J.M.D, W.O.H, X.S., G.G., B.M., and J.A.H performed experiments. S.R.P., E.W., and M.M. performed RNA-seq analysis. K.B.E, A.L-H., B.J.B., and M.P. provided key reagents. H.M.A., M.B.B., W.O.H., K.B.E., A.L.-H., M.P., B.J.B., and J.A.H wrote the manuscript. **Competing interests:** The authors declare no competing interests. **Data and materials availability:** RNA-seq data are deposited in the NCBI Gene Expression Omnibus under SuperSeries GSE117718 containing CMP dataset (GSE70520) and iHPC dataset (GSE117711). The TLR7.1 mouse strain used in this study was obtained under a materials transfer agreement (MTA) with the National Institute of Allergy and Infectious Diseases. The *P. yoelii* 17XNL parasite (S1-Red) used in this study was obtained via a MTA with the Center for Infectious Disease Research, Seattle, Washington. All other data needed to evaluate the conclusions in this paper are present either in the main text or the supplementary materials.

SUPPLEMENTARY MATERIALS

www.sciencemag.org/content/363/6423/eaao5213/suppl/DC1
Materials and Methods
Figs. S1 to S11

30 July 2017; resubmitted 4 August 2018
Accepted 28 November 2018
10.1126/science.aao5213

Downloaded from http://science.sciencemag.org/ on January 12, 2019

RESEARCH ARTICLE SUMMARY

NEUROSCIENCE

Secreted amyloid-β precursor protein functions as a $GABA_BR1a$ ligand to modulate synaptic transmission

Heather C. Rice, Daniel de Malmazet, An Schreurs, Samuel Frere, Inge Van Molle, Alexander N. Volkov, Eline Creemers, Irena Vertkin, Julie Nys, Fanomezana M. Ranaivoson, Davide Comoletti, Jeffrey N. Savas, Han Remaut, Detlef Balschun, Keimpe D. Wierda, Inna Slutsky, Karl Farrow, Bart De Strooper*, Joris de Wit*

INTRODUCTION: More than 30 years have passed since the amyloid-β precursor protein (APP) was identified. Although the role of APP in Alzheimer's disease has been studied widely, its normal physiological function in the brain has remained elusive. APP undergoes ectodomain shedding by α-, β-, or η-secretase to release secreted APP (sAPPα, sAPPβ, or sAPPη, respectively). sAPPα affects synaptic transmission and plasticity and is sufficient to rescue synaptic defects in *App* knockout mice. This has led to speculation of a yet unidentified cell-surface receptor for sAPPα.

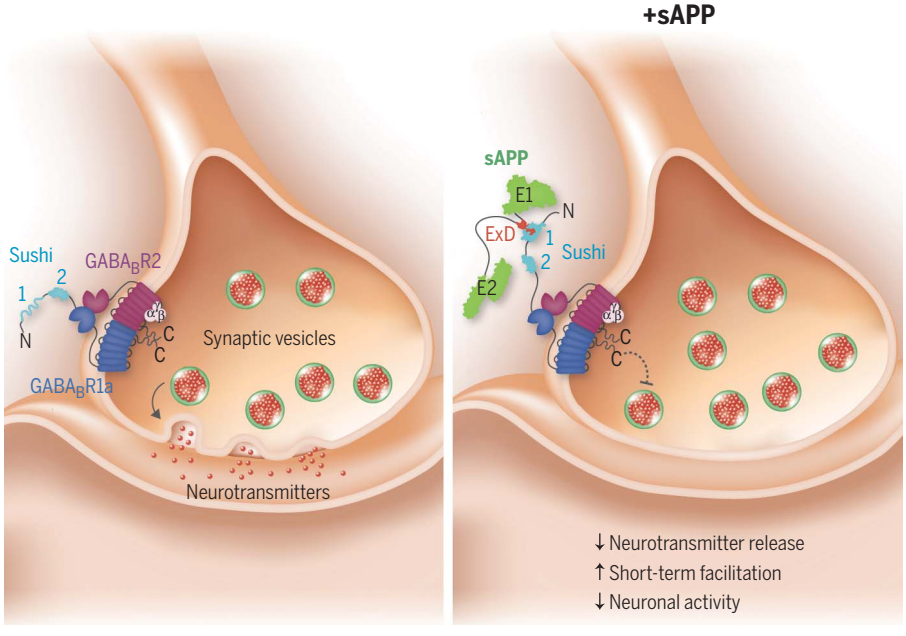
RATIONALE: To elucidate the physiological function of APP, we sought to identify the cell-surface receptor mediating its effects on synaptic function. To identify candidate synaptic interactors for sAPPα, we performed affinity-purification experiments using recombinant sAPPα to pull down interacting proteins from synaptosome extracts, followed by mass spectrometric analysis of bound proteins. We identified the γ-aminobutyric acid type B receptor ($GABA_BR$), the metabotropic receptor for the inhibitory neurotransmitter γ-aminobutyric acid (GABA), as the leading candidate for a synaptic, cell-surface receptor for sAPPα. We then performed a combination of cell-surface binding assays and in vitro biophysical techniques to determine the interacting domains and structural consequences of binding. We investigated whether sAPPα can modulate $GABA_BR$ function by assessing miniature excitatory and inhibitory postsynaptic currents (mEPSCs and mIPSCs, respectively) and synaptic vesicle recycling in mouse hippocampal neuron cultures, short-term plasticity in acute hippocampal slices from mice, and in vivo neuronal activity in the hippocampus of anesthetized mice.

RESULTS: Recombinant sAPPα selectively bound to $GABA_BR$ subunit 1a ($GABA_BR1a$)–expressing cells. Binding was mediated by the flexible, partially structured extension domain in the linker region of sAPP and the natively unstructured sushi 1 domain specific to $GABA_BR1a$. sAPPβ and sAPPη, which both contain the extension domain, also bound to $GABA_BR1a$-expressing cells. Conversely, APP family members APP-like proteins 1 and 2, which lack a conserved extension domain, failed to bind $GABA_BR1a$-expressing cells. Acute application of sAPPα reduced the frequency of mEPSCs and mIPSCs and decreased synaptic vesicle recycling in cultured mouse hippocampal neurons. In addition, sAPPα enhanced short-term facilitation in acute hippocampal slices from mice. Together, these findings demonstrate that sAPP reduces the release probability of synaptic vesicles. These effects were dependent on the presence of the extension domain in sAPP and were occluded by a $GABA_BR$ antagonist. A short APP peptide corresponding to the $GABA_BR1a$ binding region within APP stabilized the natively unstructured sushi 1 domain of $GABA_BR1a$, allowing determination of its solution structure using nuclear magnetic resonance spectroscopy and the generation of a structural model of the APP–sushi 1 complex. Application of a 17–amino acid APP peptide mimicked the effects of sAPPα on $GABA_BR1a$-dependent inhibition of synaptic vesicle release and reversibly suppressed spontaneous neuronal activity in vivo.

CONCLUSION: We identified $GABA_BR1a$ as a synaptic receptor for sAPP and revealed a physiological role for sAPP in regulating $GABA_BR1a$ function to modulate synaptic transmission and plasticity. Our findings provide a potential target for the development of $GABA_BR1a$ isoform–specific therapeutics, which is relevant to a number of neurological disorders in which $GABA_BR$ signaling is implicated. ■

ON OUR WEBSITE

Read the full article at http://dx.doi.org/10.1126/science.aao4827



sAPP is a functional $GABA_BR1a$-specific ligand. In the presence of sAPP (right), the extension domain (ExD) of sAPP binds the sushi 1 domain specific to $GABA_BR1a$. Binding induces a conformational change in the sushi 1 domain and leads to increased short-term facilitation and decreased neuronal activity via inhibition of neurotransmitter release. N, amino terminus; C, carboxyl terminus; α, β, and γ, G protein subunits coupled to $GABA_BR$ subunit 2 ($GABA_BR2$); E1 and E2, sAPP domains.

ILLUSTRATION: SOMERSAULT18:24

The list of author affiliations is available in the full article online.
*Corresponding author. Email: bart.destrooper@kuleuven.vib.be (B.D.S.); joris.dewit@kuleuven.vib.be (J.d.W.)
Cite this article as H. C. Rice *et al.*, *Science* **363**, eaao4827 (2019). DOI: 10.1126/science.aao4827

Downloaded from http://science.sciencemag.org/ on January 15, 2019

RESEARCH ARTICLE

NEUROSCIENCE

Secreted amyloid-β precursor protein functions as a $GABA_BR1a$ ligand to modulate synaptic transmission

Heather C. Rice[1,2], Daniel de Malmazet[3,4], An Schreurs[5], Samuel Frere[6], Inge Van Molle[7], Alexander N. Volkov[7,8], Eline Creemers[1,2], Irena Vertkin[6], Julie Nys[1,2], Fanomezana M. Ranaivoson[9]*, Davide Comoletti[9,10]†, Jeffrey N. Savas[11], Han Remaut[7], Detlef Balschun[5], Keimpe D. Wierda[1,2], Inna Slutsky[6], Karl Farrow[3,4,12,13], Bart De Strooper[1,2,14]‡, Joris de Wit[1,2]‡

Amyloid-β precursor protein (APP) is central to the pathogenesis of Alzheimer's disease, yet its physiological function remains unresolved. Accumulating evidence suggests that APP has a synaptic function mediated by an unidentified receptor for secreted APP (sAPP). Here we show that the sAPP extension domain directly bound the sushi 1 domain specific to the γ-aminobutyric acid type B receptor subunit 1a ($GABA_BR1a$). sAPP-$GABA_BR1a$ binding suppressed synaptic transmission and enhanced short-term facilitation in mouse hippocampal synapses via inhibition of synaptic vesicle release. A 17–amino acid peptide corresponding to the $GABA_BR1a$ binding region within APP suppressed in vivo spontaneous neuronal activity in the hippocampus of anesthetized Thy1-GCaMP6s mice. Our findings identify $GABA_BR1a$ as a synaptic receptor for sAPP and reveal a physiological role for sAPP in regulating $GABA_BR1a$ function to modulate synaptic transmission.

Amyloid-β precursor protein (APP), a type 1 transmembrane protein, was first identified more than 30 years ago (*1*–*4*) as the precursor to the amyloid-β (Aβ) peptide, the primary constituent of amyloid plaques found in the brains of Alzheimer's disease (AD) patients. APP undergoes ectodomain shedding by α-, β-, or η-secretase to release secreted APP (sAPPα, sAPPβ, or sAPPη, respectively) (*5*, *6*). Evidence suggests that the synaptic function of APP (*7*–*13*) is carried out by sAPP (*14*, *15*). sAPPα affects synaptic transmission and plasticity, including a reduction in synaptic activity and an enhancement of long-term potentiation (LTP) (*16*–*19*). Moreover, sAPPα is sufficient to rescue synaptic defects in *App* knockout (KO) mice, including defects in spine density (*20*), LTP (*21*, *22*), and spatial learning (*21*). Together, this has led to speculation of a yet-unidentified cell-surface receptor for sAPP to mediate its synaptic function (*15*, *23*, *24*).

Proteomics screen for synaptic interactors of sAPP identifies $GABA_BR$

We first confirmed, using biochemical fractionation and structured illumination imaging, that APP was abundantly expressed at presynaptic terminals (*25*) of excitatory and inhibitory hippocampal synapses (fig. S1, A and B). Next, to identify candidate synaptic receptors for sAPP, we performed an extensive series of affinity-purification experiments using recombinant sAPP-Fc [C-terminal Fc tag; affinity purified from transfected–human embryonic kidney (HEK) 293T cell supernatants; fig. S2, A and B] to pull down interacting proteins from synaptosome extracts, followed by mass spectrometric analysis of bound proteins [affinity purification–mass spectrometry (AP-MS)] (Fig. 1A) (*26*). We consistently identified, among a few intracellular proteins (Fig. 1B; fig. S3, A and B; and table S1), the γ-aminobutyric acid type B receptor subunit 1 ($GABA_BR1$) as the most abundant and reproducible cell-surface protein, using sAPPα or sAPPβ as bait, in wild-type (WT) and in *App*/*Aplp1* (APP-like protein 1) double KO synaptosome extracts (Fig. 1B; fig. S3, A and B; and table S1). Supporting our observations, APP has previously been identified in a $GABA_BR$ interactome analysis (*27*). Together, the sAPP AP-MS experiments identified $GABA_BR$ as the leading candidate for a synaptic, cell-surface receptor for sAPP.

The extension domain of APP binds the sushi 1 domain of $GABA_BR1a$

$GABA_BR$, the metabotropic receptor for the inhibitory neurotransmitter γ-aminobutyric acid (GABA), regulates presynaptic neurotransmitter release and postsynaptic membrane excitability (*28*). It consists of two subunits: $GABA_BR1$, which binds GABA, and $GABA_BR2$, which couples to G proteins (*29*). Two major isoforms, $GABA_BR1a$ and $GABA_BR1b$, differ by two N-terminal sushi repeats only present in the a-variant (*29*) (Fig. 1C). To validate the proteomics results, we performed cell-surface binding assays, applying recombinant sAPPα-Fc to HEK293T cells expressing the $GABA_BR$ ectodomain on the plasma membrane using the pDisplay vector. sAPPα-Fc, but not Fc alone, bound strongly to $GABA_BR1a$-expressing cells, but not to $GABA_BR1b$- or $GABA_BR2$-expressing cells (Fig. 1D). Biolayer interferometry experiments using recombinant sAPPα (Fc tag enzymatically removed; fig. S2, C to F) and $GABA_BR1a$ sushi domains showed that the sushi 1 peptide was sufficient for binding sAPPα (Fig. 1E). Accordingly, excess sushi 1 peptide blocked binding of sAPPα-Fc to $GABA_BR1a$-expressing cells (Fig. 1F). Isothermal titration calorimetry (ITC) determined the dissociation constant (K_D) for sAPPα–sushi 1 to be 431 nM (Fig. 1G). Thus, sAPPα binds directly and selectively to the sushi 1 domain of $GABA_BR1a$ with submicromolar affinity.

The ectodomain of the APP695 isoform of APP contains several functional domains (Fig. 2A). Surprisingly, growth factor–like domain (GFLD)–Fc, copper binding domain (CuBD)–Fc, and E2-Fc each failed to bind $GABA_BR1a$-expressing cells (Fig. 2B). However, a peptide corresponding to the natively unstructured linker region between the APP695 E1 and E2 domains (Fig. 2A) strongly bound to $GABA_BR1a$-expressing cells (Fig. 2B). The linker region includes the acidic domain (AcD) and the recently defined extension domain (ExD), which is a flexible, partially structured region (*30*). The binding affinity of the purified ExD-AcD fragment (Fc tag enzymatically removed) to sushi 1 in ITC experiments (Fig. 2C) was in the same range as that of full-length sAPPα binding to sushi 1 (Fig. 1G). To further narrow down the minimal domain in the APP linker region required for sushi 1 binding, we generated ExD-Fc and AcD-Fc fragments. ExD-Fc, but not AcD-Fc, bound to $GABA_BR1a$-expressing cells (Fig. 2B), identifying the ExD as the minimal domain required for sushi 1 binding. Consequently, deletion of the ExD in sAPPα (sAPPαΔExD-Fc) abolished binding to $GABA_BR1a$-expressing cells (Fig. 2B). sAPPβ-Fc and sAPPη-Fc, a product of the recently described η-secretase processing pathway (*6*), which both contain the ExD, also bound to $GABA_BR1a$-expressing cells (Fig. 2D). APP family members APP-like protein 1 and 2 (APLP1 and APLP2) (*31*), on the other hand, lack a conserved ExD and failed to bind $GABA_BR1a$-expressing cells (Fig. 2E). Thus, the sAPP ExD is necessary and sufficient to bind to the $GABA_BR1a$ sushi 1 domain.

[1]VIB Center for Brain & Disease Research, Leuven, Belgium. [2]Department of Neurosciences, Leuven Brain Institute, KU Leuven, Leuven, Belgium. [3]Neuro-Electronics Research Flanders, Leuven, Belgium. [4]Department of Biology, Leuven Brain Institute, KU Leuven, Leuven, Belgium. [5]Brain & Cognition, KU Leuven, Leuven, Belgium. [6]Department of Physiology and Pharmacology, Sackler Faculty of Medicine and Sagol School of Neuroscience, Tel Aviv University, Tel Aviv, Israel. [7]VIB–VUB Structural Biology Research Center, Brussels, Belgium. [8]Jean Jeener NMR Centre, VUB, Brussels, Belgium. [9]Child Health Institute of New Jersey, Robert Wood Johnson Medical School, Rutgers University, NJ, USA. [10]Department of Neuroscience and Cell Biology, Robert Wood Johnson Medical School, Rutgers University, NJ, USA. [11]Department of Neurology, Feinberg School of Medicine, Northwestern University, Chicago, IL, USA. [12]VIB, Leuven, Belgium. [13]imec, Leuven, Belgium. [14]UK–Dementia Research Institute at University College London, UK.
*Present address: Structural Motility, Institut Curie, PSL Research University, CNRS, UMR 144, Paris, France.
†Present address: School of Biological Sciences, Victoria University of Wellington, Wellington, New Zealand.
‡Corresponding author. Email: bart.destrooper@kuleuven.vib.be (B.D.S.); joris.dewit@kuleuven.vib.be (J.d.W.)

Downloaded from http://science.sciencemag.org/ on January 15, 2019

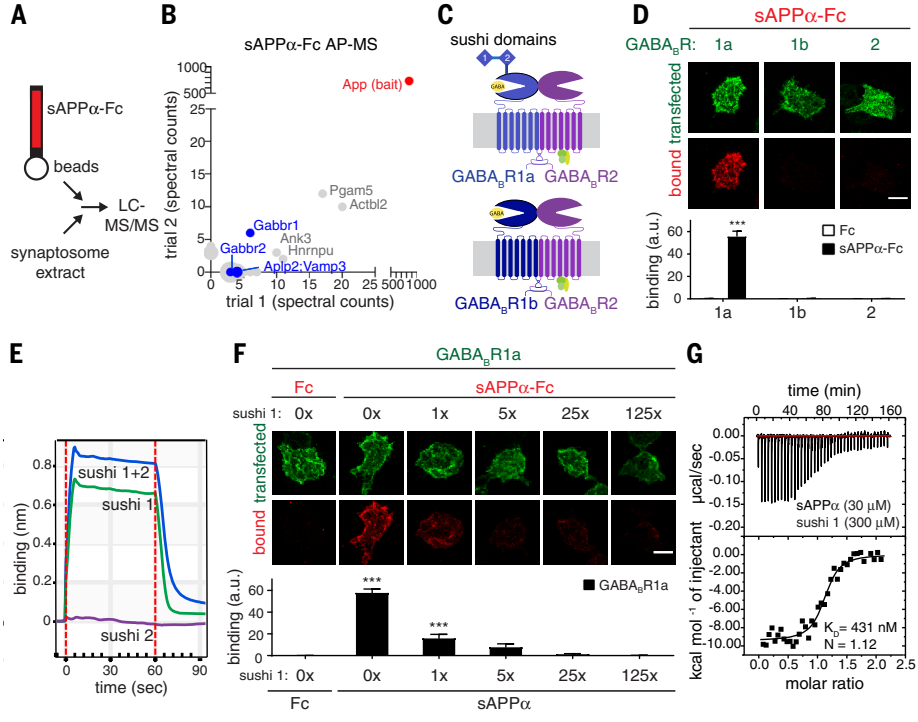


Fig. 1. sAPP selectively binds the sushi 1 domain of GABA$_B$R1a. (**A**) Cartoon illustrating the AP-MS workflow. LC-MS/MS, liquid chromatography–tandem mass spectrometry. (**B**) Spectral counts of proteins identified by MS from two independent sAPPα-Fc pull-downs on rat synaptosome extracts. Only proteins which were absent in the Fc controls and present with >2 spectral counts in a single trial are included. Cell-surface proteins are highlighted in blue. (**C**) Cartoon of GABA$_B$R subunits and isoforms. (**D**) Confocal images (top) and quantifications (bottom) of immunostaining for sAPPα-Fc or Fc binding to GABA$_B$R1a-, 1b-, or 2-expressing HEK293T cells (n = 24). a.u., arbitrary units. (**E**) Binding of sAPPα purified protein to immobilized Fc-tagged sushi 1, sushi 2, or sushi 1 and 2 peptides by biolayer interferometry. (**F**) Confocal images (top) and quantifications (bottom) of immunostaining for Fc control or sAPPα-Fc binding to GABA$_B$R1a-expressing HEK293T cells in the presence of increasing concentrations of untagged sushi 1 peptide (n = 24 to 31). X notation indicates fold increase in sushi 1 peptide concentration. (**G**) Binding of purified sAPPα and sushi 1 proteins (Fc-tag enzymatically removed from both constructs) by ITC. The red line indicates baseline. N, stoichiometry. The number of total cells from 3 to 4 independent experiments is defined as n. Graphs show means ± SEM. Two-way (D) or one-way (F) analysis of variance (ANOVA) with Bonferroni's post hoc analysis was used; ***P < 0.001. Scale bars, 10 µm.

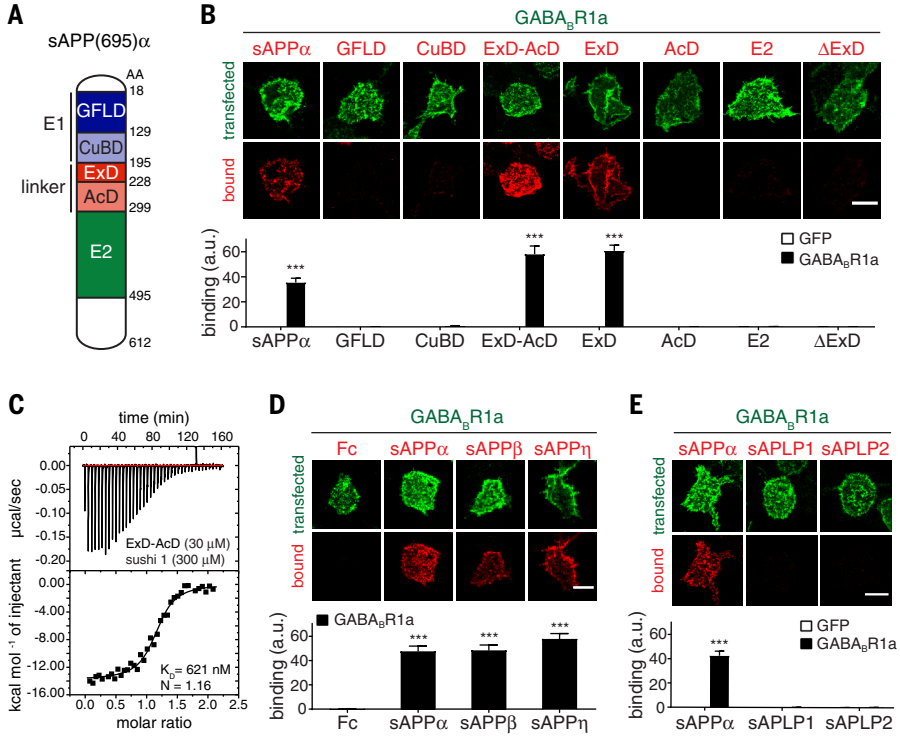


Fig. 2. The ExD of sAPP binds GABA$_B$R1a. (**A**) Cartoon of sAPPα domains. AA, amino acid. (**B**) Confocal images (top) and quantifications (bottom) of immunostaining for sAPPα-Fc, GFLD-Fc, CuBD-Fc, ExD-AcD–Fc, ExD-Fc, AcD-Fc, E2-Fc, or sAPPαΔExD-Fc binding to green fluorescent protein (GFP)– or GABA$_B$R1a-expressing HEK293T cells (n = 24 to 32). (**C**) Binding of purified ExD-AcD and sushi 1 proteins (Fc-tag enzymatically removed from both constructs) by ITC. (**D**) Confocal images (top) and quantifications (bottom) of immunostaining for Fc control, sAPPα-Fc, sAPPβ-Fc, and sAPPη-Fc binding to GABA$_B$R1a-expressing HEK293T cells (n = 24 to 30). (**E**) Confocal images (top) and quantifications (bottom) of immunostaining for sAPPα-Fc, sAPLP1-Fc, or sAPLP2-Fc binding to GFP- or GABA$_B$R1a-expressing HEK293T cells (n = 24). The number of total cells from three to five independent experiments is defined as n. Graphs show means ± SEM. Two-way (B) and (E) or one-way (D) ANOVA with Bonferroni's post hoc analysis was used; ***P < 0.001. Scale bars, 10 µm.

sAPP suppresses probability of presynaptic vesicle release via GABA$_B$R1a

Sushi domain–containing GABA$_B$R1a is the predominant isoform localized to presynaptic compartments at excitatory synapses (*32*–*34*), where it functions to inhibit neurotransmitter release (*28*). To test whether sAPPα can modulate GABA$_B$R function, we simultaneously measured miniature excitatory and inhibitory postsynaptic currents (mEPSCs and mIPSCs, respectively), which were separated on the basis of their distinct decay kinetics as described (*35*), in cultured mouse hippocampal neurons (12 to 17 days in vitro) (Fig. 3A). Consistent with previous observations (*36*, *37*), acute exposure of hippocampal neurons to 30 µM baclofen, a GABA$_B$R agonist, reduced the frequency of mEPSCs by 63 ± 5% (n = 14 cells; P < 0.001) (fig. S4, A and B). Likewise, 250 nM sAPPα (Fc tag removed) reduced the frequency of mEPSCs by 39 ± 5% (n = 13 cells; P < 0.001) (Fig. 3, B and C), an effect that was already apparent at 25 nM

Downloaded from http://science.sciencemag.org/ on January 15, 2019

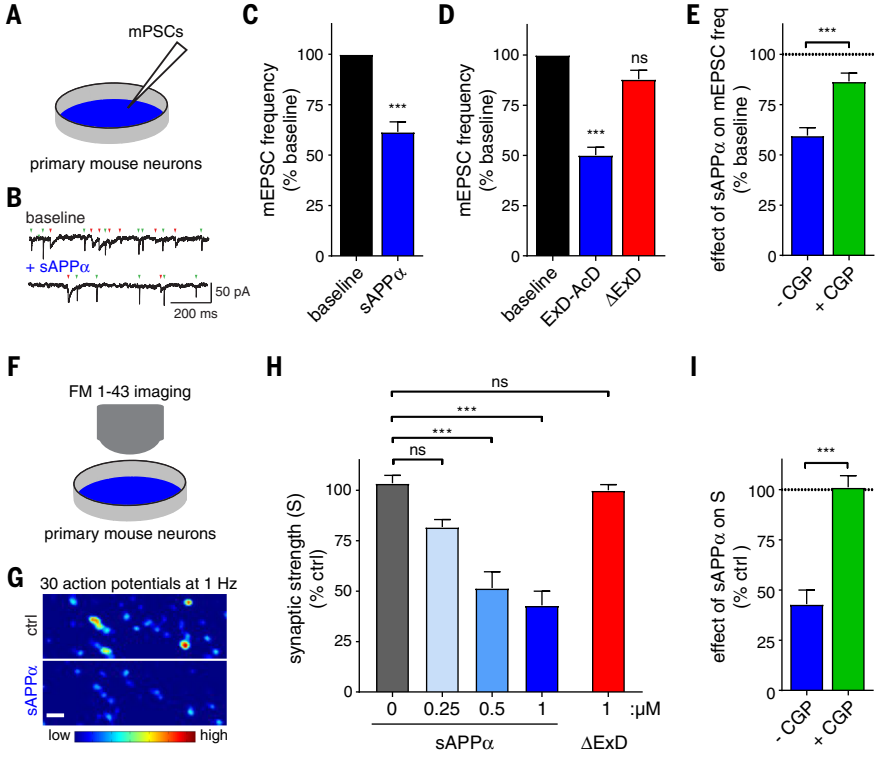


Fig. 3. sAPPα reduces the release probability of synaptic vesicles via presynaptic $GABA_BR1a$. (**A**) Cartoon of mPSC (mEPSC and mIPSC) measurements in cultured hippocampal mouse neurons reported in (B) to (E). (**B** and **C**) Example traces of mEPSCs (green arrowheads) and mIPSCs (red arrowheads) (B) and average mEPSC frequency (C) normalized to baseline recorded from primary neurons before (baseline) and after treatment with sAPPα (250 nM, Fc tag enzymatically removed; n = 13, N = 3, paired Student's t test). (**D**) Same as (C) but with either ExD-AcD or sAPPαΔExD (Fc tag enzymatically removed; n = 17 to 20, N = 3, one-way ANOVA with Dunnett's post hoc analysis). (**E**) Same as (C) but with sAPP and either without (blue) or with (green) preincubation with CGP55845 (CGP, 5 μM), a $GABA_BR$ antagonist. Dotted line indicates baseline (n = 14 to 17, N = 3, unpaired Student's t test). (**F**) Cartoon of FM1-43 measurements in cultured hippocampal mouse neurons reported in (G) to (I). (**G**) High-magnification ΔF images before and after application of sAPPα (1 μM, Fc tag enzymatically removed) to primary neurons. ctrl, control. (**H**) Summary of the dose-dependent inhibitory effect of sAPPα on presynaptic strength (S) (N = 5 to 8, one-way ANOVA analysis with post hoc Tukey's analysis). (**I**) Summary of sAPPα effect on presynaptic vesicle recycling in hippocampal neurons with or without CGP54626 (normalized to control) (N = 8). The number of neurons is defined as n, and the number of independent experiments or mice is defined as N. Graphs show means ± SEM. ***P < 0.001; ns, not significant.

(fig. S4, D and E), without affecting mEPSC amplitude (fig. S4C). sAPPβ similarly reduced mEPSC frequency (fig. S4, D and E). Acute application of the APP695 ExD-AcD fragment reduced mEPSC frequency to a similar degree as sAPPα (Fig. 3D and fig. S4F), whereas application of sAPPαΔExD had no effect (Fig. 3D and fig. S4F), indicating that the ExD of sAPP is necessary and sufficient for the suppression of spontaneous glutamatergic synaptic transmission by sAPPα. Accordingly, acute application of sAPLP1, which lacks a conserved ExD, did not reduce mEPSC frequency (fig. S4G), although we observed a minor (17 ± 9%; n = 17 cells; P < 0.05) reduction in mIPSC frequency (fig. S4H). Pretreatment with the $GABA_BR$ antagonist CGP55845 (5 μM) attenuated the sAPPα-mediated reduction of mEPSC frequency (Fig. 3E and fig. S4I), showing that the effect is mediated by $GABA_BR$.

$GABA_BR1a$ also localizes to GABAergic boutons (*34*). Consistent with previous observations (*37*, *38*), acute exposure of hippocampal neurons to 30 μM baclofen reduced the frequency of mIPSCs by 62 ± 5% (n = 14 cells; P < 0.001) (fig. S5A). Acute application of 250 nM sAPPα to hippocampal neurons reduced the frequency of mIPSCs by 44 ± 5% (n = 13 cells; P < 0.001) (Fig. 3B and fig. S5B). Application of sAPPα caused a minor (14%) reduction in mIPSC amplitude (fig. S5C), possibly owing to a small postsynaptic effect of sAPPα on $GABA_BR1a$ at postsynaptic GABAergic sites (*39*). The APP695 ExD-AcD fragment, but not sAPPαΔExD, reduced mIPSC frequency to a similar extent as sAPPα (figs. S4F and S5D). The effect of sAPPα on mIPSC frequency was blocked by pretreatment with the $GABA_BR$ antagonist CGP55845 (5 μM) (figs. S4I and S5E). Thus, sAPPα acutely reduces both glutamatergic and GABAergic quantal synaptic transmission through a $GABA_BR1a$ isoform–dependent mechanism.

sAPPα might exert its effect on synaptic transmission by interfering with a complex of full-length APP and $GABA_BR1a$. In neurons lacking APP, however, sAPPα still reduced mEPSC and mIPSC frequency (fig. S6, A and B), excluding this possibility. Application of 30 μM baclofen similarly reduced mEPSC and mIPSC frequency in *App*/*Aplp1* double KO cultures (fig. S6, C and D) as in WT cultures (Fig. 3C and fig. S5B), suggesting that the absence of full-length APP does not cause major alterations in $GABA_BR$ localization to presynaptic terminals. However, the possibility that full-length APP also interacts with and affects $GABA_BR$ signaling separate from the effects of sAPPα reported here cannot be excluded.

The decrease in mEPSC frequency, but not amplitude, following acute sAPPα application suggests a change in presynaptic release properties. We therefore assessed the effect of sAPPα on presynaptic vesicle recycling using the fluorescent membrane dye FM1-43. We measured presynaptic strength by measuring the density (D) of FM1-43–positive boutons per image area and the change in fluorescence intensity (ΔF) of FM1-43 signals at individual boutons of cultured hippocampal neurons using a combined FM1-43 loading-unloading stimulation paradigm (Fig. 3F). Application of sAPPα decreased the total presynaptic strength ($S = \Delta F \times D$) across synaptic populations (Fig. 3G and fig. S7A) in a dose-dependent manner (Fig. 3H), reaching 57 ± 7% (n = 8 experiments; P < 0.001) reduction at 1 μM sAPPα. This decrease was not observed with deletion of the ExD (sAPPαΔExD, 1 μM) (Fig. 3H and fig. S7B) and was occluded by the $GABA_BR$ antagonist CGP54626 (10 μM) (Fig. 3I and fig. S7C), indicating that $GABA_BR1a$ mediates the presynaptic inhibition induced by sAPPα.

sAPP enhances short-term plasticity at Schaffer collateral synapses in a $GABA_BR1a$-dependent manner

We next assessed the effect of sAPPα on synaptic transmission in an intact circuit at CA3-CA1 Schaffer collateral (SC) synapses, which exclusively contain $GABA_BR1a$ receptors (*32*). We measured field excitatory postsynaptic potentials (fEPSPs) evoked by low-frequency stimulation (0.1 Hz) at varying intensities (30 to 150 μA) in CA1 stratum radiatum after 90 min preincubation of acute hippocampal slices with or without 1 μM sAPPα (Fig. 4A). Treatment with sAPPα reduced fEPSP amplitude and decreased the slope of the input-output (i-o) curve by 23% (fig. S8A), indicating that sAPPα suppresses basal synaptic transmission at SC synapses. To specifically assess if sAPPα affects presynaptic properties, we applied a burst of five stimuli at three different frequencies (20, 50, and 100 Hz) to induce short-term facilitation, which inversely correlates with the probability of neurotransmitter release. Facilitation was higher for each frequency tested in sAPPα-incubated slices compared with control slices (Fig. 4B and fig. S8, B and C). Analysis of the paired-pulse ratio (PPR) for the first two

Downloaded from http://science.sciencemag.org/ on January 15, 2019

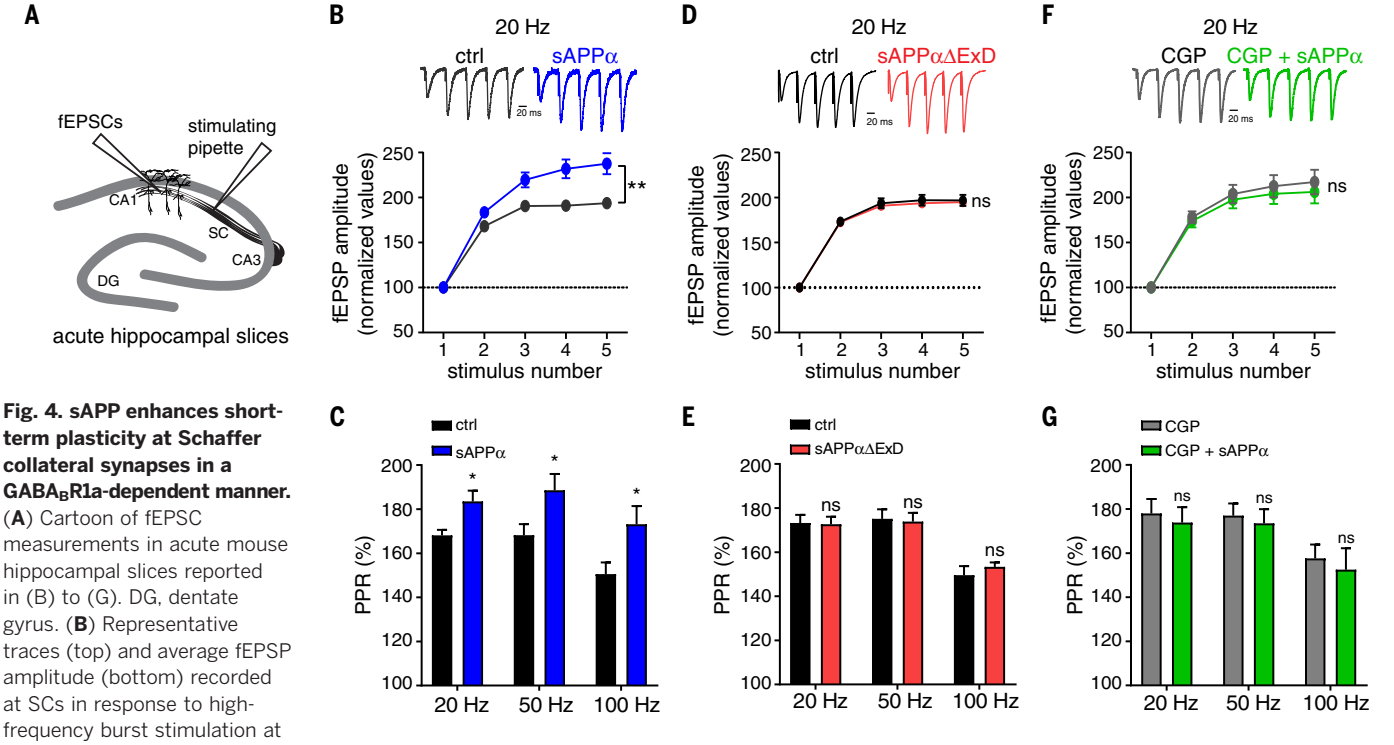


Fig. 4. sAPP enhances short-term plasticity at Schaffer collateral synapses in a $GABA_BR1a$-dependent manner. (**A**) Cartoon of fEPSC measurements in acute mouse hippocampal slices reported in (B) to (G). DG, dentate gyrus. (**B**) Representative traces (top) and average fEPSP amplitude (bottom) recorded at SCs in response to high-frequency burst stimulation at 20 Hz in mouse hippocampal slices incubated without ($n = 12$, $N = 7$) or with sAPPα (1 μM, Fc tag enzymatically removed) ($n = 10$, $N = 7$). fEPSPs were normalized to the peak amplitude of the first response. (**C**) PPRs for the first two pulses at each frequency (20, 50, and 100 Hz) for the experiment shown in (B). (**D**) Same as (B) but in slices incubated without ($n = 10$, $N = 4$) or with sAPPαΔExD (1 μM, Fc tag enzymatically removed; $n = 9$, $N = 4$). (**E**) Corresponding PPRs as in (C) for the experiment shown in (D). (**F**) Same as (B) but in slices incubated with CGP54626 (CGP, 10μM) alone ($n = 9$, $N = 4$) and slices incubated with CGP and sAPPα ($n = 8$, $N = 4$). (**G**) Corresponding PPRs as in (C) for the experiment shown in (F). The number of slices is defined as n, and the number of independent experiments or mice is defined as N. Graphs show means ± SEM. Two-way ANOVA analysis was used. *$P < 0.05$; **$P < 0.1$; ns, not significant.

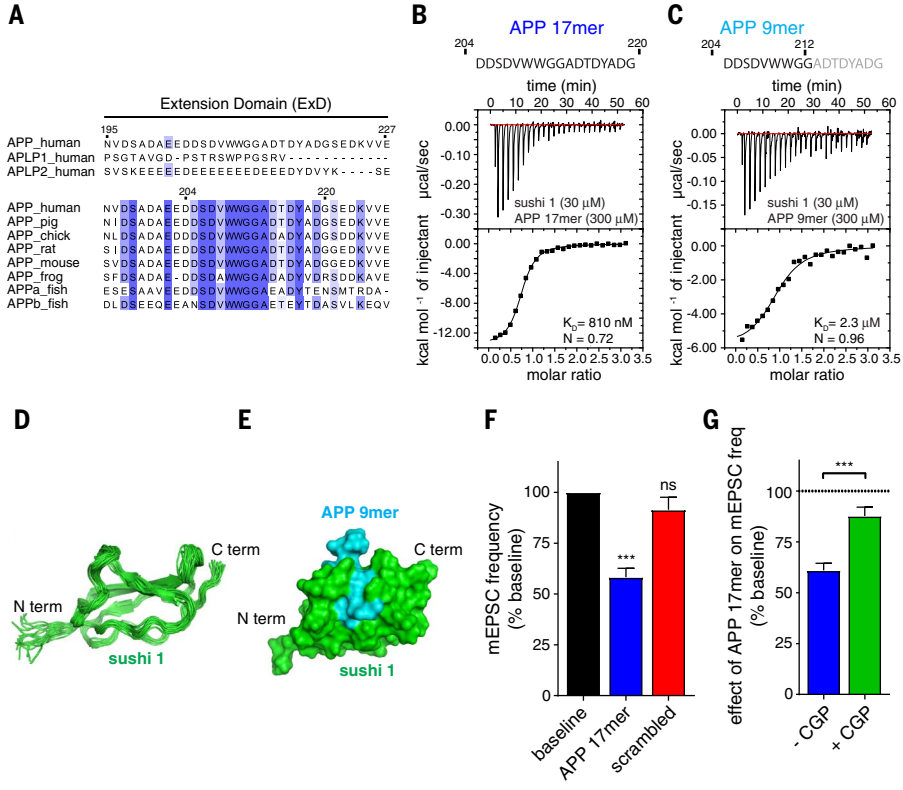


Fig. 5. A short peptide within the APP ExD suppresses synaptic vesicle release via $GABA_BR1a$. (**A**) Sequence alignment for the ExD of human APP with APLP1 and 2 and with seven vertebrate APP sequences. Numbers indicate residue positions. Single-letter abbreviations for the amino acid residues are as follows: A, Ala; C, Cys; D, Asp; E, Glu; F, Phe; G, Gly; H, His; I, Ile; K, Lys; L, Leu; M, Met; N, Asn; P, Pro; Q, Gln; R, Arg; S, Ser; T, Thr; V, Val; W, Trp; and Y, Tyr. (**B** and **C**) ITC binding experiments of purified sushi 1 and synthetic peptides within the ExD corresponding to residues 204 to 220 (B) or residues 204 to 212 (C) of APP695. (**D**) An ensemble of 20 lowest-energy NMR structures of the sushi 1 domain of $GABA_BR1a$ when bound to the APP 9-mer peptide. (**E**) A structural model of the complex between the sushi 1 domain of $GABA_BR1a$ (green) and the APP 9-mer peptide (cyan) shown as a molecular surface. Protein termini are indicated by the labels N term and C term. (**F**) Average mEPSC frequency normalized to baseline recorded from mouse primary neurons before (baseline) and after treatment with 17-mer APP peptide (250 nM, APP695 residues 204 to 220) ($n = 20$, $N = 3$) or scrambled 17-mer control peptide (250 nM; $n = 18$, $N = 4$) (one-way ANOVA with Dunnett's post hoc analysis). (**G**) Quantification of the effect of 250 nM 17-mer APP peptide (APP695 residues 204 to 220) on mEPSC frequency normalized to baseline either without ($n = 14$, $N = 3$) or with preincubation with CGP55845 (CGP, 5 μM; $n = 16$, $N = 3$) (unpaired Student's t test). Dotted line indicates baseline. The number of neurons is defined as n, and the number of independent experiments is defined as N. Graphs show means ± SEM. ***$P < 0.001$; ns, not significant.

Downloaded from http://science.sciencemag.org/ on January 15, 2019

stimuli showed an increased PPR for each frequency after sAPPα treatment (Fig. 4C), indicating a decreased release probability. Deletion of the ExD (sAPPαΔExD, 1 μM) abolished the sAPPα-mediated effect on the i-o curve (fig. S9D), short-term facilitation (Fig. 4D and fig. S8, E and F), and PPR (Fig. 4E). In addition, preincubation of slices with the $GABA_BR$ antagonist CGP54626 (10 μM) abolished the sAPPα-mediated decrease in the slope of the i-o curve (fig. S8G) and occluded the sAPPα-induced increase in short-term facilitation and PPR at each frequency (Fig. 4, F and G, and fig. S8, H and I), demonstrating the $GABA_BR$-dependence of these effects. Thus, sAPPα controls vesicle release at SC synapses by acting on presynaptic $GABA_BR1a$.

A short peptide within the APP ExD suppresses synaptic vesicle release via $GABA_BR1a$

A $GABA_BR1a$ isoform–specific modulator has potential therapeutic implications for a number of neurological disorders involving $GABA_BR$ signaling (*29*). Because we observed that purified protein corresponding to the linker region of APP (Fig. 2A) was sufficient to mimic the effects of sAPPα on mEPSC frequency (Fig. 3D), we set out to identify the minimally active region within the ExD. Alignment of the sAPP ExD [amino acid residues 195 to 227 of APP695] from seven vertebrate species revealed the strongest conservation within a 17–amino acid stretch (residues 204 to 220; Fig. 5A). The corresponding synthetic APP 17-mer peptide bound sushi 1 of $GABA_BR1a$ with a K_D of 810 nM (Fig. 5B), in the same range as the binding affinity of the entire linker region (Fig. 2C). Shortening the peptide to a synthetic 9-mer consisting of APP695 residues 204 to 212 (APP 9-mer) lowered the K_D to 2.3 μM (Fig. 5C), whereas residues 211 to 220 failed to bind sushi 1 (fig. S9A). Thus, a conserved, minimal 9–amino acid sequence within the sAPP ExD is sufficient for direct binding to the sushi 1 domain of $GABA_BR1a$.

To gain further insight into the binding of the APP 9-mer to the $GABA_BR1a$ sushi 1 domain, we used nuclear magnetic resonance (NMR) spectroscopy. As previously reported (*40*), we observed that the sushi 1 domain of $GABA_BR1a$ is natively unstructured (fig. S9B). Notably, APP 9-mer binding stabilized the sushi 1 domain of $GABA_BR1a$, allowing determination of its solution structure (Fig. 5D and fig. S9C) and generation of a structural model of the complex (Fig. 5E). In our model, valine and tryptophan at residues 208 and 209, respectively, of APP695 bind within a pocket of sushi 1, formed by the loops and the short β strand in the N-terminal part of the protein (residues 32 to 53 of full-length $GABA_BR1a$) (fig. S9D). Thus, APP binding induces a conformational change in the natively unstructured sushi 1 domain of $GABA_BR1a$. This structure-function relationship strongly supports the physiological relevance of the interaction.

Because the affinity for sushi 1 was better retained in the APP 17-mer compared with the 9-mer (Fig. 5, B and C), we next tested whether the APP 17-mer could functionally mimic sAPPα. Acute application of the APP 17-mer peptide, but not of a scrambled 17-mer control peptide, reduced mEPSC frequency in hippocampal neurons to a similar degree as sAPPα (Fig. 5F and fig. S9E) and was already apparent at 25 nM (fig. S9F). Pretreatment with the $GABA_BR$ antagonist CGP55845 (5 μM) blocks this effect (Fig. 5G and fig. S9G).

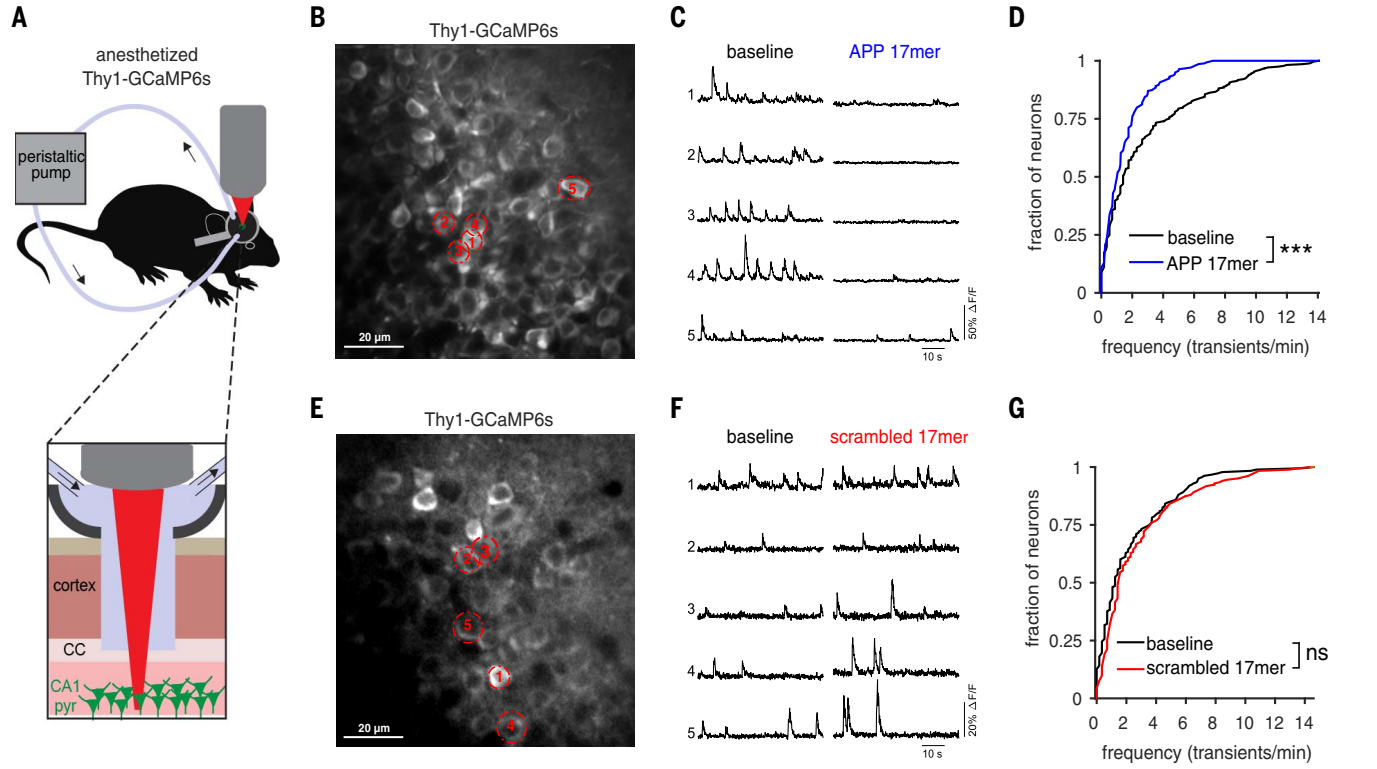


Fig. 6. A 17–amino acid peptide corresponding to the $GABA_BR1a$ binding region within APP suppresses neuronal activity in vivo. (**A**) Cartoon of in vivo two-photon calcium imaging of CA1 hippocampus of anesthetized Thy1-GCaMP6s mice with superfusion of APP 17-mer or scrambled control 17-mer. CC, corpus callosum; CA1 pyr, CA1 pyramidal cells. (**B**) In vivo two-photon image of CA1 hippocampal neurons of Thy1-GCaMP6s mice analyzed in (C) and (D). Representative neurons are indicated with a dotted outline. (**C**) Calcium traces of five representative neurons, labeled in (A), before (baseline) and during bath application of 5 μM APP 17-mer peptide corresponding to the $GABA_BR1a$ binding region within APP (APP 17-mer). ΔF/F, change in fluorescence intensity/resting fluorescence intensity. (**D**) Cumulative distribution of the frequency of calcium transients at baseline (black line) and during APP 17-mer bath application (blue line) (n = 277, N = 3). (**E**) In vivo two-photon image of CA1 hippocampal neurons of Thy1-GCaMP6s mice analyzed in (F) and (G). Representative neurons are indicated with a dotted outline. (**F**) Calcium traces of five representative neurons, labeled in (D), before (baseline) and during bath application of 5 μM scrambled 17-mer control peptide (scrambled 17-mer). (**G**) Cumulative distribution of the frequency of calcium transients at baseline (black line) and during scrambled 17-mer bath application (red line) (n = 183, N = 3). The number of neurons is defined as n, and the number of mice is defined as N. Wilcoxon rank sum test was used. ***P < 0.001; ns, P > 0.05 (not significant).

Downloaded from http://science.sciencemag.org/ on January 15, 2019

Together, these findings show that the APP 17-mer peptide mimics the effects of sAPPα on $GABA_BR1a$-dependent inhibition of synaptic vesicle release.

APP 17-mer peptide suppresses neuronal activity of CA1 pyramidal cells in vivo

In the final series of experiments, we used the APP 17-mer peptide as a tool to examine the effects of sAPP-$GABA_BR$ signaling on neuronal activity in vivo. Using two-photon calcium imaging, we measured calcium transients of CA1 hippocampal neurons in anesthetized transgenic mice expressing the genetically-encoded calcium indicator GCaMP6s under the Thy-1 promoter (Thy1-GCaMP6s) before (baseline) and after a 60 to 90 min superfusion of the exposed hippocampus with either baclofen (30 μM), APP 17-mer (5 μM), or scrambled 17-mer control peptide (5 μM) (Fig. 6A). Application of 30 μM baclofen caused a dramatic decrease in the frequency of calcium transients compared to baseline (fig. S10, A to C), indicating that activation of $GABA_BRs$ strongly suppresses neuronal activity in CA1 pyramidal neurons in vivo. Consistent with our results in cultured hippocampal neurons, application of the APP 17-mer significantly reduced the frequency of calcium transients compared to baseline (Fig. 6, B to D, and movie S1). The frequency of calcium transients was restored back to baseline after a 2-hour wash-out of the peptide (fig. S10, D to F), indicating that the suppression of CA1 neuron activity by the APP 17-mer peptide is reversible. Furthermore, the scrambled 17-mer control peptide did not affect the frequency of calcium transients (Fig. 6, E to G; fig. S10, G to I; and movie S2). Thus, APP inhibits neuronal activity in vivo, and the $GABA_BR1a$ binding domain is sufficient for such inhibition.

Discussion

Here, we found that sAPP acts as a $GABA_BR1a$-specific ligand to suppress synaptic vesicle release. Consequently, sAPP modulates hippocampal synaptic plasticity and neurotransmission in vivo. APP is among the most abundant proteins in synaptic boutons (*25*), and deletion of *App* in mice leads to synaptic deficits (*7*–*9*, *21*, *22*). Synaptic activity enhances proteolytic processing of APP (*41*, *42*), and $GABA_BR$ is a key regulator of homeostatic synaptic plasticity (*43*). Our observations raise the possibility that the sAPP-$GABA_BR1a$ interaction acts as an activity-dependent negative-feedback mechanism to suppress synaptic release and maintain proper homeostatic control of neural circuits. Although AD-causing mutations in APP all affect Aβ generation, it is not entirely clear whether other aspects of APP function contribute to AD. Network abnormalities such as hyperexcitability and hypersynchronization precede clinical onset of AD in human patients (*44*). Some studies indicate that sAPP levels may be altered in AD (*14*). Interestingly, a $GABA_BR$ antagonist can improve memory in animal models and patients with mild cognitive impairment (*45*–*47*). Moreover, because most transgenic AD mouse models overexpress sAPP, the role of sAPP in synaptic phenotypes of transgenic APP mice should be considered, particularly given evidence that network hyperexcitability in these mice is independent of Aβ production (*48*).

$GABA_BR$ signaling has been implicated in a number of neurological and psychiatric disorders, including epilepsy, depression, addiction, and schizophrenia (*49*). Selective binding partners of the $GABA_BR1a$ sushi domains are of potential therapeutic interest owing to localization and functional differences of $GABA_BR1$ isoforms (*32*, *50*) as well as the adverse effects of current nonspecific agonists (*29*). The identification of sAPP as a functional $GABA_BR1a$-specific binding partner provides a target for the development of therapeutic strategies for modulating $GABA_BR1a$-specific signaling in neurological and psychiatric disorders. The identification of short APP peptides that confer structure in the $GABA_BR1a$ sushi 1 domain and modulate neurotransmission in vivo are major steps toward development of a $GABA_BR1a$ isoform–specific therapeutic.

Methods summary

To identify candidate synaptic interactors for sAPP, affinity-purification experiments were performed using recombinant sAPP-Fc to pull down interacting proteins from synaptosome extracts, followed by MS analysis of bound proteins. Cell-surface binding assays, biolayer interferometry, and ITC were used to determine domains of interaction and apparent binding affinities between sAPP and $GABA_BR$. NMR spectroscopy was used to generate a structural model of the APP-$GABA_BR$ complex. The function of the sAPP-$GABA_BR$ interaction was investigated by accessing spontaneous postsynaptic currents and FM1-43 dye labeling in mouse hippocampal cultures, short-term facilitation in acute hippocampal slices, and two-photon in vivo calcium imaging in CA1 hippocampus of anesthetized Thy1-GCaMP6 mice. The details of each of these methods are described in the supplementary materials.

REFERENCES AND NOTES

1. D. Goldgaber, M. I. Lerman, O. W. McBride, U. Saffiotti, D. C. Gajdusek, Characterization and chromosomal localization of a cDNA encoding brain amyloid of Alzheimer's disease. *Science* **235**, 877–880 (1987). doi: 10.1126/science.3810169; pmid: 3810169
2. N. K. Robakis, N. Ramakrishna, G. Wolfe, H. M. Wisniewski, Molecular cloning and characterization of a cDNA encoding the cerebrovascular and the neuritic plaque amyloid peptides. *Proc. Natl. Acad. Sci. U.S.A.* **84**, 4190–4194 (1987). doi: 10.1073/pnas.84.12.4190; pmid: 3035574
3. R. E. Tanzi *et al*., Amyloid beta protein gene: cDNA, mRNA distribution, and genetic linkage near the Alzheimer locus. *Science* **235**, 880–884 (1987). doi: 10.1126/science.2949367; pmid: 2949367
4. J. Kang *et al*., The precursor of Alzheimer's disease amyloid A4 protein resembles a cell-surface receptor. *Nature* **325**, 733–736 (1987). doi: 10.1038/325733a0; pmid: 2881207
5. C. Haass, C. Kaether, G. Thinakaran, S. Sisodia, Trafficking and proteolytic processing of APP. *Cold Spring Harb. Perspect. Med.* **2**, a006270 (2012). doi: 10.1101/cshperspect.a006270; pmid: 22553493
6. M. Willem *et al*., η-Secretase processing of APP inhibits neuronal activity in the hippocampus. *Nature* **526**, 443–447 (2015). doi: 10.1038/nature14864; pmid: 26322584
7. G. R. Dawson *et al*., Age-related cognitive deficits, impaired long-term potentiation and reduction in synaptic marker density in mice lacking the beta-amyloid precursor protein. *Neuroscience* **90**, 1–13 (1999). doi: 10.1016/S0306-4522(98)00410-2; pmid: 10188929
8. G. R. Seabrook *et al*., Mechanisms contributing to the deficits in hippocampal synaptic plasticity in mice lacking amyloid precursor protein. *Neuropharmacology* **38**, 349–359 (1999). doi: 10.1016/S0028-3908(98)00204-4; pmid: 10219973
9. S.-H. Tyan *et al*., Amyloid precursor protein (APP) regulates synaptic structure and function. *Mol. Cell. Neurosci.* **51**, 43–52 (2012). doi: 10.1016/j.mcn.2012.07.009; pmid: 22884903
10. S. M. Fitzjohn *et al*., Similar levels of long-term potentiation in amyloid precursor protein-null and wild-type mice in the CA1 region of picrotoxin treated slices. *Neurosci. Lett.* **288**, 9–12 (2000). doi: 10.1016/S0304-3940(00)01204-0; pmid: 10869803
11. L. Yang, Z. Wang, B. Wang, N. J. Justice, H. Zheng, Amyloid precursor protein regulates $Ca_v1.2$ L-type calcium channel levels and function to influence GABAergic short-term plasticity. *Neuroscience* **29**, 15660–15668 (2009). doi: 10.1523/JNEUROSCI.4104-09.2009; pmid: 20016080
12. B. Wang *et al*., The amyloid precursor protein controls adult hippocampal neurogenesis through GABAergic interneurons. *J. Neurosci.* **34**, 13314–13325 (2014). doi: 10.1523/JNEUROSCI.2848-14.2014; pmid: 25274811
13. M. Chen *et al*., APP modulates KCC2 expression and function in hippocampal GABAergic inhibition. *eLife* **6**, e20142 (2017). pmid: 28054918
14. B. G. Mockett, M. Richter, W. C. Abraham, U. C. Müller, Therapeutic potential of secreted amyloid precursor protein APPsα. *Front. Mol. Neurosci.* **10**, 30 (2017). doi: 10.3389/fnmol.2017.00030; pmid: 28223920
15. U. C. Müller, T. Deller, M. Korte, Not just amyloid: Physiological functions of the amyloid precursor protein family. *Nat. Rev. Neurosci.* **18**, 281–298 (2017). doi: 10.1038/nrn.2017.29; pmid: 28360418
16. K. Furukawa, S. W. Barger, E. M. Blalock, M. P. Mattson, Activation of K^+ channels and suppression of neuronal activity by secreted beta-amyloid-precursor protein. *Nature* **379**, 74–78 (1996). doi: 10.1038/379074a0; pmid: 8538744
17. A. Ishida, K. Furukawa, J. N. Keller, M. P. Mattson, Secreted form of β-amyloid precursor protein shifts the frequency dependency for induction of LTD, and enhances LTP in hippocampal slices. *Neuroreport* **8**, 2133–2137 (1997). doi: 10.1097/00001756-199707070-00009; pmid: 9243598
18. C. J. Taylor *et al*., Endogenous secreted amyloid precursor protein-α regulates hippocampal NMDA receptor function, long-term potentiation and spatial memory. *Neurobiol. Dis.* **31**, 250–260 (2008). doi: 10.1016/j.nbd.2008.04.011; pmid: 18585048
19. M. Xiong *et al*., Secreted amyloid precursor protein-alpha can restore novel object location memory and hippocampal LTP in aged rats. *Neurobiol. Learn. Mem.* **138**, 291–299 (2017). doi: 10.1016/j.nlm.2016.08.002; pmid: 27521248
20. S. W. Weyer *et al*., Comparative analysis of single and combined APP/APLP knockouts reveals reduced spine density in APP-KO mice that is prevented by APPsα expression. *Acta Neuropathol. Commun.* **2**, 36 (2014). doi: 10.1186/2051-5960-2-36; pmid: 24684730
21. S. Ring *et al*., The secreted β-amyloid precursor protein ectodomain APPsα is sufficient to rescue the anatomical, behavioral, and electrophysiological abnormalities of APP-deficient mice. *J. Neurosci.* **27**, 7817–7826 (2007). doi: 10.1523/JNEUROSCI.1026-07.2007; pmid: 17634375
22. M. Hick *et al*., Acute function of secreted amyloid precursor protein fragment APPsα in synaptic plasticity. *Acta Neuropathol.* **129**, 21–37 (2015). doi: 10.1007/s00401-014-1368-x; pmid: 25432317
23. T. Saitoh *et al*., Secreted form of amyloid β protein precursor is involved in the growth regulation of fibroblasts. *Cell* **58**, 615–622 (1989). doi: 10.1016/0092-8674(89)90096-2; pmid: 2475254
24. C. Reinhard, M. Borgers, G. David, B. De Strooper, Soluble amyloid-β precursor protein binds its cell surface receptor in a cooperative fashion with glypican and syndecan proteoglycans. *J. Cell Sci.* **126**, 4856–4861 (2013). doi: 10.1242/jcs.137919; pmid: 23986479
25. B. G. Wilhelm *et al*., Composition of isolated synaptic boutons reveals the amounts of vesicle trafficking proteins. *Science* **344**, 1023–1028 (2014). doi: 10.1126/science.1252884; pmid: 24876496
26. J. N. Savas *et al*., Ecto-Fc MS identifies ligand-receptor interactions through extracellular domain Fc fusion protein

Downloaded from http://science.sciencemag.org/ on January 15, 2019

baits and shotgun proteomic analysis. *Nat. Protoc.* **9**, 2061–2074 (2014). doi: 10.1038/nprot.2014.140; pmid: 25101821
27. J. Schwenk *et al*., Modular composition and dynamics of native $GABA_B$ receptors identified by high-resolution proteomics. *Nat. Neurosci.* **19**, 233–242 (2016). doi: 10.1038/nn.4198; pmid: 26691831
28. M. Gassmann, B. Bettler, Regulation of neuronal $GABA_B$ receptor functions by subunit composition. *Nat. Rev. Neurosci.* **13**, 380–394 (2012). doi: 10.1038/nrn3249; pmid: 22595784
29. J.-P. Pin, B. Bettler, Organization and functions of mGlu and $GABA_B$ receptor complexes. *Nature* **540**, 60–68 (2016). doi: 10.1038/nature20566; pmid: 27905440
30. I. Coburger *et al*., Analysis of the overall structure of the multi-domain amyloid precursor protein (APP). *PLOS ONE* **8**, e81926 (2013). doi: 10.1371/journal.pone.0081926; pmid: 24324731
31. S. A. M. Shariati, B. De Strooper, Redundancy and divergence in the amyloid precursor protein family. *FEBS Lett.* **587**, 2036–2045 (2013). doi: 10.1016/j.febslet.2013.05.026; pmid: 23707420
32. R. Vigot *et al*., Differential compartmentalization and distinct functions of $GABA_B$ receptor variants. *Neuron* **50**, 589–601 (2006). doi: 10.1016/j.neuron.2006.04.014; pmid: 16701209
33. B. Biermann *et al*., The Sushi domains of $GABA_B$ receptors function as axonal targeting signals. *J. Neurosci.* **30**, 1385–1394 (2010). doi: 10.1523/JNEUROSCI.3172-09.2010; pmid: 20107064
34. P. C. Waldmeier, K. Kaupmann, S. Urwyler, Roles of $GABA_B$ receptor subtypes in presynaptic auto- and heteroreceptor function regulating GABA and glutamate release. *J. Neural Transm. (Vienna)* **115**, 1401–1411 (2008). doi: 10.1007/s00702-008-0095-7; pmid: 18665320
35. K. D. B. Wierda, J. B. Sørensen, Innervation by a GABAergic neuron depresses spontaneous release in glutamatergic neurons and unveils the clamping phenotype of synaptotagmin-1. *J. Neurosci.* **34**, 2100–2110 (2014). doi: 10.1523/JNEUROSCI.3934-13.2014; pmid: 24501351
36. M. Scanziani, M. Capogna, B. H. Gähwiler, S. M. Thompson, Presynaptic inhibition of miniature excitatory synaptic currents by baclofen and adenosine in the hippocampus. *Neuron* **9**, 919–927 (1992). doi: 10.1016/0896-6273(92)90244-8; pmid: 1358131
37. M. Iyadomi, I. Iyadomi, E. Kumamoto, K. Tomokuni, M. Yoshimura, Presynaptic inhibition by baclofen of miniature EPSCs and IPSCs in substantia gelatinosa neurons of the adult rat spinal dorsal horn. *Pain* **85**, 385–393 (2000). doi: 10.1016/S0304-3959(99)00285-7; pmid: 10781911
38. J. Rohrbacher, W. Jarolimek, A. Lewen, U. Misgeld, $GABA_B$ receptor-mediated inhibition of spontaneous inhibitory synaptic currents in rat midbrain culture. *J. Physiol.* **500**, 739–749 (1997). doi: 10.1113/jphysiol.1997.sp022055; pmid: 9161988
39. D. Ulrich, B. Bettler, $GABA_B$ receptors: Synaptic functions and mechanisms of diversity. *Curr. Opin. Neurobiol.* **17**, 298–303 (2007). doi: 10.1016/j.conb.2007.04.001; pmid: 17433877
40. S. Blein *et al*., Structural analysis of the complement control protein (CCP) modules of $GABA_B$ receptor 1a: Only one of the two CCP modules is compactly folded. *J. Biol. Chem.* **279**, 48292–48306 (2004). doi: 10.1074/jbc.M406540200; pmid: 15304491
41. R. M. Nitsch, S. A. Farber, J. H. Growdon, R. J. Wurtman, Release of amyloid beta-protein precursor derivatives by electrical depolarization of rat hippocampal slices. *Proc. Natl. Acad. Sci. U.S.A.* **90**, 5191–5193 (1993). doi: 10.1073/pnas.90.11.5191; pmid: 8506366
42. F. Kamenetz *et al*., APP processing and synaptic function. *Neuron* **37**, 925–937 (2003). doi: 10.1016/S0896-6273(03)00124-7; pmid: 12670422
43. I. Vertkin *et al*., $GABA_B$ receptor deficiency causes failure of neuronal homeostasis in hippocampal networks. *Proc. Natl. Acad. Sci. U.S.A.* **112**, E3291–E3299 (2015). doi: 10.1073/pnas.1424810112; pmid: 26056260
44. J. J. Palop, L. Mucke, Network abnormalities and interneuron dysfunction in Alzheimer disease. *Nat. Rev. Neurosci.* **17**, 777–792 (2016). doi: 10.1038/nrn.2016.141; pmid: 27829687
45. Y. Li *et al*., Implications of GABAergic neurotransmission in Alzheimer's disease. *Front. Aging Neurosci.* **8**, 31 (2016). doi: 10.3389/fnagi.2016.00031; pmid: 26941642
46. W. Froestl *et al*., SGS742: The first $GABA_B$ receptor antagonist in clinical trials. *Biochem. Pharmacol.* **68**, 1479–1487 (2004). doi: 10.1016/j.bcp.2004.07.030; pmid: 15451390
47. K. A. Helm *et al*., $GABA_B$ receptor antagonist SGS742 improves spatial memory and reduces protein binding to the cAMP response element (CRE) in the hippocampus. *Neuropharmacology* **48**, 956–964 (2005). doi: 10.1016/j.neuropharm.2005.01.019; pmid: 15857622
48. H. A. Born *et al*., Genetic suppression of transgenic APP rescues hypersynchronous network activity in a mouse model of Alzheimer's disease. *J. Neurosci.* **34**, 3826–3840 (2014). doi: 10.1523/JNEUROSCI.5171-13.2014; pmid: 24623762
49. B. Bettler, K. Kaupmann, J. Mosbacher, M. Gassmann, Molecular structure and physiological functions of $GABA_B$ receptors. *Physiol. Rev.* **84**, 835–867 (2004). pmid: 15269338
50. J. D. Foster, I. Kitchen, B. Bettler, Y. Chen, $GABA_B$ receptor subtypes differentially modulate synaptic inhibition in the dentate gyrus to enhance granule cell output. *Br. J. Pharmacol.* **168**, 1808–1819 (2013). doi: 10.1111/bph.12073; pmid: 23186302

ACKNOWLEDGMENTS

We thank G. Conway, A. Snellinx, K. Craessaerts, K. Horré, K. Vennekens, V. Hendrickx, and J. Verwaeren for technical help. We thank C. Martin, N. Apóstolo, G. Condomitti, G. Marcassa, and I. Chrysidou for experimental assistance. We thank L. Buts for help with NMR structure calculations; M. A. Busche for advice on in vivo calcium imaging experiments; P. Vanderheyden, S. Zels, I. Beets, L. Schoofs, H. Dunn, and K. Martemyanov for advice on and/or performing G protein–coupled receptor activity experiments; and U. Mueller for the *App/Aplp1* double KO mice. **Funding:** This work was supported by an Alzheimer's Association Research Fellowship (AARF-16-442885, H.C.R.); Stichting Voor Alzheimer Onderzoek Pilot Grant (16011, H.C.R.); Agency for Innovation by Science and Technology in Flanders (IWT 141698, A.S.); National Science Foundation BRAIN EAGER MCB-1450895 and IOS-1755189 (D.C.); Robert Wood Johnson Foundation grant no. 74260 to the Child Health Institute of New Jersey (D.C.); RO1AG061787 (J.N.S.); VUB onderzoeksfonds (SRP13, H.R.); European Research Council (ERC) (724866, I.S.); FWO Project Grant G.0946.16N (K.F.); Vlaams Initiatief voor Netwerken voor Dementie Onderzoek (VIND, Strategic Basic Research Grant 135043, B.D.S.); FWO Project Grant G.0D98.17N (B.D.S.); KU Leuven Methusalem Grant (B.D.S. and J.d.W.); ERC Starting Grant (311083, J.d.W.); FWO Odysseus Grant (J.d.W.); and FWO Project Grant G.0654.15N (J.d.W.). B.D.S. is supported by the Arthur Bax and Anna Vanluffelen chair for Alzheimer's disease, "Opening the Future" of the Leuven Universiteit Fonds (LUF), and by the "Geneeskundige Stichting Koningin Elisabeth." **Author contributions:** H.C.R., B.D.S., and J.d.W. conceived the study. All authors planned experiments. H.C.R., D.d.M., A.S., S.F., I.V.M., A.N.V., E.C., I.V., J.N., F.M.R., and K.D.W. performed the experiments. All authors interpreted data. H.C.R., B.D.S., and J.d.W. wrote the first version of the manuscript. All authors contributed to and approved the final version. **Competing interests:** H.C.R., B.D.S., and J.d.W. are inventors on a patent on the APP-$GABA_B$R interaction that is owned by VIB and the KU Leuven. Patent no. WO2018015296A1, "Therapeutic agents for neurological and psychiatric disorders." **Data and materials availability:** Resonance assignments were deposited in the Biological Magnetic Resonance Bank (accession number 27581) and the 20 lowest-energy structures were deposited in the Protein Data Bank (accession code 6HKC). All other data are provided in the main manuscript and supplementary materials.

SUPPLEMENTARY MATERIALS

www.sciencemag.org/content/363/6423/eaao4827/suppl/DC1
Materials and Methods
Figs. S1 to S10
Tables S1 to S4
References (*51*–*75*)
Movies S1 and S2

31 July 2017; resubmitted 30 September 2018
Accepted 14 November 2018
10.1126/science.aao4827

Downloaded from http://science.sciencemag.org/ on January 15, 2019

RESEARCH ARTICLE SUMMARY

CHEMISTRY

Organic synthesis in a modular robotic system driven by a chemical programming language

Sebastian Steiner, Jakob Wolf, Stefan Glatzel, Anna Andreou, Jarosław M. Granda, Graham Keenan, Trevor Hinkley, Gerardo Aragon-Camarasa, Philip J. Kitson, Davide Angelone, Leroy Cronin*

INTRODUCTION: Outside of a few well-defined areas such as polypeptide and oligonucleotide chemistry, the automation of chemical synthesis has been limited to large-scale bespoke industrial processes, with laboratory-scale and discovery-scale synthesis remaining predominantly a manual process. These areas are generally defined by the ability to synthesize complex molecules by the successive iteration of similar sets of reactions, allowing the synthesis of products by the automation of a relatively small palette of standardized reactions. Recent advances in areas such as flow chemistry, oligosaccharide synthesis, and iterative cross-coupling are expanding the number of compounds synthesized by automated methods. However, there is no universal and interoperable standard that allows the automation of chemical synthesis more generally.

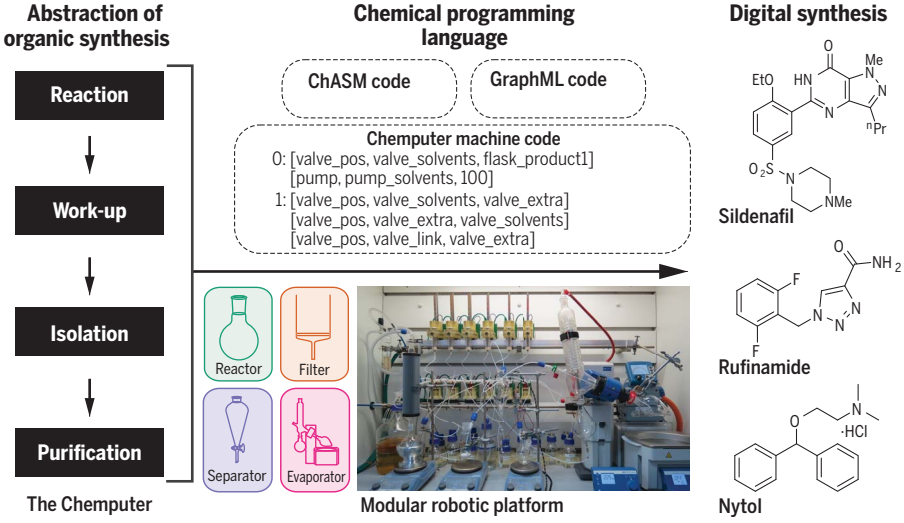
RATIONALE: We developed a standard approach that mirrors how the bench chemist works and how the bulk of the open literature is reported, with the round-bottomed flask as the primary reactor. We assembled a relatively small array of equipment to accomplish a wide variety of different syntheses, and our abstraction of chemical synthesis encompasses the four key stages of synthetic protocols: reaction, workup, isolation, and purification. Further, taking note of the incomplete way chemical procedures are reported, we hypothesized that a standardized format for reporting a chemical synthesis procedure, coupled with an abstraction and formalism linking the synthesis to physical operations of an automated robotic platform, would yield a universal approach to a chemical programming language. We call this architecture and abstraction the Chemputer.

RESULTS: For the Chemputer system to accomplish the automated synthesis of target molecules, we developed a program, the Chempiler, to produce specific, low-level instructions for modular hardware of our laboratory-scale synthesis robot. The Chempiler takes information about the physical connectivity and composition of the automated platform, in the form of a graph using the open-source GraphML format, and combines it with a hardware-independent scripting language [chemical assembly (ChASM) language], which provides instructions for the machine operations of the automated platform. The Chempiler software allows the ChASM code for a protocol to be run without editing on any unique hardware platform that has the correct modules for the synthesis. Formalization of a written synthetic scheme by using a chemical descriptive language (XDL) eliminates the ambiguous interpretation of the synthesis procedures. This XDL scheme is then translated into the ChASM file for a particular protocol. An automated robotic platform was developed, consisting of a fluidic backbone connected to a series of modules capable of performing the operations necessary to complete a synthetic sequence. The backbone allows the efficient transfer of the required chemicals into and out of any module of the platform, as well as the flushing and washing of the entire system during multistep procedures in which the modules are reused multiple times. The modules developed for the system consist of a reaction flask, a jacketed filtration setup capable of being heated or cooled, an automated liquid-liquid separation module, and a solvent evaporation module. With these four modules, it was possible to automate the synthesis of the pharmaceutical compounds diphenhydramine hydrochloride, rufinamide, and sildenafil without human interaction, in yields comparable to those achieved in traditional manual syntheses.

ON OUR WEBSITE

Read the full article at http://dx.doi.org/10.1126/science.aav2211

CONCLUSION: The Chemputer allows for an abstraction of chemical synthesis, when coupled with a high-level chemical programming language, to be compiled by our Chempiler into a low-level code that can run on a modular standard robotic platform for organic synthesis. The software and modular hardware standards permit synthetic protocols to be captured as digital code. This code can be published, versioned, and transferred flexibly between physical platforms with no modification. We validated this concept by the automated synthesis of three pharmaceutical compounds. This represents a step toward the automation of bench-scale chemistry more generally and establishes a standard aiming at increasing reproducibility, safety, and collaboration. ■



Abstraction of organic synthesis to the Chemputer software and hardware standards. The Chemputer system can perform multistep organic synthesis protocols on the bench by using a modular system with hardware and software standards.

The list of author affiliations is available in the full article online.
*Corresponding author. Email: lee.cronin@glasgow.ac.uk
Cite this article as S. Steiner *et al.*, *Science* **363**, eaav2211 (2019). DOI: 10.1126/science.aav2211

Downloaded from http://science.sciencemag.org/ on January 14, 2019

RESEARCH ARTICLE

CHEMISTRY

Organic synthesis in a modular robotic system driven by a chemical programming language

Sebastian Steiner[1*], Jakob Wolf[1], Stefan Glatzel[1], Anna Andreou[1], Jarosław M. Granda[1], Graham Keenan[1], Trevor Hinkley[1], Gerardo Aragon-Camarasa[1,2], Philip J. Kitson[1], Davide Angelone[1], Leroy Cronin[1]†

The synthesis of complex organic compounds is largely a manual process that is often incompletely documented. To address these shortcomings, we developed an abstraction that maps commonly reported methodological instructions into discrete steps amenable to automation. These unit operations were implemented in a modular robotic platform by using a chemical programming language that formalizes and controls the assembly of the molecules. We validated the concept by directing the automated system to synthesize three pharmaceutical compounds, diphenhydramine hydrochloride, rufinamide, and sildenafil, without any human intervention. Yields and purities of products and intermediates were comparable to or better than those achieved manually. The syntheses are captured as digital code that can be published, versioned, and transferred flexibly between platforms with no modification, thereby greatly enhancing reproducibility and reliable access to complex molecules.

The automation of chemical synthesis is currently expanding, and this is driven by the availability of digital labware. The field currently encompasses areas as diverse as the design of new reactions (*1*), chemistry in reactionware (*2*), reaction monitoring and optimization (*3*, *4*), flow chemistry (*5*) for reaction optimization and scale up, and even full automation of the synthesis laboratory (*6*). Established technologies such as the automated synthesis of peptides (*7*) and oligonucleotides (*8*), flow chemistry (*9*), and high-throughput experimentation (*6*) are mainstays of modern chemistry, whereas emerging technologies such as automated oligosaccharide synthesis (*10*) and iterative cross-coupling (*1*) have the potential to further transform the chemical sciences. Each of these examples, however, relies on a distinct protocol, as no current digital automation standard exists for computer control of chemical reactions (*11*). Hence, no general programming language is available for chemical operations that can direct the synthesis of organic compounds on an affordable, flexible, modular platform accessible to synthetic chemists and that could, in principle, encompass all synthetic organic chemistry. This situation is comparable to the era before digital programmable computers, when existing computational devices were fixed to a dedicated problem.

[1]School of Chemistry, The University of Glasgow, Glasgow G12 8QQ, UK. [2]School of Computer Science, The University of Glasgow, Glasgow G12 8QQ, UK.
*Present address: Department of Chemistry, University of British Columbia, Vancouver, British Columbia V6T 1Z1, Canada.
†Corresponding author. Email: lee.cronin@glasgow.ac.uk

A generalized approach to automating chemical synthesis would be beneficial because making compounds is one of the most labor-intensive branches of chemistry, requiring manual execution of a range of unit operations such as reagent mixing, liquid-liquid extractions, or filtrations. Despite the modular nature of the operations, standardization and automation are still severely limited. Furthermore, the ambiguous way in which synthetic protocols are communicated has contributed to a mounting reproducibility crisis (*12*). Syntheses are reported in prose, omitting many details explaining exactly how operations were carried out and making many assumptions about the skill level of the researcher repeating the process. We hypothesized that a more standardized format for reporting a chemical synthesis procedure, coupled with an abstraction and formalism linking the synthesis to the physical operations, could yield a universal approach to a chemical programming language; we call this architecture and abstraction the Chemputer.

In developing the Chemputer platform, we wanted to build on the 200 or more years of chemical literature and the experience of the many thousands of bench chemists active in the world today in a way that would naturally lead to a standardization embodied in a codified standard recipe, or chemical code, for molecular synthesis. For this to be possible, it was essential that the approach mirror the way the bench chemist works. As our key reaction module for implementation of the Chemputer, we selected the round-bottomed flask for batch synthesis, with well-defined inputs and outputs, because most protocols already published for complex molecule synthesis rely on this type of apparatus. Next, we identified the four key stages of a synthetic protocol from our abstraction: reaction, workup, isolation, and purification. These stages can be subdivided into several unit operations, which in turn are implemented in a specific automated platform.

Developing code for chemistry

By developing control software as well as hardware modules for laboratory-scale synthesis that can be automatically cleaned and reused in subsequent reaction steps, we were able to define a process for combining individual unit operations into full, multistep syntheses to produce desired products autonomously (Fig. 1A). For the Chemputer to operate as shown in Fig. 1B, the states of the inputs, reactor, and outputs must be defined and controlled programmatically. We therefore created a Chempiler, which is a program to produce specific low-level instructions for the modules that constitute the Chemputer architecture. The Chempiler can run commands used to control the modular platform from our abstraction layer, so that a typical written scheme can be turned into a specific code to run the modules with ease. Every module was then designed with drivers for the device or equipment and a standardized application programming interface (API) exposing the instruction set to the Chempiler (Fig. 2). The use of a program coupled to the Chemputer architecture allows users to directly run published syntheses without reconfiguration, provided the necessary modules and drivers are present within their system. Thus, the practical implementation of the Chemputer architecture converts digital code to chemical synthesis operations in accordance with the standard protocol of a chemical reaction incorporating the four processes listed in Fig. 1C. To prevent the need for manual reconfiguration, the physical modules and their connections and representation are stored in memory as a directed graph, which allows knowledge and control of their states in real time.

The physical routing that links the connected modules is described in a graph by using an open-source format, GraphML, which allows the Chempiler to find paths between a source flask and a target flask, as well as address devices such as hot plate stirrers on the basis of the vessel they are connected to. GraphML is an open-standard, extensible markup language (XML)–based exchange format for graphs (*13*) [example graphs used in the syntheses described herein can be found in data S1 (GraphML files) in the supplementary materials (SM)]. Synthetic procedures are codified by using a scripting language called Chemical Assembly (ChASM), which provides instructions for all currently implemented machine operations and supports the definition of functions and variables. To develop the ChASM code, we built a standard procedure, starting with a written synthetic scheme that is formalized by using a chemical descriptive language (XDL).

Downloaded from http://science.sciencemag.org/ on January 14, 2019

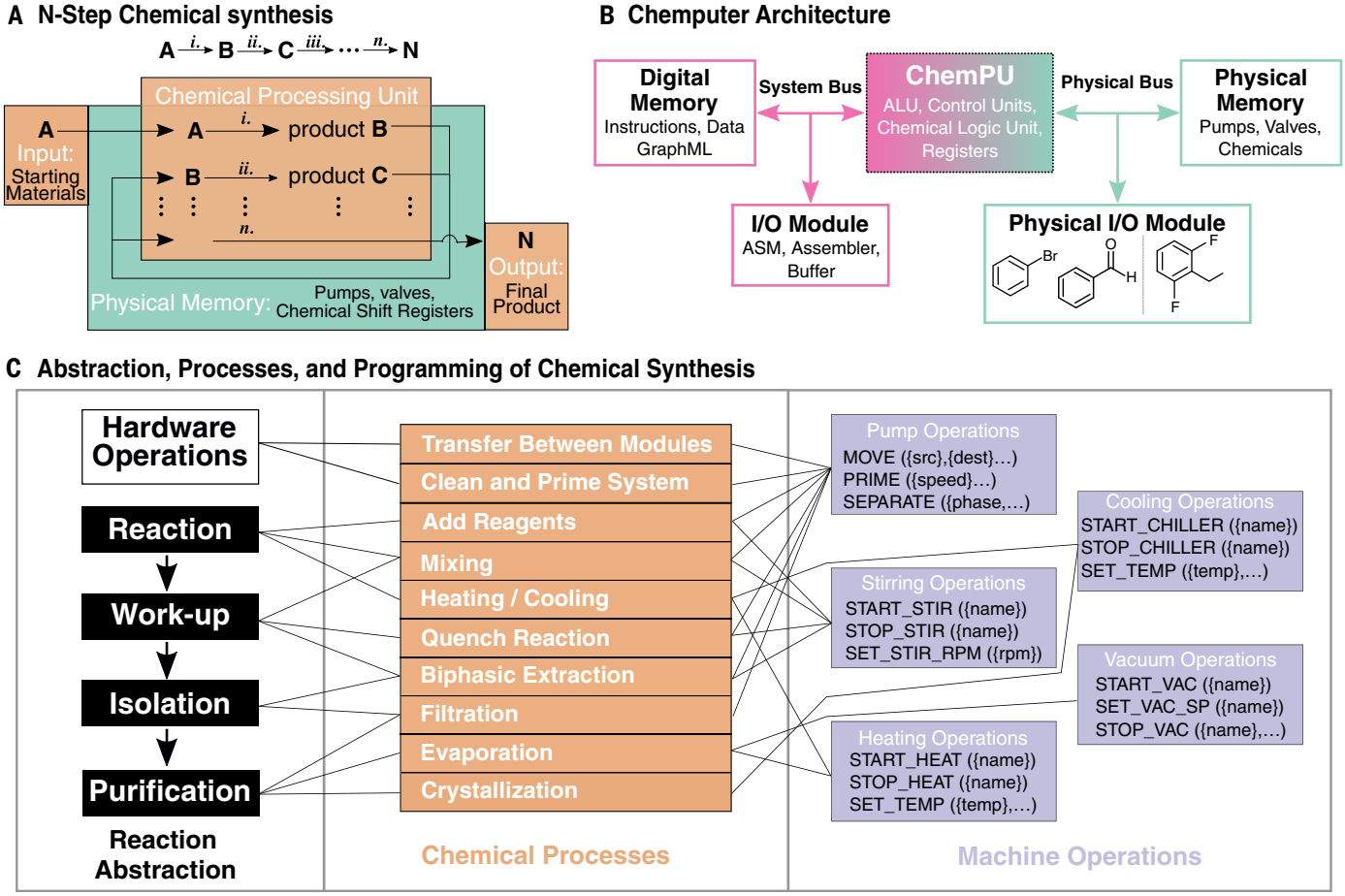


Fig. 1. Operating principles of the Chemputer. (**A**) Schematic representation of a stepwise chemical synthesis, formalizing the reagents as inputs and products as output. (**B**) Diagram outlining the computing architecture of the Chemputer. ALU, arithmetic logic unit; I/O, input/output; ASM, assembly language. (**C**) The abstraction of chemical synthesis allowing the development of an ontology that can be universally programmed by using a machine. Similar to digital computers, the Chemputer has a memory and a bus system, but these are both digital and physical. By considering chemical reagents and products in a memory bus, it is possible to break the process of complex molecule synthesis into steps or cycles that can be run using the physical hardware.

The XDL has the advantage of eliminating ambiguous interpretation of the synthesis procedures by explicitly and systematically listing all required information without making any assumptions or inferences (example ChASM files used in the syntheses described herein can be found in data S2).

To control the chemistry, the Chempiler was designed to accept ChASM commands such as "start stirring the reactor," find the module in question in the GraphML definition, and schedule the execution by using the appropriate low-level instructions. The modular Chemputer components thereby constitute a versatile and interoperable architecture for chemical synthesis. Also, a given ChASM file could be run on many different platform instances with hardware of different makes and models connected in different ways. If the required unit operation modules are present and all required reagents and solvents are provided, the hardware-agnostic ChASM code can be freely paired with a system-specific GraphML file to synthesize the same product on another, different platform without reoptimization.

During the development of the process and programming language, we found it helpful to visualize the workflow one would follow when manually reproducing the procedure. Writing the XDL and converting it to ChASM then become intuitive even for users with no programming experience. Many operations are repetitive enough to be defined as functions that can be reused many times. For instance, we have defined several functions such as "evaporate to dryness" or "add reagents and heat up to x°C," and we expect that this library can be greatly expanded with future use. Once the ChASM file is completed, a graph of the platform is drafted, following a set of rules detailed in the SM. To validate the ChASM and the graph, we implemented two simulation modes in the Chempiler. First, all operations are performed as they would be on the real system, but instead of commands being issued to physical devices, the commands are logged to a text file. Next, the system simulates the process without reagents as a dry run. The simulations flag any potential issues, such as syntax errors in the XDL representation and the ChASM, inconsistencies in the graph representation, impossible operations, or overfilling of vessels. Once the simulations run without errors, the user can load the reagents and solvents in accordance with the graph and start the synthesis. The Chempiler also has a break-point command option for additional safety and compatibility checks as needed.

Modular synthesis platform

To produce a physical platform that could implement our architecture and achieve the syntheses outlined below, we had to step away from thinking about reactions and rather adopt a process-centered way of thinking. Although the 20 most commonly used reaction classes in drug discovery (*14*) span a wide range of chemistries, from amide bond formation to Buchwald-Hartwig couplings, experimentally most of them simply involve the mixing of several reagents in the

Downloaded from http://science.sciencemag.org/ on January 14, 2019

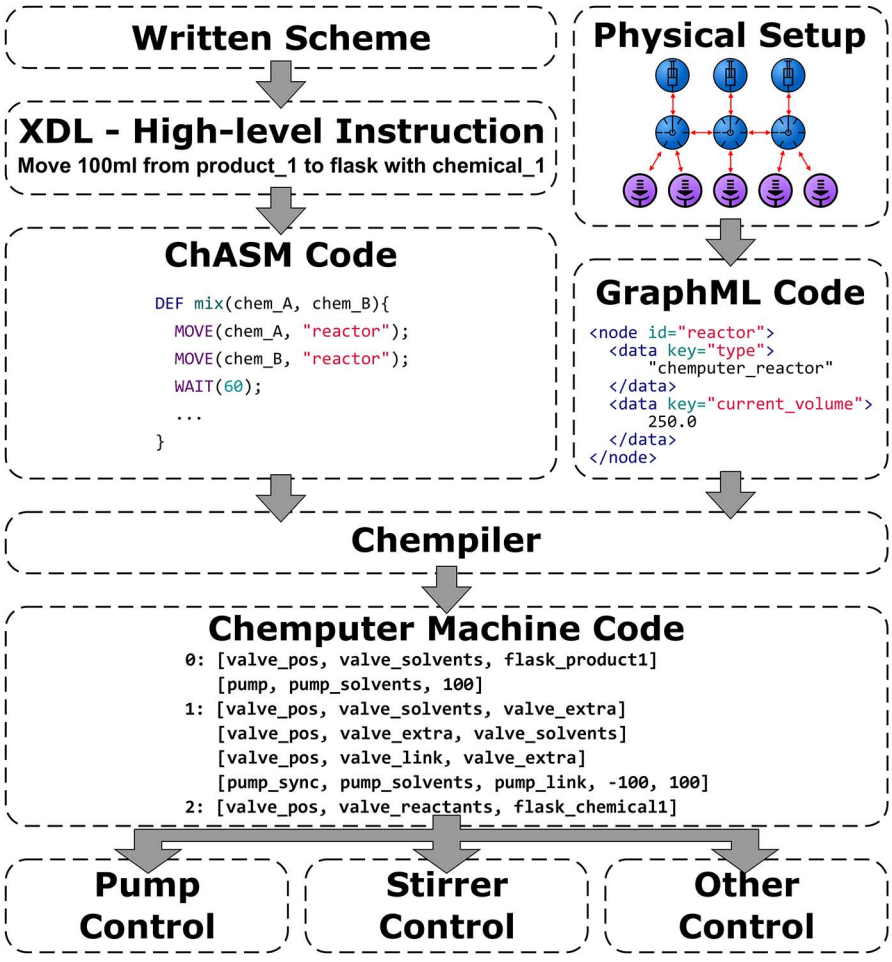


Fig. 2. Diagram showing the flow of information in the synthesis platform. To translate experimental steps into a set of pump movements or hot plate stirrer commands, the user provides the synthesis instructions in a text format similar to a written protocol. The graphical representation of the synthesis platform, which contains all necessary information about the fluidic connectivity, is represented by using GraphML. The written scheme from a published procedure or lab book entry is translated into a series of ChASM commands. Both the ChASM and the GraphML files are passed to the Chempiler. The Chempiler command dispatcher then uses those two pieces of information to control the physical labware through the respective device drivers, effectively executing the synthesis.

correct order, often under heating or cooling. These processes are typically followed by a workup and a purification technique such as distillation, recrystallization, or chromatography. We therefore concluded that a synthesis platform capable of performing the unit operations of mixing under heating or cooling, liquid-liquid separation, filtration, and solvent evaporation could in principle perform a large fraction of all organic syntheses and embody our abstraction of chemical synthesis (Fig. 1C). As those unit operations do not always occur in the same order, especially where multistep syntheses are concerned, a flexible means of moving material between the modules was required. To that end, we built the physical architecture around a fluidic backbone consisting of a series of syringe pumps and six-way selection valves (Fig. 3). The appeal of this design is that it is expandable: The user can always add more pump-valve units (backbone units) to the ends of the backbone. Material can be moved between modules in an arbitrary order, including multiple uses of the same module at different points in the sequence. The process to transfer liquid from a port on the backbone to another backbone is described in the SM (fig. S8). The pump on the source unit aspirates the appropriate amount, then the valve on the source unit and the adjacent unit switch to the bridge, and the source pump and the adjacent pump move simultaneously to transfer the liquid contents from the source syringe to the next syringe. This process is repeated, and the liquid is moved along the backbone until it reaches the destination unit, which in turn dispenses it to the destination port. Surplus ports on the six-way valves accommodate solvents and reagents, and additional backbone units may be dedicated entirely to supplying chemicals. This is in contrast with even the most advanced flow chemical setups to date (*15*), which have to be physically reconfigured for every new synthesis. In flow, the number and sequence of unit operation modules must match the number and sequence of required unit operations, whereas in our system the ability to address modules independently and reuse them as required removes the need for physical reconfiguration. This is achieved by using GraphML, which gives a complete description of the connectivity, allowing the pumps and valves to be dynamically reconfigurable resources, and facilitates the movement of solvents and solutions from reagent flasks to the various components required for a given synthesis step. To ensure modularity, we designed our own pumps and valves, controlled and powered by a single Ethernet cable plugged into each item, powered from a network switch placed next to the fume hood (see fig. S11).

In this work, we developed modules for the unit operations of mixing, filtration, liquid-liquid separation, evaporation, and chromatographic separation, which are all key to the practical implementation of our abstraction of a chemical reaction. Detailed descriptions of the individual modules can be found in figs. S34 to S44 and accompanying supplementary text. However, both the physical architecture and the architecture of the Chempiler (vide supra) were specifically designed to allow for future addition of other modules, enabling automation of even more reactions.

The reactor (fig. S34) consisted of a commercially available, two-necked, pear-shaped flask equipped with an air condenser. We decided to use common laboratory glassware rather than a jacketed reactor vessel both for simplicity and to lower the barrier for reproducing the setup. A pear-shaped flask was chosen over the more common round-bottomed flask to accommodate a wider range of reaction volumes. Heating and stirring were accomplished by using a computer-controllable stirrer hot plate and a custom-manufactured aluminum heating block for the pear-shaped flask. A 0.32-cm-outer-diameter polytetrafluoroethylene (PTFE) tube was held in place by a ground glass joint–to–GL18 thread adapter with a GL18 screw cap and insert so that its end reached the bottom of the flask. A slight argon overpressure was maintained by the inert gas system (see SM). For the sildenafil synthesis, cooling of the reactor was required, and we used a recirculation chiller with a temperature range of −30 to 160°C, giving precise temperature control of the reactor.

The liquid-liquid separation, one of the most common isolation techniques, was also the most challenging task to automate in a robust fashion. Whereas in continuous flow there are solutions using membrane technology (*16*), we found that commercially available hydrophobic frits are usually designed to be single use and therefore lack long-term reliability. We attempted to use

Downloaded from http://science.sciencemag.org/ on January 14, 2019

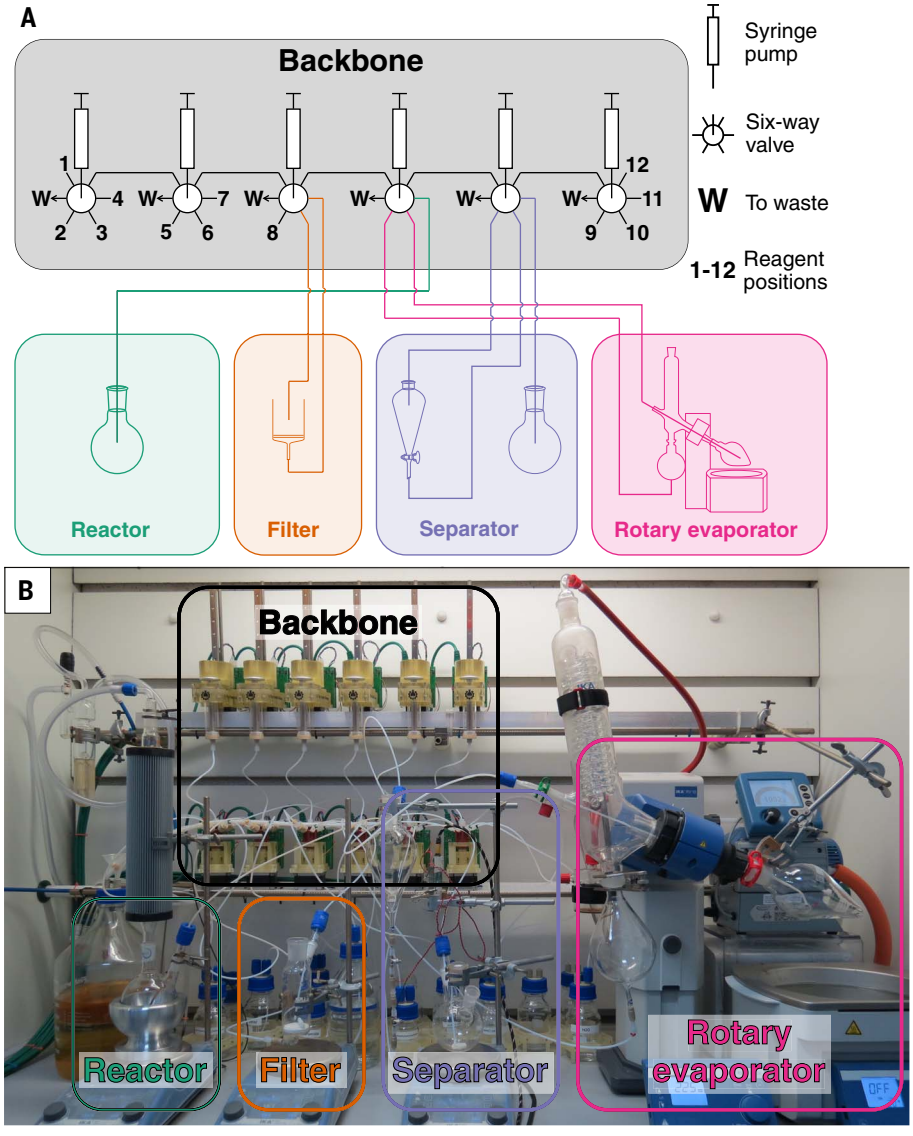


Fig. 3. Physical implementation of the synthesis platform. (**A**) Schematic representation of the Chemputer, highlighting modules used for four commonly encountered unit operations. The lines represent fluidic connections. (**B**) Photograph of one Chemputer setup used in this work. The various modules are highlighted in correspondence to the schematic.

a modified separating funnel and computer vision to directly replicate the way a human chemist would perform liquid-liquid extractions. However, we found that solutions using either a colored floater (*17*) or direct recognition of the phase boundary (*18*) worked well in a test environment but were otherwise unreliable. In real syntheses, imperfections such as poor phase separation, strongly colored or cloudy solutions, or unusual extraction solvents often lead to complete failure of the image recognition algorithms. We therefore abandoned the computer vision for a sensor-based approach. Initially, we investigated optical and capacitive sensors because they do not require direct contact with the medium. Unfortunately, those sensors also performed poorly in some cases, so ultimately, we built a conductivity sensor from two pieces of stainless-steel tubing inserted into the flow path (see SM). This sensor reliably detected phase boundaries in all test cases and enabled us to perform separations in a robust fashion. The sensor was connected to a custom-made separating funnel with a B45 ground glass joint at the top and two B14 side arms (fig. S36). Instead of a stopcock, it had a glass ¼-28 UNF (Unified fine) male threaded connector (where ¼ indicates a major diameter of 0.25 inches, or 6.35 mm, and 28 indicates a pitch of 28 threads per inch) fitted to the bottom. An Arduino Due was used to read the sensor via a simple voltage divider circuit. The top inlet tube was suspended by a ground glass joint–to–GL18 thread adapter with a GL18 screw cap and insert. To facilitate efficient extractions through thorough mixing, a computer-controlled overhead stirrer was fitted above the separator.

To perform liquid-liquid extractions, the mixture was pumped into the separator through the top inlet, or in the case of a wash, the washing solvent was added through either the top or bottom port, depending on whether it constituted the top or bottom layer of the biphasic mixture. The two layers were then stirred vigorously with the overhead stirrer, and this step was followed by a period of settling under very slow (50 rpm) stirring. Next, the bulk of the lower phase was usually transferred to the target vessel to speed up the process. The volume moved was determined empirically for every separation. The actual separation commenced with withdrawing the dead volume of the sensor and tubing from the bottom port. The volume removed was dispensed into the lower-phase target vessel. Then a sensor reading was taken and compared against a reference value. If the reading was lower than the reference, the lower phase was assumed to be organic; otherwise, the lower phase was assumed to be aqueous. One milliliter was then transferred to the lower-phase target. Another sensor reading was taken and compared against a predefined threshold value. This threshold depended on whether the lower phase was aqueous or organic. Either way, if the sensor reading was outside the threshold, it was concluded that a phase change had been detected. If not, another milliliter was withdrawn and the cycle continued until a phase change was detected. Then the dead volume of the sensor and tubing was transferred to the lower-phase target vessel. If the upper-phase target was specified as the separator, the process was concluded. Otherwise, the upper phase was withdrawn as well and transferred to the target vessel.

For the solvent evaporation, a computer-controllable rotary evaporator was modified by routing a piece of PTFE tubing through the vapor duct into the evaporation flask to pump product into and out of the flask (fig. S37). The receiver flask was fitted with a glass ¼-28 UNF male threaded connector and a PTFE tube, allowing it to be emptied in situ. One complication was that after distillation at reduced pressure, upon venting, oily products were forced back into the tube reaching into the evaporation flask. This problem was solved by affixing a magnetic stirrer bar to the tube by using PTFE shrink wrap (fig. S38). A strong magnet was then positioned in such a way that it would attract the tube and lift it out of the product, allowing the system to be vented. When the flask was lowered into the heating bath, the tube would be released and drop, thereby allowing product to be withdrawn. Solvent evaporation started with pumping the solution to be evaporated into the distillation flask of the rotary evaporator. A cartridge filled with molecular sieves could be switched into the flow path by two six-way selection valves, allowing for the solution to be dried before evaporation. The flask was then lowered into the heating bath, and the rotation was turned on. The vacuum pump was started, lowering the pressure to 900 mbar to degas the solution and avoid excessive foaming later on. The heating bath and the recirculation chiller servicing the condenser were switched on, the target temperatures were

Downloaded from http://science.sciencemag.org/ on January 14, 2019

set, and execution of the script was suspended until the target temperatures were reached. The vacuum set point was then changed to the target distillation pressure, and the vacuum pump speed was adjusted according to the solvent, to avoid bumping. Then the execution of script was suspended for a user-defined amount of time to allow the main distillation to finish. After the distillation was complete, the flask was lifted, which caused the inlet tube to be attracted by the magnet (fig. S38), lifting it out of the remaining solution. The vacuum pump was subsequently stopped, and the vacuum was vented. A user-defined amount of distillate was removed from the distillate flask and discarded. The parameters (pressure, timings, and volumes) were always chosen empirically, either through experimental trial and error or from prior experiences with the system.

At this point, we found that proceeding directly to drying the product under maximal vacuum would often lead to a few milliliters of residual solvent distilling over, which decreased the drying efficiency. Thus, the flask was lowered back into the bath and the vacuum pump was set to maximum power for 2 min, drawing out any residual solvent. The sequence of raising the flask, venting the vacuum, and emptying the distillate flask was then repeated. Next, the flask was lowered once again, the vacuum pump was set to maximum power and started, and the cooling of the condenser was switched off. The product was then dried for a user-defined amount of time. After the drying was complete, the flask was lifted once more, the vacuum was vented, and the rotation and heating bath were switched off.

The filtration unit consisted of a custom-made, jacketed, sintered glass Büchner funnel (made in-house; see SM) fitted with a B29 ground glass joint at the top, two B14 side arms, and a glass ¼-28 UNF male threaded connector at the bottom. The top inlet tube was suspended by a ground glass joint–to–GL18 thread adapter with a GL18 screw cap and insert, whereas the bottom outlet tube was connected to the threaded connector with a straight union piece. Stirring was accomplished by a computer-controllable overhead stirrer.

To allow efficient drying of the precipitate, the bottom outlet of the filter was connected to the central inlet of a six-way valve. One outlet of that valve was then connected to the backbone, and another outlet was connected to the laboratory vacuum system via a Woulff bottle. This allowed the user to switch the filter bottom between the backbone (for liquid addition or withdrawal) and vacuum (for drying). The whole platform could be cleaned automatically by pumping suitable washing solvents into the modules. This cleaning cycle would return the system to its initial state, ready for the next reaction stage. Consequently, preparing the system for another synthesis was simply a matter of swapping the reagent bottles.

Proof-of-principle automated syntheses of three drugs

To highlight the power of this approach, we chose three targets: diphenhydramine hydrochloride (**6**) (Fig. 4), rufinamide (**10**) (Fig. 5), and sildenafil (**17**) (Fig. 6). The process of digitizing a synthesis always starts with a traditional, written scheme such as an experimental procedure from a publication or a lab book entry. We chose three published syntheses, all replicated manually to establish benchmark yields and purities for comparison with the automated runs.

Diphenhydramine hydrochloride is an ethanolamine derivative used as an antihistamine and a mild sleep aid. It is marketed as Nytol in the United Kingdom and as Benadryl in the United States. The synthesis is a four-step sequence starting with a Grignard reaction. Rufinamide is a triazole derivative used as an anticonvulsant to treat various seizure disorders, and its synthesis is a relatively simple process to automate. Sildenafil is prescribed to treat erectile dysfunction and is best known under the brand name VIAGRA; its industrial synthesis route (*19*) features a chlorosulfonation with highly aggressive chlorosulfonic acid and thionyl chloride. We reasoned that successful automated handling of those aggressive reagents would demonstrate the versatility and robustness of the system, as well as highlighting the safety benefit arising from automating dangerous procedures.

After reproducing the synthesis of diphenhydramine hydrochloride (**6**) (*20*) manually, we made some small modifications and started the process on the platform. The synthesis commenced with Grignard reagent formation, for which the reactor was manually charged with dried magnesium grit. All the other required reagents and solvents were loaded into 100- or 250-ml standard GL45 bottles, and all nonaqueous storage bottles were purged with argon and stored under positive pressure. All the operations described were performed by the Chemputer under full Chempiler control, and the program used, as well as a description of the process in prose, can be found in the SM. The automated synthetic procedure was started by automatically priming the tubes to the chemical reservoirs and then autocleaning the backbone with water, isopropanol, and dry diethyl ether. The system then continued autonomously through the whole synthesis of diphenhydramine hydrochloride without human intervention as follows. Diethyl ether and a small portion of bromobenzene were added to the magnesium, and the mixture was heated under reflux to initiate the Grignard reagent formation. After cooling, the remaining bromobenzene was added at a rate of 1 ml/min, and the mixture was again

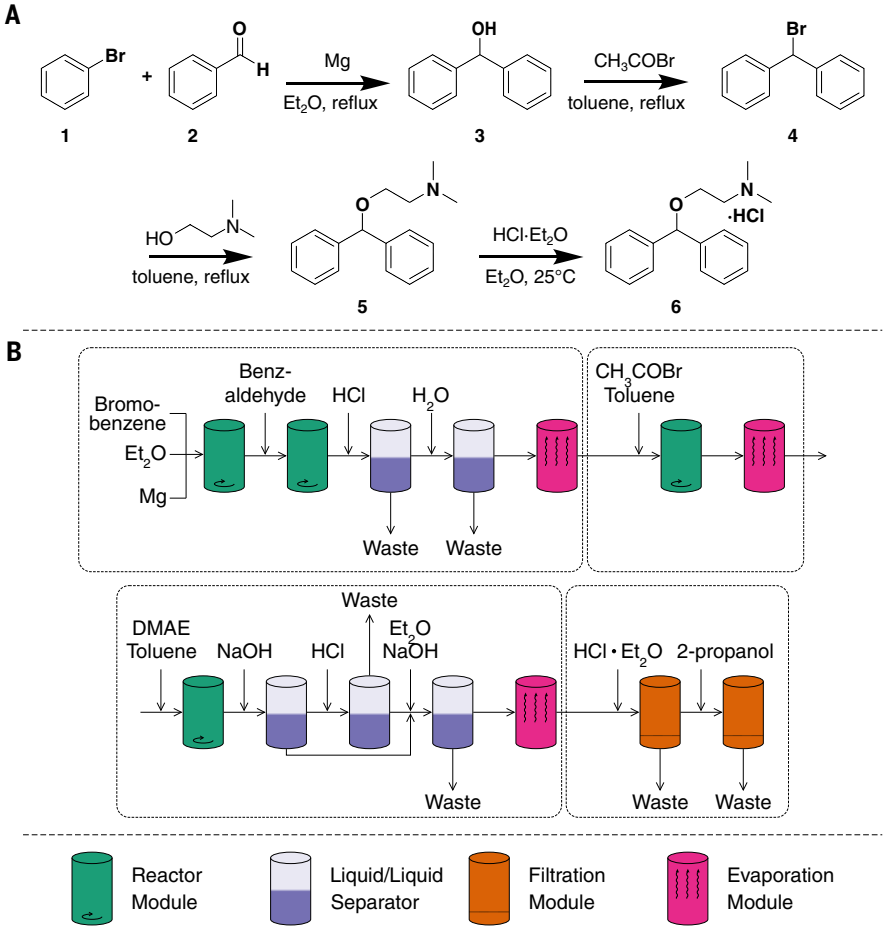


Fig. 4. Synthesis of diphenhydramine hydrochloride (6). (**A**) Modified synthetic route to diphenhydramine hydrochloride. Et, ethyl. (**B**) Sequence of unit operations required for the synthesis. The dotted boxes denote the four stages of the synthesis. DMAE, dimethylaminoethanol.

Downloaded from http://science.sciencemag.org/ on January 14, 2019

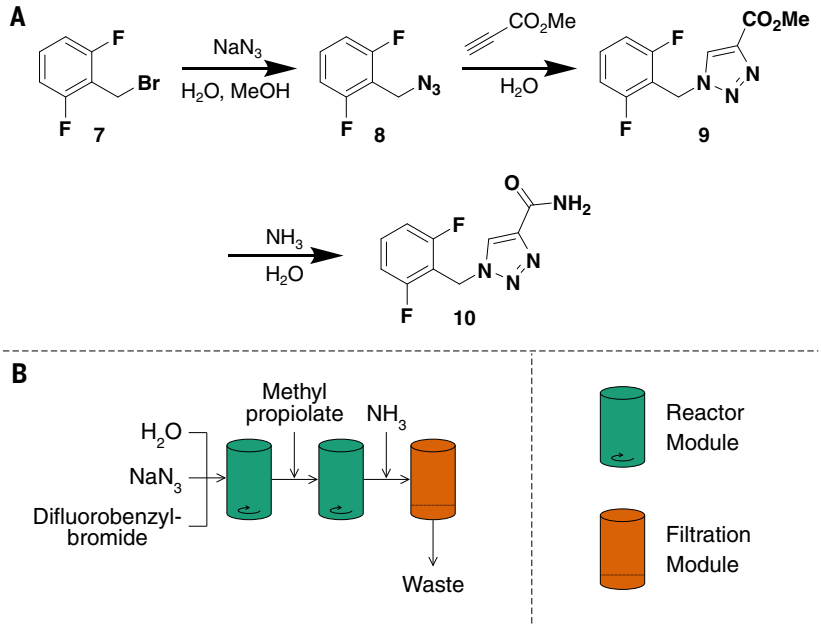


Fig. 5. Synthesis of rufinamide (10). (**A**) Synthetic route to rufinamide. Me, methyl. (**B**) Sequence of unit operations required for the synthesis.

heated to reflux. Using syringe pumps for moving material allowed us to precisely control addition rates and thus increase the reproducibility of synthetic protocols even further. Subsequently, a solution of benzaldehyde in diethyl ether was added at a rate of 1 ml/min, and the mixture was held at reflux for another 5 hours. As the platform presented herein is largely a proof of concept, no process analytical technology (PAT) has been implemented yet, so all reaction times were determined beforehand and hard-coded into the ChASM script. However, the modular architecture of the platform and control software should make adding PAT to future iterations of the platform straightforward. After quenching of the reaction with dilute HCl, the layers were separated, and the organic layer was washed with water and concentrated in vacuo as described earlier. The system then cleaned itself and directly proceeded with the bromination. To that end, the reactor was charged with acetyl bromide, the crude diphenylmethanol (**3**) was transferred from the rotary evaporator flask to the reactor with three portions of toluene, and the mixture was heated to reflux, all without human intervention. After a predetermined reaction time, the mixture was transferred to the rotary evaporator and evaporated to dryness. The subsequent Williamson ether synthesis was initiated in a similar fashion, and after a predetermined time, the reaction was quenched with aqueous sodium hydroxide. The system then automatically conducted an aqueous workup and concentrated the product in vacuo. Once again, the system cleaned itself, charged the jacketed filtration module with hydrochloric acid, and transferred the crude free base **5** to the filter with three portions of diethyl ether. To ensure smooth precipitation, the mixture was stirred vigorously and the free base solution was added very slowly. After the addition was completed, the off-white precipitate was collected by automatic filtration and recrystallized from isopropanol by using the heating and cooling capabilities of the jacketed filter. Drying at 60°C in a stream of argon for 1 hour yielded pure diphenhydramine hydrochloride, giving an isolated yield of 58% over four steps, or 87% per step on average. Although this is slightly less than the 68% overall achieved manually, the average yield per step (87% for automated versus 91% for manual) is comparable in our view. The platform performed the synthesis fully automatically in 77 hours (see movie S1), whereas the manual synthesis took 4 work days.

Next, we conducted an automated synthesis of the antiseizure drug rufinamide (**10**), a triazole derivative commonly prepared via a click reaction between the corresponding azide **8** and methyl propiolate (Fig. 5) (*21*). The synthesis began with an azide formation, for which the reactor was charged manually with 2,6-difluorobenzyl bromide (**7**); the remaining reagents were provided in bottles as described above. From this point on, unless explicitly stated otherwise, all described operations were performed by the Chemputer under full Chempiler control. An aqueous solution of sodium azide was added to the reactor to prepare the organic azide for the triazole click with methyl propiolate, which was performed inside the jacketed filtration module. Subsequent saponification with aqueous ammonia led to precipitation of the target compound. Filtration followed by three aqueous washes yielded pure rufinamide at 46% isolated yield, which was slightly better than the manual synthesis (38%). The automated synthesis took 38 hours. To demonstrate the power of the Chempiler software and the interoperability of the code, we then went on to run the same ChASM file on a "full-scale" platform equipped with slightly different hardware, which was connected in an entirely different way. The platform produced pure rufinamide in 44% yield without any problems or changes to the code (movie S2).

In the next synthesis, we prepared sildenafil, better known under the brand name VIAGRA (**17**), as shown in Fig. 6 (*13*). For this synthesis, we fitted the reactor with a heating block connected to the recirculation chiller, allowing us to cool as well as heat. From this point on, unless explicitly stated otherwise, all described operations were performed by the Chemputer under full Chempiler control. The reactor was cooled to 15°C and automatically charged with chlorosulfonic acid, thionyl chloride, and molten ethoxybenzoic acid. Chlorosulfonic acid is corrosive, so when writing the ChASM script we took great care to minimize contact times and enacted a strict cleaning regime. Chlorosulfonic acid and thionyl chloride also react violently with trace amounts of water, producing large volumes of gas. Therefore, the backbone was automatically flushed with dry diethyl ether and dried with a small amount of thionyl chloride before the reactor was charged. After a predetermined reaction time, the filtration module was charged with water and cooled to 0°C. The reaction mixture was then slowly dripped into the water, quenching the excess thionyl chloride and chlorosulfonic acid and precipitating the product (**12**), which was collected by automated filtration. The subsequent sulfonamide formation with *N*-methylpiperazine (**13**) in water was performed in the filtration module as well. Unfortunately, the sulfonamide (**14**) did not crystallize spontaneously, so a slurry of a small amount of product in water was added to seed the crystallization.

The industrial process for sildenafil uses *N*, *N*′-carbonyldiimidazole for the amide coupling in the next step. However, this reaction did not work in our hands, either manually or in automation, and thus we decided to use the acid chloride instead. The carboxylic acid (**14**) was thoroughly dried by flowing argon through the filter cake while at the same time heating the filtration module to 60°C, after which acid chloride formed with thionyl chloride in dichloromethane. The reactor module was charged with a solution of 4-amino-1-methyl-3-*n*-propyl-1*H*-pyrazole-5-carboxamide (**15**) in dichloromethane and triethylamine and cooled to 10°C. The crude acid chloride solution was then pumped from the filter module to the reactor, the reaction was quenched with water, the layers were separated, and the organic layer was dried over activated molecular sieves and evaporated to dryness, yielding amide **16** as an off-white solid. For the subsequent cyclization, the crude amide was transferred back to the reactor by dissolving it with a solution of potassium *tert*-butoxide in *tert*-butanol, and the mixture was heated at reflux for 8 hours. After the mixture was cooled to 10°C, the reaction was quenched with water, and the solution was transferred to the filter module. To induce precipitation of the sildenafil,

Downloaded from http://science.sciencemag.org/ on January 14, 2019

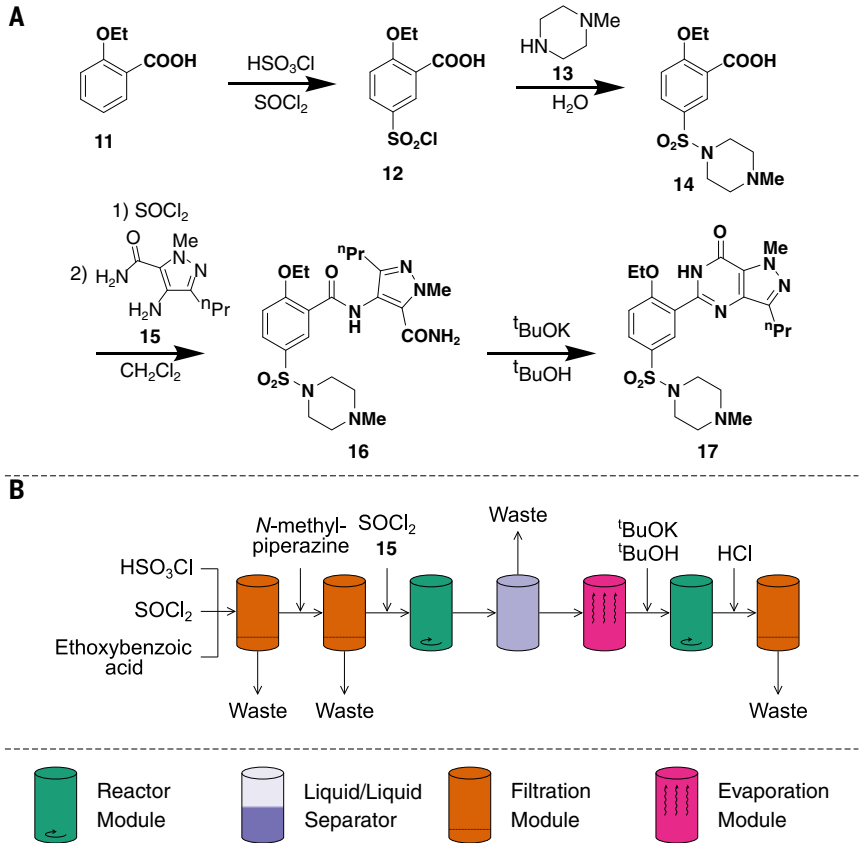


Fig. 6. Synthesis of sildenafil (17). (**A**) Synthetic route to sildenafil. ^{t}Bu, *tert*-butyl; ^{n}Pr, *normal*-propyl. (**B**) Sequence of unit operations required for the synthesis.

the mixture was neutralized with aqueous hydrochloric acid. After filtration, the solid was washed with water and dried under a stream of argon at 50°C, yielding sildenafil at 44% isolated yield over 102 hours (movie S3).

Outlook

The complete automation of all of synthesis is an ambitious objective, but this work makes a start toward that goal, as the Chemputer architecture presents a general abstraction of the process that works with traditional bench-scale techniques. The versatile programming language, the use of traditional and inexpensive labware (the total cost of the parts for the robotic modules, including nonstandard glassware, is less than $10,000 per system) (*22*), and the payoff in reproducibility after validation of the process mean that adoption could be straightforward. Initially, the synthesis of compounds will be validated reaction by reaction, but we imagine that eventually it will be possible to go straight from a reaction database to a chemical code that can run the platforms.

Materials and methods summary

The manual and automated syntheses of the three target molecules, as well as the platform and the control software, are described in detail in the SM, and this information has been deposited in Zenodo (*23*), along with the ChASM and GraphML code. Videos of the automated syntheses are available as movies S1 to S3. We will continue to update the ChASM code for the syntheses, and updates of this will be available to download (*24*). A brief summary of the syntheses is provided below.

Synthesis of diphenhydramine hydrochloride

The reactor module was charged manually with magnesium grit and dried by heating to 150°C under a stream of argon for 15 min. After cooling to room temperature (~25°C), diethyl ether and 2 ml of bromobenzene were added to the magnesium, and the mixture was heated to reflux for 20 min. After cooling below 25°C, 8.65 ml of bromobenzene was added at a rate of 1 ml/min, and the mixture was again heated to reflux for 20 min. Subsequently, a solution of benzaldehyde in diethyl ether was added at 1 ml/min, and the mixture was held at reflux for 5 hours. After quenching of the reaction with dilute HCl, the layers were separated, and the organic layer was washed with water and evaporated to dryness, yielding crude diphenylmethanol. After automatic cleaning of the system, the reactor was charged with acetyl bromide, and the crude diphenylmethanol was transferred from the rotary evaporator to the reactor with three portions of toluene. The mixture was heated to reflux for 4 hours and subsequently evaporated to dryness, yielding crude bromodiphenylmethane. The system was automatically cleaned once more, the reactor was charged with 2-(dimethylamino)ethanol and 10 ml of toluene, and the bromodiphenylmethane was transferred to the reactor with three portions of toluene. The mixture was heated to reflux for 20 hours. After cooling below 30°C, the reaction was quenched with aqueous sodium hydroxide. The layers were separated, and the organic layer was extracted with 2 M aqueous hydrochloric acid three times. Equimolar aqueous sodium hydroxide was added to the combined aqueous layers, and the mixture was extracted with diethyl ether three times. The combined etheric layers were evaporated to dryness, yielding crude diphenhydramine free base. The jacketed filter module was then charged with etheric hydrochloric acid, and the crude free base was slowly transferred to the filter with three portions of diethyl ether. The precipitate formed was collected by filtration, dried under a stream of argon, and recrystallized from isopropanol, yielding pure diphenhydramine hydrochloride as white crystalline powder.

Synthesis of rufinamide

The reactor was charged manually with 2,6-difluorobenzyl bromide. An aqueous solution of sodium azide was added to the reactor, and the mixture was heated to 75°C for 12 hours and subsequently transferred to the jacketed filter module. Neat methyl propiolate was added, and the mixture was heated to 65°C for 4 hours. An aqueous solution of ammonia was subsequently added, and the mixture was held at 75°C for an additional 12 hours, precipitating the target compound. Filtration followed by three aqueous washes yielded pure rufinamide as white crystalline powder.

Synthesis of sildenafil

The reactor was automatically charged with chlorosulfonic acid, thionyl chloride, and molten ethoxybenzoic acid. The mixture was stirred at 15°C for 30 min and then at room temperature for an additional 12 hours. Subsequently, the filtration module was charged with water and cooled to 0°C. The reaction mixture was slowly dripped into the water, quenching the excess thionyl chloride and chlorosulfonic acid and precipitating the product. The supernatant solution was removed, and the precipitate was washed with cold water, yielding 5-chlorosulfonyl-2-ethoxybenzoic acid as white powder. The wet solid remaining in the filter module was subsequently slurried in cold water, and *N*-methylpiperazine was added slowly. After 5 min, crystallization was initiated by adding a slurry of a small amount of product. The solid was collected by filtration, washed with cold water, and dried under a stream of argon at 50°C, yielding 2-ethoxy-5-(4-methyl-1-piperazinesulfonyl)-benzoic acid as a white powder. The dry carboxylic acid was slurried in dichloromethane and cooled to 5°C. Thionyl chloride and a catalytic amount of dimethylformamide were added, and the mixture was stirred for 5 hours at 25°C. Subsequently, the reactor module was charged with a solution of

Downloaded from http://science.sciencemag.org/ on January 14, 2019

4-amino-1-methyl-3-*n*-propyl-1*H*-pyrazole-5-carboxamide in dichloromethane and triethylamine and cooled to 10°C. The crude acid chloride solution was pumped from the filter module to the reactor, and the mixture was stirred for 16 hours at 25°C. After the reaction was quenched with water, the layers were separated, and the organic layer was dried over activated molecular sieves and evaporated to dryness, yielding 4-[2-ethoxy-5-(4-methyl-1-piperazinylsulfonyl)-benzamido]-1-methyl-3-propyl-1*H*-pyrazole-5-carboxamide as an off-white solid. For the subsequent cyclization, the crude amide was transferred back to the reactor by dissolving it with a solution of potassium *tert*-butoxide in *tert*-butanol, and the mixture was heated at reflux for 8 hours. After cooling to 10°C, the reaction was quenched with water, and the solution was transferred to the filter module. To induce precipitation of the sildenafil, the mixture was neutralized with aqueous hydrochloric acid. After filtration, the solid was washed with water and dried under a stream of argon at 50°C, yielding the sildenafil as white crystalline powder.

REFERENCES AND NOTES

1. J. Li *et al*., Synthesis of many different types of organic small molecules using one automated process. *Science* **347**, 1221–1226 (2015). doi: 10.1126/science.aaa5414; pmid: 25766227
2. P. J. Kitson *et al*., Digitization of multistep organic synthesis in reactionware for on-demand pharmaceuticals. *Science* **359**, 314–319 (2018). doi: 10.1126/science.aao3466; pmid: 29348235
3. C. Rougeot, H. Situ, B. H. Cao, V. Vlachos, J. E. Hein, Automated reaction progress monitoring of heterogeneous reactions: Crystallization-induced stereoselectivity in amine-catalyzed aldol reactions. *React. Chem. Eng.* **2**, 226–231 (2017). doi: 10.1039/C6RE00211K
4. F. Häse, L. M. Roch, C. Kreisbeck, A. Aspuru-Guzik, Phoenics: A Bayesian optimizer for chemistry. *ACS Cent. Sci.* **4**, 1134–1145 (2018). doi: 10.1021/acscentsci.8b00307; pmid: 30276246
5. A. Adamo *et al*., On-demand continuous-flow production of pharmaceuticals in a compact, reconfigurable system. *Science* **352**, 61–67 (2016). doi: 10.1126/science.aaf1337; pmid: 27034366
6. A. G. Godfrey, T. Masquelin, H. Hemmerle, A remote-controlled adaptive medchem lab: An innovative approach to enable drug discovery in the 21st century. *Drug Discov. Today* **18**, 795–802 (2013). doi: 10.1016/j.drudis.2013.03.001; pmid: 23523957
7. R. B. Merrifield, Automated synthesis of peptides. *Science* **150**, 178–185 (1965). doi: 10.1126/science.150.3693.178; pmid: 5319951
8. G. Alvarado-Urbina *et al*., Automated synthesis of gene fragments. *Science* **214**, 270–274 (1981). doi: 10.1126/science.6169150; pmid: 6169150
9. M. B. Plutschack, B. Pieber, K. Gilmore, P. H. Seeberger, The hitchhiker's guide to flow chemistry. *Chem. Rev.* **117**, 11796–11893 (2017). doi: 10.1021/acs.chemrev.7b00183; pmid: 28570059
10. O. J. Plante, E. R. Palmacci, P. H. Seeberger, Automated solid-phase synthesis of oligosaccharides. *Science* **291**, 1523–1527 (2001). doi: 10.1126/science.1057324; pmid: 11222853
11. P. D. Karp, Pathway databases: A case study in computational symbolic theories. *Science* **293**, 2040–2044 (2001). doi: 10.1126/science.1064621; pmid: 11557880
12. M. Baker, 1,500 scientists lift the lid on reproducibility. *Nature* **533**, 452–454 (2016). doi: 10.1038/533452a; pmid: 27225100
13. GraphML, http://graphml.graphdrawing.org/ [accessed 19 October 2018].
14. D. G. Brown, J. Boström, Analysis of past and present synthetic methodologies on medicinal chemistry: Where have all the new reactions gone? *J. Med. Chem.* **59**, 4443–4458 (2016). doi: 10.1021/acs.jmedchem.5b01409; pmid: 26571338
15. A. C. Bédard *et al*., Reconfigurable system for automated optimization of diverse chemical reactions. *Science* **361**, 1220–1225 (2018). doi: 10.1126/science.aat0650; pmid: 30237351
16. A. Adamo, P. L. Heider, N. Weeranoppanant, K. F. Jensen, Membrane-based, liquid-liquid separator with integrated pressure control. *Ind. Eng. Chem. Res.* **52**, 10802–10808 (2013). doi: 10.1021/ie401180t
17. M. O'Brien, P. Koos, D. L. Browne, S. V. Ley, A prototype continuous-flow liquid-liquid extraction system using open-source technology. *Org. Biomol. Chem.* **10**, 7031–7036 (2012). doi: 10.1039/c2ob25912e; pmid: 22858870
18. S. Eppel, T. Kachman, Computer vision–based recognition of liquid surfaces and phase boundaries in transparent vessels, with emphasis on chemistry applications. arXiv:1404.7174 [cs.CV] (6 November 2014).
19. D. J. Dale *et al*., The chemical development of the commercial route to sildenafil: A case history. *Org. Process Res. Dev.* **4**, 17–22 (2000). doi: 10.1021/op9900683
20. A. Ahmadi, M. Khalili, R. Hajikhani, N. Safari, B. Nahri-Niknafs, Anti-inflammatory effects of two new methyl and morpholine derivatives of diphenhydramine on rats. *Med. Chem. Res.* **21**, 3532–3540 (2011). doi: 10.1007/s00044-011-9891-y
21. R. D. Padmaja, K. Chanda, A short review on synthetic advances toward the synthesis of rufinamide, an antiepileptic drug. *Org. Process Res. Dev.* **22**, 457–466 (2018). doi: 10.1021/acs.oprd.7b00373
22. The total cost of the parts for robotic modules, including nonstandard glassware, is less than $10,000 per system, but this rises to $30,000 if the stirrers, evaporator, and chiller system are included, although these components might reasonably be expected to be found in most well-equipped synthesis laboratories.
23. G. Keenan, croningp/ChemputerSoftware: Chemputer first release, Zenodo (2018). doi: 10.5281/zenodo.1481731
24. Chemify; www.chemify.org.

ACKNOWLEDGMENTS

We thank M. Craven for help with the XDL development and H. Mehr, S. Zalesskiy, M. Symes, and R. Hartley for comments on the manuscript. **Funding:** We gratefully acknowledge financial support from the EPSRC (grants EP/H024107/1, EP/J015156/1, EP/K021966/1, EP/L015668/1, and EP/L023652/1) and the ERC (project 670467 SMART-POM). **Author contributions:** L.C. conceived the initial concept design approach and coordinated the team. P.J.K., G.A.-C., G.K., and L.C. developed the abstraction. L.C., T.H., and S.G. developed the fluidic backbone and initial versions of the pumps and valves, including the electronics and firmware. T.H. outlined the initial XDL with L.C. S.S. built the final versions of the rig, developed ChASM, and conducted the syntheses with help from J.W., A.A., and J.M.G. D.A. helped with the sildenafil automation. G.K. and G.A.-C. developed the software system with S.S. L.C. and S.S. wrote the manuscript. **Competing interests:** L.C. is the founder and director of DeepMatter Group PLC (deepmatter.io), which aims to digitize chemistry. **Data and materials availability:** All the software to run the Chemputer to synthesize the compounds described herein has been deposited in Zenodo (*23*).

SUPPLEMENTARY MATERIALS

www.sciencemag.org/content/363/6423/eaav2211/suppl/DC1
Materials and Methods
Supplementary Text
Figs. S1 to S58
Movies S1 to S3
Data S1 and S2

30 August 2018; accepted 12 November 2018
Published online 29 November 2018
10.1126/science.aav2211

Downloaded from http://science.sciencemag.org/ on January 14, 2019

REPORT

MEMBRANES

Complete steric exclusion of ions and proton transport through confined monolayer water

K. Gopinadhan[1,2,3]*, S. Hu[2]*, A. Esfandiar[1,4], M. Lozada-Hidalgo[1], F. C. Wang[1,5], Q. Yang[2,6], A. V. Tyurnina[2,7], A. Keerthi[1,2], B. Radha[1,2]†, A. K. Geim[1,2]†

It has long been an aspirational goal to create artificial structures that allow fast permeation of water but reject even the smallest hydrated ions, replicating the feat achieved by nature in protein channels (e.g., aquaporins). Despite recent progress in creating nanoscale pores and capillaries, these structures still remain distinctly larger than protein channels. We report capillaries made by effectively extracting one atomic plane from bulk crystals, which leaves a two-dimensional slit of a few angstroms in height. Water moves through these capillaries with little resistance, whereas no permeation could be detected even for such small ions as Na^+ and Cl^-. Only protons (H^+) can diffuse through monolayer water inside the capillaries. These observations improve our understanding of molecular transport at the atomic scale.

Protein channels use a large number of separation mechanisms, including steric (size) exclusion and electrostatic repulsion, to remove salts from water and distinguish between different ions (*1*). It is believed that angstrom-scale constrictions within these channels (*2*, *3*) play a key role in steric rejection of ions with the smallest hydration diameters $D_H \approx 7$ Å, typically present in biofluids and seawater (*1*, *4*). Such small constrictions are particularly difficult to replicate artificially because of the lack of fabrication tools capable of operating with such precision and, especially, because the surface roughness of conventional materials is much larger than the required angstrom scale (*5*). Nonetheless, several artificial systems with nanometer and subnanometer dimensions were recently demonstrated (*5*–*9*), including narrow carbon and boron nitride nanotubes (*9*–*11*), graphene oxide laminates (*12*, *13*), and atomic-scale pores in graphene and MoS_2 monolayers (*7*, *8*, *14*). The resulting devices exhibited high selectivity with respect to certain groups of ions [for example, they blocked large ions but allowed small ones (*13*) or rejected anions but allowed cations and vice versa (*6*, *7*, *9*)]. Most recently, van der Waals assembly of two-dimensional (2D) crystals (*15*) was used to make slitlike channels of several angstroms in height (*16*, *17*). They were atomically smooth and chemically inert and exhibited little ($\leq 10^{-4}$ C cm^{-2}) surface charge (*17*). The channels allowed water permeation (*16*) and blocked large ions, with a complete cutoff for diameters larger than ~10 Å (*17*). Small ions (for example, those in seawater with typical D_H of ~7 Å) still permeated through the channels with little hindrance, indicating that an angstrom-scale confinement comparable to that in aquaporins (*2*, *3*) is essential for steric exclusion of small-diameter ions. In this Report, we describe 2D channels with height h of ~3.4 Å (*18*), half the size of the smallest hydrated ions (K^+ and Cl^- with $D_H \approx 6.6$ Å) (*1*, *19*) but sufficiently large to allow water inside (effective size of water molecules is ~2.8 Å). The achieved confinement matches the size of protein channel constrictions, a critical factor in their steric selectivity (*2*, *3*).

Our devices were fabricated using the van der Waals assembly described previously (*16*, *17*). In brief, two thin (~50 and 200 nm) atomically flat monocrystals were obtained by cleaving bulk graphite or hexagonal boron nitride (hBN) and placed on top of each other, with stripes of

[1]School of Physics and Astronomy, University of Manchester, Manchester M13 9PL, UK. [2]National Graphene Institute, University of Manchester, Manchester M13 9PL, UK. [3]Department of Physics, Indian Institute of Technology Gandhinagar, Gujarat 382355, India. [4]Department of Physics, Sharif University of Technology, P.O. Box 11155-9161, Tehran, Iran. [5]Chinese Academy of Sciences Key Laboratory of Mechanical Behavior and Design of Materials, Department of Modern Mechanics, University of Science and Technology of China, Hefei, Anhui 230027, China. [6]Key Laboratory of Advanced Technologies of Materials, School of Materials Science and Engineering, Southwest Jiaotong University, Chengdu, Sichuan 610031, China. [7]Skolkovo Institute of Science and Technology, Nobel St. 3, 143026 Moscow, Russia.
*These authors contributed equally to this work.
†Corresponding author. Email: geim@manchester.ac.uk (A.K.G.); radha.boya@manchester.ac.uk (B.R.)

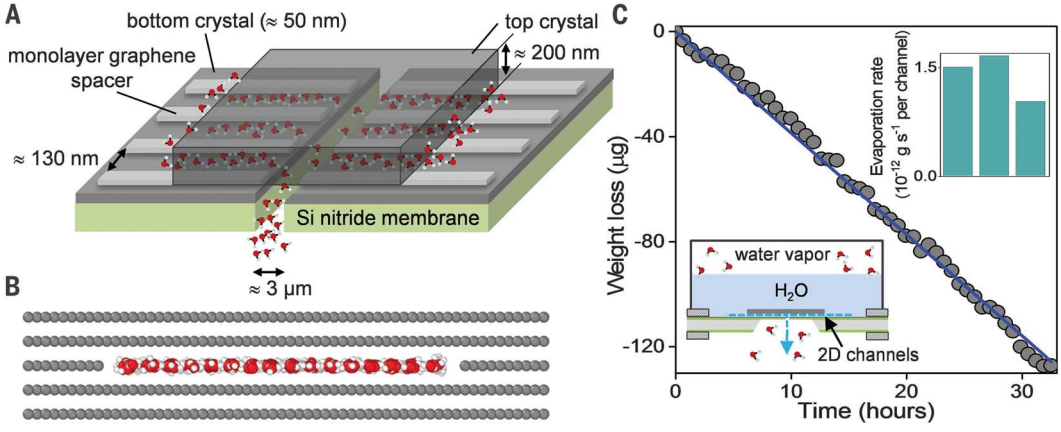


Fig. 1. Water flow through one-atom-high capillaries. (**A**) Schematic of our fluidic devices. Top and bottom layers were either graphite or hBN crystals, and monolayer graphene was used as the spacers. The trilayer assembly was supported by a free-standing membrane with a rectangular opening. (**B**) There is space for only one monolayer of water inside such 2D cavities, as indicated by MD simulations (*27*, *28*). (**C**) Weight loss due to water permeation and its subsequent evaporation (1500 graphite/graphene/graphite channels with L = 2 μm). (Top inset) Evaporation rates for three such channel devices. The indicated rates are per 1 μm channel length. (Bottom inset) Gravimetry setup. The detection limit of our gravimetry (~10^{-13} g s^{-1}) is comparable to that of helium mass spectrometers and is much lower than that achieved by mass spectrometric analysis of other gases and vapors diffusing through similar devices (*16*).

Downloaded from http://science.sciencemag.org/ on January 13, 2019

graphene serving as spacers between the two crystals (Fig. 1A). The resulting trilayer assembly can be viewed as a pair of edge dislocations connected by a 2D empty space. This space can accommodate only one atomic layer of water (Fig. 1B). The 2D channels were designed (*16*, *17*) to have a width $w \approx 130$ nm and length L of several micrometers. We primarily used many channels in parallel (≥100) to increase measurement sensitivity. The resulting structures were assembled on top of a silicon nitride membrane that separated two isolated containers so that 2D channels provided the only molecular pathway between the containers (Fig. 1A) [for further details, see the supplementary materials (*18*) and fig. S1]. The principal difference with the capillaries reported earlier (*16*, *17*) is the use of monolayer graphene as spacers. Previously, water permeation could be discerned only for capillaries with thicker spacers ($h \geq 6.7$ Å), and molecular dynamics (MD) simulations also suggested that smaller 2D cavities should collapse because of van der Waals attraction between the opposite walls (*16*). However, further MD analysis (*18*) has shown that water molecules inside the slits can act as a support and prevent the collapse of even one-atom-high slits with $h \approx 3.4$ Å (fig. S2), which agrees with our experimental results (described below) and is corroborated by Raman spectroscopy that shows liquid water inside one-atom-high channels (fig. S3). To detect minute amounts of water that can flow through them, we also needed to introduce the following improvements: (i) a 10-fold increase in the number n of channels probed in parallel, (ii) the use of thicker top crystals to avoid their sagging (*16*), and (iii) the clipping of channels' entries (Fig. 1A) by plasma etching to remove their possible blockage by thin edges of the top crystal (*18*).

The bottom inset of Fig. 1C shows a schematic of the gravimetry setup (*16*). The device containing 2D channels with graphite walls was sealed in a miniature container filled with water, and the weight loss was recorded as a function of time. For reference, we studied devices made in exactly the same way but without graphene spacers (*16*, *18*). No evaporation could be detected for these reference devices, even after many days of measurements. In contrast, the monolayer channel devices exhibited a weight loss evolving linearly in time (Fig. 1C). The slope of this curve translates directly into a water permeation rate of ~1.5×10^{-12} g/s per micrometer channel length per channel. Three such graphene devices were studied, all showing similar rates (top inset of Fig. 1C). The water permeation rate noted above is ~5% of the rates reported previously for devices with bilayer spacers ($h \approx 6.7$ Å) and is below the detection limit achieved in (*16*). The difference in water evaporation rates through mono- and bilayer capillaries is larger than a factor of 4, which is expected from the h^2 dependence for our geometry (*16*, *18*). The additional flow reduction (by another factor of 2) is perhaps not surprising because water becomes increasingly more viscous under strong confinement (*18*, *20*, *21*).

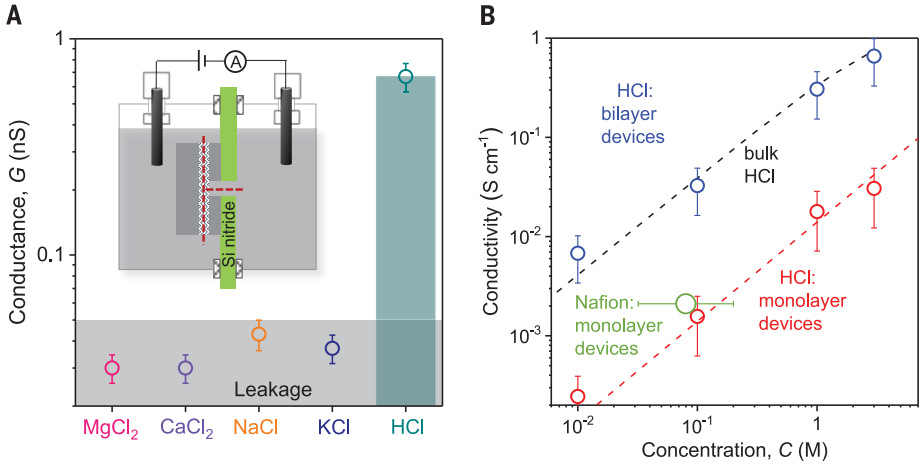


Fig. 2. Steric exclusion of salts from one-atom-high capillaries. (**A**) Conductance observed for one of our monolayer devices ($n = 100$; $L = 10$ μm; hBN/graphene/hBN) using the specified 1 M solutions (symbols). The values of G were extracted from the slopes of I-V curves over a voltage interval of ±30 mV. The error bars show standard deviations (SD) in determining G from the curves. The gray area indicates our typical detection limit given by leakage currents, as found using both reference devices and blank Si nitride membranes. Several other common salts (*17*) were tested and exhibited no discernable conductance. In total, seven devices with monolayer spacers were found to demonstrate the same behavior. For the case of HCl, G was well above our detection limit, although it varied between different devices from 0.1 to 0.64 nS (fig. S4B), yielding an average $G = 0.32 \pm 0.2$ nS. (Inset) Schematic of our measurement setup. (**B**) Conductivity σ calculated from the measured G for different HCl concentrations for mono- and bilayer capillaries [red and blue symbols, respectively; red is for the same device as in (A)]. Red line, best linear fit; black curve, literature values for bulk HCl; green symbol, σ for monolayer devices using Nafion (instead of HCl) as proton reservoirs. The horizontal error bar indicates the uncertainty in determining the proton concentration in Nafion films (*25*).

Having established that water can flow through our one-atom-high channels, we investigated their permeability with respect to ions. In these experiments, the devices separated two reservoirs filled with chloride solutions (inset of Fig. 2A). The electrical conductance G between the reservoirs was measured using chlorinated Ag/AgCl electrodes or calibrated reference electrodes (*17*) (fig. S4). First, we tested ion conductance using chloride solutions in 1 M concentrations. Within our detection limit of ~50 pS given by parasitic leakage currents of ~5 pA, no conductance could be detected for any salt (some of which are listed in Fig. 2A). This finding is in contrast to the behavior observed for capillaries with thicker spacers including bilayers (*17*). The latter ($h \approx 6.7$ Å) exhibited G of the order of 10^{-8} S (1 S = 1 A/V)—that is, three orders of magnitude above our detection limit—in agreement with the conductance expected from the known conductivity σ of the 1 M chloride solutions for the given length L and cross-sectional area $n \times h \times w$. The measurements for bilayer devices were reported previously (*17*) but, for consistency, were repeated in this work. Despite no discernable ion transport through monolayer capillaries ($h \approx 3.4$ Å), they unexpectedly showed a substantial conductance if we used HCl rather than salt solutions (Fig. 2A and fig. S4). The measured σ for the acid varied approximately linearly with its concentration C as expected (Fig. 2B), but the absolute values were 3 to 10% of the value for bulk HCl (black curve in Fig. 2B). This is again in contrast to the behavior found for bilayer devices ($h \approx 6.7$ Å), which exhibited the conductance that agreed well with that of bulk HCl in the given geometry (Fig. 2B).

The fact that no ion currents could be detected for salt solutions indicates steric rejection of all hydrated ions from the one-atom-high channels. It was previously reported (*17*) that ion permeation remained practically unaffected if $D_H \leq h$ but was sharply suppressed (by a factor of 15) if D_H exceeded h by 50%. In our case, $h \approx 3.4$ Å is half the size of D_H of the tested ions, and the extrapolation of the previously observed cutoff (quicker than exponential) (*17*) suggests that the monolayer capillaries should completely prohibit transport of any hydrated ions. This conclusion does not contradict the finite G observed for HCl because of a high concentration of protons in the latter case. They can diffuse through monolayer water present inside the capillaries, not as ions dressed in large hydration shells (hydronium) but more like subatomic particles jumping between water molecules, according to the Grotthuss mechanism (*22*, *23*).

To corroborate the suggested proton transport scenario, we used the same ion measurement setup but different HCl concentrations in the two reservoirs. The concentration gradient drives both H^+ and Cl^- in the same direction, from the high concentration (C_h) reservoir to the low concentration (C_l) one, and the sign of the electric current I at zero applied voltage V indicates whether most carriers are H^+ or Cl^- (*1*, *17*). Examples of I-V characteristics observed for our monolayer devices are shown in Fig. 3A. One

Downloaded from http://science.sciencemag.org/ on January 13, 2019

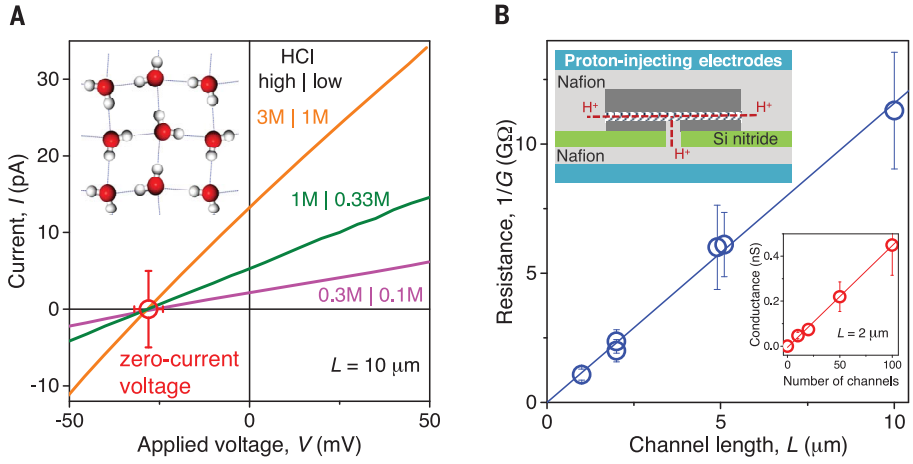


Fig. 3. Proton transport through monolayer water inside 2D channels. (**A**) *I-V* curves for different concentrations of HCl in the two reservoirs connected by monolayer capillaries. The same concentration gradient Δ was used for all curves. The red symbol denotes voltages at zero *I*. The vertical bar indicates our maximum leakage currents, whereas the horizontal bar represents the statistical error in determining V_0 by using measurements for several monolayer devices. (Inset) Square-like ice is one of the possible states of water inside one-atom-high channels at room temperature, as expected from MD simulations (*29*, *30*). (**B**) Proton transport using Nafion as proton reservoirs. (Top inset) Schematic of our Nafion devices (hBN/graphene/hBN; n = 100). Blue symbols, resistance as a function of channel length. (Bottom inset) $G(n)$ for several Nafion devices with L = 2 μm. Red and blue lines, best linear fits. Error bars indicate SD, as in Fig. 2.

can see that the current at zero V was always positive, which indicates that protons predominantly drive the system toward the equilibrium in an effort to equalize proton concentrations in the two reservoirs. Moreover, for the chosen gradient $\Delta = C_h/C_l = 3$, the *I-V* curves intersect the current axis at the same $V_0 = 28 \pm 4$ mV regardless of the C_l and C_h values. The voltage that compensates the currents caused by concentration gradients is described by the Nernst equation (*24*)

$$V_0 = (t_H - t_{Cl})(kT/e)\ln(\Delta)$$

where $t_{H,Cl} \in [0,1]$ are the so-called transport numbers for H^+ and Cl^-, k is the Boltzmann constant, T is the temperature (295 ± 3 K in our experiments), and e is the elementary charge. For $\Delta = 3$ and $V_0 \approx 28$ mV, the formula yields $t_H - t_{Cl} \approx 1$, which can be satisfied only if $t_H \approx 1$ and $t_{Cl} \approx 0$. This means that only protons diffuse through our monolayer devices, whereas Cl^- ions are rejected, in agreement with the conclusions reached from the experiments of Fig. 2.

Proton transport can be probed more directly using Nafion instead of HCl (*25*). Nafion is a polymer in which protons are the only charge carriers and the counterions (SO_3^-) are fixed within the polymer matrix (*26*). Using the approach described in (*25*), we coated our devices with Nafion from both sides and used hydrogenated Pt films as proton-injecting electrodes to convert electric current into a proton flow (top inset of Fig. 3B). For electrical measurements, these devices were placed in a hydrogen atmosphere at 100% relative humidity to ensure high Nafion proton conductivity (*25*). In comparison with our ion transport measurements, the Nafion devices were much more robust, sustained higher I values (*18*), exhibited smaller leakage currents (~1 pA), and showed little variations between similar devices. Because polymer molecules are much larger than h, they cannot enter 2D channels; therefore, Nafion served in our experiments only as a reservoir providing protons for the stationary monolayer of water inside the channels. Figure 3B shows examples of the electrical resistance $R = 1/G$ exhibited by our devices. The resistance varied linearly with L and $1/n$, as expected. Reference devices with no channels showed negligible conductance (~10^{-11} S; error bars in Fig. 3B). One can see that R accurately extrapolates to zero in the limit of zero L (blue curve in Fig. 3B), which yields that protons experience little barrier for entry into the capillaries. The experiments yield $\sigma \approx 2.1 \pm 0.2$ mS cm^{-1}, whereas the proton concentration in Nafion and, hence, inside the 2D water can be estimated from the conductivity of our Nafion coating. It was found to be ~70 mM but with a relatively large uncertainty, as the proton concentration is sensitive to details of Nafion preparation (*25*). The resulting σ (green symbol in Fig. 2B) agrees well with that found in the HCl measurements, which further substantiates our conclusion of proton-only transport through one-atom-high channels.

It is instructive to estimate the diffusion constant d_p of protons within the monolayer water that fills the capillaries. This quantity is given by $d_p = \sigma(kT/eFC_p) \approx 4 \times 10^{-6}$ cm^2 s^{-1}, where C_p is the proton concentration in HCl or Nafion, and F is the Faraday constant (*18*). This value is an order of magnitude smaller than $d_p \approx 9 \times 10^{-5}$ cm^2 s^{-1} for bulk water (*4*, *23*), which is also apparent from the difference between the red and black curves in Fig. 2B, if one recalls that the conductivity of bulk HCl is ~80% dominated by protons (*1*). On the other hand, proton transport in 3D water is several times slower than that in 1D water inside subnanometer carbon nanotubes (*9*, *11*), which exhibited $d_p \approx 4 \times 10^{-4}$ cm^2 s^{-1}. The anomalously slow proton diffusion in 2D and the nonmonotonic dependence of d_p on dimensionality seem puzzling (d_p in 2D is much smaller than in both 1D and 3D) but are consistent with different hydrogen bonding for the three cases (*18*). Indeed, MD simulations suggest (*27*, *28*) that water under 2D confinement should become ordered (icelike) at room temperature (Fig. 3A). The ordered hydrogen bonding in 2D water should suppress rotation of water molecules with respect to 3D water, which is an essential but slowest step for proton transport, according to the Grotthuss mechanism (*22*, *23*). This is in contrast to 1D water that exhibits string-like hydrogen bonding, which arguably (*9*, *11*) can strongly enhance proton diffusion (fig. S5).

In summary, our one-atom-high cavities allow one monolayer of water inside but exclude all ionic species. This finding is in contrast to the behavior of the twice-as-large slits ($h \approx 6.7$ Å), which showed little effect on such small ions as Na^+ and Cl^- ($D_H \approx 7$ Å). The extreme steric exclusion for $h \approx 3.4$ Å is attributed to the fact that it is no longer possible for any ion to squeeze inside the slits by deforming their hydration shells. Protons are different in that they diffuse not as hydrated H^+ ions but follow the Grotthuss mechanism. The slow diffusion observed for protons in 2D water suggests that it probably forms a proton-ordered ice at room temperature, in agreement with MD simulations.

REFERENCES AND NOTES

1. B. Hille, *Ion Channels of Excitable Membranes* (Sinauer, ed. 3, 2001).
2. K. Murata *et al.*, *Nature* **407**, 599–605 (2000).
3. H. Chen *et al.*, *Biophys. J.* **92**, 46–60 (2007).
4. C. A. Wraight, *Biochim. Biophys. Acta* **1757**, 886–912 (2006).
5. R. B. Schoch, J. Han, P. Renaud, *Rev. Mod. Phys.* **80**, 839–883 (2008).
6. F. Fornasiero *et al.*, *Proc. Natl. Acad. Sci. U.S.A.* **105**, 17250–17255 (2008).
7. S. C. O'Hern *et al.*, *Nano Lett.* **14**, 1234–1241 (2014).
8. T. Jain *et al.*, *Nat. Nanotechnol.* **10**, 1053–1057 (2015).
9. R. H. Tunuguntla *et al.*, *Science* **357**, 792–796 (2017).
10. A. Siria *et al.*, *Nature* **494**, 455–458 (2013).
11. R. H. Tunuguntla, F. I. Allen, K. Kim, A. Belliveau, A. Noy, *Nat. Nanotechnol.* **11**, 639–644 (2016).
12. V. Saraswat *et al.*, *ACS Nano* **12**, 7855–7865 (2018).
13. L. Chen *et al.*, *Nature* **550**, 380–383 (2017).
14. J. Feng *et al.*, *Nat. Mater.* **15**, 850–855 (2016).
15. A. K. Geim, I. V. Grigorieva, *Nature* **499**, 419–425 (2013).
16. B. Radha *et al.*, *Nature* **538**, 222–225 (2016).
17. A. Esfandiar *et al.*, *Science* **358**, 511–513 (2017).
18. See supplementary materials.
19. B. Tansel, *Separ. Purif. Tech.* **86**, 119–126 (2012).
20. M. Neek-Amal, F. M. Peeters, I. V. Grigorieva, A. K. Geim, *ACS Nano* **10**, 3685–3692 (2016).
21. O. Björneholm *et al.*, *Chem. Rev.* **116**, 7698–7726 (2016).
22. D. Marx, M. E. Tuckerman, J. Hutter, M. Parrinello, *Nature* **397**, 601–604 (1999).
23. M. Chen *et al.*, *Nat. Chem.* **10**, 413–419 (2018).
24. F. Helfferich, *Ion Exchange* (McGraw-Hill, 1962).
25. S. Hu *et al.*, *Nature* **516**, 227–230 (2014).
26. K. A. Mauritz, R. B. Moore, *Chem. Rev.* **104**, 4535–4585 (2004).

Downloaded from http://science.sciencemag.org/ on January 13, 2019

27. G. Algara-Siller *et al.*, *Nature* **519**, 443–445 (2015).
28. Y. Zhu, F. Wang, J. Bai, X. C. Zeng, H. Wu, *ACS Nano* **9**, 12197–12204 (2015).
29. J. Chen, A. Zen, J. G. Brandenburg, D. Alfè, A. Michaelides, *Phys. Rev. B* **94**, 220102 (2016).
30. I. Strauss, H. Chan, P. Král, *J. Am. Chem. Soc.* **136**, 1170–1173 (2014).

ACKNOWLEDGMENTS

Funding: This work was supported by the Lloyd's Register Foundation, Graphene Flagship, European Research Council, and Royal Society. B.R. acknowledges a Royal Society University Research Fellowship; F.C.W. acknowledges the Strategic Priority Research Program of the Chinese Academy of Sciences (XDB22040402). **Author contributions:** A.K.G. proposed and directed the research with help from K.G. and B.R.; K.G., S.H., and M.L.-H. performed ion and proton transport measurements and their analysis; A.E., A.K., S.H., and B.R. fabricated the devices; A.K., B.R., and Q.Y. did gravimetric measurements and their analysis; A.E. and A.V.T. performed Raman spectroscopy; F.C.W. carried out MD simulations with help of A.K.G.; and K.G., B.R., M.L.-H., and A.K.G. wrote the manuscript. All authors contributed to discussions. **Competing interests:** We declare no competing interests. **Data and materials availability:** All data are available in the main text and the supplementary materials. Additional information is available on reasonable request from the authors, according to their contributions.

SUPPLEMENTARY MATERIALS

www.sciencemag.org/content/363/6423/145/suppl/DC1
Materials and Methods
Supplementary Text
Figs. S1 to S5
References (*31*–*55*)

5 July 2018; accepted 23 November 2018
10.1126/science.aau6771

Downloaded from http://science.sciencemag.org/ on January 13, 2019

TOPOLOGICAL OPTICS

Observation of chiral zero mode in inhomogeneous three-dimensional Weyl metamaterials

Hongwei Jia[1,2], Ruixing Zhang[3,4], Wenlong Gao[1], Qinghua Guo[1,2], Biao Yang[1], Jing Hu[1], Yangang Bi[1], Yuanjiang Xiang[2]*, Chaoxing Liu[3]*, Shuang Zhang[1]*

Owing to the chirality of Weyl nodes, the Weyl systems can support one-way chiral zero modes under a strong magnetic field, which leads to nonconservation of chiral currents—the so-called chiral anomaly. Although promising for robust transport of optical information, the zero chiral bulk modes have not been observed in photonics. Here we design an inhomogeneous Weyl metamaterial in which a gauge field is generated for the Weyl nodes by engineering the individual unit cells. We experimentally confirm the presence of the gauge field and observe the zero-order chiral Landau level with one-way propagation. Without breaking the time-reversal symmetry, our system provides a route for designing an artificial magnetic field in three-dimensional photonic Weyl systems and may have potential for device applications in photonics.

Three-dimensional (3D) Dirac and Weyl (*1*–*12*) semimetals are topological phases of matter that support relativistic quasiparticles near the degeneracy points between two bands. Weyl points are two-fold band crossings with topological charges (or chiralities) (*3*, *4*), whose existence requires breaking time-reversal or inversion symmetry of the Dirac system (*5*, *13*). As a Weyl point has a codimension $3 = 3 - 0$, it is highly robust and cannot be eliminated unless two partners with opposite chiralities annihilate each other in momentum space (*3*, *14*). Owing to the band crossings that result from accidental degeneracy, the positions of Weyl points can be designed by introducing structural change in the unit cells (*14*). These properties provide a good opportunity for engineering gauge fields (artificial magnetic field) by designing the spatially dependent displacement of Weyl points in the momentum space.

Mechanical strain has been introduced into crystals to generate gauge field, especially in 2D systems. Within the tight binding approximation, the strain tensor can be written in the form of the vector potential. Artificial magnetic field has been generated in 2D crystal lattice by strains (*15*–*20*). However, in 3D bulk crystals, artificial magnetic fields cannot be generated readily because these systems are not flexible. Thus, research has concentrated on geometries such as films or wires to explore relevant effects induced by strains (*21*). Because of this limitation, artificially induced gauge fields have only been realized in 2D systems. Artificial magnetic field in 3D Weyl systems is expected to exhibit additional intriguing properties, such as chiral transport of Weyl fermions.

In high-energy physics, the chiral anomaly describes a phenomenon in which the conservation law of the chirality (left-handed or right-handed) for the particles or waves is broken down when external electric and magnetic fields are applied in parallel in 3D Weyl systems (*22*). It was proposed that the chiral transport may be observed in crystals that support Weyl fermions (*23*). By applying an ordinary (*24*–*26*) or an artificial magnetic field (e.g., external strain) (*21*, *27*, *28*) to a Dirac or Weyl system, Dirac types of Landau levels can be formed. In particular, a special type of zeroth Landau level is expected to propagate only in the chiral (left or right) direction that is determined by the chirality of the corresponding Weyl points and the magnetic field direction. The presence of chiral zeroth Landau levels in Dirac and Weyl systems is the physical origin of chiral transport, which has been experimentally tested through the negative magnetoresistance in electronic systems (*24*, *29*, *30*). Recently, various 3D electronic (*1*, *3*, *4*) and photonic systems (*2*, *6*–*12*) that support Dirac or Weyl degeneracies were discovered, providing a platform for experimentally detecting chiral zeroth Landau levels. However, the photonic counterpart has not been explored yet.

We experimentally realize an artificial magnetic field by designing inhomogeneous photonic structures based on the recently discovered ideal Weyl metamaterial (*8*). To engineer the photonic gauge field in 3D Weyl metamaterial, we must spatially vary the location of the Weyl points in momentum space. The designed metamaterial has a hexahedron unit cell (3 mm by 3 mm by 4.5 mm) (Fig. 1A), and each unit cell consists of a saddle-shaped connective metallic coil. The structure possesses four Weyl degeneracy points on the $k_z = 0$ plane (*8*), with k_z being the crystal wave vector. Here, through elaborate design of each individual unit cell at different locations, we introduce adiabatic variation of the unit cell structure to realize fine control over the locations of the Weyl points in the momentum space, meanwhile keeping the frequency of the Weyl points unchanged (Fig. 1A). The current distribution in the saddle-shaped coil can be solved with the resonant circuit model. Using the effective medium approach (*31*), the constitutive parameters can be obtained [see section 4 in (*32*)]. Specifically, the angle θ causes the angular shift of the Weyl points about the Γ point [see section 5 and fig. S3 in (*32*)], whereas the offset d between the metal strip and the center of the via hole is carefully tuned to maintain the Weyl frequency.

The metamaterial consists of metallic coils with spatially variant rotational angles [Fig. 1B, fig. S4, and section 6 in (*32*) for the whole structure], with a uniform angular step $\Delta\theta = 0.2°$ between adjacent unit cells along the x direction, while the translational symmetry in the y and z directions are maintained. This leads to a linear relation $\theta = ax$, with the coefficient $a = -1.1636$ rad/m. The metamaterial has 101 unit cells in the x direction, so that the rotational angle θ ranges from 10° to −10° from one end to the other. The offset parameter d has been adapted to ensure that the Weyl points are located at the same frequency everywhere in the structure. To confirm the positions of the Weyl points in the momentum space, the band structure is calculated with CST Microwave Studio (Fig. 1C, for $\theta = 0$). The system supports four type I Weyl points (Q1 to Q4). In the vicinity of each Weyl point, the effective Hamiltonian can be written as (*4*)

$$H_{\mathrm{W}} = \mathbf{w}\cdot(\mathbf{k}-\mathbf{k}_0^{\mathrm{W}})\sigma_0 + \sum_{i,j=x,y,z} v_{ij}(k_i - k_{0,i}^{\mathrm{W}})\sigma_j \qquad (1)$$

where σ_j are the Pauli matrices, σ_0 is the 2-by-2 identity, v_{ij} is the element of an anisotropic velocity tensor, $\mathbf{w}$ is a velocity vector that tilts the Weyl cone, $\mathbf{k}$ is the wave vector, and $\mathbf{k}_0^{\mathrm{W}}$ denotes the location of the Weyl point in the momentum space. Here, the first term with the identity σ_0 is introduced into the Hamiltonian to describe the tilt of the cone-like dispersion near the degeneracy point (Fig. 1C). By rotating the metallic coil with a small angle θ, the four Weyl points rotate the same angle θ around the k_z axis simultaneously, leading to a displacement of the position of the Weyl point (see Fig. 1D, taking the Weyl point Q1 in Fig. 1C as an example) $\Delta k_x^{\mathrm{W}} \approx \theta k_0^{\mathrm{W}}/\sqrt{2}$, $\Delta k_y^{\mathrm{W}} \approx -\theta k_0^{\mathrm{W}}/\sqrt{2}$. The changes of velocity components in the effective Hamiltonian are almost negligible if θ is small [section 7 and table S2 in (*32*)]. One can simply derive a new Hamiltonian that characterizes the overall system, $H_{\mathrm{W}} \approx \mathbf{w}\cdot(\mathbf{k}-\mathbf{k}_0^{\mathrm{W}}-\mathbf{A})\sigma_0 + \sum v_{ij}(k_i - k_{0i}^{\mathrm{W}} - A_i)\sigma_j$, where $\mathbf{A}$ is the gauge field. Because θ is a linear function of the spatial coordinate x, one can approximately define the gauge field as the position shift of the Weyl point

[1]School of Physics and Astronomy, University of Birmingham, Birmingham B15 2TT, UK. [2]International Collaborative Laboratory of 2D Materials for Optoelectronic Science and Technology of Ministry of Education, College of Optoelectronic Engineering, Shenzhen University, Shenzhen 518060, China. [3]Department of Physics, The Pennsylvania State University, University Park, PA 16802-6300, USA. [4]Condensed Matter Theory Center and Joint Quantum Institute, Department of Physics, University of Maryland, College Park, MD 20742, USA.
***Corresponding author. Email: yjxiang@szu.edu.cn (Y.X.); cxl56@psu.edu (C.L.); s.zhang@bham.ac.uk (S.Z.)**

Downloaded from http://science.sciencemag.org/ on January 10, 2019

$\mathbf{A} = \Delta\mathbf{k}^{W} \approx [ax k_0^W/\sqrt{2}, -ax k_0^W/\sqrt{2}, 0]^T$, where T denotes matrix transpose. The artificial magnetic field can thus be obtained by $\mathbf{B} = \nabla \times \mathbf{A}$ to be $\mathbf{B} = [0, 0, -ak_0^W/\sqrt{2}]^T$.

To confirm the existence of the gauge field in the system, we used a near-field scanning technique (Fig. 2A), with the excitation point source located at five different positions along the x direction on the bottom surface (labeled 1 to 5). For each location of the excitation source, a detector scans across the overall top surface to obtain the electric field distribution. With a discrete Fourier transform, the distribution of field amplitude in the momentum space can be obtained. The detected signal intensity in the momentum space strongly relies on the source position, where the local eigen states are strongly excited. Thus, it is expected that with the increase of x, the four Weyl points are shifted in the momentum space following the blue arrows in Fig. 2B, with the direction of the generated artificial magnetic field for each Weyl point along the z or $-z$ direction, as indicated in the right panel of Fig. 2B. Figure 2C shows the experimental results corresponding to different source locations at a frequency of 13.48 GHz, which is higher than the Weyl frequency. This selected frequency is outside the energy gap between the two first-order Landau levels, so as to avoid the impact of chiral zero modes. It is observed that the four Weyl points rotate around the k_z axis at the four excitation locations, confirming the existence of the spatially dependent pseudo–gauge field. For comparison, we plot the corresponding numerical results of Weyl point positions in Fig. 2D, which are consistent with the experimental results. The gauge fields for each Weyl node are estimated on the basis of the experimental results, which show reasonably good agreement with the simulation result, which is about 477 m^{-2} [see section 8 in (*32*)].

Chiral zeroth Landau levels for relativistic particles can be generated in 3D Dirac or Weyl systems when an external or artificial magnetic field is applied (*21*, *25*–*28*). Our designed inhomogeneous Weyl metamaterial with artificial magnetic field provides an ideal platform for observing the photonic counterpart of chiral zero modes. The dispersions of Landau levels are expressed as [see section 9 in (*32*) for deriving details]

$$\omega_n = \begin{cases} w_z k_z \pm \frac{\sqrt{v_\perp^2 - w_\perp^2}}{v_\perp}\sqrt{v_z^2 k_z^2 + 2nBv_\perp\sqrt{v_\perp^2 - w_\perp^2}}, & n > 0 \\ [w_z + \chi^z \mathrm{sgn}(B)\frac{v_z\sqrt{v_\perp^2 - w_\perp^2}}{v_\perp}]k_z, & n = 0 \end{cases} \quad (2)$$

where $v_\perp$ and $w_\perp$ are rescaled velocities taking into account the tilt of the cone-like dispersion near the Weyl points (*32*), the tilt velocity in z direction $w_z = 0$ for our sample, B is the strength of the artificial magnetic field, n is an integer representing the order of the Landau level, and χ^z is the chirality of each Weyl point. The Landau levels are calculated by Eq. 2 and presented in Fig. 3, A and B. Determined by both the directions of the artificial magnetic fields (Fig. 2B) and the chiralities of Weyl points (table S5), the zeroth Landau levels

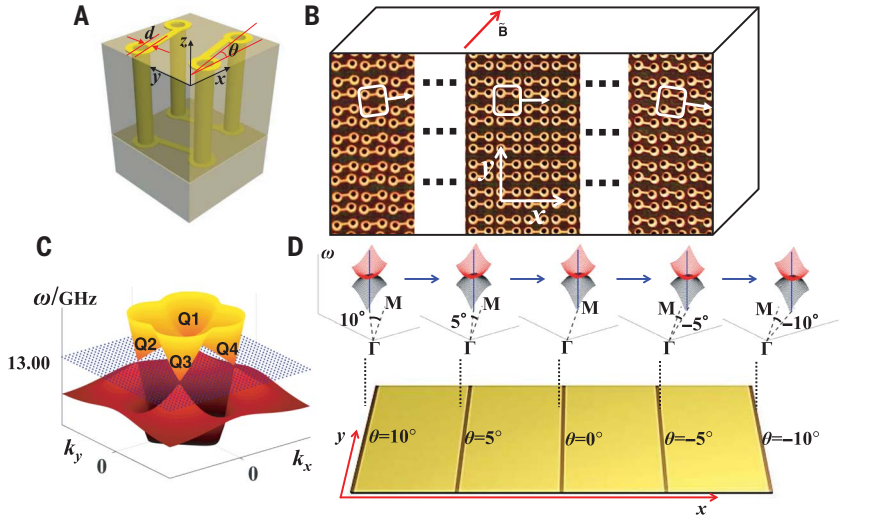


Fig. 1. Structure and dispersion of the inhomogeneous Weyl metamaterial. (**A**) Schematic of the saddle-shaped metallic coil, whose rotational angle θ and offset distance d between the center of the via hole and the metal strip can be varied to tune the positions and the frequency of the Weyl points. The metallic structure is embedded in a dielectric (dielectric constant 2.2) block with dimensions 3 mm by 3 mm by 4.5 mm. (**B**) Photograph of the top surface of the sample. The rotational angle θ has a linear gradient in x, with a variation from positive to negative with a uniform step $\Delta\theta = 0.2°$ between adjacent unit cells along the x direction. The sample has 101 unit cells in both the x and y directions, and the rotational angle θ ranges from 10° to −10°. The white squares with arrows indicate the orientation of metallic structures. $\vec{B}$, the direction of the artificial magnetic field. (**C**) Dispersion diagram of the Weyl metamaterial with θ = 0; four tilted type I Weyl cones, labeled Q1 to Q4, are located in different quadrants. The result is calculated with CST Microwave Studio. ω, frequency. (**D**) CST-simulated results of the position shift of the Weyl point Q1 as the spatial coordinate x varies. The angle of the connection of the Weyl point with the Γ point relative to the Γ-M connection varies simultaneously with the rotational angle θ from 10° to −10°. Γ, center of the Brillouin zone; M, center of the edge of the Brillouin zone.

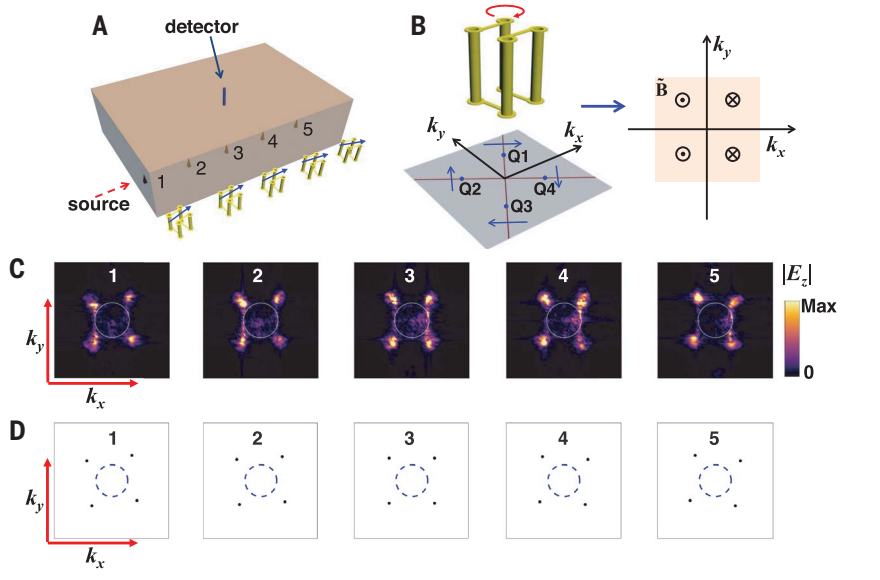


Fig. 2. Pseudo–gauge field generated by the spatially dependent rotational angle θ. (**A**) Experimental setup for detecting gauge field. The source is located at five different positions on the bottom surface, labeled from 1 to 5. (**B**) Shifting of the locations of Weyl points (left panel) and the directions of artificial magnetic field (right panel). The blue arrows indicate the shifting direction of the Weyl points Q1 to Q4 as the x coordinate (or rotational angle θ) varies. The spatial shift of the Weyl points is equivalent to the presence of a gauge field. The circles with a dot represent artificial magnetic field in the $+z$ direction; the circles with an x represent artificial magnetic field in the $-z$ direction. (**C**) Equifrequency contour ($|E_z|$) measured using the setup shown in (A) at a frequency of 13.48 GHz, with panels 1 to 5 corresponding to the results for a source located at positions 1 to 5 in (A). (**D**) Numerical results of Weyl point positions, with five panels corresponding to the five locations in (A). Results are calculated by CST Microwave Studio.

Downloaded from http://science.sciencemag.org/ on January 10, 2019

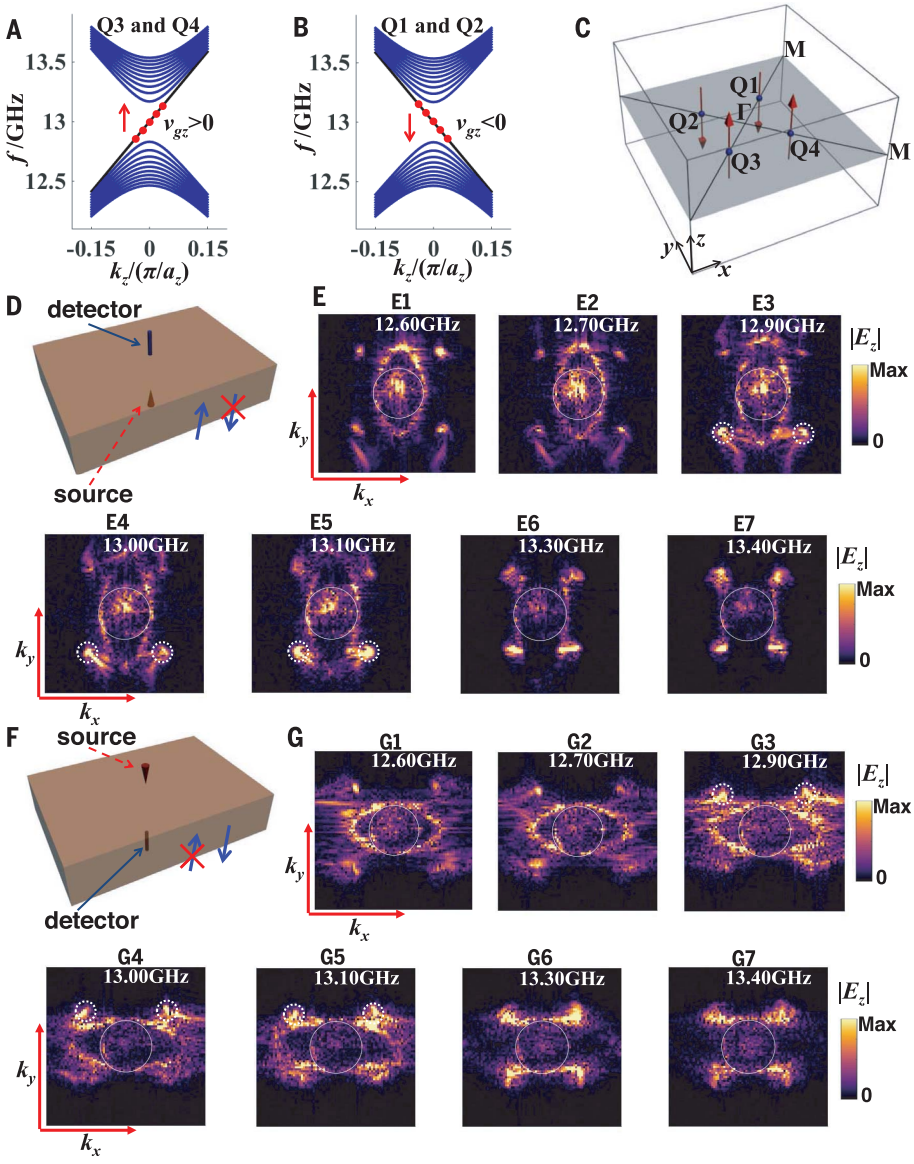


Fig. 3. Chiral zero mode in inhomogeneous Weyl metamaterial. (**A** and **B**) Band structures of Landau levels for Weyl points Q3 and Q4 (A) and Weyl points Q1 and Q2 (B), with a_z being the side length of the unit cell in the *z* direction. The group velocities of chiral zero modes in (A) and (B) are along opposite directions. *f*, frequency; v_{gz}, group velocity in the *z* direction. (**C**) Chiral transport of Weyl photons for Weyl points Q1 to Q4. The red arrows indicate the direction of group velocity at each Weyl point. (**D** and **F**) Experimental setups for detecting up-going and down-going chiral zero modes, respectively. The source is located on the upper center and bottom center of the surfaces, respectively. (**E** and **G**) Equifrequency contours ($|E_z|$) measured by setups shown in (D) and (F). Panels E1 to E7 and G1 to G7 correspond to different frequencies. Two Weyl points surrounded by white dashed circles are much more strongly excited than the other two in panels E3 to E5, and panels G3 to G5, at those frequencies close to the Weyl frequency.

in two Weyl points Q3 and Q4 (Fig. 3, A and C) have the group velocities in the positive *z* direction. By contrast, Weyl points Q1 and Q2 (Fig. 3, B and C) have chiral zero modes with group velocity in the negative *z* direction. The group velocities of zeroth Landau levels at these four Weyl points (Q1 to Q4) respect both time-reversal and mirror symmetry [see symmetry analysis in section 9 of (*32*)]. For an excitation point source located on the bottom surface (Fig. 3D), it is expected that only the up-propagating zeroth Landau levels in Q3 and Q4 can be excited and detected on the top surface. Owing to the conservation of the in-plane momentum, the reflection at the top surface cannot couple to down-going Landau levels in Q1 and Q2. In the experiments, the Fourier transform of the field patterns on the top surface shows that the Weyl points Q3 and Q4 are much more pronounced than Q1 and Q2 in the vicinity of the Weyl frequency (panels E3 to E5 in Fig. 3E). Within the gap formed between the first-order Landau levels, the ratio between the measured intensities of the up-going Landau and that of the down-going Landau levels exceeds 5 [section 10 and fig. S9 in (*32*)]. However, if the source frequency is far from the Weyl frequency (panels E1 and E2, and E6 and E7 in Fig. 3E), the four Weyl points are almost equally excited. On the contrary, for the point source located on the top surface (Fig. 3F), Weyl points Q1 and Q2 are more strongly excited than Q3 and Q4 (panels G3 to G5 in Fig. 3G) close to the Weyl frequency, whereas at other frequencies (panels G1 and G2, and G6 and G7 in Fig. 3G), all four Weyl points are equally excited. Thus, our experiments directly confirm chiral propagation of the zeroth Landau levels in Weyl systems. We further confirm the robust transport of the zero chiral modes against reflection by inserting a defect layer of dielectric slab or air into the middle of the sample and measuring the amplitude of the transmitted bulk modes [section 11 and fig. S10 in (*32*)].

We have designed an inhomogeneous Weyl metamaterial in which the positions of the Weyl points in the momentum space are dependent on the spatial coordinate. The observed shift of the Weyl point positions is equivalent to a pseudo–gauge field (or an artificial magnetic field) in the system. The ability to design the Weyl metamaterial provides a route for generating an artificial magnetic field in 3D photonic systems and an ideal platform for exploring new topological phenomena enabled by strong magnetic fields (*21*, *25*–*28*). The chiral zeroth Landau level, which is a one-way propagative bulk mode, can be applied for robust transport of photons in the bulk medium.

REFERENCES AND NOTES

1. Z. K. Liu *et al.*, *Science* **343**, 864–867 (2014).
2. Q. Guo *et al.*, *Phys. Rev. Lett.* **119**, 213901 (2017).
3. X. Wan, A. M. Turner, A. Vishwanath, S. Y. Savrasov, *Phys. Rev. B* **83**, 205101 (2011).
4. A. A. Soluyanov *et al.*, *Nature* **527**, 495–498 (2015).
5. L. Lu, L. Fu, J. D. Joannopoulos, M. Soljačić, *Nat. Photonics* **7**, 294–299 (2013).
6. L. Lu *et al.*, *Science* **349**, 622–624 (2015).
7. B. Yang *et al.*, *Nat. Commun.* **8**, 97 (2017).
8. B. Yang *et al.*, *Science* **359**, 1013–1016 (2018).
9. N. P. Armitage, E. J. Mele, A. Vishwanath, *Rev. Mod. Phys.* **90**, 015001 (2018).
10. W.-J. Chen, M. Xiao, C. T. Chan, *Nat. Commun.* **7**, 13038 (2016).
11. M. Dubois, C. Shi, X. Zhu, Y. Wang, X. Zhang, *Nat. Commun.* **8**, 14871 (2017).
12. A. Slobozhanyuk *et al.*, *Nat. Photonics* **11**, 130–136 (2017).
13. L. Lu, J. D. Joannopoulos, M. Soljačić, *Nat. Photonics* **8**, 821–829 (2014).
14. A. Weststrröm, T. Ojanen, *Phys. Rev. X* **7**, 041026 (2017).
15. F. Guinea, M. I. Katsnelson, A. K. Geim, *Nat. Phys.* **6**, 30–33 (2010).
16. J. L. Mañes, *Phys. Rev. B* **76**, 045430 (2007).
17. M. C. Rechtsman *et al.*, *Nat. Photonics* **7**, 153–158 (2012).
18. N. Levy *et al.*, *Science* **329**, 544–547 (2010).
19. G. Salerno, T. Ozawa, H. M. Price, I. Carusotto, *2D Mater.* **2**, 034015 (2015).
20. H. Abbaszadeh, A. Souslov, J. Paulose, H. Schomerus, V. Vitelli, *Phys. Rev. Lett.* **119**, 195502 (2017).
21. D. I. Pikulin, A. Chen, M. Franz, *Phys. Rev. X* **6**, 041021 (2016).
22. J. M. Ziman, *Principles of the Theory of Solids* (Cambridge Univ. Press, 1972).

Downloaded from http://science.sciencemag.org/ on January 10, 2019

23. H. B. Nielsen, M. Ninomiya, . *Phys. Lett. B* **130**, 389–396 (1983).
24. Z. M. Yu, Y. Yao, S. A. Yang, *Phys. Rev. Lett.* **117**, 077202 (2016).
25. S. Tchoumakov, M. Civelli, M. O. Goerbig, *Phys. Rev. Lett.* **117**, 086402 (2016).
26. X. Yuan *et al*., *Nat. Commun.* **9**, 1854 (2018).
27. A. G. Grushin, J. W. F. Venderbos, A. Vishwanath, R. Ilan, *Phys. Rev. X* **6**, 041046 (2016).
28. C. X. Liu, P. Ye, X. L. Qi, *Phys. Rev. B* **87**, 235306 (2013).
29. D. T. Son, B. Z. Spivak, *Phys. Rev. B* **88**, 104412 (2013).
30. X. Huang *et al*., *Phys. Rev. X* **5**, 031023 (2015).
31. R. Zhao, T. Koschny, C. M. Soukoulis, *Opt. Express* **18**, 14553–14567 (2010).
32. Materials and methods are available as supplementary materials.

ACKNOWLEDGMENTS

Funding: This work was financially supported by the European Research Council Consolidator Grant (Topological) and Horizon 2020 Action Project grant 734578 (D-SPA). S.Z. acknowledges support from the Royal Society and Wolfson Foundation. Y.X. acknowledges support from the National Natural Science Foundation of China (grant nos. 61875133 and 11874269). C.L. acknowledges the support from the Office of Naval Research (grant no. N00014-15-1-2675 and renewal no. N00014-18-1-2793). **Author contributions:** H.J., Y.X., C.L., and S.Z. planned the project. H.J., Y.X., W.G., Q.G., and B.Y. contributed to the design of the metamaterial. H.J., Q.G., J.H., and Y.B. carried out the measurements. H.J., R.Z., W.G., Y.X., C.L., and S.Z. analyzed the data and performed the theoretical modeling. H.J., C.L., and S.Z. wrote the manuscript. All authors contributed to the discussion. **Competing interests:** The authors declare no competing interests. **Data and materials availability:** All data are available in the main text or the supplementary materials.

SUPPLEMENTARY MATERIALS

www.sciencemag.org/content/363/6423/148/suppl/DC1
Materials and Methods
Figs. S1 to S10
Tables S1 to S5
References

13 July 2018; accepted 23 November 2018
10.1126/science.aau7707

Downloaded from http://science.sciencemag.org/ on January 10, 2019

ORGANIC CHEMISTRY

Finite phenine nanotubes with periodic vacancy defects

Zhe Sun[1,2]*, Koki Ikemoto[1,2], Toshiya M. Fukunaga[1], Takashi Koretsune[2,3,4], Ryotaro Arita[2,3,5], Sota Sato[1,2], Hiroyuki Isobe[1,2]†

Discrete graphitic carbon compounds serve as tunable models for the properties of extended macromolecular structures such as nanotubes. Here, we report synthesis and characterization of a cylindrical $C_{304}H_{264}$ molecule composed of 40 benzene (phenine) units mutually bonded at the 1, 3, and 5 positions. The concise nine-step synthesis featuring successive borylations and couplings proceeded with an average yield for each benzene-benzene bond formation of 91%. The molecular structure of the nanometer-sized cylinder with periodic vacancy defects was confirmed spectroscopically and crystallographically. The nanoporous nature of the compound further enabled inclusion of multiple fullerene guests. Computations suggest that fusing many such cylinders could produce carbon nanotubes with electronic properties modulated by the periodic vacancy defects.

The molecular structure of fullerenes (*1*) has inspired synthetic approaches toward curved geodesic polyarenes and larger congeners through assembly of hexagons and contorting nonhexagons, such as pentagons (*2*–*4*). The curved carbon networks of fullerenes have also led to the discovery of carbon nanotubes (CNTs), extended geodesic cylinders composed exclusively of hexagonal units (*5*–*7*). Synthesis of smaller discrete cylindrical molecules, particularly those with rigid graphitic walls, are deepening our understanding of CNT features such as chiroptical properties (*8*). However, discrete carbonaceous cylinders are not necessarily restricted to defect-free graphitic morphologies (*9*, *10*), and their structural diversity could be further enriched by congeners designed with structural defects. We report the design and synthesis of a molecular cylinder composed of multiple benzene rings. By replacing the trigonal sp^2-carbon atoms of the CNT with trigonal 1,3,5-trisubstituted benzene (phenine) units, we designed nanometer-sized cylindrical molecules, named phenine nanotube (pNT) molecules, that possess 240 sp^2-carbon atoms with six-atom vacancy defects appearing periodically throughout the cylindrical graphitic sheets.

Our previous geodesic phenine designs of a bowl and a saddle mimicked frameworks of geodesic polyarenes and adopted [*n*]cyclo-*meta*-phenylenes ([*n*]CMP) as the starting nonhexagonal omphalos (*11*, *12*). By contrast, the present target required a distinct synthetic strategy. For the design of pNT, we selected a homothetic framework from the hypothetical but long-sought Vögtle belt polyarenes (Fig. 1) (*13*, *14*). Shaping curved networks of the Vögtle belt, however, poses a difficult synthetic problem that has hampered synthetic approaches with trigonal sp2-carbon atoms.

Departing from our [*n*]CMP-omphalos strategy (*11*, *12*), we examined several synthetic strategies and finally succeeded with a concise, nine-step route (Fig. 2A and fig. S1). A two-step transformation of 1,3-dibromobenzene (**1**) through **2** afforded the terphenyl **3**, which possessed linking moieties installed on both ends, and after [3+3] cyclization (*15*), Ir-catalyzed C–H borylation (*16*) produced the [6]CMP derivative **5**, with boryl linkers at the para positions. Subsequent application of Yamago's Pt-macrocyclization (*17*) with our boryl-route modifications (*18*) gave a macrocyclic precursor (**6**) comprising a tetrameric [6]CMP array. The final three steps—iododesilylation, Suzuki coupling, and Ni-mediated Yamamoto-type coupling (*19*)—were performed with **6** to obtain the target (12,12)-pNT molecule (the nomenclature is provided below). The synthesis was completed in nine linear steps from dibromobenzene, and five coupling steps successfully resulted in 52 biaryl bonds that linked 40 benzene rings in a cylinder. Overall, the yield from dibromobenzene was 0.7%, which corresponded to an average yield of 91% per biaryl bond. This synthetic strategy manipulated the common phenine unit adopted in the previous three-dimensional (3D) geodesic phenine frameworks into one dimension (fig. S1) (*11*, *12*, *20*). Structural variations of the pNT molecules were preliminarily investigated by using minor byproducts (supplementary materials). In short, as byproducts of the macrocyclic precursor **6**, we obtained minor congeners composed of three and five [6]CMP panels. These congeners were subjected to identical synthetic transformations and allowed us to spectroscopically detect narrower and wider cylinders: (9,9)- and (15,15)-pNT molecules (Fig. 1), respectively (supplementary materials). Although our repetitive efforts failed to complete the synthesis with full requisite data, the spectroscopic detection showed that a variety of pNT congeners should become synthetically accessible in the future (*21*, *22*).

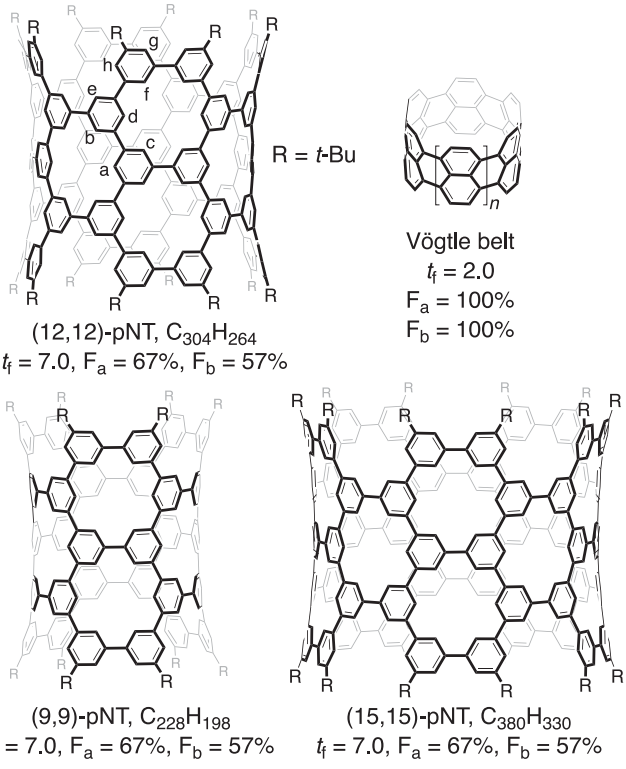


Fig. 1. pNT molecules and Vögtle belt. The positions (a to h) are labeled for assignments of the ^{1}H NMR resonances in Fig. 2.

Considering the cylindrical structure of pNT, we can apply CNT vector nomenclatures to describe the carbon arrangement (*6*, *23*). Thus, the sp^2-carbon atoms of the pNT molecules are arranged in networks of (9,9)-, (12,12)-, and (15,15)-CNTs with periodic six-atom vacancy defects. The lengths and defects in the cylinders can also be described by other vector indices, such as length index (t_f), bond-filling index (F_b), and atom-filling index (F_a) (Fig. 1) (*23*). The length index of all the pNT molecules is commonly 7.0, which is more than double the preceding largest value of 3.0 (*23*). The values of F_a (65%) and F_b (57%) assigned for pNT molecules quantitatively confirm their defect-rich nature.

The structure of the (12,12)-pNT molecule was first confirmed by means of spectroscopy. Matrix-assisted laser

Downloaded from http://science.sciencemag.org/ on January 10, 2019

desorption/ionization (MALDI) mass spectrometry showed a mass/charge ratio (m/z) value of 3917.0693 (Fig. 2), which matched well with the value calculated for the chemical composition of the molecule ($C_{304}H_{264}$). Other congeners, (9,9)- and (15,15)-pNT molecules, were also detected by means of MALDI mass spectrometry as m/z = 2938.8 ($C_{228}H_{198}$) and m/z = 4898.1 ($C_{380}H_{330}$), respectively (fig. S17). Despite their enormous molecular weight, the molecules were amenable to solution-phase analysis with nuclear magnetic resonance (NMR) spectroscopy in 1,1,2,2-tetrachloroethane-d_2. The simple ^{1}H spectrum was consistent with D_{4h} point symmetry (Fig. 2B). For example, only a single methyl ^{1}H resonance appeared for all 16 *t*-Bu groups appended to both ends of the cylinder. This symmetrization arises from elementary D_{4h} symmetry operations (*6*, *24*); eight *t*-Bu groups on one end of the cylinder are rendered equivalent by the C_4-axis/σ_v-plane along the axial direction of the cylinder, and the *t*-Bu groups on the "top" and "bottom" ends become symmetric by the orthogonal C_2-axes/σ_h-plane located at the middle of cylinder. These symmetry operations also converged the signals of the 120 aromatic protons into 8 ^{1}H resonances (Fig. 2B, a to h), which were fully assigned by a combination of nuclear Overhauser effect spectroscopy and long-range correlation spectroscopy spectra (supplementary materials). Unlike the 3D nanocarbon molecules with the phenine frameworks (bowl/saddle) (*11*, *12*), aggregation behaviors were not observed with the present 1D nanocarbon cylinder.

The cylinder shape of the (12,12)-pNT molecule was unambiguously confirmed by means of crystallography. A single crystal was obtained from chlorobenzene (PhCl)/2-propanol and analyzed with a monochromated x-ray beam at SPring-8 (BL38B1). The crystal structure revealed a nanometer-sized hydrocarbon cylinder composed of 240 sp^2-carbon atoms (Fig. 3). The 240 sp^2-carbon atoms were connected to form 40 benzene rings, and the larger hexagons of [6]CMP were fused in the homothetic network of the Vögtle belt. The cylinders were packed in the $I4/m$ space group, and the molecular structure had C_{4h} point symmetry with a C_4 axis and a σ_h plane. The C_{4h} point symmetry lacked only C_2/σ_v operations from the inherent D_{4h} symmetry and showed that the molecules in the crystal have minute structural deformations. Such packing characteristics should benefit further development of materials design via crystal engineering. The length and diameter measured at the sp^2-carbon edges were 1.71 and 1.64 nm, respectively (fig. S19), which matched well with the expected geometries of (12,12)-CNT with t_f = 7.0 (geometric length T_f = 7.0 × 0.249 = 1.74 nm and geometric diameter $d_t = (3 \times 12^2)^{1/2} \times 0.249/\pi$ = 1.65 nm) (*6*, *23*). With van der Waals radii of *t*-Bu groups, the overall length and diameter were ~2.57 and 2.54 nm, respectively. Measurement of the π-orbital axis vectors (POAVs), an indicator of structural deformations of the sp^2-carbon from planarity (*25*), revealed small values between 0.0° and 2.9° at the benzene-benzene bonds, with an average value of 1.5° (fig. S20). The average POAV angle was smaller than in preceding macrocycles of benzene, such as [12]cyclo-*para*-phenylene (average POAV angle = 2.7°), which showed the presence of small structural strains in pNT (*12*). The POAV and dihedral angles of the pNT molecule were particularly small at the circumferences (fig. S20).

The crystal data further allowed for in-depth analyses of higher-order structures, which revealed a distinct bundle assembly of pNT molecules. Unlike trigonal/hexagonal bundles conceived for CNTs (*26*–*28*), tetragonal bundles were found in the single crystal of (12,12)-pNT molecules. Thus, aligning the cylinder axes in parallel, the pNT molecules were bundled on a square plane with tetragonal packings (Fig. 3B). The minimum intercylinder distance was 2.28 nm, slightly larger than 1.98 nm, which was expected for van der Waals contacts of cylinders of the 1.64-nm diameter (1.64 + 0.34 = 1.98 nm). In the intercylinder 0.30-nm space, residual electron densities were observed (fig. S21), which was most likely due to intercalated solvent molecules (PhCl). The tetragonal packing also resulted in large interstitial sites between the cylinders at the diagonal positions (*28*, *29*), and the presence of entrapped substances there was also indicated by residual electron densities. The nanometer-sized void spaces at the interior and interstitial sites resulted in a large void fraction of 63% (fig. S22) (*29*). The tetragonal bundles persisted when multiple C_{70} molecules were entrapped in a form of $(12,12)\text{-pNT} \supset (C_{70})_3$. When the crystal was grown in the presence of an excess

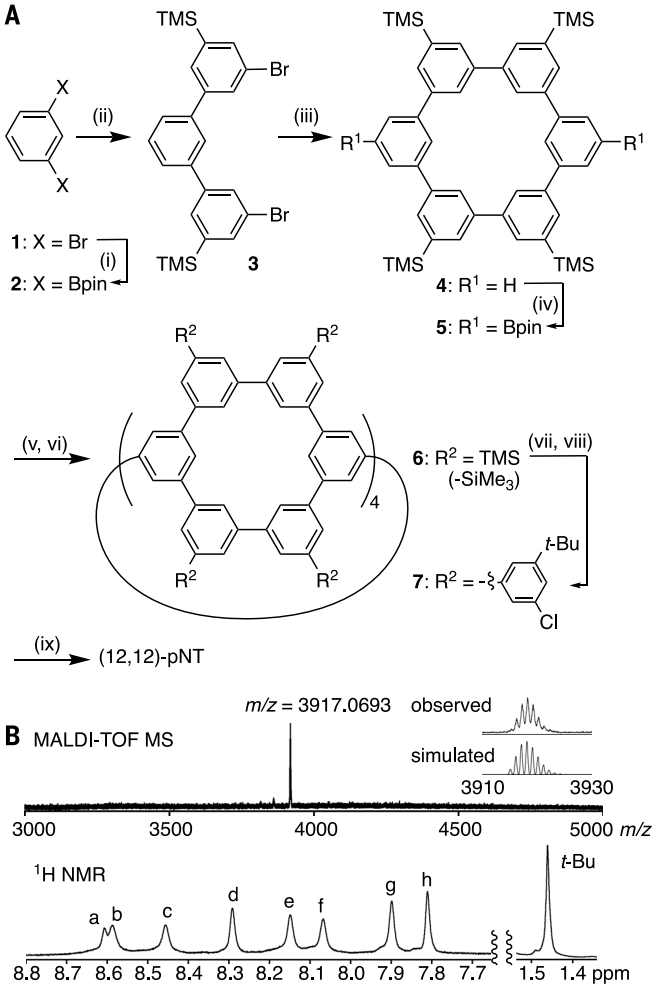


Fig. 2. Nine-step synthesis of pNT. (**A**) Reagents and conditions. (i) Bis(pinacolato)diboron [$(Bpin)_2$], $PdCl_2(dppf)\cdot CH_2Cl_2$, KOAc, dimethyl sulfoxide, 80°C, 91%. (ii) 1,3-dibromo-5-trimethylsilylbenzene, $Pd(PPh_3)_4$, K_2CO_3, *N*,*N*′-dimethylformamide (DMF)/H_2O, 80°C, 66%. (iii) $Ni(cod)_2$, 2,2′-bipyridyl (bpy), 1,5-cyclooctadiene (cod), DMF/toluene, 80°C, 84%. (iv) $(Bpin)_2$, $[Ir(cod)OMe]_2$, 4,4′-di-*t*-butyl-2,2′-bipyridyl (dtbpy), tetrahydrofuran (THF), 65°C, 92%. (v) $PtCl_2(cod)$, CsF, THF, 65°C. (vi) PPh_3, toluene, 100°C, 25% (two steps). (vii) ICl, $CHCl_3$, ambient temperature. (viii) 3-*t*-butyl-5-chlorophenylboronic acid pinacol ester, $Pd(PPh_3)_4$, K_2CO_3, THF/H_2O, 30% (two steps). (ix) $Ni(cod)_2$, bpy, cod, DMF/toluene, 80°C, 20%. (**B**) Spectra of the (12,12)-pNT molecule. (Top) MS spectrum. (Inset) HRMS; pyrene matrix, positive, $[M]^+$ calcd for $C_{304}H_{264}$ = 3917.0754. (Bottom) ^{1}H NMR spectrum in 1,1,2,2-tetrachloroethane-d_2 at 298 K. Positions corresponding to the peak assignments are shown in Fig. 1. The assignment procedures are available in the supplementary materials.

[1]Department of Chemistry, The University of Tokyo, Hongo 7-3-1, Bunkyo-ku, Tokyo 113-0033, Japan. [2]Japan Science and Technology Agency (JST), Exploratory Research for Advanced Technology (ERATO), Isobe Degenerate π-Integration Project, Hongo 7-3-1, Bunkyo-ku, Tokyo 113-0033, Japan. [3]Center for Emergent Matter Science, RIKEN, Wako 2-1, Hirosawa, Saitama 351-0198, Japan. [4]Department of Physics, Tohoku University, Aramaki Aza Aoba 6-3, Aoba-ku, Sendai, Miyagi 980-8578, Japan. [5]Department of Applied Physics, The University of Tokyo, Hongo 7-3-1, Bunkyo-ku, Tokyo, 113-8656, Japan. *Present address: Institute of Molecular Plus, Tianjin University, Building no. 11, 92 Weijin Road, Nankai District, Tianjin, 300072, P. R. China.
†Corresponding author. Email: isobe@chem.s.u-tokyo.ac.jp

Downloaded from http://science.sciencemag.org/ on January 10, 2019

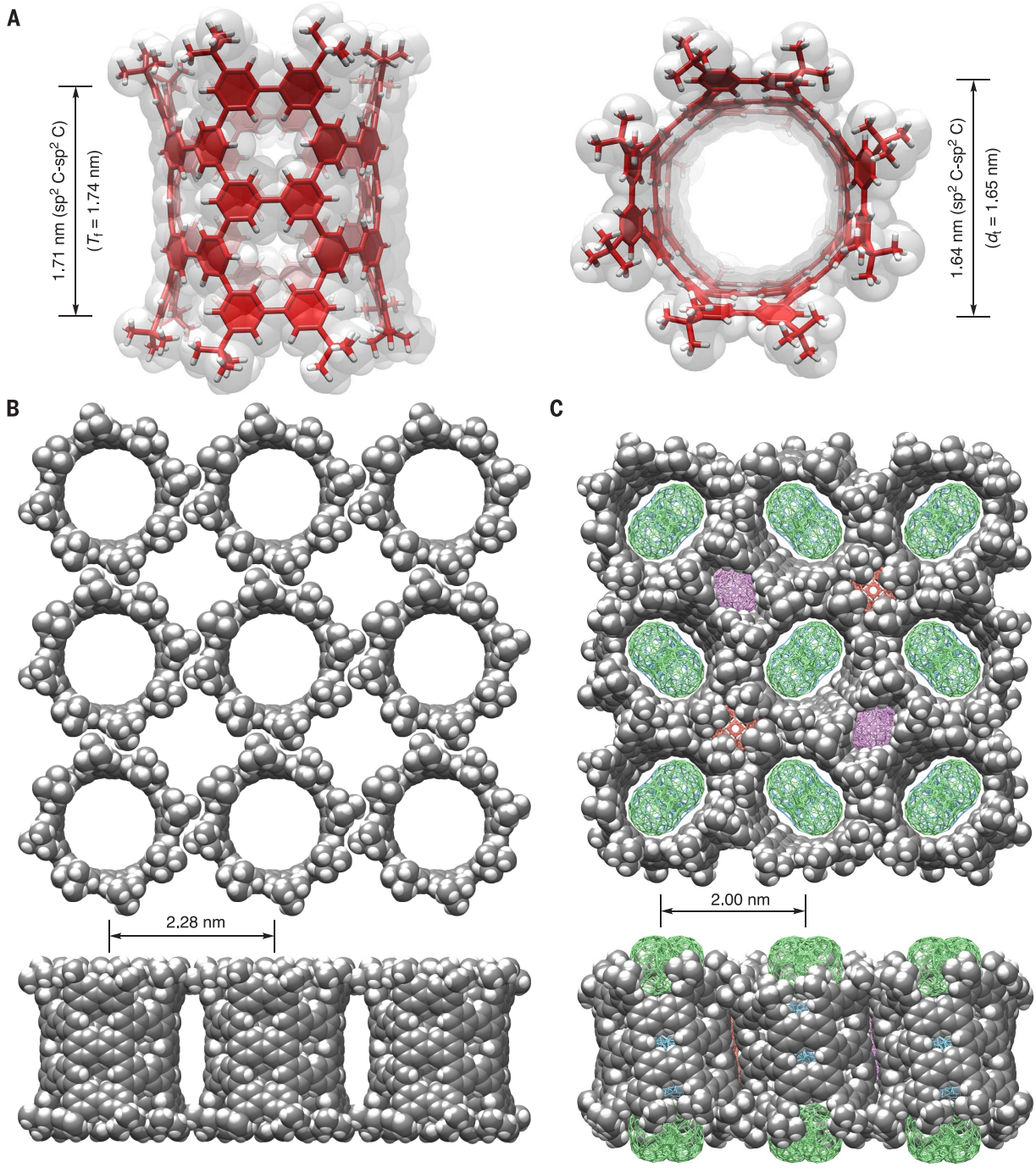


Fig. 3. Crystal structures of (12,12)-pNT. (**A**) Side and top views of the molecular structure. Carbon frameworks are highlighted in red, with hydrogen atoms colored in white. (**B**) Top and side views of the packing structure. Residual electron densities of solvent molecules were removed during the refinement process (fig. S21). (**C**) Top and side views of the packing structure of (12,12) - pNT ⊃ $(C_{70})_3$. Fullerene C_{70} molecules were found at four inequivalent locations. Two interior C_{70} molecules are shown in green and blue, and two interstitial C_{70} molecules are shown in orange and pink (fig. S23). Multiple PhCl solvent molecules and minor conformational disorders of *t*-Bu groups were omitted for clarity.

amount of C_{70} (approximately four equivalents), we obtained a single crystal that included C_{70} molecules both at the interior and interstitial sites of the tetragonal bundles (Fig. 3C and fig. S23). The cylinder structure was essentially identical to that found in the C_{70}-free crystal, with a diameter of 1.67 nm (fig. S19), and the minimum intercylinder distance was 2.00 nm. The intercylinder distance was comparable with the van der Waals contacts of 1.67-nm cylinders (1.67 + 0.34 = 2.01 nm), and the intercalated molecules were not observed in this crystal. We may interpret that the packing behaviors originate from donor-acceptor interactions between pNT and guest molecules. Supramolecular encapsulation in these constructs is a promising application to explore in the future (*30*, *31*). We believe that the persistent tetragonal packing indicates that the bundle structures are under the influence of the symmetry of the nanotubes—the D_{4h}-(12,12)-pNT molecules in this study. There are contradictory viewpoints on roles of the interstitial sites in the adsorption behaviors of

Downloaded from http://science.sciencemag.org/ on January 10, 2019

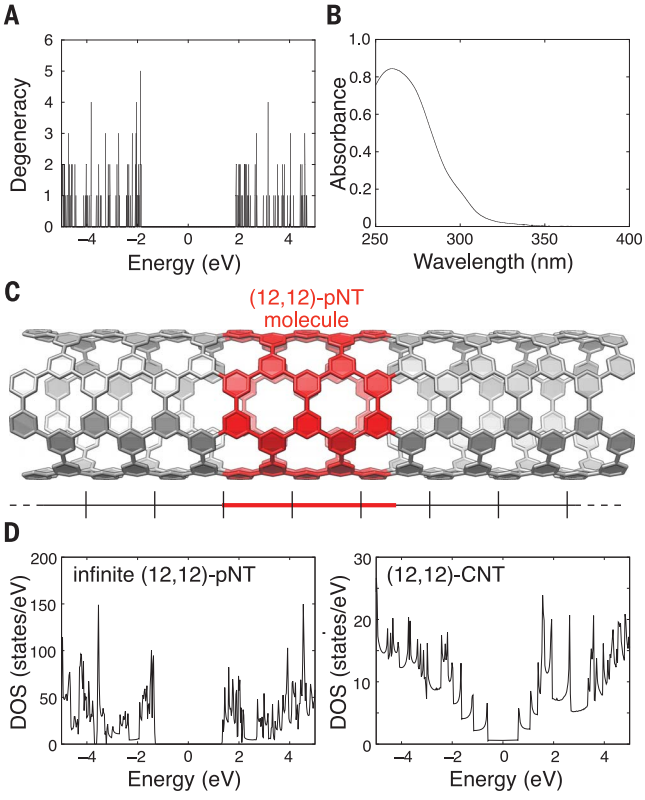


Fig. 4. Theoretical and experimental views of (12,12)-pNT with periodic defects. (**A**) Histogram sorting 192 orbitals of the (12,12)-pNT molecule by energy, from the DFT calculations. Representative orbitals are provided in figs. S24 and S25. (**B**) An absorption spectrum of a 2.0×10^{-6} M solution of (12,12)-pNT in CH_2Cl_2 at 25°C. (**C**) Posited structure of infinite (12,12)-pNT from extrapolation of the (12,12)-pNT molecule (red, 2.5 periodic layers). A ruler shows the periodicity of the pNT structure. (**D**) Electronic density of states from DFT calculations.

CNTs (*28*, *29*), which could also be due to the presence of various inhomogeneous bundles of different symmetry. The present pNT crystal may be a useful reference substance in this context.

The concise synthesis of pNT molecules should be adaptable to product lengthening. For example, installation of trimethylsilyl groups in place of *t*-Bu groups for the iododesilylation could facilitate lengthening from the halogen linkers. The lengthening reactions could readily tolerate polymerization protocols (*20*), and we theoretically investigated electronic structures of such infinite pNT by extrapolating the (12,12)-pNT molecule in density functional theory (DFT) calculations (fig. S1) (*32*). The DFT calculations of the (12,12)-pNT molecule revealed highly degenerate and dense characters of delocalized molecular orbitals (Fig. 4A and figs. S24 and S25), and a comparison with those of benzene revealed effects of π-conjugation of 40 phenines (240 p-orbitals) in a cylindrical framework (fig. S26). Further comparison of the pNT energetics with an experimental optical gap (3.59 eV, λ_{edge} = 345 nm) from an ultraviolet-visible absorption spectrum (Fig. 4B) qualitatively confirmed the validity of the calculations [highest occupied molecular orbital–lowest unoccupied molecular orbital (HOMO-LUMO) gap = 3.73 eV]. The (12,12)-pNT molecule was then used as a base template (2.5 layers) for simulation of an infinite (12,12)-pNT structure, with periodic defects (Fig. 4C). Under periodic boundary conditions, the electronic density of states (DOS) of infinite (12,12)-pNT was obtained to reveal semiconducting character with a bandgap of 2.68 eV (Fig. 4D). A reference DOS with an infinite, defect-free (12,12)-CNT was also investigated by using an identical method to show the gapless, metallic nature of the armchair-type CNT (Fig. 4D) (*6*). Therefore, the results show that installation of periodic defects in CNTs should allow for manipulations of their electronic character. Recently, both top-down and bottom-up methods have been developed for the preparation of graphenes with periodic defects (*9*, *10*), and their anomalous structures (antidot lattices and nanomeshes) have attracted attention in the interest of manipulating the electronic characteristics of nanocarbons (*33*, *34*). Our experimental and theoretical results show that the rolled variants (*5*, *6*)—CNTs with periodic defects—could be an intriguing next target for exploration.

REFERENCES AND NOTES

1. H. W. Kroto, J. R. Heath, S. C. O'Brien, R. F. Curl, R. E. Smalley, *Nature* **318**, 162–163 (1985).
2. C. Tournay, *Nat. Nanotechnol.* **3**, 637–638 (2008).
3. L. T. Scott *et al.*, *Pure Appl. Chem.* **71**, 209–219 (1999).
4. K. Tahara, Y. Tobe, *Chem. Rev.* **106**, 5274–5290 (2006).
5. S. Iijima, *Nature* **354**, 56–58 (1991).
6. R. Saito, G. Dresselhaus, M. S. Dresselhaus, *Physical Properties of Carbon Nanotubes* (Imperial, London, 1998).
7. S. E. Lewis, *Chem. Soc. Rev.* **44**, 2221–2304 (2015).
8. S. Sato *et al.*, *Proc. Natl. Acad. Sci. U.S.A.* **114**, 13097–13101 (2017).
9. J. Bai, X. Zhong, S. Jiang, Y. Huang, X. Duan, *Nat. Nanotechnol.* **5**, 190–194 (2010).
10. C. Moreno *et al.*, *Science* **360**, 199–203 (2018).
11. K. Ikemoto, R. Kobayashi, S. Sato, H. Isobe, *Angew. Chem. Int. Ed.* **56**, 6511–6514 (2017).
12. K. Ikemoto, J. Lin, R. Kobayashi, S. Sato, H. Isobe, *Angew. Chem. Int. Ed.* **57**, 8555–8559 (2018).
13. F. Vögtle, *Top. Curr. Chem.* **115**, 157–159 (1983).
14. G. Povie, Y. Segawa, T. Nishihara, Y. Miyauchi, K. Itami, *Science* **356**, 172–175 (2017).
15. A. Yoshii *et al.*, *ECS J. Solid State Sci. Technol.* **6**, M3065–M3067 (2017).
16. K. Ikemoto *et al.*, *J. Org. Chem.* **81**, 662–666 (2016).
17. S. Yamago, Y. Watanabe, T. Iwamoto, *Angew. Chem. Int. Ed.* **49**, 757–759 (2010).
18. S. Hitosugi, W. Nakanishi, T. Yamasaki, H. Isobe, *Nat. Commun.* **2**, 492 (2011).
19. T. Yamamoto, Y. Hayashi, A. Yamamoto, *Bull. Chem. Soc. Jpn.* **51**, 2091–2097 (1978).
20. Y. Segawa, H. Ito, K. Itami, *Nat. Rev. Mater.* **1**, 15002 (2016).
21. T. Iwamoto, Y. Watanabe, Y. Sakamoto, T. Suzuki, S. Yamago, *J. Am. Chem. Soc.* **133**, 8354–8361 (2011).
22. Z. Sun *et al.*, *Proc. Natl. Acad. Sci. U.S.A.* **113**, 8109–8114 (2016).
23. T. Matsuno *et al.*, *Pure Appl. Chem.* **86**, 489–495 (2014).
24. P. Neuhaus, A. Cnossen, J. Q. Gong, L. M. Herz, H. L. Anderson, *Angew. Chem. Int. Ed.* **54**, 7344–7348 (2015).
25. R. C. Haddon, L. T. Scott, *Pure Appl. Chem.* **58**, 137–142 (1986).
26. A. Thess *et al.*, *Science* **273**, 483–487 (1996).
27. P. Kondratyuk, J. T. Yates Jr., *Acc. Chem. Res.* **40**, 995–1004 (2007).
28. J. Zhao, A. Buldum, J. Han, J. P. Lu, *Nanotechnology* **13**, 195–200 (2002).
29. M. J. Turner, J. J. McKinnon, D. Jayatilaka, M. A. Spackman, *CrystEngComm* **13**, 1804–1813 (2011).
30. T. Matsuno, S. Sato, H. Isobe, in *Comprehensive Supramolecular Chemistry II*, J. L. Atwood, G. W. Gockel, L. J. Barbour, Eds., vol. 3 (Elsevier, 2017), pp. 311–328.
31. S. Bandow, M. Takizawa, K. Hirahara, M. Yudasaka, S. Iijima, *Chem. Phys. Lett.* **337**, 48–54 (2001).
32. S. Hitosugi *et al.*, *Angew. Chem. Int. Ed.* **56**, 9106–9110 (2017).
33. M. Dvorak, W. Oswald, Z. Wu, *Sci. Rep.* **3**, 2289 (2013).
34. M. S. Dresselhaus, A. Jorio, A. G. Souza Filho, R. Saito, *Philos. Trans. R. Soc. A* **368**, 5355–5377 (2010).

ACKNOWLEDGMENTS

We thank H. Yamamoto (IMS/ERATO) for valuable discussion. We were granted access to the x-ray diffraction instruments of SPring-8 (2018A1064 and 2018A1257). **Funding:** This study is partly supported by JST ERATO (JPMJER1301) and KAKENHI (17H01033, 17K05773, 17K05772, 16K04864, 25102007). **Author contributions:** H.I. launched the project; Z.S, K.I., and H.I. conceived the design; and Z.S. and T.M.F. synthesized the target. Z.S., K.I., and S.S. performed the crystallographic studies, and Z.S., K.I., T.K., and R.A. performed the DFT calculations. All authors analyzed and discussed the results, and Z.S., K.I. and H.I. wrote the manuscript. **Competing interests:** Z.S., K.I., and H.I. are inventors on U.S. patent application no. 62/745,444 submitted by the University of Tokyo, which covers the syntheses described in the manuscript. **Data and materials availability:** Crystallographic data are available free of charge from the Cambridge Crystallographic Database Centre (CCDC 1844346 and 1868931). All other data are available in the main text or the supplementary materials.

SUPPLEMENTARY MATERIALS

www.sciencemag.org/content/363/6423/151/suppl/DC1
Materials and Methods
Supplementary Text
Figs. S1 to S26
Tables S1 to S4
References (*35*–*47*)

21 June 2018; resubmitted 24 September 2018
Accepted 20 November 2018
10.1126/science.aau5441

Downloaded from http://science.sciencemag.org/ on January 10, 2019

SURFACE CHEMISTRY

Site-specific reactivity of molecules with surface defects—the case of H_2 dissociation on Pt

Richard van Lent[1,2], Sabine V. Auras[1], Kun Cao[1], Anton J. Walsh[2], Michael A. Gleeson[2], Ludo B. F. Juurlink[1]*

The classic system that describes weakly activated dissociation in heterogeneous catalysis has been explained by two dynamical models that are fundamentally at odds. Whereas one model for hydrogen dissociation on platinum(111) invokes a preequilibrium and diffusion toward defects, the other is based on direct and local reaction. We resolve this dispute by quantifying site-specific reactivity using a curved platinum single-crystal surface. Reactivity is step-type dependent and varies linearly with step density. Only the model that relies on localized dissociation is consistent with our results. Our approach provides absolute, site-specific reaction cross sections.

At the heart of any chemical transformation lie the dynamical events associated with elementary reactions. In gas-phase reactions, reactant energy is redistributed over the limited degrees of freedom available in the products. For gas-surface collisions, the bulk provides a massive sink for energy dissipation. This makes mechanistic problems for gas-surface reactions quite challenging, as exemplified by ongoing discussion regarding the role of phonons and electron-hole pairs in surface reactions (*1*, *2*). In addition, surface heterogeneity may cause site-specific reactions to dominate overall kinetics in catalysis. For example, CO oxidation was recently shown to be site-specific on both Pt and Pd (*3*, *4*).

The prototypical system in heterogeneous catalysis is H_2 dissociation on Pt, which is essential to the development of chemically accurate theoretical modeling of gas-surface interactions (*5*). H_2 dissociation occurs through dynamical processes (*6*, *7*). However, after four decades of research, two opposing dynamical models describing H_2 dissociation prevail in the literature. The fundamental discrepancy between the models lies in the assumed fate of kinetic energy of incident molecules. In the first model, the energy is conserved in the collision, and incident molecules elastically scatter into a precursor state. In the second model, incident kinetic energy is not conserved. Depending on the exact point of impact, it couples directly to the dissociation coordinate or is dissipated, for example, by excitation of a frustrated rotation.

The two models for H_2 dissociation on Pt surfaces are illustrated in Fig. 1. Model 1, schematically shown in Fig. 1A, was proposed by Poelsema, Lenz, and Comsa (*7*, *8*). Scattering experiments have previously shown that atoms and molecules may diffract into a physisorbed state (*9*, *10*). In their model, the elastic collision only leads to dissociation when an H_2 molecule also encounters a defect during friction-free diffusion across the surface. The model is summarized by:

$$H_2(g) \underset{k_{des}}{\overset{k_{ads}}{\rightleftharpoons}} H_{2,phys} \xrightarrow{k_{defect}} 2H_{ads} \quad (1)$$

The rate constant for adsorption (k_{ads}) depends on the probability to resonantly scatter into the physisorbed state ($S_{0,nL}$). The rates at which physisorbed molecules desorb (k_{des}) or encounter defects (k_{defect}) depend on their velocity (v), residence time (τ), and the average distance between defects (L_d). The model predicts a dissociation probability on the clean surface, S_0:

$$S_0 \propto S_{0,nL}\left(1 - e^{-\frac{L_d}{v\tau}}\right) \quad (2)$$

For large distances between defects, reactivity is rather sensitive to L_d. For short distances—i.e., higher defect densities—this sensitivity is lost. The transition occurs when the mean free path of the physisorbed molecule (i.e., $v\tau$) is comparable to the distance between defects.

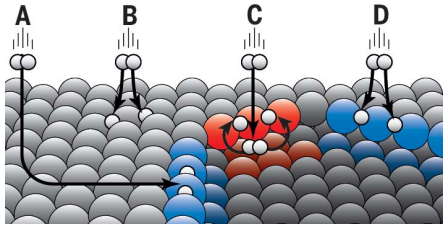


Fig. 1. Dynamical H_2 dissociation mechanisms. (**A**) Model 1: mobile precursor mechanism. (**B**) Model 2: direct activated dissociation at (111) terraces. (**C**) Model 2: trapping-mediated dissociation at step edges. (**D**) Model 2: direct dissociation at step edges. A- and B-type steps are shown in blue and red, respectively. (C) and (D) can take place at either step type, but relative contributions may vary.

In model 2, Baerends (*11*), Hayden (*12*), and Somorjai (*13*) propose parallel dynamical mechanisms for different surface sites, e.g., terraces and steps. None of these mechanisms contains a long-lived, diffusing precursor state. Dissociation is adequately represented as elementary:

$$H_2(g) \xrightarrow{k_{ave}} 2H_{ads} \quad (3)$$

The observed reactivity represents an average (k_{ave}) from site-specific contributions. Terraces contribute by direct dissociation, as illustrated in Fig. 1B. Incident kinetic energy is used to surmount activation barriers that vary with exact location and molecular orientation. Steps contribute by the two mechanisms illustrated in Fig. 1, C and D. The first occurs at the cusp and is responsible for the initial negative correlation of reactivity with incident kinetic energy (E_{kin}) (*12*, *14*). Dynamical calculations suggest that kinetic energy is converted to molecular rotation. Dissociation occurs when the dynamically trapped molecule senses the upper edge of the step (*11*). The second contribution by steps is barrier-free dissociation at the upper edge (*11*, *12*, *14*–*16*). Kinetic energy flows into the reaction coordinate and is quickly lost to the substrate. The reactivity constant in this model can be represented as the weighted average of site-specific reactivities, S_0^{site},

$$S_0 \propto \sum_{site} f^{site} S_0^{site} \quad (4)$$

In contrast to the previous one, this second model predicts a strictly linear relation between reactivity and the fractional occurrence of each type of reactive site, f^{site}. Whereas the first model also did not discriminate between defects, this model does allow for varying contributions by, e.g., the A- and B-type step edges depicted in Fig. 1.

A new approach allows us to test both models on a single sample. The step density along a curved Pt surface has been shown to vary smoothly from "defect-free" (111) to highly stepped surfaces (*17*). By combining a curved surface approach and supersonic molecular beam methods (*18*) with highly improved spatial resolution, we resolve that H_2 dissociation does not require physisorption and diffusion to defect sites. In addition, we quantify site-specific reactivities for both {100} (A-type) and {110} (B-type) step types.

A schematic illustration of the experiment is shown in Fig. 2, A to E. Our Pt single crystal is a 31° section of a cylinder along the $[1\bar{1}0]$ rotational axis. The (111) surface appears at the apex (*19*). The macroscopic curvature of the crystal is a direct result of monatomic steps (*17*). Consequently, the local surface structure on our crystal varies smoothly from Pt(335) via Pt(111) to Pt(553) (*19*). As both A- and B-type steps are spatially separated by the (111) surface,

[1]Leiden Institute of Chemistry, Leiden University, Einsteinweg 55, Leiden 2333 CC, Netherlands. [2]Dutch Institute for Fundamental Energy Research, de Zaale 20, Eindhoven 5612 AJ, Netherlands.
*Corresponding author. Email: l.juurlink@chem.leidenuniv.nl

Downloaded from http://science.sciencemag.org/ on January 10, 2019

their influence on reactivity can be probed independently. We measure initial sticking probabilities (S_0) by using the King and Wells approach (*20*). The molecular beam is incident on the surface along the [111] vector. We measure S_0 as a function of step density by translating the single-crystal surface with respect to our rectangular-shaped supersonic molecular beam (0.126 mm by 6.0 mm). Figure 2D illustrates the relative sizes of the crystal and the beam. Figure 2E quantifies the convolution of the narrow molecular beam with step density. Near (111), the probed step density is limited to 0.01 nm^{-1}. Our measurements are limited to step densities of 0.8 nm^{-1} as a result of narrowing of the crystal at high step densities in combination with the 6-mm width of our beam.

Figure 2F shows S_0 at a surface temperature (T_s) of 155 K as a function of step density and step type for E_{kin} = 9.3 meV and 100 meV. These energies are produced by (anti)seeding D_2 beams and estimated from measurements of time of flight. At the lower E_{kin}, S_0 starts at 0.01 ± 0.05 for the (111) surface and increases linearly with step density. S_0 for B-type step edges are consistently higher than A-type step edges at similar step density. At the higher E_{kin}, the influence of steps has disappeared, and S_0 is approximately constant over the entire step density range. This energy dependence is consistent with all previous King and Wells studies of H_2 dissociation on flat and stepped single-crystal surfaces (*12*, *14*–*16*, *21*, *22*).

For the lower E_{kin}, for which steps are the dominant source of dissociation, Fig. 3 compares S_0 as a function of step density for T_s= 155 K and 300 K. Results are only shown for B-type steps, but the trend is identical for A-type steps. Also shown as dashed lines are predictions for S_0 by model 1 (*8*), as described in the supporting materials. The curvature in the predicted step density dependence is a logical consequence of model 1. When the mean free path of the physisorbed state approaches or exceeds the distance between defects, increasing defect density becomes less effective in increasing S_0. Only at high defect density does S_0 become proportional to step density.

Our results are clearly at odds with the predictions by this model. Not only is S_0 underestimated over the entire defect density range, but also two crucial dependencies are not reproduced in the experiment. First, predicted curvature in the S_0 dependence on step density near the (111) surface is absent. Second, the T_s dependence opposes the predicted trend. Whereas model 1 clearly reduces S_0 with increasing T_s because of the diminishing residence time in a physisorbed state, we find that S_0 generally increases or is hardly affected. An attempt to improve the model by incorporating Debye-Waller attenuation, reducing the probability of scattering into the resonant state, would increase this discrepancy. In addition to these erroneous dependencies, the site-specific reactivity of S_0 seen in Fig. 2F is not captured in model 1. Finally, it also does not capture the observed step density independence at the higher E_{kin}.

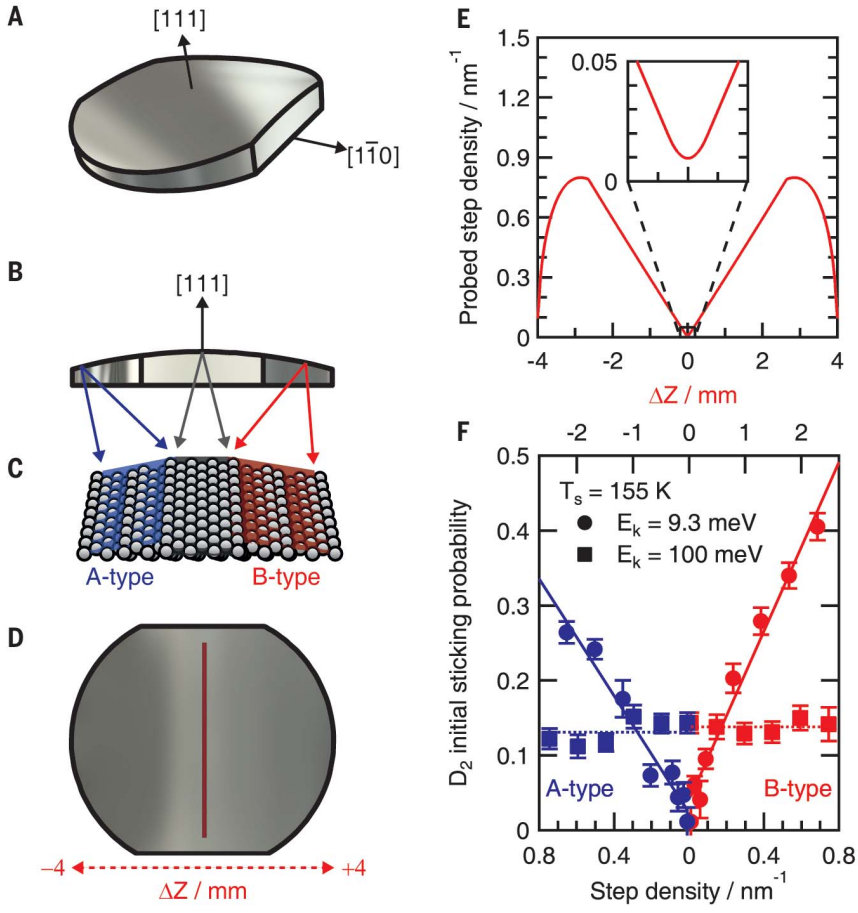


Fig. 2. Curved crystal reactivity measurement. (**A**) Bird's-eye view of the curved Pt single crystal. (**B**) Side view along the [1$\bar{1}$0] vector. (**C**) Side view showing the surface structure and surface planes of Pt(335) (A-type steps), Pt(111), and Pt(553) (B-type steps) in blue, gray, and red, respectively. (**D**) Top view with the molecular beam size in red. (**E**) Step density probed by the molecular beam at the position relative to the (111) surface. (**F**) S_0 (D_2) at T_s= 155 K as a function of step density. Results from A- and B-type step edges are depicted in blue and red, respectively. Circles and squares represent E_{kin}= 9.3 meV and E_{kin}= 100 meV. Lines are least-squares fits to the data. Error bars represent the standard deviation in S_0.

In contrast, our results are in agreement with the two underlying assumptions of model 2. Terrace and step sites contributing proportionally to their abundance and the absence of a freely diffusing precursor require a strictly linear dependence of S_0 on step density. Least-squares fitting yields a residual reactivity because of dissociation on the Pt(111) surface. Individual fits to A- and B-type steps for lower-incident energy yield 0.023 ± 0.009 and 0.040 ± 0.008. This is in good agreement with previous results (*21*, *22*) for Pt(111), even with experimental results for the clean "defect-free" surface (*7*) on which model 1 is based. This residual reactivity of the "defect-free" Pt(111) surface is explained by recent dynamical calculations for D_2 dissociation (*23*). Select impact geometries show barrier-free dissociation on the Pt(111) surface.

The slope of the linear fits in Fig. 2F reflect the summed contributions of direct barrier-free and trapping-mediated dissociation at step edges, as shown in Fig. 1, C and D. Multiplying the slope of each linear fit with the width of the unit cell yields the reaction cross section for H_2 dissociation at the step edge (*16*). For our low-E_{kin} data at T_s = 155 K, these are 0.108 ± 0.007 and 0.157 ± 0.007 nm^2 for A- and B-type steps, respectively. The reaction cross section for A-type steps agrees quantitatively with theoretical results that show the surface area of the Pt(211) unit cell where impact at the step results in dissociation (*11*). We previously showed that the direct contribution at the upper edge, shown in Fig. 1D, amounts to 0.043 nm^2 (*16*). The trapping-mediated mechanism in Fig. 1C is then responsible for the 0.065-nm^2 difference at A-type steps. As the local structure at the upper edge is identical, the larger cross section for B-type steps compared with A-type steps suggests larger and/or deeper molecular chemisorption wells at its cusp.

In summary, the model ascribing H_2 dissociation on Pt mostly to a highly mobile precursor

Downloaded from http://science.sciencemag.org/ on January 10, 2019

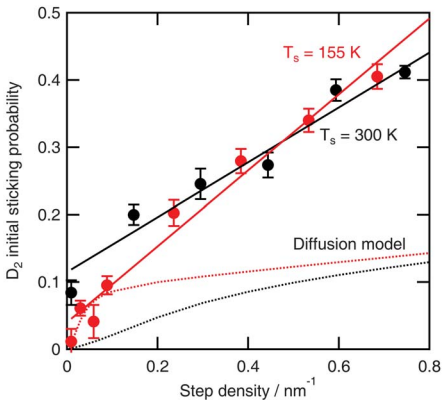


Fig. 3. Temperature and B-type step density reactivity dependences. Circles are measured data for E_{kin} = 9.3 meV. Solid lines are fits to the data. Dashed lines are predicted results from model 1. Red and black represent T_s = 155 K and 300 K, respectively. Error bars represent the standard deviation in S_0.

fails to predict the reactivity dependence on step density and surface temperature. In addition to a lack of site specificity, the model erroneously assumes that the perfect Pt(111) surface only exhibits activated adsorption (*23*). As reactivity in this model is fully ascribed to defects, the model's parameters and other conjectures must reflect this overestimate. We believe this to be represented by the unphysical assumption that all scattering occurs into the ground vibrational level of the physisorbed state. Furthermore, whereas the model's parameters are based on a fit to experimental data by using dissociation from a bulb gas at room temperature, the known complex angular dependence to dissociation (*21*, *24*) is not taken into account. More assumptions may contribute to its failure—e.g., that no other possible outcome than dissociation exists when physisorbed molecules encounter a defect.

Simultaneously, our data support that dissociation is dominated by impulsive interactions at the impact site. In the relevant regime, there is no significant surface temperature dependence, and at low kinetic energy, dissociation is strictly linear with step density. At incident energies exceeding most barriers to dissociation on the terrace, the contribution of steps becomes indiscernible; reactivity becomes independent of step density. From our low kinetic energy data, we extract site-specific reaction cross sections for A- and B-type step edges in a chemical reaction. The reaction cross section of B-type steps is significantly larger than that of A-type steps, suggesting a larger molecular chemisorption well with more efficient kinetic energy dissipation. These results present benchmarks for future construction of high dimensional potential energy surfaces and guide dynamical studies aiming to understand the kinetics of this prototypical system. In particular, the origin of the significantly larger cross section for dissociation at B-type step edges may be extracted from calculation of the potential energy surface of H_2/Pt(221). Additional (quantum) dynamical calculations, similar to those performed by Baerends and co-workers (*11*, *25*), could confirm the dominant contributions of the three parallel dynamical mechanisms captured by model 2.

REFERENCES AND NOTES

1. B. Gergen, H. Nienhaus, W. H. Weinberg, E. W. McFarland, *Science* **294**, 2521–2523 (2001).
2. J. Meyer, K. Reuter, *Angew. Chem. Int. Ed.* **53**, 4721–4724 (2014).
3. J. Neugebohren *et al.*, *Nature* **558**, 280–283 (2018).
4. S. Blomberg *et al.*, *ACS Catal.* **7**, 110–114 (2017).
5. G. J. Kroes, *Science* **321**, 794–797 (2008).
6. C. Díaz *et al.*, *Science* **326**, 832–834 (2009).
7. B. Poelsema, K. Lenz, G. Comsa, *J. Phys. Condens. Matter* **22**, 304006 (2010).
8. B. Poelsema, K. Lenz, G. Comsa, *J. Chem. Phys.* **134**, 074703 (2011).
9. J. P. Cowin, C.-F. Yu, S. J. Sibener, L. Wharton, *J. Chem. Phys.* **79**, 3537–3549 (1983).
10. A. S. Sanz, S. Miret-Artés, *Phys. Rep.* **451**, 37–154 (2007).
11. D. A. McCormack, R. A. Olsen, E. J. Baerends, *J. Chem. Phys.* **122**, 194708 (2005).
12. A. T. Gee, B. E. Hayden, C. Mormiche, T. S. Nunney, *J. Chem. Phys.* **112**, 7660–7668 (2000).
13. M. Salmeron, R. J. Gale, G. A. Somorjai, *J. Chem. Phys.* **67**, 5324–5334 (1977).
14. I. M. N. Groot, K. J. P. Schouten, A. W. Kleyn, L. B. F. Juurlink, *J. Chem. Phys.* **129**, 224707 (2008).
15. I. M. N. Groot, A. W. Kleyn, L. B. F. Juurlink, *Angew. Chem. Int. Ed.* **50**, 5174–5177 (2011).
16. I. M. N. Groot, A. W. Kleyn, L. B. F. Juurlink, *J. Phys. Chem. C* **117**, 9266–9274 (2013).
17. A. L. Walter *et al.*, *Nat. Commun.* **6**, 8903–8909 (2015).
18. C. Hahn *et al.*, *J. Chem. Phys.* **136**, 114201 (2012).
19. A. J. Walsh *et al.*, *J. Vac. Sci. Technol. A* **35**, 03E102 (2017).
20. D. A. King, M. G. Wells, *Surf. Sci.* **29**, 454–482 (1972).
21. A. C. Luntz, J. K. Brown, M. D. Williams, *J. Chem. Phys.* **93**, 5240–5246 (1990).
22. P. Samson, A. Nesbitt, B. E. Koel, A. Hodgson, *J. Chem. Phys.* **109**, 3255–3264 (1998).
23. E. Nour Ghassemi, M. Wijzenbroek, M. F. Somers, G. J. Kroes, *Chem. Phys. Lett.* **683**, 329–335 (2017).
24. K. Cao, R. van Lent, A. W. Kleyn, L. B. F. Juurlink, *Chem. Phys. Lett.* **706**, 680–683 (2018).
25. M. Luppi, D. A. McCormack, R. A. Olsen, E. J. Baerends, *J. Chem. Phys.* **123**, 164702 (2005).

ACKNOWLEDGMENTS

We thank T. Hoogenboom and P. J. van Veldhuizen for technical support. **Funding:** This work is part of the *CO2 neutral fuels* research program, which is financed by the Netherlands Organization of Scientific Research (NWO). **Author contributions:** All the authors contributed substantially to this work. **Competing interests:** The authors declare no competing interests. **Data and materials availability:** All data supporting the conclusions are available in the published work or supporting materials.

SUPPLEMENTARY MATERIALS

www.sciencemag.org/content/363/6423/155/suppl/DC1
Materials and Methods
Supplementary Text
Figs. S1 and S2
References (*26*, *27*)

4 July 2018; accepted 30 November 2018
10.1126/science.aau6716

Downloaded from http://science.sciencemag.org/ on January 10, 2019

CHEMICAL PHYSICS

The Sommerfeld ground-wave limit for a molecule adsorbed at a surface

Li Chen[1]*†‡, Jascha A. Lau[1,2]‡, Dirk Schwarzer[1], Jörg Meyer[3], Varun B. Verma[4], Alec M. Wodtke[1,2,5]*

Using a mid-infrared emission spectrometer based on a superconducting nanowire single-photon detector, we observed the dynamics of vibrational energy pooling of carbon monoxide (CO) adsorbed at the surface of a sodium chloride (NaCl) crystal. After exciting a majority of the CO molecules to their first vibrationally excited state (v = 1), we observed infrared emission from states up to v = 27. Kinetic Monte Carlo simulations showed that vibrational energy collects in a few CO molecules at the expense of those up to eight lattice sites away by selective excitation of NaCl's transverse phonons. The vibrating CO molecules behave like classical oscillating dipoles, losing their energy to NaCl lattice vibrations via the electromagnetic near-field. This is analogous to Sommerfeld's description of radio transmission along Earth's surface by ground waves.

Polar molecules in optical lattices formed by interfering laser beams are platforms for studying quantum magnetism (*1*), quantum many-body dynamics (*2*), and quantum computing (*3*, *4*). The electric fields at a crystalline surface are another form of lattice, one capable of orienting and ordering polar molecules. Hence, adsorbing molecules to low-temperature solids might be a complementary and, so far, unexplored approach to studying the lattice dynamics of polar molecules. Unfortunately, dynamical interactions between adsorbates and solid substrates are typically much stronger than those between adsorbed molecules (*5*, *6*). For example, an adsorbate's vibrational energy may flow to a solid's electrons within picoseconds (*7*, *8*) or, as a result of intrinsically anharmonic interatomic forces, to lattice vibrations within nanoseconds (*9*, *10*).

One exception (Fig. 1C) is a monolayer of CO adsorbed to NaCl(100). Here, dipole-dipole interactions between CO molecules are stronger than CO-NaCl interactions, and such conditions lead to vibrational energy pooling (VEP). Chang and Ewing (*11*) observed CO in states with vibrational quantum numbers, v, as high as v = 15 by near-resonant vibration-to-vibration (V-V) energy transfer.

$$\begin{aligned} &CO(1) + CO(1) \rightarrow CO(2) + CO(0) + \Delta\varepsilon(2) \\ &CO(2) + CO(1) \rightarrow CO(3) + CO(0) + \Delta\varepsilon(3) \\ &\vdots \\ &CO(v) + CO(1) \rightarrow CO(v+1) + CO(0) + \Delta\varepsilon(v+1) \end{aligned} \quad (1)$$

Unfortunately, detailed studies were impossible because of the low sensitivity and poor time response of infrared detectors available at that time.

To study VEP in detail, we detected time- and wavelength-resolved laser-induced infrared fluorescence with a superconducting nanowire single-photon detector (SNSPD) (*12*, *13*). Kinetic Monte Carlo (kMC) simulations (*14*–*18*) of our observations reveal V-V energy transfer occurring between CO molecules separated by more than eight lattice sites and show that the excess energy represented by $\Delta\varepsilon(v + 1)$ in Eq. 1 is selectively absorbed by NaCl's transverse phonons. Surprisingly, the vibrating CO molecules behave like classical oscillating dipoles, losing their energy to NaCl lattice vibrations via the electromagnetic near-field. These rates are quantitatively described by a theory (*19*, *20*) that has its origins in Sommerfeld's 1909 description of a radio transmitter interacting with Earth forming damped electromagnetic surface waves (*21*). This is a weak coupling limit where the anharmonic interatomic forces that are normally important to energy flow can be completely neglected.

Figure 1 shows infrared spectra of CO adsorbed to NaCl obtained in absorption (Fig. 1A) and with laser-induced infrared fluorescence (Fig. 1B). The spectrum of the CO monolayer is composed of a doublet centered at 2052 cm^{-1}, where the intensity pattern is polarization-sensitive. The feature at 2055 cm^{-1} results from the symmetric stretching of the two coupled CO molecules in the 2 × 1 unit cell (shown as a dashed rectangle in Fig. 1C) (*22*, *23*). The 2049 cm^{-1} line observed with s- and p-polarization arises from the antisymmetric stretch vibration. For comparison, Fig. 1B shows the laser-induced infrared fluorescence excitation spectrum obtained from a CO monolayer for both p- and s-polarization. There can be no doubt that the laser-induced fluorescence results from the excitation of CO molecules in the monolayer.

Figure 2, A and B, shows the experimentally obtained fluorescence emission spectrum (in black) compared to kMC simulations (in red). All features in these spectra result from the first-overtone emission of vibrationally excited CO; the emitting vibrational state is indicated by combs. Intensity peaks reflecting enhanced vibrational populations are seen near v = 7, 16, and 25; hereafter, we refer to vibrational states near these three values of v as base-camp 1, 2, and 3, respectively.

The red curve in Fig. 2A shows a kMC simulation under our experimental conditions where only nearest-neighbor V-V energy transfer is permitted, an assumption used in previous work (*14*–*18*). This approach yields a peak in population at v ~ 8 (base-camp 1), strongly resembling figure 3 of (*14*) and (*15*) but markedly different from experiment. Note that a single molecule with only four nearest neighbors can still reach v = 8 because the nearest neighbors can transport vibrational quanta from more distant molecules by process 2:

$$CO(1) + CO(0) \rightarrow CO(0) + CO(1) \quad \Delta\varepsilon(1) = 0 \quad (2)$$

Population in states higher than v ~ 8 is prevented by a one-phonon energy cutoff (*14*, *15*) that is reached when $\Delta\varepsilon(v + 1)$, the rightmost term in Eq. 1, exceeds the energy of the highest-frequency phonon of the NaCl substrate. Clearly, the nearest-neighbor assumption in these kMC simulations fails to describe the experiment.

To produce molecules in higher vibrational states, long-distance interactions between vibrationally excited molecules are needed. When VEP is modeled including V-V exchange over an area of ~1000 $Å^2$, kMC simulations reproduce the experiment well (Fig. 2B, red curve). In this case, vibrationally excited molecules in base-camp 1 states can interact with one another even though they are not likely to be nearest neighbors. For example, processes such as

$$\begin{aligned} &CO(7) + CO(7) \rightarrow CO(8) + CO(6) \\ &CO(8) + CO(7) \rightarrow CO(9) + CO(6) \\ &\vdots \\ &CO(v) + CO(7) \rightarrow CO(v+1) + CO(6) \end{aligned} \quad (3)$$

allow molecules in base-camp 1 states to climb to base-camp 2, where again the one-phonon energy cutoff slows further pooling. Subsequently, molecules in base-camp 2 climb to base-camp 3 by even longer-range interactions. Vibrational states higher than v = 27 are not seen as energy transfer to the lowest-lying excited electronic states becomes possible (V-E energy transfer). The temporal sequence of base-camp formation can also be seen by taking snapshots of the vibrational distribution in the kMC simulations at different times (see Fig. 2C). This shows that

[1]Department of Dynamics at Surfaces, Max Planck Institute for Biophysical Chemistry, 37077 Göttingen, Germany. [2]Institute for Physical Chemistry, University of Göttingen, 37077 Göttingen, Germany. [3]Leiden Institute of Chemistry, Gorlaeus Laboratories, Leiden University, 2300 RA Leiden, Netherlands. [4]National Institute of Standards and Technology, Boulder, CO, USA. [5]International Center for Advanced Studies of Energy Conversion, University of Göttingen, 37077 Göttingen, Germany.
***Corresponding author. Email: alec.wodtke@mpibpc.mpg.de (A.M.W.); li.chen@mpibpc.mpg.de (L.C.)** †Present address: State Key Laboratory of Molecular Reaction Dynamics, Dalian Institute of Chemical Physics, Chinese Academy of Sciences, Dalian, Liaoning 116023, P.R. China. ‡These authors contributed equally to this work.

Downloaded from http://science.sciencemag.org/ on January 15, 2019

base-camp 1 forms within 100 ns, base-camp 2 within 0.1 to 1 μs, and base-camp 3 only after 10 to 100 μs.

The distance dependence of dipole-dipole interactions explains the sequential formation of base-camps. From the kMC simulations of Fig. 2B, we find that the average distance between pooling molecules forming base-camp 1 is 4.1 Å (~1 lattice constant), whereas for base-camp 2 this distance is 11.7 Å, and for base-camp 3 it is 17.6 Å. One-phonon–assisted V-V rates scale with distance as R^{-8} (*24*), meaning that base-camp 1 is formed 10^3 times faster than base-camp 2, which is formed 10^2 times faster than base-camp 3. This hierarchy of rates is consistent with our experimental observations.

VEP selectively excites transverse NaCl phonons. The left panel of Fig. 3 shows four kMC simulations (red, blue, green, and brown) of emission spectra using different assumptions about the solid's phonon density of states (DOS) and compares them to experiment (black). (The assumed phonon DOS used in each simulation appears in the right panel.) Although all four simulations resemble experimental results, we find best agreement with experiment when only transverse phonons are allowed to accept energy in the ladder-climbing process. Indeed, only here do we see the formation of three base-camps.

Under conditions of this work, VEP rapidly produces CO in many vibrationally excited states. Relaxation of the system back to vibrational equilibrium proceeds more slowly, as in Fig. 4A, where we show measurements of the time-resolved infrared fluorescence (open symbols) from seven vibrational states. Asymptotically, they all exhibit

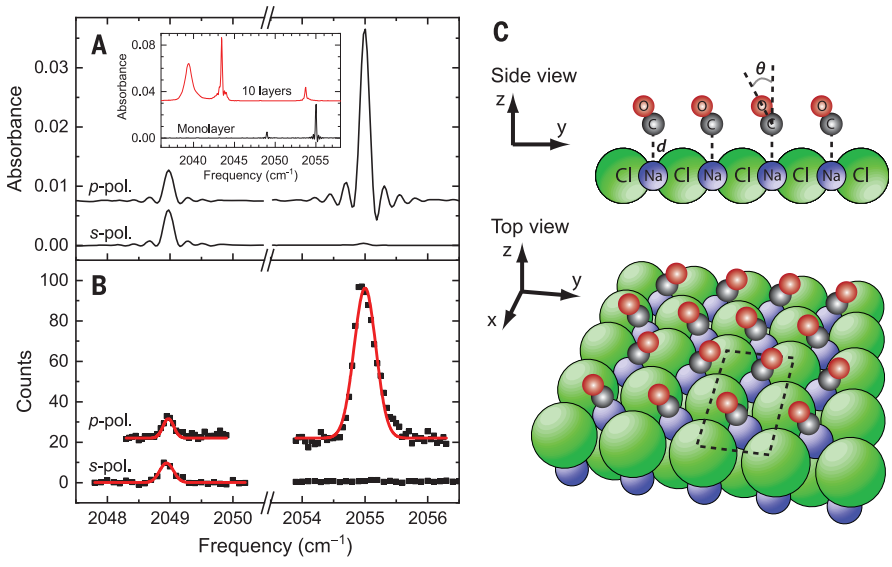


Fig. 1. Structure and infrared spectroscopy of the $^{13}C^{18}O$ monolayer on NaCl(100). (**A** and **B**) The polarization-dependent monolayer spectrum is observed with Fourier transform infrared (FTIR) absorbance spectroscopy (A) and laser-induced infrared fluorescence (B) by scanning the laser excitation frequency and integrating the total fluorescence signal between 50 and 1050 μs after the laser pulse. The spectra were recorded at a surface temperature of ~7 K. Note that the baseline of the p-polarized spectra is shifted for clarity. The inset in (A) shows that the IR absorption spectrum of the CO monolayer (black) is clearly distinguishable from that of a multilayer (red) for p-polarized light. CO molecules in the multilayer but not in contact with the NaCl surface give rise to a doublet centered at 2042 cm^{-1} (*31*, *32*). The feature at 2054 cm^{-1} arises from the CO molecules at the buried NaCl interface (*32*). The monolayer line intensities have been corrected for an offset of 18° in the polarization of the FTIR spectrometer light source. In (B), the experimental data are represented by square symbols; red lines are Gaussian fits to guide the eye. (**C**) Structure of the monolayer CO on NaCl(100) (*22*, *23*). The nearest-neighbor CO-CO distance is 3.96 Å. At a surface temperature below 35 K, the CO molecules are tilted with respect to the surface normal by an angle of 25° and are arranged in antiparallel-oriented rows to form a $p(2 \times 1)$ unit cell, as depicted by the dashed rectangle.

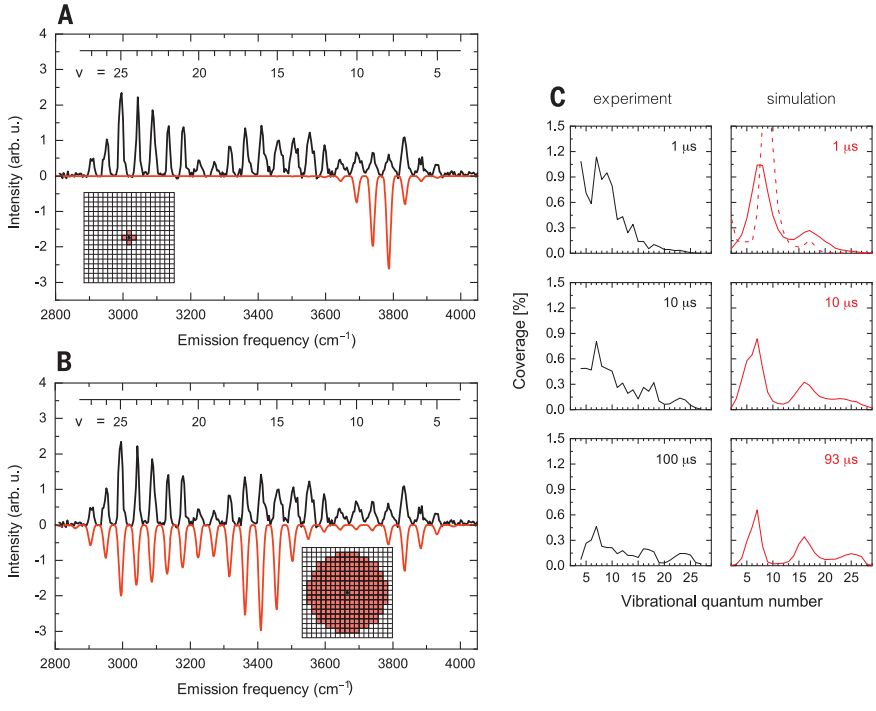


Fig. 2. Base-camp pooling mechanism operating for a monolayer of CO on NaCl(100). (**A** and **B**) Experimentally observed emission spectrum (black solid lines) and simulated spectra using kMC methods (red solid lines). The insets represent the CO lattice; the red shaded areas visualize the interaction distance around a given CO molecule (black dot) used in each kMC simulation. In (A), the simulation allows only nearest-neighbor V-V exchange, an assumption that was also made in (*14*–*16*). In (B), the simulation includes molecular interactions out to a distance of 34 Å. In each case, the monolayer feature at 2055 cm^{-1} (Fig. 1B) was excited with a narrowband infrared laser and the emission was dispersed through a monochromator and detected with a SNSPD integrating the signal counts between 50 and 250 μs after the laser pulse. (**C**) Snapshots in the experimentally derived and simulated population distributions showing sequential formation of the base-camps. The red dashed line corresponds to the population distribution at 100 ns.

Downloaded from http://science.sciencemag.org/ on January 15, 2019

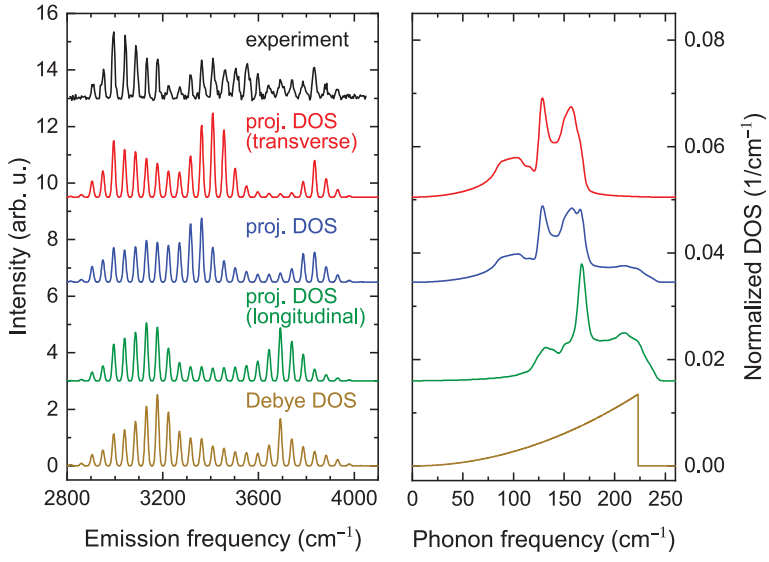


Fig. 3. Selective excitation of NaCl transverse phonons during energy pooling. The experimental emission spectrum (black solid line) is compared to kMC simulations assuming various NaCl phonon DOSs. In each simulation, the CO-to-CO interaction distance extends up to 34 Å. Each pooling step has an energy release to phonons of the solid; the probability depends on the phonon DOS at that energy. Shown are the results for a Debye DOS (brown) and three DFT-based DOSs: projection of the bulk DOS for NaCl onto the motion of the Na ions in the (100) plane (blue), longitudinal contribution to the projected DOS (green), and transverse contribution to the projected DOS (red).

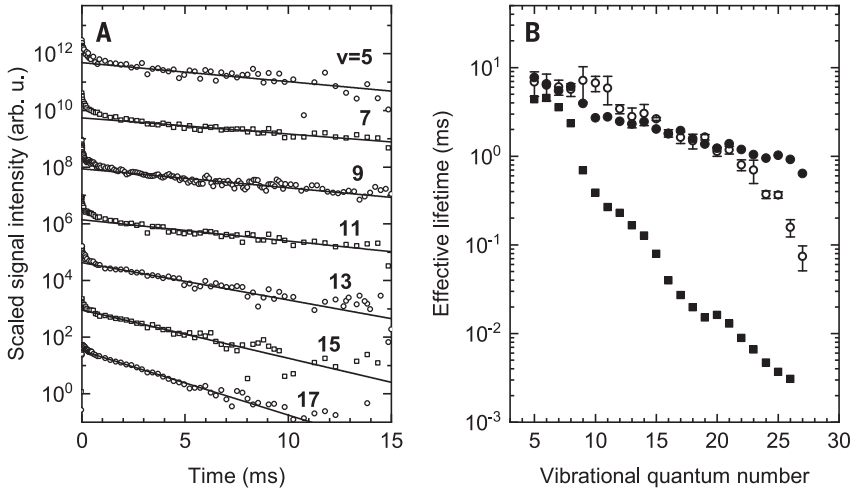


Fig. 4. Relaxation of CO to the NaCl solid follows the CPS model. (**A**) Representative temporal profiles of wavelength-resolved infrared fluorescence (open symbols); the emitting vibrational state's quantum number is indicated. The long-time relaxation exhibits an exponential decay (black solid lines). Note that the *y* axis is logarithmic and that the data are offset from one another along the *y* axis for clarity. (**B**) The effective exponential lifetime obtained from these (and other) fits (black open circles with error bars). Error bars denote SD (1σ) from three measurement results. The kMC simulations also exhibit long-time exponential behavior. The corresponding effective lifetimes are shown as solid symbols for two different vibrational relaxation models: the Skinner-Tully model (squares) and the CPS model (circles).

exponential decay (solid lines) with effective lifetimes, shown as open circles with error bars in Fig. 4B. For kMC simulations of the asymptotic exponential fall-off, we include three elementary processes: V-V energy transfer between CO molecules,

$$\mathrm{CO}(\mathrm{v}') + \mathrm{CO}(\mathrm{v}'') \rightarrow \mathrm{CO}(\mathrm{v}'+1) + \mathrm{CO}(\mathrm{v}''+1) \quad (4)$$

spontaneous radiative emission,

$$\mathrm{CO}(\mathrm{v}') \rightarrow \mathrm{CO}(\mathrm{v}'-1) + h\nu_{\mathrm{IR}} \quad (5)$$

and vibrational energy transfer to the NaCl lattice vibrations.

$$\mathrm{CO}(\mathrm{v}') \rightarrow \mathrm{CO}(\mathrm{v}'-1) + \Delta E_{\mathrm{phonon}} \quad (6)$$

For process 4, we use the same approach that allowed successful simulation of the data of Figs. 2 and 3 (*24*). For process 5, we use the known radiative emission rate constants for gas-phase CO(v′). For process 6, we have tested two models of vibrational energy transfer. The solid squares in Fig. 4B are the effective lifetimes that result from implementation of the Skinner-Tully (ST) model (*14*, *24*), where anharmonic coupling of CO vibration to NaCl phonons is mediated via the CO-NaCl surface bond (*14*–*18*). The predicted effective lifetimes are in poor agreement with experiment, and they exhibit a vibrational quantum number dependence that is far too strong. (Note the logarithmic scale.)

We also tested a model developed by Chance, Prock, and Silbey (CPS) (*19*, *20*), shown as solid circles in Fig. 4B (*24*). The agreement with experiment is striking. CPS was developed to describe fluorescence lifetimes of dye molecules interacting through an inert spacer layer with an absorbing and reflecting solid (*25*–*30*). Here, coupling occurs through electromagnetic fields. The fact that CPS accurately reproduces the observations of this work suggests that CO vibrational relaxation to NaCl lattice vibration also occurs through the electromagnetic near-field, even though there is a surface bond.

We emphasize that the weak vibrational quantum number dependence of the effective lifetime is indicative of coupling via the electromagnetic field; ST predicts a change in effective lifetime of four orders of magnitude over the same range of v where CPS predicts a change of less than an order of magnitude. Although an ab initio treatment of the coupling to the solid's phonon bath is still lacking, we expect the strong v-dependence to be retained (*24*). Referring to Fig. 4B, we speculate that the steeper slope above v ~ 23 indicates a transition to ST behavior.

Normally, we consider energy flow within an ensemble of oscillators to be a consequence of interatomic anharmonicity. This work shows that we can bind a molecule to a solid with sufficient strength to create samples that are stable over long periods of time without any influence of anharmonicity on the vibrational energy relaxation. In this Sommerfeld ground-wave limit, vibrational relaxation occurs exclusively via the electromagnetic field obeying the CPS model. Here, the strength of coupling scales with the

Downloaded from http://science.sciencemag.org/ on January 15, 2019

solid's imaginary index of refraction and the square of the molecule's transition dipole moment (*24*). Besides CO on NaCl, other similar systems are to be expected. CO on KCl and N_2 on NaCl are both interesting possibilities in which CPS coupling would be even weaker than seen here. For dipolar adsorbates that find themselves within this limit, the solid's crystalline lattice can be exploited to produce spatial registry and orientational order while the strength of dipole-dipole interactions between the adsorbate molecules still far exceeds the adsorbate coupling to the solid. Systems like the one described here appear to be promising for the study of quantum lattice dynamics.

REFERENCES AND NOTES

1. J. W. Park, Z. Z. Yan, H. Loh, S. A. Will, M. W. Zwierlein, *Science* **357**, 372–375 (2017).
2. B. Yan *et al.*, *Nature* **501**, 521–525 (2013).
3. D. DeMille, *Phys. Rev. Lett.* **88**, 067901 (2002).
4. A. André, D. DeMille *et al.*, *Nat. Phys.* **2**, 636–642 (2006).
5. K. Golibrzuch, N. Bartels, D. J. Auerbach, A. M. Wodtke, *Annu. Rev. Phys. Chem.* **66**, 399–425 (2015).
6. A. M. Wodtke, *Chem. Soc. Rev.* **45**, 3641–3657 (2016).
7. J. D. Beckerle, M. P. Casassa, R. R. Cavanagh, E. J. Heilweil, J. C. Stephenson, *Phys. Rev. Lett.* **64**, 2090–2093 (1990).
8. P. R. Shirhatti *et al.*, *Nat. Chem.* **10**, 592–598 (2018).
9. P. Guyot-Sionnest, P. Dumas, Y. J. Chabal, G. S. Higashi, *Phys. Rev. Lett.* **64**, 2156–2159 (1990).
10. K. Laß, X. Han, E. Hasselbrink, *J. Chem. Phys.* **123**, 051102 (2005).
11. H. C. Chang, G. E. Ewing, *Phys. Rev. Lett.* **65**, 2125–2128 (1990).
12. L. Chen *et al.*, *Acc. Chem. Res.* **50**, 1400–1409 (2017).
13. L. Chen *et al.*, *Opt. Express* **26**, 14859–14868 (2018).
14. S. A. Corcelli, J. C. Tully, *J. Chem. Phys.* **116**, 8079–8092 (2002).
15. S. A. Corcelli, J. C. Tully, *J. Phys. Chem. A* **106**, 10849–10860 (2002).
16. E. T. Boney, R. A. Marcus, *J. Chem. Phys.* **139**, 124107 (2013).
17. S. A. Corcelli, thesis, Yale University (2002).
18. S. A. Egorov, J. L. Skinner, *J. Chem. Phys.* **103**, 1533–1543 (1995).
19. R.R. Chance, A. Prock, R. Silbey, *Adv. Chem. Phys.* **37**, 1 (1978).
20. R. R. Chance, A. Prock, R. Silbey, *J. Chem. Phys.* **60**, 2744–2748 (1974).
21. A. Sommerfeld, *Ann. Phys.* **28**, 665 (1909).
22. J. Heidberg, E. Kampshoff, M. Suhren, *J. Chem. Phys.* **95**, 9408–9411 (1991).
23. D. Schmicker, J. P. Toennies, R. Vollmer, H. Weiss, *J. Chem. Phys.* **95**, 9412–9415 (1991).
24. See supplementary materials.
25. K. H. Drexhage, M. Fleck, H. Kuhn, F. P. Schäfer, W. Sperhing, *Ber. Bunsenges. Phys. Chem.* **70**, 1179 (1966).
26. K. H. Drexhage, *Sci. Am.* **222**, 108–119 (March 1970).
27. K. H. Drexhage, H. Kuhn, F. P. Schäfer, *Ber. Bunsenges. Phys. Chem* **72**, 329 (1968).
28. H. Kuhn, *Naturwissenschaften* **54**, 429–435 (1967).
29. H. Kuhn, *J. Chem. Phys.* **53**, 101–108 (1970).
30. K. H. Tews, O. Inacker, H. Kuhn, *Nature* **228**, 276–278 (1970).
31. H. C. Chang, H. H. Richardson, G. E. Ewing, *J. Chem. Phys.* **89**, 7561–7568 (1988).
32. J. Heidberg, M. Suhren, H. Weiss, *J. Electron Spectrosc. Relat. Phenom.* **64–65**, 227–234 (1993).

ACKNOWLEDGMENTS

We thank S. A. Corcelli for sharing his kMC simulation code, A. Kandratsenka for helpful discussions, and F. Heidrich-Meisner for providing helpful suggestions after reading an early version of this manuscript. **Funding:** Supported by Netherlands Organization for Scientific Research (NWO) Vidi grant 723.014.009 (J.M.). **Author contributions:** L.C. carried out experiments with the SNSPD-based spectrometer, analyzed data, and contributed to the manuscript; J.A.L. analyzed data, implemented and carried out the kMC calculations, and contributed to the manuscript; D.S. built and commissioned the SNSPD-based spectrometer, supervised experimentation, and contributed to the manuscript; J.M. implemented and carried out the calculations for the projected phonon DOS and contributed to the manuscript; V.B.V. developed the SNSPD devices for these experiments and reviewed drafts of the manuscript; and A.M.W. conceived the experiment and wrote the paper. **Competing interests:** None declared. **Data and materials availability:** There are no restrictions on materials used in this work. All data needed to evaluate the conclusions in the paper are present in the paper or the supplementary materials.

SUPPLEMENTARY MATERIALS

www.sciencemag.org/content/363/6423/158/suppl/DC1
Materials and Methods
Figs. S1 to S6
References (*33–49*)

15 September 2018; accepted 12 November 2018
Published online 13 December 2018
10.1126/science.aav4278

Downloaded from http://science.sciencemag.org/ on January 15, 2019

CHEMISTRY

Nematic-to-columnar mesophase transition by in situ supramolecular polymerization

Keiichi Yano[1], Yoshimitsu Itoh[1]*, Fumito Araoka[2], Go Watanabe[3], Takaaki Hikima[4], Takuzo Aida[1,2]*

Disk- and rod-shaped molecules are incompatible in coassembly, as the former tend to stack one-dimensionally whereas the latter tend to align in parallel. Because this type of incompatibility can be more pronounced in condensed phases, different-shaped molecules generally exclude one another. We report that supramolecular polymerization of a disk-shaped chiral monomer in nematic liquid crystals comprising rod-shaped molecules results in order-increasing mesophase transition into a single mesophase with a core-shell columnar geometry. This liquid crystalline material responds quickly to an applied electric field, resulting in unidirectional columnar ordering. Moreover, it can be modularly customized to be optoelectrically responsive simply by using a photoisomerizable rod-shaped module. The modular strategy allows for cooperative integration of different functions into elaborate dynamic architectures.

Polymerization in organized media has attracted attention because of the potential of the media to promote higher-order structures and the resulting physical properties (*1*–*5*). Conversely, supramolecular polymerization (*6*–*8*) in organized media has been explored very little to date (*9*, *10*), because the resultant noncovalent structures (if any) conferred by the media cannot be isolated.

We focused on supramolecular polymerization in liquid crystalline (LC) media (Fig. 1A). If the affinity between the resulting supramolecular polymer and the LC medium is large, then they are miscible, affording a uniform LC dispersion of the polymer (Fig. 1A, b). Conversely, if their affinity is poor, the polymer molecules are bundled and phase-separated from the LC medium (Fig. 1A, d). In the latter case, the insoluble polymer bundles may form a cross-linked three-dimensional network, which possibly compartmentalizes the LC phase and enhances its dynamic properties, as seen with LC physical gels (*9*). We find that supramolecular polymerization in nematic LC media induces an order-increasing mesophase transition (Fig. 1A, c), allowing highly elaborate, core-shell columnar coassembly.

Our initial motivation was to investigate whether a chiral dopant, if supramolecularly polymerized into a helical strand, could geometrically twist a nematic mesophase into a cholesteric mesophase to a greater extent than its monomeric form could (*11*). For this purpose, we chose a chiral benzenetricarboxamide (BTA) analog (*12*) as a supramolecularly polymerizable chiral dopant whose polymerization in solution has been investigated by Meijer and co-workers (*7*, *13*).

In general, different-shaped molecules, such as rods and disks, tend to exclude one another despite the large entropic penalty of the resulting phase separation (*14*). The combination of ^{OCB}Rod, a rod-shaped LC molecule affording a nematic order (Fig. 1C), and a BTA derivative monomer such as ^{C10}Disk$_{NH}$* (Fig. 1B, left) is not an exception to this general tendency. ^{C10}Disk$_{NH}$*, which carries three chiral hydrocarbon side chains, noncovalently polymerizes via triple hydrogen-bonding (H-bonding) interactions at its amide groups. We heated a mixture of ^{C10}Disk$_{NH}$* and ^{OCB}Rod (^{C10}Disk$_{NH}$*/^{OCB}Rod ratio = 1/30) (figs. S13B, S17C, and S21C) and then allowed the resulting isotropic melt to cool so that ^{C10}Disk$_{NH}$* could polymerize noncovalently in the LC medium of ^{OCB}Rod. Polarized optical microscopy (POM) revealed bundled fibers that were phase-separated from the LC medium (fig. S14, A and C). To address this incompatibility issue, we synthesized ^{OCB}Disk$_{NH}$* (Fig. 1B, center, and figs. S15A and S32) (*12*), whose hydrocarbon side chains are appended with an oxycyanobiphenyl (OCB) terminus as a potential compatibilizer with ^{OCB}Rod (*15*, *16*). A mixture of ^{OCB}Disk$_{NH}$* and ^{OCB}Rod (molar ratio, 1/30), treated thermally in a similar fashion, showed a fan-shaped POM texture (fig. S14, B and D) characteristic of columnar LC phases rather than cholesteric LC phases. Figure 1D shows a full phase diagram of the ^{OCB}Disk$_{NH}$*-^{OCB}Rod system, where a columnar mesophase at an ^{OCB}Disk$_{NH}$*/^{OCB}Rod molar ratio of 1/6 develops entirely as a single mesophase over the temperature range from 117 to −6°C (Fig. 2D and fig. S11E). When this mixture was diluted with ^{OCB}Rod, an exothermic peak assignable to its isotropic-to-nematic phase transition appeared at ~68°C, indicating that excess ^{OCB}Rod phase-separated (figs. S12 and S24). Unlike ^{OCB}Disk$_{NH}$* and ^{OCB}Rod alone (figs. S11, S16, and S19), ^{OCB}Disk$_{NH}$*-^{OCB}Rod (molar ratio, 1/6) in its synchrotron x-ray diffraction (XRD) profile at 100°C presented sharp and intense peaks in a low-angle region, whereas the wide-angle region presented only a broad diffraction peak with a *d*-spacing of 3.4 Å (Fig. 2G). We confirmed that this columnar LC material adopts a centered rectangular *c2mm* symmetry (lattice parameters, a = 75.2 Å; b = 35.0 Å), where each column contains tilted π-stacks of polymeric ^{OCB}Disk$_{NH}$* in its core (*17*), which is wrapped by a polymeric shell comprising self-assembled ^{OCB}Rod (Fig. 2A). Molecular dynamics (MD) simulations (*12*) also indicated the possibility of the formation of a core-shell columnar structure from ^{OCB}Disk$_{NH}$* and ^{OCB}Rod (figs. S54 to S57 and S60). Upon being cooled from 100 to 60°C, this columnar LC material changed its fundamental geometry from rectangular to hexagonal (a = 40.8 Å) without an exotherm (figs. S11E and S20). This phase sequence is opposite to those commonly observed (*18*) and has been observed in only rare cases (*19*).

Fourier-transform infrared (FTIR) spectroscopy (figs. S30A and S31) of an isotropic state of ^{OCB}Disk$_{NH}$*-^{OCB}Rod (molar ratio, 1/6) showed stretching vibrations due to free amide C=O and N–H moieties at 1673 and 3401 cm^{-1}, respectively (*13*). When this isotropic mixture was cooled to 100°C, allowing the phase transition into the columnar LC phase, these vibrational bands shifted abruptly to the lower wave numbers of 1640 and 3243 cm^{-1}, respectively, indicating that the amide moieties of ^{OCB}Disk$_{NH}$* H-bonded to form its supramolecular polymer. The supramolecular polymerization of ^{OCB}Disk$_{NH}$* is essential for the mesophase to adopt a columnar geometry. Chiral ^{OCB}Disk$_{NMe}$* (Fig. 1B, right, and figs. S13D, S15C, and S22), which is an N-methylated version of ^{OCB}Disk$_{NH}$*, cannot form a H-bonded supramolecular polymer. This modified version, when doped into the nematic phase of ^{OCB}Rod (^{OCB}Disk$_{NMe}$*/^{OCB}Rod ratio = 1/6), gave rise to the formation of only a cholesteric mesophase (Fig. 2, C, F, and I) and did not induce the nematic-to-columnar mesophase transition.

As described above, chiral ^{OCB}Disk$_{NH}$* carries a stereogenic center in each of its side chains that is in proximity to the H-bonding amide unit (Fig. 1B, center). We confirmed that the supramolecular polymers of (*R*)-^{OCB}Disk$_{NH}$ (^{OCB}Disk$_{NH}^{R}$) and (*S*)-^{OCB}Disk$_{NH}$ (^{OCB}Disk$_{NH}^{S}$) in methylcyclohexane were optically active and presented circular dichroism (CD) spectra that are mirror images (figs. S28A and S34). Heating to 80°C or mixing with 5 volume % methanol allowed the supramolecular polymers to depolymerize, and their characteristic CD bands virtually disappeared (fig. S28B). We also found that polymeric ^{OCB}Disk$_{NH}^{R}$ in the columnar mesophase of ^{OCB}Disk$_{NH}^{R}$-^{OCB}Rod (molar ratio, 1/6) at 100°C adopts a helical geometry, displaying a distinct chiroptical feature (Fig. 2J, red, and fig. S29C).

[1]Department of Chemistry and Biotechnology, School of Engineering, The University of Tokyo, 7-3-1 Hongo, Bunkyo-ku, Tokyo 113-8656, Japan. [2]RIKEN Center for Emergent Matter Science, 2-1 Hirosawa, Wako, Saitama 351-0198, Japan. [3]Department of Physics, School of Science, Kitasato University, 1-15-1 Kitasato, Minami-ku, Sagamihara, Kanagawa 252-0373, Japan. [4]RIKEN SPring-8 Center, 1-1-1 Kouto, Sayo-cho, Sayo-gun, Hyogo 679-5148, Japan.
***Corresponding author. Email: itoh@macro.t.u-tokyo.ac.jp (Y.I.); aida@macro.t.u-tokyo.ac.jp (T.A.)**

Downloaded from http://science.sciencemag.org/ on January 10, 2019

The MD simulation of $^{OCB}Disk_{NH}$*-^{OCB}Rod (molar ratio, 1/6) again indicated the formation of a helical BTA assembly in the core (fig. S58). As expected, when the opposite enantiomer $^{OCB}Disk_{NH}S$ was coassembled with ^{OCB}Rod (molar ratio, 1/6), the resultant CD spectrum was a mirror image of that observed for $^{OCB}Disk_{NH}R$-^{OCB}Rod (Fig. 2J, blue, and fig. S29E). Upon heating to 160°C to induce the phase transition into its isotropic melt, $^{OCB}Disk_{NH}$*-^{OCB}Rod became virtually CD silent (fig. S29A).

Columnar LC phases are known to be rigid and poorly responsive to electrical stimuli (*20*–*22*). We introduced $^{OCB}Disk_{NH}$*-^{OCB}Rod (molar ratio, 1/6) into a comb-type electrical cell, enabling in-plane application of the electric field (E-field) (Fig. 3A) (*12*). Before the application of the E-field, the sample at 100°C in POM was birefringent and displayed a fan texture characteristic of randomly oriented multidomain columnar LC phases. The two-dimensional (2D)–XRD pattern, obtained by irradiation with an x-ray beam along the *z* axis of the sample (Fig. 3A), was isotropic with a concentric diffraction feature (fig. S46A). However, when a direct-current (DC) E-field (40 V μm^{-1}) was applied to this sample along the arrow shown in Fig. 3A, the fan texture disappeared within 1 s (fig. S36 and movie S1). Upon being rotated around the *z* axis, the resulting material in POM showed bright- and dark-field images alternately at 45° intervals (fig. S35, A and B), indicating that the LC columns uniformly align unidirectionally for up to several hundred micrometers. In 2D-XRD, this oriented sample showed two distinct diffraction arcs, indexed to the (200) and (400) planes of the rectangular geometry, only in the equatorial direction (Fig. 3C), indicating parallel orientation of the core-shell columns relative to the direction of the applied DC E-field. The order parameter of the columnar orientation, as determined by scattering intensity plots, was 0.91 (fig. S47A). The observed response time of the columnar LC sample in its electrical orientation was shorter than most reported (table S1). Despite the rapid response of $^{OCB}Disk_{NH}$*-^{OCB}Rod, the unidirectional order remained unchanged for several days at 100°C after the E-field was turned off. This slow structural relaxation is not expected for the parent nematic LC material of ^{OCB}Rod. In polarized FTIR spectroscopy at 100°C, this unidirectional order presented a dichroic feature (Fig. 3D and fig. S51), where the polar plots of the H-bonded amide N–H (3239 cm^{-1}) and C≡N (2224 cm^{-1}) groups showed their absorption maxima in the meridional and equatorial directions, respectively. Together with the 2D-XRD profiles (Fig. 3C), the FTIR results make it apparent that the amide N–H and C≡N groups preferentially align parallel and perpendicular to the columnar axis, respectively, in accordance with the MD simulation (fig. S59). By switching the applied E-field from DC to AC (alternating current) (10 kHz, 24 V μm^{-1}), the columnar direction was changed from parallel to perpendicular and vice versa relative to the direction of the applied E-field (Fig. 3, B, E, and F; figs. S37 to S39; and movie S2). Such frequency-dependent behavior is reasonable considering that the C≡N and H-bonded amide groups, which are arranged orthogonally to each other in the LC column, tend to align parallel to the applied AC and DC E-fields, respectively (*22*). The orientational change profile, obtained from the scattering intensity–azimuthal angle (θ) plots, showed that two peaks (θ = 0° and 180°; perpendicular orientation) emerged at the expense of the original peaks (θ = ±90°; parallel orientation) (figs. S48 and S49). Thus, the orientational change of $^{OCB}Disk_{NH}$*-^{OCB}Rod occurred through electrical reconstruction, that is, electrical disassembly and subsequent reassembly (Fig. 3G), rather than rotation of the core-shell columns. The

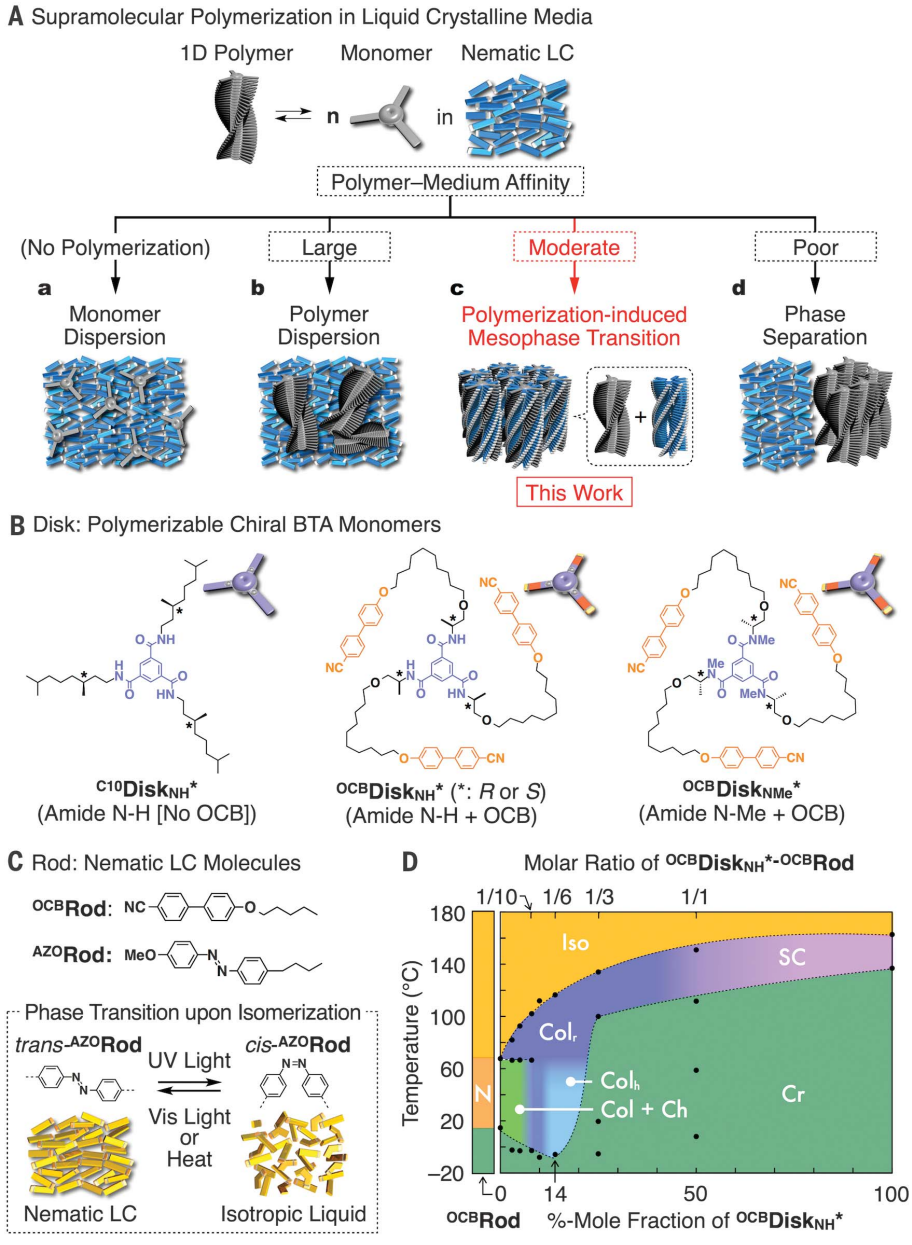


Fig. 1. Phase transition of LC media by supramolecular polymerization. (**A**) Schematic representations of possible modes of supramolecular polymerization in LC media. A monomer can form its one-dimensional supramolecular polymer in a nematic LC medium. (a to d) Depending on the affinity between the monomer or the resultant supramolecular polymer and the LC medium, four different modes are expected. (**B**) Molecular structures of disk-shaped chiral monomers derived from BTA: $^{C10}Disk_{NH}$*, $^{OCB}Disk_{NH}$*, and $^{OCB}Disk_{NMe}$*. Me, methyl. (**C**) Molecular structures of rod-shaped LC molecules affording a nematic order: ^{OCB}Rod and ^{AZO}Rod. Upon trans-cis isomerization, ^{AZO}Rod undergoes a reversible phase transition between its nematic LC phase and isotropic liquid. Vis, visible. (**D**) Phase diagram of $^{OCB}Disk_{NH}$*-^{OCB}Rod. Iso, SC, Col_r, Col_h, Col, Ch, N, and Cr denote isotropic, soft crystalline, rectangular columnar, hexagonal columnar, columnar (unidentified), cholesteric, nematic, and crystalline phases, respectively.

Downloaded from http://science.sciencemag.org/ on January 10, 2019

possible energy diagram is shown in Fig. 3G, a, where the intermediate state, featuring dissociated $^{OCB}Disk_{NH}$* and ^{OCB}Rod, substantially lowers the energetic barrier for the electrical reconstruction. Such an M-shaped energy diagram is not expected when the core and shell parts of the column are covalently connected (Fig. 3G, b).

In general, high levels of structural integrity and stimulus responsiveness are mutually exclusive. However, Zhang *et al.* recently succeeded in addressing this issue by integrating a protein crystal into a polymer network (*23*). In this work, we showed that a rod (^{OCB}Rod), when combined with a disk ($^{OCB}Disk_{NH}$*), properly operates for achieving the high levels of structural integrity and stimulus responsiveness. Furthermore, as described below, our material is customizable by modifying the rod- and disk-shaped components. An example made use of photoisomerizable ^{AZO}Rod (Fig. 1C), instead of ^{OCB}Rod, for the coassembly with $^{OCB}Disk_{NH}$*, which resulted in the formation of a core-shell columnar mesophase with a rectangular geometry (Fig. 2, B, E, and H, and fig. S23), similar to the case of $^{OCB}Disk_{NH}$*-^{OCB}Rod. The isotropic-to-columnar phase transition, which was observed for $^{OCB}Disk_{NH}$*-^{AZO}Rod (molar ratio, 1/6) at 155°C (fig. S11G), was accompanied by the H-bonding–mediated supramolecular polymerization of $^{OCB}Disk_{NH}$* (figs. S30B and S33, A to C). The columnar LC material of $^{OCB}Disk_{NH}$*-^{AZO}Rod was optically active, displaying distinct CD bands at 320 and 370 nm (Fig. 2K) originating from the OCB moieties in $^{OCB}Disk_{NH}$* [wavelength of maximum absorption (λ_{max}) = 300 nm] and ^{AZO}Rod (λ_{max} = 347 nm), respectively (fig. S25B). Thus, not only the core but also the shell in the core-shell columnar assembly adopts a helical geometry with a complementary helical handedness (Fig. 2B). Just like $^{OCB}Disk_{NH}$*-^{OCB}Rod, $^{OCB}Disk_{NH}$*-^{AZO}Rod was electrically alignable (figs. S40 and S50). Furthermore, it was optically responsive (*24*): The LC material, upon exposure to 365-nm ultraviolet (UV) light in a sandwich-type glass cell at 140°C (Fig. 4A) (*12*), underwent a phase transition into an isotropic melt, where the photoirradiated portion changed its appearance from birefringent to dark (Fig. 4C, f and g). As shown in movie S3, this reversible change occurred within seconds upon turning the UV light irradiation off and on (fig. S41). We found that this phase transition is due to the depolymerization of columnarly assembled $^{OCB}Disk_{NH}$* accompanied by the trans-to-cis photoisomerization of ^{AZO}Rod in the shell (Fig. 4B). Upon irradiation with UV light, $^{OCB}Disk_{NH}$*-^{AZO}Rod showed an enhancement of its electronic absorption intensity at 445 nm due to the cis form of ^{AZO}Rod at the expense of the absorption intensity at 347 nm due to its trans form (figs. S26 and S27). Concomitantly, the stretching vibration due to the H-bonded amide C=O moiety (1640 cm^{-1}) shifted to the higher wave number of 1671 cm^{-1}, whereas that due to the N–H moiety (3243 cm^{-1}) became highly obscure (fig. S33, D and E). The thermodynamic stability of polymeric $^{OCB}Disk_{NH}$* is highly sensitive to the polarity of the medium. From the FTIR spectral features described above, we believe that the dissociation of the polymeric $^{OCB}Disk_{NH}$* upon irradiation with UV light is caused by the enhanced polarity of the medium upon photochemical generation of highly polar *cis*-^{AZO}Rod (Fig. 4B).

A wide variety of operating principles have been reported for the realization of molecular information processors (*25*–*27*). As LC materials can provide an amplified optical output because

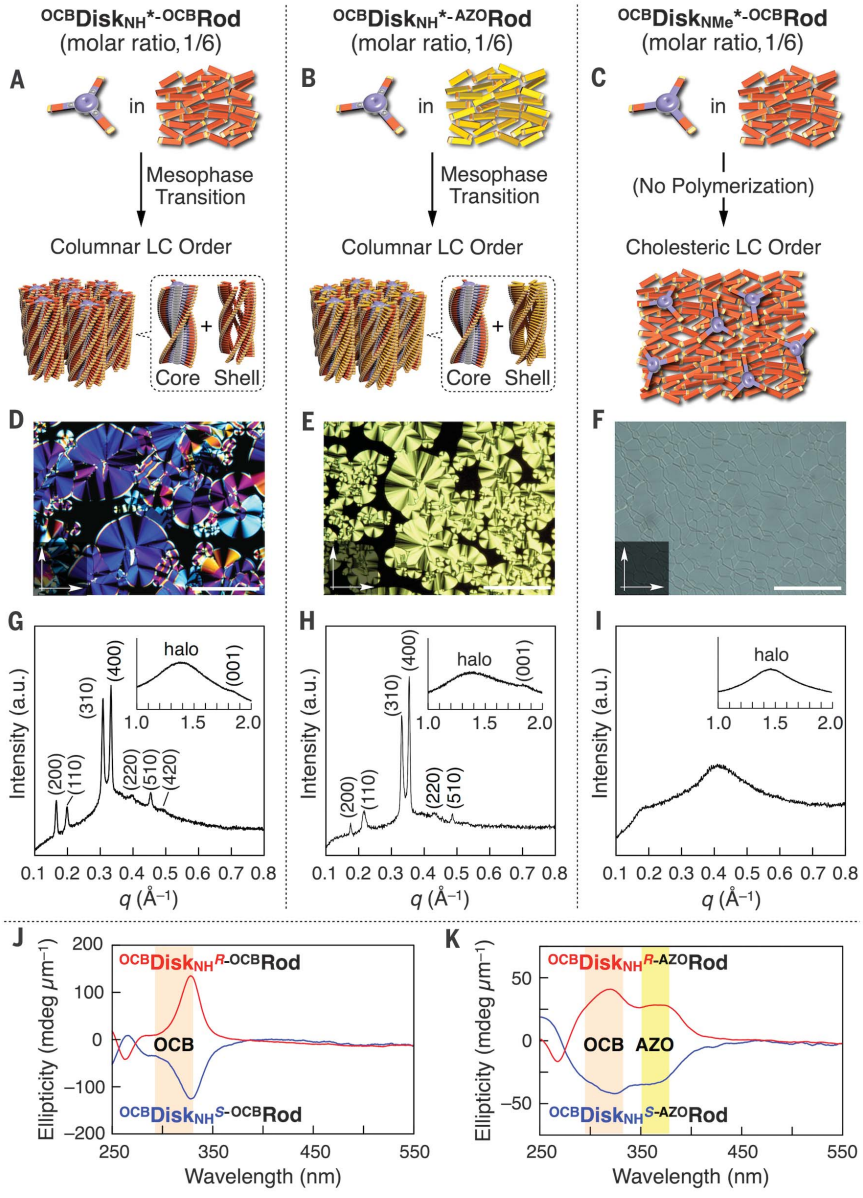


Fig. 2. Noncovalent modular approach to hierarchically ordered core-shell columnar LC phases. (**A** to **C**) Schematic representations; (**D** to **F**) POM images under crossed polarizers; (**G** to **I**) synchrotron XRD patterns; and (**J** and **K**) CD spectra of [(A), (D), (G), and (J)] $^{OCB}Disk_{NH}$*-^{OCB}Rod at 100°C, [(B), (E), (H), and (K)] $^{OCB}Disk_{NH}$*-^{AZO}Rod at 140°C, and [(C), (F), and (I)] $^{OCB}Disk_{NMe}$*-^{OCB}Rod at 30°C at disk/rod molar ratios of 1/6. Supramolecular polymerization of $^{OCB}Disk_{NH}$* in (A) ^{OCB}Rod and (B) ^{AZO}Rod results in mesophase transition into a columnar LC phase with a core-shell geometry. Each column bears a helical polymeric core composed of H-bonded $^{OCB}Disk_{NH}$*, which is surrounded by a polymeric shell comprising (A) ^{OCB}Rod and (B) ^{AZO}Rod with a complementary helical handedness. (C) Nonpolymerizable $^{OCB}Disk_{NMe}$* in ^{OCB}Rod forms a cholesteric LC phase. [(D) to (F)] For the POM observations, a sandwich-type glass cell (5 μm of separation) was employed. Scale bars represent 100 μm. [(G) to (I)] Synchrotron XRD patterns in a capillary were obtained upon cooling from isotropic melts. Miller indices are given in parentheses. a.u., arbitrary units; *q*, scattering vector. (Insets) Diffraction profiles in the wide-angle region. [(J) and (K)] For the CD spectroscopy, each of the samples was introduced into a sandwich-type quartz cell. The CD spectra were normalized by the thicknesses of their quartz cells. mdeg, millidegrees.

Downloaded from http://science.sciencemag.org/ on January 10, 2019

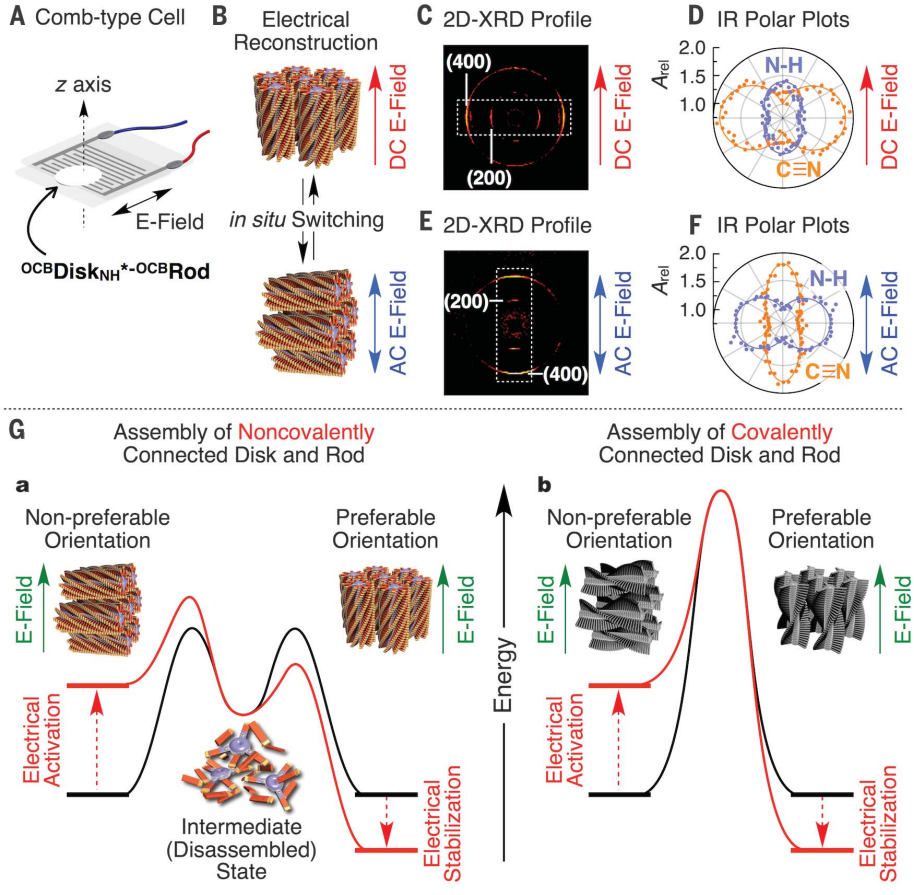


Fig. 3. Electrical reconstruction of the core-shell columnar LC material and its energy diagram. (**A**) Schematic representation of a comb-type electrical cell comprising two parallel glass plates (20 μm of separation) for in-plane E-field application. (**B**) Electrical reassembly of $^{OCB}Disk_{NH}$*-^{OCB}Rod (molar ratio, 1/6), where the core-shell LC columns can be oriented parallel and perpendicular to the directions of applied DC and AC E-fields, respectively. (**C** to **F**) [(C) and (E)] Synchrotron 2D-XRD profiles and [(D) and (F)] polar plots of the polarized IR absorption intensities of $^{OCB}Disk_{NH}$*-^{OCB}Rod at 100°C oriented by applying [(C) and (D)] a DC E-field (40 V μm^{-1}) and [(E) and (F)] an AC E-field (square wave, 10 kHz, 24 V μm^{-1}). A_{rel}, relative absorbance. [(C) and (E)] Miller indices are given in parentheses. [(D) and (F)] Polarized IR absorption intensities, arising from the H-bonded amide N–H (3239 cm^{-1}; purple) and C≡N (2224 cm^{-1}; orange) groups, were recorded upon rotation of the polarizer at 5° intervals. These intensities were normalized relative to the minimum value among them. (**G**) Energy diagrams for the electrical reconstruction of columnar LC materials. (a) The noncovalent core-shell column bears an intermediate state featuring disassembled core and shell modules, whereas (b) the covalent one does not.

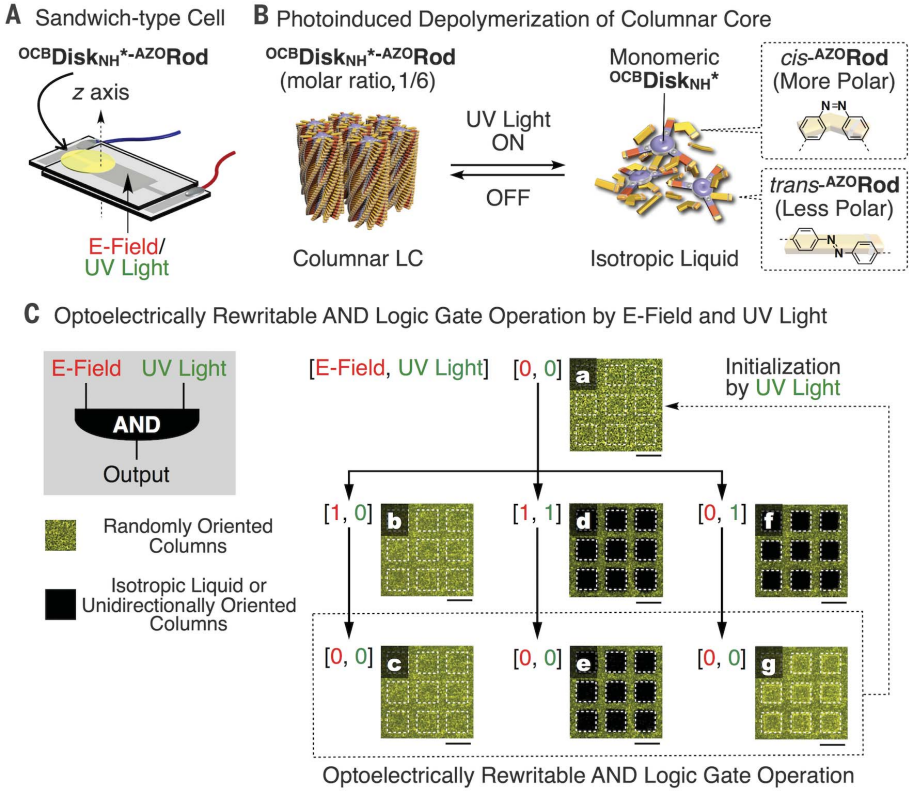


Fig. 4. LC material–based optoelectrically rewritable and logic gate operation by optical and electrical stimuli. (**A**) Schematic representation of a sandwich-type glass cell comprising two parallel glass plates (5 μm of separation) for vertical E-field application and UV light irradiation. (**B**) Schematic representations of the photoinduced depolymerization and repolymerization of $^{OCB}Disk_{NH}$*-^{AZO}Rod (molar ratio, 1/6) between the columnar LC and its isotropic liquid upon UV light irradiation (365 nm) and backward thermal relaxation. (**C**) POM images of $^{OCB}Disk_{NH}$*-^{AZO}Rod (molar ratio, 1/6) upon application of a power-tuned DC E-field (5 V μm^{-1}) and/or upon irradiation with 365-nm UV light with a lattice-patterned photomask. Dashed squares represent areas exposed to UV light, whereas the entire area was exposed to the E-field. Scale bars represent 200 μm.

Downloaded from http://science.sciencemag.org/ on January 10, 2019

of their long-range molecular ordering, the development of LC material–based logic gates is an interesting challenge. Such logic gates require LC materials that can respond differently to multiple stimuli. We developed an LC material–based optoelectrically rewritable device by using $^{OCB}Disk_{NH}$*-^{AZO}Rod (Fig. 4C), exploiting its optically and electrically responsive properties. The strategy uses a power-tuned DC E-field that cannot solely orient the LC columns but can only assist the photodissociated monomer to reassemble into a unidirectionally oriented columnar order. The as-received columnar LC phase of $^{OCB}Disk_{NH}$*-^{AZO}Rod (molar ratio, 1/6) at 140°C provided a birefringent multidomain sample (Fig. 4C, a) in a sandwich-type glass cell (Fig. 4A). This POM image could be darkened by the application of a DC E-field with a power above 5 V μm^{-1}; otherwise, it remained birefringent (Fig. 4C, b and c; fig. S42; and movie S4). By contrast, when this sample was exposed to UV light, its POM image became nonbirefringently dark by the photoinduced columnar-to-isotropic phase transition (Fig. 4C, f). However, when the UV irradiation ceased, the POM image became birefringent again because the columnar mesophase, thus reformed, presented a randomly oriented multidomain feature (Fig. 4C, g) analogous to the initial state (Fig. 4C, a). Thus, the LC logic gate device can initialize written information by light (movie S6). Meanwhile, when the DC E-field application (5 V μm^{-1}) and UV irradiation were performed simultaneously, the birefringent image quickly turned dark within a few seconds (Fig. 4C, d and e; fig. S43; and movie S5), because monomeric $^{OCB}Disk_{NH}$*, generated by the photoinduced phase transition, reassembled into a unidirectionally ordered column with the assistance of the applied DC E-field. The nonbirefringently dark image remained unchanged for several hours at 140°C after both the external inputs were turned off (fig. S44). Although this pointwise rewritable capability can be realized by using photoisomerizable ^{AZO}Rod alone, the written image became blurry because of the high fluidity of ^{AZO}Rod (fig. S45 and movie S7). As shown in Fig. 4C, the whole process can be regarded as a rewritable and logic gate because the nonbirefringently dark output appears only when the electrical and optical inputs are applied simultaneously.

REFERENCES AND NOTES

1. K. Kageyama, J. Tamazawa, T. Aida, *Science* **285**, 2113–2115 (1999).
2. K. Tajima, T. Aida, *Chem. Commun.* **2000**, 2399–2412 (2000).
3. K. Akagi *et al*., *Science* **282**, 1683–1686 (1998).
4. T. J. White, D. J. Broer, *Nat. Mater.* **14**, 1087–1098 (2015).
5. T. Kitao, Y. Zhang, S. Kitagawa, B. Wang, T. Uemura, *Chem. Soc. Rev.* **46**, 3108–3133 (2017).
6. J.-M. Lehn, *Polym. Int.* **51**, 825–839 (2002).
7. T. F. A. De Greef *et al*., *Chem. Rev.* **109**, 5687–5754 (2009).
8. T. Aida, E. W. Meijer, S. I. Stupp, *Science* **335**, 813–817 (2012).
9. T. Kato, Y. Hirai, S. Nakaso, M. Moriyama, *Chem. Soc. Rev.* **36**, 1857–1867 (2007).
10. A. Cazacu *et al*., *Proc. Natl. Acad. Sci. U.S.A.* **106**, 8117–8122 (2009).
11. R. Eelkema, B. L. Feringa, *Org. Biomol. Chem.* **4**, 3729–3745 (2006).
12. Materials and methods are available as supplementary materials.
13. S. Cantekin, T. F. A. de Greef, A. R. A. Palmans, *Chem. Soc. Rev.* **41**, 6125–6137 (2012).
14. C. Tschierske, in *Handbook of Liquid Crystals*, vol. 5, J. W. Goodby, P. J. Collings, T. Kato, C. Tschierske, H. F. Gleeson, P. Raynes, Eds. (Wiley-VCH, 2014); https://doi.org/10.1002/9783527671403.hlc074.
15. R. W. Date, D. W. Bruce, *J. Am. Chem. Soc.* **125**, 9012–9013 (2003).
16. P. H. J. Kouwer, G. H. Mehl, *J. Am. Chem. Soc.* **125**, 11172–11173 (2003).
17. J. Barberá *et al*., *J. Am. Chem. Soc.* **125**, 4527–4533 (2003).
18. C. Tschierske, *Angew. Chem. Int. Ed. Engl.* **52**, 8828–8878 (2013).
19. N. H. Tinh, J. Malthete, C. Destrade, *Mol. Cryst. Liq. Cryst.* **64**, 291–298 (1981).
20. T. Wöhrle *et al*., *Chem. Rev.* **116**, 1139–1241 (2016).
21. K. Sato, Y. Itoh, T. Aida, *J. Am. Chem. Soc.* **133**, 13767–13769 (2011).
22. D. Miyajima *et al*., *Angew. Chem. Int. Ed. Engl.* **50**, 7865–7869 (2011).
23. L. Zhang, J. B. Bailey, R. H. Subramanian, A. Groisman, F. A. Tezcan, *Nature* **557**, 86–91 (2018).
24. H. K. Bisoyi, Q. Li, *Chem. Rev.* **116**, 15089–15166 (2016).
25. A. P. de Silva, H. Q. N. Gunaratne, C. P. McCoy, *Nature* **364**, 42–44 (1993).
26. C. P. Collier *et al*., *Science* **285**, 391–394 (1999).
27. A. P. de Silva, S. Uchiyama, *Nat. Nanotechnol.* **2**, 399–410 (2007).

ACKNOWLEDGMENTS

The synchrotron radiation experiments were performed on BL44B2 and BL45XU at the Super Photon Ring (SPring-8) with the approval of RIKEN (proposal nos. 20140045, 20150022, 20160024, 20170046, and 20180044). The computations were performed by using the Research Center for Computational Science (Okazaki, Japan). We acknowledge K. Kato for generous support for the synchrotron radiation experiments. **Funding:** This work was financially supported by a JSPS Grant-in-Aid for Scientific Research (S) (18H05260) on "Innovative Functional Materials based on Multi-Scale Interfacial Molecular Science" for T.A. Y.I. is grateful for a JSPS Grant-in-Aid for Young Scientists (A) (16H06035). K.Y. thanks the Program for Leading Graduate Schools (MERIT) and the JSPS Young Scientist Fellowship. **Author contributions:** K.Y. designed and performed all experiments. Y.I. and T.A. co-designed the experiments. K.Y., Y.I., F.A., G.W., and T.A. analyzed the data and wrote the manuscript. G.W. performed MD simulations. T.H. supported the XRD measurements at SPring-8. **Competing interests:** The authors have no competing interests. **Data and materials availability:** All data are available in the main text or in the supplementary materials.

SUPPLEMENTARY MATERIALS

www.sciencemag.org/content/363/6423/161/suppl/DC1
Materials and Methods
Supplementary Text
Figs. S1 to S60
Table S1
References (*28*–*57*)
Movies S1 to S7

4 March 2017; resubmitted 12 September 2017
Accepted 23 November 2018
10.1126/science.aan1019

Downloaded from http://science.sciencemag.org/ on January 10, 2019

SEXUAL SELECTION

Problem-solving males become more attractive to female budgerigars

Jiani Chen[1], Yuqi Zou[1,2], Yue-Hua Sun[1]*, Carel ten Cate[3,4]

Darwin proposed that mate choice might contribute to the evolution of cognitive abilities. An open question is whether observing the cognitive skills of an individual makes it more attractive as a mate. In this study, we demonstrated that initially less-preferred budgerigar males became preferred after females observed that these males, but not the initially preferred ones, were able to solve extractive foraging problems. This preference shift did not occur in control experiments in which females observed males with free access to food or in which females observed female demonstrators solving these extractive foraging problems. Our results suggest that direct observation of problem-solving skills increases male attractiveness and that this could contribute to the evolution of the cognitive abilities underlying such skills.

One intriguing hypothesis for the evolution of cognitive abilities in both humans (*1*, *2*) and nonhuman animals (*3*) is that sexual selection may have contributed to their evolution. Mating with a "smart" partner can give rise to immediate benefits, such as obtaining a partner with enhanced food extraction abilities (*4*) or one that is better at coping with varying environmental conditions (*5*). In some species (*6*, *7*), variation in cognitive abilities is correlated with reproductive success. A preference for smart mates can therefore contribute to selection on cognitive abilities.

Preferences for mates with better cognitive abilities have been inferred from experiments in which mate choice was based on secondary sexual traits correlated with bigger brains or better cognitive skills (*8*–*10*), as well as from positive correlations between mate attractiveness and cognitive ability when testing these variables separately (*11*–*13*). However, the most direct support for this "mate choice for cognitive traits" hypothesis would be to demonstrate that mate preferences are affected by observing differences in cognitive abilities. We tested this hypothesis by examining whether female budgerigars alter their preference for males after observing these males' ability to open two types of problem-solving devices (referred to as "problem boxes") to get access to food.

Problem-solving tasks are frequently used to examine innovation and cognitive performance. Multiple processes and mechanisms may underlie such problem-solving, including noncognitive ones, such as motivation or neophobia (*14*–*16*). Nevertheless, an individual that can open different problem boxes, especially multistep ones involving sequential learning, demonstrates that it has acquired a complex skill. This ability may also suggest skills involving physical cognition or some degree of causal understanding (*14*, *15*).

Opening problem boxes to get access to food represents a complex food extraction task. Budgerigars are native to dry and arid areas in Australia. Although food availability may be relatively stable in parts of this range, in others it can be low, unpredictable, and variable from year to year (*17*). Detailed studies of the food extraction skills that budgerigars need in these conditions are lacking, but finding and extracting food can be challenging, and thus having cognitive skills for accessing food is likely adaptive. Moreover, because female budgerigars incubate, brood, and feed their young after hatching, while male mates provide food for the females (*18*, *19*), finding a partner with the skills to solve foraging problems is advantageous. Budgerigars also imitate demonstrators in an operant task to obtain food (*20*, *21*), and problem-solving in budgerigars correlates with detour reaching and exploration (*22*). Thus, we hypothesize that females attend to and prefer males that show cognitive skills in extracting food.

In our first experiment (experiment 1), females were exposed to two males: (i) a visibly skilled male problem solver that was able to open two different problem boxes and (ii) a male unable to do so (Fig. 1). We examined how this exposure affected female preferences for these males. To control for the effect of observing an eating male, which might affect female preferences (*4*, *23*), females in a control group were exposed to both an eating and a noneating male. In a second experiment (experiment 2), we examined whether the increased preference shown for problem-solving individuals reflected an increased social, rather than sexual, preference for problem-solving individuals. Experiment 2 was identical to experiment 1, except that females were exposed to two females, rather than two males, and their preference for both types of females was assessed.

Thirty-four males (17 pairs) and 17 females took part in experiment 1. They were divided into a problem-solving group (18 males and 9 females) and a control group (16 males and 8 females). Females in both groups were first given a series of tests (preference test 1) in which each female was tested with one pair of males in a two-choice cage (fig. S1 and movie S1). The male near which the female spent most of her time was identified as the preferred male and the other one the less-preferred male. Females in both the problem-solving group and the control group spent more time near the preferred male (problem-solving: $t = -2.395$, df = 31.99, $P = 0.023$; control: $t = -2.226$, df = 28, $P = 0.034$) (Fig. 2A). The time allocated to preferred and less-preferred males was similar for both groups (preferred males: $t = -1.290$, df = 30, $P = 0.207$; less-preferred males: $t = 0.148$, df = 30, $P = 0.883$). There were no significant morphological differences between preferred and less-preferred males (table S1).

After preference test 1, less-preferred males of the problem-solving group were trained to solve two foraging problems to get access to food—opening a petri dish and opening a three-step box. The preferred males in this group did not receive such training. During a subsequent observing phase, females were allowed to observe the problem-solving task performance of their familiar pair of males (movie S2). All nine less-preferred males, but none of the preferred males, successfully opened the petri dish and the three-step box in front of the females. After observing the successful problem-solving of the less-preferred males and the failure of the preferred males, the females were again allowed to choose among these males (preference test 2). The females significantly increased their time spent near the less-preferred males while decreasing their time spent near the preferred males compared to preference test 1 (Fig. 2A and fig. S2). The time allocated to the less-preferred males was significantly higher than that allocated to the preferred males during preference test 2 ($t = 3.129$, df = 31.99, $P = 0.004$). In addition, the time spent near the preferred male minus the time spent near the less-preferred male was significantly different between preference tests 1 and 2, showing that female preferences changed after the observing phase ($t = -3.167$, df = 15.99, $P = 0.006$).

In the observing phase for the control group, females saw the less-preferred male having free access to food in a regular food container and the preferred male having no food (movie S2). During preference test 2 (as in preference test 1), females again spent significantly more time near the preferred males than near the less-preferred males ($t = -2.642$, df = 28, $P = 0.013$) (Fig. 2A and fig. S3). The difference in time allocation to both males did not change between preference tests 1 and 2 ($t = 0.346$, df = 7.00, $P = 0.740$). Thus, a shift in preference between tests, resulting in a significant preference for less-preferred males, occurred only in the problem-solving group. Females in the problem-solving group also spent proportionally more time near the less-preferred males than did the females in the control group during preference test 2 (time near the less-preferred males divided by time near both males: $t = 2.417$, df = 14.02, $P = 0.030$).

[1]Key Laboratory of Animal Ecology and Conservation Biology, Institute of Zoology, Chinese Academy of Sciences, Beijing, China. [2]University of Chinese Academy of Sciences, Beijing, China. [3]Institute of Biology Leiden, Leiden University, Leiden, Netherlands. [4]Leiden Institute for Brain and Cognition, Leiden University, Leiden, Netherlands.
*Corresponding author. Email: sunyh@ioz.ac.cn

Downloaded from http://science.sciencemag.org/ on January 10, 2019

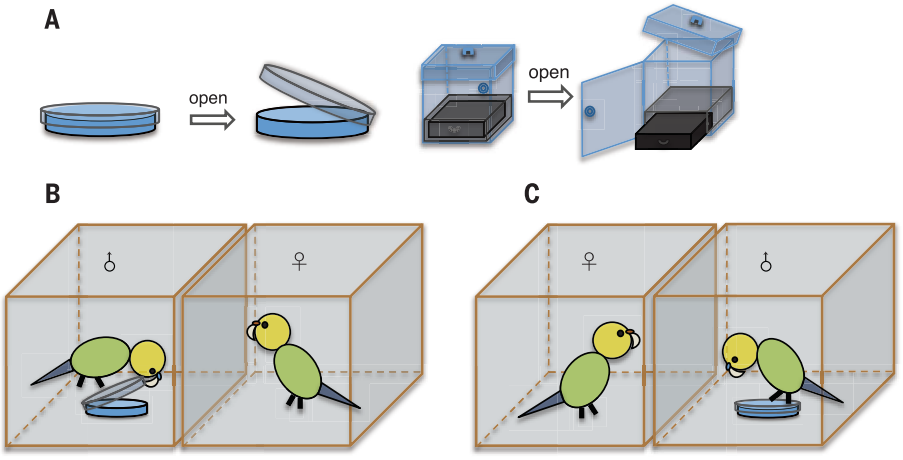


Fig. 1. Design of the observing phase. (**A**) Problem-solving devices: the petri dish and the three-step box. (**B**) A focal female observing a trained male opening the petri dish. (**C**) A focal female observing an untrained male trying unsuccessfully to open the dish.

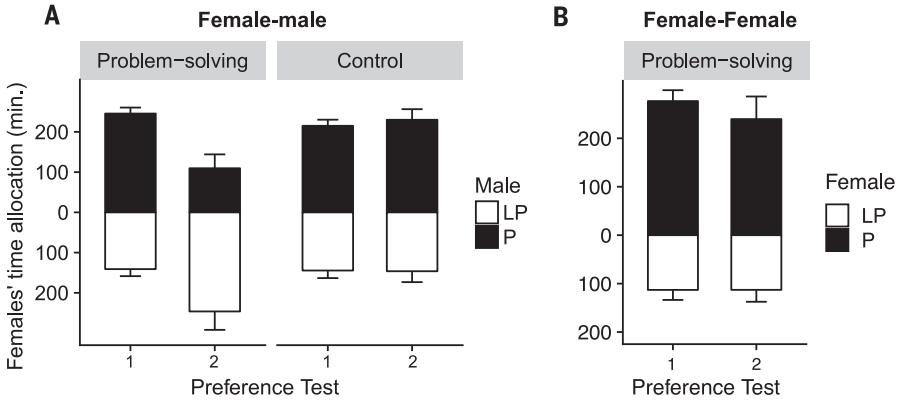


Fig. 2. Time spent by focal females near preferred and less-preferred individuals (mean ± SEM). The time spent near (**A**) males (experiment 1) and (**B**) females (experiment 2). Observation of less-preferred male demonstrators opening problem boxes resulted in a significant shift in preference toward these males. No significant preference shift was found in the control group or the female-female group. P, preferred; LP, less-preferred.

In experiment 2, eight focal females were given preference tests with two females (8 pairs of matched females) and observed female demonstrators. The focal females spent significantly more time with one female of their matched pairs in both preference test 1 (t = −3.928, df = 21, P < 0.001) and preference test 2 (t = −3.037, df = 21, P = 0.006) (Fig. 2B and fig. S4). The differences between the time allocation to the preferred and less-preferred females were similar for preference tests 1 and 2 (t = −0.556, df = 6.98, P = 0.596). Morphological characteristics were not significantly different between the preferred and less-preferred females (table S2). The preference for skilled individuals in experiment 1 is thus specifically linked to male demonstrators, suggesting that it has a clear sexual component.

The hypothesis that the evolution of cognitive abilities can be affected by a preference for smart partners has so far mainly been discussed for humans (*2*, *24*, *25*). Our results show that direct observation of behavior indicating the presence of cognitive skills in potential mates can affect mate preference in a nonhuman animal. Observing males that are more effective foragers may in itself increase attractiveness of such males (*4*, *23*), but our control experiment showed no change in the preference for males that had been observed eating without having to open problem boxes. Also, observing female instead of male demonstrators did not affect preferences. Thus, observing potential mates opening the boxes to get access to food seems to be the crucial factor for changing female preferences.

Earlier studies have shown mate choice that is based on traits that might be correlated with cognitive skills (*8*, *26*) or larger brains (*9*, *27*). Our study demonstrates that direct observation of cognitive skills can affect mate preference and, thus, that cognitive abilities may be selected by mate choice directly. This finding supports hypotheses, starting with that of Darwin (*1*), that sexual selection may affect the evolution of cognitive traits across animal species. Further studies are required to examine how general our findings are and which species are likely to undergo such selection. Species that imitate cognitive skills from conspecifics, such as budgerigars (*20*, *21*) and humans, might be those that benefit the most from discriminating mates on the basis of observing their skills.

REFERENCES AND NOTES

1. C. Darwin, *The Descent of Man, and Selection in Relation to Sex* (John Murray, ed. 1, 1871).
2. G. Miller, *The Mating Mind: How Sexual Choice Shaped the Evolution of Human Nature* (Anchor Books, ed. 1, 2001).
3. N. J. Boogert, T. W. Fawcett, L. Lefebvre, *Behav. Ecol.* **22**, 447–459 (2011).
4. L. K. Snowberg, C. W. Benkman, *J. Evol. Biol.* **22**, 762–769 (2009).
5. A. Kotrschal, B. Taborsky, *PLOS Biol.* **8**, e1000351 (2010).
6. L. Cauchard, N. J. Boogert, L. Lefebvre, F. Dubois, B. Doligez, *Anim. Behav.* **85**, 19–26 (2013).
7. B. J. Ashton, A. R. Ridley, E. K. Edwards, A. Thornton, *Nature* **554**, 364–367 (2018).
8. K. Karino, T. Utagawa, S. Shinjo, *Behav. Ecol. Sociobiol.* **59**, 1–5 (2005).
9. A. Kotrschal *et al.*, *J. Evol. Biol.* **28**, 841–850 (2015).
10. L. Cauchard, S. M. Doucet, N. J. Boogert, B. Angers, B. Doligez, *J. Avian Biol.* **48**, 1246–1253 (2017).
11. J. Keagy, J.-F. Savard, G. Borgia, *Anim. Behav.* **78**, 809–817 (2009).
12. A. J. Shohet, P. J. Watt, *J. Fish Biol.* **75**, 1323–1330 (2009).
13. M. D. Spritzer, D. B. Meikle, N. G. Solomon, *Anim. Behav.* **69**, 1121–1130 (2005).
14. J. Morand-Ferron, E. F. Cole, J. L. Quinn, *Biol. Rev. Camb. Philos. Soc.* **91**, 367–389 (2016).
15. S. Tebbich *et al.*, *Philos. Trans. R. Soc. B* **371**, 20150195 (2016).
16. A. Thornton *et al.*, *Behav. Ecol.* **25**, 1299–1301 (2014).
17. E. Wyndham, *Aust. J. Ecol.* **5**, 47–61 (1980).
18. J. Stamps, A. Clark, B. Kus, P. Arrowood, *Behaviour* **101**, 177–199 (1987).
19. C. A. Toft, T. F. Wright, *Parrots of the Wild: A Natural History of the World's Most Captivating Birds* (Univ. of California Press, 2015).
20. C. Heyes, A. Saggerson, *Anim. Behav.* **64**, 851–859 (2002).
21. R. Mui, M. Haselgrove, J. Pearce, C. Heyes, *Proc. Biol. Sci.* **275**, 2547–2553 (2008).
22. A. Medina-García, J. M. Jawor, T. F. Wright, *Behav. Ecol.* **28**, 1504–1516 (2017).
23. V. Chantal, J. Gibelli, F. Dubois, *PeerJ* **4**, e2409 (2016).
24. G. F. Miller, P. M. Todd, *Trends Cogn. Sci.* **2**, 190–198 (1998).
25. S. B. Kaufman, A. Kozbelt, M. L. Bromley, G. F. Miller, in *Mating Intelligence: Sex, Relationships, and the Mind's Reproductive System*, G. Geher, G. Miller, Eds. (Lawrence Erlbaum Associates, 2008), pp. 227–262.
26. J. Keagy, J.-F. Savard, G. Borgia, *Behav. Ecol.* **23**, 448–456 (2011).
27. J. Madden, *Proc. Biol. Sci.* **268**, 833–838 (2001).

ACKNOWLEDGMENTS

We thank C. Yan for help with the statistical analysis. **Funding:** This study was supported by the National Natural Science Foundation of China (project 31501868). **Author contributions:** J.C. and C.t.C. conceived of and designed the research. Y.-H.S. contributed to the design of the study. J.C., Y.Z., and Y.-H.S. conducted the experiments. J.C. and C.t.C. wrote the manuscript. All authors discussed and commented on the manuscript. **Competing interests:** The authors declare no competing interests. **Data and materials availability:** The video coding data are available as supplementary materials. Video recordings are available upon request.

SUPPLEMENTARY MATERIALS

www.sciencemag.org/content/363/6423/166/suppl/DC1
Materials and Methods
Figs. S1 to S4
Tables S1 to S5
References (*28*, *29*)
Movies S1 and S2
Data S1 to S4

18 July 2018; accepted 26 November 2018
10.1126/science.aau8181

Downloaded from http://science.sciencemag.org/ on January 10, 2019

NEUROSCIENCE

Emergence of preconfigured and plastic time-compressed sequences in early postnatal development

U. Farooq[1] and G. Dragoi[1,2]*

When and how hippocampal neuronal ensembles first organize to support encoding and consolidation of memory episodes, a critical cognitive function of the brain, are unknown. We recorded electrophysiological activity from large ensembles of hippocampal neurons starting on the first day after eye opening as naïve rats navigated linear environments and slept. We found a gradual age-dependent, navigational experience–independent assembly of preconfigured trajectory-like sequences from persistent, location-depicting ensembles during postnatal week 3. Adult-like compressed binding of adjacent locations into trajectories during navigation and their navigational experience–dependent replay during sleep emerged in concert from spontaneous preconfigured sequences only during early postnatal week 4. Our findings reveal ethologically relevant distinct phases in the development of hippocampal preconfigured and experience-dependent sequential patterns thought to be important for episodic memory formation.

The hippocampus is crucial for relational binding of spatial locations and events into spatial-mental trajectories and memory episodes (*1*–*3*). The rapid encoding and consolidation of sequential spatial experiences into memory episodes are achieved by representation of such trajectories within time-compressed hippocampal neuronal sequences during sleep or rest preceding (*4*) and following (*5*) novel experiences. The hippocampus undergoes a developmental critical period and functionally matures around postnatal day 24 (P24) (*6*, *7*). However, when and how hippocampal neuronal ensemble patterns of activity across different brain states underlying the encoding and consolidation of episodic-like memory develop, along with their dependence on intrinsic developmental programs and/or prior structured experience, have remained unknown. This is largely due to the difficulty of simultaneously recording electrophysiological activity from sufficient numbers of neurons in freely behaving developing animals (*8*, *9*).

Previous studies of sensory-motor brain areas have mapped how neuronal activity before and after experience (*10*) relates to the development of synaptic connectivity (*11*) and plasticity (*12*). However, the hippocampus does not directly respond to external stimuli of a single sensory modality (*13*); it integrates multimodal sensory and locomotor information across different brain states during navigation, awake rest, and sleep and expresses such information within compressed temporal neuronal sequences (*5*, *14*, *15*). Furthermore, episodic memory, thought to depend on the maturation of the hippocampal network, develops after sensory-motor systems appear sufficiently operational. Finally, structural maturation of the hippocampal formation is controlled by intrinsic signals from the stellate cells of the entorhinal cortex (*16*). These differences between the hippocampus and the sensory-motor systems further emphasize the need to understand the developmental stages of episodic-like memory function within the hippocampus.

We recorded electrophysiological activity of large ensembles of dorsal CA1 hippocampal neurons (up to 67 neurons) from 19 2- to 3-week-old freely behaving rats during ~30 min of their first ever (de novo) exploration of a 1-m linear track (i.e., the first-time run, which we refer to as Day1Run). We also recorded the preceding and following ~90-min-long sleep sessions (i.e., Pre-Run and Post-Run sleep) and awake rest epochs (awake rest) on the track (Fig. 1A). Fourteen animals reexplored the linear track on the same day (i.e., Day1Run2). On the following day, all animals reexplored the same linear track (Day2Run), and this run session was flanked by sleep sessions (Fig. 1A). Our recordings started from P15 (table S1) and included two of the previously proposed developmental landmarks corresponding to the maturation of individual CA1 place cells (on P17) and of the upstream entorhinal cortical grid cells (on P21) (*8*, *9*, *17*). The recordings of de novo run and associated sleep and rest during development were extended until P24, an age when individual hippocampal and entorhinal neuronal activities become adult-like (*8*, *9*, *17*). We also recorded the activity of dorsal CA1 hippocampal neurons in three adult rats (age ~90 days) that were undergoing a similar experimental protocol (see materials and methods).

Two movable 32-channel lightweight Neuronexus silicon octatrodes (Fig. 1, B and C) were implanted bilaterally into the hippocampus of experimentally naïve developing rats, yielding a total of 1763 single neurons for recordings on days 1 and 2 (Fig. 1, D and E). The P15 to P24 (P15–P24) animals explored the linear track in full laps and at similar velocities and angular head movement across ages (Fig. 1, F and G, and fig. S1, A to D). Place fields during run were computed for each individual putative pyramidal cell as described previously for adult rats (*15*). The P15–P24 developing animals were grouped into nonoverlapping age groups of two consecutive days (three to five animals per group), from P15–P16 to P23–P24 (Fig. 1H).

We observed an improvement with age in the metrics of spatial tuning (i.e., spatial information and place field stability within a run session) of individual place cells (Fig. 1H and fig. S2, A and B). We used a memoryless Bayesian decoder to predict the instantaneous location of an animal based on population neuronal spike trains. Despite the age-dependent increase in spatial tuning at the individual neuronal level, the decoding of animal location along its trajectory during a run was accurate as early as P15 (Fig. 1I and fig. S2C). The error in decoding location reduced with development, from ~10% track length at P15–P16 to ~5% at P23–P24 and adulthood. For all ages, the accuracy of neuronal ensembles to predict the current location of the animal was >3 times higher than that computed from shuffled data (Fig. 1J). This indicates that, from the very first exposure to a linear environment, 1 day after eye opening, hippocampal neuronal ensembles can reliably encode discrete locations along an animal's trajectory based on a firing rate code.

In addition, during a run the adult hippocampal network relationally binds past, current, and future sequential locations into trajectories at an order of magnitude faster than behavior. These compressed sequences are termed theta sequences due to their occurrence within 5- to 8-Hz theta oscillations in the hippocampus (*14*, *18*). Interventional studies suggest a relative dissociation between firing rate–based encoding of discrete locations by neuronal ensembles and binding of sequential locations into theta sequences by an ensemble temporal code (*19*, *20*). The ensemble temporal code is more strongly correlated with behavioral performance (*21*, *22*) and the role of the hippocampus in learning and memory (*21*–*23*) than the ensemble rate code. We investigated the developmental timeline of theta sequences during de novo exploration of linear tracks. Theta oscillation was present as early as P15, and its peak frequency increased as a function of age (Fig. 2A and fig. S3A). For theta cycles in the de novo run session, we decoded the trajectory based on ensemble neuronal activity (at velocities >10 cm/s). Theta sequences that bound past, current, and future animal locations within a theta cycle only occurred consistently in the P23–P24 group, and their strength [i.e., quadrant ratio (see materials and methods)] became adult-like for the first time at this age (Fig. 2, B to E, and fig. S3). Prior within-day navigational experience on the same linear track was not sufficient to accelerate the age-dependent increase in strength

[1]Interdepartmental Neuroscience Program, Yale School of Medicine, New Haven, CT, USA. [2]Departments of Psychiatry and Neuroscience, Yale School of Medicine, New Haven, CT, USA.
*Corresponding author. Email: george.dragoi@yale.edu

Downloaded from http://science.sciencemag.org/ on January 10, 2019

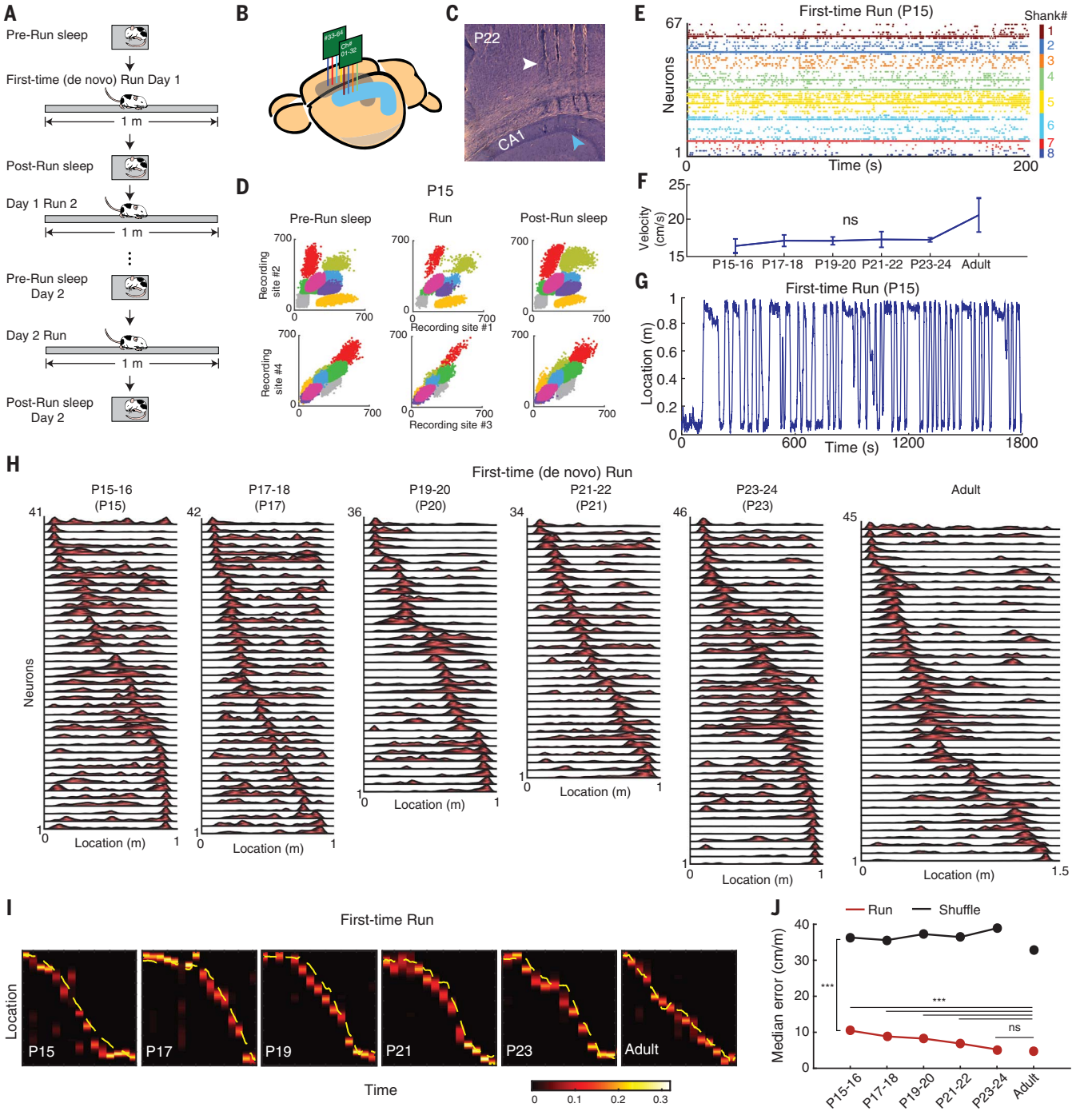


Fig. 1. Early-life development of hippocampal neuronal ensemble spatial representation during first-time navigation. (**A**) Schematic of experimental protocol. (**B**) Illustration of bilateral silicon probe implants in the dorsal hippocampal area CA1. (**C**) Sagittal brain section depicting tracks of four silicon probe shanks (white arrowhead) recording in CA1 (blue arrowhead) at P22. (**D**) Color-coded illustration of clusters of eight single cells recorded from one shank in a P15 animal during sleep-run-sleep sessions. (**E**) Simultaneous recording of 67 CA1 neurons across eight shanks at P15. (**F**) Similar velocity during first-time (de novo) run across development [$P = 0.209$; analysis of variance (ANOVA)]. (**G**) Example of first-time run trajectory at P15. (**H**) Examples of simultaneously recorded place cell sequences during first-time run across development. (**I**) Increased accuracy in neuronal ensemble representation of spatial locations during first-time navigation across ages throughout development, based on a memoryless Bayesian decoding algorithm (heatmap). Yellow line: actual animal trajectory. The color map shows the probability of a decoded location. (**J**) Significance (from P15–P16 onward, run vs. shuffle; $P < 10^{-10}$, rank sum tests) and age-dependent improvement ($P < 10^{-10}$, Kruskal-Wallis ANOVA) of neuronal ensemble–decoded locations during first-time navigation across development. Representation becomes adult-like at P23–P24. For post hoc comparisons with adult data, Dunn's test was used. ***$P < 0.001$; ns, not significant.

Downloaded from http://science.sciencemag.org/ on January 10, 2019

of theta sequences at P21–P22 (Fig. 2F). At earlier ages (P15 to P20), the hippocampal network represented well the current location of the animal on the track (Fig. 2G and fig. S3B), but the compressed binding of sequential locations within theta cycles could be variably decoded during a run starting only at P21–P22 and became adult-like at P23–P24 (Fig. 2, E and G). These changes were not due to an age-related increase in theta power (fig. S3, G and H). The later development of compressed theta sequences depicting an animal's trajectory by an ensemble temporal code contrasts with the earlier development of ensemble rate-code–based representation of individual locations.

Animals tend to rest between running individual laps on tracks. During these brief awake rest epochs, neuronal ensembles within transient periods of heightened population synchrony (termed frames) replay remembered (*24*) and preplay future (*4*) trajectories through linear space in association with 140- to 250-Hz ripple oscillations. We explored the developmental timeline of awake replay as our P15–P24 rats rested between laps during de novo run sessions. We detected frames of activity during awake rest, defined as increases in multineuronal activity (minimum of five neurons) exceeding two standard deviations (SD) above the mean at animal velocities <1 cm/s. We decoded an animal's virtual location on the track from the ensemble activity during the frames based on the corresponding activity during a run, as reported for adult animals (*15*, *25*). At P15–P16, the decoded activity from ~16% of the awake rest frames persistently depicted individual discrete locations along the track (Fig. 3, A and B) and were biased toward the current location of the animal, indicative of a behavioral bias (fig. S4). We called these frames containing discrete location-depicting ensembles stationary frames. At P15–P16, we did not observe sequential replay of trajectories (Fig. 3C, left), even when the animals had prior navigational experience on the same linear track [Fig. 3, B (right

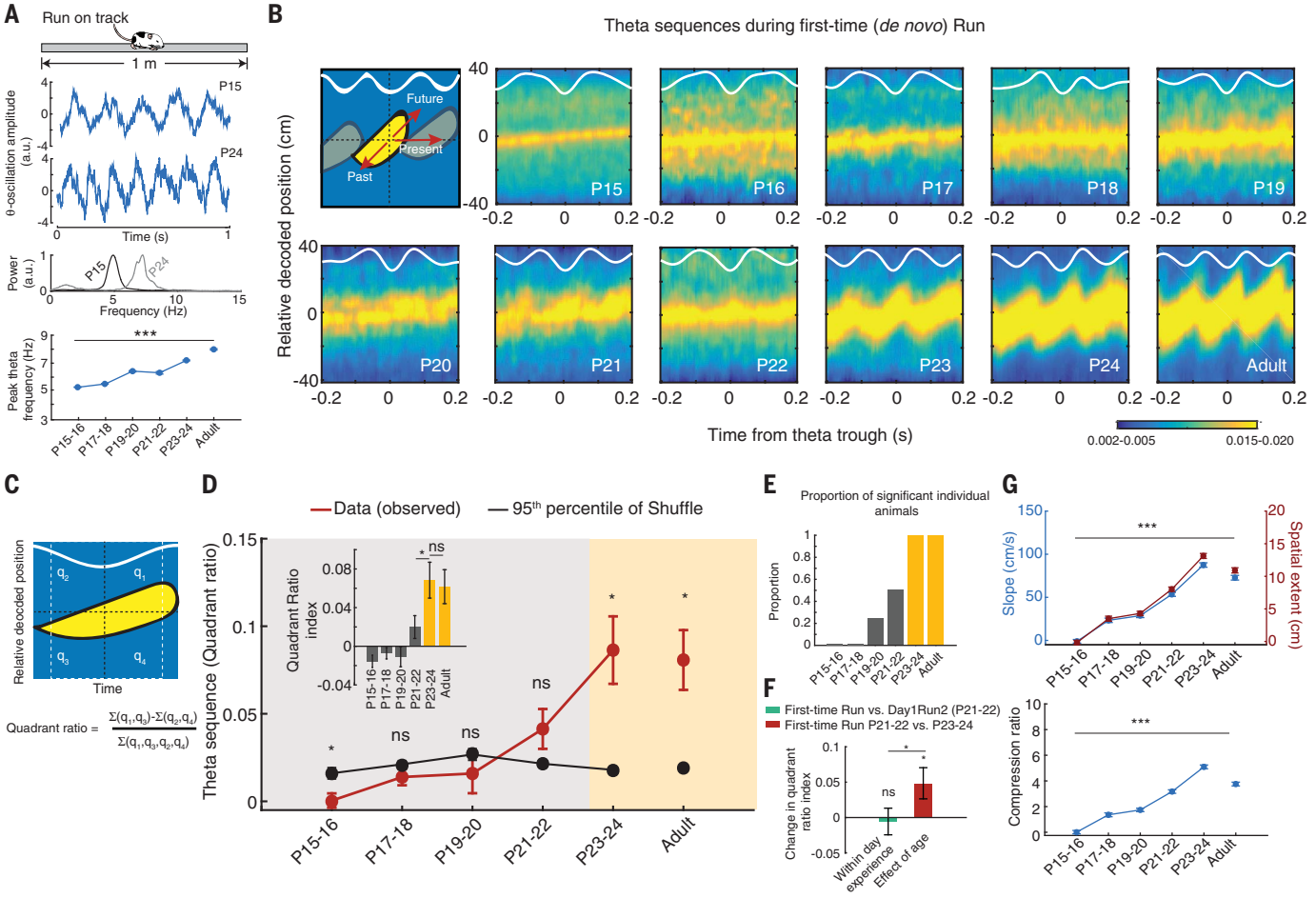


Fig. 2. Delayed development of compressed theta sequences during first-time navigation on linear tracks. (**A**) Age-dependent increase in CA1 theta oscillation frequency across development ($P < 10^{-10}$, ANOVA). The middle and bottom panels show wide band signals and the normalized power spectra for example P15 and P24 animals during the run. (**B**) Examples of developmental timeline (P15 to P24, panels 2 to 11) for compressed theta sequences binding past, current, and future locations (cartoon at top left). White curves: session-averaged theta oscillations. Note the absence of compressed theta rhythmic binding of past, current, and future locations at younger ages. (**C**) Quantification method for compressed theta sequence strength (quadrant ratio) in binding past, current, and future locations. (**D**) Developmental timeline (P15 to P24) of theta sequence strength. Note the emergence of consistent adult-like theta sequences (>shuffle) at P23–P24 (two directions per animal; n = 5, 3, 4, 4, 3, and 3 animals per age group, from P15–P16 to adult). (Inset) The quadrant ratio index significantly increases with age and becomes adult-like at P23–24. (**E**) Proportion of animals within age groups with theta sequences above the 95th percentile of their shuffles. (**F**) Effects of navigational experience on theta sequence strength (quadrant ratio index). Note that within-day experience (green bar; P = 0.75, paired t test, two directions per animal, three animals) does not reveal significant increases in theta sequence strength at P21–P22, while the increase in age, from P21–P22 to P23–P24, reveals increased strength during first-time navigation (red bar; P = 0.04, t test, two directions per animal, n = 4 and 3 animals). The effect of age is significantly higher than that of within-day experience (P = 0.03, t test). (**G**) Theta sequence slope/spatial extent (top) and compression ratio (bottom) increase with age ($P < 10^{-10}$, ANOVAs). Data are means ± SEM. ***$P < 10^{-10}$; *$P < 0.05$; ns, not significant.

Downloaded from http://science.sciencemag.org/ on January 10, 2019

two columns), and D]. Beginning on P17–P18, the activity during rest frames decoded segments of the run trajectory, which grew into extended track trajectories starting on P19–P20 (Fig. 3, A to C). From P15–P16 to P23–P24, the proportion of trajectory-depicting frames, likely replaying the extended run experience, increased gradually (Fig. 3C, left). At the same time, the strength of replay (i.e., strength of sequential trajectory-like representation by frames) and the extent of track being replayed also increased from P15–P16 to P23–P24 (Fig. 3C, middle and right). This developmental timeline of awake rest replay is important for two reasons. First, the frequent stationary frames during early development indicate that the hippocampal network initially operates in a persistent activity-like mode (*26*) at the neuronal ensemble level during offline rest epochs to represent individual spatial locations rather than sequential trajectories. The network ability to generate sequential motifs representing trajectories of sequentially explored locations develops at P17–P18 and gradually matures through P23–P24. Second, the emergence of compressed replay sequences precedes theta sequences by several days. This indicates that the phenomena of sequence compression during run (i.e., theta sequences) and during rest (i.e., awake replay) are mechanistically dissociable. This dissociation raises the question of whether offline expression of sequential motifs during rest or sleep requires prior explicit sequential spatial experience.

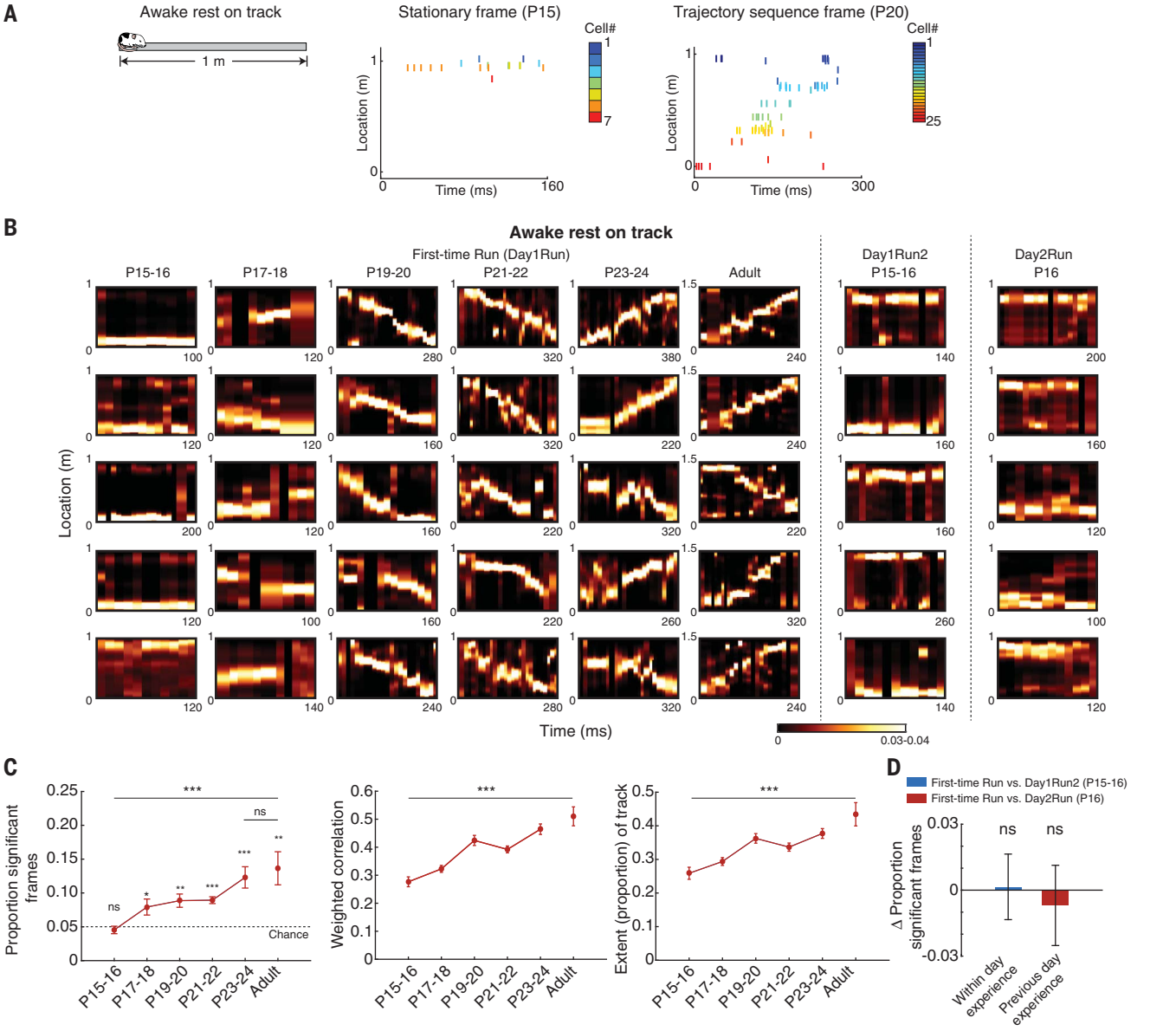


Fig. 3. Developmental timeline for trajectory-depicting sequences during on-track awake rest epochs. (**A**) Neuronal ensemble activity during rest within first-time navigation (left panel) depicts individual locations at P15–P16 (stationary ensembles in frames, middle panel) and entire trajectories from P19–P20 (right panel). (**B**) Examples of stationary location-depicting frames and partial and entire trajectory–depicting frames across age groups during on-track rest epochs for first-time navigation (Day1Run, left 30 panels), within-day runs on same track (Day1Run2, middle 5 panels), and Day2Run on the same track (right 5 panels). Bayesian decoding analysis was used. (**C**) Age-dependent increases in proportion of significant trajectory-depicting frames (left; $P < 10^{-4}$, ANOVA), correlation strength (middle; $P < 10^{-10}$), and extent of depicted trajectory (right; $P < 10^{-6}$). (**D**) Within-day ($P = 0.92$, paired t test) and previous-day ($P = 0.67$, t test) experience reveal no changes in the proportion of significant trajectory-depicting frames at P15–P16 and P16 (two directions per animal, $n = 3$ and 4 animals). Data are means ± SEM. ***$P < 0.005$; **$P < 0.01$; *$P < 0.05$; ns, not significant.

Downloaded from http://science.sciencemag.org/ on January 10, 2019

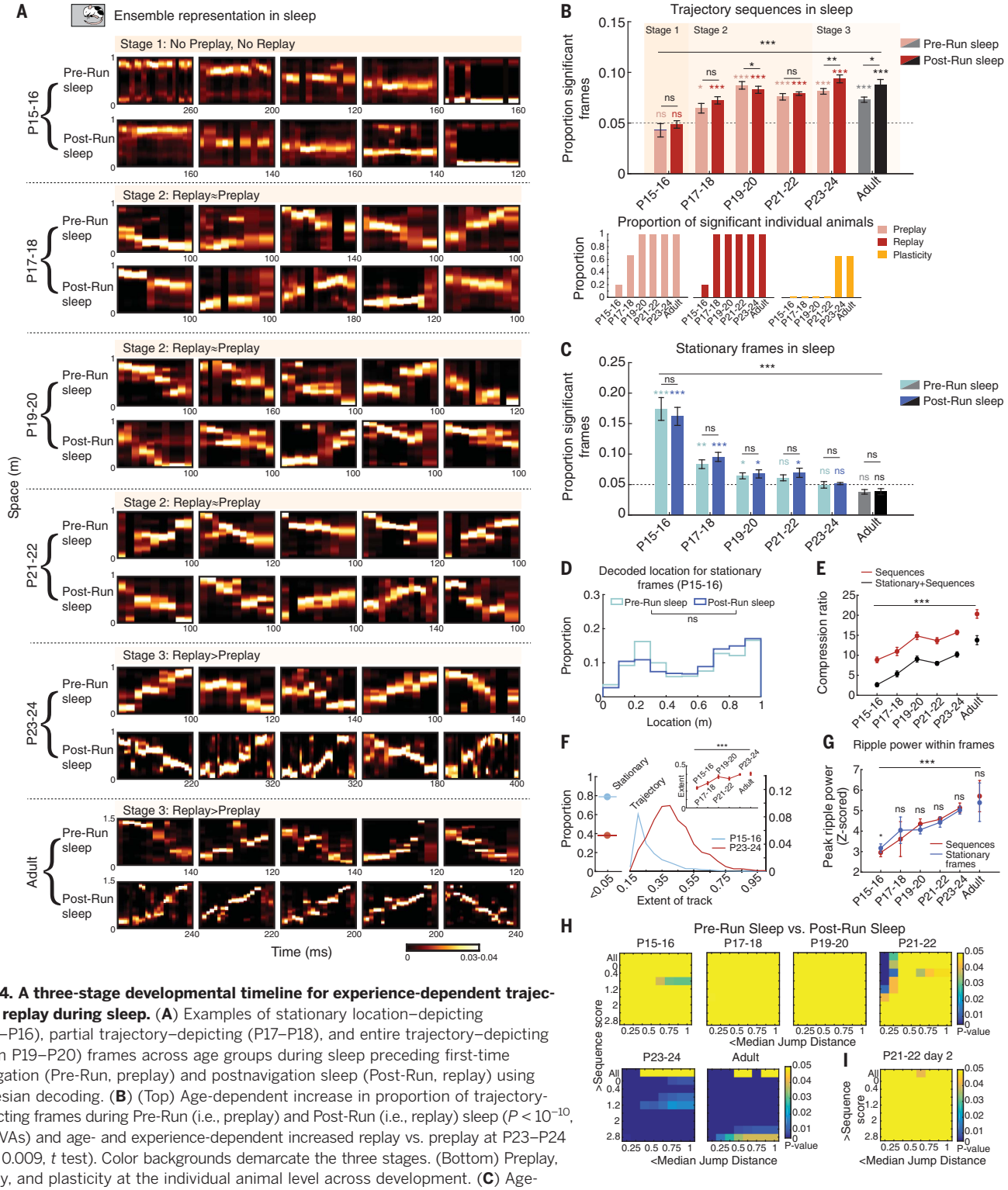


Fig. 4. A three-stage developmental timeline for experience-dependent trajectory replay during sleep. (**A**) Examples of stationary location–depicting (P15–P16), partial trajectory–depicting (P17–P18), and entire trajectory–depicting (from P19–P20) frames across age groups during sleep preceding first-time navigation (Pre-Run, preplay) and postnavigation sleep (Post-Run, replay) using Bayesian decoding. (**B**) (Top) Age-dependent increase in proportion of trajectory-depicting frames during Pre-Run (i.e., preplay) and Post-Run (i.e., replay) sleep ($P < 10^{-10}$, ANOVAs) and age- and experience-dependent increased replay vs. preplay at P23–P24 ($P < 0.009$, t test). Color backgrounds demarcate the three stages. (Bottom) Preplay, replay, and plasticity at the individual animal level across development. (**C**) Age-dependent and navigational experience–independent decreases in stationary location–depicting frames in Pre-Run and Post-Run sleep ($P < 10^{-7}$, ANOVAs). (**D**) Distribution of decoded track locations from ensemble activity within stationary frames at P15–P16. (**E**) Developmental timeline for time compression of decoded trajectory ($P < 10^{-10}$, ANOVAs). (**F**) Proportions of stationary frames out of all significant frames (>shuffles, stationary and trajectory-depicting; left) and distributions of extents of decoded track (right) at P15–P16 and P23–P24. (Inset) Age-dependent increase in extent of decoded trajectory ($P < 10^{-8}$, ANOVA). (**G**) Age-dependent increase in ripple power associated with location- and trajectory-depicting sleep frames during Pre-Run sleep ($P < 0.004$, ANOVAs). (**H**) Cross-development, two-parameter analysis of experience-dependent plastic changes in decoded trajectory from Pre-Run to Post-Run sleep (replay > preplay starting at P23–P34, Z-test for two proportions). (**I**) Prior navigational experience does not accelerate expression of Pre-Run to Post-Run sleep plasticity at P21–P22 (day 2, replay ≈ preplay). Data are means ± SEM. For (B) to (I), ***$P < 0.005$; **$P < 0.01$; *$P < 0.05$; ns, not significant. In (B) and (C), colored asterisks indicate P values from comparisons with chance.

Downloaded from http://science.sciencemag.org/ on January 10, 2019

We therefore recorded hippocampal neuronal ensemble activity while naïve animals slept in a confined enclosure distinct from the linear track, prior to and following the de novo run session. We detected frames of activity during slow-wave sleep with continuous animal immobility (velocity <2 cm/s) at minimal theta power (see materials and methods and fig. S5). This allowed us to investigate the developmental timeline for Pre-Run sleep preplay and Post-Run sleep replay (Fig. 4A and fig. S6). Similar to awake rest, we did not observe preplay and replay sequences at P15–P16 during Pre-Run and Post-Run sleep (Fig. 4, A and B); instead, the network activity frequently organized into stationary frames (Fig. 4, A and C) depicting individual locations along the track (Fig. 4D). Short preplay and replay motifs emerged at P17–P18, and from P19–P20 the ensemble activity depicted extended run trajectories within individual frames (Fig. 4, A and B). Time compression of sequential experience by the neuronal ensembles increased gradually as a function of age, starting from minimal compression at P15–P16 and approaching adult-like values at P23–P24 (Fig. 4E). In parallel, the likelihood of observing stationary frames gradually decreased with age and reached chance levels consistently at P23–P24, while the spatial extent of de novo run trajectories represented by preplay and replay increased with age (Fig. 4, C and F), with no relationship to the isolation quality of units (fig. S7). We further determined that the sequential network properties were not due to inhomogeneities in firing rate characteristics across single neurons (fig. S8) or large discontinuities (i.e., jumps) in the decoded trajectory (fig. S9) and hence represented higher-order ensemble organization. Similarly, age-dependent changes in sequential properties were not due to differences in the amount of on-track experience (fig. S10) or improved spatial representation during a run (fig. S11). Overall, the spatial experience–depicting frames co-occurred with 140- to 250-Hz ripple oscillations. The ripple oscillations exhibited an age-dependent increase in power, duration, incidence, and likelihood to occur in doublets (Fig. 4G and fig. S12). The expression of preplay of future de novo run sequences in the absence of any structured experience on linear environments and before emergence of compressed theta sequences during a run suggests that the development of preconfigured sequential motifs (*27*) is an age-dependent, potentially innate process that is likely independent of sequential experience.

Improved trajectory representation during sleep replay over preplay has been proposed as a critical mechanism for episodic-like memory formation (*5*, *28*). We investigated whether and when during development the strength and incidence of trajectory replay exceeded those of trajectory preplay. Experience-dependent plasticity, marked by a higher incidence and a higher strength of replay compared to preplay, emerged at P23–P24, when it exhibited adult-like characteristics (Fig. 4, B and H). We did not observe plasticity in location-depicting ensembles or trajectory sequences at younger ages, despite expression of preconfiguration in the form of preplay and replay phenomena as early as P17–P18 (Fig. 4H and figs. S13 to S16, two-parameter comparison). This suggests that network preconfiguration does not emerge as a result of unaccounted sequential experience in the home cage before P17–P18, as an explicit sequential experience on a linear track did not result in robust theta sequences and offline sequence plasticity until P23–P24. Previous-day navigational experience did not accelerate the developmental emergence of age- and recent experience–dependent plasticity in experienced P21–P22 animals (Fig. 4I). These results indicate that hippocampal ensembles exhibit reduced stimulus-related plasticity during the critical period, including their experience in the home cage, in apparent contrast with the heightened plasticity observed in the developing sensory cortex (*12*). This suggests that the age-dependent emergence of time-compressed trajectory sequences (Fig. 4G) depends on intrinsic, instructive signals likely provided by the upstream developing stellate cell network of the entorhinal cortex (*16*).

We have identified distinct stages in the development of sequential patterns in neuronal ensembles in the rat, which we propose are important for the relational binding of events and episodic-like memory formation, according to the following ethologically relevant scenario. In the first stage, the hippocampal network represents discrete locations explored in space but lacks the ability to bind them into temporally compressed trajectories. This occurs at P15–P16, an age when rats are naturally confined to the nest. The second stage is characterized by the emergence and gradual increase in the complexity of preconfigured sequential motifs (*27*) expressed during offline sleep or rest epochs in an age-dependent, navigational experience–independent manner (fig. S17). This stage begins around P17–P18 and continues to P21–P22, when rats start exploring increasingly beyond their nest (*9*). We suggest that the existence of genuine preconfigured sequential motifs at this stage is consistent with Kant's proposal on the a priori requirement of mental constructs of space-time for the development of other cognitive faculties (*29*). The third stage is marked by age- and navigational experience–dependent representation of entire trajectories or episodes and begins around P23–P24.

This third stage is first characterized by the relational binding and encoding of past, current, and future sequential locations into compressed trajectory-like sequences within theta oscillations during navigation, likely associated with experience-dependent, spike time–dependent plasticity. The maturation of grid cells in the medial entorhinal cortex (MEC) in the fourth postnatal week could enable the emergence of theta sequences in CA1, which depend on the integrity of MEC in adult rats (*20*) [sleep sequence replay can be expressed independently of direct MEC input to CA1 (*30*)]. Long-term plasticity due to the extended sequential run experience is likely consolidated during the following sleep period via increased replay of the run trajectory compared to its preplay (*5*). We propose that the coordinated development of time-compressed sequences during encoding and consolidation of sequential information via stronger replay in sleep at P23–P24 in the rat represents a critical network mechanism that could enable the emergence of episodic-like memory function.

REFERENCES AND NOTES

1. W. B. Scoville, B. Milner, *J. Neurol. Neurosurg. Psychiatry* **20**, 11–21 (1957).
2. L. R. Squire, *Psychol. Rev.* **99**, 195–231 (1992).
3. H. Eichenbaum, N. J. Cohen, *Neuron* **83**, 764–770 (2014).
4. G. Dragoi, S. Tonegawa, *Nature* **469**, 397–401 (2011).
5. A. K. Lee, M. A. Wilson, *Neuron* **36**, 1183–1194 (2002).
6. A. Travaglia, R. Bisaz, E. S. Sweet, R. D. Blitzer, C. M. Alberini, *Nat. Neurosci.* **19**, 1225–1233 (2016).
7. J. K. Lee, C. Wendelken, S. A. Bunge, S. Ghetti, *Child Dev.* **87**, 194–210 (2016).
8. T. J. Wills, F. Cacucci, N. Burgess, J. O'Keefe, *Science* **328**, 1573–1576 (2010).
9. R. F. Langston *et al*., *Science* **328**, 1576–1580 (2010).
10. S. Le Vay, T. N. Wiesel, D. H. Hubel, *J. Comp. Neurol.* **191**, 1–51 (1980).
11. B. L. Benedetti, Y. Takashima, J. A. Wen, J. Urban-Ciecko, A. L. Barth, *Cereb. Cortex* **23**, 2690–2699 (2013).
12. A. Maffei, G. Turrigiano, *Prog. Brain Res.* **169**, 211–223 (2008).
13. J. O'Keefe, L. Nadel, *The Hippocampus as a Cognitive Map*. (Oxford University Press, Oxford, 1978).
14. G. Dragoi, G. Buzsáki, *Neuron* **50**, 145–157 (2006).
15. G. Dragoi, S. Tonegawa, *Proc. Natl. Acad. Sci. U.S.A.* **110**, 9100–9105 (2013).
16. F. Donato, R. I. Jacobsen, M. B. Moser, E. I. Moser, *Science* **355**, eaai8178 (2017).
17. L. Muessig, J. Hauser, T. J. Wills, F. Cacucci, *Neuron* **86**, 1167–1173 (2015).
18. W. E. Skaggs, B. L. McNaughton, M. A. Wilson, C. A. Barnes, *Hippocampus* **6**, 149–172 (1996).
19. S. J. Middleton, T. J. McHugh, *Nat. Neurosci.* **19**, 945–951 (2016).
20. M. I. Schlesiger *et al*., *Nat. Neurosci.* **18**, 1123–1132 (2015).
21. G. Dragoi, S. Tonegawa, *eLife* **2**, e01326 (2013).
22. Y. Wang, S. Romani, B. Lustig, A. Leonardo, E. Pastalkova, *Nat. Neurosci.* **18**, 282–288 (2015).
23. E. Pastalkova, V. Itskov, A. Amarasingham, G. Buzsáki, *Science* **321**, 1322–1327 (2008).
24. D. J. Foster, M. A. Wilson, *Nature* **440**, 680–683 (2006).
25. T. J. Davidson, F. Kloosterman, M. A. Wilson, *Neuron* **63**, 497–507 (2009).
26. A. V. Egorov, B. N. Hamam, E. Fransén, M. E. Hasselmo, A. A. Alonso, *Nature* **420**, 173–178 (2002).
27. G. Dragoi, S. Tonegawa, *Philos. Trans. R. Soc. London B Biol. Sci.* **369**, 20120522 (2013).
28. A. D. Grosmark, G. Buzsáki, *Science* **351**, 1440–1443 (2016).
29. I. Kant, *Critique of Pure Reason*. (Cambridge University Press, Cambridge, UK, 1781).
30. J. Yamamoto, S. Tonegawa, *Neuron* **96**, 217–227.e4 (2017).

ACKNOWLEDGMENTS

We thank M. Picciotto and D. Lee for comments and J. Sibille and K. Liu for help. **Funding:** This work was supported by a Whitehall Foundation grant, NARSAD Young Investigator Fellowship, Outstanding Early Investigator Award, Charles H. Hood Foundation Award, and the NINDS of the NIH under award number 1R01NS104917 to G.D. and a Gruber Science Fellowship to U.F. The content is solely the responsibility of the authors and does not necessarily represent the official views of the NIH. **Author contributions:** G.D. conceived and designed the study. U.F. and G.D. collected and analyzed the data. G.D. and U.F. wrote the manuscript. **Competing interests:** The authors declare no conflicts of interest. **Data and materials availability:** All data are available in the manuscript or the supplementary material. The reported data are archived on file servers at Yale Medical School.

SUPPLEMENTARY MATERIALS

www.sciencemag.org/content/363/6423/168/suppl/DC1
Materials and Methods
Figs. S1 to S17
Table S1
References (*31*–*33*)

8 August 2018; accepted 4 December 2018
10.1126/science.aav0502

Downloaded from http://science.sciencemag.org/ on January 10, 2019

TROPICAL ECOLOGY

Termites mitigate the effects of drought in tropical rainforest

L. A. Ashton[1,2,3]*, H. M. Griffiths[4]*†, C. L. Parr[4,5,6], T. A. Evans[7], R. K. Didham[7,8], F. Hasan[2], Y. A. Teh[9], H. S. Tin[10], C. S. Vairappan[10], P. Eggleton[2]

Termites perform key ecological functions in tropical ecosystems, are strongly affected by variation in rainfall, and respond negatively to habitat disturbance. However, it is not known how the projected increase in frequency and severity of droughts in tropical rainforests will alter termite communities and the maintenance of ecosystem processes. Using a large-scale termite suppression experiment, we found that termite activity and abundance increased during drought in a Bornean forest. This increase resulted in accelerated litter decomposition, elevated soil moisture, greater soil nutrient heterogeneity, and higher seedling survival rates during the extreme El Niño drought of 2015–2016. Our work shows how an invertebrate group enhances ecosystem resistance to drought, providing evidence that the dual stressors of climate change and anthropogenic shifts in biotic communities will have various negative consequences for the maintenance of rainforest ecosystems.

Tropical forests have the highest productivity and biodiversity of any terrestrial system (*1*). Climate change poses a threat to these ecosystems, with the frequency and intensity of droughts predicted to increase in coming decades (*2*, *3*). Research has shown that extreme droughts cause increased tree mortality (*4*), which has implications for forest structure and functioning. Microbial decomposition and the movement of nutrients through soil are also thought to decrease during droughts because dry conditions reduce activity of microorganisms (*5*). Together, these disturbances suggest ecosystem-wide effects of increasing drought frequency and severity. However, we know little about how drought-mediated changes in invertebrate communities affect the maintenance of functioning ecosystems during periods of environmental stress.

Termites are an important macroinvertebrate group for ecosystem function (*6*), with a wide tropical and subtropical distribution, from 50°N to 45°S (*7*). All termite groups have mutualistic relationships with microbes (i.e., groups of bacteria, archaea, protists, and/or fungi), which enable them to digest cellulose (*8*). These mutualistic relationships have helped termites become dominant invertebrate leaf litter and dead wood decomposers. Termites are major ecosystem engineers (*6*, *8*) that change the soil physical environment through bioturbation, decomposition of soil organic matter (e.g., wood and leaf litter) (*9*), and facilitation of nutrient cycling (*8*), but their contributions to these ecosystem functions have not yet been experimentally quantified. Termites also regulate soil moisture (and hence the movement of nutrients through mass flow) by transporting water upward through the soil and decreasing transpiration with their "sheeting" (temporary aboveground protective structures) (*10*). These processes are likely to affect plant communities, especially during drought, because soil nutrient availability and heterogeneity influence plant growth and community structure (*11*) and promote species diversity (*12*). Moreover, soil moisture is a key factor determining the magnitude of water stress experienced by plants, which directly influences plant mortality (*13*). Termites are sensitive to changes in soil moisture and, counterintuitively, they may be more active and abundant in rainforests during droughts (*14*). Given their key role in modifying soil environments, an increase in termite activity during extended dry periods could help to maintain soil moisture and soil nutrient flow and could have indirect consequences for plant survival. Termites could therefore mitigate the ecological effects of drought in rainforest systems, as has been shown theoretically for drylands (*15*).

To investigate this potential mitigation, we carried out a large-scale in situ manipulation (*16*) of termite communities. We suppressed termite activity in old-growth tropical rainforest in Malaysian Borneo, during and after the El Niño drought of 2015–2016 (Fig. 1 and fig. S1), and monitored termite communities in control plots. This experimental approach allowed us to assess the relative contribution of termites to ecosystem functioning in drought versus post-drought conditions. Termite suppression was achieved through a targeted approach within quarter-hectare plots by physically removing termite mounds and using poisoned cellulose baits. The suppression reduced termite feeding activity on plots by 45% [ΔAIC = 59 (AIC, Akaike information criterion)] (table S2 and figs. S3B and S4) and significantly altered termite community composition (Monte Carlo permutation test within a redundancy analysis: pseudo $F = 23.6$, $P = 0.001$) (fig. S5) by reducing the activity of large wood-feeding termites (fig. S6) over 2 years (*17*). The targeted suppression did not, however, affect other invertebrate groups (table S1 and figs. S3A, S7, and S9). This experimental manipulation allowed us to partition the effects of termites from those of other organisms and to test the hypothesis that termites play a crucial role in maintaining ecosystem processes in rainforests during periods of drought.

Termite abundance in standardized survey transects (*18*) in control plots was more than twice as high during drought than in post-drought conditions (Fig. 1, inset). This drought-induced change in termite abundance influenced a number of key ecosystem processes and properties, resulting in higher leaf litter decomposition rates, soil nutrient heterogeneity, and soil moisture. Termites were responsible for all of the measured macroinvertebrate-driven leaf litter decomposition (see table S3 and fig. S3C for a detailed breakdown of microbial, macroinvertebrate, and termite contributions to litter decomposition); no other invertebrate group compensated to maintain litter decomposition on the termite suppression plots (fig. S8).

Contrary to previous findings (*19*), which have focused on microbial decay, we found that leaf litter decomposition rates of a locally abundant species [*Shorea johorensis* (Dipterocarpaceae)] increased, rather than decreased, on our control plots during the drought (Fig. 2A). We attribute this higher litter decomposition rate to the increased abundance and activity of termites during the drought. We found that the leaf litter decomposition rate increased by 41% on the control plot versus the suppression plot during drought conditions, with termite suppression contributing substantially to model fit (ΔAIC = 6), whereas termite suppression did not influence model fit under post-drought conditions (ΔAIC < 2) (Fig. 2A, table S3D, and fig. S8). Microorganisms are typically assumed to be the main drivers of litter decomposition (*20*), perhaps owing to a temperate bias in ecology, as termites are usually absent in temperate climates. Additionally, there is generally a microbial focus in tropical studies where termite effects are not considered (*21*, *22*); in studies where termites have been included, they have not been well discriminated from other non-termite macroinvertebrates (*23*). Here, we show that termites are important decomposers in tropical rainforest systems and can actually accelerate litter decomposition during dry periods.

As might be predicted from the observed increase in decomposition rates during the drought period, leaf litter depth was lower, by 22%, on the control plots (where intact termite communities were present) compared with suppression plots (Fig. 2B, table S4A, and fig. S3D). This greater

[1]School of Biological Sciences, The University of Hong Kong, Hong Kong SAR, China. [2]Department of Life Sciences, Natural History Museum, London, UK. [3]Environmental Futures Research Institute, Griffith University, Brisbane, Queensland, Australia. [4]School of Environmental Sciences, University of Liverpool, Liverpool, UK. [5]Department of Zoology and Entomology, University of Pretoria, Pretoria, South Africa. [6]School of Animal, Plant and Environmental Sciences, University of the Witwatersrand, Wits, South Africa. [7]School of Biological Sciences, University of Western Australia, Perth, Western Australia, Australia. [8]CSIRO Health and Biosecurity, Centre for Environment and Life Sciences, Perth, Western Australia, Australia. [9]School of Biological Sciences, University of Aberdeen, Aberdeen, UK. [10]Universiti Malaysia Sabah, Kota Kinabalu, Sabah, Malaysia.
*These authors contributed equally to this work.
†Corresponding author. Email: hannah.griffiths@liverpool.ac.uk

Downloaded from http://science.sciencemag.org/ on January 10, 2019

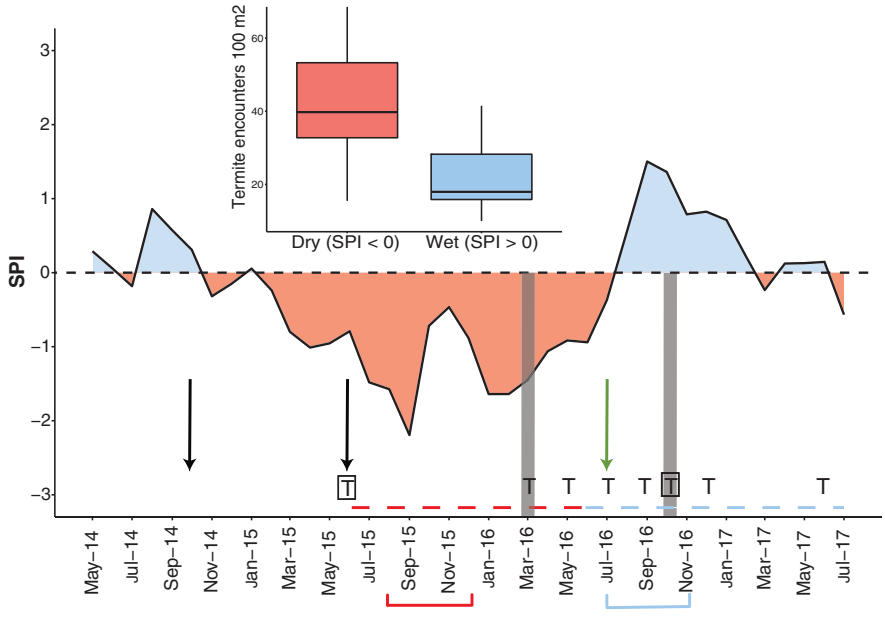


Fig. 1. Drought status during the study and timings of experiments. Three-month standardized precipitation index (SPI) calculated using rainfall data from Danum Valley Conservation Area for 1 year preceding and the 2-year duration of the study (2014–2017). SPI is a climatic proxy used to quantify and monitor drought; negative values indicate drier-than-average conditions and positive values indicate wetter-than-average conditions. See fig. S1 for a 20-year SPI plot of the region. Brackets below the *x* axis show the duration of the litter decomposition experiments during the drought (red) and post-drought (blue), which were in place for 4 months during the drought and post-drought periods. The horizontal dashed lines show the duration of the seedling survival assessment periods during the drought (red line) and post-drought (blue line) periods. "T" symbols show repeated termite transect sampling events on the control plots only, to assess the effect of drought on termite communities; "T" symbols in boxes represent termite transects that were carried out on control as well as the termite suppression plots to assess the effect of our manipulation experiment on termite communities. The black arrows indicate invertebrate sampling pre-drought and pre–termite suppression (2014) and during the drought and suppression (2015). The green arrow represents invertebrate sampling post-drought during the suppression (2016), as well as the collection of soil and leaf material for pesticide residue analysis. The gray bars indicate the soil moisture, soil nutrient analysis, and leaf litter depth sampling events. The inset shows the higher termite encounter rate (median plus interquartile range) during the dry period (SPI < 0) compared with the wet period (SPI > 0) (assessed using termite transects, which provide relative abundance data).

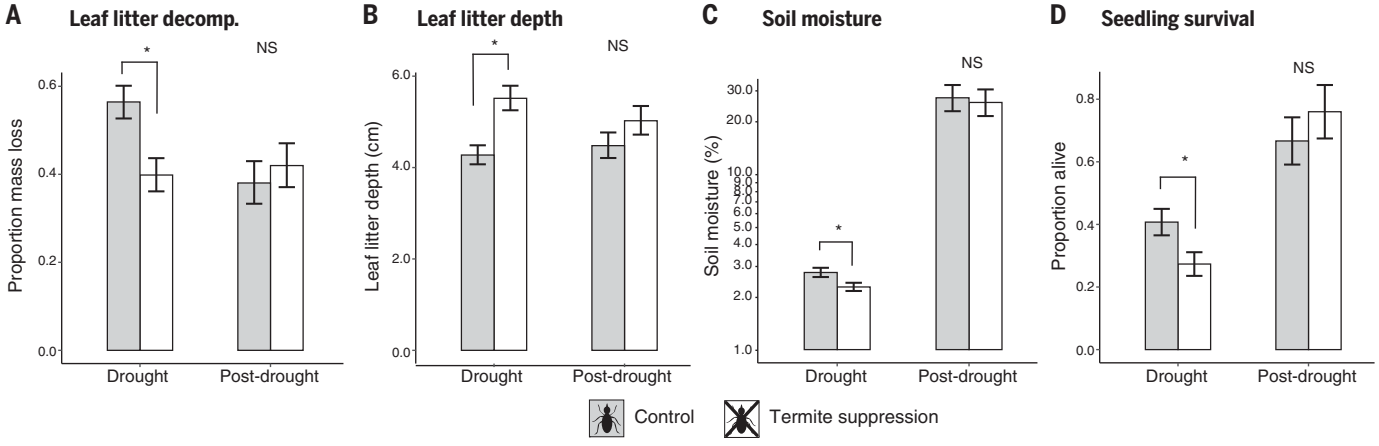


Fig. 2. The effect of drought and termite suppression on four ecosystem responses. (**A**) Proportion mass loss from open-mesh leaf litter decomposition bags (assessed after remaining on the forest floor for 4 months), (**B**) forest floor leaf litter depth, (**C**) soil moisture, and (**D**) proportion of seedlings surviving. Gray bars and white bars represent control plots and termite suppression plots, respectively, and all bars display mean values ± SE. Asterisks denote significant differences between values (see tables S3 and S4 for model outputs). Data presented are back-transformed mean predicted values from mixed effects model outputs and error bars are the back-transformed model estimates. Soil moisture (C) is presented on a $\log_{10}$ scale for ease of interpretation. NS, not significant.

accumulation of leaf litter on suppression versus control plots during the drought (suppression effect model, ΔAIC = 7) but not during post-drought conditions (suppression effect model, ΔAIC < 2) (Fig. 2B) shows an immediate ecosystem-level consequence of the change in termite activity.

This observed increase in litter cycling represents a previously unmeasured and potentially large contribution by termites to terrestrial carbon flux during drought conditions. Evidence from the 2015–2016 El Niño drought showed a net increase in tropical forest carbon flux compared with post-drought conditions (*24*), indicating that the increased termite-mediated carbon cycling is not offset by increased carbon uptake by plants. We estimate that termite-driven decomposition of leaf litter could contribute up to 1 Mg C ha^{-1} $year^{-1}$ during drought periods (*17*). These findings suggest that present models may underestimate future carbon flux from tropical rainforests (*25*, *26*). Given that termites have also been shown to contribute measurably to decomposition in the New World tropics (*27*), these results point to termites acting as a major component of carbon cycling globally.

As expected, soil moisture was lower on all plots during the drought compared with post-drought conditions. However, the presence of termites contributed substantially to soil moisture retention during the drought. At 5 cm (a depth

Downloaded from http://science.sciencemag.org/ on January 10, 2019

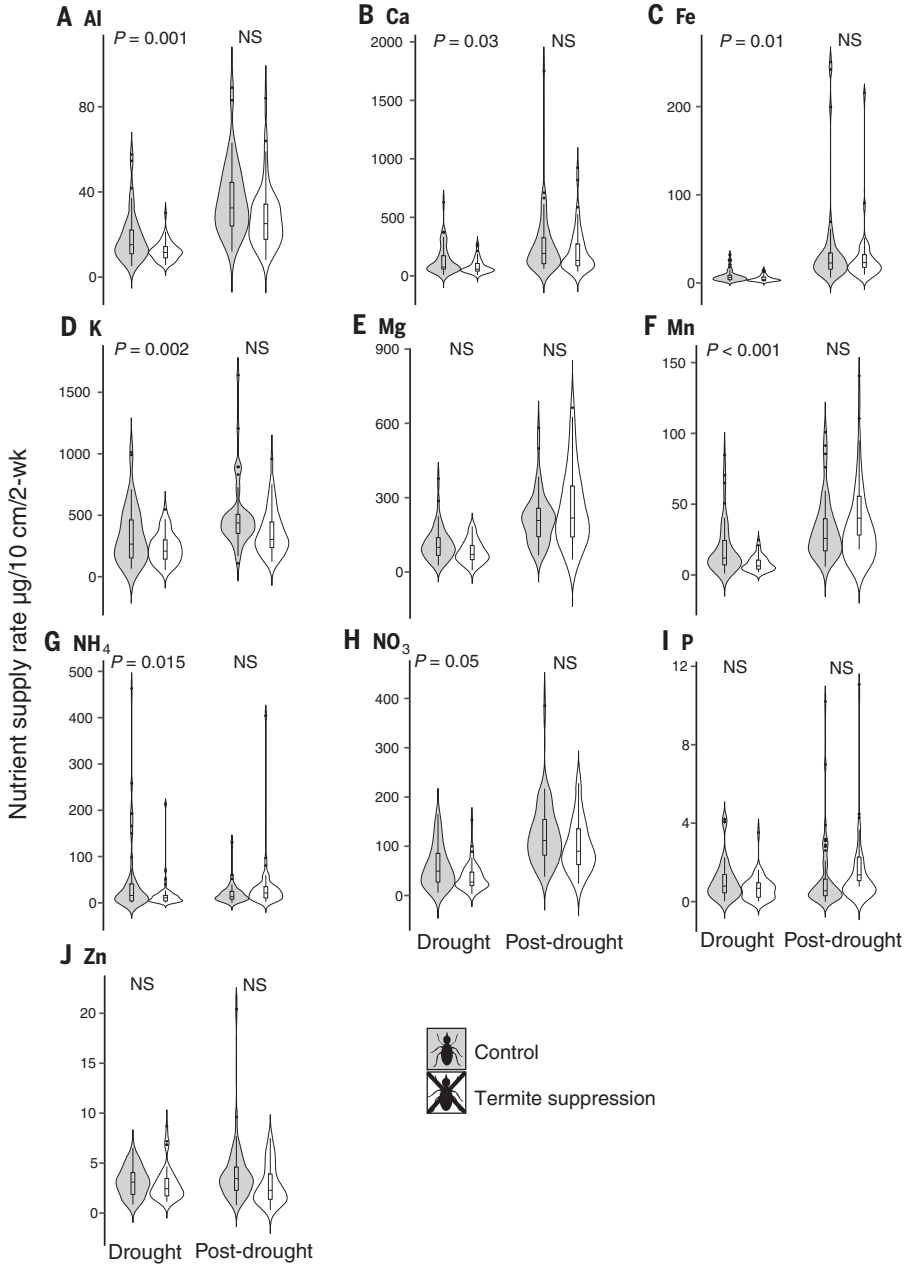


Fig. 3. The effect of drought and termite suppression on soil nutrient heterogeneity. Extent of variability in (**A**) Al, (**B**) Ca, (**C**) Fe, (**D**) K, (**E**) Mg, (**F**) Mn, (**G**) NH_4, (**H**) NO_3, (**I**) P, and (**J**) Zn soil nutrient supply over a 2-week period in control (gray violins) and termite suppression plots (white violins) during drought and post-drought conditions. Plots display (i) density of data estimated by kernel method (shaded areas), (ii) median values (horizontal line in the center of the boxplots), and (iii) interquartile range (between the top and bottom of the box). Differences in heterogeneity between treatments were assessed using Fligner-Killeen test of homogeneity of variances carried out on the residuals from linear mixed effects models. *P* values denote significant differences between values.

relevant for shallow rooted plants and seedlings), control plots displayed a 36% increase in soil moisture compared with the termite suppression plots during the drought (ΔAIC = 3) but not under post-drought conditions (ΔAIC < 2) (Fig. 2C, table S4B, and fig. S3D). These termite-driven increases in soil moisture are more than double the effect size reported by previous investigations into the influence of invertebrates on soil processes during drought (*28*).

Soil nutrient availability (*29*, *30*) and heterogeneity (*12*) contribute to plant productivity, distribution, and diversity in rainforest ecosystems. By measuring plant-available soil nutrients from multiple subsamples across each plot in the drought and post-drought periods, we show that an increase in termite activity also had consequences for the spatial heterogeneity of soil nutrients (although not for mean plot-level nutrient concentrations, which did not differ significantly between control and suppression plots under either drought or post-drought conditions) (Fig. 3). In the drought, soil nutrient heterogeneity was significantly lower in the termite suppression plots compared with the control plots for nitrate, ammonia, calcium, potassium, iron, manganese, and aluminum (Fligner-Killeen test for heterogeneity of variances) (Fig. 3). Under post-drought conditions, the suppression of termites did not influence heterogeneity of any of the soil nutrients. This could be a direct effect of the movement of organic material and/or an indirect effect of termite activity increasing soil moisture content. These data imply that termites facilitate the movement of soil nutrients when soil moisture is very low (~2.1% ± 0.1 during drought, compared with ~25.2% ± 0.8 under post-drought conditions) (Fig. 2C), leading to a more heterogeneous soil environment.

Seedling survival is often negatively affected by drought and soil desiccation (*31*). The positive impacts of termites on soil moisture and nutrient heterogeneity could therefore have positive effects for seedling survival. We investigated this using a transplant experiment to quantify the survival of liana seedlings [*Agelaea borneensis* (Fabaceae)] on our plots during and after the drought. During the drought year, we found a 51% increase in seedling survival on the control compared with the termite suppression plots, with the termite suppression treatment contributing substantially to model fit (ΔAIC = 3). Termite suppression had no effect on model fit under post-drought conditions (ΔAIC < 2) (Fig. 2D, table S4C, and fig. S3D). Our findings show that termites may buffer seedlings against the negative effects of drought by enhancing soil moisture content and nutrient heterogeneity. Given that droughts are projected to become more frequent and severe with climate change (*3*), these results suggest that termites will play an increasingly important role in structuring tropical plant communities and maintaining plant productivity and diversity in the future.

This study shows that termite activity increases in rainforests during dry conditions and that termites buffer important soil processes of consequence to seedling survival during these periods. Moreover, the buffering effect that we measured is likely to be a conservative estimate of the total effect, as we were not able to exclude all termites in our experimental plots. Common large-bodied wood-feeding termites—e.g., species belonging to *Bulbitermes*-group, *Macrotermes*, and *Prohamitermes*—were most affected by our suppression and appear to be the main drivers of the termite-mediated ecosystem processes presented here. Although soil-feeding termites and other groups that were not targeted by our suppression may also be important in maintaining ecosystem function, these occurred less frequently and contributed considerably less biomass to the overall termite community (fig. S6). Mechanisms driving the increase in

Downloaded from http://science.sciencemag.org/ on January 10, 2019

termite activity during droughts are yet to be established, but possible explanations could include favorable environmental conditions for tunneling (e.g., drier, less-waterlogged ground), increased foraging ability above ground in the absence of heavy rain, and/or reduced predation pressure from ants. This increase in termite activity is contrary to the prevailing perception that biota and ecological processes in tropical rainforests are negatively affected by drought (*4*). We show that termites form an essential link between dead plant material and the rest of the ecosystem during dry periods and that no other decomposer group compensates for the functions that termites perform.

This study is constrained by a relatively short duration, and it is possible that legacy effects in system recovery after the severe drought (*32*) could have influenced the post-drought patterns we observed. However, pre-drought abundances of non-termite invertebrates were comparable to post-drought abundances (fig. S7), indicating that our post-drought data are likely to be representative of the non–drought-stressed system. Future investigations could expand the manipulative termite suppression approach to include multifactorial environmental manipulations (e.g., drought and litter addition experiments) and monitoring of ecosystem functioning and recovery over longer-term annual cycles. This would allow us to disentangle the role of termites in ecosystem processes following periods of system stress from other confounding environmental factors.

Although small-scale manipulative experiments have shown the importance of invertebrates in alleviating the effects of drought (*28*), our large-scale data show that a major invertebrate group maintains ecosystem functioning during periods of drought, with potentially cascading consequences for plant survival. Forest disturbance is known to reduce termite abundance and diversity (*33*, *34*) and, globally, more than 50% of tropical rainforests have been modified by humans: an area of more than 10 million square kilometers (*35*). Tropical landscapes that are heavily modified by human disturbance are likely to be less resistant to drought, because of a reduction in termite-mediated buffering of ecosystem processes. Our findings suggest that climate change, along with human disturbance to invertebrate communities, will have negative and interacting (*36*) consequences for the maintenance of functioning rainforest ecosystems. This study provides further evidence of the importance of conserving natural ecosystems by showing that intact biological communities can safeguard ecosystem processes in a time of rapid environmental change.

REFERENCES AND NOTES

1. R. M. May, *Science* **329**, 41–42 (2010).
2. W. Cai *et al*., *Nat. Clim. Chang.* **4**, 111–116 (2014).
3. A. Dai, *Nat. Clim. Chang.* **3**, 52–58 (2013).
4. D. Bonal, B. Burban, C. Stahl, F. Wagner, B. Hérault, *Ann. For. Sci.* **73**, 27–44 (2016).
5. J. B. Yavitt *et al*., *Austral Ecol.* **29**, 177–188 (2004).
6. P. Jouquet *et al*., *Eur. J. Soil Biol.* **47**, 215–222 (2011).
7. P. Eggleton, in *Termites: Evolution, Sociality, Symbioses, Ecology*, T. Abe, D. E. Bignell, M. Higashi, Eds. (Springer, 2000), pp. 25–51.
8. T. Abe, D. E. Bignell, M. Higashi, Eds., *Termites: Evolution, Sociality, Symbioses, Ecology* (Springer, 2000).
9. M. D. Ulyshen, *Biol. Rev. Camb. Philos. Soc.* **91**, 70–85 (2016).
10. B. K. Gautam, G. Henderson, *Environ. Entomol.* **43**, 1399–1405 (2014).
11. D. K. Wijesinghe *et al*., *J. Ecol.* **93**, 99–112 (2005).
12. W. Xu *et al*., *Ecol. Evol.* **6**, 8719–8726 (2016).
13. N. McDowell *et al*., *New Phytol.* **178**, 719–739 (2008).
14. L. Dibog *et al*., *J. Trop. Ecol.* **14**, 841–850 (1998).
15. J. A. Bonachela *et al*., *Science* **347**, 651–655 (2015).
16. T. M. Fayle *et al*., *Trends Ecol. Evol.* **30**, 334–346 (2015).
17. Materials and methods are available as supplementary materials.
18. D. T. Jones, P. Eggleton, *J. Appl. Ecol.* **37**, 191–203 (2000).
19. M. E. Crockatt, D. P. Bebber, *Global Change Biol.* **21**, 698–707 (2015).
20. M. J. Swift, O. W. Heal, J. M. Anderson, *Decomposition in Terrestrial Ecosystems* (Univ. of California Press, 1979).
21. F. J. Xuluc-Tolosa *et al*., *For. Ecol. Manage.* **174**, 401–412 (2003).
22. K. L. Yeong, G. Reynolds, J. K. Hill, *Biotropica* **48**, 443–452 (2016).
23. G. Liu *et al*., *J. Ecol.* **103**, 1214–1223 (2015).
24. C. S. O'Connell, L. Ruan, W. L. Silver, *Nat. Commun.* **9**, 1348 (2018).
25. W. K. Cornwell *et al*., *Global Change Biol.* **15**, 2431–2449 (2009).
26. S. Luyssaert *et al*., *Global Change Biol.* **13**, 2509–2537 (2007).
27. M. Kaspari *et al*., *Ecology* **95**, 795–800 (2014).
28. S. N. Johnson *et al*., *Funct. Ecol.* **30**, 894–902 (2016).
29. R. John *et al*., *Proc. Natl. Acad. Sci. U.S.A.* **104**, 864–869 (2007).
30. G. D. Paoli *et al*., *J. Ecol.* **94**, 157–170 (2006).
31. F. Padilla, F. Pugnaire, *Funct. Ecol.* **21**, 489–495 (2007).
32. W. R. L. Anderegg *et al*., *Science* **349**, 528–532 (2015).
33. S. H. Luke *et al*., *Biodivers. Conserv.* **23**, 2817–2832 (2014).
34. P. Eggleton *et al*., *Agric. Ecosyst. Environ.* **90**, 189–202 (2002).
35. W. F. Laurance *et al*., *Trends Ecol. Evol.* **29**, 107–116 (2014).
36. I. M. Côté *et al*., *Proc. R. Soc. London Ser. B* **283**, 20152592 (2016).
37. L. A. Ashton *et al*., Termite abundance and ecosystem processes in Maliau Basin, 2015-2016, NERC Environmental Information Data Centre (2018); https://doi.org/10.5285/1e9993ae-add7-497a-b54b-745b0fc6a7ca.

ACKNOWLEDGMENTS

This work was supported by the South East Asia Rainforest Research Partnership (SEARRP) with permission from the Maliau Basin Management Committee. We thank G. Reynolds, U. Jami, and L. Kruitbos for coordinating fieldwork; S. Both and U. Kritzler for help in establishing the experimental plots; R. Walsh for providing rainfall data; and A. Zanne and A. Cheesman for discussions on experimental design. We thank J. Nash from Bayer Southeast Asia Pte-Ltd, Singapore, for donating Premise 200SC and Agenda 10SC. We thank J. Rees, A. Tagliabue, M. Begon, R. Williams, W. Cheng, C. Dahlsjö, R. Kitching, and J. Barlow for comments on the manuscript. Finally, we thank all our field assistants: R. Binti Manber, A. Jupri, F. John, Y. Binti Suffian, E. Bin Esing, D. Bin Paul, Z. Bin Angau, A. Allbanah Bin Anchun, N. Angau, D. Ku Shamirah Binti Pg Bakar, E. Binti Nahun, R. Rusili, A. Bin Rantau, R. Bin Sahamin, A. Mastor, M. Adzim Bin Rahili, M. Azuan, H. Nasir, and N. Fazzli. **Funding:** This publication is a contribution from the UK NERC-funded Biodiversity And Land-use Impacts on Tropical Ecosystem Function (BALI) consortium (NERC grant NE/L000016/1). **Author contributions:** C.L.P., H.M.G., L.A.A., P.E., and T.A.E. conceived and designed the experiment; C.L.P., P.E., and T.A.E. established the experimental plots; H.M.G., L.A.A., and P.E. collected the data; H.M.G., L.A.A., P.E., and R.K.D. analyzed the data; C.S.V., F.H., and H.S.T. carried out laboratory analysis; H.M.G. and L.A.A. led the writing of the manuscript with significant input from C.L.P., P.E., R.K.D., and Y.A.T. **Competing interests:** None declared. **Data and materials availability:** Data have been deposited in the NERC Environmental Information Data Centre (*37*).

SUPPLEMENTARY MATERIALS

www.sciencemag.org/content/363/6423/174/suppl/DC1
Materials and Methods
Figs. S1 to S9
Tables S1 to S5
Graphical Abstract
References (*38*–*49*)

31 July 2018; accepted 6 December 2018
10.1126/science.aau9565

Downloaded from http://science.sciencemag.org/ on January 10, 2019

PALEOECOLOGY

A 90,000-year record of Afromontane forest responses to climate change

Anne-Marie Lézine[1]*, Kenji Izumi[2], Masa Kageyama[2], Gaston Achoundong[3]

Pollen records from African highlands are scarce; hence, the paleoecology of the Afromontane forest and its responses to glacial cycles are poorly known. Lake Bambili (Cameroon) provides a record of vegetation changes in the tropical mountains of Africa over the past 90,000 years, with high temporal resolution. Pollen data and biome reconstructions show a diverging response of forests to climate changes; the upper tree line was extremely unstable, shifting substantially in response to glacial-interglacial climate alternation, whereas the transition between the montane and lowland forests remained remarkably stable. Such ecological instability may have had a critical influence on species richness in the Afromontane forests.

Whether stability or instability of tropical forests has produced their high biodiversity has long been debated. The high endemism and/or species richness in the rain forest of Equatorial Africa has been attributed to contraction to isolated blocks or refugia during unfavorable climates, such as those of the glacial periods of the Quaternary. It has been postulated that forest remnants persisted in refugia within a grassland-dominated landscape (*1*), with the long-term ecological stability in these restricted areas promoting high levels of species richness and endemism. Both pollen and genetic data have been invoked in support this "glacial refuge theory." Pollen records of the last glacial period mainly comes from marine cores that give information on large-scale environmental change that includes multiple vegetation zones across a large region and thus cannot be used to trace variation in plant community biodiversity locally (*2*). Continental records are scarce and located at the edge of the rain forest. The story they deliver is therefore particularly heterogeneous, with evidence for ecological stability at Ngamakala, Congo, to the south of the rain forest (*3*), contrasting with severe forest contractions at Lake Barombi Mbo, Cameroon (*4*, *5*), and Lake Bosumtwi, Ghana (*6*, *7*), to the north. Genetic data confirm that the lowland forests likely experienced multiple phases of contraction and expansion, of which the precise location and chronology remain unresolved (*8*).

Unlike the lowland areas, equatorial mountains are thought to have provided a stable moist habitat throughout the glacial episodes (*9*), allowing persistence of biodiversity-rich montane forests to the present day. Alternatively, White (*10*) hypothesized that Afromontane forest communities reached their current distribution in the highlands of western Equatorial Africa only during the Holocene and as such can be considered as "contemporary refugia." Here, we present a 90,000-year-long pollen sequence of Afromontane vegetation from Lake Bambili, a high-altitude crater lake in Cameroon (05° 56′ 11.9 N, 10°14′ 31.6 E, 2273 m above sea level) (Fig. 1) that reveals the stability and instability of equatorial Afromontane biomes through time as a driver of biological richness in one of the principal centers of biodiversity in Africa (*11*).

Lake Bambili is formed by two adjacent crater basins (Fig. 1) in the center part of the Cameroon Volcanic Line, which culminates at Mt. Oku (3011 m). The upper crater is a marsh, whereas the lower crater, situated less than 100 m below, is filled by a shallow lake (4 to 6 m deep) and receives overflow from the upper crater. Bambili is situated in the Afromontane forest belt, which currently lies ~1800 to 2800 m above sea level and is characterized by the presence of *Podocarpus milanjianus*, the only conifer indigenous to Cameroon. This forest is bounded at the top by Afroalpine grasslands and at the bottom by submontane forests and savannas, forming the transition with rain forests and seasonal forests of the Guineo-Congolian phytogeographic zone (fig. S1) (*12*). Bambili lies under the influence of the African monsoon system (Fig. 1). The average of annual precipitation is 2000 mm, with a maximum in July through September. Rains are intense and regularly distributed with 5 months above 200 mm, and mists are frequent during the rainy seasons. At the altitude of Bambili, mean monthly temperature does not exceed 18°C, and frost is very rare (*13*).

The Bambili composite record consists of two coring sections recovered at the lower crater lakeshore (B1) and inside the upper crater (B2), respectively (*14*). The sediment is uniformly organic, with less decomposed organic matter in the uppermost meters of B1. Core B1 (14 m long) has yielded a continuous pollen sequence from 20 thousand years (ka) ago to the present, described in detail elsewhere (*15*, *16*). The time scale of core B2 (12.60 m long) was constrained

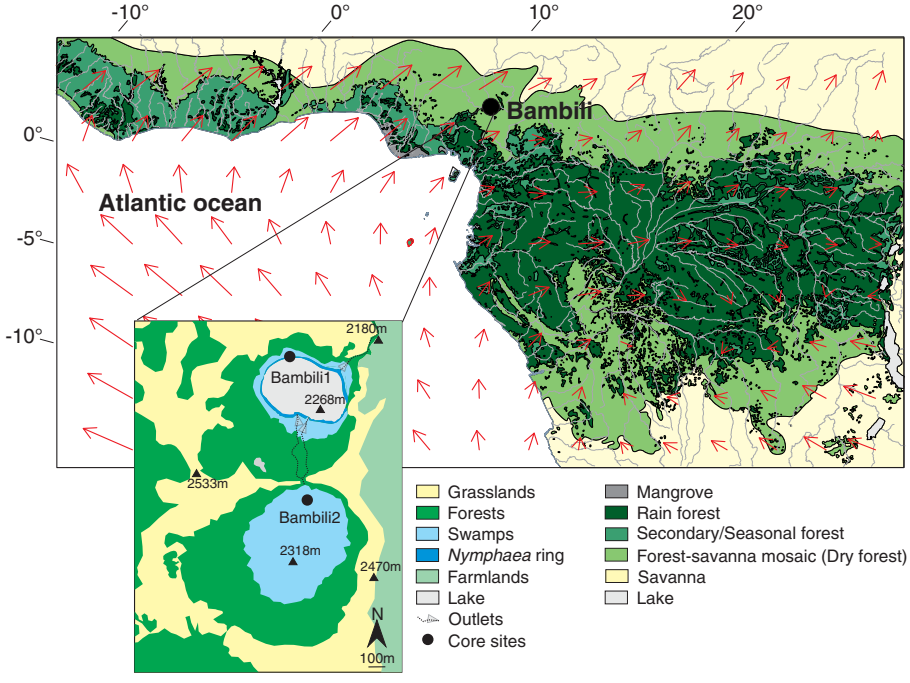


Fig. 1. Location of Bambili in western Equatorial Africa. The map shows the main vegetation types (*10*). Red arrows indicate the strength and direction of the main 925 hPa monsoonal winds during summer (NCEP-DOE AMIP-II Reanalysis). (**Inset**) The location of the core sites in the Bambili twin crater system, with details of local vegetation distribution.

[1]Laboratoire d'Océanographie et du Climat, Expérimentation et Approche numérique/Institut Pierre-Simon Laplace (IPSL), Sorbonne Université–CNRS–IRD–Muséum National d'Histoire Naturelle (MNHN), 4 Place Jussieu, 75005, Paris, France. [2]Laboratoire des Sciences du Climat et de l'Environnement/IPSL, CNRS–CEA–Université de Versailles Saint-Quentin (UVSQ), CEA-Saclay, Gif-sur-Yvette Cedex, 91191, France. [3]National Herbarium, Institut de Recherche Agricole pour le Développement, Yaoundé, Cameroon.
*Corresponding author. Email: anne-marie.lezine@locean-ipsl.upmc.fr

Downloaded from http://science.sciencemag.org/ on January 10, 2019

by fitting a third-order polynomial curve to the profile of 12 AMS radiocarbon dates against depth (tables S1 and S2). In the absence of tephra horizons, we used correlation with past phases of expanded tree cover registered in the adjacent marine pollen record from site GIK 16856-2 offshore Cameroon (*2*) to confirm the radiocarbon chronology of B2 while giving additional control points for the base of the sequence. The resulting chronology shows that core B2 represents a continuous record down to the base of the sequence, dated at 88.9 ka ago. The filling of the upper crater basin was fully completed during the early Holocene. Because the uppermost 1.54 m of B2 overlap in time with B1, they were not used. The accuracy of the B2 chronology depends on whether the pollen record of past forest expansion and contraction in marine core GIK-15856-2 is representative of the large-scale environment on the adjacent continent, including the montane forests of NW Cameroon. The Bambili chronology that resulted from peak matching of total tree percentages (excluding mangrove) at both sites is coherent and also fits with the ^{14}C-dated portion of the Bambili sequence.

The relative abundance of woody taxa (trees and shrubs pollen percentages) allows distinction of three forest phases (Figs. 2 and 3, B and D), separated by episodes of grassland development. Expansion of forests at Bambili was closely coeval with the wide development of lakes and vegetation cover and the resulting weakening of dust fluxes from the desert (fig. S2). All these testify for moist conditions over northern Africa linked to enhanced monsoon rainfall (supplementary text). Major forest phases occurred from 82.6 to 72 ka ago during the Last Interglacial (MIS 5) and from 10 to 3.3 ka ago during the Holocene. These forest phases strongly differed from each other, in that the Holocene phase consisted of two forest biomes (tables S3 to S5) (*14*), the lower-level montane forest (WAMF) and the lowland tropical seasonal forest (TSFO), whereas the MIS 5 forest phase included WAMF and upper-level Afromontane forest (AAF), which show the upper tree limit. A third phase of more moderate forest development occurred from 53 to 38 ka ago during MIS 3. As during MIS 5, this interval was characterized by WAMF and AAF, but the lower proportion of woody taxa compared with the other two forest phases, and the coeval importance of Afro-alpine grassland (AAG) and low/mid-elevation savanna (SAVA) biomes, indicates that the mountain-forest zone during MIS 3 had a relatively narrow altitudinal range.

Grass-dominated biomes were consistently present at Bambili throughout the glacial periods. Savannas occurred continuously outside the intervals of forest expansion. Afro-alpine grasslands dominated from 72 to 15.5 ka ago (from MIS 4 to MIS 2) and during a short interval at the MIS 5 ~82 ka ago. Lowland steppe (STEP) and desert (DESE) biomes occurred during the glacial maxima, particularly MIS 2. Together with the near-absence of forest elements (Fig. 2), this makes the last glacial period (MIS 2) undoubtedly the driest episode over the past 90 ka in western Equatorial Africa. By contrast, the penultimate glacial period (MIS 4) was characterized by the noticeable occurrence of subalpine trees and shrubs (such as Ericaceae), showing that the montane forests remained present in the Bambili area at that time as extremely degraded formations dominated by upper treeline elements.

In East Africa, the expansion of mountain glaciers during the last glacial period (*17*) was accompanied by a downward displacement of the upper treeline, such as subalpine taxa growing down to the surroundings of Lake Tanganyika at 773 m above sea level (*18*, *19*). Unlike East Africa, there is no evidence of past glacier formations in the highlands of western Equatorial Africa. However, continental and marine pollen data (*2*, *3*) suggest that Afromontane trees were more widely distributed during the last glacial period than today at the equator and southward (*2*). Although several living trees of *P. milanjianus* currently occur down to 900 m above sea level in Cameroon outside Mount Oku, as probable relicts of a formerly wider distribution, there is no direct evidence that this expansion took place during MIS 2: *P. milanjianus* was absent at that time from Lake Barombi Mbo (600 m above sea level) (*4*) and Lake Monoun (1083 m above sea level). It was only found in a single pollen sample dated 28,700 ± 1800 ^{14}C BP at Shum Laka at 1369 m above sea level (within the current elevation range of the species) (*20*). Another Afromontane tree, *Olea capensis*, has been extremely dynamic and able to migrate to low altitudes during the Last Glacial Maximum

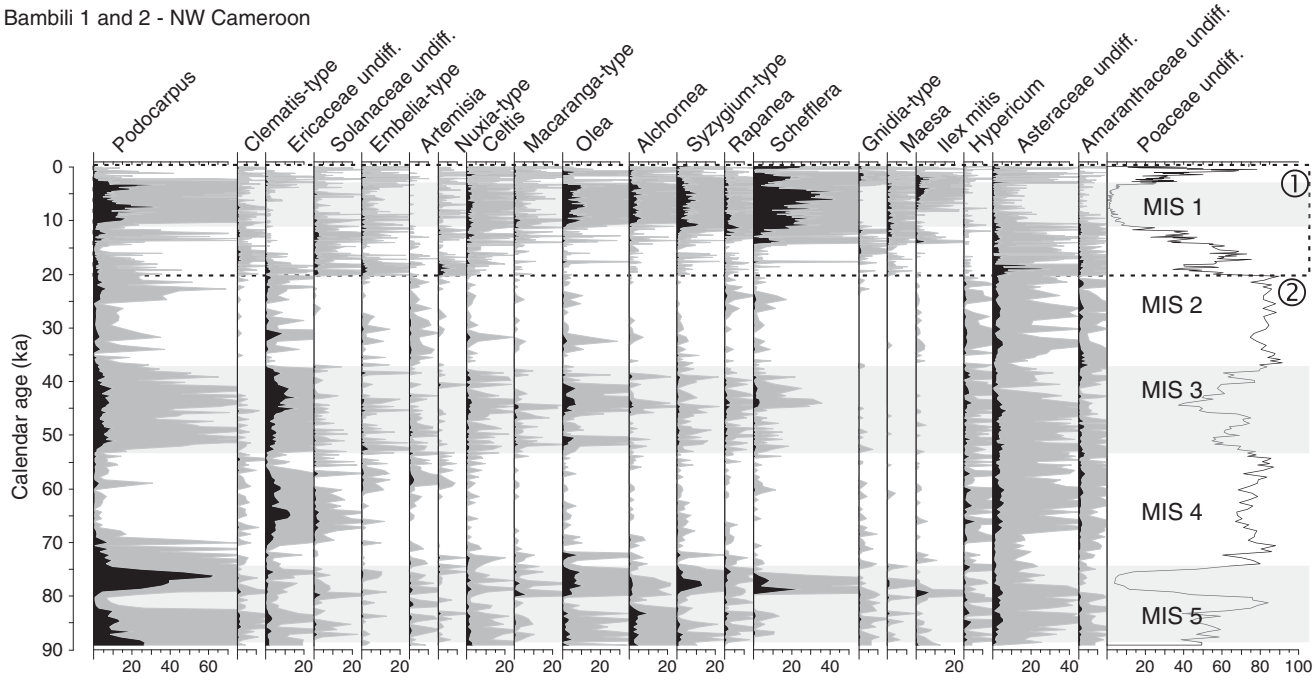


Fig. 2. Percentage pollen diagram of selected taxa from Bambili. Black shading indicates selected taxa versus time. Gray shading shows the same results, multiplied by 10 for highlighting. Percentages are calculated against the sum of terrestrial plants, excluding aquatics. The pollen analysis comprised 385 samples and 275 identified pollen and fern-spore types. Gray bands indicate the forest phases.

Downloaded from http://science.sciencemag.org/ on January 10, 2019

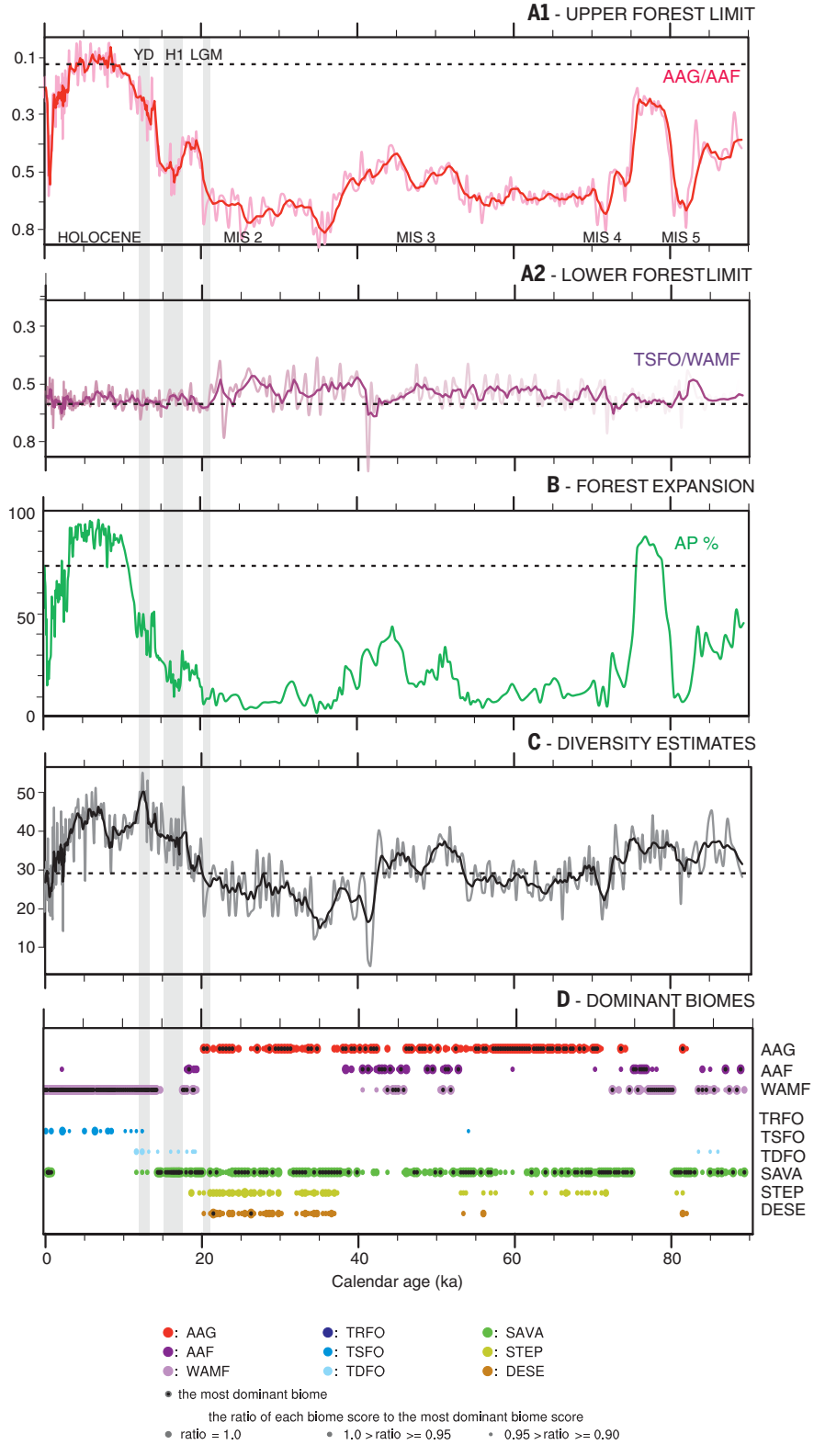


Fig. 3. Evolution of equatorial montane forests of western Africa over the past 90 ka based on Lake Bambili pollen record. (**A1** and **A2**) AAG/AAF and TSFO/WAMF biome ratios, respectively. (**B**) Tree pollen percentages. (**C**) Diversity estimates from rarefaction analyses on terrestrial pollen data. (**D**) Dominant biomes reconstruction (*14*) (tables S3-5). Horizontal dotted lines in (A), (B), and (C) show the modern-day levels. Bold lines in (A) and (C) represent the five-sample running means. Gray vertical bands show the Younger Dryas (YD); Heinrich 1 (H1) events and the Last Glacial Maximum (LGM). Biome definitions are provided in table S4.

(LGM) and then to recolonize mountain areas during the postglacial warming (*14*). However, we cannot deduce the treeline migration of Afromontane forest as a whole from the individual species behavior. To investigate the amplitude of the treeline migration and expansion/contraction of Afromontane forest range, we define the upper and lower Afromontane forest limits as follows: The upper limit is defined by the AAG/AAF ratio, and the lower limit is defined by the TSFO/WAMF ratio. Even though shifts of the upper treeline cannot be precisely quantified from the present study, evidence for the considerable amplitude of these shifts is unequivocal. Three main features arise from the AAG/AAF ratio (Fig. 3A1): (i) The upper treeline was displaced upward with respect to its current average position only during the early to mid-Holocene portion of the African Humid Period (*21*). This upslope expansion was necessarily limited because of the proximity of the summit. (ii) The upper tree line reached its lowermost elevation around 35 ka ago. Its subsequent upslope expansion started well before the LGM but accelerated immediately after it (~20 ka ago). The expansion paused and even reversed close to its LGM position during the Heinrich 1 severe drought (*22*). The upslope movement resumed at ~15 ka ago to reach the modern-day treeline elevation by the onset of the Holocene (11 ka ago). (iii) The major upslope/downslope movements of the upper tree line often occurred within a few centuries (or even a few decades), testifying to the sensitivity of the Afromontane ecosystems to change in environmental conditions. In comparison, the lower limit of the Afromontane forest displays remarkable stability around its present-day level throughout the past 90 ka (Fig. 3A2). TSFO/WAMF increased only slightly during the glacial periods and mostly during MIS 2, suggesting a moderate upward development of lowland forests at the expense of the Afromontane ones.

The most remarkable result of our study is the ecological instability of the Afromontane forest belts compared with the relative stability of lowland tropical seasonal forest over the past 90 ka. It is at its upper limit that the Afromontane forest was the most vulnerable to changing climate. By contrast, the lower limit remained relatively stable, an observation that challenges the traditional paradigm of the equatorial forest block becoming fragmented during the last glacial period (*1*). Moreover, it confirms model simulations of paleoclimate and biome distribution that point to the continuous presence of equatorial forests in Africa during the LGM (*23*). Despite the instability at the upper limit, our results show that Afromontane forest biomes have persisted over the past 90 ka, albeit at varying extent, suggesting somewhat buffered environmental conditions in the Cameroon highlands.

Unlike Afromontane forest in the Eastern Arc Mountains of Tanzania, where high modern-day biodiversity is thought to have resulted from

Downloaded from http://science.sciencemag.org/ on January 10, 2019

the remarkable long-term ecological stability observed during the past 40 ka (*24*), the diversity of vegetation in Cameroon Highlands was highly variable through time (Fig. 3C), which is consistent with the observed ecological instability (Fig. 3, A1 and B). Minimum values of diversity were coeval with the lowest position of the upper treeline between ~35 and 26 ka ago, whereas higher values than present-day pollen richness were reached during phases of forest expansion. The survival of residual forest populations in sheltered habitats within the Afromontane forest belt (such as Shum Laka) during the glacial period may have contributed to high species turnover during the last glacial-interglacial transition. The increase in diversity estimates started well before the LGM and accelerated from 20 ka ago onward. The highest diversity was then reached during the Younger Dryas dry event (~12.9 to 11.7 ka ago) (*25*), during a phase of major ecological disturbance and not during the following early Holocene phase of forest stability at 10 to 9 ka ago (*15*).

The Lake Bambili record shows that Afromontane forests of Cameroon are neither "glacial" nor "contemporary" refugia. Glacial climates did not lead to forest disappearance but had a major impact on the upper treeline, which shifted dramatically, revealing the sensitivity of the upper montane biomes to climate change.

REFERENCES AND NOTES

1. J. Maley, in *Late Quaternary Climatic Changes in the African Rain Forest: Forest Refugia and the Major Role of Sea Surface Temperature Variations*, M. Leinen, M. Sarnthein, Eds. (Kluwer 1989), pp. 585–616.
2. L. M. Dupont, S. Jahns, F. Marret, S. Ning, *Palaeogeogr. Palaeoclimatol. Palaeoecol.* **155**, 95–122 (2000).
3. H. Elenga, D. Schwartz, A. Vincens, *Palaeogeogr. Palaeoclimatol. Palaeoecol.* **109**, 345–356 (1994).
4. J. Maley, P. Brenac, *Rev. Palaeobot. Palynol.* **99**, 157–187 (1998).
5. J. Lebamba, A. Vincens, J. Maley, *Clim. Past* **8**, 59–78 (2012).
6. M. R. Talbot *et al.*, *Africa* **16**, 173–192 (1984).
7. C. Miller, W. D. Gosling, *Quat. Sci. Rev.* **84**, 7–25 (2014).
8. O. J. Hardy *et al.*, *C. R. Geosci.* **345**, 284–296 (2013).
9. G. Hewitt, *Nature* **405**, 907–913 (2000).
10. F. White, *Fragm. Florist. Geobot. Suppl.* **2**, 385–409 (1993).
11. R. A. Mittermeier, N. Myers, J. B. Thomsen, G. A. B. da Fonseca, S. Olivieri, *Conserv. Biol.* **12**, 516–520 (1998).
12. F. White, The Vegetation of Africa (UNESCO, 1983).
13. J.-B. Suchel, thesis, Université Saint-Etienne (1988).
14. Materials and methods are available as supplementary materials.
15. A.-M. Lézine, C. Assi-Kaudjhis, E. Roche, A. Vincens, G. Achoundong, *J. Biogeogr.* **40**, 183–196 (2013).
16. K. Izumi, A.-M. Lézine, *Quat. Sci. Rev.* **152**, 93–103 (2016).
17. H. A. Osmaston, S. Harrison, *Quat. Int.* **138-139**, 32–54 (2005).
18. A. Vincens, *Palaeogeogr. Palaeoclimatol. Palaeoecol.* **86**, 207–226 (1991).
19. H. Wu, J. Guiot, S. Brewer, Z. Guo, C. Peng, *Proc. Natl. Acad. Sci. U.S.A.* **104**, 9720–9724 (2007).
20. H. Kadomura, J. Kiyonaga, *Origin of Grassfields Landscape in the West Cameroon Highlands*, H. Kadomura, Ed. (Tokyo Metrop. Univ., 1994), pp. 47–85.
21. P. deMenocal *et al.*, *Quat. Sci. Rev.* **19**, 347–361 (2000).
22. J. C. Stager, D. B. Ryves, B. M. Chase, F. S. R. Pausata, *Science* **331**, 1299–1302 (2011).
23. M. Kageyama *et al.*, *Clim. Dyn.* **40**, 2469–2495 (2013).
24. J. Finch, M. J. Leng, R. Marchant, *Quat. Res.* **72**, 111–122 (2009).
25. F. Gasse, *Quat. Sci. Rev.* **19**, 189–211 (2000).

ACKNOWLEDGMENTS

Thanks are due to the Institut de Recherche pour le Développement (IRD), the Ministry of Research, and the National Herbarium in Cameroon for research facilities and authorizations; to G. Buchet, J.-P. Cazet, L. Février, and K. Lemonnier (CNRS) for laboratory and field assistance; and to D. Verschuren (Gent University, Belgium) and R. Cheddadi (CNRS Montpellier, France) for comments on earlier versions of the text. **Funding:** This research was supported by the National Research Agency (ANR), France, through IFORA (ANR-06-BDIV-0014), C3A (ANR-09-PEXT-001), VULPES (ANR-15-MASC-0003), and the BR/132/A1/AFRIFORD project in Belgium. K.I. was funded by a Marie Sklodowska-Curie European Individual Fellowship (H2020-MSCA-IF-EF, 705895), and A.-M.L. and M.K. were funded by CNRS. **Author contributions:** A.-M.L. designed the study. K.I. produced biome reconstructions. G.A. coordinated the research in the field. A.-M.L. prepared manuscript. All the authors analyzed the data and reviewed the manuscript. **Authors competing interests:** Authors have no competing interests. **Data availability:** Data are available from the NEOTOMA paleoecology database (www.neotomadb.org) and directly from the first author.

SUPPLEMENTARY MATERIALS

www.sciencemag.org/content/363/6423/177/suppl/DC1
Materials and Methods
Supplementary Text
Figs. S1 and S2
Tables S1 to S5
References (*26*–*47*)

10 October 2018; accepted 6 December 2018
10.1126/science.aav6821

Downloaded from http://science.sciencemag.org/ on January 10, 2019

ANTIBIOTIC RESISTANCE

Invertible promoters mediate bacterial phase variation, antibiotic resistance, and host adaptation in the gut

Xiaofang Jiang[1,2]*, A. Brantley Hall[2,3]*, Timothy D. Arthur[2], Damian R. Plichta[2,3], Christian T. Covington[2,3], Mathilde Poyet[1,2,4], Jessica Crothers[5], Peter L. Moses[6], Andrew C. Tolonen[2,3], Hera Vlamakis[2,3], Eric J. Alm[1,2,4]†, Ramnik J. Xavier[1,2,3,7]†

Phase variation, the reversible alternation between genetic states, enables infection by pathogens and colonization by commensals. However, the diversity of phase variation remains underexplored. We developed the PhaseFinder algorithm to quantify DNA inversion–mediated phase variation. A systematic search of 54,875 bacterial genomes identified 4686 intergenic invertible DNA regions (invertons), revealing an enrichment in host-associated bacteria. Invertons containing promoters often regulate extracellular products, underscoring the importance of surface diversity for gut colonization. We found invertons containing promoters regulating antibiotic resistance genes that shift to the ON orientation after antibiotic treatment in human metagenomic data and in vitro, thereby mitigating the cost of antibiotic resistance. We observed that the orientations of some invertons diverge after fecal microbiota transplant, potentially as a result of individual-specific selective forces.

Phase variation is a process that bacteria use to generate frequent and reversible changes within specific hypermutable loci, introducing phenotypic diversity into clonal populations. Such phenotypic diversity plays an important role in mediating preemptive adaptation to abrupt and severe selective events and is often crucial for infection by pathogens and colonization by commensals (*1*–*5*). In bacteria, phase variation often manifests through regions of DNA that invert between two states in a predictable, reversible manner (*6*). The mechanism of inversion involves enzymes called invertases, which recognize a set of inverted repeats flanking the invertible DNA region and catalyze its inversion in a reversible manner (*7*). Invertible regions commonly contain promoters oriented such that in the ON orientation, the promoter is poised to activate transcription of an operon (*7*). In the opposite OFF orientation, the promoter is oriented away from the operon, which is therefore not transcribed (*7*). Additional types of regulatory elements, such as terminators, may also be contained within these invertible DNA regions (*8*). Invertases catalyze frequent inversions—for example, one inversion in every 100 to 1000 *Escherichia coli* cells, a rate at least three orders of magnitude higher than the rate of point mutations (*7*, *9*, *10*). Thus, invertible promoters generate genetic diversity in populations, enabling rapid and reversible adaptation. Studies in specific pathogens and commensals have reported invertible promoters that regulate genes involved in virulence or colonization, such as those that encode fimbriae, flagella, and capsular polysaccharides (*1*, *2*, *4*, *7*, *11*–*17*).

Phase variation mediated by DNA inversion is an underexplored mechanism with broad consequences for adaptation to abrupt and severe selective events. Here, we sought to systematically identify invertons, which we define as single intergenic invertible DNA regions flanked by inverted repeats likely recognized and inverted by invertase proteins in a reversible manner. The term inverton encompasses invertible promoters and intergenic invertible DNA regions containing alternate types of regulatory regions. Through our systematic search for invertons, we aimed to address three long-standing questions regarding this mechanism of regulation: (i) How prevalent are invertons? (ii) What are the functions of genes regulated by invertons? (iii) In the context of a host, do individual-specific selective pressures modulate inverton orientation? We found that invertons are widely distributed across bacteria, yielding fundamental insights into bacterial infection and colonization. We confirmed and expanded upon previous observations that the orientations of some invertons regulating capsular polysaccharide biosynthesis operons of human gut bacteria are stable within individuals and divergent between individuals (*17*). Using a fecal microbiota transplant (FMT) study to observe the orientation of invertons from the same strain in multiple individuals, we observed divergences in orientation between donor and patient. We also identified invertible promoters regulating antibiotic resistance genes. We observed that antibiotic treatment results in a shift from the OFF to ON orientation of these invertons in humans, and confirmed that antibiotics cause the orientation shift in vitro, which could mitigate the fitness cost of maintaining antibiotic resistance genes in the absence of antibiotics.

We developed the PhaseFinder algorithm to computationally identify invertons and quantify their orientations with genomic or metagenomic sequencing reads by identifying regions flanked by inverted repeats, mimicking their inversion in silico, and identifying regions where sequencing reads support both orientations (figs. S1 and S2). Simulations to benchmark the performance of PhaseFinder reveal that given enough coverage, PhaseFinder can identify most invertons without a substantial rate of false positives. We reasoned that if inversion rates were high, both orientations of invertons would coexist, allowing for the identification of invertons in bacterial populations used for genome sequencing. Therefore, we used PhaseFinder to search for invertons in all available NCBI genomes from RefSeq that were sequenced using Illumina paired-end sequencing with data deposited in the NCBI Short Read Archive. In total, 54,875 bacterial genomes spanning the breadth of cultured bacterial diversity were searched, leading to the discovery of 4686 putative invertons in 2414 genomes (tables S1 and S2). Invertons were found in 10 of 19 bacterial phyla. Five phyla harbored invertons in at least 20% of their genomes (Table 1). The lack of a systematic method to identify invertons was the impetus for our study; however, the limited scope of known inverton examples may lead to biases in the PhaseFinder algorithm against invertons with features divergent from known invertible promoters. Additionally, the identification of invertons with PhaseFinder relies on the presence of both orientations of the inverton in sequenced samples. Therefore, applying the PhaseFinder algorithm to additional bacterial genomes derived from diverse conditions and sequenced at higher coverage or with longer reads will likely lead to the discovery of many more invertons.

To explore how invertons are distributed across environmental niches, we used information from ProGenomes and the Joint Genome Institute to categorize species into aquatic, terrestrial, and host-associated habitats (*18*, *19*). The prevalence of invertons was higher in host-associated species [Fisher exact test, host versus aquatic FDR (false discovery rate) $P = 3.5 \times 10^{-5}$, odds ratio = 6.4; host versus terrestrial FDR $P = 0.0053$, odds ratio = 4.8) (Fig. 1A and table S3). This overall enrichment in the prevalence of invertons is due to phylum-level enrichment in Bacteroidetes (FDR $P = 2.35 \times 10^{-15}$) and Proteobacteria (FDR $P = 8.51 \times 10^{-5}$) and the fact that all Spirochaetes and Verrucomicrobia found with invertons were associated with vertebrate hosts. Additionally, we observed an increase in the number of invertons per genome

[1]Center for Microbiome Informatics and Therapeutics, Massachusetts Institute of Technology, Cambridge, MA 02139, USA. [2]Broad Institute of MIT and Harvard, Cambridge, MA 02142, USA. [3]Center for Computational and Integrative Biology, Massachusetts General Hospital and Harvard Medical School, Boston, MA 02114, USA. [4]Department of Biological Engineering, Massachusetts Institute of Technology, Cambridge, MA 02142, USA. [5]Department of Pathology and Laboratory Medicine, University of Vermont Medical Center, Burlington, VT 05401, USA. [6]Division of Gastroenterology and Hepatology, University of Vermont, Burlington, VT 05401, USA. [7]Gastrointestinal Unit and Center for the Study of Inflammatory Bowel Disease, Massachusetts General Hospital and Harvard Medical School, Boston, MA 02114, USA.
*These authors contributed equally to this work.
†Corresponding author. Email: xavier@molbio.mgh.harvard.edu (R.J.X.); ejalm@mit.edu (E.J.A.)

Downloaded from http://science.sciencemag.org/ on January 10, 2019

in host-associated species (Wilcoxon rank sum test, host versus aquatic FDR $P = 0.00023$, W = 361,190; host versus terrestrial FDR $P = 0.007$, W = 180,680) (Fig. 1B). The enrichment of invertons in host-associated species is not due to habitat-specific differences in coverage (fig. S3). Overall, our results suggest that diverse species likely use invertons to increase their fitness in host-associated niches.

We acquired detailed information on the niches inhabited by species from the phylum Bacteroidetes (table S4). In Bacteroidetes, the prevalence of invertons was higher in host gut–associated species (Fisher exact test, host-gut versus aquatic FDR $P = 3.3 \times 10^{-35}$, odds ratio = 328.4; host-gut versus terrestrial FDR $P = 2.3 \times 10^{-34}$, odds ratio = 220.8; host-gut versus host-other, FDR $P = 3.9 \times 10^{-17}$, odds ratio = 35.2) (Fig. 1C). The number of invertons per genome was also higher in host gut–associated isolates (Wilcoxon rank sum test, host-gut versus aquatic FDR $P = 1.8 \times 10^{-26}$, W = 6911; host-gut versus terrestrial FDR $P = 2.3 \times 10^{-26}$, W = 6967; host-gut versus host-other FDR $P = 4.9 \times 10^{-13}$, W = 3956) (Fig. 1D).

Because of the observed enrichment for invertons in gut species, we performed an in-depth analysis and curation of invertons in a nonredundant selection of 49 representative species from human stool using longitudinal metagenomic data instead of the reads used to assemble reference genomes (table S5). We identified 459 putative invertons (table S6), 87.6% of which were from species in the phylum Bacteroidetes, which had an average of 19 invertons per genome. We also identified invertons in additional phyla. We found 53 invertons from two *Akkermansia* species (phylum Verrucomicrobia), two invertons from a *Eubacterium* species (phylum Firmicutes), and one inverton from a *Bifidobacterium* species (phylum Actinobacteria) (fig. S4).

We categorized the invertons according to their flanking inverted repeats (IR) and identified four canonical motifs in Bacteroidetes: three corresponding to known IR motifs in *B. fragilis* and one uncharacterized motif (Fig. 2A and tables S7 and S8) (*14*). We also identified a distinctive motif class with tandem repeats within each

Table 1. Invertons per phylum identified in a systematic search of bacterial genomes with PhaseFinder.

Phylum	Genomes searched	Genomes with invertons	Percentage of genomes with invertons	Total invertons
Acidobacteria	6	0	0	0
Actinobacteria	5,262	67	1.3	200
Armatimonadetes	2	0	0	0
Bacteroidetes	491	160	32.6	1,254
Chlamydiae	45	3	6.7	5
Chloroflexi	1	0	0	0
Cyanobacteria	20	4	20	7
Deinococcus-Thermus	14	1	7.1	1
Fibrobacteres	16	0	0	0
Firmicutes	17,010	986	5.8	1,422
Fusobacteria	10	0	0	0
Nitrospirae	1	0	0	0
Proteobacteria	14,872	1,133	7.6	1,628
Spirochaetes	138	57	41.3	140
Synergistetes	8	2	25	2
Tenericutes	21	0	0	0
Thermodesulfobacteria	3	0	0	0
Thermotogae	7	0	0	0
Verrucomicrobia	5	1	20	27

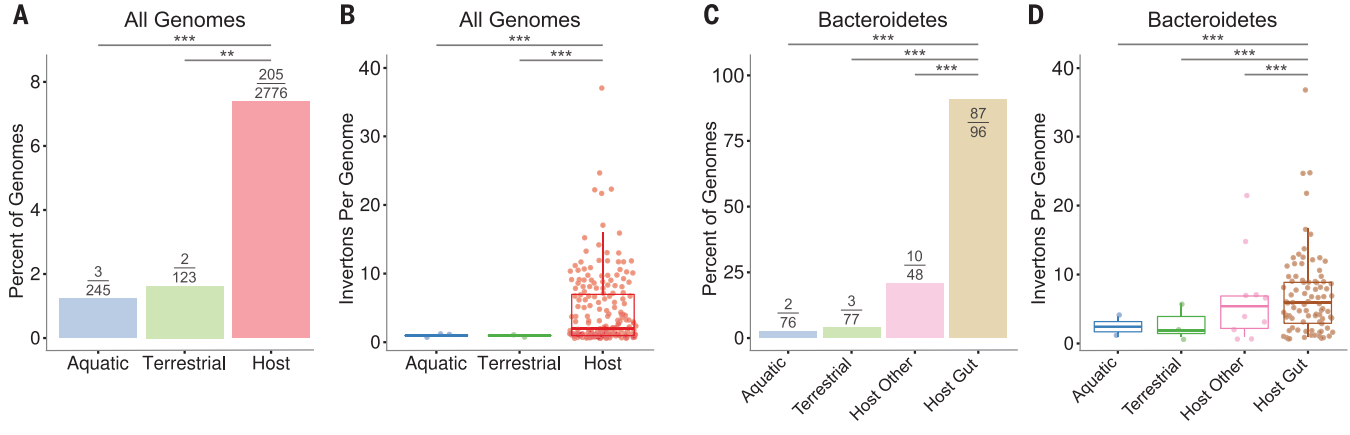


Fig. 1. Prevalence and number of invertons per genome are enriched in host-associated species. (**A** and **B**) The percentage of genomes identified with invertons (A) and the number of invertons per genome (B) from aquatic, terrestrial, and host-associated isolates. (**C** and **D**) In the phylum Bacteroidetes, the percentage of genomes identified with invertons (C) and the number of invertons per genome (D) from aquatic, terrestrial, host sites other than gut, and host gut–associated isolates. $^{**}P \leq 0.01$, $^{***}P \leq 0.001$.

Downloaded from http://science.sciencemag.org/ on January 10, 2019

inverted repeat, which we call motif 0 (fig. S5). We found conserved promoter consensus motifs in 98% (231/235) of invertons with IR motifs 1 to 4 (Fig. 2B) (*20*). In contrast, promoter motifs were not observed in any of the invertible regions of IR motif 0–containing sequences (table S9). Because of the lack of promoter motifs combined with their location downstream of operons, invertons containing motif 0 may function as another type of regulatory element, such as a phase-variable terminator (*8*). In gut Bacteroidetes, we identified a total of 255 invertible promoters. On the basis of the orientation of the promoter consensus motif in relation to surrounding genes, we determined which genes or operons were regulated by invertible promoters and whether the promoter was in the ON or OFF orientation with respect to the downstream gene (tables S7 and S8). In both species of *Akkermansia*, all invertons are flanked by inverted repeats with the same motif (Fig. 2C), contain a promoter motif (Fig. 2D), and lack upstream invertases, which suggests that they are all invertible promoters co-regulated by a single, master invertase (EAJ16_05345 in *Akkermansia muciniphila*; MK095134 in *Akkermansia* sp. aa_0143).

Through functional annotation, we found that 73% (228/312) of invertible promoters regulate genes involved in the biosynthesis of polysaccharides, fimbriae, outer membrane proteins, and autotransporters; genes involved in the utilization of polysaccharides; or genes encoding PEP-CTERM domain–containing proteins (Fig. 2A, tables S7 and S8, and fig. S4). All of these functional categories except polysaccharide utilization are enriched in genes regulated by invertible promoters (tables S10 and S11). Genes regulated by invertible promoters are enriched for cell surface products (e.g., GO:0016020, membrane, $P = 1.93 \times 10^{-14}$) (table S11). The most enriched functional class is capsular polysaccharide biosynthesis loci, for which we found at least one example regulated by an inverton in four of the five major gut phyla: Bacteroidetes, Actinobacteria, Verrucomicrobia, and Firmicutes (table S11). Previous studies show that a repertoire of phase-variable capsular polysaccharides is necessary for competitive gut colonization by *Bacteroides* species (*2*, *16*, *21*). Our data show that phase-variable capsular polysaccharide biosynthesis loci are not just a peculiarity of *Bacteroides* species but are likely a convergent response to a strong selective mechanism in the vertebrate gut that possibly originates from the immune response or phages (*2*, *21*).

We found that invertible promoters could regulate antibiotic resistance genes, such as IBP132, which is upstream of the macrolide resistance gene *ermG* in *B. stercoris*. To investigate this mechanism in vivo, we searched specifically for antibiotic resistance genes regulated by invertible promoters in a cohort of 39 Finnish children, 19 of whom had never been exposed to antibiotics and 20 of whom had been administered 9 to 15 antibiotic treatments over a 3-year period (*22*). By coupling PhaseFinder with metagenomic assembly analysis, we found three antibiotic resistance genes regulated by invertible promoters: (i) the same *ermG* macrolide resistance gene as IBP132, (ii) a *cmeABC* multidrug resistance cassette conferring resistance primarily to macrolides and cephalosporins, and (iii) *pmrEL* genes conferring resistance to cationic antimicrobial peptides such as polymixin B (Fig. 3A). At least one antibiotic resistance gene regulated by an invertible promoter was found in 38% (15/39) of individuals from this Finnish cohort: 40% (8/20) of individuals who were administered antibiotics and 37% (7/19) of individuals who were untreated. Invertons regulating antibiotic resistance genes were also detected in metagenomic data from healthy adults in the United States. All examples of invertons regulating antibiotic resistance were found in *Bacteroides* species, which are increasingly associated with multi–drug-resistant infections (*23*). Surprisingly, all *cmeABC* and *ermG* antibiotic resistance genes were regulated by an identical invertible promoter. On the basis of genomic context, the *cmeABC/ermG* invertible promoter is likely located on an integrative conjugative element homologous to CTNhyb, an antibiotic resistance–transmitting mobile element (fig. S6) (*24*).

We examined the orientation of the invertible promoters regulating antibiotic resistance genes in longitudinal metagenomic data from the Finnish children. The mean orientation of the *cmeABC/ermG* invertible promoter was 94% OFF in untreated individuals and 84% OFF in individuals administered antibiotics. We observed an individual in which the *cmeABC/ermG* invertible promoter was 99% OFF 7 days before the macrolide azithromycin was administered and 74% ON 27 days after treatment (Fig. 3B). The *cmeABC/ermG* invertible promoter reverted to 99% OFF within 5 months after azithromycin administration (Fig. 3B). A similar phenomenon was observed in a second individual (fig. S7). A permutation test revealed that macrolide treatment was positively associated with the ON orientation of the *cmeABC/ermG* invertible promoter [quantitative polymerase chain reaction (qPCR) $P = 0.0005$, metagenomic $P = 0.0465$]. Thus, it appears that macrolides may select for the ON orientation of the *cmeABC/ermG* invertible promoter, and the orientation of the invertible promoter drifts toward OFF after cessation of antibiotic treatment.

To test whether antibiotics select for resistance genes with invertible promoters in the ON orientation, we first verified that the genes regulated by the *cmeABC/ermG* invertible promoter confer macrolide resistance. We cultivated 13 *B. stercoris* isolates with and one isolate without the *cmeABC/ermG* invertible promoter upstream of the macrolide resistance gene *ermG* (table S12) (*25*). The invertible promoter was primarily ON (>75%) in 10 isolates derived from erythromycin-containing media and primarily OFF (>97%) in three isolates derived from media

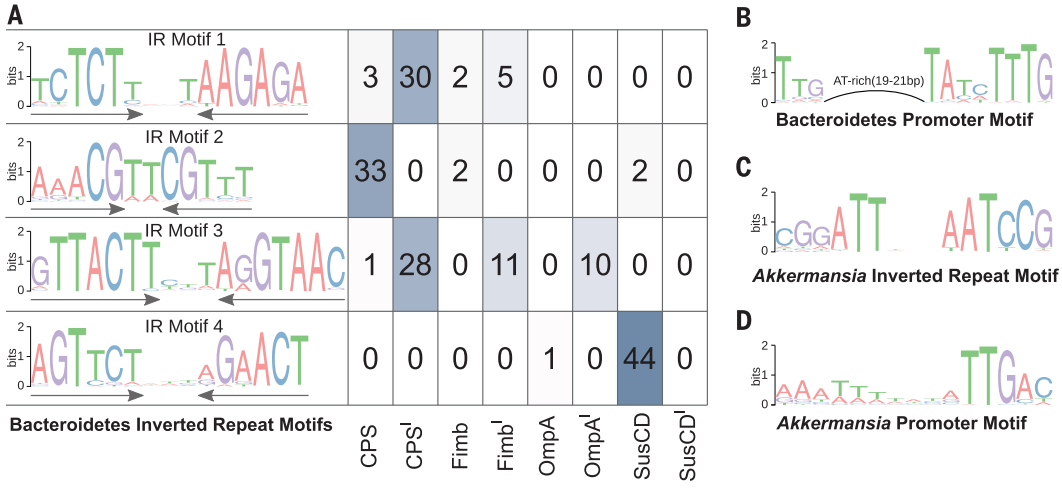


Fig. 2. Motifs found in the inverted repeats of Bacteroidetes and *Akkermansia* invertons consist of five to seven base pair palindromes with two or three intervening base pairs. (**A**) Functional profiling of operons regulated by invertons reveals specializations of each inverted repeat (IR) motif. The heat map represents the number of operons per functional class regulated by invertons with either global or local invertases. CPS, capsular polysaccharide; Fimb, fimbriae; OmpA, outer membrane protein A; SusCD, starch utilization system proteins C and D. Superscript I indicates the presence of a local invertase. The absence of local invertases directly upstream suggests that IR motifs 2 and 4 are likely regulated by global invertases. (**B**) Promoter motif identified from invertons from Bacteroidetes species. (**C**) The inverted repeat motif found in all identified invertons from *Akkermansia* spp. (**D**) Promoter motif identified from invertons from *Akkermansia* spp.

Downloaded from http://science.sciencemag.org/ on January 10, 2019

without erythromycin (Fig. 3C). We established that all *B. stercoris* isolates with *ermG* regulated by the *cmeABC/ermG* invertible promoter were resistant to erythromycin, whereas the isolate without the *ermG* gene was susceptible (fig. S8).

Next, we showed that erythromycin treatment selects for the ON orientation of the *cmeABC/ermG* invertible promoter. To quantify changes in the relative abundances of cells with the *cmeABC/ermG* invertible promoter in ON and OFF orientations, we performed qPCR comparing relative amplification using a static primer downstream of the invertible promoter paired with either a primer that amplifies the ON orientation or one that amplifies the OFF orientation (fig. S9). We transferred *B. stercoris* isolates with the *cmeABC/ermG* invertible promoter

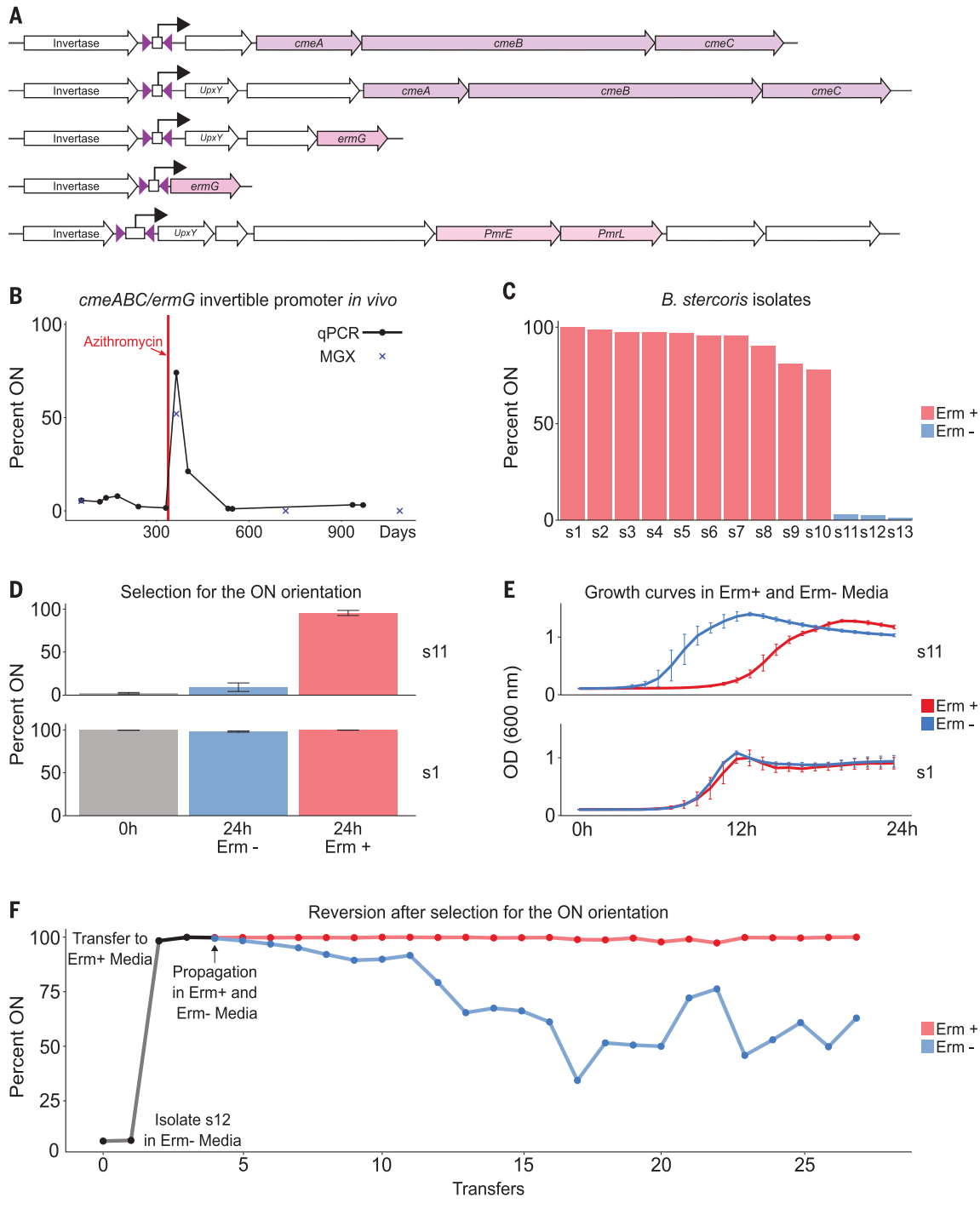


Fig. 3. Invertible promoters regulate antibiotic resistance genes. (**A**) Three classes of genes conferring antibiotic resistance are regulated by invertible promoters. The genomic contexts of the loci are shown with antibiotic resistance genes colored. Promoters are designated by hooked arrows; purple triangles represent inverted repeats. (**B**) An invertible promoter regulating the *cmeABC* multidrug efflux cassette in individual E011878 was 99% OFF before antibiotic treatment, shifted to 74% ON 7 days afterward, and then drifted back to 99% OFF over 5 months as measured by both qPCR and metagenomic (MGX) data. (**C**) The *cmeABC/ermG* invertible promoter is oriented ON in *B. stercoris* isolated in medium containing erythromycin (Erm+) and OFF in *B. stercoris* isolated in medium without erythromycin (Erm–). (**D**) The orientation of the *cmeABC/ermG* invertible promoter under antibiotic selection. Isolate s11 grown in Erm– medium remained OFF, whereas the same isolate transferred to Erm+ medium shifted to ON. Isolate s1 remained ON in Erm– and Erm+ media. (**E**) Growth of isolates under antibiotic selection. Isolate s1 grew in Erm+ medium without a lag phase relative to Erm– medium, whereas isolate s11 grew in Erm+ medium after an extended lag phase, consistent with a lower number of initially erythromycin-resistant cells. (**F**) Kinetics of the *cmeABC/ermG* invertible promoter. An isolate with the *cmeABC/ermG* invertible promoter initially in the OFF orientation, s12, was exposed to erythromycin. Half of the culture was then propagated in the presence of erythromycin and the other half in the absence of erythromycin for 24 1:1000 dilution transfers. In Erm+ medium, the promoter remained ON, whereas in Erm– medium, it drifted toward OFF. Error bars in (D) and (E) denote SD.

Downloaded from http://science.sciencemag.org/ on January 10, 2019

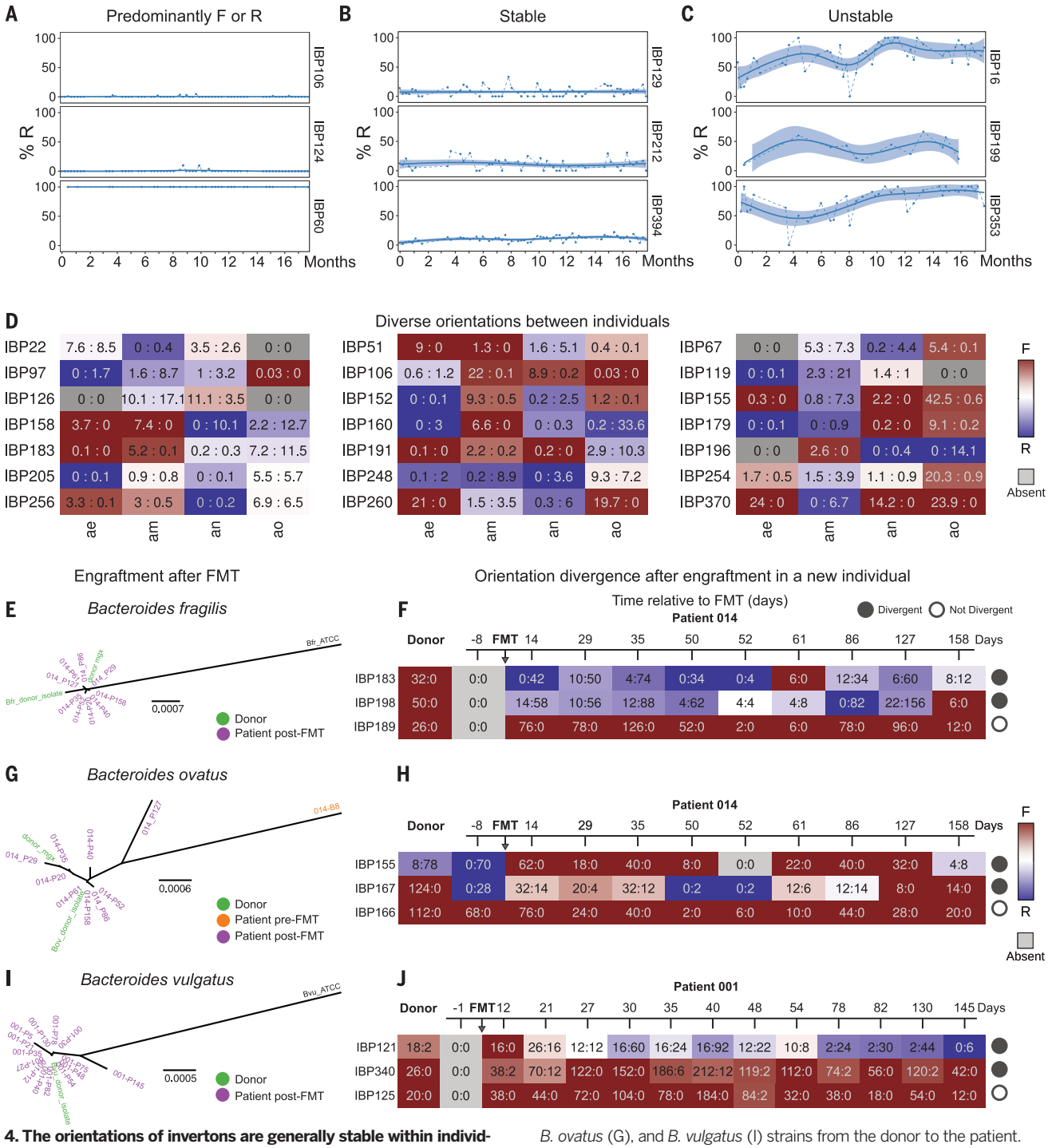


Fig. 4. The orientations of invertons are generally stable within individuals but divergent between individuals. (**A**) Examples of invertons from donor "am" found in the forward (F: IBP106, IBP124) or reverse (R: IBP60) orientation. (**B**) Examples of invertons from donor "am" (IBP129, IBP212, and IBP394) that are longitudinally stable. (**C**) Examples of invertons from donor "am" that are longitudinally unstable (IBP16, IBP199, and IBP353). (**D**) Selected examples of invertible promoters with different orientations among four individuals ("ae," "am," "an," and "ao"). Numbers in each heat map cell represent the average counts in the F and R orientations (F:R); red and blue indicate F and R orientation, respectively. (**E**, **G**, and **I**) Phylogenetic trees produced by StrainPhlAn from metagenomic data from FMT donor (green) and patient (orange, pre-FMT; purple, post-FMT) as well as isolate genomes from the donor (green) and unrelated reference genomes from the same species (black). The phylogenetic trees demonstrate engraftment and persistence of *B. fragilis* (E), *B. ovatus* (G), and *B. vulgatus* (I) strains from the donor to the patient. Phylogenetic tree legends are the number of nucleotide substitutions per site. (**F**, **H**, and **J**) Examples of divergence of invertible promoter orientations after engraftment in a patient. Black circles denote invertible promoters whose orientation was significantly different between donor and patient after FMT. White circles denote invertible promoters whose orientation is not significantly different (Wilcoxon rank sum test, FDR $P < 0.05$). Numbers in each heat map cell represent the counts in the F and R orientations (F:R). (F) After engraftment, the orientations of IBP183 and IBP198 were reversed relative to the donor. (H) A strain of *B. ovatus* was present in Patient 14 before FMT but was outcompeted by the donor strain. After engraftment, the orientation of IBP155 and IBP167 was reversed relative to the donor. (J) After *B. vulgatus* engraftment, the orientation of IBP121 was only found in the F orientation, but over the course of 135 days, the orientation reversed.

Downloaded from http://science.sciencemag.org/ on January 10, 2019

oriented either primarily ON or OFF into media with (Erm+) or without (Erm–) erythromycin and quantified the percentage of cells in the ON or OFF orientation after 24 hours (Fig. 3D). The OFF cultures grew in Erm+ medium only after an extended lag phase relative to growth in Erm– medium, whereas ON cultures grew similarly in Erm+ and Erm– media (Fig. 3E). OFF isolates grown in Erm+ medium became predominantly ON, whereas OFF isolates grown in Erm– medium remained OFF. ON isolates remained predominantly ON in both Erm+ and Erm– media (Fig. 3D).

Finally, during serial transfers in both Erm+ and Erm– media, we monitored the ON:OFF ratio of the *cmeABC/ermG* invertible promoter in a *B. stercoris* OFF isolate that had previously been switched to ON in Erm+ medium. Over the course of 24 transfers at 1:1000 dilution, the orientation of the *cmeABC/ermG* invertible promoter remained ON in Erm+ medium but gradually drifted away from 100% ON in Erm– medium, recapitulating the in vivo observations from metagenomic data (Fig. 3F).

Although strongly favored in the presence of antibiotics, high expression of antibiotic resistance genes likely incurs a substantial fitness cost, which could explain the reversion to the OFF orientation after antibiotic treatment. Many compensatory mechanisms to maintain antibiotic resistance in the absence of antibiotics have been noted (*26*), but invertons are akin to catastrophe insurance; a certain percentage of the population is always prepared to resist future antibiotic treatment and reintroduce heterogeneity after antibiotic selection.

Dense longitudinal metagenomic data allow for a detailed view of the dynamics of invertons over time in the human gut. We analyzed a dataset of samples from 54 individuals, four of whom ("ae," "am," "an," "ao") were sampled densely over 5 to 18 months, and tracked the orientations of invertons. The F orientation is the same orientation of the inverton in the reference genome, whereas the R orientation is the opposite orientation of the inverton in the reference genome. We identified 423 invertons with sufficient coverage to track their temporal dynamics in these individuals. Of these, 322 were predominantly found in one orientation within an individual with little or no fluctuation (mean > 95% and min > 75% for either the F or R orientation) (Fig. 4A); the orientations of 59 were relatively stable (max-min %R ≤ 50%) within an individual (Fig. 4B), whereas the orientations of 42 were unstable (max-min %R > 50%) within an individual (Fig. 4C and table S13).

Although the orientations of 90% of invertons in the same individual were relatively stable over time, the orientations between individuals varied extensively (Fig. 4D and fig. S10). The mean %R orientation of 214 out of 423 of the invertons varied by more than 50% between individuals. In 122 examples, averaging across time, the inverton was predominantly (>95%) in the F orientation in at least one individual and predominantly (>95%) in the R orientation in another. Additionally, 119 out of 238 invertons were significantly different (Kruskal-Wallis H test, FDR $P < 0.05$) between the four individuals for whom we had dense longitudinal metagenomic data. The differences in the orientations of invertons between individuals could be explained by divergent selective forces between individuals, different optimal orientations between strains, or stochastic variation in orientation.

Sculpted by the individual's diet, lifestyle, immune response, and genetics, the gut of every individual is a distinctive environment for resident bacteria. We observed the influence of the individual on the orientations of invertons in a cohort of patients with ulcerative colitis who were the recipients of FMT from healthy donors. The source of the fecal microbiota was donor "am," whose longitudinal metagenomic data were analyzed above. Therefore, we could monitor the orientations of invertons from the same strain for 18 months in a healthy donor and up to 5 months in the patients.

First, we identified strains from the donor that engrafted into the patient's microbiome. To identify engraftment, we found cases where the same strain was present in the donor and in at least one patient after FMT, but absent in the same patient(s) before FMT (Fig. 4, E, G, and I, and fig. S11). We found three high-abundance species with invertons from the donor that engrafted in patients: *B. fragilis*, *B. vulgatus*, and *B. ovatus*.

Then, we compared the orientations of invertons from the donor and patient after engraftment and found that the orientations of 42.8% of invertons (48/112) diverged from the donor orientation (Wilcoxon rank sum test, FDR $P < 0.05$) (Fig. 4, F, H, and J, and fig. S12). In *B. fragilis*, two invertons (IBP183 and IBP198) engrafted in the opposite orientation of the donor strain and remained predominantly (87.2% and 87.1%) in the R orientation, but drifted toward F near the end of the sampling (Fig. 4F). For *B. ovatus*, a strain existed in Patient 014 before FMT but was replaced by the donor *B. ovatus* strain (Fig. 4G; compare orange to purple). IBP155 invertons from both the donor strain and pre-FMT strain were predominantly (90.1% and 100%) in the R orientation, whereas the newly engrafted strain was oriented entirely in the F orientation and remained in the F orientation over the course of sampling (Fig. 4H). In *B. vulgatus*, an inverton was initially present completely in the F orientation but over the course of 145 days completely reversed to the R orientation (Fig. 4J, IBP121). In addition to the invertons that reversed their orientations, we also identified examples of invertons that maintained their orientations (Fig. 4F, IBP189; Fig. 4H, IBP166; Fig. 4J, IBP125).

Our findings highlight the role of invertons in host-microbe coexistence. Genes regulated by invertons were highly enriched for products located on the exterior of the cell where they are exposed to the host immune system and phages, indicating that they may be primary targets for selection that are beneficial for gut commensals to diversify their surface architectures or essential processes, such as antibiotic resistance, whose expression has a high fitness cost. The high prevalence of antibiotic resistance genes regulated by invertons containing promoters suggests that this is an example of bet-hedging (*27*). This could lead to longer persistence of antibiotic resistance genes in a microbial community, further increasing the burden to combat antibiotic resistance. Our results indicate that in the human gut, invertons help bacterial populations regain heterogeneity after bottlenecks encountered during colonization of a new host or severe perturbations. Overall, our study provides insights into a mechanism allowing adaptive tradeoffs in bacteria that have evolved to successfully colonize host-associated niches.

REFERENCES AND NOTES

1. M. J. Coyne, M. Chatzidaki-Livanis, L. C. Paoletti, L. E. Comstock, *Proc. Natl. Acad. Sci. U.S.A.* **105**, 13099–13104 (2008).
2. N. T. Porter, P. Canales, D. A. Peterson, E. C. Martens, *Cell Host Microbe* **22**, 494–506.e8 (2017).
3. J. C. Gauntlett, H.-O. Nilsson, A. Fulurija, B. J. Marshall, M. Benghezal, *Gut Pathog.* **6**, 35 (2014).
4. M. Taketani, M. S. Donia, A. N. Jacobson, J. D. Lambris, M. A. Fischbach, *mBio* **6**, e01339-15 (2015).
5. J. K. Lim *et al*., *Infect. Immun.* **66**, 3303–3310 (1998).
6. I. R. Henderson, P. Owen, J. P. Nataro, *Mol. Microbiol.* **33**, 919–932 (1999).
7. M. J. Coyne, K. G. Weinacht, C. M. Krinos, L. E. Comstock, *Proc. Natl. Acad. Sci. U.S.A.* **100**, 10446–10451 (2003).
8. P. Hinde, P. Deighan, C. J. Dorman, *J. Bacteriol.* **187**, 8256–8266 (2005).
9. T. H. Kawula, P. E. Orndorff, *J. Bacteriol.* **173**, 4116–4123 (1991).
10. C. D. Bayliss, *FEMS Microbiol. Rev.* **33**, 504–520 (2009).
11. O. Sekulovic *et al*., *PLOS Genet.* **14**, e1007332 (2018).
12. M. Silverman, M. Simon, *Cell* **19**, 845–854 (1980).
13. J. M. Abraham, C. S. Freitag, J. R. Clements, B. I. Eisenstein, *Proc. Natl. Acad. Sci. U.S.A.* **82**, 5724–5727 (1985).
14. H. Nakayama-Imaohji *et al*., *J. Bacteriol.* **191**, 6003–6011 (2009).
15. H. Nakayama-Imaohji *et al*., *PLOS ONE* **11**, e0148887 (2016).
16. E. B. Troy, V. J. Carey, D. L. Kasper, L. E. Comstock, *J. Bacteriol.* **192**, 5832–5836 (2010).
17. N. L. Zitomersky, M. J. Coyne, L. E. Comstock, *Infect. Immun.* **79**, 2012–2020 (2011).
18. D. R. Mende *et al*., *Nucleic Acids Res.* **45**, D529–D534 (2017).
19. I. V. Grigoriev *et al*., *Nucleic Acids Res.* **40**, D26–D32 (2012).
20. D. P. Bayley, E. R. Rocha, C. J. Smith, *FEMS Microbiol. Lett.* **193**, 149–154 (2000).
21. C. H. Liu, S. M. Lee, J. M. Vanlare, D. L. Kasper, S. K. Mazmanian, *Proc. Natl. Acad. Sci. U.S.A.* **105**, 3951–3956 (2008).
22. M. Yassour *et al*., *Sci. Transl. Med.* **8**, 343ra81 (2016).
23. G. N. Hartmeyer, J. Sóki, E. Nagy, U. S. Justesen, *J. Med. Microbiol.* **61**, 1784–1788 (2012).
24. F. Husain *et al*., *Mob. Genet. Elements* **4**, e29801 (2014).
25. M. Monod, S. Mohan, D. Dubnau, *J. Bacteriol.* **169**, 340–350 (1987).
26. D. I. Andersson, D. Hughes, *FEMS Microbiol. Rev.* **35**, 901–911 (2011).
27. T. Philippi, J. Seger, *Trends Ecol. Evol.* **4**, 41–44 (1989).

ACKNOWLEDGMENTS

We thank T. Poon, T. Vatanen, and M. Groussin for their assistance in obtaining samples and data; T. Reimels for comments on the manuscript; and the Microbial Omics Core of the Broad Institute and the Broad Technology Labs for their assistance with DNA

Downloaded from http://science.sciencemag.org/ on January 10, 2019

extraction, library preparation, and sequencing. The FMT research was approved by the Committee on Human Research in the Medical Sciences (CHRMS) (CHRMS 15-373). **Funding:** Supported by NIH grants DK043351 and AT009708, the Crohn's and Colitis Foundation of America, the Juvenile Diabetes Research Foundation, and the Center for Microbiome Informatics and Therapeutics at MIT (R.J.X.). A.B.H. is a Merck Fellow of the Helen Hay Whitney Foundation. **Author contributions:** Conceptualization, X.J., A.B.H., T.D.A., H.V., A.C.T., E.J.A., and R.J.X.; methodology, X.J., A.B.H., D.R.P., C.T.C., and T.D.A.; software, X.J. and A.B.H.; validation, X.J. and A.B.H.; formal analysis, X.J., A.B.H., D.R.P., C.T.C., and T.D.A.; investigation, X.J., A.B.H., and T.D.A.; resources, M.P., P.L.M., and J.C.; data curation, X.J., A.B.H., and T.D.A.; writing (original draft preparation), X.J. and A.B.H., writing (review and editing), X.J., A.B.H., H.V., A.C.T., E.J.A., and R.J.X., visualization, X.J. and A.B.H.; supervision, H.V., A.C.T., E.J.A., and R.J.X.; project administration and funding acquisition, E.J.A. and R.J.X. **Competing interests:** E.J.A. is a co-founder and shareholder of Finch Therapeutics. J.C. consults for Finch Therapeutics. P.L.M. is currently employed by Takeda Pharmaceuticals International. **Data and materials availability:** Data used in the study are available from the NCBI. Isolate genomes: PRJNA496358. Dense longitudinal metagenomic data: PRJNA503484, FMT metagenomic data: PRJNA474024. PhaseFinder is available from GitHub: https://github.com/XiaofangJ/PhaseFinder.

SUPPLEMENTARY MATERIALS

www.sciencemag.org/content/363/6423/181/suppl/DC1
Materials and Methods
Figs. S1 to S12
Tables S1 to S16
References (*28*–*50*)

19 June 2018; accepted 3 December 2018
10.1126/science.aau5238

Downloaded from http://science.sciencemag.org/ on January 10, 2019

CIRCADIAN RHYTHMS

Cell-autonomous clock of astrocytes drives circadian behavior in mammals

Marco Brancaccio*†, Mathew D. Edwards‡, Andrew P. Patton, Nicola J. Smyllie, Johanna E. Chesham, Elizabeth S. Maywood, Michael H. Hastings*

Circadian (~24-hour) rhythms depend on intracellular transcription-translation negative feedback loops (TTFLs). How these self-sustained cellular clocks achieve multicellular integration and thereby direct daily rhythms of behavior in animals is largely obscure. The suprachiasmatic nucleus (SCN) is the fulcrum of this pathway from gene to cell to circuit to behavior in mammals. We describe cell type–specific, functionally distinct TTFLs in neurons and astrocytes of the SCN and show that, in the absence of other cellular clocks, the cell-autonomous astrocytic TTFL alone can drive molecular oscillations in the SCN and circadian behavior in mice. Astrocytic clocks achieve this by reinstating clock gene expression and circadian function of SCN neurons via glutamatergic signals. Our results demonstrate that astrocytes can autonomously initiate and sustain complex mammalian behavior.

The transcription-translation negative feedback loop (TTFL) mechanisms responsible for intracellular circadian (~24-hour) timekeeping in animals are understood in molecular detail (*1*). The TTFL of mammals involves transcriptional activation by Clock/Bmal1 heterodimers, which drive daytime expression of *Period* (*Per*) and *Cryptochrome* (*Cry*) genes through E-box regulatory sequences. After dimerization and transport to the nucleus, Per-Cry complexes repress Clock-Bmal1 activity during circadian night, until progressive degradation of Per-Cry allows initiation of a new cycle. This self-sustaining cell-autonomous TTFL is universally active across mammalian tissues, so how cellular clocks interact to achieve multicellular integration and ultimately direct daily rhythms of behavior is a matter of considerable interest. The suprachiasmatic nucleus of the hypothalamus (SCN) is the fulcrum of this pathway from gene to cell to circuit to behavior. Its tightly coordinated multicellular oscillations can continue indefinitely to direct internal synchronization of cellular clocks across the body. The conventional view is that robust pacemaking relies on the intrinsic interneuronal connectivity of the SCN, albeit with principles still largely unknown (*2*). However, circadian timekeeping in the SCN is also influenced by a sophisticated interplay between its neurons and astrocytes (*3*). In common with other cell types, astrocytes have a TTFL that is assumed to be maintained by input from SCN neurons (*4*, *5*). In light of the intimacy of astrocyte-neuron interactions in the SCN, however, we wondered whether SCN astrocytes really are "slaves" to their neuronal partners, or whether the SCN pacemaker might instead be considered a bipartite cellular system in which astrocytes can also direct neuronal time-keeping and behavior.

To address this, we used adeno-associated virus vectors (AAVs) and genetics to characterize the distinctive properties of the TTFLs of SCN astrocytes and neurons. We assessed cell type–specific TTFL function with an AAV encoding a Cre recombinase–dependent reporter (*6*) in which firefly luciferase is driven by a minimal mouse Cry1 promoter (*Cry1*) containing E-boxes (Cry1-Flex-Luc; Flex represents Cre-dependent flip-excision) (*7*, *8*). Cotransduction of SCN slices with AAVs driving Cre by the glial fibrillary acidic protein (GFAP) or human synapsin 1 (Syn) promoters restricted Cry1-Flex-Luc expression to astrocytes or neurons, respectively (*3*) (Fig. 1, A to F). Bioluminescent recording revealed sustained circadian oscillations of *Cry1*-Luc in both SCN neurons and astrocytes. Although these oscillations had the same period and robustness, measured by the relative amplitude error (RAE), their waveforms differed (Fig. 1F), reminiscent of the distinctive waveforms of intracellular calcium rhythms observed in astrocytes and neurons (*3*). These SCN slices were also cotransduced with AAVs encoding the calcium reporter GCaMP3 driven by the Syn promoter (Syn-GCaMP3) to track circadian concentrations of neuronal intracellular calcium ($[Ca^{2+}]_i$). We used this reporter, which peaks during the mid-circadian day [circadian time 6.5 hours (CT6.5)] (*3*, *9*), to internally register the circadian phase of the detected *Cry1*-Luc expression in SCN astrocytes and neurons. This showed that the peak of expression of astrocytically restricted *Cry1*-Luc was phase-delayed by ~6.5 hours (~CT17) when compared with that of the neurons, which peaked at ~CT11 (Fig. 1, B, C, and F). Thus, neurons and astrocytes of the SCN exhibit cell type–specific functionally distinct Cry1-Luc reporter TTFLs characterized by different phases and waveforms.

To test the potential contribution of the astrocytic TTFL to SCN time-keeping, we used cell type–specific genetic complementation in SCN of mice lacking both *Cry* genes (Cry1/2-null mice) (*10*). In the absence of the Cry repressors, the endogenous TTFL does not function, so molecular circadian oscillations, monitored by the Per2::Luc reporter, are compromised (*11*) (Fig. 1G). Generalized (pancellular) expression of Cry1 can initiate circadian molecular rhythms in Cry-deficient SCN slices (*8*). Using Cre-dependent AAVs encoding a Cry1::EGFP (enhanced green fluorescent protein) fusion protein driven by the *Cry1* promoter (*Cry1*-Flex-Cry1::EGFP), we expressed Cry1 specifically in either neurons or astrocytes of Cry1/2-null SCN restricted by Syn-Cre or GFAP-Cre. As anticipated, expressing Cry1 in neurons was sufficient to initiate self-sustained circadian oscillations of Per2::Luc in the SCN. Expression of Cry1::EGFP solely in astrocytes was also effective, however, highlighting astrocytes as pacemakers within the SCN circuit (fig. S1 and Fig. 1, G and H). Nevertheless, there were appreciable differences in both the early and the late phases of Cry1 expression between the two cell type–specific manipulations. The effects on Per2::Luc oscillations of neuronally restricted Cry1::EGFP became apparent within ~2 days posttransduction (dpt), whereas astrocytically restricted Cry1 took appreciably longer (>7 dpt) to initiate rhythms. In the later stages (11 to 15 dpt), Cry1 maintained stable oscillations longer than 24 hours (appropriate to a Cry2-null background) (*10*) when expressed in either neurons or astrocytes, although astrocytically dependent rhythms had a significantly shorter period than neuronally driven rhythms (Fig. 1H). Thus, not only SCN neurons but also astrocytes can autonomously initiate and sustain stable oscillations of clock gene expression in the SCN, and their instructive, rather than simply permissive, role is evidenced by the observed period differences.

As shown by SCN transplantation between animals with contrasting genetically specified circadian periods (*12*, *13*), the defining property of the SCN as the master circadian pacemaker is its ability to initiate circadian patterns of behavior, imposing its intrinsic periodicity to the rest of the body. We therefore tested whether the cell-autonomous astrocytic TTFL could drive circadian locomotor activity rhythms in otherwise "clockless" adult mice and compared them to rhythms of mice with similarly restricted manipulations of the neuronal TTFL (Fig. 2). The SCN of Cry1/2-null mice were stereotaxically injected with Cre-conditional AAV-*Cry1*-Flex-Cry1::EGFP together with (i) AAV-GFAP-mCherry::Cre, (ii) AAV-Syn-mCherry::Cre, or (iii) AAV-GFAP-EGFP, as a Cre negative control group (Fig. 2, A to C, and fig. S2A). We confirmed high specificity and efficiency of Cre-dependent expression of Cry1::EGFP by evaluating post hoc the histological colocalization of the Cry1::EGFP signal with GFAP-mCherry::Cre or Syn-mCherry::Cre, respectively (Fig. 2, D and E). We further confirmed that the GFAP-driven Cre recombinase

Division of Neurobiology, MRC Laboratory of Molecular Biology, Cambridge CB2 0QH, UK.
***Corresponding author. Email: m.brancaccio@imperial.ac.uk (M.B.); mha@mrc-lmb.cam.ac.uk (M.H.H.)** †Present address: Division of Brain Sciences, Department of Medicine, Imperial College London, London W12 0NN, UK.
‡Present address: SWC for Neural Circuits and Behaviour, London W1T 4JG, UK.

Downloaded from http://science.sciencemag.org/ on January 10, 2019

efficiently restricts expression of Cry1 to astrocytes by colocalizing the Cry1::EGFP signal with the astrocytic marker AldH1L1 (*3*, *4*) (fig. S2B). Locomotor activity of mice was recorded before and after surgery under constant dim red light (DD) to assess the intrinsic free-running circadian rhythmicity. Before surgery, Cry1/2-null mice did not show any consistent circadian rhythmicity in DD (DD1). However, after surgery (DD2), and in contrast to Cre-negative control mice, both AAV-GFAP-mCherry::Cre–treated and AAV-Syn- mCherry::Cre–treated mice showed sustained circadian patterns of locomotor behavior (Fig. 2F and fig. S2A). The periods of the induced rhythms were consistent with the molecular cycles of Per2::Luc observed in SCN explants being >26 hours and with the astrocytically driven rhythm being ~1 hour shorter than that of mice with neuronally expressed Cry1 (Figs. 2F and 1H). Furthermore, across animals the number of Cry1::EGFP^{+} neurons correlated positively with the behavioral period, whereas when Cry1 was expressed in SCN astrocytes there was a negative relationship (Fig. 2G), supporting the view that increasing numbers of targeted neurons and astrocytes can drive the locomotor rhythm to a period progressively closer to that of the corresponding cell-autonomous TTFLs. Nevertheless, the daily profiles of circadian behavior were equivalent whether neuronally or astrocytically controlled (Fig. 2H and fig. S2C). Thus, SCN astrocytes can specifically instruct new circadian behavior in an otherwise-arrhythmic mouse.

Given that astrocytes are not directly connected to motor centers, we hypothesized that they rely on recruiting the (TTFL-incompetent) SCN neuronal circuitry to engage behavioral output. To test for such indirect mechanisms, we imaged single cell– and circuit–level TTFL dynamics in Cry1/2-null SCN slices during the early phases of neuronal or astrocytic Cry1 expression (Fig. 3). Neuronal expression of Cry1 immediately generated robust cellular Per2::Luc oscillations, consistent with a direct effect on the neuronal TTFL and similar to that observed after nonrestricted expression of Cry1 (*8*) (fig. S3). In contrast, although expression of Cry1 in astrocytes also initiated stable long period oscillations, it took >7 days to do so (movie S1 and Fig. 3, A and B). Analysis of individual Per2::Luc^{+} cells in the SCN revealed that Cry1 expression in astrocytes produced a progressive strengthening of Per2::Luc cellular rhythms, with periods initially differing by >16 hours and slowly converging to a single ~28.5-hour period (Fig. 3, C and D). This progressive effectiveness of astrocytes is consistent with an indirect engagement of the wider neuronal circuit.

To monitor neuronal activity directly, SCN slices expressing Cry1 only in astrocytes were supertransduced with AAVs encoding the synapsin-driven red genetically encoded calcium indicator RCaMP1h (Syn-RCaMP1h) (*3*). This revealed astrocytically driven circadian oscillations of neuronal $[Ca^{2+}]_i$ that were phase-advanced to Per2::Luc by ~6 circadian hours, as observed in wild-type SCN (Fig. 3, E to I, and movie S2). Circadian peaks of $[Ca^{2+}]_i$ and clock gene expression travel across the SCNs in a stereotypical spatio-temporal wave, with neurons in the dorsal SCN phase-leading the ventral ones in a pattern strictly dependent on the SCN circuit properties (*14*, *15*). To confirm that astrocytically restricted Cry1 expression also established appropriate spatio-temporal patterns of neuronal $[Ca^{2+}]_i$ across the SCN, we compared the calcium signal in wild-type SCN and SCN with

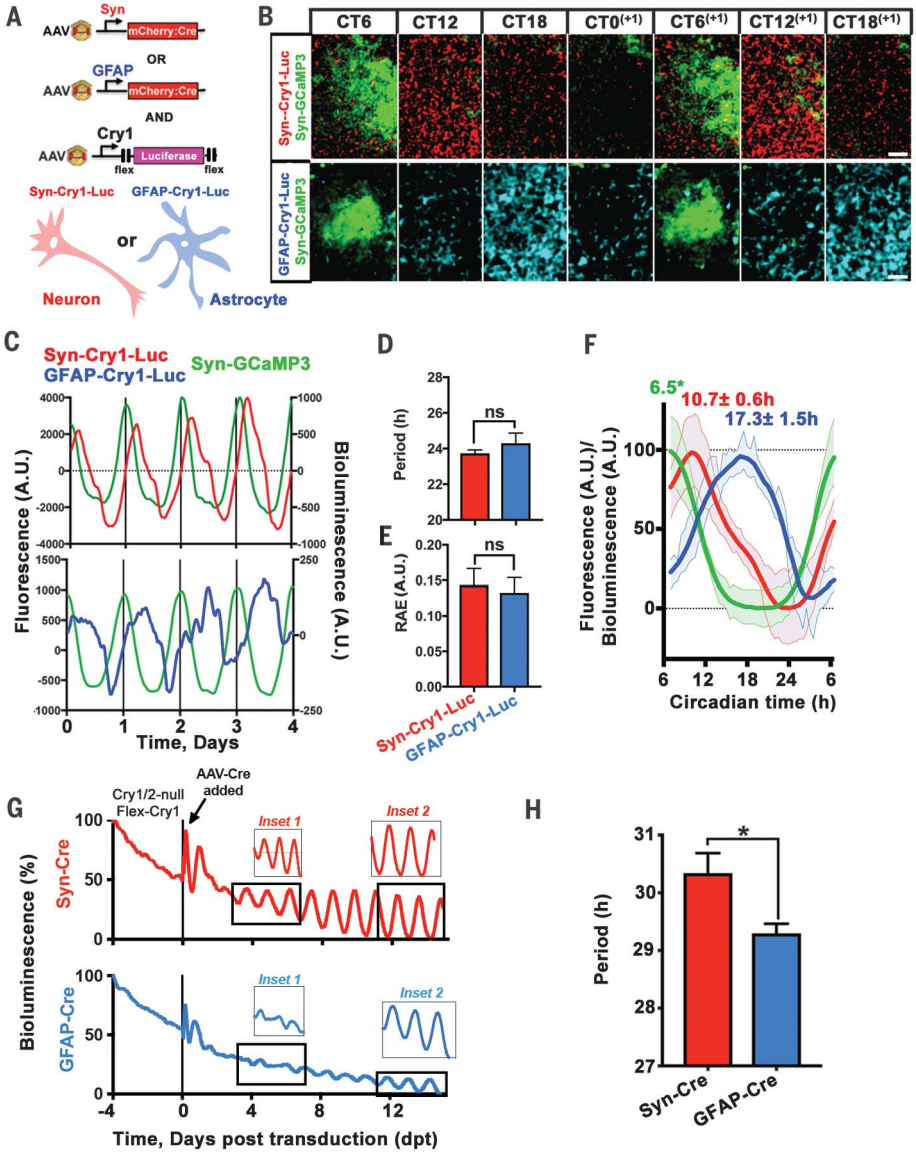


Fig. 1. An astrocytic clockwork can autonomously drive circadian clock gene expression in the SCN. (**A**) Experimental design to restrict expression of *Cry1*-Flex-Luc to neurons or astrocytes by AAVs cotransduced with Syn-mCherry::Cre or GFAP-mCherry::Cre. (**B**) Stills from live-image recordings of SCN slices cotransduced with *Cry1*-Flex-Luc, alongside Syn-mCherry::Cre or GFAP-mCherry::Cre, showing circadian variation of the bioluminescent *Cry1*-Luc signal, phase-aligned to Syn-GCaMP3. Signals are false lookup table colors. (**C**) Representative detrended traces of neuronally or astrocytically restricted *Cry1*-Flex-Luc circadian oscillations, phase-aligned to Syn-GCaMP3. A.U., arbitrary units. (**D** and **E**) Period and RAE values of *Cry1*-Luc oscillations, restricted to neurons or astrocytes. Data are means ± SEM, $n = 5$ per group. (**F**) Waveform traces of neuronal and astrocytic *Cry1*-Flex-Luc expression phase-aligned to Syn-GCaMP3. Data are means ± SEM, $n = 5$ for each experimental group. The asterisk indicates that the circadian phase is based on previous data (*3*, *9*). (**G**) Representative Per2::Luc traces from SCN slices of Cry1/2-null pups sequentially transduced with *Cry1*-Flex-Cry1::EGFP and then either Syn-mCherry::Cre or GFAP-mCherry::Cre AAVs to restore Cry1 expression in neurons or astrocytes, respectively. Insets show amplitudes of Per2::Luc in the early (inset 1) and late (inset 2) stages of neuronally and astrocytically restricted Cry1 expression. (**H**) Period values after neuronally or astrocytically restricted Cry1 expression in the late phases of the treatment. Data are means ± SEM, $n = 4$. Statistical test was an unpaired two-tailed t test. *$P < 0.05$. Scale bars, 50 μm.

Downloaded from http://science.sciencemag.org/ on January 10, 2019

astrocytically restricted Cry1 expression and found comparable dorsal-to-ventral organization of neuronal $[Ca^{2+}]_i$ (*16*) (Fig. 3, J and K, and movie S2). Given that *Per* gene promoters harbor calcium-responsive elements that phase-lock *Per* expression to neuronal $[Ca^{2+}]_i$, astrocytes may engage the E-box–based TTFL of neurons by driving neuronal $[Ca^{2+}]_i$ (*9*), sustaining intracellular oscillations of clock gene expression across SCN space and circadian time. Critically, this happens in the absence of *Cry* genes in neurons, thus revealing that the neuronal E-box–based TTFL may be dispensable for circuit-level circadian time-keeping. Thus, genetic complementation of Cry1 in SCN astrocytes can initiate and sustain mammalian circadian function by recruiting the latent SCN neuronal circuit.

To investigate the relevant mechanisms, we tested the role of connexin 43 (Cx43), a major component of gap junctions and hemichannels specifically expressed in astrocytes that coordinates astrocytic networks and was recently implicated in hypothalamic regulation of sleep-wake cycles (*17*, *18*). Cx43 is highly expressed in the SCN, extensively decorating astrocytic processes, as shown by colocalization with the GFAP-EGFP tag from control surgery mice (Figs. 2D and 4A). We then assessed the effects of Cx43 inhibition on circadian oscillations of clock gene expression in SCN slices by using the mimetic peptide TAT-Gap19 (*19*, *20*). TAT-Gap19 elicited a dose-dependent and reversible reduction in the amplitude and period lengthening of Per2::Luc oscillations (Fig. 4B and fig. S4), confirming the role of astrocytes in circadian function of wild-type SCN. We then showed that Cx43 inhibition by TAT-Gap19 significantly compromised Per2::Luc oscillations driven by astrocytically restricted expression of Cry1 in Cry1/2-null slices (Fig. 4, C and D). TAT-Gap19 specifically inhibits the hemichannel form of Cx43 that is involved in paracrine astrocytic release of gliotransmitters, including ATP and glutamate (*19*, *21*). Astrocyte-released glutamate is a major gliotransmitter in the SCN (*3*); therefore, we tested its key role in driving circadian rhythmicity in Cry1/2-null mice where Cry1 was expressed in astrocytes. Extracellular glutamate levels of Cry1/2-null SCN slices, measured using the AAV-encoded glutamate indicator iGluSnFR driven by Syn (*3*, *22*), exhibited no detectable circadian oscillations, but GFAP-Cre–restricted expression of Cry1 initiated robust circadian oscillations of glutamate. Moreover, these were strongly impaired by a Cx43 inhibitor (TAT-Gap19) (Fig. 4, E and F). These data support the role of astrocyte-derived circadian oscillations of glutamate in mediating astrocytic control of circadian oscillations in Cry1/2-null SCN.

To determine whether glutamate is specifically responsible for astrocyte-dependent circadian time-keeping in Cry1/2-null SCN, slices received DQP-1105, an antagonist for *N*-methyl-D-aspartate glutamate receptor assemblies containing the NR2C/D subunit (NMDAR2C) (*23*). NMDAR2C inhibition by DQP-1105 reversibly damps circadian rhythms of membrane potential and clock gene expression in wild-type SCN neurons (*3*).

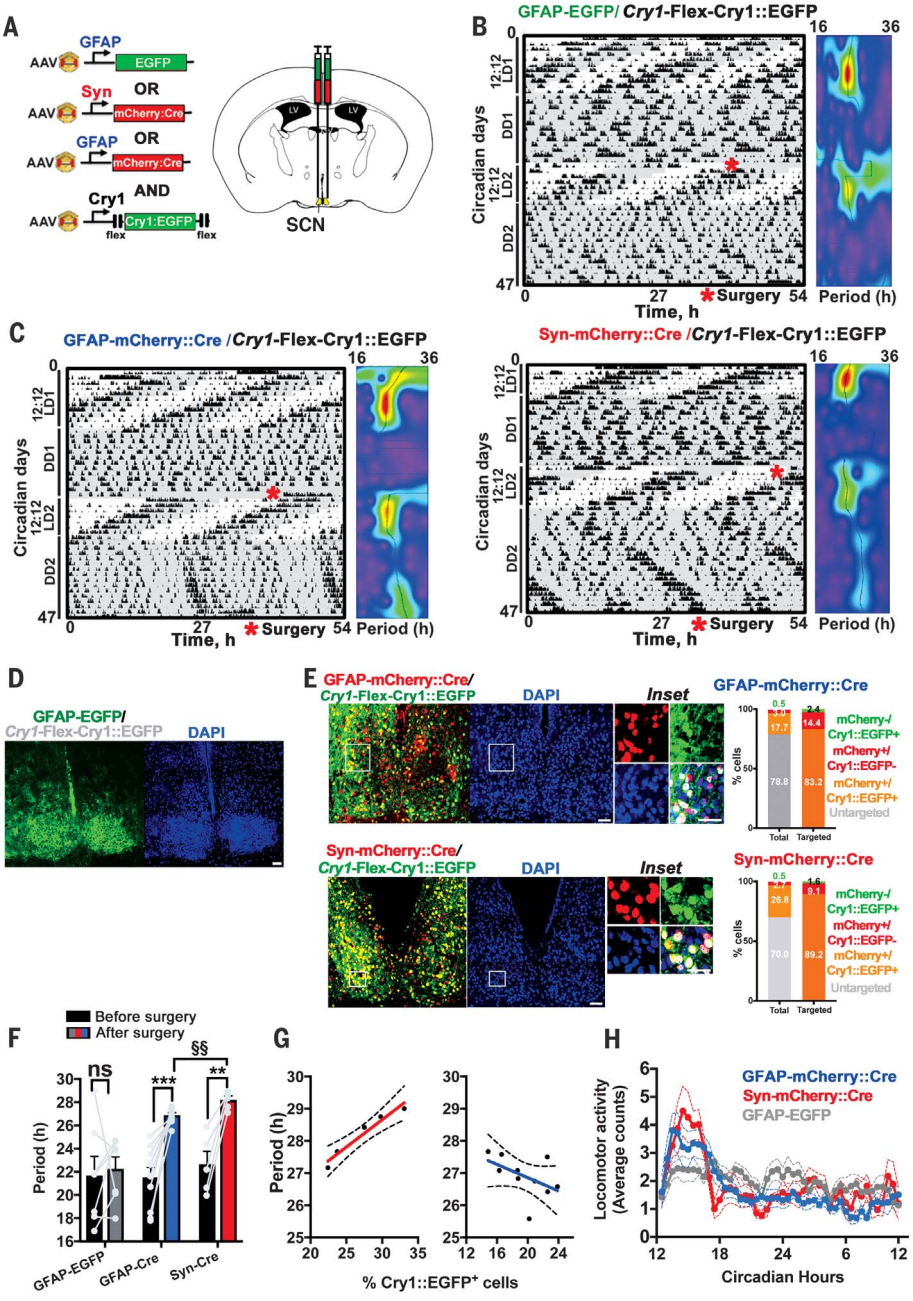


Fig. 2. Genetic complementation of Cry1 in SCN astrocytes initiates and sustains robust circadian patterns of locomotor activity in circadian-incompetent Cry1/2-null mice. (**A**) Experimental design of in vivo expression of Flex-Cry1::EGFP restricted to SCN astrocytes or neurons by Syn- or GFAP-driven Cre, respectively. (**B** and **C**) Representative actograms and wavelet analyses of Cry1/2-null mice targeted with *Cry1*-Flex-Cry1::EGFP together with AAVs expressing GFAP-EGFP (control) (B) or Cre (C). Rhythmicity in LD1 and -2 is due to a masking effect of the light-dark cycle. (**D** and **E**) Representative confocal tiled microphotographs of SCN sections from control and Cre-treated mice evaluated post hoc to assess effective targeting of the SCN. Histograms represent colocalization of fluorescence signals from mCherry::Cre and Cry1::EGFP in Cre-treated mice (insets). Total number of cells counted: GFAP-Cre, $N_{(DAPI^+)} = 5491$, $n = 5$ targeted mice; Syn-Cre, $N_{(DAPI^+)} = 6037$, $n = 5$ targeted mice. DAPI, 4′,6-diamidino-2-phenylindole. (**F**) Periods of circadian activity rhythms of control and Cre-treated mice before (DD1) and after (DD2) stereotaxic surgery. (**G**) Correlation analysis of number of Cry1::EGFP$^+$ astrocytes or neurons and behavioral period (Syn-mCherry-Cre: $r = 1$, $n = 5$, $P = 0.02$; GFAP-mCherry-Cre: $r = -0.70$, $n = 10$, $P = 0.03$, two-way Spearman test). (**H**) Locomotor activity plotted across the circadian day (means ± SEM). Group sizes were $n_{(GFAP\text{-}EGFP)} = 7$, $n_{(GFAP\text{-}Cre)} = 10$, and $n_{(Syn\text{-}Cre)} = 5$. The statistical test was a two-way repeated measures analysis of variance (RM-ANOVA) with Bonferroni correction. $^{**}P < 0.01$; $^{***}P < 0.001$; §§$P < 0.01$ (ad hoc unpaired two-tailed *t* test with Sidak-Bonferroni correction). Scale bars, 50 μm.

Downloaded from http://science.sciencemag.org/ on January 10, 2019

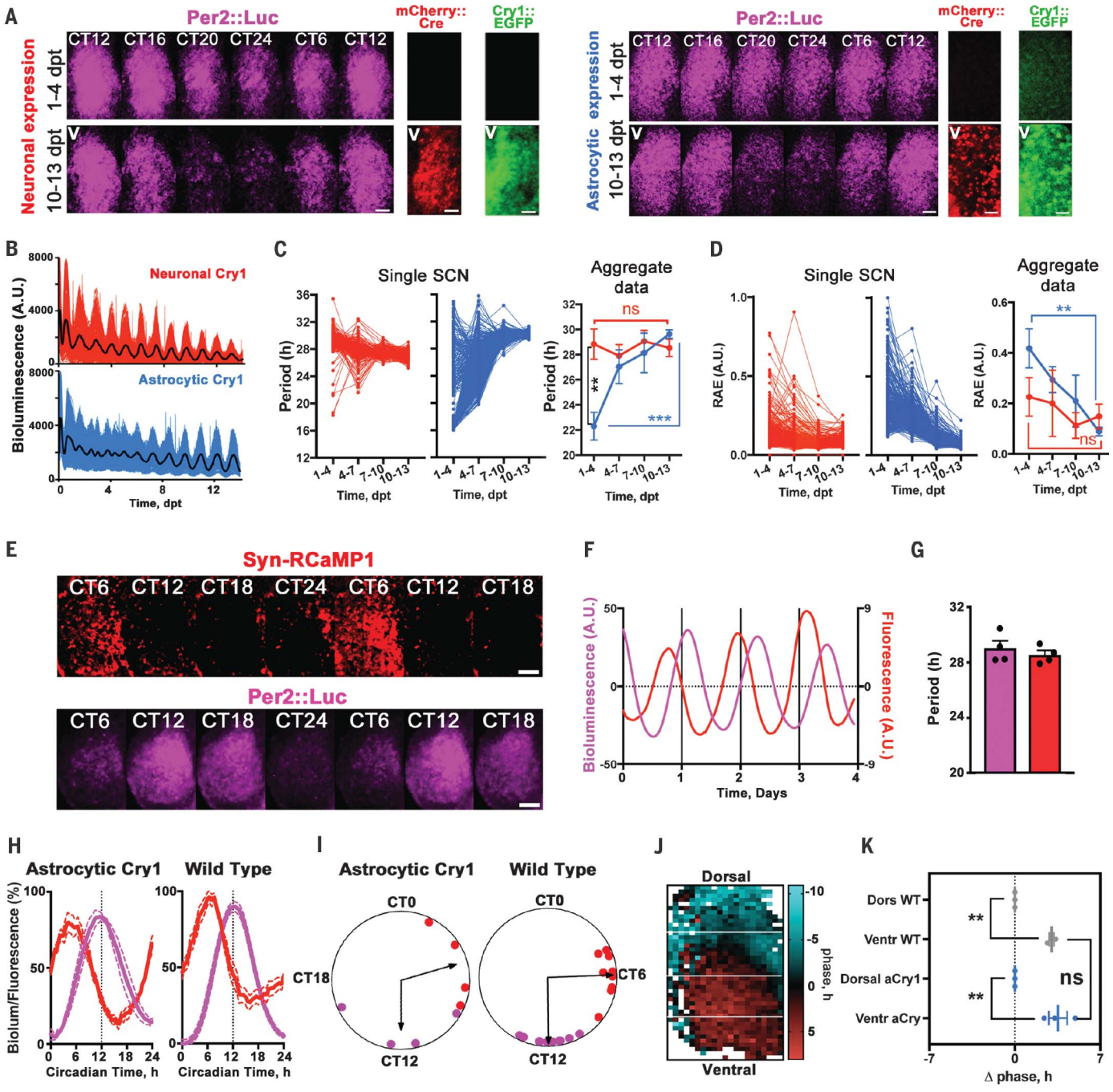


Fig. 3. Temporal dynamics of circadian bioluminescence rhythms of single cells initiated in Cry1/2-null SCN explants after neuronally or astrocytically restricted expression of Cry1. (**A**) Stills from live-image recordings of Per2::Luc expression from Cry1/2-null SCN slices, showing circadian variation of the bioluminescent signal in the early (upper rows) and late (lower rows) stages of neuronal or astrocytic Cry1 expression. Co-detected mCherry and EGFP are shown to compare spatial distribution and temporal dynamics of mCherry::Cre and Cry1::EGFP expression. (**B**) Representative single-cell (colored lines) and mean (black lines) traces of Per2::Luc oscillations after Cre-mediated expression of Cry1 in either neurons or astrocytes within SCN slices. (**C** and **D**) Period and RAE after neuronal or astrocytic expression of Cry1 in an individual SCN and across multiple explants. Traces for aggregate data are means ± SEM. Group size is $n = 3$ for each group. The statistical test was a two-way RM-ANOVA with Bonferroni correction. (**E**) Stills from live-image recordings showing circadian variations of Per2::Luc and Syn-RCaMP1h in Cry1/2-null SCN slices transduced with GFAP-mCherry::Cre or *Cry1*-Flex-Cry1::EGFP. (**F**) Representative traces of data presented in (E). (**G**) Period quantification of Per2::Luc and Syn-RCaMP1h in Cry1/2-null SCN expressing Cry1 only in astrocytes. Data are means ± SEM, $n = 4$. (**H** and **I**) Mean traces ± SEM (H) and Rayleigh plots (I) showing waveforms and phase differences of Per2::Luc and Syn-RCaMP1h oscillations in GFAP-mCherry::Cre or *Cry1*-Flex-Cry1::EGFP SCN slices and wild-type SCN. (**J** and **K**) Representative spatial phase map of Syn-RCaMP1h signal (J) and quantification of the dorsal-to-ventral phase relationship (K) in SCN expressing astrocytic Cry1 in comparison to wild type. Phase data were normalized to dorsal values. Values are means ± SEM, and group sizes are plotted. $^{**}P < 0.01$; $^{***}P < 0.001$; $^{****}P < 0.0001$. Statistical tests included a paired two-tailed *t* test (G) and unpaired ANOVA (K). Scale bars, 50 μm.

Downloaded from http://science.sciencemag.org/ on January 10, 2019

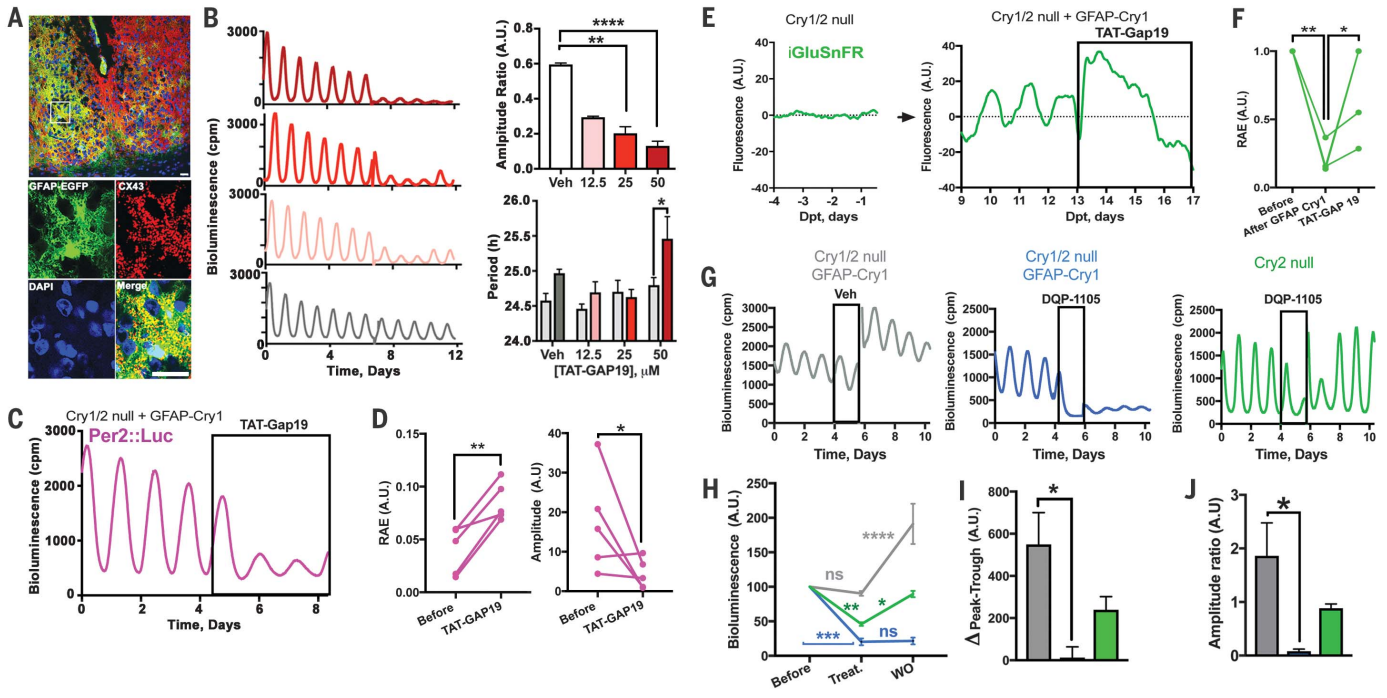


Fig. 4. Astrocytically released glutamate mediates astrocytic control of circuit-level circadian time-keeping in Cry1/2-null SCN expressing GFAP-restricted Cry1. (**A**) Confocal tiled microphotographs of adult SCN showing colocalization of GFAP-EGFP and Cx43, detected by polyclonal antiserum (results are representative of findings with three independent brains). (**B**) Representative Per2::Luc PMT traces and group data (mean + SEM), showing dose-response effects of TAT-Gap19 on the amplitude ratio (with drug/before drug) and period in wild-type SCN slices. The statistical test for the amplitude ratio was an unpaired ANOVA with Bonferroni correction. Analysis for period employed a two-way RM-ANOVA with Bonferroni correction [n = 3 for each group, except vehicle (Veh), n = 4]. (**C** and **D**) Representative Per2::Luc PMT trace (C) and paired scatter plot of RAE and amplitude (D) of Cry1/2-null SCN slices transduced with GFAP-mCherry::Cre and *Cry1*-Flex-Cry1::EGFP and treated with TAT-Gap19 (50 μM). The statistical test was a paired one-tailed t test, n = 5. (**E** and **F**) Representative iGluSnFR traces (E) and paired scatter plot of RAE (F) of Cry1/2-null SCN slices before and after GFAP-mCherry::Cre and *Cry1*-Flex-Cry1::EGFP transduction and treatment with TAT-Gap19 (50 μM). The statistical test was an RM-ANOVA with Bonferroni correction, n = 4. (**G**) Representative Per2::Luc PMT traces of Cry2-null and Cry1/2-null SCN slices transduced with GFAP-mCherry::Cre and *Cry1*-Flex-Cry1::EGFP and treated with DQP-1105 (50 μM) or vehicle, with subsequent washout. (**H**) Group data (means + SEM) of bioluminescence baseline traces represented in (G) before, in the presence of, and after removal of DQP-1105. The statistical test was a two-way RM-ANOVA with Bonferroni correction. (**I**) Group data (means + SEM) showing peak-trough differences in the presence of DQP-1105 of traces represented in (G). (**J**) Group data (means + SEM) showing amplitude ratio (after drug/with drug) of data presented in (G). The statistical test for (H) was a two-way RM-ANOVA with Bonferroni correction. The statistical test for (I) and (J) was an unpaired ANOVA with Bonferroni correction (n = 4 for Cry2-null and Veh groups; n = 3 for DQP-1105 treatment in Cry1/2-null group). *P < 0.05; **P < 0.01; ***P < 0.001; ****P < 0.0001 (n = 4). Scale bars, 20 μm.

The effect of the drug was much more marked in Cry1/2-null SCN with rhythms driven by astrocyte-expressed Cry1, as shown by the immediate drop in the baseline of the Per2::Luc rhythms and abolition of the peak-to-trough difference. Moreover, rhythmicity was restored upon washout of the drug, but the amplitude was irreversibly reduced. We interpreted this as protracted misalignment of circadian activity of SCN neurons and astrocytes. The pronounced effects of DQP-1105 were not evident in Cry2-null SCN, which retained Cry1 expression in both neurons and astrocytes, thus ruling out any confounding impact of Cry2 deficiency in our astrocytic Cry1 rescue model (Fig. 4, G to J). Thus, glutamate is a necessary mediator of astrocytic control of circadian function in the SCN, as shown by two independent pharmacological approaches: interference with glutamate release by astrocytes (via Cx43 inhibition) and with neuronal glutamate sensing (via NMDAR2C antagonism) (*2*, *3*).

A growing body of evidence has challenged a neurono-centric view of the control of behavior in mammals by showing that astrocytes can modulate complex neural processes, including cognition, fear, sleep, and circadian rhythms (*3*, *4*, *17*, *24*, *25*). However, most studies rely on the presence of a preexisting neuronally encoded behavior and show that behavioral performances are affected when astrocytic function is modified (*24*). Thus, regardless of the specificity of the astrocyte-neuron interactions described (*3*, *25*, *26*), those studies only addressed the ability of astrocytes to modulate neuronally dependent behavior; they did not establish their sufficiency in controlling behavior. Here, we have shown that astrocytes of the SCN can autonomously encode circadian information and instruct their neuronal partners, which lack a competent TTFL clock, to initiate and indefinitely sustain circadian patterns of neuronal activity and behavior.

REFERENCES AND NOTES

1. M. Koch, *Cell* **171**, 1246–1251 (2017).
2. M. H. Hastings, E. S. Maywood, M. Brancaccio, *Nat. Rev. Neurosci.* **19**, 453–469 (2018).
3. M. Brancaccio, A. P. Patton, J. E. Chesham, E. S. Maywood, M. H. Hastings, *Neuron* **93**, 1420–1435.e5 (2017).
4. C. F. Tso *et al.*, *Curr. Biol.* **27**, 1055–1061 (2017).
5. L. M. Prolo, J. S. Takahashi, E. D. Herzog, *J. Neurosci.* **25**, 404–408 (2005).
6. J. Livet *et al.*, *Nature* **450**, 56–62 (2007).
7. J. M. Fustin, J. S. O'Neill, M. H. Hastings, D. G. Hazlerigg, H. Dardente, *J. Biol. Rhythms* **24**, 16–24 (2009).
8. M. D. Edwards, M. Brancaccio, J. E. Chesham, E. S. Maywood, M. H. Hastings, *Proc. Natl. Acad. Sci. U.S.A.* **113**, 2732–2737 (2016).
9. M. Brancaccio, E. S. Maywood, J. E. Chesham, A. S. I. Loudon, M. H. Hastings, *Neuron* **78**, 714–728 (2013).
10. G. T. J. van der Horst *et al.*, *Nature* **398**, 627–630 (1999).
11. S.-H. Yoo *et al.*, *Proc. Natl. Acad. Sci. U.S.A.* **101**, 5339–5346 (2004).
12. M. R. Ralph, R. G. Foster, F. C. Davis, M. Menaker, *Science* **247**, 975–978 (1990).
13. V. M. King *et al.*, *Eur. J. Neurosci.* **17**, 822–832 (2003).
14. N. J. Smyllie, J. E. Chesham, R. Hamnett, E. S. Maywood, M. H. Hastings, *Proc. Natl. Acad. Sci. U.S.A.* **113**, 3657–3662 (2016).
15. M. Brancaccio *et al.*, *J. Neurosci.* **34**, 15192–15199 (2014).

Downloaded from http://science.sciencemag.org/ on January 10, 2019

16. R. Enoki *et al*., *Proc. Natl. Acad. Sci. U.S.A.* **114**, E2476–E2485 (2017).
17. J. Clasadonte, E. Scemes, Z. Wang, D. Boison, P. G. Haydon, *Neuron* **95**, 1365–1380.e5 (2017).
18. L. C. Mayorquin, A. V. Rodriguez, J.-J. Sutachan, S. L. Albarracín, *Front. Mol. Neurosci.* **11**, 118 (2018).
19. V. Abudara *et al*., *Front. Cell. Neurosci.* **8**, 306 (2014).
20. L. Walrave *et al*., *Glia* **66**, 1788–1804 (2018).
21. Z.-C. Ye, M. S. Wyeth, S. Baltan-Tekkok, B. R. Ransom, *J. Neurosci.* **23**, 3588–3596 (2003).
22. J. S. Marvin *et al*., *Nat. Methods* **10**, 162–170 (2013).
23. T. M. Acker *et al*., *Mol. Pharmacol.* **80**, 782–795 (2011).
24. J. F. Oliveira, V. M. Sardinha, S. Guerra-Gomes, A. Araque, N. Sousa, *Trends Neurosci.* **38**, 535–549 (2015).
25. T. Papouin, J. M. Dunphy, M. Tolman, K. T. Dineley, P. G. Haydon, *Neuron* **94**, 840–854.e7 (2017).
26. M. Martin-Fernandez *et al*., *Nat. Neurosci.* **20**, 1540–1548 (2017).

ACKNOWLEDGMENTS

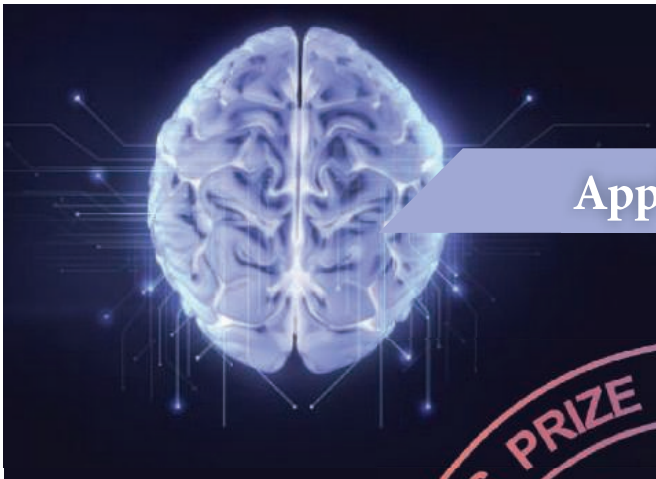
We thank LMB Biological Services Group and the Ares staff for technical support. **Funding:** The Medical Research Council UK (core funding MC_U105170643 to M.H.H.) supported this work. **Author contributions:** M.B. designed, performed, and analyzed all experiments. M.H.H. contributed to the experimental design. M.D.E and N.J.S. developed and validated the *Cry1*-Flex-Luc and *Cry1*-Flex-Cry1::EGFP constructs. A.P.P, E.S.M., and J.E.C. conducted preliminary experiments. All authors contributed to project discussions. M.B. and M.H.H. wrote the manuscript. **Competing interests:** The authors declare no competing interests. **Data and materials availability:** All data are available in the manuscript or supplementary materials.

SUPPLEMENTARY MATERIALS

www.sciencemag.org/content/363/6423/187/suppl/DC1
Materials and Methods
Figs. S1 to S4
References (*27*, *28*)
Movies S1 and S2

23 February 2018; accepted 2 November 2018
10.1126/science.aat4104

Downloaded from http://science.sciencemag.org/ on January 10, 2019



Apply for our exciting research Prize!

SCIENCE-PINS PRIZE FOR NEUROMODULATION

SCIENCE-PINS

$25, 000 Grand Prize!
Get published in *Science*!

The *Science*-PINS Prize is a highly competitive international prize that honors scientists for their excellent contributions to neuromodulation research. For purposes of the Prize, neuromodulation is any form of alteration of nerve activity through the delivery of physical (electrical, magnetic, or optical) stimulation or chemical agents to targeted sites of the nervous system.

For full details, judging criteria and eligibility requirements, visit:

www.sciencemag.org/prizes/pins

Submission Deadline: March 15, 2019

Science AAAS

PINS 品驰

Science Translational Medicine AAAS



Colony Counting and Zone Measurement System

The ProtoCOL 3 HD from Synbiosis is an automated colony-counting and zone measurement system that provides accurate, traceable results for vaccine and antibiotic development. It features a compact, light-tight cabinet, housing patented, three-color LED lighting and an ultra-high-definition 5-megapixel CCD camera integrated to user-friendly software. At the press of a button, this new system allows microbiologists to automatically read plates of up to 150-mm diameter, to detect colonies as small as 43 µm, and to measure zones with an average accuracy of more than 99.9%. The software includes, as standard, an inhibition zone measurement module to measure the diameter of inhibition zones for applications, including single radial immunodiffusion (SRD), and a pour plate module for counting colonies on pour, settle, and spread plates. All data generated can be easily exported into a spreadsheet (Excel/OpenOffice), or to the optional UNISTAT statistics package for analysis, or transferred to a laboratory information management system (LIMS).

Synbiosis
For info: +44-(0)-1223-727125
www.synbiosis.com

Nucleic Acid Stain

GoodView is a safer alternative to the traditional ethidium bromide stain for detecting nucleic acid in agarose gels. It emits green fluorescence when bound to DNA or RNA. This new stain has two fluorescence excitation maxima when bound to nucleic acid, one centered at 268 nm and another at 294 nm. In addition, it has one visible excitation at 491 nm. The fluorescence emission of GoodView bound to DNA is centered at 530 nm. The test report from the Institute for Environmental Health and Related Product Safety of the Chinese Center for Disease Control and Prevention concludes that it is nontoxic and nonmutagenic.

Beijing SBS Genetech
For info: +86-10-82784292
www.sbsbio.com/news/englishnew/index.php

NMR and EPR Explosion Protection Chamber

The NMR and EPR Explosion Protection Chamber by Wilmad-LabGlass–SP Scienceware shields researchers from flying debris and brings a new level of safety to the laboratory. High-pressure experiments have significantly grown in popularity over the last several years. As a result, the risk of tube explosion in the laboratory has also increased. The Explosion Protection Chamber solves this safety issue by preventing debris from projecting sideways toward the researcher should an explosion occur. Its one-size-fits-all design allows the chamber to be assembled in double-barrel mode for Bruker spectrometers or single-barrel mode for Varian/Agilent and JEOL spectrometers. The modular leg array ensures that the product fits securely against the upper barrel protruding from the magnet.

Wilmad-LabGlass–SP Scienceware
For info: 800-220-5171
www.wilmad-labglass.com

Anti-Glycan IgG mAbs

GlycoNex has developed and optimized a serum-free Chinese hamster ovary (CHO) platform to produce anti-glycan immunoglobulin G (IgG) monoclonal antibodies (mAbs) with remarkable purity, specificity, and affinity for glycan research. Outcompeting antibodies from hybridoma or ascites systems, GlycoBind consistently delivers accurate and precise data from Western blot, immunohistochemistry, and flow cytometry experiments by eliminating animal-serum/material contamination, unspecific antibodies, and lot-to-lot variation. More than 50 anti-glycan mAbs are coming soon. Tell us your explicit needs and pain points in dealing with ambiguous and irreproducible data. GlycoNex is willing to make your research and life easier.

GlycoNex
For info: +886-2-2697-4168
www.glyconex.com.tw/products-1.php?lang=en

Activator Cell Line for Immune Checkpoint Therapy Research

AMS Biotechnology (AMSBIO) offers a comprehensive range of purified, soluble immunoreceptors and proteins involved in key immunosignaling pathways, such as PD-1, PD-L1, PD-L2, CTLA-4, TIGIT, LAG-3, and IDO. Additionally, the company offers several cell lines (e.g., PD-L2/TCR Activator–CHO Recombinant Cell Line) and assay kits that can be used to screen for inhibitors of protein–protein interaction, as well as neutralizing antibodies to serve as positive controls for inhibition. The binding of programmed cell death protein 1 (PD-1), a receptor expressed on activated T cells, to its ligands, PD-L1 and PD-L2, negatively regulates immune responses. PD-1 ligands are found on most cancers, and PD-1/PD-L2 interaction inhibits T-cell activity and allows cancer cells to escape immune surveillance. The PD-1:PD-L1/L2 pathway is also involved in regulating autoimmune responses, making these proteins promising therapeutic targets for multiple sclerosis, arthritis, lupus, and type I diabetes.

AMS Biotechnology
For info: 617-945-5033
www.amsbio.com/immunotherapy.aspx

Back-Illuminated sCMOS Camera Platform

Featuring 95% quantum efficiency and market-leading vacuum cooling down to –45°C, the Sona back-illuminated camera platform for fluorescence microscopy represents the ultimate in sensitivity for scientific complementary metal-oxide semiconductor (sCMOS) cameras. Sona is available in two formats, each with an 11-µm pixel size. The 4.2-megapixel flagship model, Sona 4.2B-11, enables access to the entire 2048 × 2048 array, offering a 32-mm sensor diagonal and harnessing the entire field of view (FOV) available from the microscope. This model is adaptable to a range of objective lens magnifications, from 100X down to 40X. It is perfect for applications that require maximum information content, allowing large fields of cells, whole embryos, or tissue cultures to be captured with absolute clarity and maximum throughput. The Sona 2.0B-11 model features a 2-megapixel array, sized to maximize the FOV available through modern 22-mm C-mount microscope ports. Preconfigured and easily accessible regions of interest (ROIs) directly match to various smaller microscope port sizes, making the Sona 2.0B-11 usable across multiple setups.

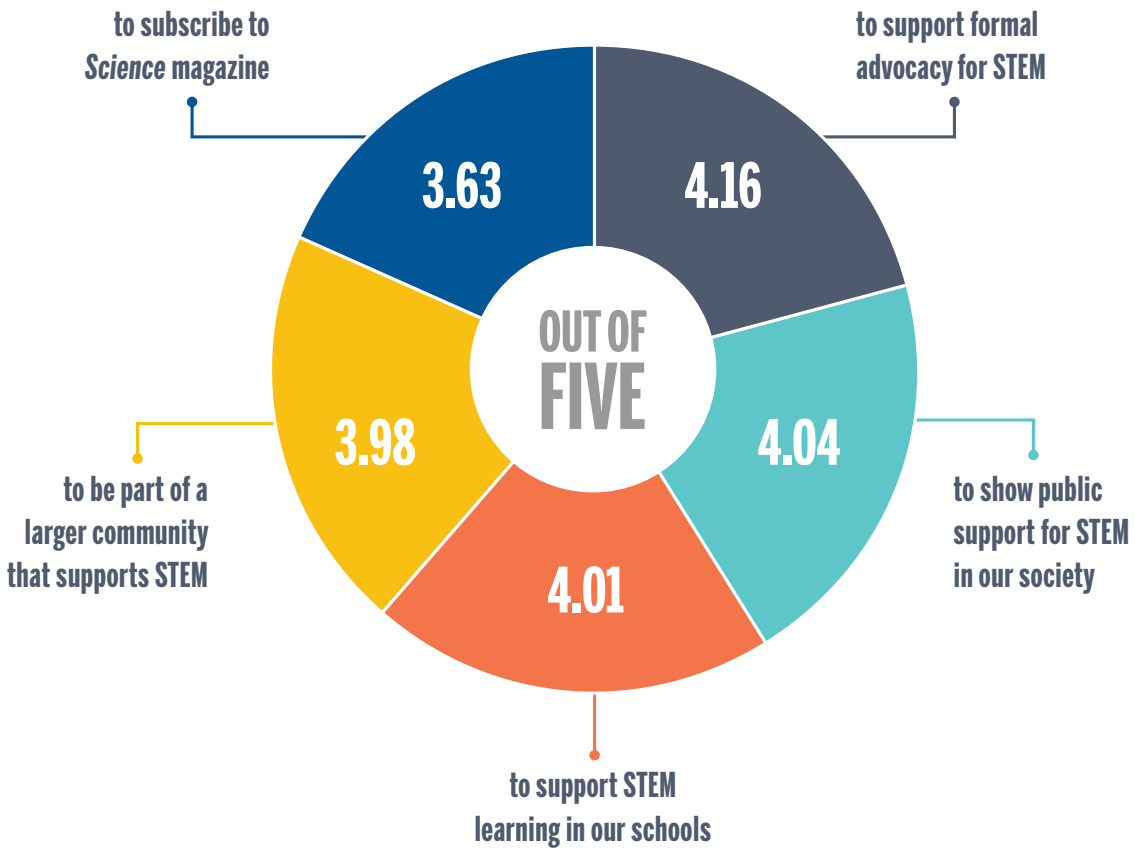
Andor Technology
For info: 847-212-0500
andor.oxinst.com/products/fast-and-sensitive-scmos-cameras

Electronically submit your new product description or product literature information! Go to www.sciencemag.org/about/new-products-section for more information.

Newly offered instrumentation, apparatus, and laboratory materials of interest to researchers in all disciplines in academic, industrial, and governmental organizations are featured in this space. Emphasis is given to purpose, chief characteristics, and availability of products and materials. Endorsement by *Science* or AAAS of any products or materials mentioned is not implied. Additional information may be obtained from the manufacturer or supplier.

AAAS IS THE FORCE FOR SCIENCE

According to the 2017 Member Survey, you joined AAAS ...



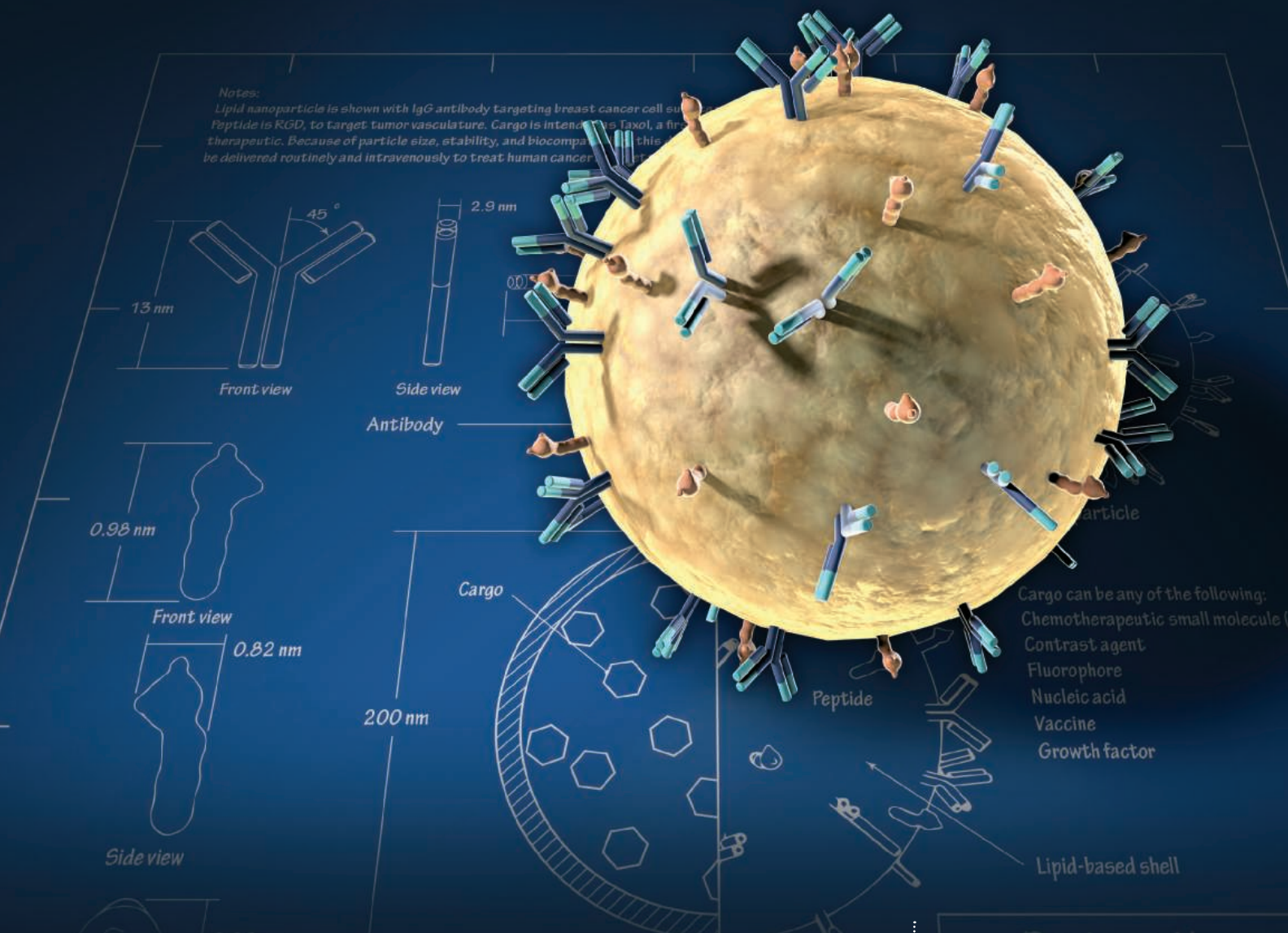


TELL US WHAT'S IMPORTANT TO YOU!

The 2018 Member Survey is launching in September. Look in your inbox for a link.

Your responses help us to better serve science, scientists, and the global community. Don't miss your chance to tell us what's most important to you!

Make Your Research Hit the Target



Science Translational Medicine publishes peer-reviewed, cutting-edge biomedical research in the fields of cardiology, cancer, immunotherapy, infectious diseases and vaccines, bioengineering and devices, neurology and neurodegenerative diseases, obesity, diabetes and metabolic disorders, drug discovery, genomic medicine, imaging, stem cell therapy and regenerative medicine.

Submit your research today

Learn more at: **ScienceTranslationalMedicine.org**

Science Translational Medicine

AAAS

SCIENCE CAREERS ADVERTISING



For full advertising details, go to ScienceCareers.org and click For Employers, or call one of our representatives.

AMERICAS
+1 (202) 326 6577
+1 (202) 326 6578
advertise@sciencecareers.org

EUROPE, INDIA, AUSTRALIA, NEW ZEALAND, REST OF WORLD
+44 (0) 1223 326527
advertise@sciencecareers.org

CHINA, KOREA, SINGAPORE, TAIWAN, THAILAND
+86 (131) 4114 0012
advertise@sciencecareers.org

JAPAN
+81 (3) 6459 4174
advertise@sciencecareers.org

JOB BOARD SUPPORT
support@sciencecareers.org

ScienceCareers
FROM THE JOURNAL SCIENCE AAAS

ScienceCareers.org

All ads submitted for publication must comply with applicable U.S. and non-U.S. laws. *Science* reserves the right to refuse any advertisement at its sole discretion for any reason, including without limitation for offensive language or inappropriate content, and all advertising is subject to publisher approval. *Science* encourages our readers to alert us to any ads that they feel may be discriminatory or offensive.

myIDP: A career plan customized for you, by you.



For your career in science, there's only one Science

my IDP
ScienceCareers

Recommended by leading professional societies and the NIH

Features in myIDP include:

- Exercises to help you examine your skills, interests, and values.
- A list of 20 scientific career paths with a prediction of which ones best fit your skills and interests.
- A tool for setting strategic goals for the coming year, with optional reminders to keep you on track.
- Articles and resources to guide you through the process.
- Options to save materials online and print them for further review and discussion.
- Ability to select which portion of your IDP you wish to share with advisors, mentors, or others.
- A certificate of completion for users that finish myIDP.

Visit the website and start planning today!
myIDP.sciencecareers.org

ScienceCareers AAAS In partnership with:

advancing the life sciences 1912-2012 FASEB Federation of American Societies for Experimental Biology
Medical College of Wisconsin
UCSF University of California San Francisco
Burroughs Wellcome Fund

Advance your career with expert advice from *Science* Careers.



Download Free Career Advice Booklets!

ScienceCareers.org/booklets

Featured Topics:

- Networking
- Industry or Academia
- Job Searching
- Non-Bench Careers
- And More



ScienceCareers

FROM THE JOURNAL SCIENCE AAAS

University of Zurich[UZH]

Faculty of Science

The Faculty of Science at the University of Zurich invites applications for an

Associate or Full Professor in Data Science for Sciences

to join us.

Through her/his research activities in the Institute for Computational Science on the Irchel Campus, the successful candidate should demonstrate the benefits of data science and modern data analytics for Sciences, with a preference in Earth, Space and/or Environmental Sciences. Her/his expertise in data science could cover for instance: computer science, machine learning, optimization, signal processing, advanced statistics. Her/his research applications could be for instance: satellite remote sensing, atmospheric science, oceanography, hydrology, glaciology, planetary science, ecology and evolution. Her/his activities at the Institute for Computational Science should in particular help demonstrating how open-source scientific software, data digitalization or new collaborative approaches (e.g. hackathon, data challenges) contribute to a successful interdisciplinary research.

Candidates for this data science position should be either
– an outstanding domain scientist with a proven track record in developing computational methods and applying modern data analytics in her/his field;
– or an outstanding data scientist with a proven track record in the proposed fields of application and a strong motivation for advancing knowledge in Earth, Space and/or Environmental Sciences.

The University of Zurich provides generous research support, including dedicated funds for personnel, running expenses and competitive start-up packages, as well as access to world class supercomputers and storage capacities. As Zurich's scientific environment includes a rich spectrum of research activities and provides extensive opportunities for collaboration with research groups at the University of Zurich and other leading Swiss research institutions.

The employment conditions for this position follow the legal regulations of the University of Zurich (see www.prof.uzh.ch/de.html), which include part-time options. The University of Zurich is an equal opportunities employer and in particular strives to increase the percentage of women in leading positions (see https://www.mnf.uzh.ch/en/mnf-gleichstellung.html). Therefore, qualified female researchers are particularly encouraged to apply. The city of Zurich combines a stimulating cultural scene in a modern European city with easy access to a beautiful natural landscape.

Academics with the appropriate qualifications are kindly invited to submit their applications including:
– a curriculum vitae
– lists of publications and research funding,
– detailed outlines of concepts for teaching and research
– vision for data science and its application to natural sciences
– names and contact details of three referees

Please address your application to Prof. Roland Sigel, Dean of the Faculty of Science. Upload your application files to http://www.mnf.uzh.ch/dss by 1 March 2019.

For further information, please contact Prof. Romain Teyssier at romain.teyssier@uzh.ch.

ScienceCareers online @sciencecareers.org

10 ways that *Science* Careers can help advance your career

1. Register for a free online account on **ScienceCareers.org**.
2. Search thousands of job postings and find your perfect job.
3. Sign up to receive e-mail alerts about job postings that match your criteria.
4. Upload your resume into our database and connect with employers.
5. Watch one of our many webinars on different career topics such as job searching, networking, and more.
6. Download our career booklets, including Career Basics, Careers Beyond the Bench, and Developing Your Skills.
7. Complete an interactive, personalized career plan at "my IDP."
8. Visit our Career Forum and get advice from career experts and your peers.
9. Research graduate program information and find a program right for you.
10. Read relevant career advice articles from our library of thousands.



Visit **ScienceCareers.org** today — all resources are free

ScienceCareers
FROM THE JOURNAL SCIENCE AAAS

SCIENCECAREERS.ORG

Department of Biotechnology
Ministry of Science & Technology
Government of India

सत्यमेव जयते

RAMALINGASWAMI RE-ENTRY FELLOWSHIP : 2018-2019

Applications are solicited from Indian Nationals working in overseas research institutions for the "Ramalingaswami Re-entry Fellowship", a Re-entry scheme of the Department of Biotechnology (DBT), Ministry of Science & Technology, Government of India.

Aim of the Fellowship

The scheme is conceptualized with the aim of attracting highly skilled researchers (Indian Nationals) working overseas in various cutting edge disciplines of Life Sciences/Biotechnology/Bio-engineering/Health Care, Agriculture/ Veterinary Sciences and all other allied areas by providing them an attractive avenue to pursue their R&D interests in Indian institutions.

Who is eligible to apply?

The applicant should possess a Ph.D., /M.D., or equivalent degree with an outstanding track record as reflected in publications and other recognitions and with at least three years of post-doctoral research experience of which last two years should be from overseas laboratory. Those who have already returned to India within one year of the closing date of this advertisement are also eligible.

Researchers upto 45 years of age as determined on closing date of application are eligible to apply.

Incentives of being a Ramalingaswami Fellow

- This is a senior fellowship programme and awardees are to be considered equivalent to Assistant Professor/Scientist-D level position. Fellows selected are entitled to take up teaching/research assignments and supervising Doctoral/MS students.
- The scheme provides a consolidated monthly remuneration of Rs. 1,00,000/- p.m. In addition, a House Rent Allowance of Rs. 18,500/- p.m. (Consolidated) is given to fellows. In case host institute provides accommodation to the fellow, no House Rent Allowance is admissible. The fellowship is taxable as per Govt. of India rules.
- Fellows will receive a research/contingency grant of Rs.10.00 lakhs for the 1st & 2nd year; Rs.7.50 lakhs for the 3rd & 4th year; Rs. 5.00 lakhs for 5th year for purchase of consumables, minor equipment, international and domestic travel, engaging manpower and other contingent expenditure to be incurred for the implementation of research proposal which is a part of fellowship and Institutional overhead @Rs. 50,000/ year.
- DBT encourages host institutions to provide medical benefits, transport allowance, leave travel allowance and other benefits as per their prevailing norms as applicable to their employees of the rank equivalent to Assistant Professor/Scientist D out of their own resources/ funds.
- Fellows retain an option for drawing either the fellowship or salary if they are appointed at a suitable permanent scientific position. Fellows opting for salary can continue to avail the research /contingency grant with prior approval of DBT.
- Ramalingaswami Re-entry Fellows could take up fellowship at any of the scientific institutes/ universities/ relevant Industries in the country. However, application should be duly forwarded by the competent authority of the host Institute. Fellows can change their host institute only once during the tenure of the fellowship with the prior No Objection Certificate from the host institute who has forwarded the application [Director/Registrar/Vice-Chancellor/Dean/ CEO/ HR Head (in case of industry) or as the case may be]. Second change will be allowed only in case the fellow gets a permanent job.
- Candidate can submit his/her nomination through single host institute only. However, institutions can nominate more than one candidate.
- Awardees are eligible to apply for research grants to any of the funding agencies towards accomplishment of research proposal. However, the Co-PI has to be a permanent employee of the host institution.

Tenure of fellowship

Fellows can draw fellowship for a term of five years. Fellowship is further extendable for another two years on a fresh appraisal. Only fellowship & HRA will be admissible during extension period. No research/contingency grant will be provided during the extension period. Those who are able to secure permanent positions will not be considered for 2nd term.

How to apply

Applications may be sent as per proforma downloadable from DBT website (www.dbtindia.nic.in) duly forwarded by the competent authority to ***Dr. Meenakshi Munshi, Adviser/Scientist 'G', Department of Biotechnology, Block-2, 7th Floor, CGO Complex, Lodhi Road,*** New Delhi -110 003, both as a hard copy as well as **Soft copy (as a single PDF file only) latest by 31st January, 2019.** The applications not forwarded by the host institution will not be considered. ***Soft copy to be mailed at Email :- rlsfellowship.dbt@nic.in***

University of Zurich[UZH]

Faculty of Science

The Faculty of Science at the University of Zurich invites applications for an

Assistant Professor Tenure Track in Next Generation Synthesis

We are seeking for candidates with an outstanding track record to build an internationally recognized research program in organic synthesis. While all areas of organic chemistry will be considered, upon equal qualifications, preference will be given to applicants with an interest in technology-driven synthesis, new molecular concepts, molecular systems engineering, «on-demand» synthesis, or new molecular frameworks. The selected candidate is expected to lead an independent research group and to participate in teaching chemistry at all levels of the BSc, MSc and PhD programs. The University of Zurich has an established program for career progression allowing promotion to associate and full professor upon successful evaluation.

The University of Zurich provides generous research support, including dedicated funds for personnel, running expenses and competitive start-up packages. Moreover, the successful applicant is expected to acquire external research funding. Zurich's scientific environment encompasses a rich spectrum of diverse activities spanning physical to biomedical research that provides extensive opportunities for collaboration with research groups at the University of Zurich and other leading Swiss research institutions.

The employment conditions for this position follow the legal regulations of the University of Zurich (see www.prof.uzh.ch/de.html), which include part-time options. The University of Zurich is an equal opportunities employer and in particular strives to increase the percentage of women in leading positions (see https://www.mnf.uzh.ch/en/mnf-gleichstellung.html). Therefore, qualified female researchers are particularly encouraged to apply. The city of Zurich combines a stimulating cultural scene in a modern European city with easy access to a beautiful natural landscape.

Academics with the appropriate qualifications are kindly invited to submit their applications including:
– a curriculum vitae
– lists of publications and research funding,
– a detailed research plan and a teaching outline
– names and contact details of three referees

Please address your application to Prof. Roland Sigel, Dean of the Faculty of Science. Upload your application files to http://www.mnf.uzh.ch/ngs by 22 Feburary 2019.

For further information, please contact Prof. Dr. Karl Gademann (email: karl.gademann@uzh.ch).

Science Careers online @sciencecareers.org

By **Robert S. Schick**

The scars we bear

I was introduced to a whale named Lucky during my first year of grad school. I study North Atlantic right whales—many of whom are scarred by traumatic injuries. Lucky's were dramatic: jagged marks from a brush with a large ship propeller when she was a juvenile. My own story, I've come to realize, is similar, although my scars are less obvious. Eleven years ago, when I was a third-year Ph.D. student, my son Silas died in my arms. He was just 3 days old. The birth nearly took my wife's life as well. Graduating the next year felt like nothing short of a miracle. I was Dr. Schick—the first in my family! I thought it meant that I had recovered from the depths of my loss and had a bright academic future. But there was more to my story—and to Lucky's.

Researchers studying Lucky were thrilled and amazed when she became pregnant. Yet as her pregnancy progressed, she gained girth, and the increasing pressure ultimately split the scar tissue. She developed sepsis, and—along with her unborn calf—Lucky died.

Two years after my son's death, pressure was building on my own internal scars. My family and I had moved to get away from the constant reminder of our loss, and at first it seemed to be working. I had a good postdoc position, my wife was healing, and my daughter was heading into kindergarten. On the surface, we were all doing relatively well.

But when I took a work trip back to our old city, suddenly everything started to fall apart. I began to struggle with anxiety. I started to have panic attacks that led to a nervous breakdown. I realized that I needed to devote time to healing instead of burying my grief. I needed to acknowledge and treat my wounds so that they wouldn't put me in danger in the future.

The best way to do this, I thought, would be to make a major change. I found a new postdoc position across the ocean, in Scotland. The change of location and perspective put me on a better track. Our 4 years abroad helped heal my family, and the challenge of living in a new culture made us even more tight-knit. I worked with a wonderful, kind therapist who helped me unpack and examine my grief. I started to feel a little bit more comfortable with our trauma—sometimes telling people about Silas rather than always keeping the story hidden.

At the same time, I needed to figure out my next career step—and I knew I had to take my emotional well-being into account. I had always hoped for a tenure-track job, and I applied for a few, but I never fully embraced the process. I didn't want to risk disappointment, and I worried that if I succeeded in landing a position, I wouldn't be able to handle the stress that would come with it. Ever since the death of my son, my anxiety threshold is much lower.



"Like the whales I study, we all carry the scars of our pasts."

Through a bit of networking and some luck, I found a job as a soft-money research scientist back at my Ph.D. institution. At first, this felt like a failure. In the 2 years since, though, a funny thing has happened: I'm not the research star I hoped I would be, and few days go by when I don't think about my son, but I find myself content. I'm doing meaningful work surrounded by colleagues whom I respect and admire.

Though I will always bear the scars from my son's death, time and emotional work help keep them from reopening, and I have found peace with how my trauma is woven into the story of my life. Like the whales I study, we all carry the scars of our pasts. The burdens can be heavy, but we needn't add to them by trying to ignore or hide them.

As for the right whales, their population now numbers approximately 410 individuals, up from an all-time low of about 50. Though the future of the species remains uncertain, for now, at least, they too have found ways to survive. ■

Robert S. Schick is a research scientist at Duke University in Durham, North Carolina. Do you have an interesting career story that you would like to share? Send it to SciCareerEditor@aaas.org.

ILLUSTRATION: ROBERT NEUBECKER

Downloaded from http://science.sciencemag.org/ on January 14, 2019

Published by AAAS